Université Paris-Sud (Orsay, France)

Thèse en vue de l'obtention d'un doctorat en Physique, présentée par

Francky LUDDENS

Laboratoire d'Informatique pour la Mécanique et les Sciences de l'Ingénieur (LIMSI),
Bât. 508, BP 133,
91403 Orsay Cedex.
École doctorale : Modélisation et Instrumentation en Physique, Énergies, Géosciences et Environnement.

Analyse théorique et numérique des équations de la magnétohydrodynamique : application à l'effet dynamo.

Soutenue le 6 décembre 2012 devant le jury composé de Messieurs et Mesdames :

Martin Costabel	*Rapporteur*
Yannick Ponty	*Rapporteur*
Frédéric Bouillault	*Examinateur*
Patrick Ciarlet	*Examinateur*
Vivette Girault	*Invitée*
Caroline Nore	*Directrice de thèse*
Jean-Luc Guermond	*Co-directeur de thèse*

Résumé

On s'intéresse dans ce mémoire aux équations de la magnétohydrodynamique (MHD) dans des milieux hétérogènes, i.e. dans des milieux pouvant présenter des variations (éventuellement brutales) de propriétés physiques. En particulier, on met ici l'accent sur la résolution des équations de Maxwell dans des milieux avec des propriétés magnétiques inhomogènes. On présentera une méthode non standard pour résoudre ce problème à l'aide d'éléments finis de Lagrange. On évoquera ensuite l'implémentation dans le code SFEMaNS, développé depuis 2002 par J.-L. Guermond, C. Nore, J. Léorat, R. Laguerre et A. Ribeiro, ainsi que les premiers résultats obtenus dans les simulations de dynamo. Nous nous intéresserons par exemple au cas de la dynamo dite de Von Kármán, afin de comprendre l'expérience VKS2. En outre, nous aborderons des cas de dynamo en précession, ou encore le problème de la dynamo au sein d'un écoulement de Taylor-Couette.

Mots-clés : équations de la magnétohydrodynamique, équations elliptiques à coefficients discontinus, éléments finis de Lagrange, effet dynamo, calcul parallèle.

Abstract

Theoretical and numerical analysis of the magnetohydrodynamics equations : application to dynamo action.

We focus on the magnetohydrodynamics (MHD) equations in hetereogeneous media, i.e. media with (possibly brutal) variations on the physical properties. In particular, we are interested in solving the Maxwell equations with discontinuous magnetic properties. We introduce a method that is, to the best of our knowledge, new to solve this problem using only Lagrange Finite Elements. We then discuss its implementation in SFEMaNS, a numerical code developped since 2002 by J.-L. Guermond, C. Nore, J. Léorat, R. Laguerre and A. Ribeiro. We show the results of the first dynamo simulations we have been able to make with this solver. For instance, we present a kinematic dynamo in a VKS setup, as well as some results about dynamo action induced either by a Taylor-Couette flow, or by a precessionnally driven flow.

Keywords : magnetohydrodynamics, elliptic equations with discontinuous coefficients, Lagrange Finite Elements, dynamo action, parallel computing.

Remerciements

Beaucoup de personnes ont contribué à la réalisation de cette thèse, et j'aimerais ici les en remercier. Je voudrais commencer par remercier mes directeurs de thèse, Caroline Nore et Jean-Luc Guermond. Tous deux ont su me faire entrer dans le monde de la recherche, et ont pu me permettre d'appréhender différents sujets avec deux approches différentes mais complémentaires que sont la physique et les mathématiques. Merci à Caroline pour m'avoir offert l'opportunité de mettre en pratique mes connaissances mathématiques à la modélisation de phénomènes physiques. Merci également à Jean-Luc, et à Texas A&M University de m'avoir accueilli pendant un an. Ce fut une expérience enrichissante, aussi bien sur le plan professionnel que personnel.

Je voudrais également remercier spécialement M. Patrick Ciarlet, qui m'a fait l'honneur et l'amitié d'accepter de présider mon jury de thèse. Mes remerciements vont également à MM. Yannick Ponty et Martin Costabel qui ont eu le courage, la patience et la gentillesse d'évaluer ma thèse. Sans oublier M. Frédéric Bouillault, qui a accepté d'examiner ma thèse. Par ailleurs, en tant que mathématicien spécialisé dans les éléments finis, je voudrais remercier tout particulièrement Mme Vivette Girault, dont la présence dans ce jury de thèse est pour moi est un grand honneur.

J'adresse également mes remerciements à M. Patrick Le Quéré, directeur du Laboratoire d'Informatique pour la Mécanique et les Sciences de l'Ingénieur, laboratoire qui m'a accueilli durant ces trois années de thèse. J'en profite également pour remercier tous les membres du laboratoire que j'ai eu la chance de cotoyer pendant trois ans ; en particulier, merci à Dang et Jalel, dont le soutien informatique et la mise à disposition d'outils de calcul ont été l'une des pierres angulaires de ce travail.

Un merci tout particulier également à Julie, Lyes, Jérémy, Benoît et Laurent, qui sont passés avant moi et ont su créer un cadre de travail particulièrement agréable, ainsi qu'à Wietze Herreman, qui a partagé son expérience du monde de la recherche, et a contribué, par ses critiques et son aide, à affiner ma formation.

Pour terminer, un grand merci à ma famille, qui m'a permis de faire, encouragé à faire, et soutenu pendant cette thèse. Sans eux et leur soutien, cette thèse n'aurait probablement pas démarré. Plus particulièrement, je voudrais remercier Marina, qui a su me porter, me supporter, et dont la présence indéfectible même dans les moments difficiles a été un précieux atout.

A Marina
et à notre enfant

Table des matières

Chapitre 1

Introduction

1.1 Objet et motivation

La magnétohydrodynamique (MHD) consiste en la description du comportement d'un fluide conducteur de l'électricité, en présence d'un champ électromagnétique. Le fluide considéré peut être par exemple du métal liquide, ou bien encore un plasma. Son caractère conducteur de l'électricité implique des interactions entre le mouvement du fluide et le champ magnétique ambiant. En astrophysique, géophysique ou même au niveau industriel, on peut trouver d'innombrables applications, mais ce présent travail de thèse se focalise sur un seul en particulier : *l'effet dynamo*, qui est considéré comme responsable de l'omniprésence des champs magnétiques dans l'Univers. La MHD fait intervenir un couplage entre les équations régissant le mouvement du fluide (ici les équations de Navier-Stokes) et les équations régissant l'évolution du champ magnétique (équations de Maxwell dans lesquelles on néglige les courants de déplacement). Deux paramètres adimensionnés apparaissent alors : R_e le nombre de Reynolds cinétique, comparant le temps visqueux au temps advectif, et R_m, le nombre de Reynolds magnétique, comparant le temps de diffusion ohmique au temps advectif. L'interaction se fait au travers de la force de Lorentz.

Jusqu'à ce jour, plusieurs expériences ont pu mettre en évidence cet effet dynamo, mais l'explication des phénomènes mis en jeu n'est pas encore claire. L'un des objectifs de ce travail est de fournir un outil de simulation numérique capable de représenter au mieux certaines configurations réalistes, afin d'étudier les mécanismes qui peuvent être à l'origine d'un effet dynamo. Il existe actuellement plusieurs codes numériques capables d'intégrer les équations de la MHD dans des géométries particulières (cf. Tilgner et al. [146, 148] pour une sphère en précession, Dormy et al. [29] dans une sphère avec prise en compte des effets thermiques, Léorat ou Willis et al. pour des cylindres axialement périodiques). Depuis 2002, l'équipe dans laquelle ce travail de thèse a été effectué s'est fixé comme objectif de développer un code non-linéaire parallélisé pouvant intégrer les équations de la MHD dans des géométries plus complexes (toutefois axisymétriques) et dans des domaines hétérogènes. Ce code, baptisé SFEMaNS (pour Spectral/Finite Element for Maxwell and Navier-Stokes), est actuellement l'un des seuls à pouvoir intégrer le système MHD non-linéaire tout en tenant compte des hétérogénéités du domaine. Il repose sur une méthode hybride, avec une décomposition de Fourier dans la direction azimutale, et une méthode d'éléments finis de Lagrange dans le plan méridien. Ce choix d'éléments finis est assez audacieux car il a déjà été mis en évidence que les méthodes standards basées sur les éléments finis de Lagrange pouvaient donner lieu à des problèmes

de convergence, notamment lors de la résolution de cas stationnaires, dans des domaines présentant des singularités géométriques et/ou des sauts de perméabilité.

Au départ de cette thèse, ce problème était contourné en n'utilisant le code que pour des calculs instationnaires, dans des géométries régulières. L'un des objectifs principaux de cette thèse a été la mise au point d'une méthode mixte autorisant tout type de géométrie, et permettant de résoudre également des problèmes d'induction stationnaires. En particulier, l'une des difficultés inhérentes aux milieux hétérogènes ou aux domaines singuliers est que la régularité des solutions est très basse. Nous nous proposons de chercher à préciser cette régularité, afin de mettre au point une méthode dépendant d'un paramètre α qui permettra d'approcher correctement les solutions. Un autre objectif de cette thèse a été la modification du code SFEMaNS : outre une nouvelle méthode de résolution, nous nous proposons de rendre le code plus efficace (en terme de temps de restitution) en ajoutant une étape de parallélisation. D'un point de vue pratique, ces améliorations apportées au code nous permettront de faire des simulations numériques dans des cas proches de cas expérimentaux, afin de mettre en évidence l'effet dynamo dans certaines configurations.

1.2 Plan détaillé du mémoire

Ce mémoire est composé de cinq courts chapitres et de huit chapitres annexes. Après un chapitre d'introduction, les chapitres 2, 3 et 4 visent à expliquer de manière plus simplifiée la nouvelle méthode pour la résolution des équations de Maxwell, à donner des détails sur son implémentation, et à résumer les différentes applications abordées au cours de cette thèse. À ces fins, de nombreuses références aux chapitres annexes y seront données. Le chapitre 5 conclut la discussion sur le travail effectué dans cette thèse. Les annexes A à H sont des reproductions d'articles publiés et/ou en préparation, qui recouvrent bien plus en détail tout ce travail. L'auteur s'excuse au passage des redondances pouvant intervenir dans ces articles, notamment au niveau des introductions, mais il lui semblait plus pertinent de laisser ces articles en l'état. C'est pourquoi ces derniers chapitres sont laissés en anglais.

Introduction générale.

Nous décrivons les équations issues de la modélisation des phénomènes MHD. On explique également succinctement ce qu'est l'effet dynamo, et on donne, parmi quelques exemples connus, ceux qui ont directement suscité notre intérêt, du point de vue de la simulation numérique.

Méthode de résolution.

On présente de manière simplifiée les idées qui ont abouti à la mise en œuvre d'une nouvelle méthode de résolution. Outre l'obtention de la méthode, ce chapitre reprend les résultats essentiels des annexes A et B, et donne quelques informations supplémentaires sur des méthodes alternatives qui pourraient paraître plus simples, mais qui présentent suffisamment d'inconvénients pour avoir été écartées.

Le code SFEMaNS.

Dans ce chapitre, on présente de façon succincte le code de calcul utilisé en pratique. On met l'accent en particulier sur les évolutions subies par ce code depuis 2009. On en présente

les principales caractéristiques, et les hypothèses nécessaires à son utilisation. Enfin, on donne quelques résultats numériques illustrant son bon comportement.

Application à l'effet dynamo.

On présente de manière simplifiée les principaux résultats de simulation numérique obtenus en utilisant le code SFEMaNS. Ce chapitre regroupe essentiellement une synthèse des annexes C à H, avec quelques résultats supplémentaires de simulations numériques d'une dynamo de type Busse & Wicht, pour laquelle la nouvelle méthode a été utilisée.

Conclusion et perspectives.

On conclut dans ce chapitre en donnant quelques axes de développement en cours pour le code SFEMaNS, afin de pouvoir obtenir de meilleurs résultats dans des configurations de type VKS notamment.

Annexe A : Fondements théoriques de la méthode.

Ce chapitre est, avec le suivant, l'un des plus importants de ce travail. Il correspond à un article théorique mathématique relatif à la régularité minimale attendue pour les solutions des équations de Maxwell. L'objectif principal de ce chapitre est de prouver une régularité minimale sur les équations de Maxwell, qui sera ensuite utilisable pour prouver la convergence de notre méthode.

A. Bonito, J.-L. Guermond & F. Luddens, Note on the regularity of the Maxwell equations in heterogeneous media, *soumis à Journal of Mathematical Analysis and Applications*

Annexe B : Convergence de la méthode.

Deuxième volet théorique important, ce chapitre correspond à un article en préparation, dans lequel on prouve la convergence de la méthode, dans le cas des équations de Maxwell avec vitesse de fluide nulle. Pour appuyer cette preuve de convergence, on développe quelques exemples simplifiés issus de benchmarks ou de solutions analytiques, afin d'illustrer notre propos.

A. Bonito, J.-L. Guermond & F. Luddens, H^1-conforming approximation of the Maxwell equations in heterogeneous media with minimal regularity, *en préparation*

Annexe C : Dynamo (cinématique) de Cadarache

Ce chapitre correspond à un premier travail en collaboration avec A. Giesecke et al. Deux codes de calcul différents (dont SFEMaNS) sont comparés dans le cadre de déclin ohmique. Après avoir montré un bon accord, on s'intéresse à une dynamo cinématique dans une configuration de type VKS, avec un écoulement axisymétrique. On donne alors quelques résultats concernant le taux de (dé)croissance pour le mode $m = 1$.

A. Giesecke, C. Nore, F. Stefani, G. Gerbeth, J. Léorat, F. Luddens & J.-L. Guermond, Electromagnetic induction in non-uniform domains, *Geophys. Astrophys. Fluid Dyn.*, 104(5-6) :509-529, 2010

Annexe D : Sauts de perméabilité.

La nouvelle méthode de résolution est appliquée au cas des équations de la MHD. Dans des configurations de type VKS, avec un milieu hétérogène (i.e. présentant des discontinuités dans la distribution de perméabilité), on essaie de déceler quelques mécanismes qui pourraient jouer un rôle important dans la dynamo de VKS observée expérimentalement.

J.-L. Guermond, J. Léorat, F. Luddens, C. Nore & A. Ribeiro, Effects of discontinuous magnetic permeability on magnetodynamic problems, *J. Comput. Phys.*, 230 :6299-6319, 2011

Annexe E : Influence des sauts de perméabilité dans la dynamo de Cadarache.

Ce chapitre correspond encore à une collaboration avec A. Giesecke et al. et présente l'article paru dans *New Journal of Physics*. On s'intéresse à l'importance des hautes valeurs de perméabilité dans la dynamo dans un modèle de type VKS. Dans la même configuration que l'annexe D, on étudie de manière plus approfondie le cas de la dynamo cinématique. On donne également quelques précisions sur le comportement du mode $m = 0$, bien qu'il s'agisse d'un mode toujours décroissant.

A. Giesecke, C. Nore, F. Stefani, G. Gerbeth, J. Léorat, W. Herreman, F. Luddens & J.-L. Guermond, Influence of high-permeability discs in an axisymmetric model of the Cadarache dynamo experiment, *New J. Phys.* 14 (2012) 053005

Annexe F : Dynamo dans une configuration Taylor-Couette.

Dans ce chapitre, on s'intéresse à une dynamo non linéaire générée par un écoulement de Taylor-Couette dans un cylindre avec un petit rapport de forme. Les résultats obtenus sont notamment comparés à des cas répertoriés de dynamo sphériques.

C. Nore, J.-L. Guermond, R. Laguerre, F. Luddens & J. Léorat, Nonlinear dynamo in a short Taylor-Couette setup, *à paraître dans Physics of Fluids*

Annexe G : Dynamo en précession dans un cylindre.

Ce chapitre correspond à nos premières simulations de dynamo générées par un écoulement dans un conteneur en précession, le but étant de déterminer si le mouvement d'un fluide dans un cylindre en précession est susceptible d'engendrer un effet dynamo. Par la suite, ces simulations numériques pourront sans doute être comparées à une expérience en cours de construction à Dresde (Allemagne).

C. Nore, J. Léorat, J.-L. Guermond & F. Luddens, Nonlinear dynamo action in a precessing cylindrical container, *Physical Review E.* 84, 016317, 2011

Annexe H : Précession dans un sphéroïde.

Ce chapitre aborde encore la dynamo en précession, mais cette fois dans un sphéroïde. Le but initial était d'évaluer la possiblité d'un effet dynamo dans un sphéroïde en précession. Toutefois, l'obtention d'un écoulement de base compatible avec des calculs référencés, notamment dans un article de Wu & Roberts (cf. [156]) a mis en évidence un comportement

instable pour certains écoulements stationnaires. Ce chapitre a donc pour but d'expliquer ces comportements, et ne concerne finalement que la partie hydrodynamique du problème.

J.-L. Guermond, J. Léorat, F. Luddens & C. Nore, Remarks on the stability of the Navier-Stokes equations supplemented with stress boundary conditions, *soumis à European Journal of Mechanics - B/Fluids*

1.3 Les équations de la MHD

Nous étudions tout au long de ce travail les équations de la magnétohydrodynamique (MHD), qui décrivent le comportement d'un fluide conducteur de l'électricité en présence d'un champ magnétique, ainsi que sa rétroaction sur ledit champ magnétique. On peut trouver une description détaillée dans [126] ou [108]. Commençons par évoquer les équations qui régissent le champ électromagnétique.

Équation d'induction

Les équations régissant le champ électromagnétique proviennent des équations de Maxwell. En notant $\mathbf{E}$ le champ électrique, $\mathbf{D}$ l'induction électrique, $\mathbf{H}$ le champ magnétique et $\mathbf{B}$ l'induction magnétique, elles s'écrivent :

$$\partial_t \mathbf{B} = -\nabla\times\mathbf{E}, \tag{1.3.1}$$

$$\nabla\times\mathbf{H} = \mathbf{j} + \partial_t \mathbf{D} + \chi\mathbf{u}, \tag{1.3.2}$$

$$\nabla\cdot\mathbf{D} = \chi, \tag{1.3.3}$$

$$\nabla\cdot\mathbf{B} = 0, \tag{1.3.4}$$

où $\mathbf{j}$ désigne la dénsité de courant électrique, χ la densité de charges électriques et $\mathbf{u}$ la vitesse du milieu considéré. On suppose que les différents champs vérifient en outre les relations constitutives suivantes, associées aux milieux considérés :

$$\mathbf{D} = \epsilon\mathbf{E}, \tag{1.3.5}$$

$$\mathbf{B} = \mu\mathbf{H}, \tag{1.3.6}$$

où ϵ (resp. μ) représente la permittivité électrique (resp. la perméabilité magnétique) du milieu considéré. Pour la MHD, on se place dans le cadre de l'approximation quasi-statique (cf. [108] pour plus de précisions), i.e. on néglige dans les équations de Maxwell les termes en χ et $\partial_t\mathbf{D}$. En particulier, les équations (1.3.2)-(1.3.3) se réécrivent :

$$\nabla\times\mathbf{H} = \mathbf{j}, \tag{1.3.7}$$

$$\nabla\cdot(\epsilon\mathbf{E}) = 0. \tag{1.3.8}$$

Avant de passer à l'adimensionnement, notons encore que l'on utilise la loi d'Ohm pour caractériser la densité de courant $\mathbf{j}$. Elle s'écrit

$$\mathbf{j} = \sigma\left(\mathbf{E} + \mathbf{u}\times\mathbf{B}\right), \tag{1.3.9}$$

où σ désigne la conductivité du milieu ; $\sigma \equiv 0$ dans toutes les parties isolantes du milieu. Pour l'adimensionnement, on prend comme perméabilité (resp. permittivité) caractéristique

la perméabilité magnétique du vide μ_0 (resp. la permittivité électrique du vide ε_0). On se donne une longueur caractéristique $\mathcal{L}$, un temps caractéristique $\mathcal{T}$ et une conductivité caractéristique σ_0. On note $\mathcal{U} = \frac{\mathcal{L}}{\mathcal{T}}$ et on introduit un nombre sans dimension

$$R_{\mathrm{m}} := \mu_0 \sigma_0 \mathcal{L}\mathcal{U}. \tag{1.3.10}$$

En réécrivant les équations sous forme adimensionnée, on considère que les deux termes dans l'équation de Maxwell-Faraday sont du même ordre de grandeur, i.e. $\frac{\mu_0|\mathbf{H}|}{\mathcal{T}} = \frac{|\mathbf{E}|}{\mathcal{L}}$. On aboutit alors à

$$\begin{aligned}
\partial_t(\mu\mathbf{H}) &= -\nabla\times\mathbf{E}, \\
\nabla\times\mathbf{H} &= R_{\mathrm{m}}\sigma\left(\mathbf{E} + \mathbf{u}\times(\mu\mathbf{H})\right), \\
\nabla\cdot(\varepsilon\mathbf{E}) &= 0, \\
\nabla\cdot(\mu\mathbf{H}) &= 0.
\end{aligned}$$

Ici, μ (resp. ε) désigne la perméabilité (resp. permittivité) relative par rapport à μ_0 (resp. ε_0). Notons que l'on peut écrire un système de deux équations portant uniquement sur le champ magnétique $\mathbf{H}$:

$$\partial_t\left(\mu\mathbf{H}\right) = -\frac{1}{R_{\mathrm{m}}}\nabla\times\left(\frac{1}{\sigma}\nabla\times\mathbf{H}\right) + \nabla\times\left(\mathbf{u}\times\mu\mathbf{H}\right), \tag{1.3.11}$$

$$\nabla\cdot(\mu\mathbf{H}) = 0. \tag{1.3.12}$$

Remarque 1.3.1. Notons que si l'on avait gardé le terme $\partial_t\mathbf{D}$ dans l'équation de Maxwell-Ampère, le terme adimensionné correspondant aurait été

$$\varepsilon_0\mu_0\mathcal{U}^2\partial_t(\varepsilon\mathbf{E}).$$

Or, avec $\mathfrak{c}$ la vitesse de la lumière, on a $\varepsilon_0\mu_0\mathfrak{c}^2 = 1$. Puisqu'on considère $\mathcal{U}$ négligeable devant $\mathfrak{c}$, le terme $\partial_t\mathbf{D}$ peut effectivement être négligé.

Signalons que, dans le cadre de la dynamo cinématique (i.e. lorsqu'on s'intéresse uniquement à la résolution des équations de Maxwell avec un champ de vitesses donné), on trouve parfois un adimensionnement différent, basé sur le temps de diffusion du champ magnétique dans le conducteur. On note alors $\mathcal{U}$ la vitesse caractéristique basée sur le champ de vitesses, et on prend comme temps caractéristique $\mathcal{T} := \mu_0\sigma_0\mathcal{L}^2$. R_{m} reste défini par (1.3.10) et on aboutit à

$$\partial_t\left(\mu\mathbf{H}\right) = -\nabla\times\left(\frac{1}{\sigma}\nabla\times\mathbf{H}\right) + R_{\mathrm{m}}\nabla\times\left(\mathbf{u}\times\mu\mathbf{H}\right). \tag{1.3.13}$$

Dans les deux cas, on voit que l'équation d'induction fait intervenir deux termes :

- un terme de diffusion, qui est prépondérant à faible R_{m}, et qui tend à dissiper le champ magnétique.
- un terme de couplage, prépondérant à fort R_{m}, et qui contient une partie d'advection pure. En effet, avec un champ de vitesses incompressible et une induction à divergence nulle, on a $\nabla\times(\mathbf{u}\times\mu\mathbf{H}) = (\mathbf{u}\cdot\nabla)(\mu\mathbf{H}) - (\mu\mathbf{H}\cdot\nabla)\mathbf{u}$. La seconde partie correspond à un cisaillement du champ magnétique par l'écoulement.

Équations de Navier-Stokes

Dans le cas de la MHD faisant intervenir un milieu fluide, on va toujours considérer un fluide newtonien incompressible, dont le mouvement est régi par les équations de Navier-Stokes. On écrit ici le terme non linéaire sous forme rotationnelle, et on utilise la pression dynamique, car c'est le choix qui a été fait pour la résolution numérique. On part alors de :

$$\partial_t \mathbf{u} + (\nabla\times\mathbf{u})\times\mathbf{u} - \nu\Delta\mathbf{u} = -\frac{1}{\rho}\nabla p + \frac{1}{\rho}\mathbf{f}, \tag{1.3.14}$$

$$\nabla\cdot\mathbf{u} = 0, \tag{1.3.15}$$

où $\mathbf{u}$ désigne le champ de vitesse, p la pression dynamique, ρ la masse volumique (supposée donc uniforme dans le fluide), ν la viscosité cinématique, et $\mathbf{f}$ représente un champ de forçage volumique. On décompose ce forçage en deux parties distinctes $\mathbf{f} = \mathbf{f}_0 + \mathbf{f}_L$, où $\mathbf{f}_L$ désigne la force de Lorentz, qui traduit l'action du champ magnétique sur le fluide, et $\mathbf{f}_0$ désigne un forçage extérieur. La force de Lorentz s'écrit $\mathbf{f}_L = \mathbf{j}\times\mathbf{B}$, ce qui entraîne, en utilisant (1.3.7),

$$\mathbf{f}_L = (\nabla\times\mathbf{H})\times(\mu\mathbf{H}). \tag{1.3.16}$$

Étant données une longueur caractéristique $\mathcal{L}$, une vitesse caractéristique $\mathcal{U}$, on utilise pour l'adimensionnement le temps d'advection $\mathcal{T} = \mathcal{L}/\mathcal{U}$, si bien que, en notant $\mathcal{P}$ (resp. $\mathcal{H}$) une échelle caractéristique de pression (resp. de champ magnétique), on obtient l'équation suivante sur les grandeurs adimensionnées :

$$\frac{\mathcal{U}}{\mathcal{T}}\partial_t\mathbf{u} + \frac{\mathcal{U}^2}{\mathcal{L}}(\nabla\times\mathbf{u})\times\mathbf{u} - \frac{\nu\mathcal{U}}{\mathcal{L}^2}\Delta\mathbf{u} = -\frac{\mathcal{P}}{\rho\mathcal{L}}\nabla p + \frac{\mathcal{H}^2\mu_0}{\rho\mathcal{L}}(\nabla\times\mathbf{H})\times(\mu\mathbf{H}). \tag{1.3.17}$$

Notons que l'on a omis le terme de forçage extérieur $\mathbf{f}_0$ pour l'adimensionnement. On pose $\mathcal{P} = \rho\mathcal{U}^2$, et on introduit deux paramètres sans dimension $A^2 := \frac{\mu_0\mathcal{H}^2}{\rho\mathcal{U}^2}$ et le nombre de Reynolds cinétique $R_\mathrm{e} := \frac{\mathcal{U}\mathcal{L}}{\nu 0}$; on obtient alors

$$\partial_t\mathbf{u} + (\nabla\times\mathbf{u})\times\mathbf{u} - \frac{1}{R_\mathrm{e}}\Delta\mathbf{u} = -\nabla p + A^2(\nabla\times\mathbf{H})\times(\mu\mathbf{H}), \tag{1.3.18}$$

$$\nabla\cdot\mathbf{u} = 0. \tag{1.3.19}$$

Lorsqu'on ne considère que les équations de Maxwell, on se rend compte que le choix de l'intensité de référence du champ magnétique $\mathcal{H}$ peut être arbitraire, car il n'intervient pas directement dans les équations adimensionnées. Dans le cadre de la magnétohydrodynamique en revanche, il apparaît par l'intermédiaire du paramètre d'interaction A. Sauf mention contraire, on considère que la vitesse caractéristique est égale à la vitesse d'Alfvén, i.e. $\mathcal{U} = \mathcal{H}\sqrt{\frac{\mu_0}{\rho}}$. Cela correspond alors à $A = 1$.

Les équations dans le code

Dans le code numérique que nous utiliserons (cf. section 3), on gardera dans les équations de Maxwell un terme de courant externe $\mathbf{j}$ (supposé adimensionné) et dans les équations de Navier-Stokes, un terme de forçage externe $\mathbf{f}$ (supposé adimensionné), i.e. on s'intéressera aux

équations suivantes :

$$\partial_t(\mu\mathbf{H}) + \frac{1}{R_\mathrm{m}}\nabla\times\left(\frac{1}{\sigma}\nabla\times\mathbf{H}\right) - \nabla\times(\mathbf{u}\times\mu\mathbf{H}) = \frac{1}{R_\mathrm{m}}\nabla\times\left(\frac{1}{\sigma}\mathbf{j}\right), \tag{1.3.20}$$

$$\nabla\cdot(\mu\mathbf{H}) = 0, \tag{1.3.21}$$

$$\partial_t\mathbf{u} + (\nabla\times\mathbf{u})\times\mathbf{u} - \frac{1}{R_\mathrm{e}}\Delta\mathbf{u} = -\nabla p + A^2(\nabla\times\mathbf{H})\times(\mu\mathbf{H}) + \mathbf{f}, \tag{1.3.22}$$

$$\nabla\cdot\mathbf{u} = 0, \tag{1.3.23}$$

où $A = 0$ ou 1 selon que l'on s'intéresse à un cas hydrodynamique pur, ou un cas de MHD non linéaire.

1.4 L'effet dynamo

L'effet dynamo peut être, de manière simplifiée, décrit comme étant l'émergence et l'entretien d'un champ par les mouvements d'un fluide (ou d'un solide) conducteur de l'électricité. En effet, la présence d'un terme de couplage dans l'équation d'induction (1.3.11) peut entraîner des instabilités par rapport au paramètre adimensionné R_m. Plus précisément, c'est le terme d'étirement $(\mu\mathbf{H}\cdot\nabla)\mathbf{u}$ qui est le terme clef de la dynamo. Soulignons que les écoulements ne sont pas tous susceptibles d'entretenir un champ magnétique. En particulier, certaines symétries dans les champs de vitesse ou magnétique peuvent rendre impossible cet effet dynamo. Pour une description plus détaillée de certains théorèmes anti-dynamo, on renvoie à [108]. On peut néanmoins citer les résultats suivants :

1. (Cowling, [39]) Un écoulement axisymétrique ne peut pas engendrer un champ magnétique axisymétrique. Notons que l'on peut avoir un effet dynamo, mais alors le champ magnétique sera porté par des modes non nuls.
2. Lorsque le conducteur a des propriétés électromagnétiques homogènes, un écoulement plan ne peut pas produire d'effet dynamo.

À l'opposé, on peut citer des résultats positifs de dynamo : en premier lieu, on peut mentionner des cas de dynamo solide (i.e. le champ magnétique est entretenu par le mouvement d'un solide conducteur de l'électricité), comme la dynamo de Bullard (cf. [27]) ou la dynamo de Lowes et Wilkinson (cf. [98, 99]). Toutefois, puisqu'il semble admis par la communauté que la présence du champ magnétique terrestre actuel pourrait être expliquée par un phénomène de dynamo fluide, c'est ce type de dynamo sur lequel on va mettre l'accent dans ce mémoire. Citons alors quelques résultats positifs de dynamo fluide.

La dynamo de G. O. Roberts

Cette dynamo a été mise en évidence expérimentalement à Karlsruhe (Allemagne) en 2000 (cf. [139, 147, 150, 112]). Elle s'inspire de l'écoulement analytique de G. O. Roberts [125], qui est périodique et indépendant de la variable verticale. Son expression est :

$$\mathbf{u} = \sin(y)\mathbf{e}_x + \sin(x)\mathbf{e}_y + (\cos(x) - \cos(y))\,\mathbf{e}_z.$$

Afin de réaliser expérimentalement un écoulement proche de cet écoulement analytique, le dispositif mis en place à Karlsruhe consiste en un ensemble d'écoulements hélicoïdaux de composantes verticales opposées, engendrés dans un réseau de tubes à l'aide de pompes. On

reporte en figure 1.1 un schéma de ce dispositif. Un dipôle magnétique stationnaire (perpendiculaire à l'axe des tubes) a ainsi été mis en évidence. La valeur de ce champ à saturation est de l'ordre de $250G$, à 10% au dessus du seuil.

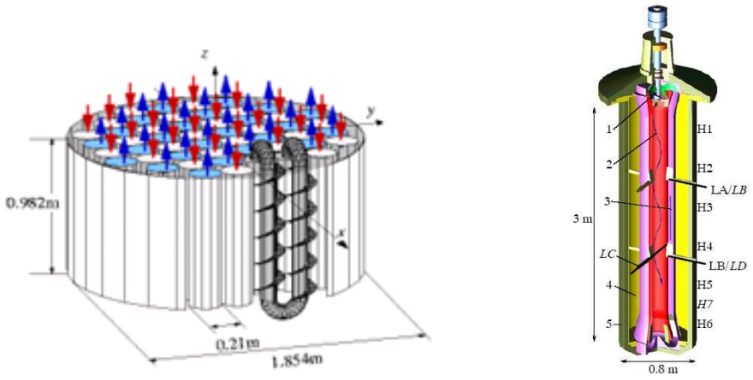

FIG. 1.1: Schéma des dispositifs pour la dynamo de Karlsruhe (à gauche, [139]) et Riga (à droite, [51])

La dynamo Ponomarenko (Riga)

Cette dynamo a été obtenue expérimentalement à Riga (Lettonie) en 1999. L'écoulement utilisé, appelé écoulement de Ponomarenko [121], est assez simple et offre l'avantage d'être instable vis à vis de l'effet dynamo pour des petites valeurs de R_m (de l'ordre de quelques dizaines). On donne un schéma du dispositif expérimental en figure 1.1. Le fluide est entraîné en translation, puis en rotation grâce à une hélice dans un tube. Il est ensuite redirigé par un écoulement vertical vers l'entrée du tube, dans une chemise entourant le cylindre. L'ensemble est immergé dans du sodium au repos. Des simulations numériques de Stefani et al. [135] ont permis l'optimisation de la configuration. L'effet dynamo a été observé pour différents nombres de Reynolds magnétiques très proches du seuil cinématique [52].

L'expérience Von Kármán Sodium (VKS)

Cette expérience est menée conjointement depuis quelques années par des équipes du CEA Saclay, du CEA Cadarache et des Écoles Normales Supérieures de Paris et Lyon. Il s'agit d'obtenir un effet dynamo à partir d'un écoulement de Von Kármán dans du sodium liquide. Le dispositif expérimental, représenté de façon simplifiée en figure 1.2, consiste essentiellement en un cylindre de rayon R, de hauteur H et de rapport de forme $\Gamma := H/R = 1.8$. L'écoulement est forcé par deux disques munis de pales et tournant en contra-rotation. Pour de grandes valeurs du nombre de Reynolds cinétique R_e, l'écoulement obtenu est très turbulent et hélicitaire. Néanmoins, il n'est pas forcément générateur de dynamo. En effet, une première expérience dans laquelle disques et pales étaient faits d'acier n'a pas permis de mettre en évidence un effet dynamo, mais a tout de même permis d'identifier divers mécanismes d'induction [20, 103, 101, 118]. En 2006, en remplaçant l'acier par du fer doux, l'effet dynamo a pu être observé, mais sa compréhension demeure incomplète. Les sauts de perméabilité magnétique semblent jouer un rôle essentiel dans cette dynamo et c'est pourquoi nous y avons consacré trois articles (en chapitres annexes) dans cette thèse.

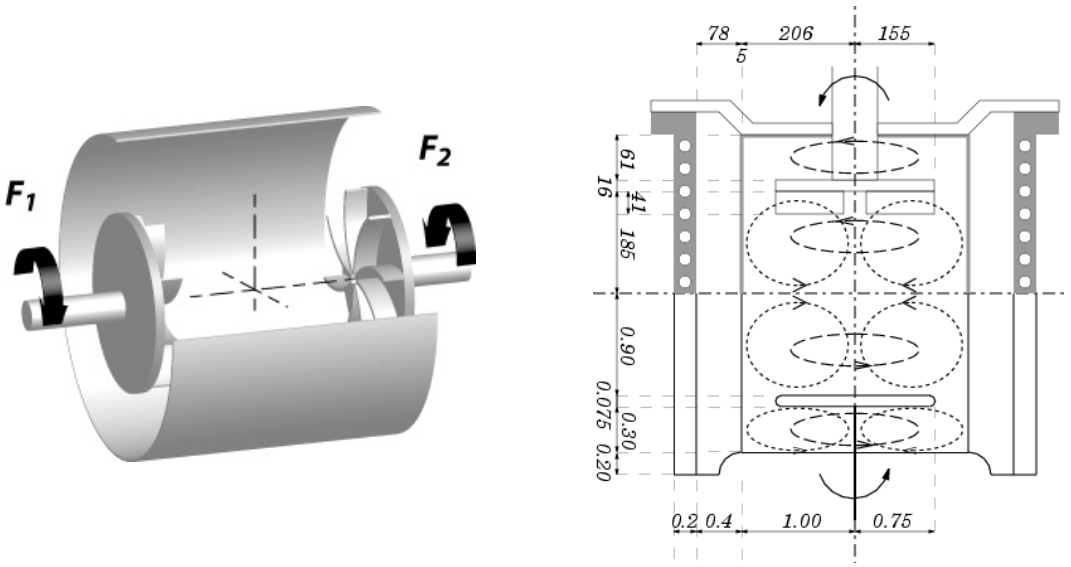

FIG. 1.2: Dispositif de Cadarache : à gauche, schéma du dispositif (Von Kármán Sodium collaboration) ; à droite, détails techniques pour le cas réel (en haut) et géométrie simplifiée pour les simulations numériques (en bas), cf. [67]. La structure du flot moyen est également représentée.

La dynamo en précession

L'effet dynamo engendré par un mouvement de précession a été fortement étudié en géométrie sphérique, car la précession est considérée comme une source (tout au moins partielle) possible du champ magnétique terrestre (cf. [100, 148] par exemple). Des études paléomagnétiques tendent d'ailleurs à confirmer cette idée [30]. La configuration est assez simple : un fluide conducteur de l'électricité est placé dans un conteneur en rotation par rapport à un axe de symétrie (conteneur axisymétrique). Cet axe de symétrie est lui-même en rotation dans le référentiel du laboratoire. Une expérience est en cours de montage à Dresde (Allemagne), afin d'étudier cette dynamo [134]. L'un des attraits de cette dynamo en précession est le fait qu'elle est un modèle de dynamo *homogène* ; en effet, le fluide homogène est mis en rotation autour de deux axes, sans guidage (comme à Karlsruhe) ni dispositif d'injection (comme à Riga), et ne nécessite pas de forçage externe par un matériau solide en fer doux (crucial dans la dynamo de Cadarache).

Chapitre 2

Approximation des équations de Maxwell en milieu hétérogène

Dans ce chapitre plutôt mathématique, on essaie de présenter de manière simplifiée les fondements de la méthode numérique mise en place pour la résolution des équations de Maxwell. On commence par écrire un problème simplifié sous forme variationnelle, et on discute de l'approximation dans les espaces fonctionnels naturellement mis en jeu. On donne ensuite une formulation permettant de retrouver de la convergence. Les résultats importants de ce chapitre sont :

- l'estimation de régularité (2.1.20), qui correspond au résultat principal prouvé dans l'annexe A, qui donne une régularité a priori des solutions,
- les théorèmes 2.3.1 et 2.3.2, qui correspondent aux principaux résultats prouvés dans l'annexe B, et qui justifient de la convergence de la méthode, aussi bien sur des problèmes aux limites que pour la recherche de valeurs propres.

Après avoir illustré numériquement la convergence de la méthode, on discute également rapidement d'une autre formulation, qui pourrait sembler un peu plus naturelle, mais qui est également plus contraignante sur les espaces d'approximation, et sera donc écartée.

2.1 Cadre fonctionnel

2.1.1 Modèle simplifié

Pour bien comprendre la méthode développée et mise en place numériquement, on se place dans le cadre suivant : dans tout ce chapitre, on considère un domaine borné Ω conducteur, et on suppose que $\Omega = \bigcup_{i=1,N} \Omega_i$, avec dans chaque Ω_i, des propriétés physiques (i.e. μ et σ) uniformes et isotropes. Pour simplifier, on considère même que σ et μ sont constants sur chaque Ω_i. On fait en outre l'hypothèse que tous les domaines Ω et Ω_i ont une frontière Lipschitz. On peut écrire les équations régissant l'évolution du champ magnétique sous la forme suivante :

$$\partial_t(\mu\mathbf{H}) + \nabla\times\left(\frac{1}{\sigma}\nabla\times\mathbf{H}\right) = \mathbf{g} \quad \text{dans } \Omega, \tag{2.1.1}$$

$$\nabla\cdot(\mu\mathbf{H}) = 0 \quad \text{dans } \Omega, \tag{2.1.2}$$

où $\mathbf{g}$ contient le terme de couplage (on écrit les équations sous cette forme car numériquement, le terme de couplage sera traitée de manière explicite). Afin de simplifier notre propos, suppo-

sons que $\mathbf{g}$ est une donnée et considérons également que le domaine Ω est entouré par un milieu de perméabilité infinie, i.e. on impose la condition de bord suivante sur $\Gamma := \partial\Omega$: $\mathbf{H}\times\mathbf{n} = 0$, où $\mathbf{n}$ désigne la normale unitaire sortante. Enfin, on note Σ l'interface au niveau de laquelle μ et σ peuvent présenter des discontinuités, i.e. $\Sigma := \bigcup_{i\neq j} \left(\overline{\partial\Omega_i} \cap \overline{\partial\Omega_j}\right)$. On rappelle alors que l'on a les relations de continuité suivantes :

$$\mathbf{H}_i\times\mathbf{n}_i + \mathbf{H}_j\times\mathbf{n}_j = 0 \text{ sur } \Sigma, \tag{2.1.3}$$

$$\mu_i\mathbf{H}_i\cdot\mathbf{n}_i + \mu_j\mathbf{H}_j\cdot\mathbf{n}_j = 0 \text{ sur } \Sigma, \tag{2.1.4}$$

où les indices i et j indiquent le sous-domaine sur lequel on considère chaque quantité, et sont tels que $\overline{\partial\Omega_i} \cap \overline{\partial\Omega_j} \neq \emptyset$. Il ne faut pas oublier d'ajouter une donnée initiale, $\mathbf{H}_{|t=0} = \mathbf{H}_0$, où $\mathbf{H}_0$ est supposé connu. La difficulté de l'approximation de ces équations par éléments finis réside notamment dans la recherche d'une solution stationnaire de (2.1.1). En effet, dans le cas instationnaire, avec l'hypothèse que $\nabla\cdot\mathbf{g} = 0$, si on part de $\nabla\cdot(\mu\mathbf{H}_0) = 0$, alors l'équation d'induction (2.1.1) assure que $\mu\mathbf{H}$ est toujours à divergence nulle. En revanche, lorsque l'on cherche une solution stationnaire, i.e. lorsqu'on veut résoudre

$$\nabla\times\left(\frac{1}{\sigma}\nabla\times\mathbf{H}\right) = \mathbf{g} \text{ dans } \Omega, \tag{2.1.5}$$

$$\nabla\cdot(\mu\mathbf{H}) = 0 \text{ dans } \Omega, \tag{2.1.6}$$

$$\mathbf{H}\times\mathbf{n} = 0 \text{ sur } \Gamma, \tag{2.1.7}$$

la seconde équation devient *une contrainte* qu'il faut gérer proprement. Ce problème soulève naturellement le problème de valeurs propres suivant : trouver λ et $\mathbf{H}$ tels que

$$\nabla\times\left(\frac{1}{\sigma}\nabla\times\mathbf{H}\right) = \lambda\mu\mathbf{H} \text{ dans } \Omega, \tag{2.1.8}$$

$$\nabla\cdot(\mu\mathbf{H}) = 0 \text{ dans } \Omega, \tag{2.1.9}$$

$$\mathbf{H}\times\mathbf{n} = 0 \text{ sur } \Gamma. \tag{2.1.10}$$

C'est pour répondre à ces deux problèmes (2.1.5)-(2.1.6)-(2.1.7) et (2.1.8)-(2.1.9)-(2.1.10) que nous allons développer une nouvelle méthode d'approximation, en utilisant les éléments finis de Lagrange.

2.1.2 Espaces fonctionnels

Définissons ici le cadre fonctionnel dont nous allons avoir besoin par la suite. Sauf mention contraire, tous les espaces utilisés ici seront équipés de leur norme naturelle. On peut retrouver ces définitions dans les introductions des annexes A et B, mais on les redonne ici par souci de clarté. Pour un ouvert E de $\mathbb{R}^d$, $d = 2, 3$ donné, on notera $L^2(E)$ l'ensemble des fonctions (scalaires) mesurables de carré intégrables sur E. On note également $W^{1,2}(E)$ l'ensemble des fonctions de $L^2(E)$ dont toutes les dérivées sont encore de carré intégrable. Le sous-ensemble de $W^{1,2}(E)$ formé de toutes les fonctions qui s'annulent sur le bord de E sera noté $W_0^{1,2}(E)$. Lorsque E est borné dans au moins une direction, en utilisant l'inégalité de Poincaré (cf. par exemple [23, chapitre 9]), on considère la norme suivante sur $W_0^{1,2}(E)$:

$$\|q\|_{W_0^{1,2}(E)} := \|\nabla q\|_{\mathbf{L}^2(E)}.$$

Pour distinguer les espaces de fonctions à valeurs scalaires et les espaces de fonctions à valeurs vectorielles, on utilisera des caractères gras. On utilise encore les espaces suivants :

$$\mathbf{H}_{\mathrm{curl}}(E) := \left\{\mathbf{F} \in \mathbf{L}^2(E) \mid \nabla\times\mathbf{F} \in \mathbf{L}^2(E)\right\}, \tag{2.1.11}$$

$$\mathbf{H}_{0,\mathrm{curl}}(E) := \left\{\mathbf{F} \in \mathbf{H}_{\mathrm{curl}}(E) \mid \mathbf{F}\times\mathbf{n}_{|\partial E} = 0\right\}, \tag{2.1.12}$$

$$\mathbf{H}_{\mathrm{div}}(E) := \left\{\mathbf{F} \in \mathbf{L}^2(E) \mid \nabla\cdot\mathbf{F} \in L^2(E)\right\}, \tag{2.1.13}$$

$$\mathbf{H}_{\mathrm{div}=0}(E) := \left\{\mathbf{F} \in \mathbf{L}^2(E) \mid \nabla\cdot\mathbf{F} = 0\right\}, \tag{2.1.14}$$

$$\mathbf{X}(E) := \mathbf{H}_{0,\mathrm{curl}}(E) \cap \mathbf{H}_{\mathrm{div}=0}(E), \tag{2.1.15}$$

$$\mathbf{X}_\mu(E) := \{\mathbf{F} \in \mathbf{H}_{0,\mathrm{curl}}(E) \mid \nabla\cdot(\mu\mathbf{F}) = 0\}. \tag{2.1.16}$$

On définit enfin les espaces de Sobolev fractionnaires, en utilisant l'interpolation réelle (cf. [96] ou [143, chapitre 22] par exemple) : pour $0 < s < 1$,

$$W^{s,2}(E) := \left[L^2(E), W^{1,2}(E)\right]_{s,2} \qquad \text{et} \qquad W_0^{s,2}(E) := \left[L^2(E), W_0^{1,2}(E)\right]_{s,2}. \tag{2.1.17}$$

On notera $W^{-s,2}(E)$ le dual de $W_0^{s,2}(E)$. Notons que les espaces $W^{s,2}$ et $W_0^{s,2}$ correspondent aux espaces H^s et H_0^s introduits dans le chapitre A. On évite ici la notation H pour éviter toute confusion avec le champ magnétique considéré dans le problème. Dans la suite, on notera $(\cdot,\cdot)_E$ le produit scalaire sur E, i.e.

$$\forall f, g \in L^2(E), \qquad (f,g)_E := \int_E fg. \tag{2.1.18}$$

Bien souvent, lorsque $E = \Omega$, on omettra les références à E.

Remarque 2.1.1. Les espaces d'interpolation $W^{s,2}(E)$ peuvent être vus comme des espaces intermédiaires entre $L^2(E)$ et $W^{1,2}(E)$.

Pour comprendre ces espaces intermédiaires, on donne (sans démonstration) le résultat suivant : il existe c dépendant uniquement de E et de s tel que,

$$\forall f \in W^{s,2}(E),\ \forall t > 0,\ \exists f_t \in W^{1,2}(E), \qquad \begin{cases} \|f - f_t\|_{L^2(E)} & \leq & ct^s \|f\|_{W^{s,2}(E)}, \\ \|f_t\|_{W^{1,2}(E)} & \leq & ct^{s-1}\|f\|_{W^{s,2}(E)}. \end{cases}$$

Ce résultat signifie que, pour tout élément de $W^{s,2}(E)$, on peut trouver une suite d'approximations dont on peut contrôler à la fois la vitesse de convergence dans $L^2(E)$ et la vitesse de divergence (lorsque la suite diverge) dans $W^{1,2}(E)$.

2.1.3 Formulation variationnelle et régularité (Résultats principaux de l'annexe A)

Nous utilisons une formulation variationnelle pour résoudre le problème (2.1.5)-(2.1.6)-(2.1.7) : on dira que $\mathbf{H} \in \mathbf{X}_\mu$ est solution de (2.1.5)-(2.1.6)-(2.1.7) lorsque

$$\forall \mathbf{F} \in \mathbf{X}_\mu, \qquad \left(\frac{1}{\sigma}\nabla\times\mathbf{H}, \nabla\times\mathbf{F}\right) = (\mathbf{g}, \mathbf{F}). \tag{2.1.19}$$

Le caractère bien posé de cette formulation, ainsi que la régularité a priori des solutions, est plus compliqué à établir qu'il n'y paraît, en particulier dans le cas où μ présente des discontinuités. Nous y avons consacré un article, reporté en annexe A. On renvoie le lecteur à ce chapitre pour les détails, et on ne cite ici que les résultats importants :

– En utilisant la Proposition A.4.1, on a la coercivité de la forme bilinéaire définie par le membre de gauche de (2.2.1). Le théorème de Lax-Milgram (cf. [23, Chap. 5] par exemple) assure alors l'existence et l'unicité d'une solution $\mathbf{H} \in \mathbf{X}_\mu$.
– En utilisant le théorème A.5.1, on montre qu'il existe $\tau_\mu > 0$ (resp $\tau_\sigma > 0$) dépendant uniquement de Ω et μ (resp. σ) et tels que la solution $\mathbf{H} \in \mathbf{X}_\mu$ de (2.1.19) vérifie :

$$\|\mathbf{H}\|_{\mathbf{W}^{s_\mu,2}(\Omega)} + \|\nabla\times\mathbf{H}\|_{\mathbf{W}^{s_\sigma,2}(\Omega)} \leq c\|\mathbf{g}\|_{\mathbf{L}^2(\Omega)}, \tag{2.1.20}$$

pour une constante c ne dépendant que de Ω et des indices $s_\mu \in [0, \tau_\mu)$ et $s_\sigma \in [0, \tau_\sigma)$.
Il s'agit maintenant d'approcher la solution de (2.1.19) par une méthode d'éléments finis. La difficulté réside dans la contrainte de divergence nulle. Une première idée est d'ajouter un terme de stabilisation dans la forme bilinéaire, pour assurer une divergence nulle. Nous allons voir que le choix de cette stabilisation n'est pas anodin.

2.2 Cas simplifié, $\mu = 1$

Dans cette section, on explique pourquoi la stabilisation de la divergence dans $L^2(\Omega)$, qui paraît naturelle, peut poser problème. On se limite au cas $\mu \equiv 1$, $\sigma \equiv 1$, et on suppose $\mathbf{g}$ à divergence nulle (et indépendante du temps bien sûr).

2.2.1 Formulation faible du problème continu.

La formulation variationnelle (2.1.19) s'écrit alors : trouver $\mathbf{H} \in \mathbf{X}$ tel que, pour tout $\mathbf{F} \in \mathbf{X}$,

$$(\nabla\times\mathbf{H}, \nabla\times\mathbf{F}) = (\mathbf{g}, \mathbf{F}), \tag{2.2.1}$$

la contrainte de divergence nulle étant contenue dans l'espace $\mathbf{X}$. Toutefois, il n'est pas commode de construire des espaces d'approximations qui vérifient la contrainte de divergence nulle (rappelons que nous voulons utiliser des éléments de Lagrange continus). On peut alors considérer un nouveau problème variationnel : trouver $\mathbf{H} \in \mathbf{H}_{0,\mathrm{curl}}(\Omega) \cap \mathbf{H}_{\mathrm{div}}(\Omega)$ tel que, pour tout $\mathbf{F} \in \mathbf{H}_{0,\mathrm{curl}}(\Omega) \cap \mathbf{H}_{\mathrm{div}}(\Omega)$,

$$(\nabla\times\mathbf{H}, \nabla\times\mathbf{F}) + (\nabla\cdot\mathbf{H}, \nabla\cdot\mathbf{F}) = (\mathbf{g}, \mathbf{F}). \tag{2.2.2}$$

Le caractère bien posé de ces deux formulations découle directement du théorème de Lax-Milgram grâce à l'inégalité

$$\forall \mathbf{F} \in \mathbf{H}_{0,\mathrm{curl}}(\Omega) \cap \mathbf{H}_{\mathrm{div}}(\Omega), \qquad c\|\mathbf{F}\|^2_{\mathbf{L}^2(\Omega)} \leq \|\nabla\times\mathbf{F}\|^2_{\mathbf{L}^2(\Omega)} + \|\nabla\cdot\mathbf{F}\|^2_{L^2(\Omega)}, \tag{2.2.3}$$

où c est une constante qui ne dépend que du domaine Ω (voir par exemple [35]). Utilisant le lemme 2.2.1 ci-après, on peut montrer que les deux formulations sont équivalentes.

Proposition 2.2.1. Pour $\mathbf{g}$ à divergence nulle, la solution $\mathbf{H}$ de (2.2.1) est également solution de (2.2.2).

Preuve. Soit $\mathbf{g}$ à divergence nulle, et notons $\mathbf{H} \in \mathbf{X}$ la solution de (2.2.1). On considère $\mathbf{F} \in \mathbf{H}_{0,\mathrm{curl}}(\Omega) \cap \mathbf{H}_{\mathrm{div}}(\Omega)$. On utilise la décomposition de Helmholtz donnée par le lemme 2.2.1, et l'on écrit

$$\mathbf{F} = \mathbf{w} + \nabla q,$$

avec $\mathbf{w} \in \mathbf{X}$ et $q \in W_0^{1,2}(\Omega)$. Il s'en suit que $\nabla\times\mathbf{F} = \nabla\times\mathbf{w}$ et $\Delta q = \nabla\cdot\mathbf{F} \in L^2(\Omega)$. On peut appliquer la forme bilinéaire dans (2.2.2), et l'on obtient :

$$\begin{aligned}(\nabla\times\mathbf{H}, \nabla\times\mathbf{F}) + (\nabla\cdot\mathbf{H}, \nabla\cdot\mathbf{F}) &= (\nabla\times\mathbf{H}, \nabla\times\mathbf{w}) \\ &= (\mathbf{g}, \mathbf{w})\,.\end{aligned}$$

Or, $\mathbf{g}$ est à divergence nulle, et $q \in W_0^{1,2}(\Omega)$, si bien que $(\mathbf{g}, \nabla q) = 0$. Il s'en suit que

$$(\nabla\times\mathbf{H}, \nabla\times\mathbf{F}) + (\nabla\cdot\mathbf{H}, \nabla\cdot\mathbf{F}) = (\mathbf{g}, \mathbf{F})\,.$$

□

Remarque 2.2.1. Puisque les deux problèmes (2.2.1) et (2.2.2) admettent chacun une unique solution, on a bien montré qu'ils étaient équivalents (pour une donnée à divergence nulle).

Lemme 2.2.1. On a la décomposition suivante :

$$\mathbf{H}_{0,\mathrm{curl}}(\Omega) = \mathbf{X} \oplus \nabla W_0^{1,2}(\Omega), \tag{2.2.4}$$

la décomposition étant orthogonale dans $\mathbf{L}^2(\Omega)$.

Preuve. Soit $\mathbf{F} \in \mathbf{H}_{0,\mathrm{curl}}(\Omega)$. On note $p \in W_0^{1,2}(\Omega)$ la solution du problème de Laplace avec conditions de Dirichlet homogènes suivant :

$$\forall q \in W_0^{1,2}(\Omega), \qquad (\nabla p, \nabla q) = (\mathbf{F}, \nabla q)\,.$$

On pose ensuite $\mathbf{w} := \mathbf{F} - \nabla p$. Puisque $\mathbf{F} \in \mathbf{H}_{\mathrm{curl}}(\Omega)$ et que $\nabla\times\nabla p = 0$, on a $\mathbf{w} \in \mathbf{H}_{\mathrm{curl}}(\Omega)$. En outre, la condition de Dirichlet homogène sur p implique $\nabla p\times\mathbf{n} = 0$ sur $\partial\Omega$. Il s'en suit que $\mathbf{w}\times\mathbf{n} = 0$ sur $\partial\Omega$. Enfin, on a $\mathbf{F} \in \mathbf{H}_{\mathrm{div}}(\Omega)$ et par définition, $\Delta p = \nabla\cdot\mathbf{F}$, ce qui implique $\nabla\cdot\mathbf{w} = 0$. On a donc bien montré que $\mathbf{w} \in \mathbf{X}$. Par ailleurs, puisque $\mathbf{w}$ est à divergence nulle et $q \in W_0^{1,2}(\Omega)$, on a bien

$$(\mathbf{w}, \nabla p) = 0.$$

□

La formulation (2.2.2) est une version simplifiée de la formulation utilisée dans [66], qui était en premier lieu implémentée dans le code SFEMaNS. On va voir qu'elle n'est pas toujours adaptée aux éléments finis de Lagrange continus, et on présentera une alternative.

2.2.2 Éléments finis de Lagrange.

Dans toute la suite du chapitre, on note $\{\mathcal{T}_h\}_{h>0}$ une famille régulière de maillages affines quasi-uniformes, de taille caractéristique h, i.e. on fait les trois hypothèses suivantes sur la famille de maillages :

1. (famille régulière) Il existe $\beta_0 > 0$ tel que, pour tout $h > 0$ et tout $K \in \mathcal{T}_h$,

$$\frac{h_k}{\rho_K} \leq \beta_0, \tag{2.2.5}$$

où h_K désigne le diamètre de l'élément K, et ρ_K le diamètre de la plus grosse boule incluse dans K.

2. (maillages quasi-uniformes) Il existe $\beta > 0$ tel que, pour tout $h > 0$,

$$h = \max_{K\in\mathcal{T}_h} h_K \leq \beta \min_{K\in\mathcal{T}_h} h_K. \tag{2.2.6}$$

3. (maillages affines) Il existe un élément de référence $\hat{K}$ tel que, pour tout $h > 0$ et tout $K \in \mathcal{T}_h$ on peut trouver une application affine bijective $T_K : \hat{K} \to K$.

On introduit l'espace d'approximation suivant :

$$\mathbf{X}_h := \left\{ \mathbf{F}_h \in \boldsymbol{\mathcal{C}}^0(\bar{\Omega}) \mid \forall K \in \mathcal{T}_h,\ \mathbf{F}_{h|K} \in \mathbb{P}^\ell \right\}, \tag{2.2.7}$$

où l'on note $\mathbb{P}^\ell$ l'espace des polynômes de degré inférieur ou égal à ℓ. On voit alors dans ce cas que $\mathbf{X}_h \subset \mathbf{W}^{1,2}(\Omega)$. Pour simplifier le propos, on suppose ici en outre que $\mathbf{X}_h \subset \mathbf{H}_{0,\mathrm{curl}}(\Omega)$, i.e., la condition de bord est bien vérifiée. On note alors $\mathbf{H}_h \in \mathbf{X}_h$ tel que

$$\forall \mathbf{F}_h \in \mathbf{X}_h, \qquad (\nabla\times\mathbf{H}_h, \nabla\times\mathbf{F}_h) + (\nabla\cdot\mathbf{H}_h, \nabla\cdot\mathbf{F}_h) = (\mathbf{g}, \mathbf{F}_h). \tag{2.2.8}$$

Là encore, l'existence et l'unicité d'un tel $\mathbf{H}_h$ sont assurées par (2.2.3). On montre alors le résultat (classique) d'approximation suivant :

Proposition 2.2.2. Il existe $c > 0$ tel que, pour tout $\mathbf{g} \in \mathbf{L}^2(\Omega)$, en notant $\mathbf{H} \in \mathbf{H}_{0,\mathrm{curl}}(\Omega) \cap \mathbf{H}_{\mathrm{div}}(\Omega)$ la solution de (2.2.2) et $\mathbf{H}_h \in \mathbf{X}_h$ la solution de (2.2.8),

$$\|\mathbf{H} - \mathbf{H}_h\|_{\mathbf{H}_{0,\mathrm{curl}}(\Omega)\cap\mathbf{H}_{\mathrm{div}}(\Omega)} \leq c \inf_{\mathbf{F}_h\in\mathbf{X}_h} \|\mathbf{H} - \mathbf{F}_h\|_{\mathbf{H}_{0,\mathrm{curl}}(\Omega)\cap\mathbf{H}_{\mathrm{div}}(\Omega)}, \tag{2.2.9}$$

où la norme dans $\mathbf{H}_{0,\mathrm{curl}}(\Omega) \cap \mathbf{H}_{\mathrm{div}}(\Omega)$ est définie par :

$$\|\mathbf{F}\|^2_{\mathbf{H}_{0,\mathrm{curl}}(\Omega)\cap\mathbf{H}_{\mathrm{div}}(\Omega)} := \|\mathbf{F}\|^2_{\mathbf{L}^2(\Omega)} + \|\nabla\times\mathbf{F}\|^2_{\mathbf{L}^2(\Omega)} + \|\nabla\cdot\mathbf{F}\|^2_{L^2(\Omega)}. \tag{2.2.10}$$

Preuve. Dans la preuve, c désigne une constante qui ne dépend que de Ω et σ. Sa valeur peut changer entre chaque occurrence, pour alléger les notations. En utilisant encore la coercivité (2.2.3), on obtient :

$$\begin{aligned}\|\mathbf{H} - \mathbf{H}_h\|^2_{\mathbf{H}_{0,\mathrm{curl}}(\Omega)\cap\mathbf{H}_{\mathrm{div}}(\Omega)} &\leq c\left(\|\nabla\times(\mathbf{H} - \mathbf{H}_h)\|^2_{\mathbf{L}^2(\Omega)} + \|\nabla\cdot(\mathbf{H} - \mathbf{H}_h)\|^2_{L^2(\Omega)}\right)\\ &\leq c\left(\frac{1}{\sigma}\nabla\times(\mathbf{H} - \mathbf{H}_h), \nabla\times(\mathbf{H} - \mathbf{H}_h)\right) + c\left(\nabla\cdot(\mathbf{H} - \mathbf{H}_h), \nabla\cdot(\mathbf{H} - \mathbf{H}_h)\right).\end{aligned}$$

Or, par définition de $\mathbf{H}$ et $\mathbf{H}_h$, pour tout $\mathbf{F}_h \in \mathbf{X}_h$, on a :

$$\left(\frac{1}{\sigma}\nabla\times(\mathbf{H} - \mathbf{H}_h), \nabla\times\mathbf{F}_h\right) + (\nabla\cdot(\mathbf{H} - \mathbf{H}_h), \nabla\cdot\mathbf{F}_h) = 0.$$

En combinant ces deux dernières relations, on obtient, pour tout $\mathbf{F}_h \in \mathbf{X}_h$,

$$\|\mathbf{H} - \mathbf{H}_h\|^2_{\mathbf{H}_{0,\mathrm{curl}}(\Omega)\cap\mathbf{H}_{\mathrm{div}}(\Omega)} \leq c\left(\frac{1}{\sigma}\nabla\times(\mathbf{H} - \mathbf{H}_h), \nabla\times(\mathbf{H} - \mathbf{F}_h)\right) + c\left(\nabla\cdot(\mathbf{H} - \mathbf{H}_h), \nabla\cdot(\mathbf{H} - \mathbf{F}_h)\right).$$

La forme bilinéaire étant continue (avec norme 1) sur $\mathbf{H}_{0,\mathrm{curl}}(\Omega) \cap \mathbf{H}_{\mathrm{div}}(\Omega)$, on obtient au final, pour tout $\mathbf{F}_h \in \mathbf{X}_h$,

$$\|\mathbf{H} - \mathbf{H}_h\|_{\mathbf{H}_{0,\mathrm{curl}}(\Omega)\cap\mathbf{H}_{\mathrm{div}}(\Omega)} \leq c\|\mathbf{H} - \mathbf{F}_h\|_{\mathbf{H}_{0,\mathrm{curl}}(\Omega)\cap\mathbf{H}_{\mathrm{div}}(\Omega)}.$$

Le résultat voulu est alors obtenu en prenant l'infimum sur toutes les fonctions $\mathbf{F}_h$. □

Notons $\varepsilon_h := \inf_{\mathbf{F}_h \in \mathbf{X}_h} \|\mathbf{H} - \mathbf{F}_h\|_{\mathbf{H}_{0,\mathrm{curl}}(\Omega)\cap\mathbf{H}_{\mathrm{div}}(\Omega)}$. La proposition précédente assure qu'il existe une constante c indépendante de h telle que,

$$\varepsilon_h \leq \|\mathbf{H} - \mathbf{H}_h\|_{\mathbf{H}_{0,\mathrm{curl}}(\Omega)\cap\mathbf{H}_{\mathrm{div}}(\Omega)} \leq c\varepsilon_h.$$

Ainsi, une condition nécessaire et suffisante pour que l'approximation $\mathbf{H}_h$ converge vers $\mathbf{H}$ lorsque h tend vers 0 est que $\varepsilon_h \to 0$. Or, puisque $\mathbf{X}_h \subset \mathbf{W}^{1,2}(\Omega)$, on obtient :

$$\forall h > 0, \qquad \varepsilon_h \geq \inf_{\mathbf{F}_h \in \mathbf{W}^{1,2}(\Omega)} \|\mathbf{H} - \mathbf{F}_h\|_{\mathbf{H}_{\mathrm{curl}}(\Omega)\cap\mathbf{H}_{\mathrm{div}}(\Omega)} =: \varepsilon. \tag{2.2.11}$$

Rappelons maintenant un résultat dû à Costabel :

Théorème 2.2.1 (cf. [35]). Si Ω n'est pas convexe et que sa frontière n'est pas de classe $\mathcal{C}^1$, alors l'espace $\mathbf{W}^{1,2}(\Omega)$ est un sous-espace strict et fermé de $\mathbf{H}_{\mathrm{curl}}(\Omega) \cap \mathbf{H}_{\mathrm{div}}(\Omega)$.

En d'autres termes, pour certains domaines Ω présentant des singularités (notamment des coins ou des arêtes rentrantes), on a $\varepsilon > 0$, ce qui implique que le schéma peut, pour certaines données, ne pas converger. En illustration, on renvoie à la figure 2.1. Notons que le résultat démontré dans [35] est plus précis car il donne des indications précises sur la codimension de $\mathbf{W}^{1,2}(\Omega)$ dans $\mathbf{H}_{\mathrm{curl}}(\Omega)\cap\mathbf{H}_{\mathrm{div}}(\Omega)$, en utilisant la géométrie de Ω. Nous allons mettre au point une méthode qui nécessite le moins d'informations possibles sur Ω, c'est pourquoi nous nous contentons de cette forme du théorème 2.2.1.

2.3 Contrôle de la divergence

La stabilisation dans $L^2(\Omega)$ de l'induction magnétique n'assurant pas la convergence, on doit se tourner vers un autre type de stabilisation. Une approche est celle de la stabilisation dans des espaces pondérés, suggérée par Costabel et al. (cf. [37] par exemple), et reprise par la suite par Buffa et al. [24]. On peut également trouver une autre approche, proposée par Bramble et al. [22, 21], qui consiste en une méthode de moindres carrés, et évite encore l'utilisation d'éléments finis complexes. Le point commun de ces méthodes est qu'elles sont basées sur des espaces intermédiaires. On utilise ici également des espaces intermédiaires, dans la continuité du travail de Bonito & Guermond [17]. On va démontrer un résultat d'approximation pour une formulation abstraite, car c'est sur cette formulation qu'on va se baser pour développer une formulation plus facile à implémenter. Dans toute la suite, on considère $\mu > 0$ et $\sigma > 0$, constants sur chaque sous-domaine Ω_i.

2.3.1 Stabilisation dans des espaces intermédiaires

En s'inspirant du problème (2.2.2), on peut introduire l'espace suivant :

$$\mathbf{X}^s := \left\{ \mathbf{F} \in \mathbf{H}_{0,\mathrm{curl}}(\Omega) \;\middle|\; \nabla\cdot(\mu\mathbf{F}) \in W^{s-1,2}(\Omega) \right\},$$

pour $s \in (0,1)$. On cherche alors $\mathbf{H} \in \mathbf{X}^s$ tel que,

$$\forall \mathbf{F} \in \mathbf{X}^s, \qquad \left(\frac{1}{\sigma}\nabla\times\mathbf{H}, \nabla\times\mathbf{F}\right) + \langle \nabla\cdot(\mu\mathbf{H}), \nabla\cdot(\mu\mathbf{F})\rangle_{W^{s-1,2}(\Omega)} = (\mathbf{g}, \mathbf{F}), \tag{2.3.1}$$

où $\langle\cdot,\cdot\rangle_{W^{s-1,2}(\Omega)}$ désigne le produit scalaire sur $W^{s-1,2}(\Omega)$. Notons que (2.2.2) correspond au cas $s = 1$. Pour l'instant, nous considérerons que $\mathbf{g}$ est à divergence nulle.

2.3.2 Coercivité et consistance

Là encore, on fait appel aux résultats de l'annexe A.

Proposition 2.3.1. Le problème (2.3.1) est bien posé.

Preuve. En utilisant la proposition A.4.1, on a l'existence de $\tau > 0$ dépendant uniquement de Ω et μ, et tel que $\mathbf{X}^s$ s'injecte continument dans $\mathbf{W}^{s,2}(\Omega)$, pour $s \in [0, \tau)$. En outre, on a l'inégalité :

$$\forall \mathbf{F} \in \mathbf{X}^s, \qquad \|\mathbf{F}\|^2_{\mathbf{W}^{s,2}(\Omega)} \leq c \left(\|\nabla \times \mathbf{F}\|^2_{\mathbf{L}^2(\Omega)} + \|\nabla \cdot (\mu \mathbf{F})\|^2_{W^{s-1,2}(\Omega)} \right),$$

où la constante c ne dépend que de Ω, μ et s. Il s'en suit que la forme bilinéaire définie par le membre de gauche de (2.3.1) est coercive sur $\mathbf{X}^s$, pour $s \in [0, \tau)$. En appliquant une nouvelle fois le théorème de Lax-Milgram, on a existence et unicité d'une solution au problème (2.3.1). □

Remarque 2.3.1. Dans toute la suite, on suppose sans perte de généralité que

$$\tau < \min \left(\tau_\mu, \tau_\sigma, \frac{1}{2} \right),$$

où τ_μ et τ_σ sont définis par (2.1.20).

En s'inspirant de la preuve de la proposition 2.2.1, on peut également montrer le résultat suivant :

Proposition 2.3.2. Pour $\mathbf{g} \in \mathbf{H}_{\text{div}=0}(\Omega)$, la solution de (2.1.19) est également la solution de (2.3.1).

Preuve. Soit $\mathbf{g} \in \mathbf{H}_{\text{div}=0}(\Omega)$ et $\mathbf{H} \in \mathbf{X}_\mu$ la solution de (2.1.19). On a bien $\mathbf{H} \in \mathbf{X}^s$, pour tout $s \in (0, 1)$. Soit $\mathbf{F} \in \mathbf{X}^s$. On résout le problème elliptique suivant : trouver $p \in W^{1,2}_0(\Omega)$ tel que,

$$\forall q \in W^{1,2}_0(\Omega), \qquad (\mu \nabla p, \nabla q) = (\mu \mathbf{F}, \nabla q).$$

On pose ensuite $\mathbf{w} := \mathbf{F} - \nabla p$. On voit immédiatement que $\mathbf{w} \in \mathbf{H}_{\text{curl}}(\Omega)$ et $\nabla \times \mathbf{w} = \nabla \times \mathbf{F}$. Par ailleurs, la condition $p_{|\Gamma} = 0$ implique que $\nabla p \times \mathbf{n} = 0$, et donc $\mathbf{w} \in \mathbf{H}_{0,\text{curl}}(\Omega)$. Enfin, par définition de p, on a $\nabla \cdot (\mu \mathbf{w}) = 0$, ce qui implique que $\mathbf{w} \in \mathbf{X}_\mu$. En utilisant (2.1.19), on obtient :

$$\begin{aligned} \left(\frac{1}{\sigma} \nabla \times \mathbf{H}, \nabla \times \mathbf{F} \right) + \langle \nabla \cdot (\mu \mathbf{H}), \nabla \cdot (\mu \mathbf{F}) \rangle_{W^{s-1,2}(\Omega)} &= \left(\frac{1}{\sigma} \nabla \times \mathbf{H}, \nabla \times \mathbf{w} \right) + \langle 0, \nabla \cdot (\mu \mathbf{F}) \rangle_{W^{s-1,2}(\Omega)} \\ &= (\mathbf{g}, \mathbf{w}). \end{aligned}$$

Or, $p \in W^{1,2}_0(\Omega)$ et $\mathbf{g}$ est à divergence nulle, ce qui implique que $(\mathbf{g}, \nabla p) = 0$. Au final, on a bien :

$$\left(\frac{1}{\sigma} \nabla \times \mathbf{H}, \nabla \times \mathbf{F} \right) + \langle \nabla \cdot (\mu \mathbf{H}), \nabla \cdot (\mu \mathbf{F}) \rangle_{W^{s-1,2}(\Omega)} = (\mathbf{g}, \mathbf{F}),$$

i.e. $\mathbf{H}$ est la solution de (2.3.1). □

Les deux problèmes étant équivalents, on s'intéresse à l'approximation de (2.3.1) par éléments finis.

2.3.3 Approximation par éléments finis de Lagrange

On introduit un espace d'approximation qui prend en compte l'interface Σ où les coefficients σ et μ peuvent présenter des discontinuités.

$$\mathbf{X}_h := \left\{ \mathbf{F}_h \in \mathbf{L}^1(\Omega),\ |\ \forall i,\ \mathbf{F}_h \in \boldsymbol{\mathcal{C}}^0(\overline{\Omega_i}),\ \forall K \in \mathcal{T}_h,\ \mathbf{F}_{h|K} \in \mathbb{P}^\ell \right\}. \tag{2.3.2}$$

On peut alors montrer que, pour tout $s \in \left[0, \frac{1}{2}\right)$, on a $\mathbf{X}_h \subset \mathbf{X}^s$. Dans toute la suite, on prend $s < \tau < \frac{1}{2}$. On peut alors définir une approximation $\mathbf{H}_h \in \mathbf{X}_h$ par :

$$\forall \mathbf{F}_h \in \mathbf{X}_h, \qquad \left(\frac{1}{\sigma}\nabla\times\mathbf{H}_h, \nabla\times\mathbf{F}_h\right) + \langle \nabla\cdot(\mu\mathbf{H}_h), \nabla\cdot(\mu\mathbf{F}_h)\rangle_{W^{s-1,2}(\Omega)} = (\mathbf{g}, \mathbf{F}_h). \tag{2.3.3}$$

En utilisant des arguments similaires à la partie précédente, on peut montrer le résultat d'approximation suivant :

Proposition 2.3.3. Pour $\mathbf{g} \in \mathbf{H}_{\mathrm{div}=0}(\Omega)$, on note $\mathbf{H} \in \mathbf{X}^s$ la solution de (2.3.1) et $\mathbf{H}_h \in \mathbf{X}_h$ la solution de (2.3.3). Il existe c uniforme en h telle que :

$$\|\mathbf{H} - \mathbf{H}_h\|_{\mathbf{X}^s} \leq c \inf_{\mathbf{F}_h \in \mathbf{X}_h} \|\mathbf{H} - \mathbf{F}_h\|_{\mathbf{X}^s}. \tag{2.3.4}$$

On rappelle que la norme sur $\mathbf{X}^s$ est définie par :

$$\|\mathbf{F}\|^2_{\mathbf{X}^s} := \|\mathbf{F}\|^2_{\mathbf{L}^2(\Omega)} + \|\nabla\times\mathbf{F}\|^2_{\mathbf{L}^2(\Omega)} + \|\nabla\cdot(\mu\mathbf{F})\|^2_{W^{s-1,2}(\Omega)}.$$

Enfin, on termine cette partie par le résultat d'approximation suivant :

Proposition 2.3.4. Soient $s \in [0, \tau)$ et $\mathbf{g} \in \mathbf{H}_{\mathrm{div}=0}(\Omega)$. On note $\mathbf{H} \in \mathbf{X}^s$ la solution de (2.3.1) et $\mathbf{H}_h \in \mathbf{X}_h$ la solution de (2.3.3). Il existe c uniforme en h et $r > 0$ tels que :

$$\|\mathbf{H} - \mathbf{H}_h\|_{\mathbf{X}^s} \leq c h^r \|\mathbf{g}\|_{\mathbf{L}^2(\Omega)}. \tag{2.3.5}$$

Preuve. Avec la proposition précédente, il suffit de montrer que l'on peut trouver $r > 0$ et $\mathbf{F}_h \in \mathbf{X}_h$ tels que

$$\|\mathbf{H} - \mathbf{F}_h\|_{\mathbf{X}^s} \leq c h^r \|\mathbf{g}\|_{\mathbf{L}^2(\Omega)},$$

avec c uniforme en h. Pour cela, on utilise les opérateurs d'approximation $\mathcal{K}_\delta$ et $\mathcal{C}_h$ définis dans l'annexe B (cf. (B.3.15) et (B.4.2)). On prend $t \in (s, \tau)$. On choisit alors $\mathbf{F}_h := \mathcal{C}_h\mathcal{K}_\delta\mathbf{H}$, pour un $\delta > 0$ à choisir. Traitons les trois termes intervenant dans la norme séparément, en utilisant une inégalité triangulaire faisant intervenir $\mathcal{K}_\delta\mathbf{H}$.

– En utilisant les résultats d'approximation (B.4.3), (B.3.18) et (B.3.16), on obtient :

$$\begin{aligned}\|\mathbf{H} - \mathbf{F}_h\|_{\mathbf{L}^2(\Omega)} &\leq \|\mathbf{H} - \mathcal{K}_\delta\mathbf{H}\|_{\mathbf{L}^2(\Omega)} + \|\mathcal{K}_\delta\mathbf{H} - \mathcal{C}_h\mathcal{K}_\delta\mathbf{H}\|_{\mathbf{L}^2(\Omega)} \\ &\leq c\delta^t \|\mathbf{H}\|_{\mathbf{W}^{t,2}(\Omega)} + ch^{\ell+1}\delta^{t-\ell-1}\|\mathbf{H}\|_{\mathbf{W}^{t,2}(\Omega)}\end{aligned}$$

– Pour le deuxième terme, on utilise les résultats d'approximation (B.4.3), (B.3.18) et (B.3.17) :

$$\begin{aligned}\|\nabla\times\mathbf{H} - \nabla\times\mathbf{F}_h\|_{\mathbf{L}^2(\Omega)} &\leq \|\nabla\times\mathbf{H} - \nabla\times\mathcal{K}_\delta\mathbf{H}\|_{\mathbf{L}^2(\Omega)} + \|\nabla\times\mathcal{K}_\delta\mathbf{H} - \nabla\times\mathcal{C}_h\mathcal{K}_\delta\mathbf{H}\|_{\mathbf{L}^2(\Omega)} \\ &\leq c\delta^t \|\nabla\times\mathbf{H}\|_{\mathbf{W}^{t,2}(\Omega)} + ch^{\ell}\delta^{t-\ell-1}\|\mathbf{H}\|_{\mathbf{W}^{t,2}(\Omega)}\end{aligned}$$

– Enfin, pour la divergence, on utilise le fait que $\|\nabla\cdot\mathbf{F}\|_{W^{s-1,2}(\Omega)} \leq \|\mathbf{F}\|_{\mathbf{W}^{s,2}(\Omega)}$, pour obtenir,

$$\begin{aligned}\|\nabla\cdot(\mu(\mathbf{H}-\mathbf{F}_h))\|_{W^{s-1,2}(\Omega)} &\leq \|\mu(\mathbf{H}-\mathbf{F}_h)\|_{\mathbf{W}^{s,2}(\Omega)}\\ &\leq c\|\mathbf{H}-\mathbf{F}_h\|_{\mathbf{W}^{s,2}(\Omega)}.\end{aligned}$$

La dernière inégalité, non triviale (c'est l'objet de la proposition A.2.1), est vraie puisque $s<\frac{1}{2}$. La constante c dépend alors de μ et de la décomposition de Ω en sous-domaines Ω_i. Enfin, on applique les résultats d'approximation (B.4.3), (B.3.18) et (B.3.16), pour aboutir à :

$$\begin{aligned}\|\nabla\cdot(\mu(\mathbf{H}-\mathbf{F}_h))\|_{W^{s-1,2}(\Omega)} &\leq c\|\mathbf{H}-\mathcal{K}_\delta\mathbf{H}\|_{\mathbf{W}^{s,2}(\Omega)} + c\|\mathcal{K}_\delta\mathbf{H}-\mathcal{C}_h\mathcal{K}_\delta\mathbf{H}\|_{\mathbf{W}^{s,2}(\Omega)}\\ &\leq c\delta^{t-s}\|\mathbf{H}\|_{\mathbf{W}^{t,2}(\Omega)} + ch^{\ell+1-s}\delta^{t-\ell-1}\|\mathbf{H}\|_{\mathbf{W}^{t,2}(\Omega)}.\end{aligned}$$

Enfin, on regroupe toutes ces inégalités en utilisant (2.1.20), pour obtenir :

$$\|\mathbf{H}-\mathbf{F}_h\|_{\mathbf{X}^s} \leq c\left(\delta^{t-s}+h^\ell\delta^{t-\ell-1}\right)\|\mathbf{g}\|_{\mathbf{L}^2(\Omega)}.$$

On peut maintenant choisir δ de sorte que $\delta^{t-s}=h^\ell\delta^{t-\ell-1}$, i.e. $\delta=h^{\frac{\ell}{1-s+\ell}}$. On obtient alors :

$$\|\mathbf{H}-\mathbf{F}_h\|_{\mathbf{X}^s} \leq ch^r\|\mathbf{g}\|_{\mathbf{L}^2(\Omega)},$$

avec $r=\frac{(t-s)\ell}{1-s+\ell}$. □

2.3.4 Inconvénients de cette méthode

À ce stade, on a construit (tout au moins de manière théorique) une méthode basée sur des espaces intermédiaires qui assure la convergence des solutions discrètes vers la solution continue. Néanmoins, deux inconvénients sont à noter :

– Nous avons uniquement prouvé la convergence de la méthode pour le problème aux limites, i.e. le problème (2.1.5)-(2.1.6)-(2.1.7), lorsque le second membre est à divergence nulle. Or, les formulations variationnelles (2.1.19) ou (2.3.1) autorisent un second membre à divergence non nulle. Dans ce cas, les deux problèmes ne sont plus équivalents. Ce problème a déjà été soulevé dans [17], et implique que la méthode ne sera pas adaptée à la recherche de valeurs propres (i.e. à l'approximation du problème (2.1.8)-(2.1.9)-(2.1.10)).
– Le deuxième inconvénient de cette méthode est qu'elle met en jeu le produit scalaire dans l'espace $W^{s-1,2}(\Omega)$. Il faut donc savoir calculer (ou au moins approcher numériquement) ce produit scalaire, ce qui n'est pas aisé.

En conséquence, on va devoir modifier quelque peu cette méthode, afin de remplir ces deux objectifs : obtenir de la convergence quel que soit le second membre, et ne faire intervenir que des termes faciles à calculer.

2.3.5 Formulation mixte

Expliquons comment nous passons de la formulation (2.3.1) à une formulation mixte, plus adaptée. Il ne s'agit ici que de donner les idées directrices, mais pas de démonstrations au sens propre. On démarre de la forme bilinéaire a_h^1 sur $\mathbf{X}_h$ définie par :

$$a_h^1(\mathbf{F}_h,\mathbf{G}_h) := \left(\frac{1}{\sigma}\nabla\times\mathbf{F}_h, \nabla\times\mathbf{G}_h\right) + \langle\nabla\cdot(\mu\mathbf{F}_h), \nabla\cdot(\mu\mathbf{G}_h)\rangle_{W^{s-1,2}(\Omega)}.$$

On procède en quatre étapes :

1. On se débarrasse du produit scalaire dans $W^{s-1}(\Omega)$. En vertu de l'inégalité inverse

$$\|\nabla\cdot(\mu\mathbf{F}_h)\|_{W^{s-1,2}(\Omega)} \leq ch^{-s}\|\nabla\cdot(\mu\mathbf{F}_h)\|_{W^{-1,2}(\Omega)},$$

vraie pour tout $\mathbf{F}_h \in \mathbf{X}_h$, on remplace a_h^1 par a_h^2 définie par :

$$a_h^2(\mathbf{F}_h,\mathbf{G}_h) := \left(\frac{1}{\sigma}\nabla\times\mathbf{F}_h, \nabla\times\mathbf{G}_h\right) + h^{-2s}\left\langle\nabla\cdot(\mu\mathbf{F}_h), \nabla\cdot(\mu\mathbf{G}_h)\right\rangle_{W^{-1,2}(\Omega)}.$$

2. On traite le produit scalaire dans $W^{-1,2}(\Omega)$ à l'aide d'une formulation mixte. À ces fins, on introduit l'opérateur $(-\Delta_\mu)^{-1} : W^{-1,2}(\Omega) \to W_0^{1,2}(\Omega)$ défini par :

$$\forall q \in W_0^{1,2}(\Omega), \qquad \left(\mu\nabla\left((-\Delta_\mu)^{-1}f\right), \nabla q\right) = -\left\langle f, q\right\rangle_{W^{-1,2}(\Omega),W_0^{1,2}(\Omega)},$$

le membre de droite étant le crochet de dualité. On peut alors vérifier que la forme bilinéaire b définie sur $W^{-1,2}(\Omega)$ par :

$$\forall f,g \in W^{-1,2}(\Omega), \qquad b(f,g) = -\left\langle f, (-\Delta_\mu)^{-1}g\right\rangle_{W^{-1,2}(\Omega),W_0^{1,2}(\Omega)}$$

est un produit scalaire équivalent au produit scalaire usuel sur $W^{-1,2}(\Omega)$ (voir par exemple [41, Chapitre 4] pour le cas $\mu \equiv 1$, i.e. le cas où $(-\Delta_\mu)^{-1}$ est l'inverse de l'opérateur de Laplace avec conditions de Dirichlet homogènes). Soient alors $\mathbf{F}_h, \mathbf{G}_h \in \mathbf{X}_h$. On note $p := (-\Delta_\mu)^{-1}(\nabla\cdot(\mu\mathbf{F}_h))$. On remplace alors a_h^2 par a_h^3 en utilisant ce nouveau produit scalaire :

$$\begin{aligned} a_h^3(\mathbf{F}_h,\mathbf{G}_h) &= \left(\frac{1}{\sigma}\nabla\times\mathbf{F}_h, \nabla\times\mathbf{G}_h\right) - h^{-2s}\left\langle\nabla\cdot(\mu\mathbf{G}_h), p\right\rangle_{W^{-1,2}(\Omega),W_0^{1,2}(\Omega)} \\ &= \left(\frac{1}{\sigma}\nabla\times\mathbf{F}_h, \nabla\times\mathbf{G}_h\right) + h^{-2s}\left(\mu\mathbf{G}_h, \nabla p\right). \end{aligned}$$

On a par ailleurs, pour tout $q \in W_0^{1,2}(\Omega)$,

$$(\mu\nabla p, \nabla q) = -\left\langle\nabla\cdot(\mu\mathbf{F}_h), q\right\rangle_{W^{-1,2}(\Omega),W_0^{1,2}(\Omega)} = \left(\mu\mathbf{F}_h, \nabla q\right). \tag{2.3.6}$$

On introduit donc une nouvelle inconnue p, que l'on va également approcher par éléments finis. On utilise alors l'espace d'approximation suivant :

$$M_h := \left\{q_h \in \mathcal{C}^0(\overline{\Omega}) \cap W_0^{1,2}(\Omega) \mid \forall K \in \mathcal{T}_h,\ q_{h|K} \in \mathbb{P}^{\ell_p}\right\}.$$

On note $p_h \in M_h$ un élément dont le but est d'approcher $h^{-2s}p$. En combinant la forme bilinéaire a_h^3 et (2.3.6), on utilise à présent la forme bilinéaire a_h^4 définie sur $[\mathbf{X}_h\times M_h]^2$ par :

$$\begin{aligned} a_h^4\left((\mathbf{F}_h,p_h),(\mathbf{G}_h,q_h)\right) := &\left(\frac{1}{\sigma}\nabla\times\mathbf{F}_h, \nabla\times\mathbf{G}_h\right) + (\mu\nabla p_h, \mathbf{G}_h) \\ &+ h^{2s}\left(\mu\nabla p_h, \nabla q_h\right) - \left(\mu\mathbf{F}_h, \nabla q_h\right). \end{aligned}$$

3. On ajoute enfin un terme de stabilisation qui, on le verra par la suite, facilite le caractère bien posé de la formulation discrète et évite d'imposer des contraintes importantes sur les espaces d'approximation. On utilise finalement la forme bilinéaire suivante :

$$a_h\left((\mathbf{F}_h,p_h),(\mathbf{G}_h,q_h)\right) := \left(\frac{1}{\sigma}\nabla\times\mathbf{F}_h,\nabla\times\mathbf{G}_h\right) + \sum_i h^{2(1-s)}\left(\nabla\cdot(\mu\mathbf{F}_h),\nabla\cdot(\mu\mathbf{G}_h)\right)_{\Omega_i} + \left(\mu\nabla p_h,\mathbf{G}_h\right) + h^{2s}\left(\mu\nabla p_h,\nabla q_h\right) - \left(\mu\mathbf{F}_h,\nabla q_h\right). \tag{2.3.7}$$

4. Partant de cette forme bilinéaire, on est tenté de chercher $(\mathbf{H}_h,p_h)\in\mathbf{X}_h\times M_h$ tels que,

$$\forall(\mathbf{F}_h,q_h)\in\mathbf{X}_h\times M_h,\qquad a_h\left((\mathbf{H}_h,p_h),(\mathbf{F}_h,q_h)\right)=\left(\mathbf{g},\mathbf{F}_h\right).$$

Si $\mathbf{g}$ est à divergence nulle, cela ne pose aucun problème. Si $\mathbf{g}$ n'est pas à divergence nulle en revanche, la formulation n'est pas consistante. On pallie à ce problème en résolvant :

$$\forall(\mathbf{F}_h,q_h)\in\mathbf{X}_h\times M_h,\qquad a_h\left((\mathbf{H}_h,p_h),(\mathbf{F}_h,q_h)\right)=\left(\mathbf{g},\mathbf{F}_h\right)+h^{2s}\left(\mathbf{g},\nabla q_h\right).$$

Remarque 2.3.2. Dans la suite, la nouvelle inconnue p_h sera appelée abusivement *pression magnétique*, mais elle n'a rien à voir avec la quantité physique homonyme $\dfrac{|\mathbf{B}|^2}{2\mu_0}$.

Afin d'être le plus complet possible, on montre maintenant la relation d'orthogonalité de Galerkin suivante (consistance de la méthode).

Proposition 2.3.5. Soit $\mathbf{g}\in\mathbf{L}^2(\Omega)$. Soit $\mathbf{H}\in\mathbf{X}_\mu$ la solution de (2.1.19). Il existe $p\in W_0^{1,2}(\Omega)$ tel que,

$$\forall(\mathbf{F},q)\in\mathbf{X}^s\times W_0^{1,2}(\Omega),\qquad a_h\left((\mathbf{H},p),(\mathbf{F},q)\right)=\left(\mathbf{g},\mathbf{F}\right)+h^{2s}\left(\mathbf{g},\nabla q\right).$$

Preuve. Soit $\mathbf{g}\in\mathbf{L}^2(\Omega)$. On note $\mathbf{H}\in\mathbf{X}_\mu$ la solution de (2.1.19) et $p\in W_0^{1,2}(\Omega)$ la solution du problème suivant :

$$\forall q\in W_0^{1,2}(\Omega),\qquad \left(\mu\nabla p,\nabla q\right)=\left(\mathbf{g},\nabla q\right).$$

On prend alors $(\mathbf{F},q)\in\mathbf{X}^s\times W_0^{1,2}(\Omega)$. On introduit également $r\in W_0^{1,2}(\Omega)$ la solution de :

$$\forall z\in W_0^{1,2}(\Omega),\qquad \left(\mu\nabla r,\nabla z\right)=\left(\mu\mathbf{F},\nabla z\right),$$

et on note $\mathbf{w}=\mathbf{F}-\nabla r$. Avec cette construction, on a $\mathbf{w}\in\mathbf{X}_\mu(\Omega)$ et $\nabla\times\mathbf{w}=\nabla\times\mathbf{F}$. On calcule alors $a_h\left((\mathbf{H},p),(\mathbf{F},q)\right)$. Puisque $\nabla\cdot(\mu\mathbf{H})=0$, il n'y a que quatre termes à évaluer (cf. (2.3.7)) : en utilisant (2.1.19), les définitions de p et r, ainsi que $\nabla\cdot(\mu\mathbf{H})=0$, on obtient :

$$\begin{aligned}\left(\frac{1}{\sigma}\nabla\times\mathbf{H},\nabla\times\mathbf{F}\right)+\left(\mu\nabla p,\mathbf{F}\right)+h^{2s}\left(\mu\nabla p,\nabla q\right)-\left(\mu\mathbf{H},\nabla q\right)&\\ =\left(\frac{1}{\sigma}\nabla\times\mathbf{H},\nabla\times\mathbf{F}\right)+\left(\mu\nabla p,\nabla r\right)+h^{2s}\left(\mathbf{g},\nabla q\right)&\\ =\left(\mathbf{g},\mathbf{w}\right)+\left(\mathbf{g},\nabla r\right)+h^{2s}\left(\mathbf{g},\nabla q\right)&\\ =\left(\mathbf{g},\mathbf{F}\right)+h^{2s}\left(\mathbf{g},\nabla q\right),&\end{aligned}$$

ce qui est le résultat attendu. □

2.3.6 Convergence (Résultats principaux de l'annexe B)

En pratique, il n'est pas forcément aisé de construire un espace d'approximation conforme dans $\mathbf{H}_{0,\mathrm{curl}}(\Omega)$. On va alors ajouter des termes de pénalisation. On renvoie à l'annexe B pour tous les détails concernant la formulation employée en pratique. Notons que l'annexe B est une version préliminaire d'un article, qui n'a pas encore été soumis. Néanmoins, déjà deux résultats importants sont démontrés dans cette annexe. Le premier, à savoir le théorème B.5.3 concerne la convergence de notre approximation dans le cadre d'un problème aux limites. Il peut s'écrire de la manière suivante :

Théorème 2.3.1. Soit $\mathbf{g} \in \mathbf{L}^2(\Omega)$. On note $\mathbf{H}$ la solution de (2.1.19) et $(\mathbf{H}_h, p_h)$ la solution discrète obtenue par notre nouvelle méthode. Il existe $t > 0$ tel que, si $s \in (0,t)$ (s étant l'indice utilisé dans la définition de la forme bilinéaire),

$$\|\mathbf{H} - \mathbf{H}_h\|_{\mathbf{L}^2(\Omega)} \leq c h^r \|\mathbf{g}\|_{\mathbf{L}^2(\Omega)},$$

avec $r > 0$ et c uniforme en h et ne dépendant pas de $\mathbf{H}$ ou $\mathbf{g}$.

Remarque 2.3.3. Dans l'annexe B, on introduit un paramètre $\alpha \in (0,1)$ dans la forme bilinéaire. Ce paramètre correspond en fait à $\alpha = 1 - s$. Dans la suite, on utilisera plutôt α commme paramètre.

Le deuxième résultat important de cette annexe B concerne les valeurs propres. Il s'agit de la section B.6, dont le résultat principal peut être énoncé ainsi :

Théorème 2.3.2. Pour $\alpha \in (1-t, 1)$ (i.e. $s \in (0,t)$), cette nouvelle méthode d'approximation est spectralement correcte, i.e. permet d'approcher sans pollution de spectre les valeurs propres du problème (2.1.8)-(2.1.9)-(2.1.10).

Pour les détails (notamment mathématiques) concernant cette assertion, on renvoie à l'annexe B. Ces deux résultats assurent donc que la méthode mise au point est correcte aussi bien pour résoudre des problèmes aux limites que pour calculer des valeurs propres.

2.3.7 Illustrations numériques

Nous terminons notre description de la méthode par quelques illustrations numériques, qui concernent à la fois le problème aux limites et le problème de valeurs propres. Nous présentons ici uniquement des calculs 2D.

Singularité géométrique

Pour justifier les restrictions sur les valeurs de α (cf. 2.3.3 pour la définition), à savoir α proche de 1, on commence par résoudre le même problème que dans [17], avec différentes valeurs de α. Rappelons le cadre. On se place dans un domaine plan en forme de L.

$$\Omega := (-1,1)^2 \backslash ([0,1]\times[-1,0])\,.$$

On prend $\sigma = 1$, $\mu = 1$, et on cherche $\mathbf{H}$ tel que :

$$\nabla\times\nabla\times\mathbf{H} = 0, \qquad \nabla\cdot\mathbf{H} = 0, \qquad \mathbf{H}\times\mathbf{n}_{|\partial\Omega} = \mathbf{G}\times\mathbf{n}, \tag{2.3.8}$$

où $\mathbf{G}$ est une donnée ; ici, on prend $\mathbf{G} = \nabla\phi$, où ϕ est défini en coordonnées polaires par $\phi(r,\theta) = r^{\frac{2}{3}} \sin\left(\frac{2}{3}\theta\right)$. On peut noter que $\mathbf{G}\times\mathbf{n}$ est suffisamment régulière au bord pour que ce

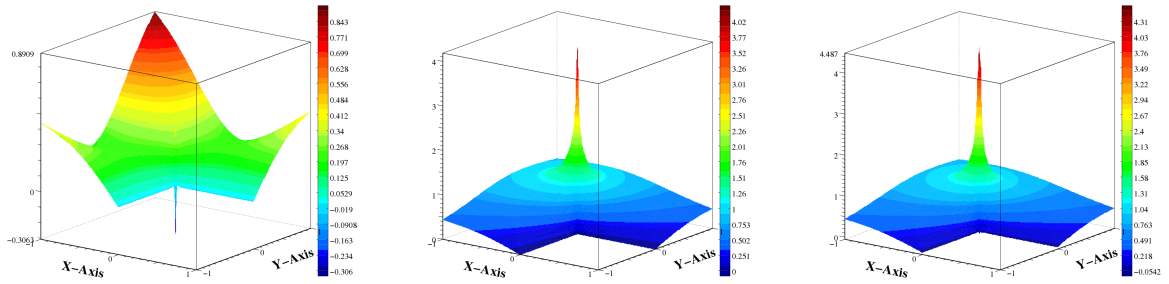

FIG. 2.1: Comparaison des approximations pour $\alpha = 0$ (à gauche) et $\alpha = 0,75$ (à droite) avec la solution exacte (au centre).

problème soit équivalent à un problème du type $\nabla\times\nabla\times\mathbf{H} = \mathbf{g}$, avec condition de divergence nulle et condition de bord homogène. Dans ces conditions, la solution cherchée est en fait $\mathbf{H} = \nabla\phi$, qui présente des singularités. Plus précisément, pour tout $t \in \left[0, \frac{2}{3}\right)$, $\mathbf{H} \in \mathbf{W}^{t,2}(\Omega)$. La figure 2.1 illustre le défaut de convergence lorsque α est proche de 0 (i.e. s proche de 1). Sur un même maillage, on compare la composante radiale de la solution approchée obtenue pour $\alpha = 0$ (à gauche), de la solution réelle (au milieu) et de la solution approchée obtenue pour $\alpha = 0.75$ (à droite). Notons que le cas $\alpha = 0$ correspond au cas 2.2.2 dont on a prédit le défaut de convergence.

Sauts de perméabilité

Illustrons maintenant le comportement de l'approximation pour des cas où les perméabilités sont discontinues. On reprend un exemple présenté dans [32]. On garde Ω le domaine en L, que l'on décompose en trois sous-domaines :

$$\Omega_1 = (0,1)^2, \qquad \Omega_2 = (-1,0)\times(0,1), \qquad \Omega_3 = (-1,0)^2.$$

On prend alors une distribution de perméabilité telle que $\mu_{|\Omega_2} = 1$ et $\mu_{|\Omega_1} = \mu_{|\Omega_3} =: \mu_r$. On note $\lambda > 0$ une solution de

$$\tan\left(\frac{\lambda\pi}{4}\right)\tan\left(\frac{\lambda\pi}{2}\right) = \mu_r.$$

On définit alors le potentiel scalaire $S_\lambda(r,\theta) = r^\lambda\phi_\lambda(\theta)$, où la fonction ϕ_λ est définie par :

$$\begin{aligned}
\phi_\lambda(\theta) &= \sin(\lambda\theta) && \text{si } 0 \le \theta < \frac{\pi}{2},\\
\phi_\lambda(\theta) &= \frac{\sin\left(\frac{\lambda\pi}{2}\right)}{\cos\left(\frac{\lambda\pi}{4}\right)}\cos\left(\lambda\left(\theta - \frac{3\pi}{4}\right)\right) && \text{si } \frac{\pi}{2} \le \theta < \pi,\\
\phi_\lambda(\theta) &= \sin\left(\lambda\left(\frac{3\pi}{2} - \theta\right)\right) && \text{si } \pi \le \theta \le \frac{3\pi}{2}.
\end{aligned}$$

On résout à présent le problème suivant :

$$\nabla\times\nabla\times\mathbf{H} = 0, \qquad \nabla\cdot(\mu\mathbf{H}) = 0, \qquad \mathbf{H}\times\mathbf{n}_{|\partial\Omega} = \nabla S_\lambda\times\mathbf{n},$$

La solution de ce problème est alors $\mathbf{H} = \nabla S_\lambda$. On présente deux séries de calculs, pour $\lambda = 0.535$ et $\lambda = 4.535$. Dans ces deux cas, on a $\mu_r = 0.499 \pm 10^{-3}$. On s'intéresse à la norme L^2 de

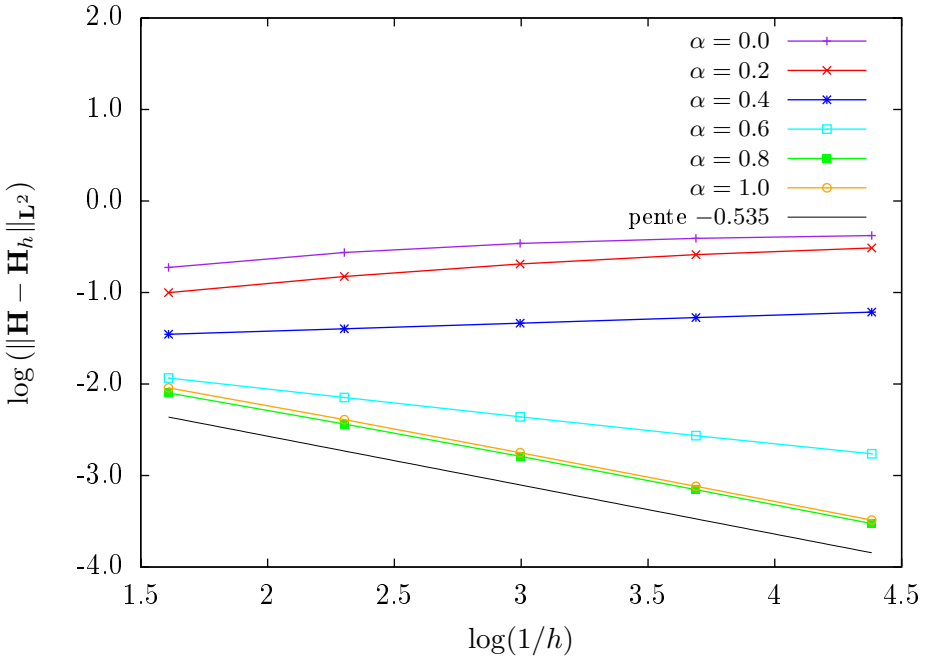

FIG. 2.2: Courbes de convergence pour le cas $\lambda = 0.535$. On note qu'on retrouve numériquement l'ordre de convergence optimal 0.535 pour $\alpha = 0.8$ ou 1.

la différence entre $\mathbf{H}$ et $\mathbf{H}_h$. Le cas $\lambda = 0.535$ correspond à une solution singulière, pour laquelle on s'attend à un ordre de convergence inférieur à 0.535. Le deuxième cas, correspondant à une solution régulière, peut donner des ordres de convergence supérieurs à 2. Les courbes sont présentées en figure 2.2 et 2.3.

Calcul de valeurs propres

Enfin, on termine ces illustrations par un calcul de valeurs propres. On se place sur un domaine

$$\Omega = (-1,1)^2,$$

découpé en quatre sous-domaines :

$$\Omega_1 = (0,1)^2, \qquad \Omega_2 = (-1,0)\times(0,1), \qquad \Omega_3 = (-1,0)^2, \qquad \Omega_4 = (0,1)\times(-1,0).$$

On choisit alors une distribution de perméabilité telle que $\mu_{|\Omega_1} = \mu_{|\Omega_3} = 1$ et $\mu_{|\Omega_2} = \mu_{|\Omega_4} =: \mu_r$. Un benchmark des valeurs propres pour les cas $\mu_r \in \{\frac{1}{2}, \frac{1}{10}, \frac{1}{100}, \frac{1}{10^8}\}$ a été effectué par Dauge et al. [40]. On présente ici le cas $\mu_r = 0.1$, avec $\alpha = 0.7$, et on compare les résultats avec le benchmark. Le tableau 2.1 présente les résultats pour les quatre premières valeurs propres. La colonne "coc" désigne l'ordre de convergence calculé à partir des erreurs. On peut remarquer que la deuxième valeur propre est plus difficile à approcher. Cela tient au fait qu'elle présente une singularité au niveau de l'origine.

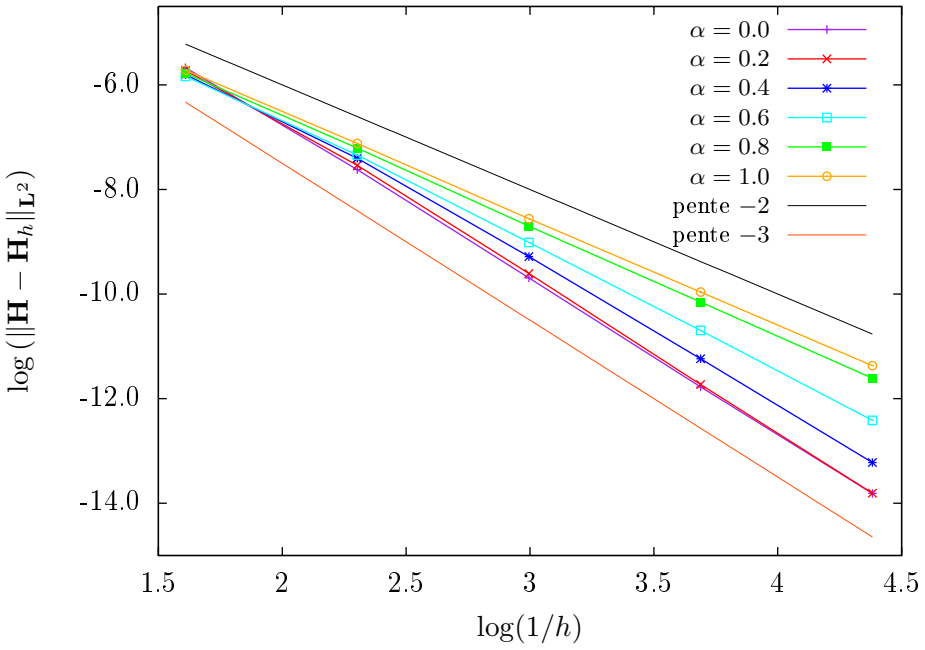

FIG. 2.3: Courbes de convergence pour le cas $\lambda = 4.535$. Il semble que l'ordre de convergence soit $3-\alpha$, mais nous n'avons pas été en mesure de le prouver précisément de manière théorique.

	$\lambda_1 \simeq 4.534$			$\lambda_2 \simeq 6.250$		
1/h	val.	rel. err.	coc	val.	rel. err.	coc
5	4.538	$8.358\,10^{-4}$	N/A	7.047	$1.274\,10^{-1}$	N/A
10	4.534	$9.592\,10^{-5}$	3.12	7.038	$1.261\,10^{-1}$	0.01
20	4.534	$3.992\,10^{-5}$	1.26	6.764	$8.218\,10^{-2}$	0.62
40	4.534	$1.606\,10^{-5}$	1.31	6.506	$4.096\,10^{-2}$	1.00
	$\lambda_3 \simeq 7.037$			$\lambda_4 \simeq 22.342$		
1/h	val.	rel. err.	coc	val.	rel. err.	coc
5	9.076	$2.897\,10^{-1}$	N/A	22.51	$7.489\,10^{-3}$	N/A
10	7.404	$5.220\,10^{-2}$	2.47	22.36	$9.487\,10^{-4}$	3.05
20	7.037	$2.274\,10^{-5}$	11.1	22.34	$9.935\,10^{-5}$	3.26
40	7.037	$2.597\,10^{-6}$	3.13	22.34	$9.718\,10^{-6}$	3.35

TAB. 2.1: Approximation des valeurs propres dans un carré, avec une perméabilité variable.

2.4 Un résultat sans stabilisation

On a vu dans la partie précédente que la nouvelle méthode de résolution faisait intervenir un terme de stabilisation sur la divergence de $\mu\mathbf{H}$. On peut raisonnablement se demander si ce terme est vraiment nécessaire pour la convergence du schéma numérique. On va montrer dans cette partie que, dans un cadre simplifié, on peut parfois s'en passer. Néanmoins, pour assurer la convergence, des contraintes sur les espaces d'approximation sont nécessaires. Par ailleurs, on verra que numériquement, l'un des cas de figure qui nous intéresse semble ne pas donner de convergence, ce qui explique qu'on garde en pratique le terme de stabilisation.

2.4.1 Cadre

On s'intéresse au cas μ, σ constants (on les prend égaux à 1 sans perte de généralité) et $\alpha = 1$. On veut montrer que, pour certains choix d'éléments finis, on peut considérer une forme bilinéaire sans stabilisation de la divergence, i.e. sans le terme $h^2\left(\nabla\cdot\mathbf{H}, \nabla\cdot\mathbf{F}\right)$. On note donc dans cette partie a_s la forme bilinéaire définie sur $\left[\mathbf{H}_{0,\mathrm{curl}}\left(\Omega\right)\times W_0^{1,2}(\Omega)\right]^2$ par : $\forall(\mathbf{H},p),(\mathbf{F},q)\in\mathbf{H}_{0,\mathrm{curl}}\left(\Omega\right)\times W_0^{1,2}(\Omega)$,

$$a_s\left((\mathbf{H},p),(\mathbf{F},q)\right) = \left(\nabla\times\mathbf{H},\nabla\times\mathbf{F}\right) + \left(\nabla p,\mathbf{F}\right) - \left(\mathbf{H},\nabla q\right) + \left(\nabla p,\nabla q\right). \tag{2.4.1}$$

On va utiliser la norme naturelle sur $\mathbf{H}_{0,\mathrm{curl}}\left(\Omega\right)\times W_0^{1,2}(\Omega)$ définie par

$$|\!|\!|\mathbf{H},q|\!|\!|^2 := \|\mathbf{H}\|^2_{\mathbf{L}^2(\Omega)} + \|\nabla\times\mathbf{H}\|^2_{\mathbf{L}^2(\Omega)} + \|\nabla p\|^2_{\mathbf{L}^2(\Omega)}. \tag{2.4.2}$$

On considère toujours une famille de maillages $\{\mathcal{T}_h\}_{h>0}$ comme en 2.2. On note toujours $\hat{K}$ un élément de référence, et on se donne une fonction $\hat{b}$ définie sur $\hat{K}$, nulle sur le bord (fonction "bulle"). Pour tout $K\in\mathcal{T}_h$, on définit $b_K := \hat{b}\circ T_K^{-1}$. On va montrer que la nouvelle méthode converge lorsqu'on choisit les espaces d'approximation suivants :

$$\mathbf{X}_h := \left\{\mathbf{F}_h\in\boldsymbol{\mathcal{C}}^0(\bar{\Omega})\mid\forall K\in\mathcal{T}_h,\ \mathbf{F}_{h|K}\in\mathbb{P}^1\right\}, \tag{2.4.3}$$

$$M_h := \left\{q_h\in W_0^{1,2}(\Omega),\ \forall K\in\mathcal{T}_h,\ q_{|K}\in\mathbb{P}^1\oplus\mathbb{R}b_K\right\}. \tag{2.4.4}$$

On suppose encore (pour simplifier le propos) que

$$\mathbf{X}_h\subset\mathbf{H}_{0,\mathrm{curl}}\left(\Omega\right). \tag{2.4.5}$$

On utilise une technique à la Fortin (cf. [49] ou [47, Lemme 5.2.6]).

2.4.2 Un projecteur utile

Lemme 2.4.1. Pour tout h, il existe une application linéaire $\pi_h : W_0^{1,2}(\Omega)\to M_h$ vérifiant les deux conditions suivantes :

$$\forall q\in W_0^{1,2}(\Omega),\ \forall\mathbf{F}_h\in\mathbf{X}_h,\ \left(\nabla\cdot\mathbf{F}_h,\pi_h q\right) = \left(\nabla\cdot\mathbf{F}_h,q\right), \tag{2.4.6}$$

$$\exists c>0,\ \forall q\in W_0^{1,2}(\Omega),\ \|\pi_h q\|_{W_0^{1,2}(\Omega)}\le\|q\|_{W_0^{1,2}(\Omega)}, \tag{2.4.7}$$

où la constante c est uniforme en h.

Preuve. Remarquons que la relation (2.4.6) ne fait intervenir que des fonction $\mathbf{F}_h \in \mathbf{X}_h$. Il s'en suit que sur chaque élément $K \in \mathcal{T}_h$, $\nabla\cdot\mathbf{F}_h$ est constante. Ainsi, une condition suffisante pour que (2.4.6) soit satisfaite est que :

$$\forall q \in W_0^{1,2}(\Omega),\ \forall K \in \mathcal{T}_h, \qquad \int_K \pi_h q = \int_K q. \tag{2.4.8}$$

On note $\mathcal{C}_h$ un interpolateur $W_0^{1,2}(\Omega) \to M_h$ de type Clément (cf. [33, 16] par exemple), et on cherche, pour $q \in W_0^{1,2}(\Omega)$, $\pi_h q$ sous la forme

$$\pi_h q = \mathcal{C}_h q + \sum_{K\in\mathcal{T}_h} \gamma_K b_K,$$

où les γ_K sont des nombres réels à déterminer. Rappelons qu'il existe c uniforme en h telle que, pour tout $q \in W_0^{1,2}(\Omega)$,

$$\|\mathcal{C}_h q\|_{W_0^{1,2}(\Omega)} \le c\|q\|_{W_0^{1,2}(\Omega)}, \tag{2.4.9}$$

$$\|\mathcal{C}_h q - q\|_{L^2(\Omega)} \le ch\|q\|_{W_0^{1,2}(\Omega)}. \tag{2.4.10}$$

Puisqu'on cherche à imposer (2.4.8), on obtient :

$$\forall K \in \mathcal{T}_h, \qquad \gamma_K = \frac{\int_K (q - \mathcal{C}_h q)}{\int_K b_K}.$$

En supposant, sans perte de généralité, que $|\hat{K}|^{-1}\int_{\hat{K}} \hat{b} = 1$, un changement de variable affine assure que $\int_K b_K = |K|$, ce qui induit :

$$\forall K \in \mathcal{T}_h, \qquad \gamma_K = |K|^{-1}\int_K (q - \mathcal{C}_h q)\,.$$

On a donc construit un candidat π_h, dont on sait par construction qu'il vérifie (2.4.6). Par ailleurs, par construction, il est bien linéaire. Il ne reste donc plus qu'à vérifier (2.4.7). Utilisant l'inégalité triangulaire, la partie $\mathcal{C}_h q$ est immédiate, en utilisant (2.4.9). Pour la seconde partie, on remarque que :

$$\left\| \sum_{K\in\mathcal{T}_h} \gamma_K b_K \right\|^2_{W_0^{1,2}(\Omega)} = \sum_{K\in\mathcal{T}_h} \gamma_K^2 \|\nabla b_K\|^2_{\mathbf{L}^2(K)}.$$

En appliquant l'inégalité de Cauchy-Schwarz dans la définition de γ_K, et on calculant par changement de variables $\|\nabla b_K\|_{\mathbf{L}^2(K)}$, on obtient :

$$\gamma_K^2 \le |K|^{-1}\|q - \mathcal{C}_h q\|_{L^2(K)},$$

$$\|\nabla b_K\|^2_{\mathbf{L}^2(K)} \le \beta_0^2 \frac{h_{\hat{K}}^2}{h_K^2}\frac{|K|}{|\hat{K}|}\|\hat{\nabla}\hat{b}\|^2_{\mathbf{L}^2(\hat{K})},$$

où β_0 est défini par (2.2.5). Puisque $\hat{K}$ et $\hat{b}$ sont indépendants de h, on obtient donc, en utilisant l'hypothèse (2.2.6) :

$$\|\nabla b_K\|^2_{\mathbf{L}^2(K)} \le c\frac{|K|}{h^2},$$

où c est uniforme en h. On peut alors sommer et utiliser (2.4.10), pour aboutir à :

$$\left\| \sum_{K\in\mathcal{T}_h} \gamma_K b_K \right\|^2_{W_0^{1,2}(\Omega)} \leq ch^{-2} \sum_{K\in\mathcal{T}_h} \|q - \mathcal{C}_h q\|^2_{L^2(K)} = ch^{-2}\|q - \mathcal{C}_h q\|^2_{L^2(\Omega)}$$
$$\leq c\|q\|_{W_0^{1,2}(\Omega)}.$$

Au final, on a bien montré que

$$\|\pi_h q\|_{W_0^{1,2}(\Omega)} \leq c\|q\|_{W_0^{1,2}(\Omega)},$$

i.e. (2.4.7) est bien vérifiée. □

Lemme 2.4.2. Il existe $c > 0$ uniforme en h telle que,

$$\forall \mathbf{F}_h \in \mathbf{X}_h,\ \|\nabla\cdot\mathbf{F}_h\|_{W^{-1,2}(\Omega)} \leq c \sup_{0\neq q_h\in M_h} \frac{(\mathbf{F}_h, \nabla q_h)}{\|\nabla q_h\|_{\mathbf{L}^2(\Omega)}}. \tag{2.4.11}$$

Preuve. Rappelons tout d'abord que, étant donnée la définition de la norme sur $W_0^{1,2}(\Omega)$, on a :

$$\forall \mathbf{F} \in \mathbf{L}^2(\Omega), \qquad \|\nabla\cdot\mathbf{F}\|_{W^{-1,2}(\Omega)} := \sup_{0\neq q\in W_0^{1,2}(\Omega)} \frac{(\mathbf{F}, \nabla q)}{\|\nabla q\|_{\mathbf{L}^2(\Omega)}}.$$

Soient alors $\mathbf{F}_h \in \mathbf{X}_h$ et $q \in W_0^{1,2}(\Omega)$. On utilise le projecteur π_h défini précédemment, et l'on obtient :

$$(\mathbf{F}_h, \nabla q) = -(\nabla\cdot\mathbf{F}_h, q) = -(\nabla\cdot\mathbf{F}_h, \pi_h q) = (\mathbf{F}_h, \nabla\pi_h q).$$

En utilisant (2.4.7), on a alors :

$$\frac{(\mathbf{F}_h, \nabla q)}{\|\nabla q\|_{\mathbf{L}^2(\Omega)}} \leq c\frac{(\mathbf{F}_h, \nabla\pi_h q)}{\|\nabla\pi_h q\|_{\mathbf{L}^2(\Omega)}} \leq c \sup_{0\neq q_h\in M_h} \frac{(\mathbf{F}_h, \nabla q_h)}{\|\nabla q_h\|_{\mathbf{L}^2(\Omega)}}.$$

Le résultat est ensuite obtenu en prenant le sup sur tous les $q \in W_0^{1,2}(\Omega)$. □

2.4.3 Coercivité et continuité

La forme bilinéaire considérée n'est pas à proprement parler coercive sur les espaces considérés. Néanmoins, elle vérifie la condition inf-sup suivante.

Proposition 2.4.1. Il existe $c > 0$ uniforme en h telle que, pour tout $(\mathbf{F}_h, q_h) \in \mathbf{X}_h\times M_h$,

$$c|\!|\!|\mathbf{F}_h, q_h|\!|\!| \leq \sup_{(0,0)\neq(\mathbf{G}_h,r_h)\in\mathbf{X}_h\times M_h} \frac{a_s\left((\mathbf{F}_h, q_h), (\mathbf{G}_h, r_h)\right)}{|\!|\!|\mathbf{G}_h, r_h|\!|\!|} \tag{2.4.12}$$

Preuve. Soit $(\mathbf{F}_h, q_h) \in \mathbf{X}_h\times M_h$ différent de $(0,0)$. On note $\mathbb{S}$ le sup présent dans le membre de droite de (2.4.12). On a immédiatement :

$$|\!|\!|\mathbf{F}_h, q_h|\!|\!|^2 - \|\mathbf{F}_h\|^2_{\mathbf{L}^2(\Omega)} = \|\nabla\times\mathbf{F}_h\|^2_{\mathbf{L}^2(\Omega)} + \|\nabla q_h\|^2_{\mathbf{L}^2(\Omega)} = a_s\left((\mathbf{F}_h, q_h), (\mathbf{F}_h, q_h)\right) \leq \mathbb{S}|\!|\!|\mathbf{F}_h, q_h|\!|\!|.$$

Par ailleurs, en utilisant par exemple [17, Lemme 3.1], il existe c ne dépendant que de Ω telle que

$$c\|\mathbf{F}_h\|_{\mathbf{L}^2(\Omega)} \leq \|\nabla\times\mathbf{F}_h\|_{\mathbf{L}^2(\Omega)} + \|\nabla\cdot\mathbf{F}_h\|_{W^{-1,2}(\Omega)}$$

En utilisant le lemme 2.4.2, on obtient alors :

$$\|\mathbf{F}_h\|_{\mathbf{L}^2(\Omega)} \leq c\mathbb{S}^{\frac{1}{2}}\|\mathbf{F}_h, q_h\|\!\|^{\frac{1}{2}} + c\sup_{0\neq r_h\in M_h}\frac{(\mathbf{F}_h,\nabla r_h)}{\|\nabla r_h\|_{\mathbf{L}^2(\Omega)}}.$$

Or, par définition de $\mathbb{S}$, on a, pour tout $r_h \in M_h$ non nul,

$$\begin{aligned}\mathbb{S} &\geq \frac{a_s\left((\mathbf{F}_h,q_h),(0,-r_h)\right)}{\|\!|0,-r_h|\!\|} = \frac{(\mathbf{F}_h,\nabla r_h)}{\|\nabla r_h\|_{\mathbf{L}^2(\Omega)}} - \frac{(\nabla q_h,\nabla r_h)}{\|\nabla r_h\|_{\mathbf{L}^2(\Omega)}}\\ &\geq \frac{(\mathbf{F}_h,\nabla r_h)}{\|\nabla r_h\|_{\mathbf{L}^2(\Omega)}} - \|\nabla q_h\|_{\mathbf{L}^2(\Omega)}.\end{aligned}$$

En prenant le sup sur r_h, on obtient alors :

$$\sup_{0\neq r_h\in M_h}\frac{(\mathbf{F}_h,\nabla r_h)}{\|\nabla r_h\|_{\mathbf{L}^2(\Omega)}} \leq \mathbb{S} + \mathbb{S}^{\frac{1}{2}}\|\mathbf{F}_h, q_h\|\!\|^{\frac{1}{2}}.$$

En combinant ces inégalités, on obtient alors :

$$\|\mathbf{F}_h, q_h\|\!\|^2 \leq c\left(\mathbb{S}^2 + \mathbb{S}\|\mathbf{F}_h, q_h\|\!\|\right),$$

ce qui induit le résultat voulu. □

Proposition 2.4.2 (continuité). La forme bilinéaire a_s est continue sur $\mathbf{H}_{0,\mathrm{curl}}(\Omega)\times W_0^{1,2}(\Omega)$.

Preuve. En utilisant directement des inégalités de Cauchy-Schwarz, on obtient, pour tous $(\mathbf{H},p),(\mathbf{F},q)\in\mathbf{H}_{0,\mathrm{curl}}(\Omega)\times W_0^{1,2}(\Omega)$,

$$|a_s\left((\mathbf{H},p),(\mathbf{F},q)\right)| \leq c\|\!|\mathbf{H},p|\!\|\,\|\!|\mathbf{F},q|\!\|, \tag{2.4.13}$$

ce qui implique la continuité de a_s. □

2.4.4 Consistance et convergence

Proposition 2.4.3 (consistance). Soit $\mathbf{g}\in\mathbf{H}_{\mathrm{div}=0}(\Omega)$. On note $\mathbf{H}$ la solution de (2.2.1) et on prend $p=0$. Alors, pour tout $(\mathbf{F},q)\in\mathbf{H}_{0,\mathrm{curl}}(\Omega)\times W_0^{1,2}(\Omega)$:

$$a_s\left((\mathbf{H},p),(\mathbf{F},q)\right) = (\mathbf{g},\mathbf{F}). \tag{2.4.14}$$

Preuve. En procédant comme dans la proposition 2.2.1, on montre que, pour tout $\mathbf{F}\in\mathbf{H}_{0,\mathrm{curl}}(\Omega)$:

$$(\nabla\times\mathbf{H},\nabla\times\mathbf{F}) = (\mathbf{g},\mathbf{F}).$$

Par ailleurs, puisque $\mathbf{H}$ est à divergence nulle, pour tout $q\in W_0^{1,2}(\Omega)$, on a

$$(\mathbf{H},\nabla q) = 0.$$

En combinant ces deux relations et la définition $p=0$, on obtient le résultat voulu. □

Proposition 2.4.4 (convergence). Soit $\mathbf{g} \in \mathbf{H}_{\mathrm{div}=0}(\Omega)$. On note $\mathbf{H}$ la solution de (2.2.1). On note $(\mathbf{H}_h, p_h) \in \mathbf{X}_h \times M_h$ la solution de :

$$\forall (\mathbf{F}_h, q_h) \in \mathbf{X}_h \times M_h,\ a_s\left((\mathbf{H}_h, p_h), (\mathbf{F}_h, q_h)\right) = (\mathbf{g}, \mathbf{F}_h)\,. \tag{2.4.15}$$

Alors il existe $s > 0$ tel que :

$$|\!|\!| \mathbf{H}_h - \mathbf{H}, p_h |\!|\!| \leq c h^s \|\mathbf{g}\|_{\mathbf{L}^2(\Omega)}. \tag{2.4.16}$$

Preuve. On commence par prouver l'inégalité suivante :

$$|\!|\!| \mathbf{H}_h - \mathbf{H}, p_h |\!|\!| \leq c \inf_{(0,0)\neq(\mathbf{F}_h,q_h)\in \mathbf{X}_h\times M_h} |\!|\!| \mathbf{F}_h - \mathbf{H}, q_h |\!|\!|, \tag{2.4.17}$$

pour une constante c indépendante de h, $\mathbf{H}$, $\mathbf{H}_h$ et p_h. Soit alors $(\mathbf{F}_h, q_h) \in \mathbf{X}_h \times M_h$. Utilisant l'inégalité triangulaire, on a :

$$|\!|\!| \mathbf{H}_h - \mathbf{H}, p_h |\!|\!| \leq |\!|\!| \mathbf{H}_h - \mathbf{F}_h, p_h - q_h |\!|\!| + |\!|\!| \mathbf{F}_h - \mathbf{H}, q_h |\!|\!|.$$

On traite le premier terme en utilisant la condition inf-sup (2.4.12) :

$$|\!|\!| \mathbf{H}_h - \mathbf{F}_h, p_h - q_h |\!|\!| \leq c \sup_{(0,0)\neq(\mathbf{G}_h,r_h)\in \mathbf{X}_h\times M_h} \frac{a_s\left((\mathbf{H}_h - \mathbf{F}_h, p_h - q_h), (\mathbf{G}_h, r_h)\right)}{|\!|\!| \mathbf{G}_h, r_h |\!|\!|}.$$

Or, la relation de consistance (2.4.14) implique que pour tout $\mathbf{G}_h, r_h$, on a :

$$a_s\left((\mathbf{H}_h - \mathbf{F}_h, p_h - q_h), (\mathbf{G}_h, r_h)\right) = a_s\left((\mathbf{H} - \mathbf{F}_h, -q_h), (\mathbf{G}_h, r_h)\right).$$

Enfin, on utilise la continuité (2.4.13) pour obtenir

$$|\!|\!| \mathbf{H}_h - \mathbf{F}_h, p_h - q_h |\!|\!| \leq c |\!|\!| \mathbf{H} - \mathbf{F}_h, -q_h |\!|\!|.$$

En prenant l'inf sur $\mathbf{F}_h, q_h$, on aboutit à (2.4.17). Il ne reste plus qu'à montrer qu'on peut choisir un couple $\mathbf{F}_h, q_h$ ad hoc. Pour cela, on utilise

$$\mathbf{F}_h := \mathcal{C}_h \mathcal{K}_\delta \mathbf{H}, \qquad q_h := 0,$$

où $\mathcal{C}_h$ et $\mathcal{K}_\delta$ sont définis au chapitre B (cf. (B.3.15), (B.4.2) et (B.4.3)) et $\delta > 0$ reste à choisir. Remarquons au passage que $\mathbf{G}_h \in \mathbf{W}_0^{1,2}(\Omega)$. On obtient alors :

$$\begin{aligned}
|\!|\!| \mathbf{H}_h - \mathbf{H}, p_h |\!|\!| &\leq c \left(\|\mathcal{C}_h \mathcal{K}_\delta \mathbf{H} - \mathbf{H}\|_{\mathbf{L}^2(\Omega)} + \|\nabla\times(\mathcal{C}_h \mathcal{K}_\delta \mathbf{H} - \mathbf{H})\|_{\mathbf{L}^2(\Omega)} \right) \\
&\leq c \left(\|\mathcal{C}_h \mathcal{K}_\delta \mathbf{H} - \mathcal{K}_\delta \mathbf{H}\|_{\mathbf{L}^2(\Omega)} + \|\nabla\times(\mathcal{C}_h \mathcal{K}_\delta \mathbf{H} - \mathcal{K}_\delta \mathbf{H})\|_{\mathbf{L}^2(\Omega)} \right) \\
&\quad + c \left(\|\mathcal{K}_\delta \mathbf{H} - \mathbf{H}\|_{\mathbf{L}^2(\Omega)} + \|\nabla\times(\mathcal{K}_\delta \mathbf{H} - \mathbf{H})\|_{\mathbf{L}^2(\Omega)} \right)
\end{aligned}$$

En utilisant les propriétés d'approximation de $\mathcal{C}_h$ et $\mathcal{K}_\delta$, on aboutit à :

$$|\!|\!| \mathbf{H}_h - \mathbf{H}, p_h |\!|\!| \leq c \left(h^2 \delta^{-\frac{3}{2}} + h\delta^{-\frac{3}{2}} + \delta^{\frac{1}{2}} \right) \left(\|\mathbf{H}\|_{W^{\frac{1}{2},2}(\Omega)} + \|\nabla\times\mathbf{H}\|_{W^{\frac{1}{2},2}(\Omega)} \right).$$

Or, on peut remarquer que (cf. par exemple [17, Proposition 2.1])

$$\|\mathbf{H}\|_{W^{\frac{1}{2},2}(\Omega)} + \|\nabla\times\mathbf{H}\|_{W^{\frac{1}{2},2}(\Omega)} \leq c \|\mathbf{g}\|_{\mathbf{L}^2(\Omega)}.$$

On choisit alors δ de sorte que $\delta^{\frac{1}{2}} = h\delta^{-\frac{3}{2}}$, i.e. $\delta = \sqrt{h}$. On a alors :

$$|\!|\!| \mathbf{H}_h - \mathbf{H}, p_h |\!|\!| \leq c h^{\frac{1}{4}} \|\mathbf{g}\|_{\mathbf{L}^2(\Omega)},$$

ce qui est le résultat voulu, avec $s = \frac{1}{4}$. □

Remarque 2.4.1. Étant donné le choix de $\mathbf{G}_h \in \mathbf{W}_0^{1,2}(\Omega)$ dans la preuve précédente, on voit que l'hypothèse (2.4.5) n'est pas restrictive, puisqu'on peut même prendre $\mathbf{X}_h \subset \mathbf{W}_0^{1,2}(\Omega)$.

2.4.5 Illustration numérique et conclusion

On propose trois figures pour illustrer le propos développé dans cette partie. On résout encore le problème (2.3.8) en utilisant la forme bilinéaire a_s introduite précédemment, à l'aide du logiciel FreeFem++ (cf. [120]). Dans les figures 2.4, 2.5 et 2.6, pour chaque graphe, la courbe rouge correspond au cas sans stabilisation de la divergence (i.e. celui qu'on vient de décrire), et la courbe bleue est la référence avec stabilisation (et $\alpha = 1$ bien sûr). On propose à chaque fois quatre courbes :

- En haut à gauche : la norme $\mathbf{L}^2(\Omega)$ de $\mathbf{H} - \mathbf{H}_h$, en fonction du nombre total de degrés de liberté ($\propto h^{-2}$), en coordonnées log-log.
- En haut à droite : la norme $\mathbf{L}^2(\Omega)$ de $\nabla\times(\mathbf{H} - \mathbf{H}_h)$, en fonction du nombre total de degrés de liberté, en coordonnées log-log.
- En bas à gauche : la norme $L^2(\Omega)$ de $\nabla\cdot(\mathbf{H} - \mathbf{H}_h)$, en fonction du nombre total de degrés de liberté, en coordonnées log-log. Notons que l'on n'a pas ici de convergence. Cela traduit bien le fait que la solution est singulière : en effet, en vertu du théorème 2.2.1, il existe des éléments de $\mathbf{H}_{\mathrm{curl}}(\Omega) \cap \mathbf{H}_{\mathrm{div}}(\Omega)$ qui ne peuvent pas être approchés par des éléments de $W^{1,2}(\Omega)$. C'est exactement ce qui se produit ici pour cette solution singulière.
- En bas à droite : la norme $\mathbf{L}^2(\Omega)$ de ∇p_h, en fonction du nombre total de degrés de liberté, en coordonnées log-log.

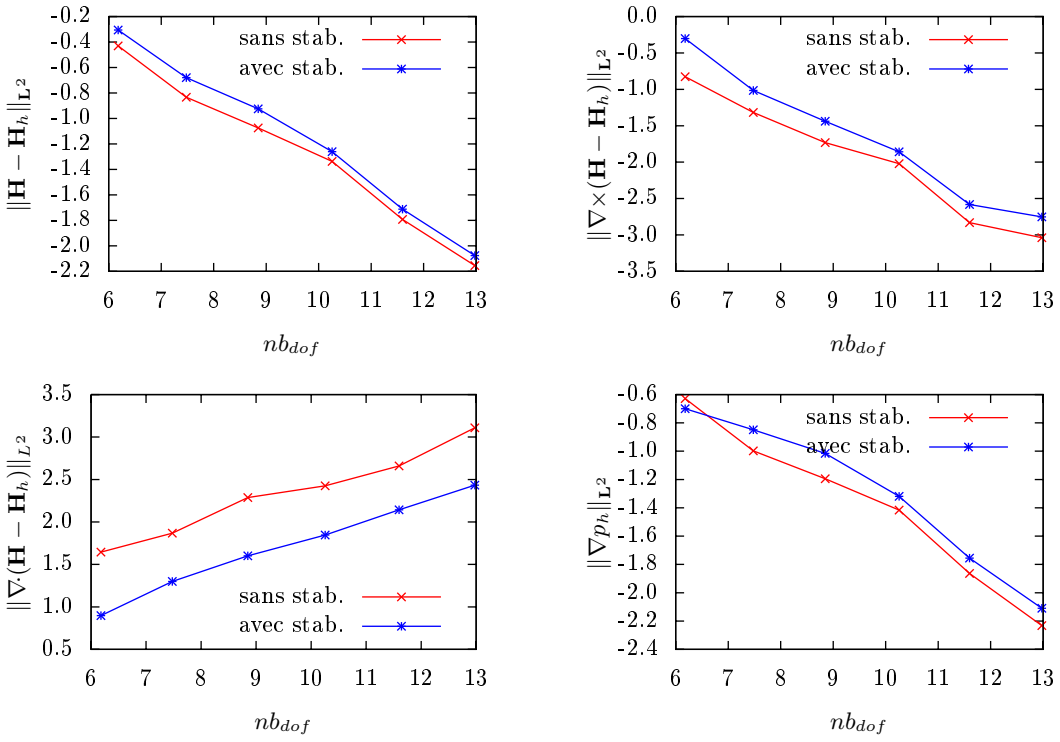

FIG. 2.4: Sans stabilisation, éléments $P1$ pour $\mathbf{H}_h$, éléments $P1$-bulle pour p_h.

On voit alors que la méthode sans stabilisation est convergente pour d'autres choix d'éléments finis. Toutefois, les figures 2.5-2.6 suggèrent que, sans stabilisation, il faut un espace de "pression magnétique" plus riche que l'espace de champ magnétique. Or, la convergence énoncée dans le théorème 2.3.1 ne requiert que la condition $M_h \subset W_0^{1,2}(\Omega)$ (cf. annexe B pour les détails), ce qui nous motive à essayer de trouver une méthode faisant intervenir pour M_h des polynômes de degré 1, quel que soit le degré choisi pour $\mathbf{X}_h$. En conclusion, il vaut mieux (et c'est ce qu'on fera) garder le terme de stabilisation, qui donne une convergence sans hypothèse particulière sur les espaces discrets.

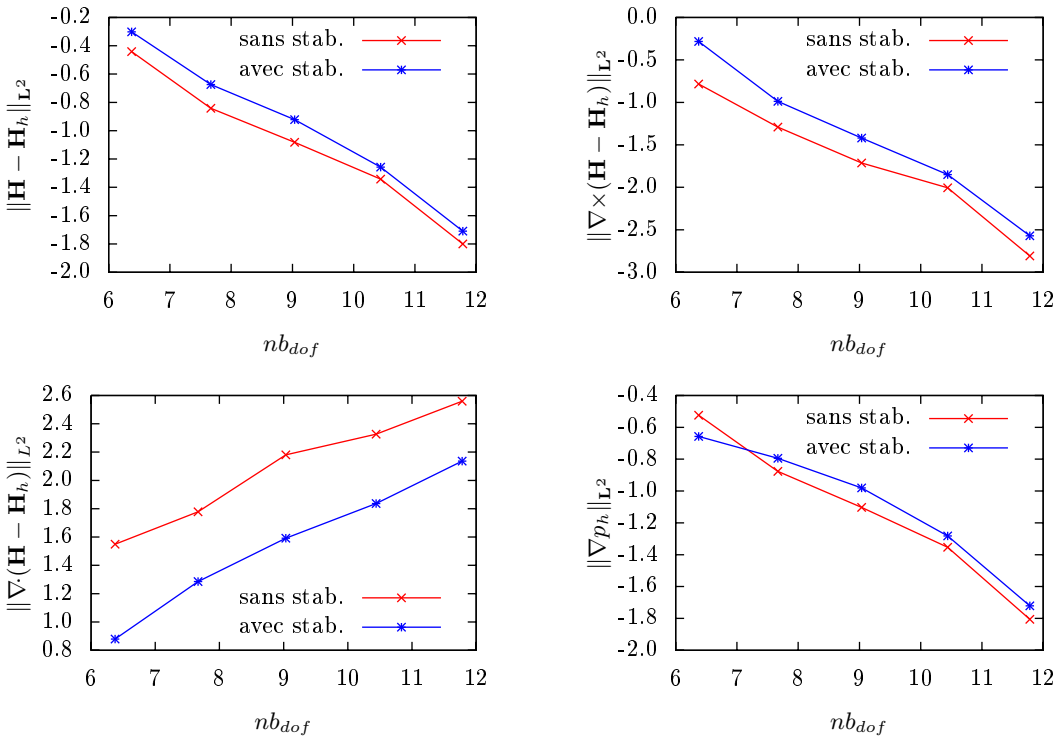

FIG. 2.5: Sans stabilisation, éléments $P1$ pour $\mathbf{H}_h$, éléments $P2$ pour p_h.

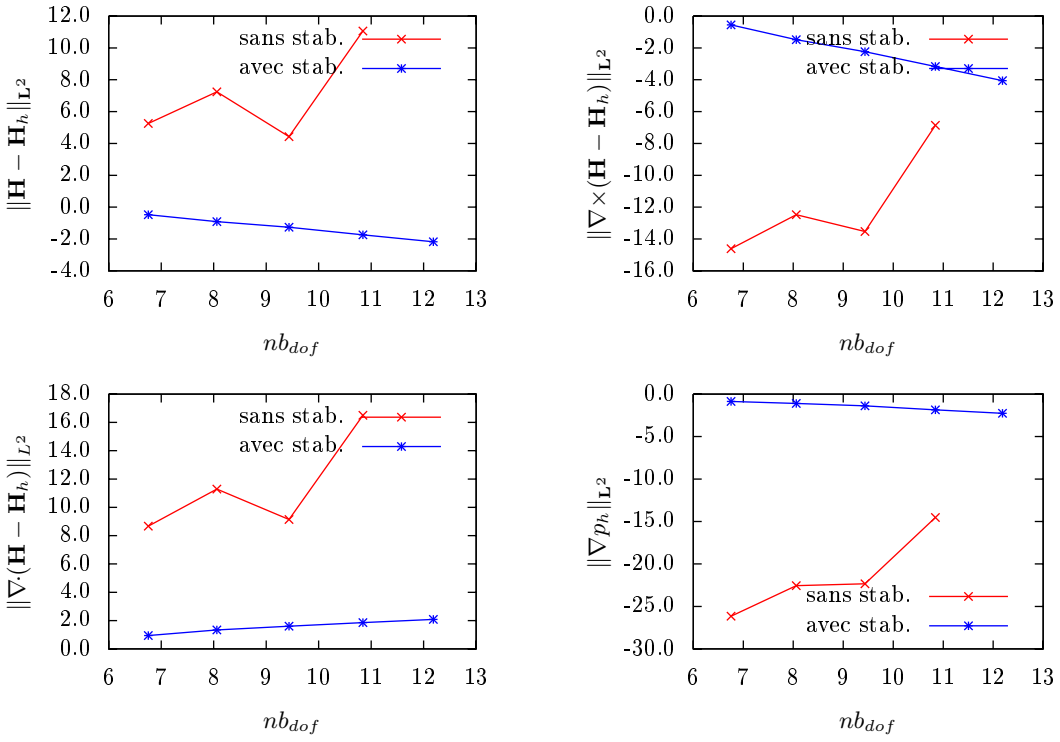

FIG. 2.6: Sans stabilisation, éléments $P2$ pour $\mathbf{H}_h$, éléments $P1$ pour p_h.

Chapitre 3

Le code SFEMaNS

Cette partie a pour but de décrire de façon succincte le code utilisé pour la résolution des équations de la MHD. On discute également des modifications apportées au cours de cette thèse pour enrichir ce code. Enfin, on donne quelques résultats qui illustrent le bon fonctionnement de SFEMaNS.

3.1 Présentation générale

Le code numérique SFEMaNS (Spectral / Finite Element code for Maxwell and Navier-Stokes equations) est un outil développé en Fortran90 depuis 2002 par J.-L. Guermond et al. Il s'agit d'une méthode hybride spectrale/éléments finis de Lagrange, qui permet d'intégrer le système complet d'équations de la MHD. Nous en donnons ici les principales caractéristiques.

3.1.1 Hypothèses de base

Deux hypothèses de base sont faites pour ce code, et nous discuterons de leur impact sur les configurations étudiées.

1. Le domaine de calcul est supposé *axisymétrique*. Cette hypothèse est sans doute la plus restrictive (elle empêche par exemple de modéliser parfaitement des configurations comme celle de la dynamo de Cadarache (expérience VKS), les pales faisant perdre l'axisymétrie), mais elle est à la base de notre méthode. En effet, on se sert de cette symétrie cylindrique pour faire une décomposition de Fourier dans la direction azimutale, et l'on résout les problèmes dans le plan méridien par une méthode d'éléments finis de Lagrange. On suppose en outre que les distributions μ et σ sont également axisymétriques, et indépendantes du temps.
2. Pour la résolution des équations de Maxwell, on suppose que le domaine possède deux parties distinctes : une partie conductrice Ω_c dans laquelle la conductivité σ est uniformément positive, et une partie isolante Ω_v, appelée *vide*, dans laquelle $\sigma \equiv 0$. En outre, sur Ω_v, on suppose $\mu \equiv 1$. La seule hypothèse restrictive que l'on fait est l'hypothèse que Ω_v est simplement connexe, ce qui nous permet de chercher le champ magnétique dans le vide sous la forme d'un gradient.

Outre la décomposition des champs selon des modes de Fourier (réels) dans la direction azimutale, on tire également parti de la symétrie cylindrique en explicitant tous les termes susceptibles de mêler les modes (les termes non linéaires ou de couplage). On obtient alors des

systèmes indépendants sur chacun des modes de Fourier considérés. L'interaction entre les modes de Fourier se fait uniquement par le second membre des systèmes à résoudre.

Les hypothèses concernant l'axisymétrie peuvent sembler restrictives, mais nous pensons que ce code couvre (presque) tous les cas de dynamos réalistes, astrophysiques ou expérimentales (sphères, cylindres, tores...) et décrit également correctement un certain nombre de situations MHD pratiques. Nous admettons tout de même que nous ne pouvons pas représenter correctement le dispositif VKS. Néanmoins, nous pouvons, en modélisant les régions "disques+pales", utiliser le code de calcul pour obtenir quelques informations sur la dynamo de Cadarache (cf. section 4.2)

L'hypothèse d'un isolant simplement connexe est cruciale pour la recherche du champ magnétique sous forme d'un gradient. Lorsque ce n'est plus le cas, écrire le champ comme un gradient revient à faire une hypothèse de courant moyen nul dans le conducteur, ce qui est raisonnable dans nos applications.

3.1.2 Cadre d'application

Ce code permet de résoudre des problèmes de trois types différents :

- des problèmes purement hydrodynamiques : étant donnée une source de forçage $\mathbf{f}$ (non nécessairement la force de Lorentz), on ne résout que les équations de Navier-Stokes (1.3.22)-(1.3.23) avec $A = 0$.
- des problèmes d'induction magnétique : étant donnés un courant externe $\mathbf{j}$ et la vitesse du conducteur $\mathbf{u}$, on ne résout que les équations de Maxwell (1.3.20)-(1.3.21) dans le conducteur, ainsi que le potentiel magnétique. Dans ce cas, on parle de *dynamo cinématique.*
- le problème de MHD non linéaire, pour lequel on résout à la fois les équations de Navier-Stokes et les équations de Maxwell. Dans ce cas, on parle de *dynamo non linéaire*

Signalons encore que, pour déterminer si une configuration donnée permet de générer un effet dynamo (on parlera parfois abusivement de *configuration dynamogène*), on procède en trois étapes. La première étape est purement hydrodynamique : on étudie le champ de vitesses produit par différentes valeurs du nombre de Reynolds R_e. Si le flot obtenu est stationnaire, on l'utilise ensuite pour des calculs d'induction, qui nous permettent d'évaluer un seuil de dynamo cinématique, i.e. un nombre de Reynolds magnétique critique R_mc à partir duquel on a une croissance exponentielle du champ magnétique. Si le flot est instationnaire, les calculs de dynamo cinématique prennent l'une des deux formes suivantes :

- soit on prend un (ou plusieurs) flot(s) figé(s) provenant du calcul hydrodynamique pour évaluer un nombre de Reynolds magnétique critique R_mc,
- soit on calcule à la fois le champ magnétique et le champ de vitesses, mais en enlevant le couplage par la force de Lorentz dans les équations de Navier-Stokes (i.e. on résout (1.3.22) avec $A = 0$).

Enfin, on lance des simulations non linéaires dans la gamme de paramètres établie par le calcul de dynamo cinématique.

3.1.3 Implémentation

On renvoie à [66] pour les détails concernant la discrétisation en temps des équations de Navier-Stokes. En ce qui concerne la discrétisation des équations de Maxwell, la méthode initialement mise en œuvre est expliquée dans [65]. Elle a été au cours de cette thèse modifiée,

pour prendre en compte l'ajout de la "pression magnétique" (cf. Remarque 2.3.2). On en trouve une description dans [67], article qui est reporté en annexe D. Dans le cas d'un calcul de MHD non linéaire, on peut résumer la marche en temps (basée sur une méthode à deux pas) de la façon schématique suivante :

- Initialisation du champ de vitesses $\mathbf{u}^0, \mathbf{u}^1$, de la pression dynamique p^0, p^1, du champ magnétique dans le conducteur $\mathbf{H}^0, \mathbf{H}^1$ et du potentiel dans le vide ϕ^0, ϕ^1.
- Approximation des termes non linéaires et de couplage dans l'équation de Navier-Stokes (à l'instant t^{n+1}) par des extrapolations à partir de $\mathbf{u}^n, \mathbf{u}^{n-1}, \mathbf{H}^n, \mathbf{H}^{n-1}$.
- Calcul de $\mathbf{u}^{n+1}$ puis p^{n+1} en utilisant ces extrapolations.
- Approximation du terme de couplage dans les équations de Maxwell (à l'instant t^{n+1}) par des extrapolations à partir de $\mathbf{u}^{n+1}, \mathbf{H}^n, \mathbf{H}^{n-1}$.
- Calcul de $\mathbf{H}^{n+1}$ et ϕ^{n+1}.

On peut remarquer qu'il existe un décalage en temps entre les champs magnétiques et le champ de vitesses. Pour les cas où on veut ne résoudre que les équations de Maxwell ou que les équations de Navier-Stokes, on adapte aisément ce schéma.

Signalons enfin que le code de calcul permet de traiter des conditions de périodicité, pour prendre en compte des géométries infinies (par exemple un cylindre infini) dans la direction de l'axe de symétrie.

3.2 Parallèlisation sur les modes de Fourier

On a souligné que les modes de Fourier pouvaient être résolus de manière quasi-indépendante, puisque l'interaction des modes de Fourier n'apparaît que dans les seconds membres. Cette caractéristique est donc propice à une parallélisation selon les modes de Fourier, mise en œuvre dès l'origine. Les détails concernant cette parallélisation peuvent être trouvés dans [66].

3.3 Parallèlisation dans le plan méridien

Une nouvelle étape de parallélisation a été mise en place. Il s'agit de découper le plan méridien en un certain nombre de sous-domaines, afin de répartir le calcul sur plusieurs processeurs. Dans un souci d'équilibre des charges de travail réparties sur chacun des processeurs, on distingue trois parties dans le plan méridien :

- une partie Ω_{NS}^{2D} dans laquelle on doit résoudre les équations de Navier-Stokes pour le champ de vitesses, ainsi que l'équation d'induction pour le champ magnétique,
- une partie Ω_{MXW}^{2D} dans laquelle la vitesse de la partie conductrice est supposée connue, et où l'on ne résout que l'équation d'induction pour le champ magnétique,
- une partie Ω_v^{2D} dans laquelle on ne résout que l'équation d'induction pour le potentiel magnétique dans le vide.

On utilise dans le code la librairie Metis (cf. [80, 85]) afin de créer une partition équilibrée par rapport à la charge de calculs, i.e. on s'arrange pour que les sous-domaines de Ω_{NS}^{2D} contiennent moins d'éléments que les autres, et que les sous-domaines de Ω_v^{2D}, au contraire, en contiennent le plus : le but de ce découpage est de répartir équitablement tous les degrés de liberté sur les processeurs. Pour la résolution des systèmes linéaires, nous avons remplacé l'utilisation d'un solveur itératif par une méthode directe, en utilisant MUMPS (cf. [4, 5, 6]) au travers d'une interface fournie par la librairie PETSc (cf. [14, 12, 13]). On présente dans la suite quelques résultats qui confirment le bon comportement du code, aussi bien du point de vue

de la précision que du point de vue de la parallélisation. La figure 3.1 montre un exemple de ce découpage du plan méridien.

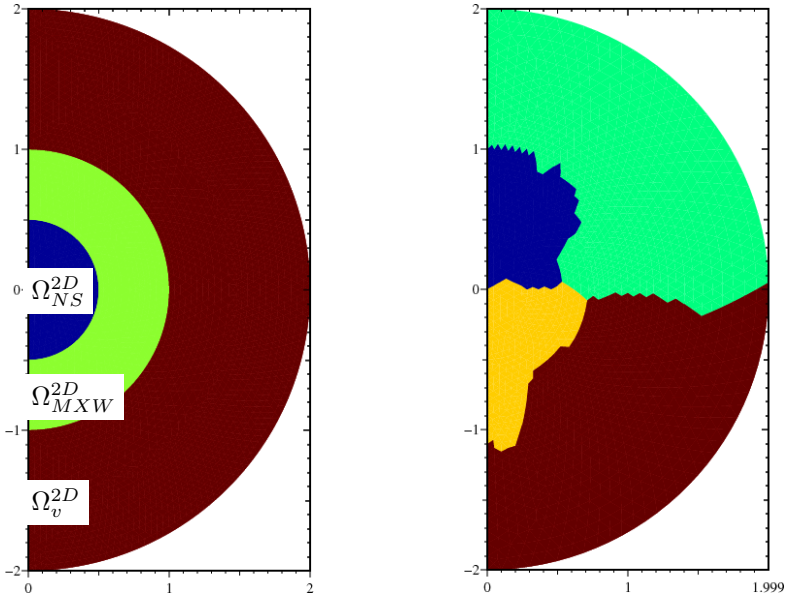

FIG. 3.1: Exemple de découpage du plan méridien : à gauche, représentation des domaines Ω_{NS}^{2D} (bleu), Ω_{MXW}^{2D} (vert) et Ω_v^{2D}(marron), à droite, répartition des degrés de liberté sur 4 processeurs (une couleur par processeur)

3.4 Tests du code

Dans cette partie, on présente une série de tests qui attestent du bon comportement du code numérique. Nous avons implémenté dans le code sept cas tests analytiques, pour les problèmes purement hydrodynamiques et d'induction magnétique, et nous les présentons ici. Afin de couvrir le cas de la MHD non linéaire, on reporte également une comparaison avec des calculs faits avec le code non parallélisé, sans la stabilisation de la divergence. Ces calculs proviennent de [66] et sont reproduits ici avec un très bon accord. Enfin, on termine par quelques résultats sur la parallélisation dans le plan méridien. Notons pour être complet que des résultats concernant la parallélisation sur les modes de Fourier peuvent être trouvés dans [66].

3.4.1 Précision pour la résolution des équations de Navier-Stokes

Deux tests ont été mis en place pour vérifier le bon comportement du code vis à vis des équations hydrodynamiques. Pour ces deux tests, on se donne une solution analytique $(\mathbf{u}, p)$ et une géométrie, et l'on calcule la solution en utilisant un terme de forçage $\mathbf{f}$ ad hoc, i.e.

$$\mathbf{f} := \partial_t \mathbf{u} + (\nabla \times \mathbf{u}) \times \mathbf{u} - \frac{1}{R_\mathrm{e}} \Delta \mathbf{u} + \nabla p.$$

On impose des conditions de Dirichlet sur la vitesse au bord du domaine. Les deux tests font intervenir $R_\mathrm{e} = 1$.

Test 1

On se place dans un domaine Ω cylindrique, de hauteur 1 et de rayon 1. On cherche à approcher la solution suivante :

$$\begin{aligned}
u_r(r,\theta,z,t) &= \left(\left(r^2z^3 - 3r^3z^2\right)\cos(\theta) - \left(r^2z^3 + 3r^3z^2\right)\sin(\theta)\right)\cos(t),\\
u_\theta(r,\theta,z,t) &= 3\left(r^3z^2 - r^2z^3\right)\left(\cos(\theta) + \sin(\theta)\right)\cos(t),\\
u_z(r,\theta,z,t) &= \left(3r^2z^3\cos(\theta) + 5r^2z^3\sin(\theta)\right),\\
p(r,\theta,z,t) &= rz\left(\cos(\theta) + \sin(\theta)\right)\sin(t).
\end{aligned}$$

On illustre la convergence en maillage en utilisant un pas de temps $\delta t = \frac{1}{2000}$, et en calculant l'erreur au temps $t = 1$. Plusieurs maillages sont utilisés, de taille caractéristique $h \in \left\{\frac{1}{2}, \frac{1}{5}, \frac{1}{10}, \frac{1}{20}, \frac{1}{40}, \frac{1}{80}\right\}$, et les résultats sont reportés en figure 3.2. Le calcul a été effectué en utilisant trois modes de Fourier.

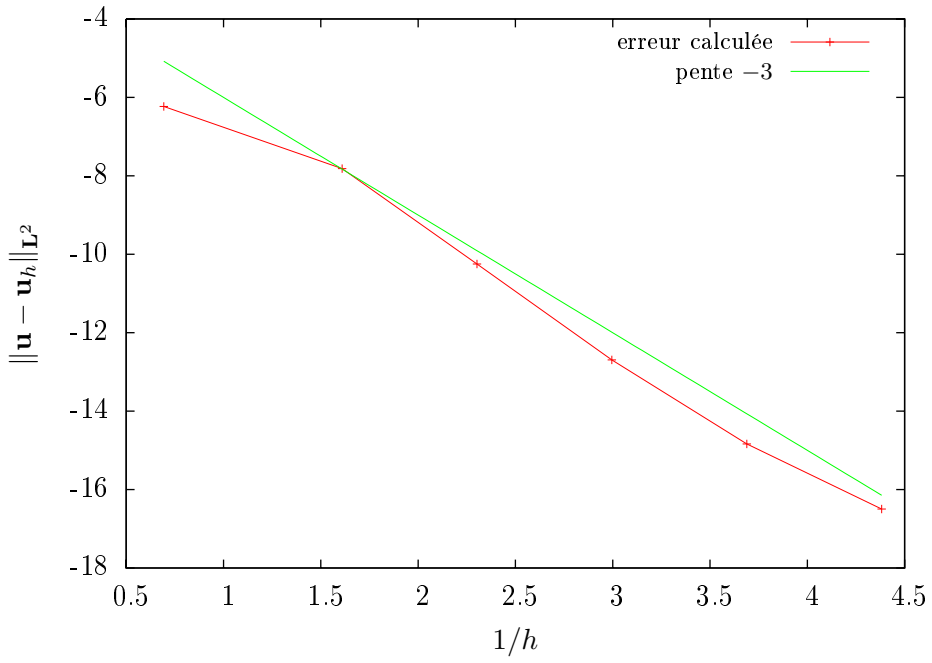

FIG. 3.2: Test 1 : erreur $\mathbf{L}^2$ sur le champ de vitesses : la courbe est en échelle logarithmique, et on s'attend à une convergence d'ordre 3, obtenue ici.

Test 2

Le domaine de calcul est le même que précédemment, mais on impose cette fois une condition de périodicité sur la vitesse et la pression, en $z = 0$ et $z = 1$. On cherche à approcher

la solution suivante :

$$\begin{aligned} u_r(r,\theta,z,t) &= -r^2\left(1-2\pi r\sin(2\pi z)\right)\sin(\theta)\cos(t),\\ u_\theta(r,\theta,z,t) &= -3r^2\cos(\theta)\cos(t),\\ u_z(r,\theta,z,t) &= r^2\left(4\cos(2\pi z)+1\right)\sin(\theta)\cos(t),\\ p(r,\theta,z,t) &= r^2\cos(2\pi z)\cos(\theta)\cos(t). \end{aligned}$$

On illustre en figure 3.3 la convergence en maillage, avec un pas de temps $\delta t = \frac{1}{4000}$, pour des maillages de taille caractéristique $h \in \left\{\frac{1}{2}, \frac{1}{5}, \frac{1}{10}, \frac{1}{20}, \frac{1}{40}, \frac{1}{80}\right\}$. Les calculs ont été réalisés en utilisant trois modes de Fourier, et les erreurs sont calculées après 4000 itérations (i.e. au temps $t = 1$).

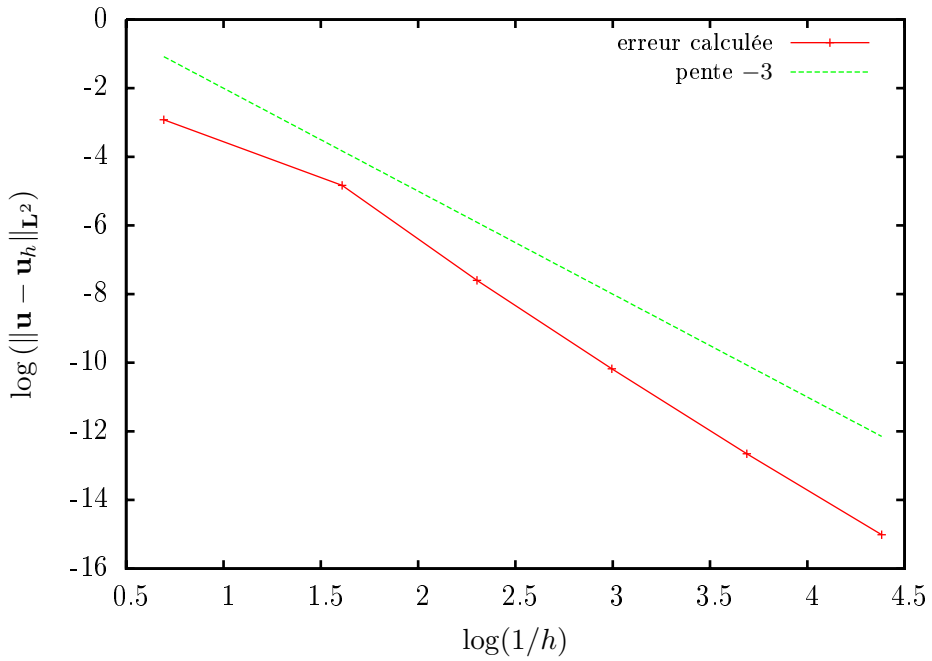

FIG. 3.3: Test 2 : erreur $\mathbf{L}^2$ sur le champ de vitesses : la courbe est en échelle logarithmique, et on s'attend à une convergence d'ordre 3, obtenue ici.

3.4.2 Précision pour la résolution des équations de Maxwell

Pour l'équation d'induction, 5 tests ont été mis en place, au fur et à mesure du développement du code. Ils sont numérotés dans la continuité des tests sur les équations de Navier-Stokes. À l'instar des tests hydrodynamiques, on se donne d'abord une solution analytique $(\mathbf{H}, \phi)$, et éventuellement un champ de vitesses $\mathbf{u}$. Ensuite, on calcule une source de courant $\mathbf{j}$ et un champ électrique $\mathbf{E}$ pour que les équations soient satisfaites. On impose des conditions de Dirichlet sur ϕ au bord du domaine de calcul. Dans certains cas, le domaine conducteur touche le bord du domaine de calcul. On impose alors des conditions de Dirichlet soit sur $\mathbf{H}\times\mathbf{n}$, soit sur $\mathbf{E}\times\mathbf{n}$.

Test 3

Le domaine conducteur est un cylindre de hauteur 1 et de rayon 0.5. Pour le calcul, le vide correspond à la coquille cylindrique définie par $z \in [0,1]$ et $r \in [0.5,1]$. Des conditions de Dirichlet sont appliquées sur $\mathbf{H}\times\mathbf{n}$ en $z=0$ et $z=1$. On suppose que le domaine a une perméabilité constante $\mu \equiv 1$ et que la conductivité est uniforme dans le conducteur $\sigma \equiv 1$. On utilise $R_\mathrm{m} = 1$, et on suppose que la vitesse du conducteur est portée par des modes non nuls, et peut s'écrire :

$$\begin{aligned}
u_r(r,\theta,z,t) &= \sum_{m=m_0}^{m_1} \frac{1}{m^3}\left(\alpha_m z r^{m-1} m\cos(m\theta) + \beta_m z r^{m-1} m \sin(m\theta)\right),\\
u_\theta(r,\theta,z,t) &= \sum_{m=m_0}^{m_1} \frac{1}{m^3}\left(\beta_m z r^{m-1} m\cos(m\theta) - \alpha_m z r^{m-1} m \sin(m\theta)\right),\\
u_z(r,\theta,z,t) &= \sum_{m=m_0}^{m_1} \frac{1}{m^3}\left(\alpha_m r^{m} \cos(m\theta) + \beta_m r^{m} \sin(m\theta)\right),
\end{aligned}$$

avec $0 < m_0 \leq m_1$. On cherche à approcher la solution suivante :

$$\text{(3.4.1)} \qquad \begin{cases}
H_r(r,\theta,z,t) = \displaystyle\sum_{m=m_0}^{m_1} \frac{1}{m^3}\left(\alpha_m z r^{m-1} m\cos(m\theta) + \beta_m z r^{m-1} m \sin(m\theta)\right)\cos(t),\\
H_\theta(r,\theta,z,t) = \displaystyle\sum_{m=m_0}^{m_1} \frac{1}{m^3}\left(\beta_m z r^{m-1} m\cos(m\theta) - \alpha_m z r^{m-1} m \sin(m\theta)\right)\cos(t),\\
H_z(r,\theta,z,t) = \displaystyle\sum_{m=m_0}^{m_1} \frac{1}{m^3}\left(\alpha_m r^{m} \cos(m\theta) + \beta_m r^{m} \sin(m\theta)\right)\cos(t),\\
\phi(r,\theta,z,t) = \displaystyle\sum_{m=m_0}^{m_1} \frac{1}{m^3}\left(\alpha_m z r^{m} \cos(m\theta) + \beta_m z r^{m} \sin(m\theta)\right)\cos(t).
\end{cases}$$

La figure 3.4 montre le domaine utilisé pour le calcul (vue dans un plan méridien). La figure 3.5 illustre la convergence en maillage, pour différentes valeurs de notre paramètre α. Les calculs ont été réalisés avec $m_0 = 1$, $m_1 = 3$, en utilisant seulement 3 modes de Fourier (cela est possible car le terme non linéaire $\mathbf{u}\times(\mu\mathbf{H})$ est en fait nul), sur 2000 itérations avec un pas de temps $\delta t = \frac{1}{2000}$. Les coefficients α_m et β_m sont tous pris égaux à 1, et les maillages utilisés ont des tailles caractéristiques $h \in \left\{\frac{1}{5}, \frac{1}{10}, \frac{1}{20}, \frac{1}{40}, \frac{1}{80}\right\}$. Notons que la solution est suffisamment régulière pour que toutes les valeurs de α donnent de la convergence. On peut néanmoins noter quelques légères différences sur l'ordre de convergence, qui semble être proche de $3-\alpha$.

Test 4

Ce deuxième test sur l'équation d'induction a pour but de vérifier le bon comportement du code vis à vis de conditions aux limites périodiques. On prend encore comme domaine de calcul le domaine représenté en figure 3.4. Cette fois, on impose des conditions périodiques, à savoir

$$\mathbf{H}(z=1) = \mathbf{H}(z=0), \qquad \phi(z=1) = \phi(z=0).$$

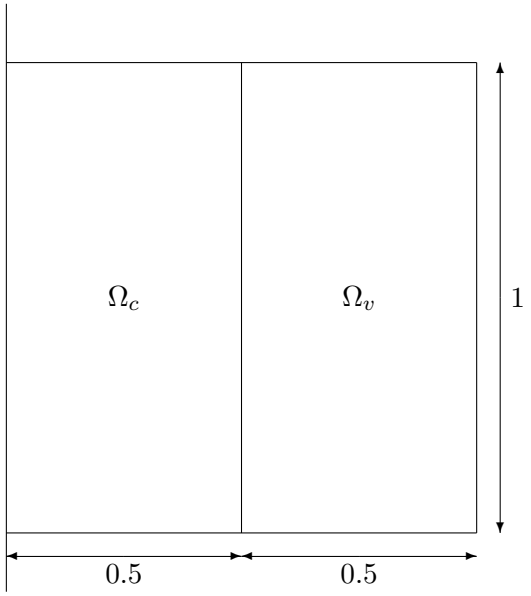

FIG. 3.4: Schéma du domaine de calcul pour les tests 3 et 4

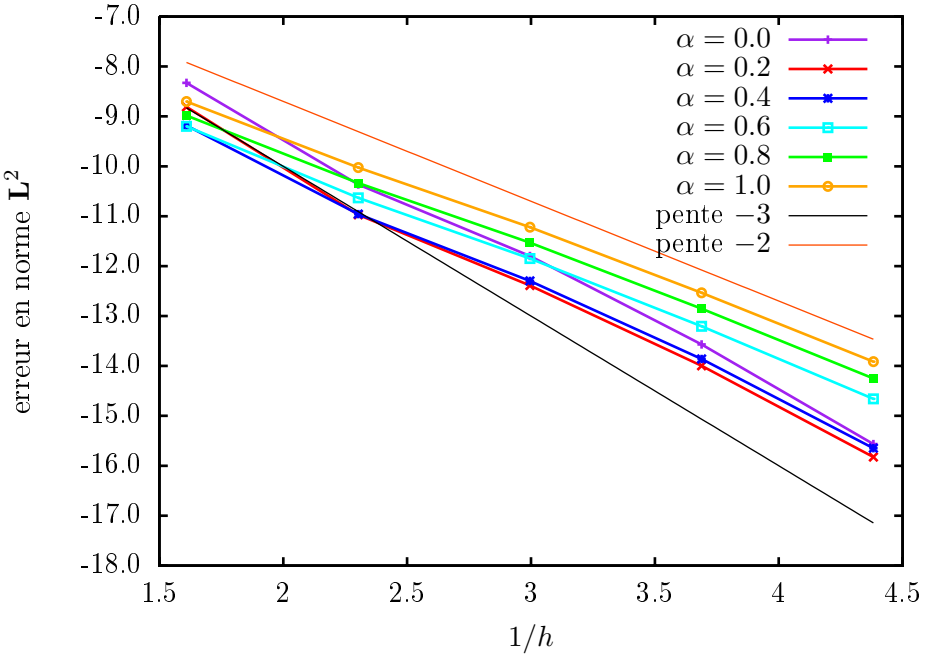

FIG. 3.5: Test 3 : erreur $\mathbf{L}^2$ sur le champ magnétique : la courbe est en échelle logarithmique, et on remarque que l'ordre de convergence semble être $3 - \alpha$.

Là encore, on suppose que $\mu \equiv 1$ dans tout le domaine, et que $\sigma \equiv 1$ dans le conducteur. En revanche, on suppose que le conducteur est au repos, i.e. $\mathbf{u} = 0$. On prend $R_\mathrm{m} = 1$, et on

cherche à approcher la solution suivante :

$$\text{(3.4.2)} \qquad \begin{cases} H_r(r,\theta,z,t) = \cos(t)\cos(\theta)\cos(2\pi z)\left(\dfrac{r}{r_0^2} - 2\pi\left(\dfrac{r}{r_0}\right)^2\left(A + B\dfrac{r}{r_0}\right)\right), \\ H_\theta(r,\theta,z,t) = \cos(t)\sin(\theta)\cos(2\pi z)\left(2\pi\left(\dfrac{r}{r_0}\right)^2 C - 2\dfrac{r}{r_0^2}\right), \\ H_z(r,\theta,z,t) = \cos(t)\cos(\theta)\sin(2\pi z)\dfrac{r}{r_0^2}\left(3A + 4B\dfrac{r}{r_0} - C\right), \\ \phi(r,\theta,z,t) = \cos(t)\cos(\theta)\cos(2\pi z)K_1(2\pi r), \end{cases}$$

où $r_0 = 0.5$ et K_1 désigne la fonction de Bessel modifiée de seconde espèce. Les paramètres A, B et C sont ajustés de sorte que les relations de passage soient vérifiées en $r = r_0$. On donne en figure 3.6 une illustration de la convergence en maillage. Le pas de temps choisi ici est $\delta t = \frac{1}{2000}$ et on représente la norme $\mathbf{L}^2$ de l'erreur après 2000 itérations. Différents maillages sont utilisés, de taille caractéristique $h \in \left\{\frac{1}{10}, \frac{1}{20}, \frac{1}{40}, \frac{1}{80}\right\}$, et on compare les calculs pour différentes valeurs de α. Encore une fois, on voit une légère différence entre les ordres de convergence, tout de même moins marquée que dans le test 3.

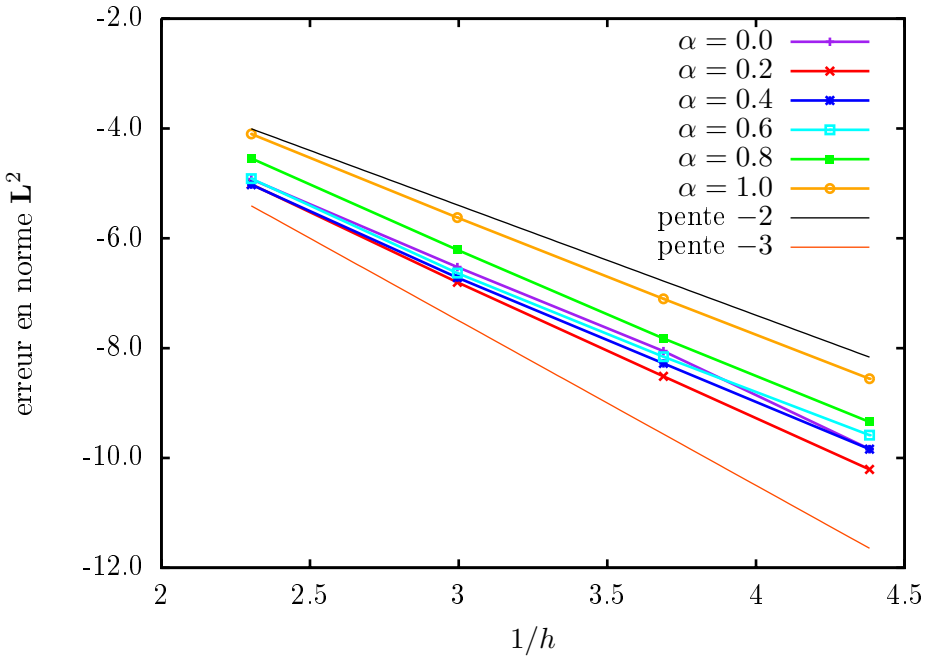

FIG. 3.6: Test 4 : erreur $\mathbf{L}^2$ sur le champ magnétique : la courbe est en échelle logarithmique. L'ordre de convergence est entre 2 et 3 et varie selon α.

Test 5

Ce test est essentiellement le même que le test numéro 3, à ceci près que l'on découpe maintenant le domaine conducteur en deux parties, et on introduit artificiellement une interface entre ces deux sous-domaines (cf. figure 3.7). La solution est encore donnée par les

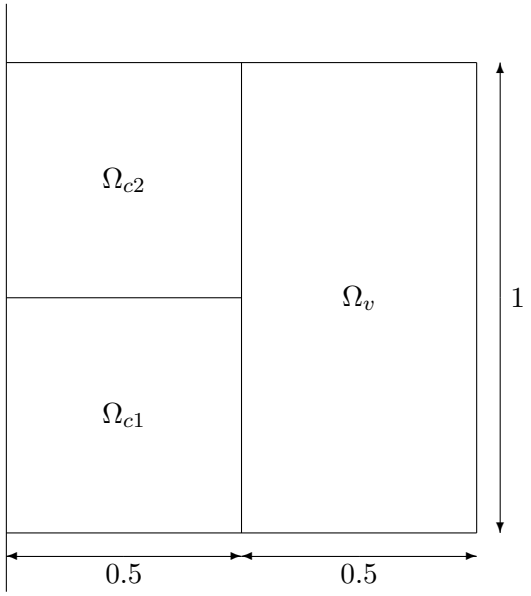

FIG. 3.7: Schéma du domaine de calcul pour le test 5

équations (3.4.1), avec $m_0 = 2$, $m_1 = 4$, $\alpha_m = \beta_m = 1$. On prend $\mu \equiv 1$ sur l'ensemble du domaine, et $\sigma \equiv 1$ dans le conducteur. Ce cas a été mis en place pour tester la présence d'une interface. Nous présentons donc uniquement une comparaison entre ce test et le test numéro 3, pour un maillage fixé, de taille caractéristique $h = 0.1$. On prend un pas de temps $\delta t = 0.01$ et on calcule 100 itérations. Dans les deux calculs, on a pris seulement 3 modes de Fourier $m \in \{2, 3, 4\}$ et $\alpha = 0.6$: on reporte la comparaison (très satisfaisante) dans le tableau 3.1.

	$\|\mathbf{H} - \mathbf{H}_h\|_{\mathbf{L}^2}$	$\|\nabla\times(\mathbf{H} - \mathbf{H}_h)\|_{\mathbf{L}^2}$	$\|\nabla\cdot(\mathbf{H} - \mathbf{H}_h)\|_{\mathbf{L}^2}$	$\|\phi - \phi_h\|_{W^{1,2}}$
Test 3	$2.40\ 10^{-4}$	$3.18\ 10^{-4}$	$2.08\ 10^{-3}$	$9.37\ 10^{-5}$
Test 5	$2.72\ 10^{-4}$	$3.72\ 10^{-4}$	$2.28\ 10^{-3}$	$9.59\ 10^{-5}$

TAB. 3.1: Comparaison des erreurs obtenues pour les tests 3 et 5 : on voit que les erreurs calculées sont sensiblement les mêmes, ce qui assure que la prise en compte des interfaces par une méthode de pénalisation permet une bonne approximation des solutions.

Test 6

Ce test correspond au cas de la sphère de Durand, présenté dans [67], cf. D.4.2, cas 1. On cherche une solution stationnaire, et notre nouvelle méthode nous permet de faire le calcul en une seule itération, en utilisant un pas de temps $\delta t = 10^{10}$. La figure 3.8 rassemble les résultats obtenus pour un saut de μ égal à 20 et différentes valeurs du paramètre α, sur des maillages de taille caractéristique $h \in \{0.16, 0.08, 0.04, 0.02, 0.01\}$. Notons ici que la régularité de la solution influence de deux façons la méthode :

- toutes les valeurs de α donnent une approximation convergente,
- les ordres de convergence sont proches de 3 et semblent moins différents que dans le cas de la figure 2.3.

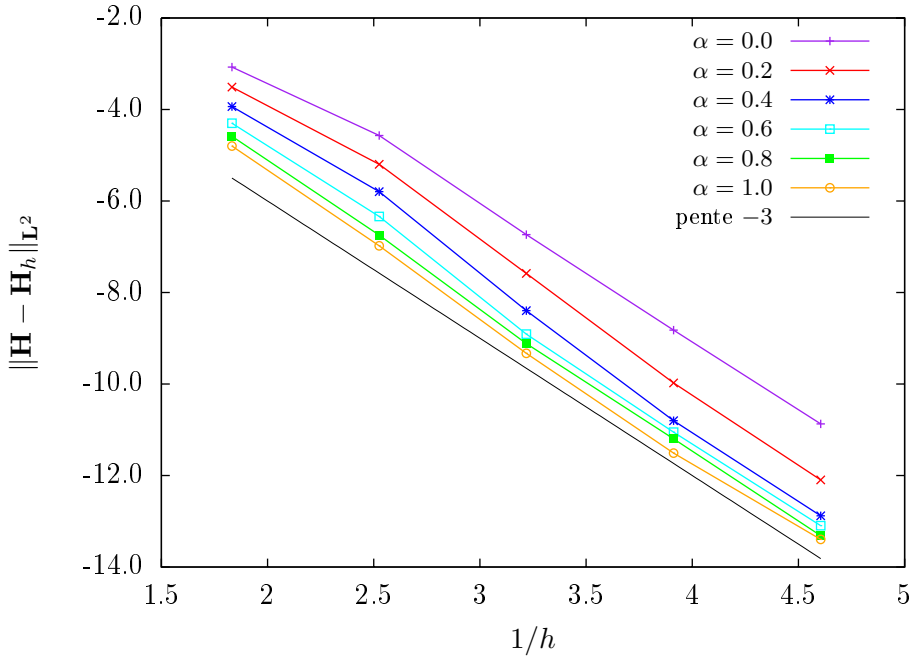

FIG. 3.8: Test 6 : erreur en norme $\mathbf{L}^2$ sur le champ magnétique dans le conducteur. La courbe est en échelle logarithmique.

Test 7

Ce test correspond encore au cas de la sphère de Durand, mais où l'on suppose cette fois que la sphère interne est isolante (cf. D.4.2, cas 2). Cette hypothèse ne change pas la solution analytique, mais elle change la méthode de résolution des équations. On fait encore le calcul en une itération, avec un pas de temps $\delta t = 10^{10}$. On utilise $\mu = 20$ dans le conducteur, et on présente en figure 3.9 l'erreur en norme $\mathbf{L}^2$, sur différents maillages, de taille caractéristique $h \in \{0.16, 0.08, 0.04, 0.02, 0.01\}$. On utilise différentes valeurs du paramètre α et, comme pour le test 6, toutes ces valeurs donnent une méthode convergente et les ordres de convergence ne semblent pas très différents : cela est encore dû à la régularité de la solution.

3.4.3 Cohérence avec la version non parallélisée du code

Depuis 2009, le code a subi de profondes modifications, avec des changements dans la méthode de résolution, au niveau théorique (méthode présentée plus haut) et pratique (changement de solveur linéaire). Il semble donc pertinent de vérifier sur un exemple que cela n'affecte pas les résultats obtenus précédemment. On reprend ici un cas de dynamo dans une configuration Taylor-Couette présenté dans [66]. Deux configurations sont étudiées, l'une faisant intervenir des conditions de périodicité, l'autre dans un cylindre fini. La configuration utilisée est la suivante : le domaine conducteur est compris entre deux cylindres coaxiaux de rayons respectifs 1 et 2. Le reste du domaine est considéré comme du vide. Le cylindre extérieur est au repos, alors que le cylindre intérieur tourne avec une vitesse angulaire de 1.

– Dans le cas périodique, le domaine de calcul utilisé a pour hauteur 4, et l'on applique des conditions de périodicité sur les bords $z = \pm 2$.

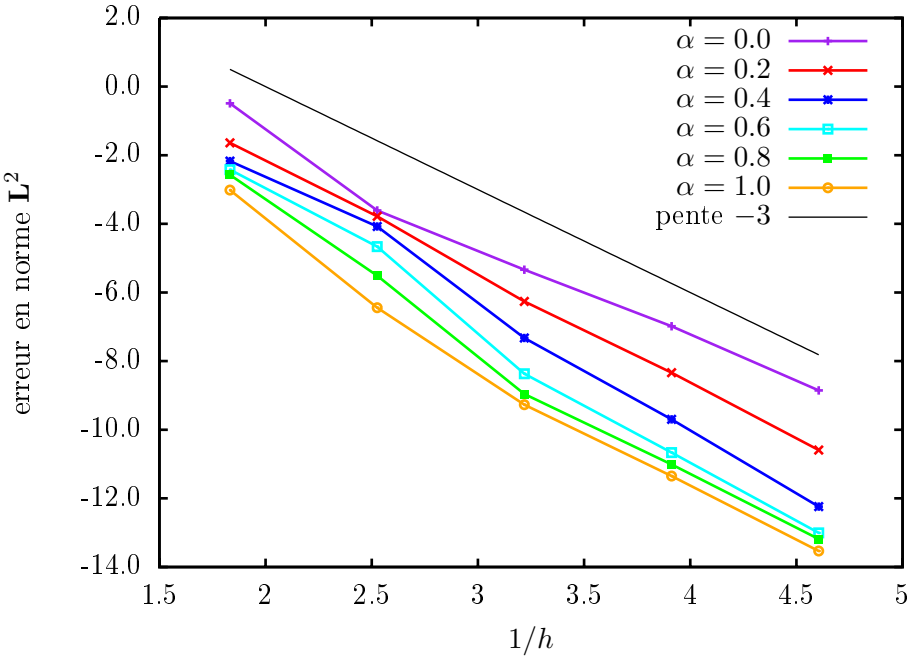

FIG. 3.9: Test 7 : erreur en norme $\mathbf{L}^2$ sur le champ magnétique dans le conducteur. La courbe est en échelle logarithmique.

– Dans le cas fini, le domaine de calcul utilisé a pour hauteur 2π, et l'on applique pour le champ de vitesses des conditions de Dirichlet homogènes à $z = \pm\pi$.

Dans chaque cas, on commence par calculer l'écoulement $\mathbf{u}_0$ obtenu par le seul forçage engendré par le mouvement des parois, avec un nombre de Reynolds $R_\mathrm{e} = 120$. À partir de ce champ, on fait ensuite des calculs de dynamo.

Dynamo cinématique

En gardant l'écoulement de base $\mathbf{u}_0$ stationnaire calculé juste avant, on calcule les taux de croissance pour différents nombres de Reynolds magnétiques. Les résultats obtenus sont reportés en figure 3.10. On note un excellent accord avec les calculs réalisés en 2007, malgré de légères différences entre les tailles caractéristiques et les pas de temps utilisés.

Dynamo non linéaire

On fixe $R_\mathrm{m} = 240$, et on lance des calculs non linéaires, où l'on fait évoluer à la fois le champ de vitesses et le champ magnétique. Pour le champ de vitesses, on prend comme condition initiale le champ de vitesses $\mathbf{u}_0$ précédemment calculé. Pour le champ magnétique, on prend comme condition initiale le champ obtenu dans le calcul de dynamo cinématique à $R_\mathrm{m} = 240$. Les figures 3.11 et 3.12 montrent l'évolution temporelle des énergies cinétiques et magnétiques. Dans le cas périodique, l'énergie magnétique croit jusqu'à un certain seuil (tandis que l'énergie cinétique décroit) et l'accord est excellent. Dans le cas fini en revanche, on voit un phénomène d'oscillations (non linéaires). À même taille caractéristique de maille, on voit des différences assez importantes : le calcul fait avec PETSC donne une évolution dont les

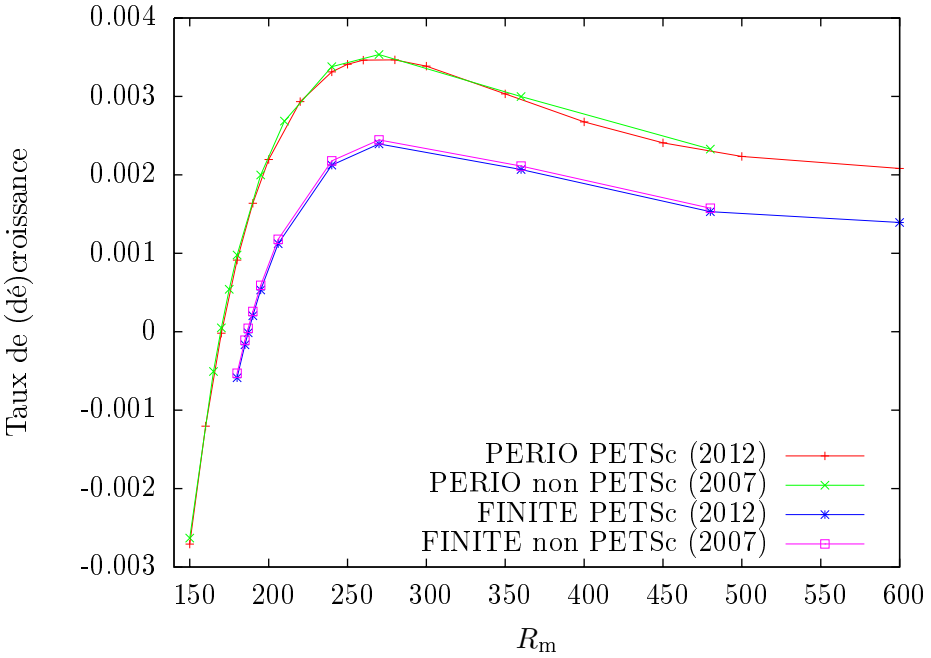

FIG. 3.10: Taux de croissance pour les cas de cylindre infini avec conditions périodiques (PERIO) et cylindre fini (FINITE).

non-linéarités sont plus apparentes, c'est pourquoi nous avons représenté plusieurs courbes. Trois ont été réalisées sans PETSC, avec une résolution de systèmes linéaires par méthode itérative. Deux ont été réalisées avec PETSC et une méthode directe de résolution (PETSC DIR), et la dernière utilise PETSC, mais avec une méthode itérative, pour laquelle on a utilisé la même précision que celle utilisée dans les calculs de 2007. Plusieurs tailles de mailles ont été utilisées. Pour le calcul utilisant PETSC avec une méthode itérative, on a relancé le calcul provenant de la méthode directe, ce qui explique que les courbes soient proches au début. En revanche, après quelques temps, on voit moins les non-linéarités dans le calcul utilisant la méthode itérative, et la forme se rapproche des calculs de 2007. On peut dire que les différences s'expliquent par le changement du solveur linéaire, et les courbes obtenues en 2012 semblent donc mieux correspondre au phénomène. En tout état de cause, le comportement observé est similaire (oscillations non linéaires), les périodes sont légèrement différentes, mais les extrema sont sensiblement les mêmes, ce qui constitue une bonne comparaison.

3.4.4 Efficacité de la parallélisation

On a déjà signalé que le code SFEMaNS était dès l'origine parallélisé selon les modes de Fourier. Des détails sur cette implémentation et sur les tests de performance peuvent être trouvés dans [66]. Ainsi, on ne s'intéresse ici qu'à l'efficacité de la parallélisation dans le plan méridien. Pour les modes de fonctionnnement "nst" et "mxw", on présente deux valeurs. Dans un premier temps, on fixe le maillage (assez fin), et l'on fait plusieurs calculs avec différents

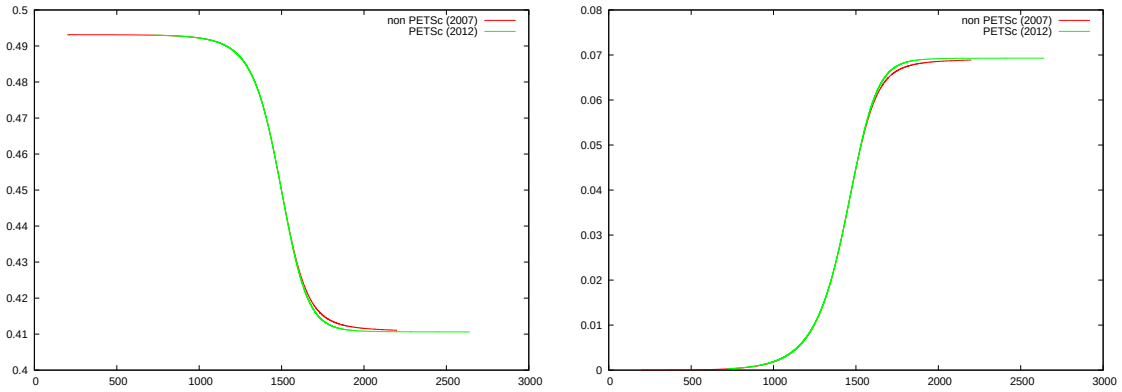

FIG. 3.11: Évolution temporelle de l'énergie cinétique (à gauche) et magnétique (à droite) dans le cas périodique

nombres de processeurs. On calcule alors

$$S(N) := \frac{T_{N_r} N_r}{T_N N},$$

où T_i représente le temps moyen d'une itération pour un découpage en i sous-domaines, et N_r est le nombre minimal de processeurs que l'on a utilisé pour faire le calcul (en général, on essaie de prendre $N_r = 1$, mais il peut arriver que les données soient trop importantes pour êtres traitées sur seulement 1 domaine). On fait également un test de parallélisation "faible", i.e. on lance plusieurs simulations avec différents nombres de processeurs, en faisant en sorte que le nombre moyen de degrés de liberté sur chaque processeur soit toujours le même. On s'attend alors à ce que la quantité

$$W(N) := \frac{T_{N_r}}{T_N},$$

où T_i représente le temps moyen d'une itération pour un découpage en i sous-domaines, soit proche de 1. Les résultats sont présenté dans le tableau 3.2. On peut remarquer que la paral-

N/N_r	NST ($N_r = 1$)		MXW ($N_r = 2$)	
	$S(N)$	$W(N)$	$S(N)$	$W(N)$
2	0.94	0.95	0.91	0.90
4	0.92	0.84	0.86	0.80
8	0.87	0.87	0.65	0.62
16	0.75	0.74	0.55	0.52

TAB. 3.2: Efficacité de la parallélisation, pour différents modes de fonctionnement de SFEMaNS. Les calculs pour le cas "nst" ont été réalisés via le test numéro 1 : pour $S(N)$, le maillage compte environ 200000 points dans le plan méridien ; pour $W(N)$, le maillage comporte environ 12000 points dans chaque sous-domaine du plan méridien. Les calculs pour le cas "mxw" ont été réalisés via le test numéro 4 : pour $S(N)$, le maillage compte environ 700000 points dans le plan méridien ; pour $W(N)$, le maillage comporte environ 40000 points dans chaque sous-domaine du plan méridien.

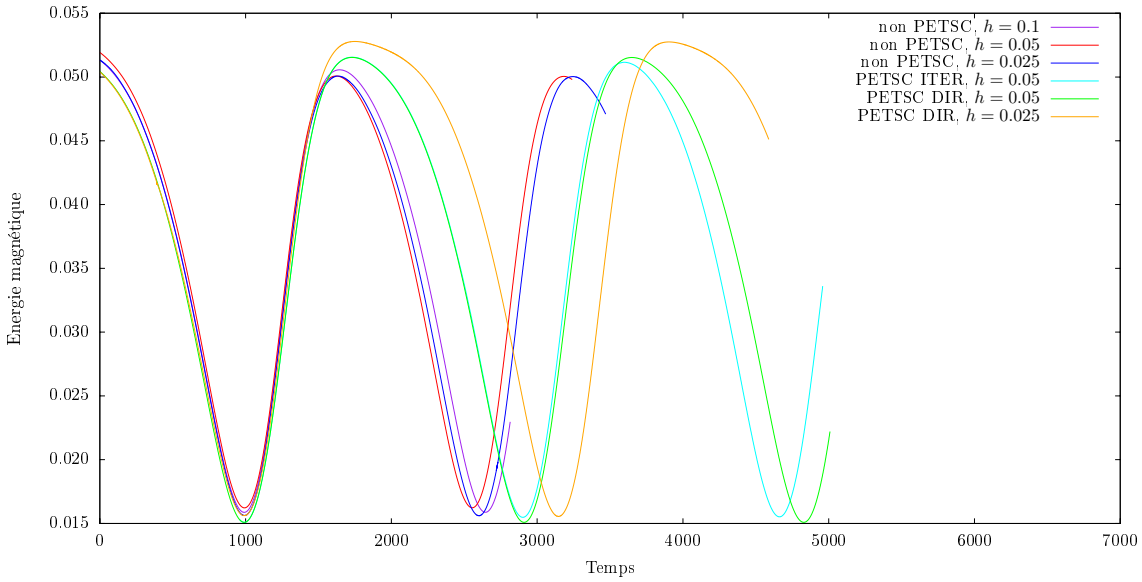

FIG. 3.12: Évolution temporelle de l'énergie magnétique dans un cylindre fini. Le graphique montre des résultats produits avec l'ancienne version du code (non PETSC), pour des maillages de taille caractéristique $h \in \{0.1, 0.05, 0.025\}$. En comparaison sont donnés des résultats faits avec PETSC, soit par méthode directe de résolution des systèmes linéaires (DIR), soit par méthode itérative (ITER)

lélisation est très bonne pour les calculs hydrodynamiques. Pour la résolution des équations de Maxwell, la parallélisation n'est pas optimale, et il y a sans doute encore des modifications à apporter au code afin de l'améliorer.

Chapitre 4

Application à l'effet dynamo

Ce chapitre a pour but de discuter les différentes applications testées au cours de cette thèse, concernant l'effet dynamo : excepté pour la section 4.1, les résultats sont présentés comme des résumés des annexes C à H. On renverra le lecteur à ces articles pour plus de détails. Notons également que l'implémentation de notre nouvelle méthode de résolution a été cruciale pour pouvoir résoudre correctement des problèmes dans des configurations de type VKS (cf. 4.2) dans lesquelles il y a de fortes variations de perméabilité.

4.1 Dynamo de Busse & Wicht

4.1.1 Configuration étudiée et adimensionnement

En 1992, Busse & Wicht ont proposé une configuration simple génératrice de dynamo [28]. L'idée est de faire circuler un fluide conducteur de l'électricité au dessus d'un matériau présentant des variations de conductivité. Cette étude a été poursuivie par B. Gallet dans le cas de matériau présentant des sauts de perméabilité [53]. Inspiré par des calculs de W. Herreman, on adapte ici cette configuration plane à un cas cylindrique. On considère deux cylindres coaxiaux, de rayons respectifs R et $R+g$ (cf. fig. 4.1 pour une vue de dessus), et d'axe Oz. Le cylindre intérieur Ω_1, de conductivité constante σ_1 et de perméabilité constante μ_1, tourne

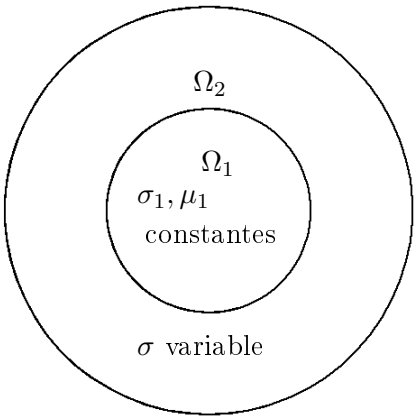

FIG. 4.1: Vue de dessus du dispositif

à vitesse angulaire ω. La couronne externe Ω_2 est immobile, et présente des variations de

perméabilité et/ou de conductivité. L'adimensionnement est basé sur le temps diffusif , i.e., on choisit les échelles de longueur, de vitesse et de temps suivantes :

$$\mathcal{L} = R, \qquad \mathcal{U} = \omega R, \qquad \mathcal{T} = \sigma_1 \mu_1 R^2.$$

L'équation adimensionnée vérifiée par le champ magnétique est alors l'équation (1.3.13)

$$\partial_t (\mu \mathbf{H}) = -\nabla\times \left(\frac{1}{\sigma} \nabla\times \mathbf{H} \right) + R_\mathrm{m} \nabla\times (\mathbf{u}\times\mu\mathbf{H}),$$

où $R_\mathrm{m} = \sigma_1\mu_1\omega R^2$. On choisit dans cette partie $\mathbf{u}(x,y) = (-y, x, 0)$. On ne s'intéresse qu'à des solutions périodiques dans la direction Oz, et on ne résout que pour un nombre d'ondes fixé, noté k_z. Ainsi, on se ramène à un problème en deux dimensions dans un plan orthogonal à l'axe Oz.

4.1.2 Dynamo cinématique avec sauts de conductivité

Dans un premier temps, on prend $\mu \equiv 1$ dans tout le domaine, et on fait varier σ dans la couronne de la manière suivante :

$$\sigma(r,\theta) = \frac{1}{\xi_0 + \kappa_0 \cos(\alpha_0 \theta)},$$

où (r,θ) désignent les coordonnées polaires, et $\xi_0, \kappa_0, \alpha_0$ sont des paramètres. On calcule pour différentes valeurs des paramètres $\xi_0, \kappa_0, \alpha_0, k_z, R_\mathrm{m}$ le taux de croissance (ou décroissance) du champ magnétique. Deux codes de calcul différents ont été utilisés : le premier (WH sur la figure), développé par W. Herreman, calcule des valeurs propres par une méthode implicite, et présente l'avantage de ne résoudre l'équation d'induction que dans la couronne (ainsi, elle évite le calcul dans des couches très fines aux alentours de l'interface $r = 1$). Le second code (FL sur la figure) utilise la méthode d'éléments finis avec stabilisation de la divergence dans les espaces intermédiaires présentée dans ce manuscrit, et calcule le champ magnétique dans le domaine complet. La figure 4.2 présente une comparaison satisfaisante pour des nombres de Reynolds magnétique variant de 100 à 15000. Pour notre méthode d'éléments finis, tous les calculs ont été faits avec le même maillage, qui s'avère être trop grossier pour des grandes valeurs de R_m, ce qui explique l'écart pour le calcul à $R_\mathrm{m} = 20000$. On note une évolution du taux de croissance proportionnelle à $R_\mathrm{m}^{1/3}$, ce qui induit une dynamo peu efficace. Les paramètres choisis pour ce calcul sont : $\alpha_0 = 1$, $k_z = 1$, $\xi_0 = 1$ et $\kappa_0 = 0.9$. Le seuil de dynamo trouvé est $R_\mathrm{mc} \simeq 11300$. Ce seuil est très élevé, et l'on aimerait trouver une configuration qui le fasse significativement baisser. Une idée est d'ajouter des variations de perméabilité en plus, par exemple, considérer $\mu = \mu_1$ constante sur Ω_1 et $\mu = \mu_2$ constante sur Ω_2. Une étude plus approfondie est en cours, mais il semblerait que $\mu_1 > \mu_2$ aide à baisser le seuil de dynamo, alors que dans la limite opposée, le seuil tend vers l'infini. Des calculs réalisés avec $\mu_1 = 10$, $\mu_2 = 1$ donnent un seuil $R_\mathrm{mc} \simeq 1520$ par exemple, ce qui est bien inférieur au cas $\mu_1 = 1$. Ce comportement n'est pas tellement étonnant, car, si l'on met de côté les conditions de compatabilité induites par ce saut de perméabilité, on remarque que, pour $\mu_2 = 1$ fixé, la variation de μ_1 influe directement sur le nombre de Reynolds. Augmenter μ_1 revient grosso modo à augmenter R_m, et donc contribue à abaisser le seuil.

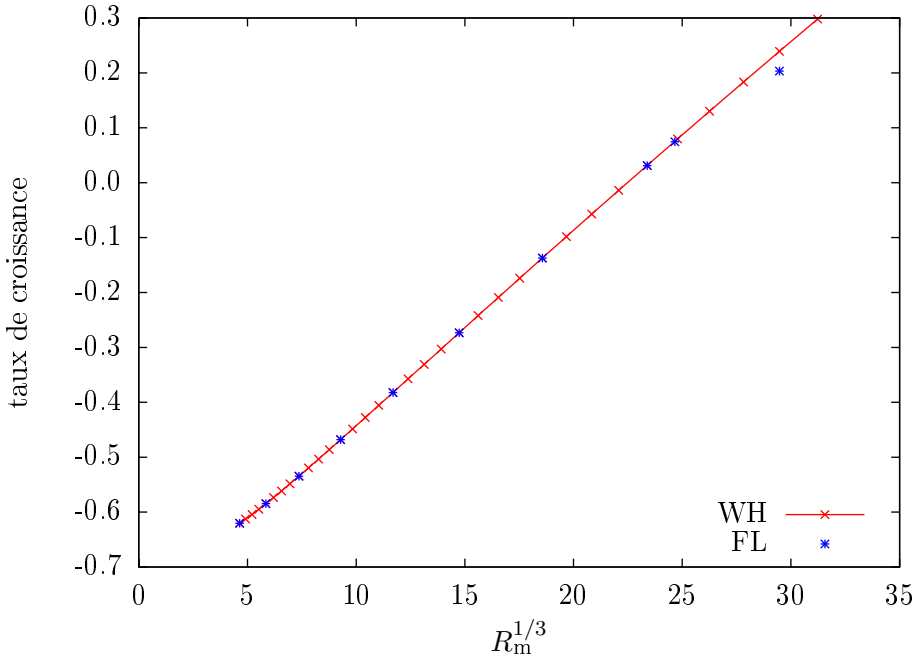

FIG. 4.2: Taux de croissance en fonction de R_m, pour $\alpha_0 = 1$, $k_z = 1$, $\xi_0 = 1$ et $\kappa_0 = 0.9$.

4.1.3 Dynamo cinématique avec sauts de perméabilité

On peut également utiliser notre méthode d'éléments finis pour faire des calculs avec $\sigma \equiv 1$ dans tout le domaine, et μ variable dans la couronne. En choisissant μ constant par morceaux dans la couronne, on décrit alors une situation plus réaliste. On choisit pour cet exemple $\mu = \mu_2$ constant dans la partie supérieure de la couronne, et $\mu = \mu_3$ constant dans la partie inférieure (cf. fig. 4.3). On présente en figure 4.4 les taux de croissance calculés pour différentes

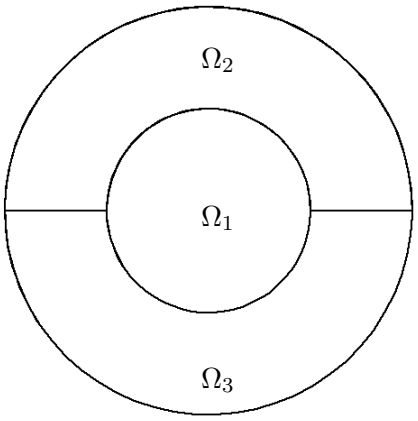

FIG. 4.3: Configuration avec sauts de perméabilité (vue de dessus).

valeurs de R_m avec les valeurs suivantes : $\mu_1 = 1$, $\mu_2 = 0.5$ et $\mu_3 = 0.1$. On trouve un nombre de Reynolds magnétique critique $R_m \simeq 7050$. Ce taux reste très élevé malgré les discontinuités de μ. Une étude plus approfondie concernant les valeurs de μ_1, μ_2 et μ_3 suscpetibles d'abaisser

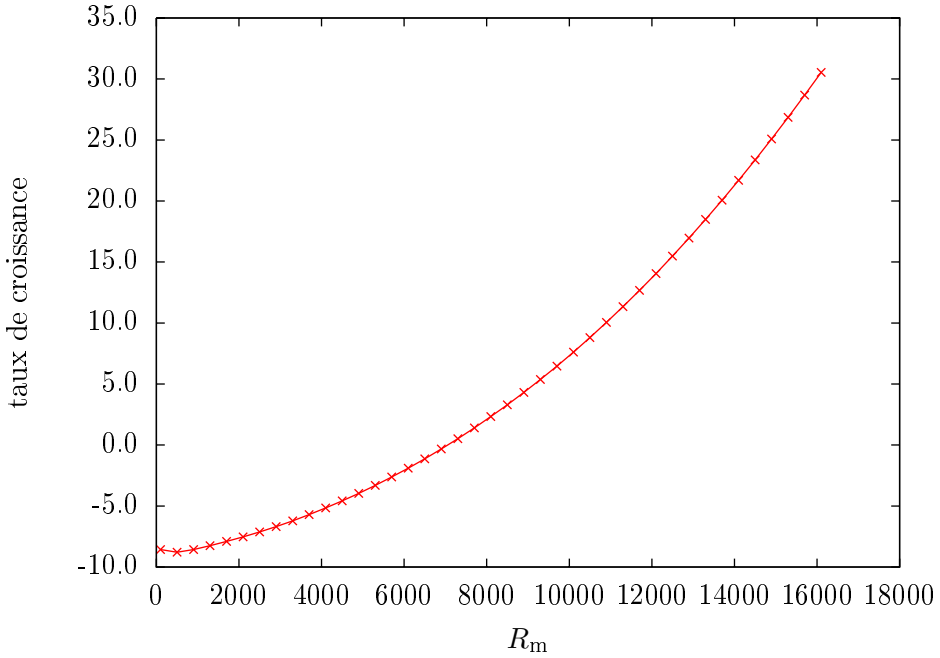

FIG. 4.4: Taux de croissance en fonction de R_m, dans la couronne avec sauts de perméabilité.

ce seuil dans des proportions raisonnables est à envisager.

4.1.4 Perspectives

Une étude plus approfondie du seuil de dynamo en fonction des variations de perméabilité est envisagée, mais n'a pas encore pu être réalisée. Il semble toutefois que des fortes variations de perméabilité (avec des valeurs importantes dans la zone où le fluide est en mouvement) contribuent fortement à l'abaissement du seuil de dynamo. Par ailleurs, nous étudions la possibilité d'ajouter une composante verticale sur la vitesse, pour ainsi étudier des configurations de type Ponomarenko. On pourra alors étudier encore l'influence de zones à fortes perméabilités. Enfin, une étude de la dynamo dans des configurations plus réalistes est envisagée, afin éventuellement de proposer un dispositif expérimental réalisable : une idée est par exemple d'ajouter une couronne entre le disque central et la couronne présentant des sauts de perméabilité, et d'y imposer un écoulement de type Taylor-Couette, i.e. de la forme $\mathbf{u} = \left(Ar + \frac{B}{r}\right)\mathbf{e}_\theta$.

4.2 Dynamo de type VKS

L'explication des phénomènes à l'origine de la dynamo obtenue par l'expérience VKS2 reste encore vague et non unanimement acceptée. Nous avons essayé de produire à partir de données expérimentales des simulations permettant de mieux comprendre le phénomène. Nous résumons ici les principaux résultats obtenus et discutons de leur possible signification vis à vis de l'expérience VKS.

4.2.1 Configuration étudiée

L'expérience menée à Cadarache consiste en la génération d'un champ magnétique par le mouvement de sodium liquide dans une cuve cylindrique, de rayon $R = 1.4$ et de hauteur $Z = 2.6$. Deux disques, de rayon $R_d = 0.95$ et d'épaisseur $h = 0.1$, munis de pales, sont mis en contrarotation pour forcer le mouvement du sodium liquide. La distance entre les deux disques est $H_i = 1.8$. Ce liquide est entouré d'une fine chemise de cuivre, elle-même entourée par une couronne de sodium au repos. Ce dispositif est contenu dans une cuve en cuivre. On renvoie à la figure 4.5 pour les détails sur les positions relatives des différents éléments. Notons que, numériquement, on ne modélise pas la fine chemise de cuivre séparant les deux couches de sodium liquide, ce qui revient à supposer qu'elle est suffisamment fine pour ne pas influencer le système. Par ailleurs, le code SFEMaNS ne peut pas prendre en compte les pales sur les disques, donc nous avons dans un premier temps modélisé uniquement un cas sans pales, afin de préserver l'axisymétrie. On distingue dans le domaine fluide trois zones distinctes :

- la zone située entre les disques $r \in [0, R_d]$, $z \in \left[-\frac{H_i}{2}, \frac{H_i}{2}\right]$, appelée "bulk-flow",
- la zone proche de la paroi latérale $r \in [R_d, R]$, $z \in \left[-\frac{H_i}{2}, \frac{H_i}{2}\right]$, appelée "side-layer",
- les zones situées derrière les disques $r \in [0, R]$, $|z| \in \left[\frac{H_i}{2} + h, \frac{Z}{2}\right]$, appelées "lid'flow".

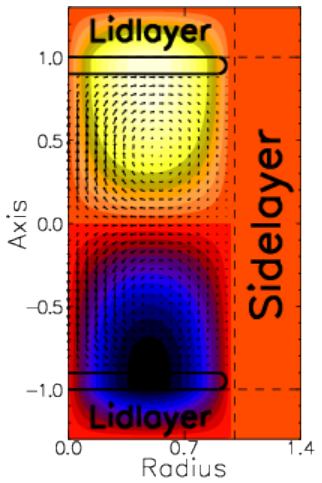

FIG. 4.5: Schéma simplifié du dispositif VKS. Nous représentons également la forme du flot MND (4.2.1) : les couleurs indiquent la vitesse toroïdale, alors que les vecteurs indiquent la vitesse poloïdale. Les traits noirs représentent le contour des disques.

Dans les notations adimensionnées, le fluide a une conductivité $\sigma = 1$ et une perméabilité $\mu = 1$. Les disques ont une conductivité $\sigma = \sigma_r$ et $\mu = \mu_r$. Rappelons que l'expérience a mis en évidence un effet dynamo dans le cas où les disques et les pales étaient en fer doux (ce qui correspond à une configuration du type $\sigma_r = 1$, $\mu_r >> 1$). Il semble important pour l'expérience que l'ensemble disque+pales en fer doux soit en rotation pour produire de l'effet dynamo. La question naturelle qui se pose est la suivante : est-ce que la présence d'une zone de forte perméabilité magnétique en mouvement est nécessaire à l'obtention d'un effet dynamo, ou est-ce qu'elle permet simplement de réduire le seuil de dynamo à un niveau réalisable expérimentalement ? Nous essayons par la suite de produire des simulations numériques pour tenter de répondre à cette question. Les différentes simulations que nous allons présenter

sont des calculs de dynamo cinématique, i.e. avec un champ de vitesses fixé. Par ailleurs, ce champ, décrit par (4.2.1), est axisymétrique. Il s'en suit que les champs magnétiques obtenus ne peuvent pas représenter le cas réellement observé par l'expérience, pour lequel la dynamo présente un mode axisymétrique. Néanmoins, l'étude de la dynamo cinématique nous donne quelques indications sur des mécanismes possibles pour la dynamo de Cadarache. Dans la suite, on ne s'intéresse qu'aux modes $m = 0$ et $m = 1$, et l'on sépare le mode $m = 0$ en une composante toroïdale et une composante poloïdale, dont on étudie les variations séparément.

4.2.2 Résultats principaux de l'annexe C

Décroissance ohmique

Dans un premier temps, on compare deux codes de calcul sur des cas de décroissance ohmique, i.e. on suppose que le fluide est au repos dans la cuve, et on regarde la décroissance du champ magnétique. Au delà du bon accord entre les deux codes de calcul (cf. figure C.8), on évalue l'influence des sauts de perméablité et/ou de conductivité sur le taux de décroissance du champ magnétique. Cette influence est étudiée pour deux valeurs différentes de h, l'épaisseur des disques. On note λ le taux de décroissance calculé ($\lambda < 0$). Lorsque les disques sont épais ($h = 0.6$), une augmentation du saut de perméabilité ou du saut de conductivité réduit la vitesse d'atténuation du champ magnétique (i.e. $|\lambda|$ diminue pour les trois cas considérés, i.e. les composantes toroïdale et poloïdale du mode $m = 0$, et le mode $m = 1$). En revanche, dans le cas de disques fins ($h = 0.1$, plus proches du cas expérimental), des différences nettes apparaissent entre les modes. En effet, si le mode $m = 1$ se comporte comme pour les disques épais, on n'observe presque aucune influence du saut de perméabilité (resp. saut de conductivité) sur la décroissance de la composante poloïdale (resp. toroïdale) du mode $m = 0$. Ce comportement est intéressant car on voit que les fortes variations de perméabilité atténuent fortement la composante poloïdale du champ magnétique, mais pas sa composante toroïdale, ce qui confère au champ magnétique une forme plus proche de celle trouvée expérimentalement.

Dynamo cinématique (mode $m = 1$)

Pour les calculs de dynamo cinématique, on utilise comme champ de vitesses le flot MND (Marié-Normand-Daviaud, [102]) :

$$\left\{ \begin{array}{rcl} u_r &=& -\dfrac{\pi}{H_i} r(1-r)^2(1+2r)\cos\left(\dfrac{2\pi z}{H_i}\right), \\ u_\theta &=& 4\epsilon r(1-r)\sin\left(\dfrac{\pi z}{H_i}\right), \\ u_z &=& (1-r)(1+r-5r^2)\sin\left(\dfrac{2\pi z}{H_i}\right), \end{array} \right. \tag{4.2.1}$$

où ϵ est le rapport entre la vitesse toroïdale et la vitesse poloïdale et H_i est la distance entre les deux disques. Ici, on utilise $H_i = 1.8$ pour respecter le rapport de forme et $\epsilon = 0.7259$ d'après une étude précédente [137]. On ne s'intéresse qu'au mode $m = 1$. Les simulations reportées (pour différentes valeurs de R_m) en figure C.13 montrent trois choses intéressantes :

- les variations de conductivité n'aident pas à augmenter λ, et on n'obtient pas de dynamo pour les Reynolds considérés,

- en revanche, pour des sauts de perméabilité, on obtient un seuil autour de $R_{\mathrm{mc}} \simeq 55$. On voit par ailleurs qu'au delà d'une certaine valeur de μ_r, le taux de (dé)croissance du champ magnétique semble indépendant de μ_r,
- les taux de croissance sont très sensibles à la forme du champ de vitesses dans la région du "bulk-flow" : de petites variations dans le flot provoquent d'importantes variations du taux de croissance.

Ces calculs renforcent donc l'idée que la présence de zones à fortes perméabilités est cruciale pour la dynamo de Cadarache, alors que des sauts de conductivité semblent la freiner. Ils soulignent également l'importance d'une modélisation aussi précise que possible de ces zones de forte perméabilité, ainsi qu'une évaluation précise du champ de vitesses. Dans le cadre de notre approximation, on peut néanmoins noter que le seuil calculé pour le mode $m = 1$ est supérieur au Reynolds magnétique estimé dans les expériences, ce qui est en accord avec le fait que la dynamo observée expérimentalement présente un mode axisymétrique.

4.2.3 Résultats principaux de l'annexe D

On résume ici les résultats de dynamo cinématique présentés dans l'annexe D. On a souligné précédemment que la forme de l'écoulement dans la zone du "bulk-flow" influait fortement sur les seuils calculés. On essaie d'utiliser un écoulement plus proche de celui réellement observé. Pour ce faire, on prend ici comme champ de vitesses un flot axisymétrique provenant de mesures dans une expérience réalisée avec de l'eau dans une configuration VKS (cf. [123]). On ne s'intéresse ici qu'au mode $m = 1$. On montre alors que dans le cas de disques de forte perméabilité ($\mu_r >> 1$), la forme du flot derrière les disques ("lid-flow") n'influe pas sur le seuil de la dynamo (cf. tableau F.1) : la présence de disques de fortes perméabilités écrante l'effet du "lid-flow". Dans le cas de disques de perméabilité $\mu_r = 1$ en revanche, l'effet du "lid-flow" est visible, et influe sur le seuil de dynamo. Cela suggère donc qu'il est surtout nécessaire de se concentrer sur la zone du "bulk-flow", et la zone latérale ('side layer'), mais que les régions derrière les disques ne sont pas importantes dans la dynamo de Cadarache.
Un autre résultat intéressant dans cette optique est un calcul effectué dans un modèle encore plus simplifié de l'expérience VKS. On ne s'intéresse ici qu'à la zone entre les deux disques. Les domaines simplifiés sont présentés en figure 4.6. On distingue trois cas :

- Cas 1 : on considère la région du "bulk-flow", la "side-layer" contenant du sodium immobile, et une chemise en cuivre autour. Le reste est considéré comme isolant (en particulier, cela modélise un cas où les disques sont isolants) : on trouve $R_{\mathrm{mc}} = 45$.
- Cas 2 : on garde le même domaine que pour le cas 1, mais on impose sur le champ magnétique la condition $\mathbf{H}\times\mathbf{n} = 0$ sur $\{z = \pm\frac{1}{2}H_i,\ 0 \leq r \leq R_0\}$. Cela correspond au cas où les disques ont une perméabilité infinie : on trouve $R_{\mathrm{mc}} = 40$.
- Cas 3 : on ne garde que la région du "bulk-flow", que l'on considère entourée d'une enveloppe de perméabilité infinie (i.e. on impose $\mathbf{H}\times\mathbf{n}$ partout). Il n'y a pas de région isolante ici : on trouve $R_{\mathrm{mc}} = 52$.

On peut déduire de ces calculs que la présence de disques de forte perméabilité aide à réduire le seuil de dynamo. Par ailleurs, la présence de sodium immobile autour de l'écoulement semble également jouer un rôle important, alors que le confinement du flot dans une enveloppe de perméabilité infinie se révèle contre-productif. En particulier, cela montre que la présence de zones à forte perméabilité, si elle est cruciale dans l'expérience VKS, n'est pas la seule condition à la dynamo. Il faut en outre que ces zones soient placées à des endroits spécifiques, avec pour effet des contraintes géométriques liées aux conditions de continuité du champ magnétique.

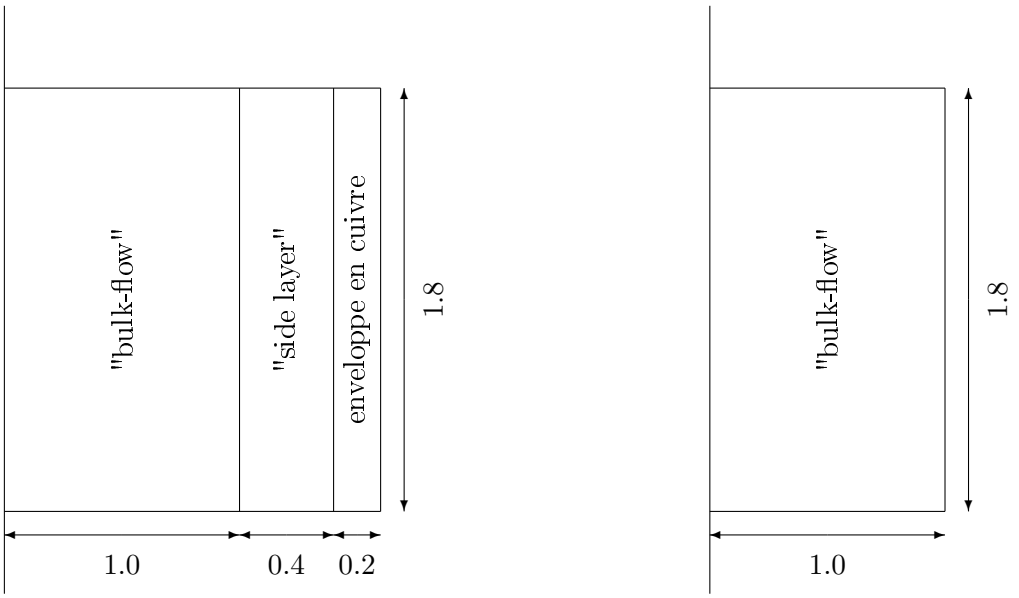

FIG. 4.6: Modèles simplifiés pour VKS : à gauche pour les cas 1 et 2, à droite pour le cas 3.

Ces contraintes pourraient alors donner des champs magnétiques plus propices à la dynamo.

4.2.4 Résultats principaux de l'annexe E

Les deux articles précédents ont pu attester de l'importance de disques de forte perméabilité dans l'expérience de Cadarache. Dans cet article, on pousse plus avant l'étude de l'influence de μ_r sur les seuils de dynamo. Outre une loi d'échelle pour le comportement de R_{mc} en fonction de μ_r mise en évidence pour le mode $m = 1$ avec l'écoulement MND donné en (4.2.1), l'étude montre des résultats probants sur le mode $m = 0$. Pour celui-ci, on note que le flot n'a pas ou peu d'importance : par conséquent, on se limite à l'étude du cas de décroissance ohmique. Par ailleurs, on voit qu'au delà d'un certain seuil de μ_r, c'est la composante toroïdale du mode $m = 0$ qui est la moins atténuée. Cet effet, visible sur des disques de faible épaisseur, est lié à un phénomène de 'pompage paramagnétique' (cf. section E.4). On montre alors que la composante toroïdale du mode $m = 0$ est localisée au niveau des disques, et que son taux de décroissance augmente de façon inversement proportionnelle à μ_r, ce qui implique que c'est cette composante qui est la moins atténuée pour de grandes valeurs de μ_r.

4.2.5 Conclusions

Les différentes simulations numériques ont confirmé que la présence de disques de forte perméabilité était essentielle, car elle permet de réduire significativement le Reynolds magnétique critique. Il semblerait que les contraintes géométriques induites par les conditions de continuité du champ magnétique soient également impliquées dans la dynamo, ce qui suggère que même pour de grandes valeurs de R_{m}, on ne peut pas obtenir de dynamo avec des disques en acier. Par ailleurs, il semble que des variations de conductivité dans les disques soient un obstacle à la dynamo. Enfin, l'utilisation de disques fins de forte perméabilité permet de réduire l'atténuation du mode $m = 0$, même sans champ de vitesses. On peut alors penser que l'effet de pompage paramagnétique, qui intervient sur la composante purement toroïdale du

mode $m = 0$, puisse par la suite agir sur la partie poloïdale par l'intermédiaire des termes de couplage, lorsque les distributions de perméabilités ne sont plus axisymétriques (comme dans le cas réel) et/ou pour des champs de vitesses non axisymétriques. Cela pourrait jouer un rôle important dans la dynamo de Cadarache.
En revanche, les simulations numériques ne permettent pour le moment pas de comprendre l'importance de la rotation des disques dans le mécanisme de dynamo.

4.3 Dynamo non linéaire Taylor-Couette

4.3.1 Écoulement de Taylor-Couette dans un cylindre de petit rapport de forme

Dans cette partie, on s'intéresse à un écoulement de type Taylor-Couette dans le domaine suivant : le domaine conducteur est constitué de deux cylindres coaxiaux de rayons respectifs R_i et R_o, et de hauteur L_z. Le rapport de forme est $\Gamma = \frac{L_z}{\mathcal{L}}$ où $\mathcal{L} = R_o - R_i$. Le cylindre intérieur est supposé solide et tourne à vitesse angulaire Ω_i. L'espace entre les deux cylindres est supposé fluide. On considère que la conductivité et la perméabilité sont constantes dans tout le domaine. Enfin, on suppose que ces cylindres sont entourés de vide. Le dispositif est similaire à celui de la section 3.4.3. Deux différences sont à noter : tout d'abord, on s'intéresse ici à un plus petit rapport de forme $\Gamma = 2$. Par ailleurs, le haut et le bas du domaine tournent ici avec la même vitesse angulaire que le cylindre intérieur. On va s'intéresser à la possibilité de générer un champ magnétique avec un écoulement dans cette géométrie.

4.3.2 Résultats principaux de l'annexe F

Rapport vitesse poloïdale / vitesse toroïdale

Dans un premier temps, on utilise cette configuration pour calculer l'écoulement de base, pour un petit nombre de Reynolds $R_\mathrm{e} = 120$. On obtient un écoulement stationnaire axisymétrique. On utilise alors cet écoulement pour des calculs de dynamo cinématique, à bas Reynolds magnétique ($R_\mathrm{m} \leq 200$). On remarque alors que l'écoulement de base ne permet pas d'engendrer de la dynamo. On modifie alors cet écoulement de base, pour étudier l'influence du rapport entre vitesse poloïdale et vitesse toroïdale sur le champ magnétique. On reporte en figure 4.7 l'évolution du taux de croissance du champ magnétique en fonction de ϵ, paramètre adimensionné proportionnel au rapport entre vitesse poloïdale et vitesse toroïdale. On voit alors apparaître, pour $R_\mathrm{m} = 200$, une fenêtre de dynamo pour certaines valeurs de ϵ. Par exemple, on voit que pour $\epsilon = 1$, qui correspond au cas de l'écoulement de base non modifié, on n'a pas de dynamo (et le rapport entre vitesses poloïdale et toroïdale est $\Lambda = 0.235$). En revanche, on dépasse le seuil de dynamo à $\epsilon = 6.5$ (i.e. $\Lambda = 1.5275$) par exemple.

Calculs avec forçage

L'écoulement utilisé pour obtenir une dynamo (avec $\epsilon \neq 1$) n'est pas physique : on essaie donc par la suite d'imposer un forçage sur le champ de vitesses afin d'obtenir un écoulement de base présentant un rapport $\Lambda \simeq 1.53$ entre vitesse poloïdale et vitesse toroïdale compatible avec la fenêtre de dynamo précédemment observée. Ce forçage est localisé à proximité des parois supérieure et inférieure du cylindre, et peut être interprété comme l'action de pales sur l'écoulement. Avec ce forçage, on calcule un nouvel écoulement de base, utilisé ensuite

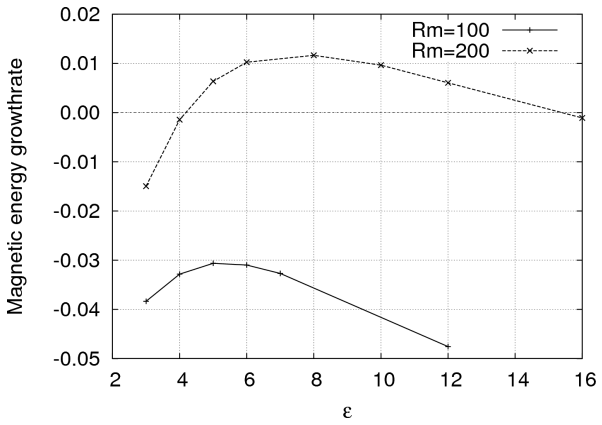

FIG. 4.7: Taux de croissance du champ magnétique en fonction du rapport entre vitesse poloïdale et toroïdale, pour deux valeurs de R_{m}

pour des calculs de dynamo cinématique : on obtient alors un seuil de dynamo $R_{\mathrm{mc}} \simeq 180$. Il est bon de noter que ce seuil est en accord avec des calculs réalisés en géométrie sphérique (cf. [44]) ou dans des cas de plus grand rapport d'aspect (cf. [66]). On peut également utiliser ces données pour un calcul non-linéaire complet de MHD, à $R_{\mathrm{m}} = 200$. Au cours du temps, on peut percevoir des changements dans la structure de cette dynamo. Dans un premier temps, on a une évolution du champ magnétique similaire au cas de dynamo cinématique (pour le mode $m = 1$). Une fois que le champ magnétique est suffisamment important pour nourrir la force de Lorentz, les autres modes de Fourier commencent à contribuer à la dynamo, et le champ de vitesses perd sa symétrie cylindrique. En revanche, la symétrie équatoriale des champs est encore respectée. Cette symétrie finit par être brisée au cours d'une courte phase de transition, provoquée par la croissance des modes pairs du champ magnétique. Il s'en suit une phase dont la dynamique est dominée par les grands modes de Fourier. Un régime non linéaire est finalement atteint lorsque les modes pairs du champ magnétique cessent de croître. Cette dynamo présente dans un premier temps les caractéristiques d'un dipôle équatorial, mais dans le régime non linéaire final, une composante verticale du dipôle magnétique apparaît et présente des inversions.

4.3.3 Conclusions

On a montré que, dans une configuration de type Taylor-Couette dans un cylindre de petit rapport de forme, un écoulement non forcé ne permet pas d'obtenir de dynamo à faible Reynolds magnétique. En revanche, il est possible d'ajouter un forçage ad hoc qui permet au flot de présenter un rapport entre vitesse poloïdale et vitesse toroïdale compatible avec une dynamo. On interprète ce forçage comme une action de pales sur le fluide. On peut alors imaginer une expérience dans cette configuration, dans le but d'optimiser encore le rapport entre vitesse poloïdale et vitesse toroïdale. Ce pourrait être un bon indicateur sur la forme des pales et/ou sur la puissance à fournir dans un tel dispositif. Il semble être réalisable expérimentalement, et la puissance à fournir pourrait être inférieure à celle utilisée dans l'expérience de Cadarache car, pour des géométries similaires, les turbulences induites par des turbines co-rotatives sont moins importantes que dans le cas de turbines contra-rotatives. Une expérience de dynamo est d'ailleurs envisagée par Colgate et al. [34].

4.4 Dynamo en précession

4.4.1 Cadre

Dans cette section, on s'intéresse à un cas de dynamo fluide homogène, et plus particulièrement à la possibilité d'engendrer un effet dynamo à partir d'un fluide contenu dans une cuve en précession. Le cadre général est le suivant : on considère une cuve présentant une symétrie cylindrique. Cette cuve est remplie par un fluide conducteur de l'électricité (on supposera ici $\mu = 1$ et $\sigma = 1$ dans cette partie). L'axe de symétrie de la cuve est mis en précession autour d'un axe dirigé par un vecteur unitaire $\mathbf{e}_p$ dans le référentiel du laboratoire. En outre, on suppose que la cuve tourne autour de son axe de symétrie (dirigé par $\mathbf{e}_z$). La cuve est entourée de vide, et nous négligeons les effets éventuels liés à l'épaisseur de la cuve. On se place dans le référentiel en précession, i.e. dans un référentiel pour lequel le seul mouvement de la cuve est la rotation autour de son axe de symétrie. Ainsi, les équations de Navier-Stokes prennent une forme légèrement différente de (1.3.22), en faisant maintenant intervenir la force de Coriolis :

$$\partial_t \mathbf{u} + (\nabla\times\mathbf{u})\times\mathbf{u} - \frac{1}{R_\mathrm{e}}\Delta\mathbf{u} + 2\epsilon\mathbf{e}_p\times\mathbf{u} = -\nabla p + (\nabla\times\mathbf{H})\times(\mu\mathbf{H}) + \mathbf{f}, \tag{4.4.1}$$

où ϵ est le taux de précession, i.e. le rapport entre la vitesse angulaire de la précession autour de $\mathbf{e}_p$ et la vitesse angulaire de rotation autour de l'axe de symétrie.

4.4.2 Précession dans un cylindre (résultats principaux de l'annexe G)

Dans un premier article, on étudie la possiblité d'une dynamo dans une cuve cylindrique en précession. On se place dans un cylindre de rapport de forme $\frac{H}{R} = 2$, où H est la hauteur totale du cylindre, et R son rayon. On se restreint au cas $\epsilon = 0.15$, et on considère que les axes de précession et de rotation sont orthogonaux.

Régime hydrodynamique

Dans un premier temps, on se focalise sur les équations de Navier-Stokes uniquement. Le seul forçage ici provient de la rotation de la cuve, i.e. on prend $\mathbf{H} = 0$ et $\mathbf{f} = 0$ dans l'équation (4.4.1), et on impose que le champ de vitesses sur le bord corresponde à la rotation de la cuve. En faisant varier le nombre de Reynolds R_e, on observe un comportement similaire à celui décrit dans des cavités sphériques en précession : à bas nombre de Reynolds, le champ de vitesses est stationnaire et centrosymétrique (i.e. $\mathbf{u}(-\mathbf{x}) = -\mathbf{u}(\mathbf{x})$). Lorsqu'on augmente le nombre de Reynolds, le flot perd à la fois son caractère symétrique et stationnaire. L'énergie cinétique est transférée de façon cyclique entre la partie supérieure et la partie inférieure du cylindre. S'inspirant de [148, 156], on s'attend à ce que la dynamo soit facilitée par un écoulement asymétrique instationnaire, c'est pourquoi on utilise par la suite $R_\mathrm{e} = 1200$.

Dynamo

Afin de déterminer des valeurs de R_m susceptibles de générer une dynamo, on commence par effectuer des calculs de dynamo cinématique. Comme le champ de vitesses calculé pour $R_\mathrm{e} = 1200$ n'est pas stationnaire, on résout à la fois l'équation d'induction et les équations de Navier-Stokes, mais on retire le couplage dans la partie hydrodynamique (i.e. on résout (1.3.22) avec $A = 0$). Le calcul à $R_\mathrm{e} = 1200$ donne alors un seuil de dynamo $R_\mathrm{mc} \simeq 750$. Des calculs non

linéaires ont ensuite été effectués, pour différents nombres de Reynolds magnétiques, variant de 600 à 2400, et ont permis de prouver qu'une dynamo pouvait être générée par un cylindre en précession. Par ailleurs, la figure 4.8 (reproduction de la figure G.10) montre une coïncidence remarquable sur l'évolution de l'énergie magnétique dans trois cas distincts, à $R_\mathrm{m} = 1200$:

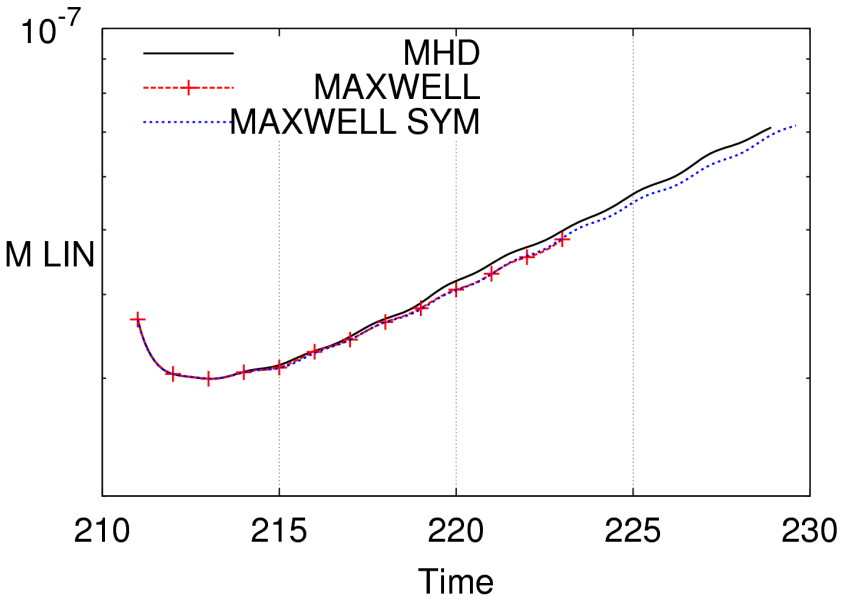

FIG. 4.8: Évolution de l'énergie magnétique en fonction du temps ($R_\mathrm{e} = 1200$, $R_\mathrm{m} = 1200$)

- le premier cas (MHD sur la figure) correspond au calcul de MHD non linéaire, avec $R_\mathrm{e} = 1200$
- le deuxième cas (MAXWELL sur la figure) correspond au calcul de dynamo cinématique à partir d'un champ de vitesses figé, provenant d'un calcul hydrodynamique à $R_\mathrm{e} = 1200$,
- le troisième cas (MAXWELL SYM sur la figure) correspond au calcul de dynamo cinématique pour lequel on ne prend que la partie symétrique du champ de vitesses utilisé dans le cas MAXWELL.

Cela suggère que ni la rupture de symétrie, ni la dépendance temporelle du champ n'influe de façon drastique sur cette dynamo. Enfin, il est bon de souligner que, en admettant que le seuil est fixé par la valeur de R_mc et pas par la valeur de nombre de Prandtl $P_\mathrm{m} = \frac{R_\mathrm{m}}{R_\mathrm{e}}$, les valeurs de paramètres permettant l'effet dynamo semblent atteignables expérimentalement, et nous espérons pouvoir bientôt comparer ces simulations numériques à l'expérience DresDyn, actuellement en cours de montage en Allemagne [134].

4.4.3 Précession dans un sphéroïde (résultats principaux de l'annexe H)

Là encore, on étudie une configuration où l'axe de précession et l'axe de rotation sont orthogonaux. La cuve est ici considérée comme étant un sphéroïde (i.e. un ellipsoïde avec une symétrie cylindrique). Le point de départ de cet article était l'étude de la dynamo dans une telle configuration. Comme pour toutes les configurations étudiées, la première étape est de vérifier que l'on peut calculer un écoulement de base. Là encore, le seul forçage vient de la rotation de la cuve. Stewartson et Roberts [138] ont montré que, dans la limite d'un fluide peu visqueux

et avec un faible taux de précession, le champ de vitesses a une expression analytique simple, excepté dans de fines couches d'Ekman au niveau de la frontière du domaine. Ce flot, linéaire, est souvent appelé *solution de Poincaré*, et on donne son expression en (H.3.6). S'inspirant de [156], on modifie les conditions aux limites sur le champ de vitesses, afin de ne pas avoir à traiter ces couches limites. On introduit une nouvelle formulation (cf. (H.3.2) à (H.3.7)), qui s'est avérée être plus délicate que prévu à résoudre, ce qui explique qu'on ne s'intéresse dans cet article qu'au régime hydrodynamique. L'avantage de ce nouveau jeu de conditions aux limites est que le système admet une solution stationnaire simple, en l'occurrence la solution de Poincaré. Mais l'inconvénient majeur est que cette solution n'est ni unique (d'autres solutions non physiques apparaissent), ni stable. Nous nous sommes donc efforcés de comprendre ce qui posait problème, tout en essayant de proposer une méthode numérique qui permette dans une certaine mesure d'approcher une solution du système. Dans le même esprit que [138], nous avons été en mesure de prouver que, si le produit ϵR_e (où ϵ désigne le taux de précession) est suffisamment faible, alors toute solution de (H.3.2)– (H.3.7) tend vers un champ stationnaire de la forme $\mathbf{u}_P + \mathbf{w}$, où $\mathbf{u}_P$ désigne la solution de Poincaré, et $\mathbf{w}$ est une rotation solide autour de l'axe de symétrie. Des comparaisons avec d'autres codes de calcul ont été effectuées, soulignant toutes ce problème lié aux rotations autour de l'axe de symétrie. Numériquement, l'un des problèmes principaux est le contrôle de la composante verticale du moment cinétique,

$$M_z = \int_\Omega \mathbf{x}\times\mathbf{u}\cdot\mathbf{e}_z.$$

Dans le cas $\epsilon = 0$, nous avons pu mettre au point une méthode permettant numériquement de contrôler M_z, évitant ainsi l'apparition d'une composante supplémentaire de rotation solide. Dans le cas $\epsilon \neq 0$, il n'est toutefois pas encore clair de savoir si un tel ajustement est possible, sans imposer une nouvelle condition sur le moment cinétique, qui pourrait être incompatible avec la physique. En revanche, nous avons proposé un nouveau jeu de conditions aux limites, dans le même esprit mais en cassant la symétrie de la formulation, qui semble éviter ces problèmes de stabilité. Des calculs de dynamo sont envisagés par la suite, une fois que ce problème hydrodynamique sera mieux compris.

4.4.4 Conclusions

Nous avons montré que le mouvement de précession pouvait à lui seul être générateur de dynamo, dans le cas d'une géométrie cylindrique. Par ailleurs, l'étude de cette dynamo a montré de façon surprenante une relative indépendance de la croissance du champ magnétique vis à vis de l'asymétrie et de l'instationnarité du champ de vitesses. Ce comportement, contraire aux prédictions de Tilgner [148], peut n'être qu'un cas particulier à $R_\mathrm{e} = 1200 = R_\mathrm{m}$. Il serait intéressant d'étudier l'influence des brisures de symétrie et de l'instationnarité du flot sur la dynamo, pour une gamme plus large de paramètres.
Par ailleurs, nous avons commencé à explorer le cas d'un sphéroïde en précession. Le changement de conditions aux limites sur le champ de vitesses, qui devait nous permettre de faciliter la résolution en supprimant les couches limites, a finalement soulevé des problèmes de stabilité auxquels nous avons répondu en nous démarquant de [156]. Nous espérons pouvoir par la suite obtenir des calculs satisfaisants de dynamo.

Chapitre 5

Conclusion et perspectives

5.1 Bilan général

Cette thèse s'inscrit comme un prolongement naturel de celles de R. Laguerre ([87], soutenue en Décembre 2006) et A. Ribeiro ([124], soutenue en Juillet 2010). Le fil conducteur de ce travail a été l'amélioration constante du code de calcul SFEMaNS, qui est l'un des seuls outils capables d'intégrer le système complet d'équations de la MHD, dans n'importe quelle configuration axisymétrique. L'un des principaux objectifs était de modifier la méthode de résolution des équations de Maxwell, afin d'obtenir une méthode capable de résoudre efficacement les problèmes faisant intervenir une distribution hétérogène de perméabilité et/ou de conductivité, ou des singularités géométriques, dans le cas stationnaire.

À ces fins, une nouvelle inconnue, appelée *pression magnétique*, a été introduite dans les équations et une formulation mixte a pu être écrite. Cette *pression magnétique* peut à la fois être vue comme un multiplicateur de Lagrange associée à la contrainte de divergence nulle, et comme un terme de stabilisation. Par ailleurs, un autre terme de stabilisation a été ajouté, et nous a permis de valider la méthode numérique avec des choix relativement simples d'éléments finis. En particulier, cette méthode autorise les éléments finis de Lagrange, et ne requiert que peu d'hypothèses sur l'espace d'approximation pour la pression magnétique. Les différentes conditions de continuité (au sein du conducteur ou entre conducteur et isolant) sont traitées par des méthodes de pénalisation. Un travail théorique important a été effectué afin de valider la méthode dans un cadre général. En particulier, les résultats de régularité présentés en annexe A peuvent ne pas être nouveaux dans la communauté mathématique, mais les références à de tels résultats sont difficiles à trouver, et nous pensons que cet article les résume bien. La validation théorique inclut également la preuve de convergence du schéma dans un modèle simplifié 2D. Cette convergence a été illustrée par de nombreux exemples recouvrant les difficultés possibles : singularités géométriques, sauts de perméabilité, calcul de valeurs propres. Nous avons ensuite adapté cette méthode au sein du code SFEMaNS.

Outre la méthode de résolution de l'équation d'induction, un profond remaniement au sein du code SFEMaNS a été effectué au cours de cette thèse, afin d'en améliorer les performances. Alors qu'il était jusque là parallélisé uniquement selon les modes de Fourier, nous avons ajouté un niveau de parallélisation, concernant la résolution des systèmes linéaires dans les plans méridiens. Nous avons également exploré différents solveurs linéaires, pour finalement renoncer à une méthode itérative au profit d'une méthode directe, qui nous fait gagner énormément de temps de calcul. La contrepartie est une dépense de mémoire plus importante, mais nous

pensons qu'à l'heure actuelle, étant données les capacités des calculateurs, cette contrepartie est plus qu'acceptable. Après toutes ces modifications, une étape de validation du code a été nécessaire. Elle a été effectuée de deux façons différentes et complémentaires. Dans un premier temps, on a montré sur des cas analytiques que le code convergeait de façon convenable, que ce soit sur des calculs hydrodynamiques ou sur des calculs de dynamo cinématique. Par ailleurs, nous avons vérifié que le code était cohérent avec d'anciennes versions, au travers d'un exemple de dynamo non-linéaire dans une configuration de type Taylor-Couette.

Grâce à cette *pression magnétique*, nous avons pu en application faire de nombreux calculs dans des configurations de type VKS, pour lesquelles il y a de forts sauts de perméabilité. En particulier, nous avons pu illustrer numériquement l'importance de la présence de disques *fins* en fer. L'un des atouts de ces disques est qu'ils écrantent l'effet de l'écoulement derrière eux, écoulement qui est apparu défavorable à la dynamo dans d'autres simulations. Par ailleurs, l'épaisseur des disques et les conditions de compatibilité induites par les sauts de perméabilité semblent réduire l'atténuation de la composante toroïdale du mode $m = 0$ du champ magnétique, même sans écoulement. On peut alors penser que dans un cas réel, avec un champ de vitesses non axisymétrique, ils peuvent jouer un rôle dans la création d'un champ magnétique axisymétrique. Dans le modèle simplifié que nous avons étudié, nous avons également pu montrer qu'une enceinte à haute perméabilité serait un frein à la dynamo, ce qui suggère que la position et la géométrie des zones à haute perméabilité dans la dynamo de Cadarache sont importantes. On peut alors penser que les conditions de continuité induites par ces sauts de perméabilité et/ou conductivité sont un élément clef de la dynamo. Enfin, nous avons également illustré numériquement l'effet néfaste à la dynamo d'une variation de conductivité dans le dispositif.

Nous avons par ailleurs élargi le champ d'action du code SFEMaNS, en rendant possible l'intégration dans l'équation de Navier-Stokes de la force de Coriolis, permettant ainsi de faire des calculs de dynamo homogène en précession. Les calculs de dynamo dans un sphéroïde n'ont malheureusement pas encore pu être traités, car le régime hydrodynamique soulève des problèmes de stabilité, mais des calculs de dynamo dans un cylindre ont donné des résultats assez encourageants, et ont confirmé la possibilité de générer de l'effet dynamo. Par ailleurs, les plages de dynamo obtenues semblent raisonnables. Une expérience est en cours de montage à Dresde (Allemagne) [134] et nous espérons pouvoir à l'avenir comparer simulations numériques et expériences.

Enfin, nous avons également pu appliquer cette méthode de *pression magnétique* à un modèle cylindrique de type Busse & Wicht, pour lequel nous avons mis en évidence un potentiel dynamogène. En revanche, ces dynamos sont très peu efficaces, en ce sens qu'elles requièrent un très haut nombre de Reynolds magnétique. La présence de fortes perméabilités dans la zone en rotation contribue à faire baisser le seuil.

5.2 Vers encore plus de réalisme ?

La configuration Busse & Wicht présentée dans ce mémoire n'a été étudiée que vers la fin de la thèse, ce qui explique que les résultats soient encore sommaires. Néanmoins, une étude plus approfondie de configurations de même type est envisagée, notamment en ajoutant dans le cas de la figure 4.3 une couronne interne avec un écoulement de type Taylor-Couette. Une autre piste d'étude est l'ajout d'une composante verticale sur la vitesse, afin de se rapprocher de configurations de type Ponomarenko, et de pouvoir étudier l'influence d'une couronne avec

sauts de perméabilité dans ce cas.

Nous avons discuté des capacités du code de calcul SFEMaNS, qui n'ont cessé d'augmenter depuis sa création. Néanmoins, d'autres modifications importantes sont en cours, afin de représenter des modèles aussi réalistes que possible. Nous avons mis en avant la difficulté pour un code axisymétrique de bien modéliser les pales dans l'expérience VKS. Une approche éventuelle serait de considérer des disques dont la perméabilité varie en fonction de l'azimut θ, et éventuellement en fonction du temps. Pour cela, une adaptation de la méthode de résolution de l'équation d'induction est nécessaire, et étudiée par J.-L. Guermond et D. Castanon.

Du point de vue hydrodynamique également, nous savons que certaines configurations réelles présentent un écoulement très turbulent ($R_e > 10^5$), qui n'est actuellement pas réalisable par notre méthode de simulation numérique directe. Une méthode de stabilisation est étudiée en ce moment par J.-L. Guermond et L. Cappanera notamment, afin de permettre une résolution des équations de Navier-Stokes à grands nombres de Reynolds cinétique, sans nécessiter un maillage trop fin.

En application, ces deux améliorations du code pourraient permettre de faire des calculs non-linéaires dans une géométrie de type VKS, et nous espérons qu'ils pourraient donner des informations sur la dynamo de Cadarache. Jusque là, deux types de calcul non linéaires avaient été effectués : dans un premier temps, dans le modèle simplifié de disques sans pales, les calculs non linéaires n'ont pas permis d'apporter d'information sur le mécanisme de dynamo. Un scénario avancé dans [89, 119] justifie la création du champ magnétique par un effet α (cf. [117]) induit près des pales par l'écoulement très turbulent et hélicoïdal, suggérant l'importance des pales dans la dynamo (importance relayée par les expériences). Des calculs ont donc été réalisés (cf. [89, 88]) dans une configuration de type VKS avec un forçage modélisant l'effet α. Ces calculs ont mis en évidence un champ magnétique axisymétrique au même seuil que dans l'expérience, mais pour des valeurs non réalistes pour la modélisation de l'effet α. On peut alors se demander si les conditions de continuité sur le champ magnétique induites par la géométrie des zones entre les pales peuvent influer sur le champ magnétique de manière à obtenir un effet α comparable à celui utilisé. Nous travaillons à l'élaboration d'un modèle simplifié qui pourrait nous fournir des illustrations numériques.

Annexe A

Note on the regularity of the Maxwell equations in heterogeneous media

A. Bonito [a], J.-L. Guermond [a], F. Luddens [b]

Abstract

This note establishes regularity estimates for the solution of the Maxwell equations in Lipschitz domains with non-smooth coefficients and minimal regularity assumptions.

A.1 Introduction

The purpose of this note is to prove regularity estimates for the solution of the Maxwell equations in Lipschitz domains with non-smooth coefficients and minimal regularity assumptions. More precisely, given a Lipschitz domain Ω, we are interested in the time harmonic Maxwell System,

$$\nabla\times\mathbf{E} - \mathrm{i}\omega\mu\mathbf{H} = 0 \quad \text{and} \quad \nabla\times\mathbf{H} + \mathrm{i}\omega\varepsilon\mathbf{E} = \mathbf{J}, \tag{A.1.1}$$

where $\mathbf{E}$ is the electric field, $\mathbf{H}$ is the magnetic field, $\mathbf{J}$ is a given (divergence-free) current density, ε is the electrical permittivity of the material, and μ is the magnetic permeability. The tensor fields $\mathbf{x}\mapsto\varepsilon(\mathbf{x})$ and $\mathbf{x}\mapsto\mu(\mathbf{x})$ are only assumed to be piecewise smooth. The Maxwell system (A.1.1) must be supplemented with boundary conditions. In this work, we assume that Ω is a perfect conductor, i.e.

$$\mathbf{E}\times\mathbf{n}|_\Gamma = 0, \tag{A.1.2}$$

where $\mathbf{n}$ is the outer unit normal of Ω. Eliminating the magnetic field from (A.1.1), the electric field satisfies the following system:

$$\nabla\times\left(\mu^{-1}\nabla\times\mathbf{E}\right) - \omega^2\varepsilon\mathbf{E} = i\omega\mathbf{J}, \quad \nabla\cdot(\varepsilon\mathbf{E}) = 0, \quad \mathbf{E}\times\mathbf{n}|_\Gamma = 0. \tag{A.1.3}$$

If the electric field is eliminated instead, we obtain

$$\nabla\times\left(\varepsilon^{-1}\nabla\times\mathbf{H}\right) - \omega^2\mu\mathbf{H} = \nabla\times\left(\varepsilon^{-1}\mathbf{J}\right), \quad \nabla\cdot(\mu\mathbf{H}) = 0, \quad \mu\mathbf{H}\cdot\mathbf{n}|_\Gamma = 0, \tag{A.1.4}$$

[a] Department of Mathematics, Texas A&M University 3368 TAMU, College Station, TX 77843-3368, USA
[b] Laboratoire d'Informatique pour la Mécanique et les Sciences de l'Ingénieur, CNRS, BP 133, 91403 Orsay Cedex, France

where the boundary condition $\mathbf{H}\cdot\mathbf{n}|_\Gamma = 0$ is a consequence of (A.1.2).

Establishing regularity estimates for (A.1.3) and (A.1.4) requires studying the following model problem

$$\nabla\times\left(\mu^{-1}\nabla\times\mathbf{F}\right) = \mathbf{g}, \qquad \nabla\cdot(\varepsilon\mathbf{F}) = 0, \qquad \mathbf{F}\times\mathbf{n}|_\Gamma = 0. \tag{A.1.5}$$

The main result (Theorem A.5.1) established in this paper is that, under very mild assumptions on the fields μ and ε, there is $\tau(\varepsilon,\mu) < \frac{1}{2}$ so that the mapping $\mathbf{g} \longmapsto (\mathbf{F}, \nabla\times\mathbf{F})$ is continuous from $\mathbf{L}^2(\Omega)$ to $\mathbf{H}^s(\Omega)\times\mathbf{H}^s(\Omega)$ for all $0 \le s < \tau(\varepsilon,\mu)$. Theorem A.5.1 relies on the following two embedding estimates established in Proposition A.4.1 and Proposition A.4.2, respectively: There are constants $c(\varepsilon)$, $c(\mu)$ so that

$$\|\mathbf{F}\|_{\mathbf{H}^s(\Omega)} \le c(\varepsilon)\left(\|\nabla\times\mathbf{F}\|_{\mathbf{L}^2(\Omega)} + \|\nabla\cdot(\varepsilon\mathbf{F})\|_{H^{s-1}(\Omega)}\right), \qquad \forall s \in [0,\tau(\varepsilon)) \tag{A.1.6}$$

holds for all smooth vector field $\mathbf{F}$ with zero tangent trace, and

$$\|\mathbf{G}\|_{\mathbf{H}^s(\Omega)} \le c(\mu)\|\nabla\times\mathbf{G}\|_{\mathbf{L}^2(\Omega)}, \qquad \forall s \in [0,\tau(\mu)) \tag{A.1.7}$$

holds for all smooth vector field $\mathbf{G}$ with zero normal trace and such that $\nabla\cdot(\mu\mathbf{G}) = 0$. The estimate (A.1.6) is of particular interest when approximating the Maxwell equations with Lagrange finite elements and when using a stabilization technique that requires controlling the divergence of the electric field in $\mathbf{H}^{s-1}(\Omega)$ with $s \in (0,\frac{1}{2})$, see e.g. [17]. The estimates (A.1.6)-(A.1.7) are also useful to establish compactness on the electric field and its curl. More precisely, assuming that $\mathbf{F}$ solves (A.1.5) and upon setting $\mathbf{G} = \mu^{-1}\nabla\times\mathbf{F}$, we observe that $\mathbf{G}\cdot\mathbf{n}|_\Gamma = 0$, $\nabla\cdot(\mu\mathbf{G}) = 0$, and (A.1.7) implies that $\mathbf{G}$ is a member of $\mathbf{H}^s(\Omega)$, which in turn, under mild assumptions on the multiplier μ, implies that $\nabla\times\mathbf{F}$ is in $\mathbf{H}^s(\Omega)$.

To the best of our knowledge, the results stated in Theorem A.5.1, Proposition A.4.1 and Proposition A.4.2 are new in the range $s \in (0,\frac{1}{2})$. In particular Proposition A.4.1 and Proposition A.4.2 generalize the now well-known fact, established in particular in [35], that $\mathbf{H}_{0,\mathrm{curl}}(\Omega)\cap\mathbf{H}_{\mathrm{div}}(\Omega)$ and $\mathbf{H}_{\mathrm{curl}}(\Omega)\cap\mathbf{H}_{0,\mathrm{div}}(\Omega)$ are continuously embedded in $\mathbf{H}^{\frac{1}{2}}(\Omega)$. The proofs of Proposition A.4.1 and Proposition A.4.2 use regularity estimates on the Laplace equation with non-smooth coefficients supplemented with either Dirichlet or Neumann data. These regularity estimates are established in Theorem A.3.1. It is likely that these estimates are not new, and may be found scattered in the literature in various guises. We nevertheless have included the proof of this theorem in the paper to make it self-contained. For instance, Savaré [129] has proved similar results for Dirichlet data by assuming some global integrability of the right-hand side of the Laplace equation and assuming that the multiplier is piecewise constant over two sub-domains. Later, Jochmann [77] removed the extra integrability assumption, considered finitely many sub-domains and mixed Dirichlet-Neumann boundary conditions. His proof technique is based on local maps and requires some mild regularity on the boundary of the domain (each map is Lipschitz and its Jacobian is piecewise $\mathcal{C}^{0,\frac{1}{2}}$). Following the arguments proposed by Meyers [107] and Jochmann [77], we provide in Theorem A.3.1 a regularity result for both types of boundary conditions assuming only Lipschitz regularity on the boundary of the domain and piecewise smoothness on the multiplier. Our proof is different from that of Jochmann in the sense that we only use the Jerison-Kenig [76] regularity results on Lipschitz domains for the Laplace equation.

The paper is organized as follows. We introduce some notation and prove preliminary results on multipliers in §A.2. Regularity properties of the Laplace equation with non-smooth

coefficients are discussed in §A.3. The main result of this section is Theorem A.3.1. We establish embedding results in §A.4; these results are stated in Proposition A.4.1 and Proposition A.4.2 and are used to prove regularity estimates on the Maxwell system. Finally §A.5 focuses on the Maxwell system with non-smooth coefficients, e.g. electrical conductivity, magnetic permeability, or electrical permittivity. The main result of this section is Theorem A.5.1. The main thrust for the present work is our ongoing research program to establish convergence estimates for the approximation of the Maxwell system using H^1-conforming Lagrange finite elements in the spirit of [17].

A.2 Preliminaries

A.2.1 Notation

Henceforth Ω is a simply-connected Lipschitz polyhedron in $\mathbb{R}^d$, $d = 2, 3$. We assume that Ω is partitionned into M Lipschitz subdomains $\Omega_1, \cdots, \Omega_M$. We denote Γ the boundary of the domain, i.e., $\Gamma := \Gamma$ and Σ the interface between the subdomains Ω_i, i.e.,

$$\Sigma := \bigcup_{i \neq j} \Gamma_i \cap \Gamma_j. \tag{A.2.1}$$

Let $E \subset \Omega$ be a non-empty open Lipschitz subset of Ω. We denote $(\cdot,\cdot)_E$ the inner product in $\mathbf{L}^2(E)$ for vector-valued field, in $L^2(E)$ for scalar-valued fields, or in $L^2(E)^{d\times d}$ for tensor-valued fields. The subscript is omitted if the domain of integration is Ω. Let $\dot{L}^2(E)$ and $\dot{H}^1(E)$ be respectively the subspaces of $L^2(E)$ and $H^1(E)$ composed of the function with zero average over E. Owing to the Poincaré and Poincaré-Friedrichs inequalities, we equip $H^1_0(E)$ and $\dot{H}^1(E)$ with the following norms:

$$\|u\|_{H^1_0(E)} := \|\nabla u\|_{\mathbf{L}^2(E)}, \qquad \|u\|_{\dot{H}^1(E)} := \|\nabla u\|_{\mathbf{L}^2(E)}. \tag{A.2.2}$$

The norm of $\big(H^1_0(E)\big)'$ is then defined by

$$\|F\|_{(H^1_0(E))'} := \sup_{0\neq u\in H^1_0(E)} \frac{\langle F, u\rangle_{(H^1_0(E)',H^1_0(E)}}{\|\nabla u\|_{\mathbf{L}^2(E)}}, \tag{A.2.3}$$

and the norm of $\big(H^1(E)\big)'$ is defined similarly.

We define the Sobolev spaces $H^s(E)$, $\dot{H}^s(E)$ for $0 < s < 1$, by using the real interpolation method (K-method) between $L^2(E)$ and $H^1(E)$ and between $\dot{L}^2(E)$ and $\dot{H}^1(E)$, respectively; see for instance [96] or [143, Chapter 22]. We also define $H^s_0(E)$ by interpolation between $L^2(E)$ and $H^1_0(E)$, so that for any $0 \leq s < \frac{1}{2}$, the spaces $H^s_0(E)$ and $H^s(E)$ coincide (cf. [95, Thm 11.1] or [63, Cor. 1.4.4.5]). For the sake of conciseness, we denote

$$\mathcal{H}^s(E) := \begin{cases} H^s_0(E) & \text{for Dirichlet boundary conditions,} \\ \dot{H}^s(E) & \text{for Neumann boundary conditions,} \end{cases} \tag{A.2.4}$$

for $s \in [0, 1]$, and $\mathcal{H}^s(E) := (\mathcal{H}^{-s}(E))'$ for $s \in [-1, 0]$. Note that when we use $\mathcal{H}^1(E) = \dot{H}^1(E)$, the elements of the dual space $\mathcal{H}^s(E)$, $s \in [-1, 0)$, cannot be identified with distributions in $(\mathcal{D}(E))'$ in general. For instance, for any $g \in L^2(\partial E)$ and $s \in [-1, -\frac{1}{2})$, the linear form

$\mathcal{H}^{-s}(E) \ni p \mapsto \int_{\partial E} gp$ is in $\mathcal{H}^s(E)$ and cannot be represented by a distribution in $(\mathcal{D}(E))'$. The above definitions naturally extend to vector fields and in this case we use bold letters to avoid confusion. For $s \in [0,1]$, we abusively denote $\mathcal{H}^{1+s}(E)$ the following spaces:

$$\mathcal{H}^{1+s}(E) = \begin{cases} \{p \in H^1_0(E),\ \nabla p \in \mathbf{H}^s(E)\} & \text{if } \mathcal{H}^1(E) = H^1_0(E) \\ \{p \in \dot{H}^1(E),\ \nabla p \in \mathbf{H}^s(E)\} & \text{if } \mathcal{H}^1(E) = \dot{H}^1(E), \end{cases} \tag{A.2.5}$$

and we equip $\mathcal{H}^{1+s}(E)$ with the following norm:

$$\|p\|_{\mathcal{H}^{1+s}(E)} := \|\nabla p\|_{\mathbf{H}^s(E)}\,. \tag{A.2.6}$$

The Poincaré constant over each sudomain Ω_i is denoted C_{Ω_i}, i.e.,

$$\forall \mathbf{u} \in \mathbf{H}^1_0(\Omega_i), \qquad \|\mathbf{u}\|_{L^2(\Omega_i)} \le C_{\Omega_i} \|\nabla \mathbf{u}\|_{L^2(\Omega_i)^{d\times d}}, \tag{A.2.7}$$

and we set

$$C_\Omega := \max_{1\le i\le M} C_{\Omega_i}. \tag{A.2.8}$$

The norm of the natural injection from $\mathbf{H}^s(\Omega_i)$ to $\mathbf{H}^s_0(\Omega_i)$ is denoted D_{s,Ω_i} for all $s \in [0, \frac{1}{2})$ and all $i = 1, \ldots, M$, i.e.,

$$\|\mathbf{v}\|_{\mathbf{H}^s_0(\Omega_i)} \le D_{s,\Omega_i} \|\mathbf{v}\|_{\mathbf{H}^s(\Omega_i)}, \qquad \forall \mathbf{v} \in \mathbf{H}^s(\Omega_i). \tag{A.2.9}$$

In addition, we set

$$D_{s,\Omega} := \max(\max_{1\le i\le M} D_{s,\Omega_i}, 1). \tag{A.2.10}$$

Assuming that X and Y are two Banach spaces, $\mathcal{L}(X,Y)$ denotes the space of bounded linear operator $X \to Y$ equipped with its natural norm, $\|\cdot\|_{X\to Y}$.

In the rest of the paper we use the generic notation c for constants. The value of c may change at each occurrence.

A.2.2 Multipliers

We now introduce notation to stipulate the regularity that we require on the tensor fields ε and μ. For this purpose we define

$$W^{1,\infty}_\Sigma(\Omega)^{d\times d} := \left\{ \nu \in L^\infty(\Omega)^{d\times d} \mid \nabla(\nu_{|\Omega_i}) \in L^\infty(\Omega_i)^{d\times d\times d},\ i = 1, \cdots, M \right\}. \tag{A.2.11}$$

For all ν in $W^{1,\infty}_\Sigma(\Omega)^{d\times d}$ we define $\nu_{\max} \in \mathbb{R}$ such that

$$\boldsymbol{\xi}^T \nu \boldsymbol{\xi} \le \nu_{\max} \boldsymbol{\xi}^T \boldsymbol{\xi}, \quad \text{a.e. in } \Omega,\ \forall \boldsymbol{\xi} \in \mathbb{R}^d \tag{A.2.12}$$

and $\Lambda_\nu \in \mathbb{R}$ by

$$\Lambda_\nu := \frac{\max_{i=1,\cdots,M} \left\|\nabla(\nu_{|\Omega_i})\right\|_{L^\infty(\Omega_i)^{d\times d\times d}}}{\nu_{\max}}, \quad \text{if} \quad \nu_{\max} \neq 0, \quad \Lambda_\nu := 0 \quad \text{otherwise.}$$

Given a tensor field ν in $W^{1,\infty}_\Sigma(\Omega)^{d\times d}$, we call multiplier $\mathcal{E}_\nu$ associated with ν the linear operator $\mathcal{E}_\nu : \mathbf{L}^2(\Omega) \to \mathbf{L}^2(\Omega)$ so that

$$(\mathcal{E}_\nu(\mathbf{u}))(\mathbf{x}) := \nu(\mathbf{x})\mathbf{u}(\mathbf{x}) \text{ for a.e. } \mathbf{x} \text{ in } \Omega, \quad \forall \mathbf{u} \in \mathbf{L}^2(\Omega). \tag{A.2.13}$$

The main result of this section is the following

Proposition A.2.1. *Let $\nu \in W^{1,\infty}_{\Sigma}(\Omega)^{d\times d}$. Then $\mathcal{E}_\nu \in \mathcal{L}(\mathbf{H}^s(\Omega), \mathbf{H}^s(\Omega))$ for every $s \in \left[0, \frac{1}{2}\right)$ and*

$$\|\mathcal{E}_\nu\|_{\mathbf{H}^s(\Omega)\to\mathbf{H}^s_0(\Omega)} \leq \nu_{\max} N_{s,\nu}, \quad \text{where} \quad N_{s,\nu} := D_{s,\Omega}(2(1+C_\Omega^2\Lambda_\nu^2))^{s/2}. \tag{A.2.14}$$

Moreover, the following holds for all $r \in [0, \frac{1}{2})$,

$$\|\mathcal{E}_\nu\|_{H^s\to H^s_0} \leq \nu_{\max} N_{r,\nu}^{\frac{s}{r}}, \quad \forall s \in [0, r]. \tag{A.2.15}$$

Proof. Let $0 \leq s < \frac{1}{2}$ and $\mathbf{u} \in \mathbf{H}^s(\Omega)$. We set $\mathbf{u}_i := \mathbf{u}_{|\Omega_i}$ for $i = 1, \cdots M$. Then owing to Lemma B.7.3 below, $\mathbf{u}_i \in \mathbf{H}^s(\Omega_i)$ for all $i = 1, \ldots, M$. This in turn implies that $\mathbf{u}_i \in \mathbf{H}^s_0(\Omega_i)$ since $0 \leq s < \frac{1}{2}$. We want to use the K-interpolation theory. For any $\mathbf{u}_i \in [\mathbf{L}^2(\Omega_i), \mathbf{H}^1_0(\Omega_i)]_s = \mathbf{H}^s_0(\Omega)$, we set

$$\mathcal{K}(t, \mathbf{u}_i, \mathbf{L}^2(\Omega_i), \mathbf{H}^1_0(\Omega_i)) := \inf_{\mathbf{v}\in\mathbf{H}^1_0(\Omega_i)} \left\{ \|\mathbf{u}_i - \mathbf{v}\|^2_{\mathbf{L}^2(\Omega_i)} + t^2 \|\mathbf{v}\|^2_{\mathbf{H}^1_0(\Omega_i)} \right\}.$$

Then asserting that $\mathbf{u}_i$ is in $\mathbf{H}^s_0(\Omega_i)$ is equivalent to say that the mapping $\mathbb{R}^+ \ni t \mapsto \mathcal{K}(t, \mathbf{u}_i, \mathbf{L}^2(\Omega_i), \mathbf{H}^1_0(\Omega_i))$ is in $L^1\left(\mathbb{R}^+, \frac{dt}{t^{1+2s}}\right)$. For any $t > 0$, we define $\mathbf{u}_{i,t} \in \mathbf{H}^1_0(\Omega_i)$ so that the following holds for all $\mathbf{v}_i \in \mathbf{H}^1_0(\Omega_i)$,

$$(\mathbf{u}_{i,t}, \mathbf{v}_i)_{\Omega_i} + t^2 (\nabla \mathbf{u}_{i,t}, \nabla \mathbf{v}_i)_{\Omega_i} = (\mathbf{u}_i, \mathbf{v}_i)_{\Omega_i}.$$

This definition implies that

$$\|\mathbf{u}_i - \mathbf{u}_{i,t}\|^2_{\mathbf{L}^2(\Omega_i)} + t^2 \|\mathbf{u}_{i,t}\|^2_{\mathbf{H}^1_0(\Omega_i)} = \mathcal{K}(t, \mathbf{u}_i, \mathbf{L}^2(\Omega_i), \mathbf{H}^1_0(\Omega_i)).$$

Now we estimate $\mathcal{K}(t, \mathcal{E}_\nu \mathbf{u}, \mathbf{L}^2(\Omega), \mathbf{H}^1_0(\Omega))$. For this purpose we define $\mathbf{u}_t$ by $\mathbf{u}_{t|\Omega_i} = \mathbf{u}_{i,t}$. Since every $\mathbf{u}_{i,t}$ vanishes on Σ, we have $\mathbf{u}_t \in \mathbf{H}^1_0(\Omega)$, $\mathcal{E}_\nu \mathbf{u}_t \in \mathbf{H}^1_0(\Omega)$ with the estimates

$$\|\mathcal{E}_\nu(\mathbf{u} - \mathbf{u}_t)\|^2_{\mathbf{L}^2(\Omega)} = \sum_{i=1}^M \|\nu(\mathbf{u}_i - \mathbf{u}_{i,t})\|^2_{\mathbf{L}^2(\Omega_i)} \leq \nu^2_{\max} \sum_{i=1}^M \|\mathbf{u}_i - \mathbf{u}_{i,t}\|^2_{\mathbf{L}^2(\Omega_i)},$$

and

$$\begin{aligned}
\|\mathcal{E}_\nu \mathbf{u}_t\|^2_{\mathbf{H}^1_0(\Omega)} := \|\nabla(\mathcal{E}_\nu \mathbf{u}_t)\|^2_{L^2(\Omega)^{d\times d}} &\leq 2 \sum_{i=1}^M \|\nu \nabla \mathbf{u}_{i,t}\|^2_{L^2(\Omega_i)^{d\times d}} + \|(\nabla \nu)\mathbf{u}_{i,t}\|^2_{L^2(\Omega_i)^{d\times d}} \\
&\leq 2\nu^2_{\max}\left(1 + C_\Omega^2 \Lambda_\nu^2\right) \sum_{i=1}^M \|\nabla \mathbf{u}_{i,t}\|^2_{L^2(\Omega_i)^{d\times d}}
\end{aligned}$$

where we used the Poincaré inequality on every Ω_i in the second estimate. Combining the above two inequalities and setting $\alpha^2 := 2\left(1 + C_\Omega^2 \Lambda_\nu^2\right)$ gives

$$\begin{aligned}
\mathcal{K}(t, \mathcal{E}_\nu \mathbf{u}, \mathbf{L}^2(\Omega), \mathbf{H}^1_0(\Omega)) &\leq \|\mathcal{E}_\nu(\mathbf{u} - \mathbf{u}_{\alpha t})\|^2_{\mathbf{L}^2(\Omega)} + t^2 \|\mathcal{E}_\nu \mathbf{u}_{\alpha t}\|^2_{\mathbf{H}^1_0(\Omega)} \\
&\leq \nu^2_{\max} \sum_{i=1}^M \left(\|\mathbf{u}_i - \mathbf{u}_{i,\alpha t}\|^2_{\mathbf{L}^2(\Omega_i)} + \alpha^2 t^2 \|\nabla \mathbf{u}_{i,\alpha t}\|^2_{L^2(\Omega_i)^{d\times d}} \right) \\
&\leq \nu^2_{\max} \sum_{i=1}^M \mathcal{K}(\alpha t, \mathbf{u}_i, \mathbf{L}^2(\Omega_i), \mathbf{H}^1_0(\Omega_i)).
\end{aligned}$$

As a result $\mathcal{E}_\nu \mathbf{u} \in \mathbf{H}_0^s(\Omega)$, and using the injection $\|\mathbf{u}_i\|_{\mathbf{H}_0^s(\Omega_i)} \leq D_{s,\Omega_i} \|\mathbf{u}_i\|_{\mathbf{H}^s(\Omega_i)}$ we deduce

$$\begin{aligned}
\|\mathcal{E}_\nu \mathbf{u}\|^2_{\mathbf{H}_0^s(\Omega)} &\leq \nu_{\max}^2 \sum_{i=1}^M \int_0^\infty \mathcal{K}(\alpha t, \mathbf{u}_i, \mathbf{L}^2(\Omega_i), \mathbf{H}_0^1(\Omega_i)) t^{-1-2s} dt \\
&\leq \nu_{\max}^2 \alpha^{2s} \sum_{i=1}^M \|\mathbf{u}_i\|^2_{\mathbf{H}_0^s(\Omega_i)} \leq \nu_{\max}^2 \alpha^{2s} \sum_{i=1}^M D^2_{s,\Omega_i} \|\mathbf{u}_i\|^2_{\mathbf{H}^s(\Omega_i)} \\
&\leq \nu_{\max}^2 N^2_{s,\nu} \sum_{i=1}^M \|\mathbf{u}_i\|^2_{\mathbf{H}^s(\Omega_i)}.
\end{aligned}$$

Then we finally obtain (A.2.14) by using Lemma B.7.3.

Noticing that $N_{0,\nu} = 1$, the inequality (A.2.15) directly follows from the re-interpolation formula

$$\mathbf{H}^s(\Omega) = \left[\mathbf{L}^2(\Omega), \mathbf{H}^r(\Omega)\right]_{\frac{s}{r}}.$$

This completes the proof. □

Lemma A.2.1. *The following holds for all $s \in [0,1]$ and for all $\mathbf{v} \in \mathbf{H}^s(\Omega)$,*

$$\sum_{i=1}^M \|\mathbf{v}_{|\Omega_i}\|^2_{\mathbf{H}^s(\Omega_i)} \leq \|\mathbf{v}\|^2_{\mathbf{H}^s(\Omega)}. \tag{A.2.16}$$

Proof. The result is evident for $s = 0$ and $s = 1$. Let us assume now that $s \in (0,1)$. Let $\mathbf{v}$ be a member of $\mathbf{H}^s(\Omega)$. Recall that

$$\begin{aligned}
\|\mathbf{v}\|_{\mathbf{H}^s(\Omega)} &:= \left(\int_0^\infty \mathcal{K}(t, \mathbf{v}, \mathbf{L}^2(\Omega), \mathbf{H}^1(\Omega))^2 t^{-1-2s} \mathrm{d}t \right)^{1/2}, \\
\mathcal{K}(t, \mathbf{v}, \mathbf{L}^2(\Omega), \mathbf{H}^1(\Omega))^2 &:= \inf_{\mathbf{w} \in \mathbf{H}^1(\Omega)} \left(\|\mathbf{v} - \mathbf{w}\|^2_{\mathbf{L}^2(\Omega)} + t^2 \|\mathbf{w}\|^2_{\mathbf{H}^1(\Omega)} \right).
\end{aligned}$$

For all $t \in \mathbb{R}_+$, let us denote $\mathbf{v}_t$ the function in $\mathbf{H}^1(\Omega)$ that achieves the infimum in the definition of $\mathcal{K}(t, \mathbf{v}, \mathbf{L}^2(\Omega), \mathbf{H}^1(\Omega))$, i.e., $-t^2 \Delta \mathbf{v}_t + t^2 \mathbf{v}_t + (\mathbf{v}_t - \mathbf{v}) = 0$ over Ω with homogeneous Neumann boundary condition. Then

$$\begin{aligned}
\sum_{i=1}^M \|\mathbf{v}_{|\Omega_i}\|^2_{\mathbf{H}^s(\Omega_i)} &= \sum_{i=1}^M \int_0^\infty \mathcal{K}(t, \mathbf{v}_{|\Omega_i}, \mathbf{L}^2(\Omega_i), \mathbf{H}^1(\Omega_i))^2 t^{-1-2s} \mathrm{d}t \\
&\leq \sum_{i=1}^M \int_0^\infty \left(\|\mathbf{v}_{|\Omega_i} - \mathbf{v}_{t|\Omega_i}\|^2_{\mathbf{L}^2(\Omega_i)} + t^2 \|\mathbf{v}_{t|\Omega_i}\|^2_{\mathbf{H}^1(\Omega_i)} \right) t^{-1-2s} \mathrm{d}t \\
&= \int_0^\infty \left(\sum_{i=1}^M \|\mathbf{v}_{|\Omega_i} - \mathbf{v}_{t|\Omega_i}\|^2_{\mathbf{L}^2(\Omega_i)} + t^2 \|\mathbf{v}_{t|\Omega_i}\|^2_{\mathbf{H}^1(\Omega_i)} \right) t^{-1-2s} \mathrm{d}t \\
&= \int_0^\infty \mathcal{K}(t, \mathbf{v}, \mathbf{L}^2(\Omega), \mathbf{H}^1(\Omega))^2 t^{-1-2s} \mathrm{d}t := \|\mathbf{v}\|^2_{\mathbf{H}^s(\Omega)}.
\end{aligned}$$

This completes the proof. □

A.3 Non-constant coefficient Laplace equation

We establish regularity estimates for the Laplace equation with non-constant coefficients in this section.

A.3.1 The main result

Let ν be a tensor field in $W^{1,\infty}_{\Sigma}(\Omega)^{d\times d}$ and assume that

$$\exists \nu_{\min} > 0 \text{ such that } \boldsymbol{\xi}^T \nu \boldsymbol{\xi} \geq \nu_{\min} \boldsymbol{\xi}^T \boldsymbol{\xi} \text{ a.e. in } \Omega, \quad \forall \boldsymbol{\xi} \in \mathbb{R}^d. \tag{A.3.1}$$

Consider the following problem: given $f \in \mathcal{H}^{-1}(\Omega)$, find $p \in \mathcal{H}^1(\Omega)$ such that,

$$\forall q \in \mathcal{H}^1(\Omega), \qquad (\nu \nabla p, \nabla q) = \langle f, q \rangle_{\mathcal{H}^{-1}(\Omega),\mathcal{H}^1(\Omega)}\,. \tag{A.3.2}$$

The existence and uniqueness of a solution to the above problem is ensured by the Lax-Milgram lemma since

$$\forall p \in \mathcal{H}^1(\Omega), \qquad \nu_{\min} \|p\|^2_{\mathcal{H}^1(\Omega)} = \nu_{\min} (\nabla p, \nabla p) \leq (\nu \nabla p, \nabla p)\,.$$

We re-write the above problem (A.3.2) in the symbolic form $-\Delta^{\mathcal{H}^1}_{\nu} p = f$.

The objective of this section is to prove the following

Theorem A.3.1. *Let $\nu \in W^{1,\infty}_{\Sigma}(\Omega)^{d\times d}$ be satisfying* (A.3.1). *There exists $\tau \in (0, \frac{1}{2})$, only depending on ν, Ω, and the partition $\{\Omega_i\}_{i=1}^M$ such that, for every $s \in [0, \tau)$ and every $f \in \mathcal{H}^{s-1}(\Omega)$, the solution $p \in \mathcal{H}^1(\Omega)$ of the problem* (A.3.2) *is in $\mathcal{H}^{1+s}(\Omega)$ and satisfies the estimate*

$$\|p\|_{\mathcal{H}^{s+1}(\Omega)} \leq c \|f\|_{\mathcal{H}^{s-1}(\Omega)}\,, \tag{A.3.3}$$

where c depends only on Ω, ν, the partition $\{\Omega_i\}_{i=1}^M$, and s.

We postpone the proof of Theorem A.3.1 to §A.3.3. We will use a technique similar to that in [77], where the author proves the result for a more general class of spaces, but requires some additional regularity conditions on the boundary Γ and assumes (A.2.14). One novelty of our proof is that, owing to the assumptions on ν, the Lipschitz condition on the boundary of the domain is sufficient; we also derive an almost explicit admissible range for τ.

A.3.2 Key lemmas

Using the same notation as in [77], we introduce the operators $\mathcal{J} \in \mathcal{L}(\mathcal{H}^{-1}(\Omega), \mathcal{H}^1(\Omega))$ and $\mathcal{S} \in \mathcal{L}(\mathbf{L}^2, \mathcal{H}^{-1}(\Omega))$ defined as follows:

$$\forall f \in \mathcal{H}^{-1}(\Omega),\ \forall q \in \mathcal{H}^1(\Omega), \qquad (\nabla(\mathcal{J} f), \nabla q) = \langle f, q \rangle_{\mathcal{H}^{-1}(\Omega),\mathcal{H}^1(\Omega)}\,. \tag{A.3.4}$$

and

$$\forall \mathbf{F} \in \mathbf{L}^2,\ \forall q \in \mathcal{H}^1(\Omega), \qquad \langle \mathcal{S}\mathbf{F}, q \rangle_{\mathcal{H}^{-1}(\Omega),\mathcal{H}^1(\Omega)} := (\mathbf{F}, \nabla q)\,. \tag{A.3.5}$$

Note that $\mathcal{J}$ is well defined owing to the definition of $\mathcal{H}^1(\Omega)$ and the Lax-Milgram lemma. Notice that formally

$$\mathcal{S}\mathbf{F} = \begin{cases} -\nabla\cdot\mathbf{F} & \text{when} \quad \mathcal{H}^1 = H^1_0(\Omega), \\ -\nabla\cdot\mathbf{F} + \mathbf{F}\cdot\mathbf{n}\delta_\Gamma & \text{when} \quad \mathcal{H}^1 = \dot{H}^1(\Omega), \end{cases}$$

where δ_Γ is the Dirac measure supported on Γ.

Lemma A.3.1. *For any $s \in [0,1]$ and $\mathbf{F} \in \mathbf{H}_0^s(\Omega)$, we have*

$$\mathcal{S}\mathbf{F} \in \mathcal{H}^{s-1}(\Omega) \text{ and } \|\mathcal{S}\mathbf{F}\|_{\mathcal{H}^{s-1}(\Omega)} \leq \|\mathbf{F}\|_{\mathbf{H}_0^s(\Omega)}. \tag{A.3.6}$$

Proof. This is again a standard interpolation argument. We start with $s = 0$ and $\mathbf{F} \in \mathbf{L}^2(\Omega)$. Then the following series of bounds holds for all $p \in \mathcal{H}^1(\Omega)$,

$$\langle \mathcal{S}\mathbf{F}, p\rangle_{\mathcal{H}^{-1}(\Omega),\mathcal{H}^1(\Omega)} = (\mathbf{F}, \nabla p) \leq \|\mathbf{F}\|_{\mathbf{L}^2(\Omega)} \|\nabla p\|_{\mathbf{L}^2(\Omega)} = \|\mathbf{F}\|_{\mathbf{L}^2(\Omega)} \|p\|_{\mathcal{H}^1(\Omega)},$$

which leads to

$$\|\mathcal{S}\mathbf{F}\|_{\mathcal{H}^{-1}(\Omega)} \leq \|\mathbf{F}\|_{\mathbf{L}^2(\Omega)}. \tag{A.3.7}$$

When $s = 1$ and $\mathbf{F} \in \mathbf{H}_0^1(\Omega)$, we have for $p \in \mathcal{H}^0(\Omega)$

$$\langle \mathcal{S}\mathbf{F}, p\rangle_{\mathcal{H}^{-1}(\Omega),\mathcal{H}^1(\Omega)} = (\mathbf{F}, \nabla p) = -(\nabla\cdot\mathbf{F}, p) \leq \|\nabla\cdot\mathbf{F}\|_{L^2(\Omega)} \|p\|_{\mathcal{H}^0(\Omega)}.$$

Using the fact that

$$\|\nabla\cdot\mathbf{F}\|^2_{L^2(\Omega)} \leq \|\nabla\cdot\mathbf{F}\|^2_{L^2(\Omega)} + \|\nabla\times\mathbf{F}\|^2_{\mathbf{L}^2(\Omega)} = \|\nabla\mathbf{F}\|^2_{L^2(\Omega)} = \|\mathbf{F}\|^2_{\mathbf{H}_0^1(\Omega)},$$

and recalling that for $\mathbf{F} \in \mathbf{H}_0^1(\Omega)$ $\mathcal{S}\mathbf{F} = -\nabla\cdot\mathbf{F}$ and $\int_\Omega \mathcal{S}\mathbf{F} = 0$, we deduce

$$\sup_{0\neq p\in\mathcal{H}^0(\Omega)} \frac{\langle \mathcal{S}\mathbf{F}, p\rangle_{\mathcal{H}^{-1}(\Omega),\mathcal{H}^1(\Omega)}}{\|p\|_{\mathcal{H}^0(\Omega)}} = \|\mathcal{S}\mathbf{F}\|_{\mathcal{H}^0} = \|\mathcal{S}\mathbf{F}\|_{\dot{L}^2(\Omega)} = \|\mathcal{S}\mathbf{F}\|_{L^2(\Omega)} \leq \|\mathbf{F}\|_{\mathbf{H}_0^1(\Omega)}. \tag{A.3.8}$$

We conclude by the using the Riesz-Thorin Theorem. □

Lemma A.3.2. *For all $r \in [0, \frac{1}{2})$, there is $K := K(\Omega, r)$ such the following holds that for all $f \in \mathcal{H}^{r-1}(\Omega)$,*

$$\mathcal{J}f \in \mathcal{H}^{1+r}(\Omega) \text{ and } \|\mathcal{J}f\|_{\mathcal{H}^{1+r}(\Omega)} \leq K \|f\|_{\mathcal{H}^{r-1}(\Omega)}. \tag{A.3.9}$$

and for all $s \in [0, r]$ and all $f \in \mathcal{H}^{s-1}(\Omega)$,

$$\mathcal{J}f \in \mathcal{H}^{1+s}(\Omega) \text{ and } \|\mathcal{J}f\|_{\mathcal{H}^{1+s}(\Omega)} \leq K^{\frac{s}{r}} \|f\|_{\mathcal{H}^{s-1}(\Omega)}. \tag{A.3.10}$$

Proof. The result is proved by using a standard interpolation technique. We first establish the estimate for $s = 0$. Taking $f \in \mathcal{H}^{-1}(\Omega)$ and using the definition of $\mathcal{J}$ together with the norm in $\mathcal{H}^1(\Omega)$ gives

$$\|\mathcal{J}f\|^2_{\mathcal{H}^1(\Omega)} = \langle f, \mathcal{J}f\rangle_{\mathcal{H}^{-1}(\Omega),\mathcal{H}^1(\Omega)} \leq \|f\|_{\mathcal{H}^{-1}(\Omega)} \|\mathcal{J}f\|_{\mathcal{H}^1(\Omega)},$$

thereby leading to

$$\forall f \in \mathcal{H}^{-1}(\Omega),\ \|\mathcal{J}f\|_{\mathcal{H}^1(\Omega)} \leq \|f\|_{\mathcal{H}^{-1}(\Omega)}. \tag{A.3.11}$$

We must distinguish two cases for $r < \frac{1}{2}$ depending whether $\mathcal{H}^1(\Omega) = H_0^1(\Omega)$ or $\mathcal{H}^1(\Omega) = \dot{H}^1(\Omega)$. If $\mathcal{H}^1(\Omega) = H_0^1(\Omega)$, then a standard result from [76] (cf. Theorem 0.5) implies that

there exists K only depending on Ω and r such that, for any $f \in \mathcal{H}^{r-1}(\Omega) = H^{r-1}(\Omega)$, $\mathcal{J}f \in H^{1+r}(\Omega)$ and

$$\|\mathcal{J}f\|_{H^{1+r}(\Omega)} \leq K \|f\|_{H^{r-1}(\Omega)}.$$

The Neumann boundary case, $\mathcal{H}^1(\Omega) = \dot{H}^1(\Omega)$, does not seem to be as clear as the Dirichlet case. It appears however to be a by-product of Theorem 3 in [129]; it is proved therein that $\mathcal{J}f \in H^{1+r}(\Omega)$ for any $r \in [0, \frac{1}{2})$, i.e., (abusing the notation) there exists K only depending on Ω and r such and the following estimate holds for any $f \in (H^{1-r}(\Omega))'$

$$\|\nabla\mathcal{J}f\|_{H^r(\Omega)} \leq K \|f\|_{(H^{1-r}(\Omega))'}.$$

In conclusion, for any $0 < r < \frac{1}{2}$ there exists $K = K(r, \Omega)$ such that (A.3.9) holds. The estimate (A.3.10) is obtained by interpolation using (A.3.11) and (A.3.9). □

Remark A.3.1. Owing to the property $\mathcal{J}\mathcal{S}\nabla u = u$ for all $u \in \mathcal{H}^1(\Omega)$, we infer that $\|\mathcal{J}\|_{\mathcal{H}^{r-1}\to\mathcal{H}^{r+1}}\|\mathcal{S}\|_{H_0^r\to\mathcal{H}^{r-1}}$ 1, which in turn implies the following lower bound $K(\Omega, r) \geq \|\mathcal{J}\|_{\mathcal{H}^{r-1}\to\mathcal{H}^{r+1}} \geq 1$.

A.3.3 Proof of Theorem A.3.1

We want to use a perturbation argument à la Meyer [107]. Let $k > 0$ be a positive number yet to be chosen. Let $f \in \mathcal{H}^{-1}(\Omega)$ and let $p \in \mathcal{H}^1(\Omega)$ be the solution to (A.3.2). Let us start by observing that the following holds in the distribution sense if $f \in (H_0^1(\Omega))'$:

$$f = -\nabla\cdot(\nu\nabla p) = -k\Delta p + \nabla\cdot((kI - \nu)\nabla p) = -\Delta(kp) + \nabla\cdot((I - \frac{1}{k}\nu)\nabla(kp)),$$

where $I \in \mathbb{R}^{d\times d}$ is the identity matrix. To account for boundary conditions, (in particular for Neumann boundary conditions, i.e., $f \in (H^1(\Omega))'$), we actually have

$$f = \mathcal{S}(\nu\nabla p) = k\mathcal{S}\nabla p - \mathcal{S}((kI - \nu)\nabla p) = \mathcal{S}\nabla(kp) - \mathcal{S}((I - \frac{1}{k}\nu)\nabla(kp)).$$

Upon setting $\bar{\nu} := I - \frac{1}{k}\nu$ and $q = kp$, and using that $\mathcal{J}\mathcal{S}\nabla$ is the identity operator in $\mathcal{H}^1(\Omega)$, we arrive at

$$q - \mathcal{J}(\mathcal{S}(\bar{\nu}\nabla q)) = \mathcal{J}f.$$

Let us denote $\mathcal{Q} := \mathcal{J}\mathcal{S}\mathcal{E}_{\bar{\nu}}\nabla$ and let us assume for a moment that we can establish that $\mathcal{Q}$ is a bounded operator from $\mathcal{H}^{s+1}(\Omega)$ to $\mathcal{H}^{s+1}(\Omega)$ and that the norm of $\mathcal{Q}$ in $\mathcal{L}(\mathcal{H}^{s+1}(\Omega), \mathcal{H}^{s+1}(\Omega))$ is less than 1, say $\|\mathcal{Q}\|_{\mathcal{H}^{s+1}\to\mathcal{H}^{s+1}} < 1$. Then

$$k\|p\|_{\mathcal{H}^{s+1}(\Omega)} = \|q\|_{\mathcal{H}^{s+1}(\Omega)} \leq \frac{\|\mathcal{J}\|}{1 - \|\mathcal{Q}\|}\|f\|_{\mathcal{H}^{s-1}(\Omega)}$$

and the conclusion follows readily. In summary, the crux of the matter is to prove $\|\mathcal{Q}\|_{\mathcal{H}^{s+1}\to\mathcal{H}^{s+1}} < 1$.

Since q is in $\mathcal{H}^{1+s}(\Omega)$, we infer that $\nabla q \in \mathbf{H}^s(\Omega)$. The hypothesis $s < \frac{1}{2}$ together with Proposition A.2.1 implies that $\mathcal{E}_{\bar{\nu}}\nabla q \in \mathbf{H}_0^s(\Omega)$. Using Lemma A.3.1, we infer that $\mathcal{S}\mathcal{E}_{\bar{\nu}}\nabla q \in \mathcal{H}^{s-1}(\Omega)$ so that Lemma A.3.2 yields $\mathcal{Q}q = \mathcal{J}\mathcal{S}\mathcal{E}_{\bar{\nu}}\nabla q \in \mathcal{H}^{s+1}(\Omega)$. In addition, we have

$$\begin{aligned}\|\mathcal{Q}\|_{\mathcal{H}^{s+1}\to\mathcal{H}^{s+1}} &\leq \|\mathcal{J}\|_{\mathcal{H}^{s-1}\to\mathcal{H}^{s+1}}\|\mathcal{S}\|_{H_0^s\to\mathcal{H}^{s-1}}\|\mathcal{E}_{\bar{\nu}}\|_{\mathbf{H}^s\to\mathbf{H}_0^s}\\ &\leq K^{\frac{s}{r}}(1 - \frac{\nu_{\min}}{k})N_{r,\bar{\nu}}^{\frac{s}{r}}\end{aligned}$$

provided $k \geq \nu_{\max}$. Then by choosing $k = \nu_{\max}$, we deduce the following bound

$$\|\mathcal{Q}\|_{\mathcal{H}^{s+1}\to\mathcal{H}^{s+1}} \leq \frac{\nu_{\max}-\nu_{\min}}{\nu_{\max}} K^{\frac{s}{r}} N_{r,\bar{\nu}}^{\frac{s}{r}},$$

which implies that $\|\mathcal{Q}\|_{\mathcal{H}^{s+1}\to\mathcal{H}^{s+1}} < 1$ for all $s \in [0,\tau)$ where

$$\tau := r \min\left(1, \frac{\log\left(\frac{\nu_{\max}}{\nu_{\max}-\nu_{\min}}\right)}{\log(KN_{r,\bar{\nu}})}\right).$$

Note that $KN_{r,\bar{\nu}} \geq 1$ owing to Remark A.3.1 and definitions (A.2.10), (A.2.14). Observe also that $\tau \in (0, \frac{1}{2})$. Finally we arrive at

$$\|p\|_{\mathcal{H}^{s+1}(\Omega)} \leq \frac{K^{\frac{s}{r}}}{\nu_{\max} - (\nu_{\max}-\nu_{\min})K^{\frac{s}{r}} N_{r,\bar{\nu}}^{\frac{s}{r}}} \|f\|_{\mathcal{H}^{s-1}(\Omega)}.$$

This concludes the proof of Theorem A.3.1.

A.4 $\mathbf{H}^s$ embeddings

In this section, we prove two embedding results which are used in §A.5 to establish regularity estimates on the Maxwell problem (A.1.5). The main results of this section are propositions A.4.1 and A.4.2. Both these results are consequences of TheoremA.4.1, which by itself is an improvement of [35, Theorem 2].

A.4.1 Notations

In the rest of the paper we use the following spaces characterizing the regularity of vector fields:

$$\mathbf{H}_{\mathrm{curl}}(\Omega) := \left\{\mathbf{F} \in \mathbf{L}^2(\Omega) \mid \nabla\times\mathbf{F} \in \mathbf{L}^2(\Omega)\right\}, \tag{A.4.1}$$

$$\mathbf{H}_{\mathrm{div}}(\Omega) := \left\{\mathbf{F} \in \mathbf{L}^2(\Omega) \mid \nabla\cdot\mathbf{F} \in \mathbf{L}^2(\Omega)\right\}. \tag{A.4.2}$$

Let s be a real number in the range $s \in [0, \frac{1}{2})$. We consider the following space equipped with its canonical norm:

$$\mathbf{Z}^{1-s}(\Omega) := \left\{\mathbf{F} \in \mathbf{L}^2(\Omega) \mid \nabla\times\mathbf{F} \in \mathbf{H}^{-s}(\Omega),\ \nabla\cdot\mathbf{F} \in H^{-s}(\Omega)\right\}. \tag{A.4.3}$$

The tangential trace $\mathbf{v}\times\mathbf{n}$ of a function $\mathbf{v} \in \mathbf{H}^{-s}(\Omega)$ with $\nabla\times\mathbf{v} \in \mathbf{H}^{-s}(\Omega)$ is defined as an element of $\mathbf{H}^{-s-\frac{1}{2}}(\Gamma)$, $s \in [0, \frac{1}{2})$, by

$$\begin{aligned}\langle \mathbf{v}\times\mathbf{n}, \boldsymbol{\psi}\rangle_{\mathbf{H}^{-s-\frac{1}{2}}(\Gamma),\mathbf{H}^{s+\frac{1}{2}}(\Gamma)} :=& \langle \nabla\times\mathbf{v}, E(\boldsymbol{\psi})\rangle_{\mathbf{H}^{-s}(\Omega),\mathbf{H}^{s}(\Omega)} \\ &- \langle \mathbf{v}, \nabla\times E(\boldsymbol{\psi})\rangle_{\mathbf{H}^{-s}(\Omega),\mathbf{H}^{s}(\Omega)},\end{aligned} \tag{A.4.4}$$

for all $\boldsymbol{\psi} \in \mathbf{H}^{s+\frac{1}{2}}(\Gamma)$. Here $E(\boldsymbol{\psi})$ denote any extension to Ω guaranteed by the continuity and surjectivity of the trace operator from $\mathbf{H}^{1+s}(\Omega)$ to $\mathbf{H}^{s+\frac{1}{2}}(\Gamma)$, $s \in [0, \frac{1}{2})$ [76, Thm 3.1]. Note that the above definition is consistent with the usual tangential traces when $\mathbf{v} \in \mathbf{H}_{\mathrm{curl}}(\Omega)$ and

is independent of the extension chosen using the density of $\boldsymbol{\mathcal{C}}_0^\infty(\Omega)$ in $\mathbf{H}_0^{1+s}(\Omega)$. In addition, the following estimate holds

$$\|\mathbf{v}\times\mathbf{n}\|_{\mathbf{H}^{-s-\frac{1}{2}}(\Gamma)} \leq c\left(\|\mathbf{v}\|_{\mathbf{H}^{-s}(\Omega)} + \|\nabla\times\mathbf{v}\|_{\mathbf{H}^{-s}(\Omega)}\right). \tag{A.4.5}$$

Similarly, for $\mathbf{v} \in H^{-s}(\Omega)$ with $\nabla\cdot\mathbf{v} \in H^{-s}(\Omega)$, we define $\mathbf{v}\cdot\mathbf{n} \in H^{-s-\frac{1}{2}}(\Gamma)$ by

$$\begin{aligned}\langle \mathbf{v}\cdot\mathbf{n}, \psi\rangle_{H^{-s-\frac{1}{2}}(\Gamma),H^{s+\frac{1}{2}}(\Gamma)} :=& \langle \nabla\cdot\mathbf{v}, E(\psi)\rangle_{H^{-s}(\Omega),H^s(\Omega)} \\ &+ \langle \mathbf{v}, \nabla E(\boldsymbol{\psi})\rangle_{\mathbf{H}^{-s}(\Omega),\mathbf{H}^s(\Omega)},\end{aligned} \tag{A.4.6}$$

for all $\psi \in H^{s+\frac{1}{2}}(\Gamma)$. Moreover, the normal trace $\mathbf{v}\cdot\mathbf{n}$ satisfies

$$\|\mathbf{v}\cdot\mathbf{n}\|_{H^{-s-\frac{1}{2}}(\Gamma)} \leq c\left(\|\mathbf{v}\|_{\mathbf{H}^{-s}(\Omega)} + \|\nabla\cdot\mathbf{v}\|_{H^{-s}(\Omega)}\right). \tag{A.4.7}$$

The above arguments show that it is legitimate to consider the following spaces:

$$\mathbf{Z}_T^{1-s}(\Omega) := \left\{\mathbf{v} \in \mathbf{Z}^{1-s} \mid \mathbf{v}\cdot\mathbf{n}_{|\Gamma} = 0\right\}, \tag{A.4.8}$$

$$\mathbf{Z}_N^{1-s}(\Omega) := \left\{\mathbf{v} \in \mathbf{Z}^{1-s} \mid \mathbf{v}\times\mathbf{n}_{|\Gamma} = 0\right\}. \tag{A.4.9}$$

A.4.2 Case of constant coefficients

Theorem 2 in [35] asserts that $\mathbf{Z}_T^1(\Omega)$ and $\mathbf{Z}_N^1(\Omega)$ are continuously embedded in $\mathbf{H}^{\frac{1}{2}}(\Omega)$. The objective of this section is to establish the following generalization:

Theorem A.4.1. *For any $s \in [0, \frac{1}{2})$ and any $\mathbf{u} \in \mathbf{Z}^{1-s}(\Omega)$, the following conditions are equivalent:*

(i) $\mathbf{u}\times\mathbf{n} \in \mathbf{L}^2(\Gamma)$,

(ii) $\mathbf{u}\cdot\mathbf{n} \in L^2(\Gamma)$.

Moreover, there is a constant $c > 0$ so that the following embedding estimates hold:

$$\|\mathbf{u}\|_{\mathbf{H}^{\frac{1}{2}}(\Omega)} \leq c\left(\|\nabla\times\mathbf{u}\|_{\mathbf{H}^{-s}(\Omega)} + \|\nabla\cdot\mathbf{u}\|_{H^{-s}(\Omega)} + \|\mathbf{u}\times\mathbf{n}\|_{\mathbf{L}^2(\Gamma)}\right), \tag{A.4.10}$$

$$\|\mathbf{u}\|_{\mathbf{H}^{\frac{1}{2}}(\Omega)} \leq c\left(\|\nabla\times\mathbf{u}\|_{\mathbf{H}^{-s}(\Omega)} + \|\nabla\cdot\mathbf{u}\|_{H^{-s}(\Omega)} + \|\mathbf{u}\cdot\mathbf{n}\|_{L^2(\Gamma)}\right). \tag{A.4.11}$$

In order to prove Theorem A.4.1, we introduce $\mathcal{B}$ an open ball containing $\bar{\Omega}$, we set $\Gamma_0 = \partial\mathcal{B}$ and $\mathcal{O} := \mathcal{B}\backslash\bar{\Omega}$, and we establish the following lemma:

Lemma A.4.1. *For any $s \in [0, \frac{1}{2})$ and for any $g \in H^{-s-\frac{1}{2}}(\Gamma)$, there exists $\chi \in \dot{H}^{1-s}(\mathcal{O})$ such that*

$$\langle \nabla\chi, \nabla\psi\rangle_{\mathbf{H}^{-s}(\mathcal{O}),\mathbf{H}^s(\mathcal{O})} = \langle g, \psi\rangle_{H^{-s-\frac{1}{2}}(\Gamma),H^{s+\frac{1}{2}}(\Gamma)}, \qquad \forall\psi \in \dot{H}^{1+s}(\mathcal{O}) \tag{A.4.12}$$

$$\|\chi\|_{\dot{H}^{1-s}(\mathcal{O})} \leq c\,\|g\|_{H^{-s-\frac{1}{2}}(\Gamma)}, \tag{A.4.13}$$

where c is a constant that only depends on s and Γ. If in addition, $\langle g, 1\rangle_{H^{-s-\frac{1}{2}}(\Gamma),H^{s+\frac{1}{2}}(\Gamma)} = 0$, then (A.4.12) *holds for any $\psi \in H^{1+s}(\mathcal{O})$.*

Proof. Owing to the closed range Theorem, proving (A.4.12) is equivalent to prove the following inf-sup condition:

$$\inf_{0\neq\psi\in\dot{H}^{1+s}(\mathcal{O})}\sup_{0\neq\phi\in\dot{H}^{1-s}(\mathcal{O})}\frac{\langle\nabla\phi,\nabla\psi\rangle_{\mathbf{H}^{-s}(\mathcal{O}),\mathbf{H}^{s}(\mathcal{O})}}{\|\phi\|_{\dot{H}^{1-s}(\mathcal{O})}\|\psi\|_{\dot{H}^{1+s}(\mathcal{O})}}\geq\alpha,$$

for some $\alpha>0$. Using the notations of Section A.3 with $\mathcal{H}^s(\mathcal{O})=\dot{H}^s(\mathcal{O})$, the following holds

$$\langle\nabla\phi,\nabla\psi\rangle_{\mathbf{H}^{-s}(\mathcal{O}),\mathbf{H}^{s}(\mathcal{O})}=\langle\mathcal{S}\nabla\psi,\phi\rangle_{\mathcal{H}^{s-1}(\mathcal{O}),\mathcal{H}^{1-s}(\mathcal{O})}$$

for any $\phi\in\dot{H}^{1-s}(\mathcal{O})$ and $\psi\in\dot{H}^{1+s}(\mathcal{O})$, As a result, for any $\psi\in\dot{H}^{s+1}(\mathcal{O})$, we have

$$\sup_{0\neq\phi\in\dot{H}^{1-s}}\frac{\langle\nabla\phi,\nabla\psi\rangle_{\mathbf{H}^{-s}(\mathcal{O}),\mathbf{H}^{s}(\mathcal{O})}}{\|\phi\|_{\dot{H}^{1-s}(\mathcal{O})}}=\|\mathcal{S}\nabla\psi\|_{\mathcal{H}^{s-1}(\mathcal{O})}\,,\tag{A.4.14}$$

where $\mathcal{S}:\mathbf{L}^2(\mathcal{O})\to(\dot{H}^1(\mathcal{O}))'$ is defined by

$$\forall\mathbf{f}\in\mathbf{L}^2(\mathcal{O}),\ \forall q\in\dot{H}^1(\mathcal{O}),\qquad\langle\mathcal{S}\mathbf{f},q\rangle_{(\dot{H}^1(\mathcal{O}))',\dot{H}^1(\mathcal{O})}=(\mathbf{f},\nabla q)\,.$$

Since $\mathcal{O}$ is a Lipschitz domain, we can use $\mathcal{J}\mathcal{S}\nabla\psi=\psi$ for any $\psi\in\dot{H}^1(\mathcal{O})$, where $\mathcal{J}:(\dot{H}^1(\mathcal{O}))'\to\dot{H}^1(\mathcal{O})$ is defined by

$$\forall\mathbf{f}\in\mathbf{L}^2(\mathcal{O}),\ \forall q\in\dot{H}^1(\mathcal{O}),\qquad\langle\mathcal{S}\mathbf{f},q\rangle_{(\dot{H}^1(\mathcal{O}))',\dot{H}^1(\mathcal{O})}=(\mathbf{f},\nabla q)\,.$$

Thus, upon applying Lemma A.3.2 we obtain:

$$\|\nabla\psi\|_{\mathbf{H}^s(\mathcal{O})}=\|\psi\|_{\mathcal{H}^{1+s}(\mathcal{O})}=\|\mathcal{J}\mathcal{S}\nabla\psi\|_{\mathcal{H}^{1+s}(\mathcal{O})}\leq K(\mathcal{O},s)\,\|\mathcal{S}\nabla\psi\|_{\mathcal{H}^{s-1}(\mathcal{O})}\,.\tag{A.4.15}$$

Combining (A.4.14) and (A.4.15) together with the Poincaré-Friedrichs inequality on $\mathcal{O}$ leads to the inf-sup condition, with $\alpha^{-1}=K(\mathcal{O},r)$. This in turn implies the existence of χ with (A.4.12) and the estimate (A.4.13) with $c=\alpha^{-1}$ (see for instance [48, Lemma A.42]). Since the left-hand side of (A.4.12) only involves gradients, if in addition g satisfies the condition

$$\langle g,1\rangle_{H^{-s-\frac{1}{2}}(\Gamma),H^{s+\frac{1}{2}}(\Gamma)}=0,$$

the definition (A.4.12) holds for any $\psi\in H^{1+s}(\mathcal{O})$, i.e.,

$$\forall\psi\in H^{1+s}(\mathcal{O}),\qquad\langle\nabla\chi,\nabla\psi\rangle_{\mathbf{H}^{-s}(\mathcal{O}),\mathbf{H}^{s}(\mathcal{O})}=\langle g,\psi\rangle_{H^{-s-\frac{1}{2}}(\Gamma),H^{s+\frac{1}{2}}(\Gamma)}\,.\tag{A.4.16}$$

□

Let D be an open Lipschitz domain in $\mathbb{R}^d$. For any $F\in L^1(D)$, we denote E_DF the extension of F by 0, i.e.,

$$E_DF(\mathbf{x})=\begin{cases}F(\mathbf{x}) & \text{if } \mathbf{x}\in D,\\ 0 & \text{elsewhere.}\end{cases}\tag{A.4.17}$$

We use the same definition for vector-valued functions in $\mathbf{L}^1(D)$.

Proof of Theorem A.4.1. The proof is similar to that of Theorem 2 in [35]. Taking $\mathbf{u} \in \mathbf{Z}^{1-s}(\Omega)$, we build an extension of $\nabla\times\mathbf{u}$ in $\mathbf{H}^{-s}(\mathbb{R}^d)$ in order to be able to construct $\mathbf{w} \in \mathbf{H}^{1-s}(\Omega)$ such that $\mathbf{u}-\mathbf{w}$ is curl-free. Then we use results from Jerison and Kenig (cf. [75]) to obtain some regularity on $\mathbf{u}-\mathbf{w}$.

Taking $\mathbf{u} \in \mathbf{Z}^{1-s}(\Omega)$, we have $\nabla\times\mathbf{u} \in \mathbf{H}^{-s}(\Omega)$ and $\nabla\cdot\nabla\times\mathbf{u} = 0$, so that $(\nabla\times\mathbf{u})\cdot\mathbf{n}$ is well-defined as an element of $H^{-s-\frac{1}{2}}(\Gamma)$, owing to (A.4.6). Note also that this normal trace satisfies

$$\langle(\nabla\times\mathbf{u})\cdot\mathbf{n}, 1\rangle_{H^{-s-\frac{1}{2}}(\Gamma),H^{s+\frac{1}{2}}(\Gamma)} = 0.$$

Thus we can apply Lemma A.4.1, and there exists $\chi \in H^{1-s}(\mathcal{O})$ such that

$$\langle\nabla\chi, \nabla\psi\rangle_{\mathbf{H}^{-s}(\mathcal{O}),\mathbf{H}^s(\mathcal{O})} = \langle-(\nabla\times\mathbf{u})\cdot\mathbf{n}, \psi\rangle_{H^{-s-\frac{1}{2}}(\Gamma),H^{s+\frac{1}{2}}(\Gamma)}, \qquad \forall\psi \in H^{1+s}(\mathcal{O}).$$

We now set $\mathbf{f} = E_\Omega\nabla\times\mathbf{u} + E_\mathcal{O}\nabla\chi$. Since $s < \frac{1}{2}$, $\mathbf{H}^s(\Omega) = \mathbf{H}^s_0(\Omega)$ and $\mathbf{H}^s(\mathcal{B}) = \mathbf{H}^s_0(\mathcal{B})$, $\mathbf{f}$ can also be seen as an element of $\mathbf{H}^{-s}(\mathbb{R}^d)$, i.e., the following holds:

$$\langle\mathbf{f}, \Psi\rangle_{\mathbf{H}^{-s}(\mathbb{R}^d),\mathbf{H}^s(\mathbb{R}^d)} := \left\langle\nabla\times\mathbf{u}, \Psi_{|\Omega}\right\rangle_{\mathbf{H}^{-s}(\Omega),\mathbf{H}^s(\Omega)} + \left\langle\nabla\chi, \Psi_{|\mathcal{O}}\right\rangle_{\mathbf{H}^{-s}(\mathcal{O}),\mathbf{H}^s(\mathcal{O})},$$

for all $\Psi \in \mathbf{H}^s(\mathbb{R}^d)$. Moreover, since the restrictions $\mathbf{H}^s(\mathbb{R}^d) \to \mathbf{H}^s(\Omega)$ and $\mathbf{H}^s(\mathbb{R}^d) \to \mathbf{H}^s(\mathcal{O})$ are continuous with norm 1, combining (A.4.13) and (A.4.7) leads to

$$\begin{aligned}
\|\mathbf{f}\|_{\mathbf{H}^{-s}(\mathbb{R}^d)} &\le \|\nabla\times\mathbf{u}\|_{\mathbf{H}^{-s}(\Omega)} + \|\nabla\chi\|_{\mathbf{H}^{-s}(\mathcal{O})} \\
&\le \|\nabla\times\mathbf{u}\|_{\mathbf{H}^{-s}(\Omega)} + c\,\|(\nabla\times\mathbf{u})\cdot\mathbf{n}\|_{H^{-s-\frac{1}{2}}(\Gamma)} \\
&\le c\,\|\nabla\times\mathbf{u}\|_{\mathbf{H}^{-s}(\Omega)},
\end{aligned}$$

Owing to the definition of the trace $(\nabla\times\mathbf{u})\cdot\mathbf{n}$ and the definition of χ we infer that, the following hold for all $\phi \in \mathcal{C}^\infty_0(\mathbb{R}^d)$:

$$\begin{aligned}
\langle\mathbf{f}, \nabla\phi\rangle_{\mathbf{H}^{-s}(\mathbb{R}^d),\mathbf{H}^s(\mathbb{R}^d)} &= \left\langle\nabla\times\mathbf{u}, \nabla\phi_{|\Omega}\right\rangle_{\mathbf{H}^{-s}(\Omega),\mathbf{H}^s(\Omega)} + \left\langle\nabla\chi, \nabla\phi_{|\mathcal{O}}\right\rangle_{\mathbf{H}^{-s}(\mathcal{O}),\mathbf{H}^s(\mathcal{O})}, \\
&= \left\langle\nabla\times\mathbf{u}, \nabla\phi_{|\Omega}\right\rangle_{\mathbf{H}^{-s}(\Omega),\mathbf{H}^s(\Omega)} - \langle(\nabla\times\mathbf{u})\cdot\mathbf{n}, \phi\rangle_{H^{-s-\frac{1}{2}}(\Gamma),H^{s+\frac{1}{2}}(\Gamma)}, \\
&= \left\langle\nabla\times\mathbf{u}, \nabla\phi_{|\Omega}\right\rangle_{\mathbf{H}^{-s}(\Omega),\mathbf{H}^s(\Omega)} - \left\langle\nabla\times\mathbf{u}, \nabla\phi_{|\Omega}\right\rangle_{\mathbf{H}^{-s}(\Omega),\mathbf{H}^s(\Omega)} \\
&\quad - \langle\nabla\cdot\nabla\times\mathbf{u}, \phi\rangle_{H^{-s}(\Omega),H^s(\Omega)} = 0,
\end{aligned}$$

implying that $\nabla\cdot\mathbf{f} = 0$. As a result there exists $\mathbf{\Phi} \in \mathbf{H}^{2-s}(\mathbb{R}^d)$ such that

$$-\Delta\mathbf{\Phi} = \mathbf{f} \text{ with } \nabla\cdot\mathbf{\Phi} = 0 \text{ and } \|\mathbf{\Phi}\|_{\mathbf{H}^{2-s}(\mathbb{R}^d)} \le c\,\|\mathbf{f}\|_{\mathbf{H}^{-s}(\mathbb{R}^d)}.$$

Setting $\mathbf{w} := \nabla\times\mathbf{\Phi}$, we infer that

$$\|\mathbf{w}\|_{\mathbf{H}^{1-s}(\mathbb{R}^d)} \le c\,\|\mathbf{f}\|_{\mathbf{H}^{-s}(\mathbb{R}^d)}, \qquad \nabla\times\mathbf{w} = \mathbf{f}, \qquad \nabla\cdot\mathbf{w} = 0.$$

This in turn implies that

$$\nabla\times\mathbf{w}_{|\Omega} = \nabla\times\mathbf{u} \in \mathbf{H}^{-s}(\Omega), \qquad \nabla\cdot\mathbf{w}_{|\Omega} = 0, \qquad \left\|\mathbf{w}_{|\Omega}\right\|_{\mathbf{H}^{1-s}(\Omega)} \le c\,\|\mathbf{f}\|_{\mathbf{H}^{-s}(\mathbb{R}^d)}.$$

We set now $\mathbf{z} := \mathbf{u}-\mathbf{w}_{|\Omega}$. Using the fact that Ω is simply-connected together with $\nabla\times\mathbf{z} = 0$, we infer from [59, Theorem 2.9] that there exists $v \in H^1(\Omega)$ such that $\mathbf{z} = \nabla v$. We now split v to

be able to apply a regularity result on a homogeneous Laplace equation with non homogeneous boundary conditions. Let $E_\Omega \nabla\cdot\mathbf{u}$ be the zero extension of $\nabla\cdot\mathbf{u}$. Clearly $E_\Omega \nabla\cdot\mathbf{u} \in H^{-s}(\mathcal{B})$ since

$$\langle E_\Omega \nabla\cdot\mathbf{u}, \psi\rangle_{H^{-s}(\mathcal{B}),H^s(\mathcal{B})} := \left\langle \nabla\cdot\mathbf{u}, \psi_{|\Omega}\right\rangle_{H^{-s}(\Omega),H^s(\Omega)}, \qquad \forall \psi \in H_0^s(\mathcal{B}),$$

and

$$\|E_\Omega \nabla\cdot\mathbf{u}\|_{H^{-s}(\mathcal{B})} \leq \|\nabla\cdot\mathbf{u}\|_{H^{-s}(\Omega)},$$

since $s < \frac{1}{2}$. Let $p \in H_0^1(\mathcal{B})$ be the solution of $-\Delta p = E_\Omega \nabla\cdot\mathbf{u}$. Then elliptic regularity implies that $p \in H^{2-s}(\mathcal{B})$ (see for instance [76, Theorem 0.5]) and the following estimate holds:

$$\|\nabla p\|_{\mathbf{H}^{1-s}(\mathcal{B})} \leq c \|E_\Omega \nabla\cdot\mathbf{u}\|_{H^{-s}(\mathcal{B})} \leq c' \|\nabla\cdot\mathbf{u}\|_{H^{-s}(\Omega)}.$$

Finally, let us define $r := v - p_{|\Omega}$, so that $\mathbf{u} = (\mathbf{w} + \nabla p)_{|\Omega} + \nabla r$. By definition of $\mathbf{w}$ and p, we have

$$\Delta r = 0 \text{ in } H^{-s}(\Omega).$$

Let us assume that (i) holds, i.e., $\mathbf{u}\times\mathbf{n} \in \mathbf{L}^2(\Gamma)$. Since $\mathbf{w} \in \mathbf{H}^{1-s}(\Omega)$, we have $\mathbf{w}\times\mathbf{n} \in \mathbf{H}^{\frac{1}{2}-s}(\Gamma) \subset \mathbf{L}^2(\Gamma)$. Similarly, $p_{|\Omega} \in H^{2-s}(\Omega)$ so that $\nabla p\times\mathbf{n} \in \mathbf{H}^{\frac{1}{2}-s}(\Gamma) \subset \mathbf{L}^2(\Gamma)$. As a result, we have $\nabla r\times\mathbf{n}_{|\Gamma} = (\mathbf{u}\times\mathbf{n} - \mathbf{w}\times\mathbf{n} - \nabla p\times\mathbf{n})_{|\Gamma} \in \mathbf{L}^2(\Gamma)$, which together with $r_{|\Gamma} \in L^2(\Gamma)$ implies $r_{|\Gamma} \in H^1(\Gamma)$. Thus we have

$$\Delta r = 0 \text{ in } \Omega, \qquad r_{|\Gamma} \in H^1(\Gamma).$$

Consequently $r \in H^{\frac{3}{2}}(\Omega)$ and the following estimate holds

$$\|\nabla r\|_{\mathbf{H}^{\frac{1}{2}}(\Omega)} \leq c \|r\|_{H^1(\Gamma)} \leq c' \|\nabla r\times\mathbf{n}\|_{\mathbf{L}^2(\Gamma)}.$$

Hence, because $\mathbf{u} = (\mathbf{w}+\nabla p)_{|\Omega} + \nabla r$ with $\mathbf{w}_{|\Omega} \in \mathbf{H}^{1-s}(\Omega)$, $\nabla p_{|\Omega} \in H^{1-s}(\Omega)$, and $\nabla r \in \mathbf{H}^{\frac{1}{2}}(\Omega)$, we deduce that $\mathbf{u} \in \mathbf{H}^{\frac{1}{2}}(\Omega)$. Note also that $(\mathbf{w}\cdot\mathbf{n} + \nabla p\cdot\mathbf{n})_{|\Gamma} \in L^2(\Gamma)$, which implies that $\mathbf{u}\cdot\mathbf{n}_{|\Gamma} = (\mathbf{w}\cdot\mathbf{n} + \nabla p\cdot\mathbf{n} + \nabla r\cdot\mathbf{n})_{|\Gamma} \in L^2(\Gamma)$ thereby proving (ii). The proof of the converse implication is similar, we leave the details to the reader. In summary, we have proved that (i) and (ii) are equivalent, and that both these assumptions imply $\mathbf{u} \in \mathbf{H}^{\frac{1}{2}}(\Omega)$. Using $s < \frac{1}{2}$ and gathering all the previous estimates, we end up with:

$$\begin{aligned}
\|\mathbf{u}\|_{\mathbf{H}^{\frac{1}{2}}(\Omega)} &\leq c\left(\|\mathbf{w}\|_{\mathbf{H}^{1-s}(\Omega)} + \|\nabla p\|_{\mathbf{H}^{1-s}(\Omega)} + \|\nabla r\|_{\mathbf{H}^{\frac{1}{2}}(\Omega)}\right) \\
&\leq c\left(\|\mathbf{w}\|_{\mathbf{H}^{1-s}(\Omega)} + \|\nabla p\|_{\mathbf{H}^{1-s}(\Omega)} + \|\mathbf{u}\times\mathbf{n}\|_{\mathbf{L}^2(\Gamma)} + \|\mathbf{w}\times\mathbf{n}\|_{\mathbf{L}^2(\Gamma)} + \|\nabla p\times\mathbf{n}\|_{\mathbf{L}^2(\Gamma)}\right) \\
&\leq c\left(\|\mathbf{w}\|_{\mathbf{H}^{1-s}(\Omega)} + \|\nabla p\|_{\mathbf{H}^{1-s}(\Omega)} + \|\mathbf{u}\times\mathbf{n}\|_{\mathbf{L}^2(\Gamma)}\right) \\
&\leq c\left(\|\mathbf{f}\|_{\mathbf{H}^{-s}(\mathbb{R}^d)} + \|E_\Omega \nabla\cdot\mathbf{u}\|_{H^{-s}(\mathcal{B})} + \|\mathbf{u}\times\mathbf{n}\|_{\mathbf{L}^2(\Gamma)}\right) \\
&\leq c\left(\|\nabla\times\mathbf{u}\|_{\mathbf{H}^{-s}(\Omega)} + \|\nabla\cdot\mathbf{u}\|_{H^{-s}(\Omega)} + \|\mathbf{u}\times\mathbf{n}\|_{\mathbf{L}^2(\Gamma)}\right),
\end{aligned}$$

which is the desired result. The inequality involving $\mathbf{u}\cdot\mathbf{n}$ is obtained similarly; in particular we must use the fact that the scalar field $r := v - p_{|\Omega}$ is such that

$$\Delta r = 0 \text{ in } \Omega, \qquad \mathbf{n}\cdot\nabla r \in L^2(\Gamma),$$

which again implies $r \in H^{\frac{3}{2}}(\Omega)$, (see for instance [75] or [35, Lemma 1]). □

A.4.3 Case of non-constant coefficients

Throughout §A.4 and §A.5 we assume that the tensor fields ε and μ satisfy the following property:

Assumption A.4.1. *We assume that* $\varepsilon, \mu \in W^{1,\infty}_{\Sigma}(\Omega)^{d\times d}$ *and there exist* $\varepsilon_{\min}$, $\mu_{\min} > 0$ *such that*

$$\boldsymbol{\xi}^T\varepsilon\boldsymbol{\xi} \geq \varepsilon_{\min}\boldsymbol{\xi}^T\boldsymbol{\xi} \quad \textit{a.e. in } \Omega, \quad \forall \boldsymbol{\xi} \in \mathbb{R}^d,$$
$$\boldsymbol{\xi}^T\mu\boldsymbol{\xi} \geq \mu_{\min}\boldsymbol{\xi}^T\boldsymbol{\xi} \quad \textit{a.e. in } \Omega, \quad \forall \boldsymbol{\xi} \in \mathbb{R}^d.$$

The analysis of the regularity of Maxwell problem (A.1.5) requires introducing the following two spaces:

$$\mathbf{Y}^s(\Omega) := \left\{\mathbf{F} \in \mathbf{L}^2(\Omega) \mid \nabla\times\mathbf{F} \in \mathbf{H}^{-s}(\Omega),\ \nabla\cdot(\mu\mathbf{F}) = 0,\ \mu\mathbf{F}\cdot\mathbf{n}_{|\Gamma} = 0\right\}, \tag{A.4.18}$$

$$\mathbf{X}^s(\Omega) := \left\{\mathbf{F} \in \mathbf{L}^2(\Omega) \mid \nabla\times\mathbf{F} \in \mathbf{H}^{-s}(\Omega),\ \nabla\cdot(\varepsilon\mathbf{F}) \in H^{s-1}(\Omega),\ \mathbf{F}\times\mathbf{n}_{|\Gamma} = 0\right\}. \tag{A.4.19}$$

We define the following semi-norms in $\mathbf{X}^s(\Omega)$ and $\mathbf{Y}^s(\Omega)$:

$$|\mathbf{F}|^2_{\mathbf{X}^s(\Omega)} := \|\nabla\times\mathbf{F}\|^2_{\mathbf{H}^{-s}(\Omega)} + \|\nabla\cdot(\varepsilon\mathbf{F})\|^2_{H^{s-1}(\Omega)}, \quad |\mathbf{F}|_{\mathbf{Y}^s(\Omega)} := \|\nabla\times\mathbf{F}\|_{\mathbf{H}^{-s}(\Omega)}. \tag{A.4.20}$$

Two embedding results for $\mathbf{X}^s$ and $\mathbf{Y}^s(\Omega)$ are established in this section.

Proposition A.4.1. *Let Assumption A.4.1 hold. There exists* $\tau_\varepsilon > 0$*, only depending on* Ω *and* ε*, such that, for any* $s \in [0, \tau_\varepsilon)$*,* $\mathbf{X}^s(\Omega)$ *is continuously embedded in* $\mathbf{H}^s(\Omega)$*, and there is* $c > 0$ *so that*

$$\|\mathbf{F}\|_{\mathbf{H}^s(\Omega)} \leq c\,|\mathbf{F}|_{\mathbf{X}^s(\Omega)}, \qquad \forall \mathbf{F} \in \mathbf{X}^s(\Omega). \tag{A.4.21}$$

Proof. Owing to Assumption A.4.1, we can apply Theorem A.3.1 with $\nu = \varepsilon$ and $\mathcal{H}^1(\Omega) = H^1_0(\Omega)$. Let $\tau_\varepsilon < \frac{1}{2}$ be the parameter defined in Theorem A.3.1. Let us consider $\mathbf{F} \in \mathbf{X}^s(\Omega)$ with $s \in [0, \tau_\varepsilon)$. We define $p \in H^1_0(\Omega)$ such that

$$(\nabla p, \nabla q) = (\mathbf{F}, \nabla q), \qquad \forall q \in H^1_0(\Omega),$$

and we set $\mathbf{w} := \mathbf{F} - \nabla p$. This definition implies that $\mathbf{w} \in \mathbf{Z}^{1-s}(\Omega)$ since $\nabla\times\mathbf{w} = \nabla\times\mathbf{F}$ and $\nabla\cdot\mathbf{w} = 0$. Observing also that $\mathbf{w}\times\mathbf{n}_{|\Gamma} = 0$ and applying Theorem A.4.1, we deduce that $\mathbf{w} \in \mathbf{H}^{\frac{1}{2}}(\Omega)$ and $\|\mathbf{w}\|_{\mathbf{H}^{\frac{1}{2}}(\Omega)} \leq c\,\|\nabla\times\mathbf{w}\|_{\mathbf{H}^{-s}(\Omega)}$. In addition, $s < \frac{1}{2}$ and $\nabla\times\mathbf{w} = \nabla\times\mathbf{F}$, imply that

$$\|\mathbf{w}\|_{\mathbf{H}^s(\Omega)} \leq c\,\|\nabla\times\mathbf{F}\|_{\mathbf{H}^{-s}(\Omega)}. \tag{A.4.22}$$

Moreover, since $\mathbf{w} \in \mathbf{H}^s(\Omega)$, Proposition A.2.1 ensures that $\varepsilon\mathbf{w} \in \mathbf{H}^s(\Omega)$; as a result, $\nabla\cdot(\varepsilon\mathbf{w}) \in H^{s-1}(\Omega)$ and

$$\|\nabla\cdot(\varepsilon\mathbf{w})\|_{H^{s-1}(\Omega)} \leq c\|\varepsilon\mathbf{w}\|_{H^s(\Omega)} \leq c'\|\mathbf{w}\|_{H^s(\Omega)} \leq c''\,\|\nabla\times\mathbf{F}\|_{\mathbf{H}^{-s}(\Omega)}. \tag{A.4.23}$$

Let us now turn our attention to p. In view of the following equality

$$(\varepsilon\nabla p, \nabla q) = (\varepsilon\mathbf{F}, \nabla q) - (\varepsilon\mathbf{w}, \nabla q), \qquad q \in H^1_0(\Omega),$$

and upon introducing the linear form $f : \mathcal{H}^1(\Omega) \ni q \mapsto (\varepsilon\mathbf{F} - \varepsilon\mathbf{w}, \nabla q)$, i.e., $f = -\nabla\cdot(\varepsilon(\mathbf{F}-\mathbf{w}))$, we infer that p solves:

$$(\varepsilon\nabla p, \nabla q) = \langle f, q\rangle_{\mathcal{H}^{-1}(\Omega),\mathcal{H}(\Omega)}, \qquad \forall q \in \mathcal{H}^1(\Omega).$$

The definition of $\mathbf{X}^s(\Omega)$ implies that $\nabla\cdot(\varepsilon\mathbf{F}) \in H^{s-1}(\Omega)$. This, together with (A.4.23), implies that $\|f\|_{\mathcal{H}^{s-1}(\Omega)} \le c|\mathbf{F}|_{\mathbf{X}^s(\Omega)}$. Applying Theorem A.3.1, we infer that $p \in H^{1+s}(\Omega)$ and

$$\|\nabla p\|_{\mathbf{H}^s(\Omega)} \le c|\mathbf{F}|_{\mathbf{X}^s(\Omega)}. \tag{A.4.24}$$

Using (A.4.22), (A.4.24), and recalling the definition $\mathbf{F} = \mathbf{w}+\nabla p$, we conclude that $\mathbf{F} \in \mathbf{H}^s(\Omega)$ and there exists a constant c that only depends on Ω, ε, and s such that

$$\|\mathbf{F}\|_{\mathbf{H}^s(\Omega)} \le c\,|\mathbf{F}|_{\mathbf{X}^s(\Omega)}\,. \tag{A.4.25}$$

This concludes the proof. □

Proposition A.4.2. *Let Assumption A.4.1 hold. There exists τ_μ only depending on Ω and μ such that, for any $s \in [0, \tau_\mu)$, the space $\mathbf{Y}^s(\Omega)$ is continuously embedded in $\mathbf{H}^s(\Omega)$.*

Proof. We proceed as in the proof of Proposition A.4.1. We consider $\mathbf{F} \in \mathbf{Y}^s(\Omega)$ and we want to decompose $\mathbf{F}$ as follows:

$$\mathbf{F} = \mathbf{w} + \nabla p,$$

where $\mathbf{w}$ is a regular part and p is the solution of an elliptic system with discontinuous coefficients. We first focus on the construction of $\mathbf{w}$. We introduce

$$\mathbf{H}_{0,\mathrm{curl}}(\Omega) := \{\mathbf{G} \in \mathbf{H}_{\mathrm{curl}}(\Omega) \mid \mathbf{G}\times\mathbf{n} = 0\},$$
$$\mathbf{H}_{\mathrm{div}=0}(\Omega) := \{\mathbf{G} \in \mathbf{H}_{\mathrm{div}}(\Omega) \mid \nabla\cdot\mathbf{G} = 0\}.$$

Owing to (A.4.10) with $s = 0$ (see also [35, Theorem 2]) and the Lax-Milgram lemma, there exists a unique $\mathbf{G} \in \mathbf{H}_{0,\mathrm{curl}}(\Omega) \cap \mathbf{H}_{\mathrm{div}=0}(\Omega)$ such that the following holds:

$$(\nabla\times\mathbf{G}, \nabla\times\mathbf{f}) = (\mathbf{F}, \nabla\times\mathbf{f}), \qquad \mathbf{f} \in \mathbf{H}_{0,\mathrm{curl}}(\Omega) \cap \mathbf{H}_{\mathrm{div}=0}(\Omega). \tag{A.4.26}$$

Since the above definition only involves $\nabla\times\mathbf{f}$, we infer that the following holds also

$$(\nabla\times\mathbf{G}, \nabla\times\mathbf{f}) = (\mathbf{F}, \nabla\times\mathbf{f}), \qquad \forall\mathbf{f} \in \mathbf{H}_{0,\mathrm{curl}}(\Omega).$$

Setting $\mathbf{w} := \nabla\times\mathbf{G}$, the above equality implies that $\nabla\times\mathbf{w} = \nabla\times\mathbf{F}$. The equality $\nabla\times\mathbf{w} = \nabla\times\mathbf{F}$ first holds in the distribution space $\mathcal{D}'(\Omega)$, and then in $\mathbf{H}^{-s}(\Omega)$ taking advantage of the regularity $\nabla\times\mathbf{F} \in \mathbf{H}^{-s}(\Omega)$. We have $\mathbf{w} \in \mathbf{L}^2(\Omega)$ with $\nabla\cdot\mathbf{w} = 0$ and $\nabla\times\mathbf{w} \in \mathbf{H}^{-s}(\Omega)$, i.e. $\mathbf{w} \in \mathbf{Z}^{1-s}(\Omega)$. Moreover, the condition $\mathbf{G}\times\mathbf{n}_{|\Gamma} = 0$ implies $\mathbf{w}\cdot\mathbf{n}_{|\Gamma} = 0$. Then Theorem A.4.1 implies that $\mathbf{w} \in \mathbf{H}^{\frac{1}{2}}(\Omega)$ and

$$\|\mathbf{w}\|_{\mathbf{H}^{\frac{1}{2}}(\Omega)} \le c\,\|\nabla\times\mathbf{w}\|_{\mathbf{H}^{-s}(\Omega)} = c\,\|\nabla\times\mathbf{F}\|_{\mathbf{H}^{-s}(\Omega)}\,. \tag{A.4.27}$$

The equality $\nabla\times\mathbf{w} = \nabla\times\mathbf{F}$ yields the existence of $p \in H^1(\Omega)$ such that $\mathbf{F} = \mathbf{w} + \nabla p$ [59, Theorem 2.9]. Up to an additive constant, we assume that $p \in \dot{H}^1(\Omega)$ and now derive $H^s(\Omega)$ estimates. The definition of p together with the assumption $\nabla\cdot(\mu\mathbf{F}) = 0$ implies that

$$(\mu\nabla p, \nabla q) = (\mu\mathbf{F}, \nabla q) - (\mu\mathbf{w}, \nabla q) = -(\mu\mathbf{w}, \nabla q), \qquad \forall q \in H^1(\Omega).$$

As a result, we have

$$(\mu\nabla p, \nabla q) = -(\mathcal{S}(\mu\mathbf{w}), q), \qquad \forall q \in \dot{H}^1(\Omega).$$

Proposition A.2.1 ensures that $\mu\mathbf{w} \in \mathbf{H}^s(\Omega)$ for all $s < \frac{1}{2}$, and Lemma A.3.1 implies that $\mathcal{S}(\mu\mathbf{w}) \in \mathcal{H}^{s-1}(\Omega)$, so that

$$\|\mathcal{S}(\mu\mathbf{w})\|_{\mathcal{H}^{s-1}(\Omega)} \leq \|\mu\mathbf{w}\|_{\mathbf{H}^s_0(\Omega)} \leq \mu_{\max} N_{s,\mu} \|\mathbf{w}\|_{\mathbf{H}^s(\Omega)} \leq c \|\mathbf{w}\|_{\mathbf{H}^{\frac{1}{2}}(\Omega)}.$$

We now can apply Theorem A.3.1 with $\mathcal{H}^1(\Omega) = \dot{H}^1(\Omega)$ and $\nu = \mu$. Let τ_μ be the parameter defined in Theorem A.3.1. Then $p \in H^{1+s}(\Omega)$ for all $s \in [0, \tau_\mu)$ and there is a constant c so that

$$\|\nabla p\|_{\mathbf{H}^s(\Omega)} \leq c \|\mathcal{S}(\mu\mathbf{w})\|_{\mathcal{H}^{s-1}(\Omega)} \leq c' \|\mathbf{w}\|_{\mathbf{H}^{\frac{1}{2}}(\Omega)}. \tag{A.4.28}$$

Recalling that and $\mathbf{F} = \mathbf{w} + \nabla p$, we finally conclude that $\mathbf{F} \in \mathbf{H}^s$, and owing to (A.4.27) and (A.4.28) we obtain the following estimate:

$$\|\mathbf{F}\|_{\mathbf{H}^s} \leq c \|\mathbf{w}\|_{\mathbf{H}^{\frac{1}{2}}} \leq c' \|\nabla\times\mathbf{F}\|_{\mathbf{H}^{-s}(\Omega)} = c' |\mathbf{F}|_{\mathbf{Y}^s(\Omega)}. \tag{A.4.29}$$

This concludes the proof. □

Remark A.4.1. The counterpart of Proposition A.4.1 and Proposition A.4.2 when ε are μ are constant or smooth functions is that $\mathbf{X}^s(\Omega)$ and $\mathbf{Y}^s(\Omega)$ are continuously embedded in $\mathbf{H}^{\frac{1}{2}}(\Omega)$. The discontinuities in the fields ε are μ imply regularity losses. See also [38].

A.5 Application to Maxwell problem

We turn our attention in this section to the Maxwell problems mentioned in the introduction. Using Theorem A.3.1, we establish a priori estimates for the following problem: Given $\mathbf{g}$ and b, find $\mathbf{E}$ so that

$$\nabla\times(\mu^{-1}\nabla\times\mathbf{E}) = \mathbf{g}, \quad \nabla\cdot(\varepsilon\mathbf{E}) = b, \quad \mathbf{E}\times\mathbf{n}|_\Gamma = 0. \tag{A.5.1}$$

A.5.1 Notation and preliminaries

Let us consider the following space:

$$\mathbf{X}^s_{\mathrm{div}=0}(\Omega) := \{\mathbf{F} \in \mathbf{X}^s(\Omega) \mid \nabla\cdot(\varepsilon\mathbf{F}) = 0\}, \tag{A.5.2}$$

equipped with the canonical norm

$$\|\mathbf{F}\|^2_{\mathbf{X}^s_{\mathrm{div}=0}(\Omega)} := \|\mathbf{E}\|^2_{\mathbf{L}^2(\Omega)} + \|\nabla\times\mathbf{E}\|^2_{\mathbf{H}^{-s}(\Omega)}. \tag{A.5.3}$$

The case $b \neq 0$ reduces to the case $b = 0$ upon decomposing $\mathbf{E} := \widetilde{\mathbf{E}} + \nabla p$ where $\widetilde{\mathbf{E}}$ is the solution of the Maxwell system with $b = 0$ and p solves

$$(\epsilon\nabla p, \nabla r) = (b, r), \qquad \forall r \in H^1_0(\Omega).$$

As a consequence, we focus from now on to the case $b = 0$. Problem (A.5.1) can be reformulated as follows: Find $\mathbf{E} \in \mathbf{X}^0_{\mathrm{div}=0}(\Omega)$ such that the following holds:

$$\left(\mu^{-1}\nabla\times\mathbf{E}, \nabla\times\mathbf{F}\right) = (\mathbf{g}, \mathbf{F}), \qquad \forall \mathbf{F} \in \mathbf{X}^0_{\mathrm{div}=0}(\Omega). \tag{A.5.4}$$

Let us denote $A : \mathbf{L}^2(\Omega) \ni g \mapsto E \in \mathbf{X}^0_{\mathrm{div}=0}(\Omega)$ the solution mapping for the model problem Problem (A.5.4). We deduce an existence result as an immediate consequence of Proposition A.4.1, i.e., the linear operator A is well defined.

Proposition A.5.1. *Let the Assumption* (A.4.1) *hold. Problem* (A.5.4) *has a unique solution* $\mathbf{E} := A\mathbf{g}$ *in* $\mathbf{X}^0_{div=0}(\Omega)$ *for any* $\mathbf{g} \in \mathbf{L}^2(\Omega)$ *and there is a constant* c*, independent of* $\mathbf{g}$*, so that*

$$\|A\mathbf{g}\|_{\mathbf{X}^0(\Omega)} \leq c\|\mathbf{g}\|_{\mathbf{L}^2(\Omega)}. \tag{A.5.5}$$

Proof. This is a direct application of the Lax-Milgram lemma. Indeed, for any $\mathbf{F} \in \mathbf{X}^0_{\mathrm{div}=0}(\Omega)$, Proposition A.4.1 implies that

$$\|\mathbf{F}\|^2_{\mathbf{X}^0(\Omega)} = \|\mathbf{F}\|^2_{\mathbf{L}^2(\Omega)} + \|\nabla\times\mathbf{F}\|^2_{\mathbf{L}^2(\Omega)} \leq c\,|\mathbf{F}|^2_{\mathbf{X}^0(\Omega)} + \|\nabla\times\mathbf{F}\|^2_{\mathbf{L}^2}\,.$$

After observing that $|\mathbf{F}|_{\mathbf{X}^0(\Omega)} = \|\nabla\times\mathbf{F}\|_{\mathbf{L}^2}$, since $\mathbf{F} \in \mathbf{X}^0_{\mathrm{div}=0}(\Omega)$, we conclude that

$$\|\mathbf{F}\|^2_{\mathbf{X}^0(\Omega)} \leq c\,\|\nabla\times\mathbf{F}\|^2_{\mathbf{L}^2} \leq c\mu_{\max}\left(\mu^{-1}\nabla\times\mathbf{F}, \nabla\times\mathbf{F}\right),$$

and the bilinear form $\left(\mu^{-1}\nabla\times\mathbf{F}, \nabla\times\mathbf{G}\right)$ is coercive in $\mathbf{X}^0_{\mathrm{div}=0}(\Omega)$. The rest of the proof is standard. □

A.5.2 Regularity of the Maxwell problem

We now establish regularity estimates for the solution of the Maxwell problem (A.5.4).

Theorem A.5.1. *Let the regularity Assumption A.4.1 hold. There exist* τ_ε*,* τ_μ*, depending only on* Ω*,* ε*, and* μ *so that,*

$$\mathbf{g} \in \mathbf{L}^2(\Omega) \mapsto A\mathbf{g} \in \mathbf{H}^s(\Omega) \text{ is continuous for all } s \in [0, \tau_\varepsilon), \tag{A.5.6}$$

$$\mathbf{g} \in \mathbf{L}^2(\Omega) \mapsto \nabla\times A\mathbf{g} \in \mathbf{H}^s(\Omega) \text{ is continuous for all } s \in [0, \tau_\mu). \tag{A.5.7}$$

Proof. By applying Proposition A.4.1 and Proposition H.2.2, we infer that

$$\|A\mathbf{g}\|_{\mathbf{H}^s(\Omega)} \leq c\,|A\mathbf{g}|_{\mathbf{X}^s(\Omega)} \leq c\,\|\nabla\times A\mathbf{g}\|_{\mathbf{L}^2(\Omega)} \leq c'\,\|\mathbf{g}\|_{\mathbf{L}^2(\Omega)}\,,$$

which proves (A.5.6). Note in passing that this also proves that $\mu^{-1}\nabla\times A\mathbf{g} \in \mathbf{L}^2(\Omega)$.

We now prove (A.5.7). We first establish that there exists $p \in H^1_0(\Omega)$ so that $\nabla\times\left(\mu^{-1}\nabla\times A\mathbf{g}\right) = g - \varepsilon\nabla p$. Let $\mathbf{F} \in \boldsymbol{\mathcal{C}}^\infty_0(\Omega)$ and let $q \in H^1_0(\Omega)$ be so that

$$(\varepsilon\nabla q, \nabla r) = (\varepsilon\mathbf{F}, \nabla r), \qquad \forall r \in H^1_0(\Omega),$$

and set $\mathbf{w} := \mathbf{F} - \nabla q$. The definition of q implies that $\mathbf{w}\times\mathbf{n}|_\Gamma = 0$, $\nabla\cdot(\varepsilon\mathbf{w}) = 0$, and $\nabla\times\mathbf{w} = \nabla\times\mathbf{F} \in \mathbf{L}^2(\Omega)$. As a result, $\mathbf{w}$ is a member of $\mathbf{X}^0(\Omega)$. This in turn implies that

$$\left(\mu^{-1}\nabla\times A\mathbf{g}, \nabla\times\mathbf{F}\right) = \left(\mu^{-1}\nabla\times A\mathbf{g}, \nabla\times\mathbf{w}\right) = (\mathbf{g}, \mathbf{w}) = (\mathbf{g}, \mathbf{F} - \nabla q)\,.$$

Now let us define $p \in H_0^1(\Omega)$ so that

$$(\varepsilon \nabla p, \nabla r) = (\mathbf{g}, \nabla r), \qquad \forall r \in H_0^1(\Omega).$$

Then,

$$\left(\mu^{-1}\nabla\times A\mathbf{g}, \nabla\times\mathbf{F}\right) = (\mathbf{g}, \mathbf{F}) - (\varepsilon\nabla p, \nabla q) = (\mathbf{g}, \mathbf{F}) - (\varepsilon\mathbf{F}, \nabla p)\,.$$

Since $\mathbf{F}$ is an arbitrary member of $\boldsymbol{\mathcal{C}}_0^\infty(\Omega)$, the above equality implies that

$$\nabla\times\left(\mu^{-1}\nabla\times A\mathbf{g}\right) + \varepsilon\nabla p = \mathbf{g}, \qquad \text{in } (\boldsymbol{\mathcal{D}}(\Omega))'.$$

The equality actually holds in $\mathbf{L}^2(\Omega)$ since $q \in \mathbf{L}^2(\Omega)$ and $p \in H_0^1(\Omega)$, and

$$\|\nabla\times\left(\mu^{-1}\nabla\times A\mathbf{g}\right)\|_{\mathbf{L}^2(\Omega)} \le \|\mathbf{g}\|_{\mathbf{L}^2(\Omega)} + \varepsilon_{\max}\|\nabla p\|_{\mathbf{L}^2(\Omega)} \le (1 + \varepsilon_{\max}\varepsilon_{\min}^{-1})\|\mathbf{g}\|_{\mathbf{L}^2(\Omega)}.$$

In conclusion $\mu^{-1}\nabla\times A\mathbf{g}$ is a member of $\mathbf{H}_{\mathrm{curl}}(\Omega)$.

Now let us observe that since $\nabla\times A\mathbf{g}$ is a member of $\mathbf{H}_{\mathrm{div}}\,(\Omega)$, the condition $\nabla\cdot(\nabla\times A\mathbf{g}) = 0$ together with the boundary condition $A\mathbf{g}\times\mathbf{n}|_\Gamma = 0$ implies that $(\mu^{-1}\nabla\times A\mathbf{g})\cdot\mathbf{n}|_\Gamma = 0$. Moreover it is clear that $\nabla\cdot(\mu(\mu^{-1}\nabla\times A\mathbf{g})) = 0$. In conclusion, $\mu^{-1}\nabla\times A\mathbf{g}$ is a member of $\mathbf{Y}^0(\Omega)$. Using Proposition A.4.2, we infer that there is $\tau_\mu > 0$ so that the following holds for all $s \in [0, \tau_\mu)$:

$$\begin{aligned}
\left\|\mu^{-1}\nabla\times A\mathbf{g}\right\|_{\mathbf{H}^s(\Omega)} &\le c\left\|\mu^{-1}\nabla\times A\mathbf{g}\right\|_{\mathbf{Y}^0(\Omega)} \\
&= c\left(\left\|\mu^{-1}\nabla\times A\mathbf{g}\right\|_{\mathbf{L}^2(\Omega)} + \left\|\nabla\times(\mu^{-1}\nabla\times A\mathbf{g})\right\|_{\mathbf{L}^2(\Omega)}\right) \\
&\le c'\|\mathbf{g}\|_{\mathbf{L}^2(\Omega)}.
\end{aligned}$$

We conclude by using the fact that $\mathcal{E}_\mu$ is a continuous operator from $\mathbf{H}^s(\Omega)$ to $\mathbf{H}^s(\Omega)$ for all $s \le \tau_\mu < \frac{1}{2}$. □

Annexe B

H^1-conforming approximation of the Maxwell equations in heterogeneous media with minimal regularity

A. Bonito [a], J.-L. Guermond [a], F. Luddens [b]

Abstract

In this note, we propose and analyse an approximation technique for the Maxwell equations in heterogeneous domains, using Lagrange finite elements. In the spirit of [17], the idea consists of controlling the divergence of the electric field in a Sobolev space with fractional negative exponent. We prove that the method is suitable for boundary value problems as well as for eigenvalue problems.

B.1 Introduction

B.1.1 The Maxwell problem

We start from the time-harmonic Maxwell equations with perfect conductor boundary conditions in a simply connected, bounded, Lipschitz domain $\Omega \subset \mathbb{R}^d$:

$$\nabla\times\mathbf{E} - i\omega\mu\mathbf{H} = 0 \text{ and } \nabla\times\mathbf{H} + i\omega\varepsilon\mathbf{E} = \mathbf{J} \text{ in } \Omega,$$
$$\mathbf{E}\times\mathbf{n} = 0 \text{ and } \mathbf{H}\cdot\mathbf{n} = 0 \text{ on } \partial\Omega.$$

We assume that Ω is made of heterogenous media, i.e. the permittivity ε and the permeability μ may have discontinuities. Eliminating the magnetic field $\mathbf{H}$ from the above equations, the electric field $\mathbf{E}$ satisfies a system of the kind

$$\nabla\times\left(\mu^{-1}\nabla\times\mathbf{E}\right) - \omega^2\varepsilon\mathbf{E} = \varepsilon\mathbf{g} \qquad \text{and} \qquad \nabla\cdot(\varepsilon\mathbf{E}) = 0, \text{ in } \Omega.$$

This naturally leads to the following two problems:

[a] Department of Mathematics, Texas A&M University 3368 TAMU, College Station, TX 77843-3368, USA
[b] Laboratoire d'Informatique pour la Mécanique et les Sciences de l'Ingénieur, CNRS, BP 133, 91403 Orsay Cedex, France

- the boundary value problem; given $\mathbf{g}$ a field such that $\nabla\cdot(\varepsilon\mathbf{g}) = 0$, find $\mathbf{E}$ such that:

$$\begin{cases} \nabla\times\left(\mu^{-1}\nabla\times\mathbf{E}\right) = \varepsilon\mathbf{g} \\ \nabla\cdot(\varepsilon\mathbf{E}) = 0 \\ \mathbf{E}\times\mathbf{n} = 0 \end{cases}$$

- the eigenvalue problem; find $(\lambda, \mathbf{E})$ such that:

$$\begin{cases} \nabla\times\left(\mu^{-1}\nabla\times\mathbf{E}\right) = \lambda\varepsilon\mathbf{E} \\ \nabla\cdot(\varepsilon\mathbf{E}) = 0 \\ \mathbf{E}\times\mathbf{n} = 0 \end{cases}$$

In the following, we will often use $\kappa := \mu^{-1}$.

B.1.2 Mixed formulation

It can be shown (cf. [18] e.g.) that the boundary value problem may extend for any square-integrable data $\mathbf{g}$, using the following mixed formulation:

$$\begin{cases} \nabla\times(\kappa\nabla\times\mathbf{E}) + \varepsilon\nabla q = \varepsilon\mathbf{g}, \\ \nabla\cdot(\varepsilon\mathbf{E}) = 0 \\ \mathbf{E}\times\mathbf{n}_{|\Gamma} = 0, \quad q_{|\Gamma} = 0. \end{cases} \tag{B.1.1}$$

This formulation is the starting point for approximation. In the homogeneous case (i.e. κ and ε constant), it is well-known that the use of Lagrange finite element is challenging, because it often relies on convergence in the L^2-norm for both the curl and the divergence of the electric field. It has been shown by Costabel [35] that such techniques may fail to converge if Ω is non-smooth and non-convex.

In the present paper, we follow the idea of controlling the divergence of the electric field in a an intermediate space between $L^2(\Omega)$ and $H^{-1}(\Omega)$. The idea has already been used by Bramble et al. [22, 21], Costabel and Dauge [37]. Here, we develop a technique in the spirit of [17], based on estimates in fractional Sobolev spaces with negative exponents.

The paper is organized as follows: in §2, we introduce the functional framework and recall a regularity result from [18] for the solution of the Maxwell system. In §3, we introduce a regularization operator with good approximation and commutating properties. In §4, we present the discrete formulation we want to use, and prove that the method is well-defined and consistent. Several convergence results (for different norms) for the boundary value problem are stated. Finally, in §5, we focus on the eigenvalue problem, and prove that in some sense, the approximation technique we have developed is suitable to approximate both eigenvalues and eigenvectors.

B.2 Preliminaries

B.2.1 Spaces

Let D be an open connected Lipschitz domain in $\mathbb{R}^d$. (In the rest of the paper D denotes a generic open Lipschitz domain that may differ from Ω.) The space of the smooth functions

with compact support in D is indifferently denoted by $\mathcal{C}_0^\infty(D)$ or $\mathcal{D}(D)$. We define the norm in $H^1(D)$ as follows:

$$\|v\|^2_{H^1(D)} := \|v\|^2_{L^2(D)} + \|\nabla v\|^2_{\mathbf{L}^2(D)}. \tag{B.2.1}$$

The space $H^s(D)$ for $s \in (0,1)$ is defined by the method of real interpolation between $H^1(D)$ and $L^2(D)$ (see e.g. [143])

$$H^s(D) = [L^2(D), H^1(D)]_{s,2}. \tag{B.2.2}$$

We also consider the space $H^1_0(D)$ to be the completion of $\mathcal{D}(D)$ with respect to the following norm

$$\|v\|_{H^1_0(D)} := \|\nabla v\|_{\mathbf{L}^2(D)}. \tag{B.2.3}$$

This allows us again to define the space $H^s_0(D)$ for $s \in (0,1)$ by the method of real interpolation between $H^1_0(D)$ and $L^2(D)$

$$H^s_0(D) = [L^2(D), H^1_0(D)]_{s,2}. \tag{B.2.4}$$

(This definition is slightly different from what is usually done; the only differences occurs at $s = \frac{1}{2}$. What we hereafter denote by $H^{\frac{1}{2}}_0(D)$ is usually denoted by $H^{\frac{1}{2}}_{00}(D)$ elsewhere.) Recall that the spaces $H^s_0(D)$ and $H^s(D)$ coincide for $s \in [0, \frac{1}{2})$ and their norms are equivalent, (see e.g. [95, Thm 11.1], [63, Cor 1.4.4.5], or [143, Chap. 33]). The space $H^{-s}(D)$ is defined by duality with $H^s_0(D)$ for $0 \le s \le 1$, i.e., with a slight abuse of notation

$$\|v\|_{H^{-s}(D)} = \sup_{0 \neq w \in H^s_0(D)} \frac{\int_D vw}{\|w\|_{H^s_0(D)}}.$$

It is a standard result that $H^{-s}(D) = [L^2(D), H^{-1}(D)]_{s,2}$.

The above definitions are naturally extended to the vector-valued Sobolev spaces $\mathbf{H}^s(D)$ and $\mathbf{H}^s_0(D)$. We additionally introduce the spaces

$$\mathbf{H}_{\mathrm{curl}}(D) = \{\mathbf{v} \in \mathbf{L}^2(D) \mid \nabla\times\mathbf{v} \in \mathbf{L}^2(D)\}, \tag{B.2.5}$$

$$\mathbf{H}_{0,\mathrm{curl}}(D) = \{\mathbf{v} \in \mathbf{L}^2(D) \mid \nabla\times\mathbf{v} \in \mathbf{L}^2(D),\ \mathbf{v}\times\mathbf{n}|_{\partial D} = 0\}, \tag{B.2.6}$$

$$\mathbf{H}^r_{\mathrm{curl}}(D) = \{\mathbf{v} \in \mathbf{L}^2(D) \mid \nabla\times\mathbf{v} \in \mathbf{H}^r(D)\}, \tag{B.2.7}$$

$$\mathbf{H}^r_{0,\mathrm{curl}}(D) = \{\mathbf{v} \in \mathbf{L}^2(D) \mid \nabla\times\mathbf{v} \in \mathbf{H}^r(D),\ \mathbf{v}\times\mathbf{n}|_{\partial D} = 0\}, \tag{B.2.8}$$

all equipped with their natural norm; for instance, $\|\mathbf{v}\|^2_{\mathbf{H}_{\mathrm{curl}}(D)} = \|\mathbf{v}\|^2_{\mathbf{L}^2(D)} + \|\nabla\times\mathbf{v}\|^2_{\mathbf{L}^2(D)}$.

B.2.2 The domain

The domain Ω is a bounded open set in $\mathbb{R}^d$, $d = 2, 3$. The boundary is assumed to have the Lipschitz regularity. To simplify the presentation we also assume that $0 \in \Omega$ and Ω is star-shaped with respect to an open neighborhood of 0. More precisely, there is an open neighborhood of the origin, say $\mathcal{V}$, such that Ω is star-shaped with respect to all the points on $\mathcal{V}$. This assumption is equivalent to assuming that Ω is a star-shaped domain with respect

to the origin and there exists a real number $\chi \in (0,1)$ such that the following holds for any $\delta \in (0,1)$:

$$(1-\delta)\Omega + B(0,\delta\chi) \subset\subset \Omega, \tag{B.2.9}$$

where $B(0,r)$ is the ball centered at 0 of radius r and $\subset\subset$ denotes compact embedding.

A key piece of the convergence analysis of the method that we propose in this paper is based on the existence of a family of smoothing operators in $\mathbf{H}_{0,\mathrm{curl}}(\Omega)$. This construction is discussed in detail in §B.3. The main challenge one encounters when constructing this family of operators is to make it compatible with the boundary condition and to commutes with the curl operator. The purpose of the hypothesis (B.2.9) is to make this construction possible. The hypothesis (B.2.9) may seem restrictive, but, using a partition of unity technique, the results presented in this paper remain valid for any domain that can be divided into finitely many domains that are star-shaped with respect to a open neighborhood.

B.2.3 Formulation of the problem

We want to approximate the solution to the following boundary value problem: Given a vector field $\mathbf{g}$, find $\mathbf{E}$ and p such that

$$\nabla\times(\mu^{-1}\nabla\times\mathbf{E}) + \varepsilon\nabla p = \varepsilon\mathbf{g}; \quad \nabla\cdot(\varepsilon\mathbf{E}) = 0, \quad \mathbf{E}\times\mathbf{n}_{|\Gamma} = 0, \quad p_{|\Gamma} = 0, \tag{B.2.10}$$

where the fields μ and ε are piecewise smooth. More precisely we assume that Ω is partitioned into N Lipschitz subdomains $\Omega_1, \cdots, \Omega_N$ and we define

$$\Sigma := \bigcup_{i\neq j} \partial\Omega_i \cap \partial\Omega_j. \tag{B.2.11}$$

$$W^{1,\infty}_{\Sigma}(\Omega) := \left\{\nu \in L^\infty(\Omega) \mid \nabla(\nu_{|\Omega_i}) \in \mathbf{L}^\infty(\Omega_i),\ i = 1,\cdots,N\right\}. \tag{B.2.12}$$

We refer to Σ as the interface between the subdomains Ω_i. In the rest of the paper we assume that the fields ε and μ satisfy the following properties: There exist $\varepsilon_{\min}$, $\mu_{\min} > 0$ such that

$$\varepsilon, \mu \in W^{1,\infty}_{\Sigma}(\Omega), \qquad \text{and} \qquad \varepsilon \geq \varepsilon_{\min}, \quad \mu \geq \mu_{\min} \quad \text{a.e. in } \Omega. \tag{B.2.13}$$

The following stability results proved in [18] play important roles in the stability of the finite element method developed in this paper:

Theorem B.2.1. *Assuming that $\varepsilon\mathbf{g} \in \mathbf{L}^2(\Omega)$, Problem* (B.2.10) *has a unique solution in $\mathbf{H}_{0,\mathrm{curl}}(\Omega)$. Moreover, assuming* (B.2.13)*, there exist c, depending on Ω and the fields ε and μ, and there exist τ_ε and τ_μ depending on Ω and the fields ε and μ, respectively, so that*

$$\|\mathbf{E}\|_{\mathbf{H}^s(\Omega)} \leq c\|\varepsilon\mathbf{g}\|_{\mathbf{L}^2(\Omega)}, \qquad \forall s \in [0,\tau_\varepsilon), \tag{B.2.14}$$

$$\|\nabla\times\mathbf{E}\|_{\mathbf{H}^s(\Omega)} \leq c\|\varepsilon\mathbf{g}\|_{\mathbf{L}^2(\Omega)}, \qquad \forall s \in [0,\tau_\mu). \tag{B.2.15}$$

$$\|\nabla\times(\mu^{-1}\nabla\times\mathbf{E})\|_{\mathbf{L}^2(\Omega)} + \|\nabla p\|_{L^2(\Omega)} \leq c\|\varepsilon\mathbf{g}\|_{\mathbf{L}^2(\Omega)}, \tag{B.2.16}$$

B.3 Smooth approximation in $\mathbf{H}_{0,\mathrm{curl}}(\Omega)$

We introduce in this section a smoothing operator in $\mathbf{H}_{0,\mathrm{curl}}(\Omega)$ that will be used to prove the convergence of the finite element approximation. The key difficulty that we are facing is to find an approximation that is compatible with the boundary condition in $\mathbf{H}_{0,\mathrm{curl}}(\Omega)$ and commutes with the curl operator. We essentially proceed as in [17] but modify the argument to correct an incorrect statement made therein. When invoking $\mathcal{C}_h(A\mathbf{e})_\varepsilon$ in the proof of Lemma 3.3 in [17] it was incorrectly assumed that $(A\mathbf{E})\varepsilon$ is in $\mathbf{H}_{0,\mathrm{curl}}(\Omega)$, which is not the case. We resolve this issue in the present construction by introducing an additional scaling operator, S_D^δ.

B.3.1 Extension operator

Let D be an open Lipschitz domain in $\mathbb{R}^d$. For any $\mathbf{F} \in \mathbf{L}^1(D)$, we denote $E_D\mathbf{F}$ the extension of $\mathbf{F}$ by 0, i.e.,

$$E_D\mathbf{F}(\mathbf{x}) = \begin{cases} \mathbf{F}(\mathbf{x}) & \text{if } \mathbf{x} \in D, \\ 0 & \text{elsewhere.} \end{cases} \tag{B.3.1}$$

Let $\delta \in [0, \frac{1}{2}]$, define $\bar{\delta} := 1 - \delta$ and set $D_\delta := \bar{\delta} D$. We define the scaling operator $S_D^\delta : \mathbf{L}^1(D) \longmapsto \mathbf{L}^1(D_\delta)$ by

$$\forall \mathbf{F} \in \mathbf{L}^1(D),\ \forall \mathbf{x} \in D_\delta, \quad (S_D^\delta \mathbf{F})(\mathbf{x}) := \mathbf{F}\left(\mathbf{x}\bar{\delta}^{-1}\right). \tag{B.3.2}$$

Lemma B.3.1. *The following commuting properties hold:*

$$S_{\mathbb{R}^d}^\delta E_D = E_{D_\delta} S_D^\delta \tag{B.3.3}$$

$$\partial_{x_i}(S_D^\delta \mathbf{F}) = \bar{\delta}^{-1} S_D^\delta(\partial_{x_i}\mathbf{F}), \quad \forall \mathbf{F} \in \mathbf{L}^1(D),\ \forall i = 1, \ldots, d, \tag{B.3.4}$$

$$\nabla\times(E_D\mathbf{F}) = E_D(\nabla\times\mathbf{F}), \quad \forall \mathbf{F} \in \mathbf{H}_{0,\mathrm{curl}}(D), \tag{B.3.5}$$

$$\nabla(E_D\mathbf{F}) = E_D(\nabla\mathbf{F}), \quad \forall \mathbf{F} \in \mathbf{H}_0^1(D). \tag{B.3.6}$$

Proof. (B.3.3) is evident and (B.3.4) is just the chain rule. We only prove (B.3.5) since the proof of the (B.3.6) is similar. Let $\mathbf{F}$ be a member of $\mathbf{H}_{0,\mathrm{curl}}(D)$, then the following holds:

$$\langle \nabla\times(E_D\mathbf{F}), \boldsymbol{\phi}\rangle = \int_{\mathbb{R}^d} (E_D\mathbf{F})\cdot\nabla\times\boldsymbol{\phi} = \int_D \mathbf{F}\cdot\nabla\times\boldsymbol{\phi} = \int_D \nabla\times\mathbf{F}\cdot\boldsymbol{\phi}, \quad \forall \boldsymbol{\phi} \in \boldsymbol{\mathcal{D}}(\mathbb{R}^d),$$

where the last equality holds owing to $\mathbf{F}$ being in $\mathbf{H}_{0,\mathrm{curl}}(D)$. Then

$$\langle \nabla\times(E_D\mathbf{F}), \boldsymbol{\phi}\rangle = \int_{\mathbb{R}^d} E_D(\nabla\times\mathbf{F})\cdot\boldsymbol{\phi}, \quad \forall \boldsymbol{\phi} \in \boldsymbol{\mathcal{D}}(\mathbb{R}^d),$$

which proves the statement. □

Lemma B.3.2. *For all $r \in [0,1]$, (i) the linear operator $E_D : \mathbf{H}_0^r(D) \to \mathbf{H}_0^r(\mathbb{R}^d)$ is bounded; (ii) the family of operators $\{S_D^\delta\} : \mathbf{H}^r(D) \to \mathbf{H}^r(D_\delta)$ is uniformly bounded with respect to $\delta \in [0, \frac{1}{2}]$.*

Proof. It is a standard result that E_D is a continuous operator from $\mathbf{L}^2(D)$ to $\mathbf{L}^2(\mathbb{R}^d)$ and from $\mathbf{H}_0^1(D)$ to $\mathbf{H}_0^1(\mathbb{R}^d)$, [2]. Then the first assertion follows directly from the interpolation theory. For the second part, a scaling argument ensures that S_D^δ is a continuous operator from $\mathbf{L}^2(D)$ to $\mathbf{L}^2(D_\delta)$. Using (B.3.4), we infer that it is also a continuous operator from $\mathbf{H}^1(D)$ to $\mathbf{H}^1(D_\delta)$. The conclusion follows from the interpolation theory. □

Taking $r \in \left[0, \frac{1}{2}\right)$ and using the fact that the spaces $\mathbf{H}_0^r(\Omega)$ and $\mathbf{H}^r(\Omega)$ coincide (with equivalent norms), we infer that there exists c such that,

$$\forall \mathbf{F} \in \mathbf{H}^r(\Omega), \qquad \|E_\Omega \mathbf{F}\|_{\mathbf{H}^r(\mathbb{R}^d)} \leq c \, \|\mathbf{F}\|_{\mathbf{H}^r(\Omega)}. \tag{B.3.7}$$

Moreover, using this inequality and the second part of Lemma B.3.2 with $D = \mathbb{R}^d$, we infer that $S^\delta_{\mathbb{R}^d} E_\Omega : \mathbf{H}^r(\Omega) \to \mathbf{H}^r(\mathbb{R}^d)$ is a linear continuous operator, and there exists c, uniform in δ, such that

$$\forall \mathbf{F} \in \mathbf{H}^r(\Omega), \qquad \|S^\delta_{\mathbb{R}^d} E_\Omega \mathbf{F}\|_{\mathbf{H}^r(\mathbb{R}^d)} \leq c \, \|\mathbf{F}\|_{\mathbf{H}^r(\Omega)}. \tag{B.3.8}$$

Lemma B.3.3. *The following holds:*

$$\forall \mathbf{F} \in \mathbf{H}_{0,\mathrm{curl}}(\Omega), \qquad \nabla\times(S^\delta_{\mathbb{R}^d} E_\Omega \mathbf{F}) = \bar{\delta}^{-1} S^\delta_{\mathbb{R}^d} E_\Omega (\nabla\times\mathbf{F}). \tag{B.3.9}$$

Proof. Let $\mathbf{F} \in \mathbf{H}_{0,\mathrm{curl}}(\Omega)$. By (B.3.4) we infer that

$$\nabla\times(S^\delta_{\mathbb{R}^d} E_\Omega \mathbf{F}) = \bar{\delta}^{-1} S^\delta_{\mathbb{R}^d} \nabla\times(E_\Omega \mathbf{F}).$$

Then (B.3.5) from Lemma B.3.1 implies

$$\nabla\times(S^\delta_{\mathbb{R}^d} E_\Omega \mathbf{F}) = \bar{\delta}^{-1} S^\delta_{\mathbb{R}^d} E_\Omega (\nabla\times\mathbf{F}),$$

since $\mathbf{F} \in \mathbf{H}_{0,\mathrm{curl}}(\Omega)$. This concludes the proof. □

Lemma B.3.4. *The linear operator $S^\delta_{\mathbb{R}^d} E_\Omega : \mathbf{H}^r_{0,\mathrm{curl}}(\Omega) \longrightarrow \mathbf{H}^r_{0,\mathrm{curl}}\left(\mathbb{R}^d\right)$ is bounded for all $r \in [0, \frac{1}{2})$. More precisely there is c, uniform with respect to δ, so that the following holds:*

$$\|\nabla\times(S^\delta_{\mathbb{R}^d} E_\Omega \mathbf{F})\|_{\mathbf{H}^r(\mathbb{R}^d)} \leq c \|\nabla\times\mathbf{F}\|_{\mathbf{H}^r(\Omega)}. \tag{B.3.10}$$

Proof. The identity (B.3.9) implies that $S^\delta_{\mathbb{R}^d} E_\Omega$ is a continuous map from $\mathbf{H}_{0,\mathrm{curl}}(\Omega)$ to $\mathbf{H}_{0,\mathrm{curl}}\left(\mathbb{R}^d\right)$. Let r$\in [0, \frac{1}{2})$ and let $\mathbf{F}$ be a member of $\mathbf{H}^r_{0,\mathrm{curl}}(\Omega)$. A simple scaling argument implies that $S^\delta_\Omega \mathbf{F}$ is a member of $\mathbf{H}^r_{0,\mathrm{curl}}(\Omega_\delta)$. Since $\nabla\times S^\delta_\Omega \mathbf{F}$ is in $\mathbf{H}^r(\Omega)$ and $r \in [0, \frac{1}{2})$, the extension by zero is stable in $\mathbf{H}^r(\mathbb{R}^d)$, i.e., $E_{\Omega_\delta} \nabla\times S^\delta_\Omega \mathbf{F}$ is a member of $\mathbf{H}^r(\mathbb{R}^d)$ and there is a constant c, uniform with respect to $\mathbf{F}$ and δ, so that

$$\begin{aligned} \|E_{\Omega_\delta} \nabla\times S^\delta_\Omega \mathbf{F}\|_{\mathbf{H}^r(\mathbb{R}^d)} &\leq c' \|\nabla\times S^\delta_\Omega \mathbf{F}\|_{\mathbf{H}^r(\Omega_\delta)} = c' \bar{\delta}^{-1} \|S^\delta_\Omega \nabla\times\mathbf{F}\|_{\mathbf{H}^r(\Omega_\delta)} \\ &\leq c \|\nabla\times\mathbf{F}\|_{\mathbf{H}^r(\Omega)}. \end{aligned}$$

Note that c is uniform with respect to δ since $\bar{\delta} \in [\frac{1}{2}, 1]$. Then, applying (B.3.3) and (B.3.5) to the above inequality gives

$$\begin{aligned} \|\nabla\times(S^\delta_{\mathbb{R}^d} E_\Omega \mathbf{F})\|_{\mathbf{H}^r(\mathbb{R}^d)} &= \|\nabla\times(E_{\Omega_\delta} S^\delta_\Omega \mathbf{F})\|_{\mathbf{H}^r(\mathbb{R}^d)} = \|E_{\Omega_\delta} \nabla\times S^\delta_\Omega \mathbf{F}\|_{\mathbf{H}^r(\mathbb{R}^d)} \\ &\leq c \|\nabla\times\mathbf{F}\|_{\mathbf{H}^r(\Omega)}, \end{aligned}$$

which concludes the proof. □

We now state a lemma that gives some important approximation properties of the operator $\mathbf{F} \mapsto S^\delta_{\mathbb{R}^d} E_\Omega \mathbf{F}$.

Lemma B.3.5. *There exists K_1 for all $r \in [0,1]$ such that the following holds for every $\mathbf{F} \in \mathbf{H}^r_0(\Omega)$:*

$$\left\|\mathbf{F} - S^\delta_{\mathbb{R}^d} E_\Omega \mathbf{F}\right\|_{\mathbf{H}^s_0(\Omega)} \leq K_1 \delta^{r-s} \left\|\mathbf{F}\right\|_{\mathbf{H}^r_0(\Omega)} \qquad 0 \leq s \leq r \leq 1, \tag{B.3.11}$$

and for all $r \in [0, \frac{1}{2})$ there exists $K_2(r)$, such that the following holds every $\mathbf{F} \in \mathbf{H}^r_{0,\mathrm{curl}}(\Omega)$

$$\left\|\nabla\times(\mathbf{F} - S^\delta_{\mathbb{R}^d} E_\Omega \mathbf{F})\right\|_{\mathbf{H}^s(\Omega)} \leq K_2(r) \delta^{r-s} \left\|\nabla\times\mathbf{F}\right\|_{\mathbf{H}^r(\Omega)} \qquad 0 \leq s \leq r < \frac{1}{2}. \tag{B.3.12}$$

Proof. We prove the first inequality (B.3.11) by means of an interpolation technique. Using Lemma B.3.1 together with $d \geq 2$, we have

$$\begin{aligned}
\left\|\mathbf{F} - S^\delta_{\mathbb{R}^d} E_\Omega \mathbf{F}\right\|_{\mathbf{L}^2(\Omega)} &\leq \left\|\mathbf{F}\right\|_{\mathbf{L}^2(\Omega)} + \left\|S^\delta_{\mathbb{R}^d} E_\Omega \mathbf{F}\right\|_{\mathbf{L}^2(\Omega)} \leq \left(1 + \bar{\delta}^{\frac{d}{2}}\right) \left\|\mathbf{F}\right\|_{\mathbf{L}^2(\Omega)} \leq 2 \left\|\mathbf{F}\right\|_{\mathbf{L}^2(\Omega)}. \\
\left\|\mathbf{F} - S^\delta_{\mathbb{R}^d} E_\Omega \mathbf{F}\right\|_{\mathbf{H}^1_0(\Omega)} &= \left\|\nabla(\mathbf{F} - S^\delta_{\mathbb{R}^d} E_\Omega \mathbf{F})\right\|_{\mathbf{L}^2(\Omega)} \leq \left\|\nabla\mathbf{F}\right\|_{\mathbf{L}^2(\Omega)} + \left\|\nabla S^\delta_{\mathbb{R}^d} E_\Omega \mathbf{F}\right\|_{\mathbf{L}^2(\Omega)} \\
&= \left\|\nabla\mathbf{F}\right\|_{\mathbf{L}^2(\Omega)} + \bar{\delta}^{-1} \left\|S^\delta_{\mathbb{R}^d} \nabla(E_\Omega \mathbf{F})\right\|_{\mathbf{L}^2(\Omega)} = \left\|\nabla\mathbf{F}\right\|_{\mathbf{L}^2(\Omega)} + \bar{\delta}^{\frac{d}{2}-1} \left\|E_\Omega \nabla\mathbf{F}\right\|_{\mathbf{L}^2(\Omega)} \\
&= \left(1 + \bar{\delta}^{\frac{d}{2}-1}\right) \left\|\nabla\mathbf{F}\right\|_{\mathbf{L}^2(\Omega)} \leq 2 \left\|\mathbf{F}\right\|_{\mathbf{H}^1_0(\Omega)}.
\end{aligned}$$

We now derive an estimate for the mapping $\mathbf{H}^1_0(\Omega) \ni \mathbf{F} \mapsto \mathbf{F} - S^\delta_{\mathbb{R}^d} E_\Omega \mathbf{F} \in \mathbf{L}^2(\Omega)$. The definition of $S^\delta_{\mathbb{R}^d} E_\Omega \mathbf{F}$ implies that

$$\begin{aligned}
\left\|\mathbf{F} - S^\delta_{\mathbb{R}^d} E_\Omega \mathbf{F}\right\|^2_{\mathbf{L}^2(\Omega)} &= \int_\Omega \left|(E_\Omega \mathbf{F})(\mathbf{x}) - (E_\Omega \mathbf{F})\left(\mathbf{x}\bar{\delta}^{-1}\right)\right|^2 \, \mathrm{d}\mathbf{x} \\
&= \int_\Omega \left|\int_0^1 \nabla(E_\Omega \mathbf{F})\left((1-t)\mathbf{x} + t\mathbf{x}\bar{\delta}^{-1}\right) \cdot \frac{\delta}{\bar{\delta}}\mathbf{x} \, \mathrm{d}t\right|^2 \, \mathrm{d}\mathbf{x} \\
&\leq \int_\Omega \frac{\delta^2}{\bar{\delta}^2} |\mathbf{x}|^2 \int_0^1 \left|\nabla(E_\Omega \mathbf{F})\left((1-t)\mathbf{x} + t\mathbf{x}\bar{\delta}^{-1}\right)\right|^2 \, \mathrm{d}t \, \mathrm{d}\mathbf{x}
\end{aligned}$$

Then, we introduce $M := \max_{\mathbf{x}\in\Omega} |\mathbf{x}|$, and we apply Fubini's lemma:

$$\left\|\mathbf{F} - S^\delta_{\mathbb{R}^d} E_\Omega \mathbf{F}\right\|^2_{\mathbf{L}^2(\Omega)} \leq M^2 \frac{\delta^2}{\bar{\delta}^2} \int_0^1 \int_\Omega \left|\nabla(E_\Omega \mathbf{F})\left((1-t)\mathbf{x} + t\mathbf{x}\bar{\delta}^{-1}\right)\right|^2 \, \mathrm{d}\mathbf{x}\mathrm{d}t$$

Using a change of variable in the inner integral, we finally obtain

$$\begin{aligned}
\left\|\mathbf{F} - S^\delta_{\mathbb{R}^d} E_\Omega \mathbf{F}\right\|^2_{\mathbf{L}^2(\Omega)} &\leq M^2 \frac{\delta^2}{\bar{\delta}^2} \left\|\nabla E_\Omega \mathbf{F}\right\|^2_{\mathbf{L}^2(\Omega_\delta)} \int_0^1 \left(\frac{\bar{\delta}}{\bar{\delta} + \delta t}\right)^d \, \mathrm{d}t \\
&\leq M^2 \delta^2 \bar{\delta}^{-2} \left\|\nabla(E_\Omega \mathbf{F})\right\|^2_{\mathbf{L}^2(\mathbb{R}^d)}.
\end{aligned}$$

Since $\mathbf{F} \in \mathbf{H}^1_0(\Omega)$, we have $\left\|\nabla E_\Omega \mathbf{F}\right\|_{\mathbf{L}^2(\mathbb{R}^d)} = \left\|E_\Omega \nabla\mathbf{F}\right\|_{\mathbf{L}^2(\mathbb{R}^d)} = \left\|\nabla\mathbf{F}\right\|_{\mathbf{L}^2(\Omega)}$. Using now the assumption $\delta \leq \frac{1}{2}$, i.e., $\bar{\delta}^{-1} \leq 2$, we finally deduce that

$$\left\|\mathbf{F} - S^\delta_{\mathbb{R}^d} E_\Omega \mathbf{F}\right\|_{\mathbf{L}^2(\Omega)} \leq 2M\delta \left\|\nabla\mathbf{F}\right\|_{\mathbf{L}^2(\Omega)} = 2M\delta \left\|\mathbf{F}\right\|_{\mathbf{H}^1_0(\Omega)}. \tag{B.3.13}$$

We now set $K_1 := \max(2, 2M)$ and we have proven that

$$\begin{aligned}
\left\|\mathbf{F} - S^\delta_{\mathbb{R}^d} E_\Omega \mathbf{F}\right\|_{\mathbf{L}^2(\Omega)} &\leq K_1 \|\mathbf{F}\|_{\mathbf{L}^2(\Omega)}\,, \\
\left\|\mathbf{F} - S^\delta_{\mathbb{R}^d} E_\Omega \mathbf{F}\right\|_{\mathbf{L}^2(\Omega)} &\leq K_1 \delta \|\mathbf{F}\|_{\mathbf{H}^1_0(\Omega)}\,, \\
\left\|\mathbf{F} - S^\delta_{\mathbb{R}^d} E_\Omega \mathbf{F}\right\|_{\mathbf{H}^1_0(\Omega)} &\leq K_1 \|\mathbf{F}\|_{\mathbf{H}^1_0(\Omega)}\,.
\end{aligned}$$

We conclude that (B.3.11) holds by using the Lions-Peetre Reiteration Theorem.

We now turn our attention to (B.3.12). Let $r \in [0, \frac{1}{2})$ and consider $s \in [0, r]$. Let $\mathbf{F}$ be a member of $\mathbf{H}^r_{0,\mathrm{curl}}(\Omega)$. We observe first that $S^\delta_{\mathbb{R}^d} E_\Omega \mathbf{F}$ is also in $\mathbf{H}^r_{0,\mathrm{curl}}(\Omega)$ owing to Lemma B.3.4. Using (B.3.9) gives

$$\begin{aligned}
\left\|\nabla\times(\mathbf{F} - S^\delta_{\mathbb{R}^d} E_\Omega \mathbf{F})\right\|_{\mathbf{H}^s_0(\Omega)} &= \left\|\nabla\times\mathbf{F} - \bar\delta^{-1} S^\delta_{\mathbb{R}^d} E_\Omega \nabla\times\mathbf{F}\right\|_{\mathbf{H}^s_0(\Omega)} \\
&\leq \left\|\nabla\times\mathbf{F} - \bar\delta^{-1}\nabla\times\mathbf{F}\right\|_{\mathbf{H}^s_0(\Omega)} + \bar\delta^{-1}\left\|\nabla\times\mathbf{F} - S^\delta_{\mathbb{R}^d} E_\Omega(\nabla\times\mathbf{F})\right\|_{\mathbf{H}^s_0(\Omega)} \\
&\leq \delta\bar\delta^{-1}\|\nabla\times\mathbf{F}\|_{\mathbf{H}^s_0(\Omega)} + K_1\bar\delta^{-1}\delta^{r-s}\|\nabla\times\mathbf{F}\|_{\mathbf{H}^r_0(\Omega)}\,.
\end{aligned}$$

Using $\delta < \frac{1}{2}$, i.e., $\bar\delta^{-1} \leq 2$, we have

$$\left\|\nabla\times(\mathbf{F} - S^\delta_{\mathbb{R}^d} E_\Omega \mathbf{F})\right\|_{\mathbf{H}^s_0(\Omega)} \leq 2(K_1 + \delta^{1-r+s})\delta^{r-s}\|\nabla\times\mathbf{F}\|_{\mathbf{H}^r_0(\Omega)}\,,$$

Remembering that $\mathbf{H}^s(\Omega)$ and $\mathbf{H}^s_0(\Omega)$ coincide for $0 \leq r < \frac{1}{2}$ and that their norm are equivalent, the above inequality yields (B.3.12) since $1 - r + s \geq 1 - r > 0$. □

B.3.2 Smooth approximation

We now use the above extension operator $S^\delta_{\mathbb{R}^d} E_\Omega$ together with a mollification to construct a smooth approximation operator. For $0 < \delta < \frac{1}{2}$, we set

$$\rho_\delta(\mathbf{x}) := \delta^{-d}\rho(\mathbf{x}/\delta), \text{ where } \rho(\mathbf{x}) := \begin{cases} \eta \exp\left(-\frac{1}{1-|\mathbf{x}|^2}\right), & \text{if } |\mathbf{x}| < 1, \\ 0, & \text{if } |\mathbf{x}| \geq 1, \end{cases} \tag{B.3.14}$$

where η is chosen so that $\int_{\mathbb{R}^d}\rho = 1$. We define a family of approximation operators $\{\mathcal{K}_\delta\}_{\delta>0}$ in the following way:

$$\mathcal{K}_\delta\mathbf{F} = \rho_{\delta\chi} \star (S^\delta_{\mathbb{R}^d} E_\Omega \mathbf{F}), \qquad \forall \mathbf{F} \in \mathbf{L}^1(\Omega) \tag{B.3.15}$$

where χ is the constant introduced in (B.2.9).

Theorem B.3.1. *$\mathcal{K}_\delta\mathbf{F}|_\Omega$ is in $\mathcal{C}^\infty_0(\Omega)$ for all $\mathbf{F} \in \mathbf{L}^1(\Omega)$. There exists a constant K such that the following estimates hold for any $0 < \delta < \frac{1}{2}$:*

$$\|\mathbf{F} - \mathcal{K}_\delta\mathbf{F}\|_{\mathbf{H}^s_0(\Omega)} \leq K\delta^{r-s}\|\mathbf{F}\|_{\mathbf{H}^r_0(\Omega)} \qquad 0 \leq s \leq r \leq 1 \tag{B.3.16}$$

$$\|\nabla\times\mathbf{F} - \nabla\times\mathcal{K}_\delta\mathbf{F}\|_{\mathbf{H}^s(\Omega)} \leq K\delta^{r-s}\|\nabla\times\mathbf{F}\|_{\mathbf{H}^r(\Omega)} \qquad 0 \leq s \leq r < \tfrac{1}{2} \tag{B.3.17}$$

$$\|\mathcal{K}_\delta\mathbf{F}\|_{\mathbf{H}^r(\Omega)} \leq K\chi^{s-r}\delta^{s-r}\|\mathbf{F}\|_{\mathbf{H}^s(\Omega)} \qquad 0 \leq s \leq r,\ s < \tfrac{1}{2} \tag{B.3.18}$$

and all $\mathbf{F} \in \mathbf{H}^r_0(\Omega)$, all $\mathbf{F} \in \mathbf{H}_{0,\mathrm{curl}}(\Omega)$, and all $\mathbf{F} \in \mathbf{H}^r(\Omega)$, respectively.

Proof. Owing to the properties of the mollification operator, we have $\mathcal{K}_\delta\mathbf{F}|_\Omega \in \mathcal{C}^\infty(\Omega)$. We now prove that the support of $\mathcal{K}_\delta\mathbf{F}$ is compact in Ω. The definition of the convolution operation implies that the following holds for all $\mathbf{x} \in \mathbb{R}^d$:

$$\mathcal{K}_\delta\mathbf{F}(\mathbf{x}) = \int_{\mathbb{R}^d} (S^\delta_{\mathbb{R}^d} E_\Omega \mathbf{F})(\mathbf{y}) \rho_{\delta\chi}(\mathbf{x}-\mathbf{y})\, \mathrm{d}\mathbf{y} = \int_{\bar\delta\Omega} \mathbf{F}(\mathbf{y}/\bar\delta)\rho_{\delta\chi}(\mathbf{x}-\mathbf{y})\, \mathrm{d}\mathbf{y}.$$

If $\mathbf{x} \notin \bar\delta\Omega + B(0,\delta\chi)$, then for all $\mathbf{y} \in \bar\delta\Omega$, we have $\rho_{\delta\chi}(\mathbf{x}-\mathbf{y}) = 0$ and then $\mathcal{K}_\delta\mathbf{F}(\mathbf{x}) = 0$. As a result, $\mathcal{K}_\delta\mathbf{F}$ is supported in $\bar\delta\Omega + B(0,\delta\chi)$ which is compactly embedded in Ω owing to the assumption (B.2.9). Hence, $\mathcal{K}_\delta\mathbf{F} \in \mathcal{C}^\infty_0(\Omega)$; in particular, we have $\mathcal{K}_\delta\mathbf{F} \in \mathbf{H}_{0,\mathrm{curl}}(\Omega)$. We now prove the estimates (B.3.16) to (B.3.18). Let us first consider $\mathbf{F} \in \mathbf{H}^r_0(\Omega)$. Using standard approximation properties of the mollification operator, we deduce that there exists a uniform constant $K_3 > 0$ so that

$$\left\| S^\delta_{\mathbb{R}^d} E_\Omega \mathbf{F} - \mathcal{K}_\delta\mathbf{F} \right\|_{\mathbf{H}^s_0(\Omega)} \le K_3(\delta\chi)^{r-s} \left\| S^\delta_{\mathbb{R}^d} E_\Omega \mathbf{F} \right\|_{\mathbf{H}^r_0(\mathbb{R}^d)}, \qquad 0 \le s \le r \le 1.$$

Using the triangle inequality and Lemma B.3.5 we have

$$\begin{aligned}
\|\mathbf{F} - \mathcal{K}_\delta\mathbf{F}\|_{\mathbf{H}^s_0(\Omega)} &\le \|\mathbf{F} - S^\delta_{\mathbb{R}^d} E_\Omega\mathbf{F}\|_{\mathbf{H}^s_0(\Omega)} + \left\| S^\delta_{\mathbb{R}^d} E_\Omega \mathbf{F} - \mathcal{K}_\delta\mathbf{F} \right\|_{\mathbf{H}^s_0(\Omega)} \\
&\le K_1\delta^{r-s} \|\mathbf{F}\|_{\mathbf{H}^r_0(\Omega)} + K_3\chi^{r-s}\delta^{r-s} \left\| S^\delta_{\mathbb{R}^d} E_\Omega \mathbf{F} \right\|_{\mathbf{H}^r_0(\mathbb{R}^d)} \\
&\le (K_1 + 2K_3\chi^{r-s})\delta^{r-s} \|\mathbf{F}\|_{\mathbf{H}^r_0(\Omega)}.
\end{aligned}$$

This proves (B.3.16) with $K = K_1 + 2K_3$ since $\chi \le 1$ and $s \le r$. Let us now consider $\mathbf{F} \in \mathbf{H}^r_{0,\mathrm{curl}}(\Omega)$. Using that $\nabla\times\mathcal{K}_\delta\mathbf{F} = \rho_{\delta\chi} \star \nabla\times(S^\delta_{\mathbb{R}^d} E_\Omega\mathbf{F})$, we infer that

$$\left\| \nabla\times(S^\delta_{\mathbb{R}^d} E_\Omega\mathbf{F} - \mathcal{K}_\delta\mathbf{F}) \right\|_{\mathbf{H}^s(\Omega)} \le K_3(\delta\chi)^{r-s} \left\| \nabla\times(S^\delta_{\mathbb{R}^d} E_\Omega\mathbf{F}) \right\|_{\mathbf{H}^r(\mathbb{R}^d)} \qquad 0 \le s \le r$$

Using the triangle inequality together with (B.3.10), Lemma B.3.5, and assuming that $r < \frac{1}{2}$ we have

$$\begin{aligned}
\|\nabla\times(\mathbf{F} - \mathcal{K}_\delta\mathbf{F})\|_{\mathbf{H}^s(\Omega)} &\le \left\| \nabla\times(\mathbf{F} - S^\delta_{\mathbb{R}^d} E_\Omega\mathbf{F}) \right\|_{\mathbf{H}^s(\Omega)} + \left\| \nabla\times(S^\delta_{\mathbb{R}^d} E_\Omega\mathbf{F} - \mathcal{K}_\delta\mathbf{F}) \right\|_{\mathbf{H}^s(\Omega)} \\
&\le K_2(r)\delta^{r-s} \|\nabla\times\mathbf{F}\|_{\mathbf{H}^r(\Omega)} + K_3(\delta\chi)^{r-s} \left\| \nabla\times(S^\delta_{\mathbb{R}^d} E_\Omega\mathbf{F}) \right\|_{\mathbf{H}^r(\mathbb{R}^d)} \\
&\le (K_2(r) + K_2\chi^{r-s}) \|\nabla\times\mathbf{F}\|_{\mathbf{H}^r(\Omega)},
\end{aligned}$$

which proves (B.3.17) with $K = K_1 + 2K_2(r)$ since $\chi \le 1$ and $s \le r$. Let us finally assume that $\mathbf{F} \in \mathbf{H}^r(\Omega)$. Using again the properties of the mollification operator, we infer

$$\|\mathcal{K}_\delta\mathbf{F}\|_{\mathbf{H}^r(\Omega)} \le \|\mathcal{K}_\delta\mathbf{F}\|_{\mathbf{H}^r(\mathbb{R}^d)} \le K_3(\delta\chi)^{s-r} \left\| S^\delta_{\mathbb{R}^d} E_\Omega\mathbf{F} \right\|_{\mathbf{H}^s(\mathbb{R}^d)} \qquad 0 \le s \le r.$$

Applying (B.3.8), we obtain (B.3.18). Note that the assumption $s < \frac{1}{2}$ is required in order to ensure that $S^\delta_{\mathbb{R}^d} E_\Omega\mathbf{F} \in \mathbf{H}^r(\mathbb{R}^d)$. □

Remark B.3.1. In the following, we will use (B.3.18) without χ in the right hand sides. Indeed, we will use the inequality with r bounded from above by the polynomial degree of the approximation; as a result, χ^{s-r} is uniformly bounded.

We end this section with a commuting property on $\mathcal{K}_\delta$.

Lemma B.3.6. *The following holds for any* $\mathbf{F} \in \mathbf{H}_{\mathrm{curl}}(\Omega)$*:*

$$\bar{\delta}\nabla\times\mathcal{K}_\delta\mathbf{F} = \mathcal{K}_\delta(\nabla\times\mathbf{F}). \tag{B.3.19}$$

Proof. Owing to the properties of the convolution, the following holds for any $\mathbf{F} \in \mathbf{H}_{\mathrm{curl}}(\Omega)$:

$$\nabla\times\mathcal{K}_\delta\mathbf{F} = \rho_{\delta\chi} \star \left(\nabla\times\left(S^\delta_{\mathbb{R}^d} E_\Omega \mathbf{F}\right)\right).$$

Applying (B.3.9), we infer

$$\begin{aligned}\nabla\times\mathcal{K}_\delta\mathbf{F} &= \rho_{\delta\chi} \star \left(\bar{\delta}^{-1} S^\delta_{\mathbb{R}^d} E_\Omega(\nabla\times\mathbf{F})\right)\\ &= \bar{\delta}^{-1}\rho_{\delta\chi} \star \left(S^\delta_{\mathbb{R}^d} E_\Omega(\nabla\times\mathbf{F})\right) = \bar{\delta}^{-1}\mathcal{K}_\delta(\nabla\times\mathbf{F}).\end{aligned}$$

This completes the proof. □

B.4 Finite Element Approximation of the boundary value problem

We introduce and study the stability properties of a Lagrange finite element technique for solving the boundary value problem (B.2.10).

B.4.1 Finite Element Spaces

Let $\{\mathcal{T}_h\}_{h>0}$ be a shape regular family of conforming affine meshes with typical mesh size h. We assume that the sub-domains Ω_i, $i = 1, \ldots, N$ are polyhedra and the interface Σ is captured by the meshes in $\{\mathcal{T}_h\}_{h>0}$, i.e., Σ is partitioned by a set of mesh interfaces. We introduce the following discrete space:

$$\mathbf{X}_h := \left\{\mathbf{F} \in \prod_{i=1}^{N} \mathcal{C}^0(\bar{\Omega}_i),\ |\ \forall K \in \mathcal{T}_h,\ \mathbf{F}_{|K} \in \mathbb{P}^{\ell-1}\right\} \tag{B.4.1}$$

where $\mathbb{P}^{\ell-1}$ denotes the vector space of vector-valued polynomial of total degree at most $\ell-1$, $\ell \geq 2$. Note that the approximation space is non-conforming, i.e., $\mathbf{X}_h \not\subset \mathbf{H}_{0,\mathrm{curl}}(\Omega)$ and $\mathbf{X}_h \not\subset \mathbf{H}_{\mathrm{div}}(\Omega, \epsilon)$. From the standard approximation theory of finite elements, we know that there exists a family of operators $\mathcal{C}_h : \mathbf{H}_{0,\mathrm{curl}}(\Omega) \to \mathbf{X}_h$ satisfying the following properties (cf. e.g. [131]): there exist c uniform in h such that, for every $\mathbf{F} \in \mathbf{H}_{0,\mathrm{curl}}(\Omega) \cap \mathbf{H}^l(\Omega)$

$$\|\mathcal{C}_h\mathbf{F}\|_{\mathbf{H}^l(\Omega)} \leq c\,\|\mathbf{F}\|_{\mathbf{H}^l(\Omega)} \qquad 0 \leq l \leq \tfrac{3}{2} \tag{B.4.2}$$

$$\|\mathcal{C}_h\mathbf{F} - \mathbf{F}\|_{\mathbf{H}^t(\Omega)} \leq c h^{l-t}\,\|\mathbf{F}\|_{\mathbf{H}^l(\Omega)} \qquad 0 \leq t \leq l \leq \ell,\ t < \tfrac{3}{2} \tag{B.4.3}$$

We additionally introduce the scalar-valued discrete space

$$\mathbf{M}_h := \left\{q \in \mathcal{C}^0(\bar{\Omega}),\ |\ \forall K \in \mathcal{T}_h,\ q \in \mathbb{P}^{\ell-1},\ q_{|\Gamma} = 0\right\} \subset H^1_0(\Omega). \tag{B.4.4}$$

Again, the approximation theory of finite elements ensures that there exists an approximation operator $\mathcal{P}_h : H_0^1(\Omega) \longrightarrow M_h$ satisfying the scalar counterparts of (B.4.2) and (B.4.3) for all $q \in H_0^1(\Omega) \cap H^l(\Omega)$.

$$\|\mathcal{P}_h q\|_{H^l(\Omega)} \leq c \|q\|_{H^l(\Omega)} \qquad 0 \leq l \leq \tfrac{3}{2} \tag{B.4.5}$$

$$\|\mathcal{P}_h q - q\|_{H^t(\Omega)} \leq c h^{l-t} \|q\|_{\mathbf{H}^l(\Omega)} \qquad 0 \leq t \leq l \leq \ell,\ t < \tfrac{3}{2} \tag{B.4.6}$$

Note that the construction of M_h and $\mathcal{P}_h$ is possible since the mesh is conforming.

We denote $\mathcal{F}_h^i$ the set of the mesh interfaces: F is an interface if there are two elements in $\mathcal{T}_h$, say K_m and K_n so that $F = K_m \cap K_n$ and F is a $d-1$ manifold. We denote $\mathcal{F}_h^\partial$ the set of the boundary faces: F is a boundary face if there is an element in $\mathcal{T}_h$, say K_i so that $F = K_m \cap \Gamma$ and F is a $d-1$ manifold. To simplify notation we also introduce $\mathcal{F}_h := \mathcal{F}_h^i \cup \mathcal{F}_h^\partial$. For any mesh interface $F \in \mathcal{F}_h^i$, $F = K_m \cap K_n$ and any function $\mathbf{v}$ whose restrictions over K_m and K_n are continuous, we define the tangent and normal jump of $\mathbf{v}$ across F by

$$[\![\mathbf{v} \times \mathbf{n}]\!](\mathbf{x}) := (\mathbf{v}_{|K_m} \times \mathbf{n}_m)(\mathbf{x}) + (\mathbf{v}_{|K_n} \times \mathbf{n}_n)(\mathbf{x}), \qquad \forall \mathbf{x} \in F, \tag{B.4.7}$$

$$[\![\mathbf{v} \cdot \mathbf{n}]\!](\mathbf{x}) := (\mathbf{v}_{|K_m} \cdot \mathbf{n}_m)(\mathbf{x}) + (\mathbf{v}_{|K_n} \cdot \mathbf{n}_n)(\mathbf{x}), \qquad \forall \mathbf{x} \in F, \tag{B.4.8}$$

where $\mathbf{n}_l$ is the unit outer normal to K_l. The average of $\mathbf{v}$ across across F is defined by

$$\{\!\{\mathbf{v}\}\!\}(\mathbf{x}) := \frac{1}{2}\left(\mathbf{v}_{|K_m}(\mathbf{x}) + \mathbf{v}_{|K_n}(\mathbf{x})\right), \qquad \forall \mathbf{x} \in F. \tag{B.4.9}$$

Whenever F is a boundary face we set $[\![\mathbf{v} \times \mathbf{n}]\!](\mathbf{x}) := \mathbf{v}_{|K_m} \times \mathbf{n}_m(\mathbf{x})$, $[\![\mathbf{v} \cdot \mathbf{n}]\!](\mathbf{x}) := \mathbf{v}_{|K_m} \cdot \mathbf{n}_m(\mathbf{x})$ and $\{\!\{\mathbf{v}\}\!\}(\mathbf{x}) := \mathbf{v}_{|K_m}(\mathbf{x})$.

Remark B.4.1. We may assume the following: for any $\mathbf{F} \in \mathbf{H}_0^1(\Omega)$, $\mathcal{C}_h \mathbf{F} \in \mathbf{H}_0^1(\Omega)$. In particular, we have

$$[\![\mathcal{C}_h \mathbf{F} \times \mathbf{n}]\!] = 0.$$

B.4.2 Discrete formulation

It will be useful to work with broken norms; for instance, we introduce the following notation:

$$\|v\|_{L^2(\Omega_\Sigma)}^2 := \sum_{i=1}^N \|v\|_{L^2(\Omega_i)}^2, \qquad (v,w)_{\Omega_\Sigma} := \sum_{i=1}^N \int_{\Omega_i} vw, \tag{B.4.10}$$

$$\|v\|_{L^2(\Sigma \cup \Gamma)}^2 := \|v\|_{L^2(\Sigma)}^2 + \|v\|_{L^2(\Sigma)}^2, \qquad (v,w)_{\Sigma \cup \Gamma} := \int_\Sigma vw + \int_\Gamma vw. \tag{B.4.11}$$

To simplify the notation we set $\kappa := \mu^{-1}$. We construct a discrete formulation of (B.2.10) by proceeding as in [17]. Let $\alpha \in [0,1]$ be a parameter yet to be chosen. We define the following bilinear form $a_h : \mathbf{X}_h \times \mathbf{M}_h \longrightarrow \mathbb{R}$,

$$\begin{aligned}
a_h((\mathbf{E}_h, p_h), (\mathbf{F}_h, q_h)) := {} & (\kappa \nabla \times \mathbf{E}_h, \nabla \times \mathbf{F}_h)_{\Omega_\Sigma} + \left(\{\!\{\kappa \nabla \times \mathbf{E}_h\}\!\}, [\![\mathbf{F}_h \times \mathbf{n}]\!]\right)_{\Sigma \cup \Gamma} \\
& + \theta \left(\{\!\{\kappa \nabla \times \mathbf{F}_h\}\!\}, [\![\mathbf{E}_h \times \mathbf{n}]\!]\right)_{\Sigma \cup \Gamma} \\
& + \gamma h^{-1} \left(\{\!\{\kappa\}\!\} [\![\mathbf{E}_h \times \mathbf{n}]\!], [\![\mathbf{F}_h \times \mathbf{n}]\!]\right)_{\Sigma \cup \Gamma} \\
& + (\varepsilon \nabla p_h, \mathbf{F}_h)_\Omega - (\varepsilon \mathbf{E}_h, \nabla q_h)_\Omega \\
& + c_\alpha \Big(h^{2\alpha} \left(\nabla \cdot (\varepsilon \mathbf{E}_h), \nabla \cdot (\varepsilon \mathbf{F}_h)\right)_{\Omega_\Sigma} + h^{2(1-\alpha)} \left(\varepsilon \nabla p_h, \nabla q_h\right)_\Omega \\
& + h^{(2\alpha - 1)} \left([\![\varepsilon \mathbf{E}_h \cdot \mathbf{n}]\!], [\![\varepsilon \mathbf{F}_h \cdot \mathbf{n}]\!]\right)_\Sigma \Big),
\end{aligned} \tag{B.4.12}$$

where $\gamma, c_\alpha > 0$, and $\theta \in \{-1, 0, +1\}$ are user-defined parameters. We say that the formulation is anti-symmetric, incomplete, or symmetric depending whether θ is equal to -1, 0, or 1, respectively. The choice $\theta = 1$ ensures the adjoint consistency of the method. The term proportional to γ enforces the weak continuity of the tangent component of $\mathbf{E}$. The purpose of the term proportional to c_α is to penalize $\nabla\cdot(\varepsilon\mathbf{E}_h)$ in $\mathbf{H}^{-\alpha}(\Omega)$.

The discrete formulation that we consider in the rest of the manuscript consists of defining $(\mathbf{E}_h, p_h) \in \mathbf{X}_h \times \mathbf{M}_h$ such that the following holds for all $(\mathbf{F}_h, q_h) \in \mathbf{X}_h \times \mathbf{M}_h$:

$$a_h\left((\mathbf{E}_h, p_h), (\mathbf{F}_h, q_h)\right) = (\varepsilon\mathbf{g}, \mathbf{F}_h)_\Omega + c_\alpha h^{2(1-\alpha)} (\varepsilon\mathbf{g}, \nabla q_h)_\Omega . \tag{B.4.13}$$

To perform the consistency analysis of the method we are led to introduce

$$\mathbf{Z}^s(\Omega) = \{\mathbf{F} \in \mathbf{H}^s_{0,\mathrm{curl}}(\Omega)\,;\, \nabla\times(\kappa\nabla\times\mathbf{F}) \in \mathbf{L}^2(\Omega),\ \nabla\cdot(\varepsilon\mathbf{F}) \in \mathbf{L}^2(\Omega)\}. \tag{B.4.14}$$

Owing to Theorem B.2.1, it is a priori known that there exists $s > 0$ such that the solution to the boundary value problem (B.2.10) is in $\mathbf{Z}^s(\Omega)$. We shall use the notation $\mathbf{Z}^s$ instead of $\mathbf{Z}^s(\Omega)$ when no confusion is possible.

Proposition B.4.1. *Assuming* (B.2.13)*, it is possible to extend the bilinear form a_h to $\left[(\mathbf{Z}^s + \mathbf{X}_h)\times H^1_0(\Omega)\right]^2$ for all $s > 0$.*

Proof. Note first that $M_h \subset H^1_0(\Omega)$ and the extension of the bilinear form to scalar fields in $H^1_0(\Omega)$ does not pose any difficulty. We decompose a_h into three pieces:

$$\begin{aligned}
a_{0h}((\mathbf{E}_h, p_h), (\mathbf{F}_h, q_h)) &:= (\{\!\{\kappa\nabla\times\mathbf{E}_h\}\!\}, [\![\mathbf{F}_h\times\mathbf{n}]\!])_{\Sigma\cup\Gamma} + \theta\,(\{\!\{\kappa\nabla\times\mathbf{F}_h\}\!\}, [\![\mathbf{E}_h\times\mathbf{n}]\!])_{\Sigma\cup\Gamma} \\
a_{1h}((\mathbf{E}_h, p_h), (\mathbf{F}_h, q_h)) &:= (\kappa\nabla\times\mathbf{E}_h, \nabla\times\mathbf{F}_h)_{\Omega_\Sigma} + \gamma h^{-1} (\{\!\{\kappa\}\!\}\, [\![\mathbf{E}_h\times\mathbf{n}]\!], [\![\mathbf{F}_h\times\mathbf{n}]\!])_{\Sigma\cup\Gamma} \\
a_{2h}((\mathbf{E}_h, p_h), (\mathbf{F}_h, q_h)) &:= c_\alpha \Big(h^{2\alpha} (\nabla\cdot(\varepsilon\mathbf{E}_h), \nabla\cdot(\varepsilon\mathbf{F}_h))_{\Omega_\Sigma} + h^{2(1-\alpha)} (\varepsilon\nabla p_h, \nabla q_h)_\Omega \\
&\quad + h^{(2\alpha-1)} ([\![\varepsilon\mathbf{E}_h\cdot\mathbf{n}]\!], [\![\varepsilon\mathbf{F}_h\cdot\mathbf{n}]\!])_\Sigma \Big) + (\varepsilon\nabla p_h, \mathbf{F}_h)_\Omega - (\varepsilon\mathbf{E}_h, \nabla q_h)_\Omega .
\end{aligned}$$

The bilinear form a_{1h} can clearly be extended to $\left[(\mathbf{Z}^s + \mathbf{X}_h)\times H^1_0(\Omega)\right]^2$, since every function $\mathbf{E}$ in $\mathbf{Z}^s$ is such that $[\![\mathbf{E}\times\mathbf{n}]\!]_{\Sigma\cup\Gamma}$ is zero. Hence, if either $(\mathbf{E}, \mathbf{F}) \in \mathbf{Z}^s\times(\mathbf{Z}^s + \mathbf{X}_h)$ or $(\mathbf{E}, \mathbf{F}) \in (\mathbf{Z}^s + \mathbf{X}_h)\times\mathbf{Z}^s$, we set

$$a_{1h}((\mathbf{E}, p), (\mathbf{F}, q)) := (\kappa\nabla\times\mathbf{E}, \nabla\times\mathbf{F})_{\Omega_\Sigma} ,$$

for all $(p, q) \in H^1_0(\Omega)$. The bilinear form a_{2h} can also be extended to $\left[(\mathbf{Z}^s + \mathbf{X}_h)\times H^1_0(\Omega)\right]^2$, since every function $\mathbf{E}$ in $\mathbf{Z}^s$ is such that $[\![\mathbf{E}\cdot\mathbf{n}]\!]_{\Sigma\cup\Gamma}$ is zero. Hence, if either $(\mathbf{E}, \mathbf{F}) \in \mathbf{Z}^s\times(\mathbf{Z}^s + \mathbf{X}_h)$ or $(\mathbf{E}, \mathbf{F}) \in (\mathbf{Z}^s + \mathbf{X}_h)\times\mathbf{Z}^s$, we set

$$\begin{aligned}
a_{2h}((\mathbf{E}, p), (\mathbf{F}, q)) &:= c_\alpha \Big(h^{2\alpha} (\nabla\cdot(\varepsilon\mathbf{E}), \nabla\cdot(\varepsilon\mathbf{F}))_{\Omega_\Sigma} + h^{2(1-\alpha)} (\varepsilon\nabla p, \nabla q)_\Omega \Big) \\
&\quad + (\varepsilon\nabla p, \mathbf{F})_\Omega - (\varepsilon\mathbf{E}, \nabla q)_\Omega .
\end{aligned}$$

for all $(p, q) \in H^1_0(\Omega)$.

The question of the extension of a_{0h} is more subtle, and we must now distinguish the trial and test spaces. We are going to use Lemma B.7.4 that shows that the bilinear form $(\mathbf{H}^s(\Omega) \cap \mathbf{H}_{\mathrm{curl}}(\Omega))\times\mathbf{X}_h \ni (\boldsymbol{\phi}, \mathbf{F}_h) \longmapsto \int_F \boldsymbol{\phi}\cdot(\mathbf{F}_h\times\mathbf{n}) \in \mathbb{R}$ is well defined for all $F \in \mathcal{F}_h$. Let $\mathbf{E}$ be a member of $\mathbf{Z}^s$, then $\nabla\times\mathbf{E} \in \mathbf{H}^s(\Omega)$. If $s \geq \frac{1}{2}$, then $\nabla\times\mathbf{E} \in \mathbf{H}^{s'}(\Omega)$ for all $s' \in (0, \frac{1}{2})$.

We henceforth abuse the notation by assuming that $\nabla\times\mathbf{E} \in \mathbf{H}^s(\Omega)$ with $s \in (0, \frac{1}{2})$. Owing to (B.2.13), κ can be shown to be in $W^{1,\infty}_\Sigma(\Omega)$ and $\kappa\nabla\times\mathbf{E} \in \mathbf{H}^s(\Omega)$, see e.g. [18]. Note in addition that $\mathbf{E}$ being a member of $\mathbf{Z}^s$ implies that $\nabla\times(\kappa\nabla\times\mathbf{E}) \in \mathbf{L}^2(\Omega)$, which in turn also implies that $\{\!\{\kappa\nabla\times\mathbf{E}\}\!\}_{|\Sigma} = \kappa\nabla\times\mathbf{E}_{|\Sigma}$. In conclusion can use Lemma B.7.4 to make sense of $\int_F \kappa\nabla\times\mathbf{E}\cdot(\mathbf{F}_h\times\mathbf{n})$ for all $F \in \mathcal{F}_h$ and for all $(\mathbf{E}, \mathbf{F}_h) \in \mathbf{Z}^s\times\mathbf{X}_h$. The extension of a_{0h} for $(\mathbf{E}_h, \mathbf{F}) \in \mathbf{X}_h\times\mathbf{Z}^s$ is justified similarly. The extension of a_{0h} for $(\mathbf{E}, \mathbf{F}) \in \mathbf{Z}^s\times\mathbf{Z}^s$ is trivial since the tangent jumps of $\mathbf{E}$ and $\mathbf{F}$ across F are zero. In conclusion a_{0h} can be extended to $\left[(\mathbf{Z}^s + \mathbf{X}_h)\times H^1_0(\Omega)\right]^2$ by setting

$$a_{0h}((\mathbf{E}+\mathbf{E}_h, p), (\mathbf{F}+\mathbf{F}_h, q)) := (\kappa\nabla\times\mathbf{E}, [\![\mathbf{F}_h\times\mathbf{n}]\!])_{\Sigma\cup\Gamma} + (\{\!\{\kappa\nabla\times\mathbf{E}_h\}\!\}, [\![\mathbf{F}_h\times\mathbf{n}]\!])_{\Sigma\cup\Gamma} + \theta\,(\kappa\nabla\times\mathbf{F}, [\![\mathbf{E}_h\times\mathbf{n}]\!])_{\Sigma\cup\Gamma} + \theta\,(\{\!\{\kappa\nabla\times\mathbf{F}_h\}\!\}, [\![\mathbf{E}_h\times\mathbf{n}]\!])_{\Sigma\cup\Gamma}$$

for all $(\mathbf{E}, \mathbf{E}_h) \in \mathbf{Z}^s\times\mathbf{X}_h$, all $(\mathbf{F}, \mathbf{F}_h) \in \mathbf{Z}^s\times\mathbf{X}_h$, and all $(p, q) \in H^1_0(\Omega)$. □

Lemma B.4.1. *Assume* (B.2.13) *and let* $(\mathbf{E}, p)$ *be the solution of* (B.2.10). *Let* $s > 0$ *be such that* $\mathbf{E} \in \mathbf{Z}^s$. *The following holds for any* $(\mathbf{F}+\mathbf{F}_h, q) \in (\mathbf{Z}^s + \mathbf{X}_h)\times H^1_0(\Omega)$*:*

$$a_h\left((\mathbf{E}, p), (\mathbf{F}+\mathbf{F}_h, q)\right) = (\varepsilon\mathbf{g}, \mathbf{F}+\mathbf{F}_h)_\Omega + c_\alpha h^{2(1-\alpha)}\,(\varepsilon\mathbf{g}, \nabla q)_\Omega\,.$$

Proof. Let us observe first that

$$a_h\left((\mathbf{E}, p), (\mathbf{F}+\mathbf{F}_h, q)\right) = (\kappa\nabla\times\mathbf{E}, \nabla\times\mathbf{F}+\mathbf{F}_h)_{\Omega_\Sigma} + (\kappa\nabla\times\mathbf{E}, [\![\mathbf{F}_h\times\mathbf{n}]\!])_{\Sigma\cup\Gamma} + (\varepsilon\nabla p, \mathbf{F}+\mathbf{F}_h)_\Omega + c_\alpha h^{2(1-\alpha)}(\varepsilon\nabla p, \nabla q)_\Omega,$$

where all the terms make sense owing to the extension properties of a_h stated in Proposition B.4.1. We now test (B.2.10) with $\mathbf{F}+\mathbf{F}_h \in (\mathbf{Z}^s + \mathbf{X}_h)$,

$$(\nabla\times\kappa\nabla\times\mathbf{E}, \mathbf{F})_\Omega + \sum_{i=1}^N (\nabla\times\kappa\nabla\times\mathbf{E}, \mathbf{F}_h)_{\Omega_i} + (\varepsilon\nabla p, \mathbf{F}+\mathbf{F}_h)_\Omega = (\varepsilon\mathbf{g}, \mathbf{F}+\mathbf{F}_h)_\Omega,$$

and we perform the integration by parts over Ω when the test function is $\mathbf{F}$ and over each sub-domain when the test function is $\mathbf{F}_h$,

$$(\kappa\nabla\times\mathbf{E}, \nabla\times\mathbf{F})_\Omega + \sum_{i=1}^N (\kappa\nabla\times\mathbf{E}, \nabla\times\mathbf{F}_h)_{\Omega_i} + (\kappa\nabla\times\mathbf{E}, [\![\mathbf{F}_h\times\mathbf{n}]\!])_{\Sigma\cup\Gamma} + (\varepsilon\nabla p, \mathbf{F}+\mathbf{F}_h)_\Omega = (\varepsilon\mathbf{g}, \mathbf{F}+\mathbf{F}_h)_\Omega.$$

Note that the term $(\kappa\nabla\times\mathbf{E}, [\![\mathbf{F}_h\times\mathbf{n}]\!])_{\Sigma\cup\Gamma}$ is meaningful owing to $\mathbf{E}$ being a member of $\mathbf{Z}^s$. This implies that

$$a_h\left((\mathbf{E}, p), (\mathbf{F}+\mathbf{F}_h, q)\right) = (\varepsilon\mathbf{g}, \mathbf{F}+\mathbf{F}_h)_\Omega + c_\alpha h^{2(1-\alpha)}(\varepsilon\nabla p, \nabla q)_\Omega.$$

Upon testing again (B.2.10) with ∇q, $q \in H^1_0(\Omega)$, we infer that

$$(\varepsilon\nabla p, \nabla q)_\Omega = (\varepsilon\mathbf{g}, \nabla q)_\Omega,$$

which in turn implies the desired result. □

Lemma B.4.2 (Galerkin Orthogonality). *Assume* (B.2.13), *then the Galerkin orthogonality holds, i.e., let* $(\mathbf{E}, p)$ *be the solution of* (B.2.10) *and* $(\mathbf{E}_h, p_h)$ *be the solution of* (B.4.13), *then*

$$a_h\left((\mathbf{E}-\mathbf{E}_h, p-p_h), (\mathbf{F}_h, q_h)\right) = 0. \tag{B.4.15}$$

Proof. This is a direct consequence of Lemma B.4.1 and the formulation (B.4.13). □

Remark B.4.2 (Continuous Approximation of p). Observe that the approximation of the Lagrange multiplier p is globally continuous. This will lead to a global control of $\nabla\cdot(\varepsilon\mathbf{E})$ in $\mathbf{H}^{-\alpha}(\Omega)$ instead of $\prod_{i=1}^{N}\mathbf{H}^{-\alpha}(\Omega_i)$.

B.4.3 Well posedness of the discrete formulation

We discuss in this section the existence and uniqueness of a solution $(\mathbf{E}_h, p_h)$ to (B.4.13). This issue is addressed by equipping $\mathbf{X}_h\times\mathbf{M}_h$ with the following discrete norm:

$$\begin{aligned}\|\mathbf{F}_h, q_h\|_h^2 := &\left\|\kappa^{\frac{1}{2}}\nabla\times\mathbf{F}_h\right\|^2_{\mathbf{L}^2(\Omega_\Sigma)} + \gamma h^{-1}\left\|\{\!\{\kappa\}\!\}^{\frac{1}{2}}\,[\![\mathbf{F}_h\times\mathbf{n}]\!]\right\|^2_{L^2(\Sigma\cup\Gamma)}\\ &+ c_\alpha\Big(h^{2\alpha}\left\|\nabla\cdot(\varepsilon\mathbf{F}_h)\right\|^2_{L^2(\Omega_\Sigma)} + h^{2(1-\alpha)}\left\|\varepsilon^{\frac{1}{2}}\nabla q_h\right\|^2_{\mathbf{L}^2(\Omega)}\\ &+ h^{(2\alpha-1)}\left\|[\![\varepsilon\mathbf{F}_h\cdot\mathbf{n}]\!]\right\|^2_{\mathbf{L}^2(\Sigma)}\Big)\end{aligned} \tag{B.4.16}$$

and by proving a coercivity property, uniform in h, and by establishing some continuity estimates for the bilinear form $a_h(.,.)$. We first establish the coercivity of a_h.

Proposition B.4.2 (Coercivity). *If* $\theta\in\{0,1\}$, *there exists* $\gamma_0>0$ *and* $c(\gamma_0)>0$, *uniform with respect to* h, *so that the following holds for all* $\gamma\geq\gamma_0$*:*

$$a_h((\mathbf{E}_h,p_h),(\mathbf{E}_h,p_h)) \geq c(\gamma_0)\left\|\mathbf{E}_h,p_h\right\|_h^2, \qquad \forall(\mathbf{E}_h,p_h)\in\mathbf{X}_h\times M_h, \tag{B.4.17}$$

and this inequality holds with $c(\gamma_0)=1$ *if* $\theta=-1$.

Proof. We first observe that

$$a_h((\mathbf{E}_h,p_h),(\mathbf{E}_h,p_h)) = \|\mathbf{E}_h,p_h\|_h^2 + (1+\theta)\left(\{\!\{\kappa\nabla\times\mathbf{E}_h\}\!\},[\![\mathbf{E}_h\times\mathbf{n}]\!]\right)_{\Sigma\cup\Gamma}.$$

The conclusion is evident if $\theta=-1$. Otherwise we have to control the term $\left(\{\!\{\kappa\nabla\times\mathbf{E}_h\}\!\},[\![\mathbf{E}_h\times\mathbf{n}]\!]\right)_{\Sigma\cup\Gamma}$. Invoking a trace and a Young inequality yields

$$\begin{aligned}\left(\{\!\{\kappa\nabla\times\mathbf{F}_h\}\!\},[\![\mathbf{F}_h\times\mathbf{n}]\!]\right)_{\Sigma\cup\Gamma} \leq \frac{1}{4}&\left\|\kappa^{\frac{1}{2}}\nabla\times\mathbf{F}_h\right\|^2_{L^2(\Omega_\Sigma)}\\ &+ c_0h^{-1}\left\|\{\!\{\kappa\}\!\}^{\frac{1}{2}}\,[\![\mathbf{F}_h\times\mathbf{n}]\!]\right\|^2_{L^2(\Sigma\cup\Gamma)}.\end{aligned} \tag{B.4.18}$$

Hence, if $\gamma\geq\gamma_0:=4c_0$, we infer that the following holds:

$$a_h\left((\mathbf{E}_h,p_h),(\mathbf{E}_h,p_h)\right) \geq \frac{1}{2}\left\|\mathbf{E}_h,p_h\right\|_h^2 \geq 0. \tag{B.4.19}$$

This completes the proof. □

We now establish the uniform boundedness of the bilinear form a_h.

Proposition B.4.3 (Continuity). *For any $s \in \left(0, \frac{1}{2}\right)$, there is $c > 0$, uniform in h such that the following holds for every $(\mathbf{E}, p) \in \mathbf{Z}^s \times H_0^1(\Omega)$ and $(\mathbf{G}_h, d_h), (\mathbf{F}_h, q_h) \in \mathbf{X}_h \times M_h$:*

$$
\begin{aligned}
c\,\frac{a_h\left((\mathbf{E}-\mathbf{G}_h, p-d_h), (\mathbf{F}_h, q_h)\right)}{\|\mathbf{F}_h, q_h\|_h} &\leq \|\mathbf{E}-\mathbf{G}_h\|_h + h^{\alpha-1}\,\|\mathbf{E}-\mathbf{G}_h\|_{\mathbf{L}^2(\Omega)} \\
&\quad + h^{\sigma}\,\|\kappa\nabla\times(\mathbf{E}-\mathbf{G}_h)\|_{H^{\sigma}(\mathcal{T}_h)} \\
&\quad + h\,\|\nabla\times\kappa\nabla\times(\mathbf{E}-\mathbf{G}_h)\|_{L^2(\mathcal{T}_h)} \\
&\quad + h^{-\alpha}\,\|p-d_h\|_{L^2(\Omega)} + h^{(\frac{1}{2}-\alpha)}\,\|p-d_h\|_{L^2(\Sigma)}\,.
\end{aligned} \tag{B.4.20}
$$

where $\|.\|^2_{L^2(\mathcal{T}_h)} := \sum_{K\in\mathcal{T}_h}\|.\|^2_K$.

Proof. We first realize that Cauchy-Schwarz inequalities yield

$$
\begin{aligned}
&(\kappa\nabla\times(\mathbf{E}-\mathbf{G}_h), \nabla\times\mathbf{F}_h)_{\Omega} + \gamma h^{-1}\,(\{\!\{\kappa\}\!\}\,[\![(\mathbf{E}-\mathbf{G}_h)\times\mathbf{n}]\!], [\![\mathbf{F}_h\times\mathbf{n}]\!])_{\Sigma\cup\Gamma} \\
&\quad + c_\alpha\Big(h^{2\alpha}\,(\nabla\cdot(\varepsilon(\mathbf{E}-\mathbf{G}_h)), \nabla\cdot(\varepsilon\mathbf{F}_h))_{\Omega_\Sigma} + h^{2(1-\alpha)}\,(\varepsilon\nabla(p-d_h), \nabla q_h)_{\Omega} \\
&\quad + h^{(2\alpha-1)}\,([\![\varepsilon(\mathbf{E}-\mathbf{G}_h)\cdot\mathbf{n}]\!], [\![\varepsilon\mathbf{F}_h\cdot\mathbf{n}]\!])_{\Sigma}\Big), \\
&\quad \leq \|\mathbf{F}_h, q_h\|_h\,\|\mathbf{E}-\mathbf{G}_h, p-d_h\|_h\,.
\end{aligned}
$$

We now bound separately the remaining terms appearing in the definition (B.4.12) of $a_h(.,.)$:

$$
\begin{aligned}
-(\varepsilon(\mathbf{E}-\mathbf{G}_h), \nabla q_h)_{\Omega} \leq& \varepsilon_{\max} h^{\alpha-1}\,\|\nabla q_h\|_{L^2(\Omega)}\,h^{1-\alpha}\,\|\mathbf{E}-\mathbf{G}_h\|_{L^2(\Omega)}\,, \\
(\varepsilon\nabla(p-d_h), \mathbf{F}_h)_{\Omega} \leq& h^{\alpha}\,\|\nabla\cdot(\varepsilon\mathbf{F}_h)\|_{L^2(\Omega_\Sigma)}\,h^{-\alpha}\,\|p-d_h\|_{L^2(\Omega)} \\
&+ h^{(\alpha-\frac{1}{2})}\,\|[\![\varepsilon\mathbf{F}_h\cdot\mathbf{n}]\!]\|_{L^2(\Sigma)}\,h^{(\frac{1}{2}-\alpha)}\,\|p-d_h\|_{L^2(\Sigma)}\,,
\end{aligned}
$$

where we used an integration by parts for the second estimate. It remains to bound the consistency terms

$$
(\{\!\{\kappa\nabla\times(\mathbf{E}-\mathbf{G}_h)\}\!\}, [\![\mathbf{F}_h\times\mathbf{n}]\!])_{\Sigma\cup\Gamma} + \theta\,(\{\!\{\kappa\nabla\times\mathbf{F}_h\}\!\}, [\![(\mathbf{E}-\mathbf{G}_h)\times\mathbf{n}]\!])_{\Sigma\cup\Gamma}\,. \tag{B.4.21}
$$

For the first term in (B.4.21), we apply Lemma B.7.4 with $\mathbf{v} = [\![\mathbf{F}_h\times\mathbf{n}]\!]$, which is a polynomial of degree $\ell-1$, and $\boldsymbol{\phi} = \{\!\{\kappa\nabla\times(\mathbf{E}-\mathbf{G}_h)\}\!\}$. Then for any $F \in \Sigma\cup\Gamma$, we infer that

$$
\begin{aligned}
(\{\!\{\kappa\nabla\times(\mathbf{E}-\mathbf{G}_h)\}\!\}, [\![\mathbf{F}_h\times\mathbf{n}]\!])_F \leq& ch^{-\frac{1}{2}}\,\|[\![\mathbf{F}_h\times\mathbf{n}]\!]\|_{L^2(F)} \\
&\times\sum_{i=1}^{2}\Big(h^s\,\|\kappa\nabla\times(\mathbf{E}-\mathbf{G}_h)\|_{H^s(K_i)} + h\,\|\nabla\times\kappa\nabla\times(\mathbf{E}-\mathbf{G}_h)\|_{L^2(K_i)} \\
&\qquad + \|\kappa\nabla\times(\mathbf{E}-\mathbf{G}_h)\|_{L^2(K_i)}\Big),
\end{aligned}
$$

where $K_1, K_2 \in \mathcal{T}_h$ such that $F = \overline{K_1}\cap\overline{K_2}$. Hence, summing over all the faces we arrive at

$$
\begin{aligned}
(\{\!\{\kappa\nabla\times(\mathbf{E}-\mathbf{G}_h)\}\!\}, [\![\mathbf{F}_h\times\mathbf{n}]\!])_{\Sigma\cup\Gamma} \leq& ch^{-\frac{1}{2}}\,\|[\![\mathbf{F}_h\times\mathbf{n}]\!]\|_{L^2(\Sigma\cup\Gamma)} \\
&\times\Big(h^s\,\|\kappa\nabla\times(\mathbf{E}-\mathbf{G}_h)\|_{H^s(\mathcal{T}_h)} + h\,\|\nabla\times\kappa\nabla\times(\mathbf{E}-\mathbf{G}_h)\|_{L^2(\mathcal{T}_h)} \\
&\qquad + \|\kappa\nabla\times(\mathbf{E}-\mathbf{G}_h)\|_{L^2(\mathcal{T}_h)}\Big).
\end{aligned}
$$

For the second term in (B.4.21) we notice that $[\![(\mathbf{E}-\mathbf{G}_h)\times\mathbf{n}]\!] = -[\![\mathbf{G}_h\times\mathbf{n}]\!]$ owing to the regularity of $\mathbf{E}$. The by proceeding as above, we arrive at

$$\begin{aligned}(\{\!\{\kappa\nabla\times\mathbf{F}_h\}\!\}, [\![(\mathbf{E}-\mathbf{G}_h\times\mathbf{n}]\!])_{\Sigma\cup\Gamma} &\le ch^{-\frac{1}{2}} \|[\![\mathbf{G}_h\times\mathbf{n}]\!]\|_{L^2(\Sigma\cup\Gamma)} \|\kappa\nabla\times\mathbf{F}_h\|_{L^2(\mathcal{T}_h)} \\ &\le ch^{-\frac{1}{2}} \|[\![(\mathbf{E}-\mathbf{G}_h)\times\mathbf{n}]\!]\|_{L^2(\Sigma\cup\Gamma)} \|\kappa\nabla\times\mathbf{F}_h\|_{L^2(\mathcal{T}_h)},\end{aligned}$$

where we used the inverse inequalities

$$\begin{aligned}h\,\|\nabla\times\kappa\nabla\times\mathbf{F}_h\|_{L^2(\mathcal{T}_h)} &\le c\,\|\kappa\nabla\times\mathbf{F}_h\|_{L^2(\mathcal{T}_h)}, \\ h^s\,\|\kappa\nabla\times\mathbf{F}_h\|_{H^s(\mathcal{T}_h)} &\le c\,\|\kappa\nabla\times\mathbf{F}_h\|_{L^2(\mathcal{T}_h)}.\end{aligned}$$

The desired result is obtained by gathering the above estimates. □

The following result will be useful in order to prove a convergence result in $\mathbf{L}^2(\Omega)$.

Proposition B.4.4 (Adjoint continuity). *For any $s \in \left(0, \frac{1}{2}\right)$, there is $c > 0$, uniform in h such that the following holds for every $(\mathbf{E}, p), (\mathbf{F}, q) \in \mathbf{Z}^s\times H_0^1(\Omega)$, $\mathbf{F}_h \in \mathbf{X}_h \cap \mathbf{H}_{0,\mathrm{curl}}(\Omega)$, $q_h \in M_h$ and $(\mathbf{G}_h, d_h) \in \mathbf{X}_h\times M_h$:*

$$\begin{aligned}c\,\frac{a_h((\mathbf{E}-\mathbf{G}_h, p-d_h), (\mathbf{F}-\mathbf{F}_h, q-q_h))}{\|\mathbf{E}-\mathbf{G}_h, p-d_h\|_h} &\le \|\mathbf{F}-\mathbf{F}_h, q-q_h\|_h + h^{\alpha-1}\,\|\mathbf{F}-\mathbf{F}_h\|_{\mathbf{L}^2(\Omega)} \\ &\quad + h^s\,\|\kappa\nabla\times(\mathbf{F}-\mathbf{F}_h)\|_{H^s(\mathcal{T}_h)} \\ &\quad + h\,\|\nabla\times\kappa\nabla\times(\mathbf{F}-\mathbf{F}_h)\|_{L^2(\mathcal{T}_h)} \\ &\quad + h^{-\alpha}\,\|q-q_h\|_{L^2(\Omega)} + h^{(\frac{1}{2}-\alpha)}\,\|q-q_h\|_{L^2(\Sigma)}.\end{aligned} \tag{B.4.22}$$

Proof. The proof proceeds similarly as in the proof of Proposition B.4.3. The only difference here is that we have $(\{\!\{\nabla\times(\mathbf{E}-\mathbf{G}_h)\}\!\}, [\![(\mathbf{F}-\mathbf{F}_h)\times\mathbf{n}]\!])_{\Sigma\cup\Gamma} = 0.$ owing to the assumption on $\mathbf{F}_h$. This identity makes the analysis of the consistency term (B.4.21) tractable. □

Remark B.4.3. Note that the coercivity and the continuity of a_h have been established for any $\alpha \in [0, 1]$.

B.5 Convergence analysis for the boundary value problem

In the first part of this section, we prove two convergence results for the discrete problem (B.4.13) using the discrete norm $\|\cdot\|_h$, one assuming minimal regularity and the other assuming full smoothness. In the second part of the section we use a Nitsche-Aubin duality argument to establish convergence in $\mathbf{L}^2(\Omega)$. The performance of the method is numerically illustrated at the end of the section.

B.5.1 Convergence in the discrete norm.

We assume first that the solution to the boundary value problem (B.2.10) has minimal regularity properties.

Theorem B.5.1. *Let* $\mathbf{g} \in \mathbf{L}^2(\Omega)$ *and denote* $(\mathbf{E}, p)$ *the solution of* (B.2.10). *Let* $\tau < \min(\tau_\varepsilon, \tau_\mu)$ *where* τ_ε *and* τ_μ *are defined in Theorem B.2.1. Denote* $(\mathbf{E}_h, p_h)$ *the solution of* (B.4.13). *Then, for any* $\alpha \in \left(\frac{\ell(1-\tau)}{\ell-\tau}, 1\right)$, *there exists* $c > 0$, *uniform in* h, *such that*

$$\|\mathbf{E} - \mathbf{E}_h, p - p_h\|_h \leqslant c h^r \|\mathbf{g}\|_{\mathbf{L}^2(\Omega)}, \tag{B.5.1}$$

with $r = \min\left(1-\alpha, \alpha - 1 + \tau\left(1 - \frac{\alpha}{r}\right)\right)$.

Proof. We first recall that, owing to Theorem B.2.1, we have $\mathbf{E} \in \mathbf{H}^\tau(\Omega) \cap \mathbf{H}^\tau_{0,\mathrm{curl}}(\Omega)$, together with the estimates

$$\|\mathbf{E}\|_{\mathbf{H}^\tau(\Omega)} + \|\nabla\times\mathbf{E}\|_{\mathbf{H}^\tau(\Omega)} + \|\nabla\times(\kappa\nabla\times\mathbf{E})\|_{\mathbf{L}^2(\Omega)} + \|\nabla p\|_{\mathbf{L}^2(\Omega)} \leq c\|\mathbf{g}\|_{\mathbf{L}^2(\Omega)}.$$

We establish (B.5.1) by using the triangular inequality

$$\begin{aligned}\|\mathbf{E} - \mathbf{E}_h, p - p_h\|_h \leqslant & \|\mathbf{E} - \mathcal{K}_\delta\mathbf{E}, 0\|_h + \|\mathcal{K}_\delta\mathbf{E} - \mathcal{C}_h\mathcal{K}_\delta\mathbf{E}, p - \mathcal{P}_h p\|_h \\ & + \|\mathcal{C}_h\mathcal{K}_\delta\mathbf{E} - \mathbf{E}_h, \mathcal{P}_h p - p_h\|_h,\end{aligned}$$

for some $\delta > 0$ to be defined later, and by bounding from above the three terms separately.

Using the definition of $\|\cdot\|_h$ together with the approximation properties of $\mathcal{K}_\delta$, cf. (B.3.16)-(B.3.17)-(B.3.18), we infer:

$$\|\mathbf{E} - \mathcal{K}_\delta\mathbf{E}, 0\|_h \leq c\delta^\tau \|\nabla\times\mathbf{E}\|_{\mathbf{H}^\tau(\Omega)} + ch^\alpha\delta^{\tau-1}\|\mathbf{E}\|_{\mathbf{H}^\tau(\Omega)} + h^{\alpha-\frac{1}{2}}\|\mathcal{K}_\delta\mathbf{E}\|_{\mathbf{L}^2(\Sigma)}.$$

Note that the estimate (B.3.17) is critical to obtain a bound that depends only on $\|\nabla\times\mathbf{E}\|_{\mathbf{H}^\tau(\Omega)}$ instead of $\|\mathbf{E}\|_{\mathbf{H}^{1+\tau}(\Omega)}$. To estimate the last term in the above inequality, we apply (B.7.6) with $\Theta = \frac{1-2\tau}{2(1-\tau)}$,

$$\begin{aligned}h^{\alpha-\frac{1}{2}}\|\mathcal{K}_\delta\mathbf{E}\|_{\mathbf{L}^2(\Sigma)} &\leq ch^{\alpha-\frac{1}{2}}\|\mathcal{K}_\delta\mathbf{E}\|^{1-\Theta}_{\mathbf{H}^\tau(\Omega)}\|\mathcal{K}_\delta\mathbf{E}\|^{\Theta}_{\mathbf{H}^1(\Omega)} \\ &\leq ch^{\alpha-\frac{1}{2}}\delta^{\Theta(\tau-1)}\|\mathbf{E}\|_{\mathbf{H}^\tau(\Omega)} \leq ch^{\alpha-\frac{1}{2}}\delta^{\tau-\frac{1}{2}}\|\mathbf{E}\|_{\mathbf{H}^\tau(\Omega)}.\end{aligned}$$

Finally, we arrive at

$$\|\mathbf{E} - \mathcal{K}_\delta\mathbf{E}, 0\|_h \leq c\left(\delta^\tau + h^\alpha\delta^{\tau-1} + h^{\alpha-\frac{1}{2}}\delta^{\tau-\frac{1}{2}}\right)\|\mathbf{g}\|_{\mathbf{L}^2(\Omega)}. \tag{B.5.2}$$

Let us now turn our attention to $\|\mathcal{K}_\delta\mathbf{E} - \mathcal{C}_h\mathcal{K}_\delta\mathbf{E}, p - \mathcal{P}_h p\|_h$. Owing to the definition of $\mathcal{C}_h$ and the regularity of $\mathcal{K}_\delta\mathbf{E}$, we have $\mathcal{C}_h\mathcal{K}_\delta\mathbf{E} \in \mathbf{H}_{0,\mathrm{curl}}(\Omega)$, so that we only have four terms to bound (the jumps of $\mathcal{C}_h\mathcal{K}_\delta\mathbf{E}$ across the mesh interfaces and the tangent trace on Γ are zero, cf. Remark B.4.1). Using the properties of $\mathcal{K}_\delta$ and $\mathcal{C}_h$ together with (B.7.5) we deduce that:

$$\begin{aligned}\|\kappa^{\frac{1}{2}}\nabla\times(\mathcal{K}_\delta\mathbf{E} - \mathcal{C}_h\mathcal{K}_\delta\mathbf{E})\|_{\mathbf{L}^2(\Omega)} \leq & ch^{\ell-1}\|\mathcal{K}_\delta\mathbf{E}\|_{\mathbf{H}^\ell(\Omega)} \leq ch^{\ell-1}\delta^{\tau-\ell}\|\mathbf{E}\|_{\mathbf{H}^\tau(\Omega)}, \\ h^\alpha\|\nabla\cdot(\varepsilon(\mathcal{K}_\delta\mathbf{E} - \mathcal{C}_h\mathcal{K}_\delta\mathbf{E}))\|_{L^2(\Omega)} \leq & ch^{\alpha+\ell-1}\|\mathcal{K}_\delta\mathbf{E}\|_{\mathbf{H}^\ell(\Omega)} \leq ch^{\alpha+\ell-1}\delta^{\tau-\ell}\|\mathbf{E}\|_{\mathbf{H}^\tau(\Omega)}, \\ h^{1-\alpha}\|\varepsilon^{\frac{1}{2}}\nabla(p - \mathcal{P}_h p)\|_{\mathbf{L}^2(\Omega)} \leq & ch^{1-\alpha}\|p\|_{H^1_0(\Omega)}, \\ h^{\alpha-\frac{1}{2}}\|[\![\varepsilon(\mathcal{K}_\delta\mathbf{E} - \mathcal{C}_h\mathcal{K}_\delta\mathbf{E})\cdot\mathbf{n}]\!]\|_{\mathbf{L}^2(\Sigma)} \leq & ch^{\alpha-\frac{1}{2}}\|\mathcal{K}_\delta\mathbf{E} - \mathcal{C}_h\mathcal{K}_\delta\mathbf{E}\|_{\mathbf{L}^2(\Sigma)} \\ \leq & ch^{\alpha-\frac{1}{2}}\|\mathcal{K}_\delta\mathbf{E} - \mathcal{C}_h\mathcal{K}_\delta\mathbf{E}\|^{1-\frac{1}{2\alpha}}_{\mathbf{L}^2(\Omega)}\|\mathcal{K}_\delta\mathbf{E} - \mathcal{C}_h\mathcal{K}_\delta\mathbf{E}\|^{\frac{1}{2\alpha}}_{\mathbf{H}^\alpha(\Omega)} \\ \leq & ch^{\alpha-\frac{1}{2}}h^{\ell\left(1-\frac{1}{2\alpha}\right)}h^{(\ell-\alpha)\frac{1}{2\alpha}}\|\mathcal{K}_\delta\mathbf{E}\|_{\mathbf{H}^\ell(\Omega)} \\ \leq & ch^{\alpha+\ell-1}\delta^{\tau-\ell}\|\mathbf{E}\|_{\mathbf{H}^\tau(\Omega)}.\end{aligned}$$

These estimates lead to

$$\|\mathcal{K}_\delta \mathbf{E} - \mathcal{C}_h\mathcal{K}_\delta \mathbf{E}, p - \mathcal{P}_h p\|_h \leq c\left(h^{\ell-1}\delta^{\tau-\ell} + h^{1-\alpha}\right)\|\mathbf{g}\|_{\mathbf{L}^2(\Omega)}. \tag{B.5.3}$$

The last term, $\|\mathcal{C}_h\mathcal{K}_\delta\mathbf{E} - \mathbf{E}_h, \mathcal{P}_h p - p_h\|_h$, is a little more subtle to handle. We start from the coercivity of a_h (B.4.19) and use both the Galerkin orthogonality (B.4.15) and the continuity of a_h (B.4.20) with $s = 1-\alpha$ to get the following estimate:

$$\begin{aligned}
&\|\mathcal{C}_h\mathcal{K}_\delta\mathbf{E} - \mathbf{E}_h, \mathcal{P}_h p - p_h\|_h \\
&\quad\leq c\,\frac{a_h\left((\mathcal{C}_h\mathcal{K}_\delta\mathbf{E} - \mathbf{E}_h, \mathcal{P}_h p - p_h), (\mathcal{C}_h\mathcal{K}_\delta\mathbf{E} - \mathbf{E}_h, \mathcal{P}_h p - p_h)\right)}{\|\mathcal{C}_h\mathcal{K}_\delta\mathbf{E} - \mathbf{E}_h, \mathcal{P}_h p - p_h\|_h} \\
&\quad\leq c\,\frac{a_h\left((\mathcal{C}_h\mathcal{K}_\delta\mathbf{E} - \mathbf{E}, \mathcal{P}_h p - p), (\mathcal{C}_h\mathcal{K}_\delta\mathbf{E} - \mathbf{E}_h, \mathcal{P}_h p - p_h)\right)}{\|\mathcal{C}_h\mathcal{K}_\delta\mathbf{E} - \mathbf{E}_h, \mathcal{P}_h p - p_h\|_h} \\
&\quad\leq c\,\big(\|\mathcal{C}_h\mathcal{K}_\delta\mathbf{E} - \mathbf{E}, \mathcal{P}_h p - p\|_h + h^{\alpha-1}\|\mathbf{E} - \mathcal{C}_h\mathcal{K}_\delta\mathbf{E}\|_{\mathbf{L}^2(\Omega)} \\
&\qquad + h^{1-\alpha}\|\kappa\nabla\times(\mathbf{E} - \mathcal{C}_h\mathcal{K}_\delta\mathbf{E})\|_{\mathbf{H}^{1-\alpha}(\Omega)} + h^{-\alpha}\|p - \mathcal{P}_h p\|_{L^2(\Omega)} \\
&\qquad + h\|\nabla\times\kappa\nabla\times(\mathbf{E} - \mathcal{C}_h\mathcal{K}_\delta\mathbf{E})\|_{\mathbf{L}^2(\mathcal{T}_h)} + h^{\frac{1}{2}-\alpha}\|p - \mathcal{P}_h p\|_{L^2(\Sigma)}\big).
\end{aligned}$$

We now handle each term in the right hand side separately. Using the triangle inequality $\|\mathcal{C}_h\mathcal{K}_\delta\mathbf{E} - \mathbf{E}, \mathcal{P}_h p - p\|_h \leq \|\mathcal{C}_h\mathcal{K}_\delta\mathbf{E} - \mathcal{K}_\delta\mathbf{E}, \mathcal{P}_h p - p\|_h + \|\mathcal{K}_\delta\mathbf{E} - \mathbf{E}, 0\|_h$ and the estimates (B.5.2)-(B.5.3), we obtain

$$\|\mathcal{C}_h\mathcal{K}_\delta\mathbf{E} - \mathbf{E}, \mathcal{P}_h p - p\|_h \leq c\left(\delta^\tau + h^\alpha\delta^{\tau-1} + h^{\alpha-\frac{1}{2}}\delta^{\tau-\frac{1}{2}} + h^{\ell-1}\delta^{\tau-\ell} + h^{1-\alpha}\right)\|\mathbf{g}\|_{\mathbf{L}^2(\Omega)}.$$

Similarly, we obtain

$$\begin{aligned}
h^{\alpha-1}\|\mathbf{E} - \mathcal{C}_h\mathcal{K}_\delta\mathbf{E}\|_{\mathbf{L}^2(\Omega)} &\leq c\left(h^{\alpha-1}\delta^\tau + h^{\alpha+\ell-1}\delta^{\tau-\ell}\right)\|\mathbf{g}\|_{\mathbf{L}^2(\Omega)}, \\
h^{1-\alpha}\|\kappa\nabla\times(\mathbf{E} - \mathcal{C}_h\mathcal{K}_\delta\mathbf{E}\|_{\mathbf{H}^{1-\alpha}(\Omega)} &\leq c\left(h^{1-\alpha}\delta^{\tau+\alpha-1} + h^{\ell-1}\delta^{\tau-\ell}\right)\|\mathbf{g}\|_{\mathbf{L}^2(\Omega)}.
\end{aligned}$$

Note that the previous computation is valid since $1-\alpha \leq \tau$ owing to the assumption $\alpha \in \left(\frac{\ell(1-\tau)}{\ell-\tau}, 1\right)$. For the last term involving $\mathbf{E}$ we use the commuting property $\bar{\delta}\nabla\times\mathcal{K}_\delta\mathbf{E} = \mathcal{K}_\delta\nabla\times\mathbf{E}$, see (B.3.19) as follows:

$$\begin{aligned}
h\|\nabla\times\kappa\nabla\times(\mathbf{E} - \mathcal{C}_h\mathcal{K}_\delta\mathbf{E})\|_{\mathbf{L}^2(\mathcal{T}_h)} &\leq h\|\nabla\times\kappa\nabla\times\mathbf{E}\|_{\mathbf{L}^2(\mathcal{T}_h)} + h\|\nabla\times\kappa\nabla\times\mathcal{K}_\delta\mathbf{E}\|_{\mathbf{L}^2(\mathcal{T}_h)} \\
&\quad + h\|\nabla\times\kappa\nabla\times(\mathcal{K}_\delta\mathbf{E} - \mathcal{C}_h\mathcal{K}_\delta\mathbf{E})\|_{\mathbf{L}^2(\mathcal{T}_h)} \\
&\leq c\left(h\|\mathbf{g}\|_{\mathbf{L}^2(\Omega)} + h\|\nabla\times\mathcal{K}_\delta\mathbf{E}\|_{\mathbf{H}^1(\Omega)} + h^{\ell-1}\|\mathcal{K}_\delta\mathbf{E}\|_{\mathbf{H}^\ell(\Omega)}\right) \\
&\leq c\left(h\|\mathbf{g}\|_{\mathbf{L}^2(\Omega)} + h\|\mathcal{K}_\delta\nabla\times\mathbf{E}\|_{\mathbf{H}^1(\Omega)} + h^{\ell-1}\delta^{\tau-\ell}\|\mathbf{E}\|_{\mathbf{H}^\tau(\Omega)}\right) \\
&\leq c\left(h + h\delta^{\tau-1} + h^{\ell-1}\delta^{\tau-\ell}\right)\|\mathbf{g}\|_{\mathbf{L}^2(\Omega)}.
\end{aligned}$$

For the remaining terms involving p, we use (B.7.5) together with the approximation properties of $\mathcal{C}_h$:

$$\begin{aligned}
h^{-\alpha}\|p - \mathcal{P}_h p\|_{L^2(\Omega)} &\leq ch^{1-\alpha}\|p\|_{H_0^1(\Omega)} \leq ch^{1-\alpha}\|\mathbf{g}\|_{\mathbf{L}^2(\Omega)}, \\
h^{\frac{1}{2}-\alpha}\|p - \mathcal{P}_h p\|_{L^2(\Sigma)} &\leq h^{\frac{1}{2}-\alpha}\|p - \mathcal{P}_h p\|_{L^2(\Omega)}^{1-\frac{1}{2\alpha}}\|p - \mathcal{P}_h p\|_{H^\alpha(\Omega)}^{\frac{1}{2\alpha}} \\
&\leq h^{\frac{1}{2}-\alpha}h^{1-\frac{1}{2\alpha}}h^{(1-\alpha)\frac{1}{2\alpha}}\|p\|_{H_0^1(\Omega)} \leq ch^{1-\alpha}\|\mathbf{g}\|_{\mathbf{L}^2(\Omega)}.
\end{aligned}$$

Gathering all the above estimates together with (B.5.2) and (B.5.3), we finally obtain

$$\begin{aligned}\|\mathbf{E}-\mathbf{E}_h, p-p_h\|_h \leq & c\big(\delta^\tau + h^{1-\alpha} + h + h\delta^{\tau-1} + h^{\ell-1}\delta^{\tau-\ell} + h^{\alpha-1}\delta^\tau \\ & + h^{1-\alpha}\delta^{\tau+\alpha-1} + h^\alpha\delta^{\tau-1} + h^{\alpha-\frac{1}{2}}\delta^{\tau-\frac{1}{2}}\big)\|\mathbf{g}\|_{\mathbf{L}^2(\Omega)}.\end{aligned} \tag{B.5.4}$$

We want to use $\delta = h^\beta$ for some $\beta \in (0,1)$, i.e., $\delta h^{-1} \to +\infty$ as $h \to 0$. Once the negligible terms are removed in (B.5.4), we derive the following estimate:

$$\|\mathbf{E}-\mathbf{E}_h, p-p_h\|_h \leq c\big(h^{\alpha-1}\delta^\tau + h^{1-\alpha} + h^{\ell-1}\delta^{\tau-\ell}\big)\|\mathbf{g}\|_{\mathbf{L}^2(\Omega)}.$$

Using $\delta = h^{1-\frac{\alpha}{\ell}}$ implies that $h^{\alpha-1}\delta^\tau = h^{\ell-1}\delta^{\tau-\ell}$ and we arrive at

$$\|\mathbf{E}-\mathbf{E}_h, p-p_h\|_h \leq c(h^{\alpha-1+\tau\left(1-\frac{\alpha}{\ell}\right)} + h^{1-\alpha})\|\mathbf{g}\|_{\mathbf{L}^2(\Omega)},$$

which leads to (B.5.1) with $r := \min\left(1-\alpha, \alpha-1+\tau\left(1-\frac{\alpha}{\ell}\right)\right)$. Note that the assumed lower bound on α ensures that we have a convergence result as $h \to 0$. □

Remark B.5.1. Note that the best choice for α is such that $1-\alpha = \alpha-1+\tau\left(1-\frac{\alpha}{\ell}\right)$. This choice gives the following convergence rate $\frac{\tau}{2}(1-\frac{1}{\ell}) < r = \tau\frac{\ell-1}{2\ell-\tau} < \frac{\tau}{2}$.

We now derive a convergence estimate assuming that the solution of (B.2.10) is smooth.

Theorem B.5.2. *Let* $\mathbf{g} \in \mathbf{L}^2(\Omega)$ *and denote* $(\mathbf{E}, p)$ *the solution of* (B.2.10). *Assume that* $\mathbf{E} \in \mathbf{H}^{k+1}(\Omega)$ *and* $p \in H^{k+\alpha}(\Omega)$ *for some* $0 < k \leq \ell - 1$ *and* $\alpha \in [0,1]$. *Denote* $(\mathbf{E}_h, p_h)$ *the solution of* (B.4.13). *Then there exists* $c > 0$, *uniform in* h, *such that*

$$\|\mathbf{E}-\mathbf{E}_h, p-p_h\|_h \leq c\, h^k\left(\|\mathbf{g}\|_{\mathbf{L}^2(\Omega)} + \|\mathbf{E}\|_{\mathbf{H}^{k+1}(\Omega)} + \|p\|_{H^{k+\alpha}(\Omega)}\right). \tag{B.5.5}$$

Proof. The proof is similar to that of Theorem B.5.1. We start from the triangular inequality

$$\|\mathbf{E}-\mathbf{E}_h, p-p_h\|_h \leq \|\mathbf{E}-\mathcal{C}_h\mathbf{E}, p-\mathcal{P}_h p\|_h + \|\mathcal{C}_h\mathbf{E}-\mathbf{E}_h, \mathcal{P}_h p - p_h\|_h.$$

We bound the two terms in the right hand side separately. For the first one, we use the approximation properties of $\mathcal{C}_h$ to get:

$$\begin{aligned}\|\mathbf{E}-\mathcal{C}_h\mathbf{E}, p-\mathcal{P}_h p\|_h \leq & c\Big(h^k\|\mathbf{E}\|_{\mathbf{H}^{k+1}(\Omega)} + h^{k+\alpha}\|\mathbf{E}\|_{\mathbf{H}^{k+1}(\Omega)} + h^{-\frac{1}{2}}\|\mathbf{E}-\mathcal{C}_h\mathbf{E}\|_{\mathbf{L}^2(\Sigma\cup\Gamma)} \\ & + h^{1-\alpha}h^{k+\alpha-1}\|p\|_{H^{k+\alpha}(\Omega)} + h^{\alpha-\frac{1}{2}}\|\mathbf{E}-\mathcal{C}_h\mathbf{E}\|_{\mathbf{L}^2(\Sigma)}\Big).\end{aligned}$$

Using (B.7.5) for any $\sigma \in \left(\frac{1}{2}, 1\right)$, we have

$$\|\mathbf{E}-\mathcal{C}_h\mathbf{E}\|_{\mathbf{L}^2(\Sigma)} \leq c\,\|\mathbf{E}-\mathcal{C}_h\mathbf{E}\|_{\mathbf{L}^2(\Omega)}^{1-\frac{1}{2\sigma}}\|\mathbf{E}-\mathcal{C}_h\mathbf{E}\|_{\mathbf{H}^\sigma(\Omega)}^{\frac{1}{2\sigma}} \leq c\,h^{k+\frac{1}{2}}\|\mathbf{E}\|_{\mathbf{H}^{k+1}(\Omega)}.$$

As a result, we obtain

$$\|\mathbf{E}-\mathcal{C}_h\mathbf{E}, p-\mathcal{P}_h p\|_h \leq ch^k\left(\|\mathbf{E}\|_{\mathbf{H}^{k+1}(\Omega)} + \|p\|_{H^{k+\alpha}(\Omega)}\right). \tag{B.5.6}$$

Now we turn our attention to $\|\mathcal{C}_h\mathbf{E}-\mathbf{E}_h, \mathcal{P}_h p-p_h\|_h$. We use the coercivity of a_h, the Galerkin orthogonality and the continuity of a_h (for any $\sigma \in \left(0, \frac{1}{2}\right)$) to get

$$\begin{aligned}\|\mathcal{C}_h\mathbf{E}-\mathbf{E}_h, \mathcal{P}_h p-p_h\|_h \leq c\big(&\|\mathbf{E}-\mathcal{C}_h\mathbf{E}, p-\mathcal{P}_h p\|_h + h^{\alpha-1}\|\mathbf{E}-\mathcal{C}_h\mathbf{E}\|_{\mathbf{L}^2(\Omega)}\\ &+ h^{\sigma}\|\kappa\nabla\times(\mathbf{E}-\mathcal{C}_h\mathbf{E})\|_{\mathbf{H}^{\sigma}(\mathcal{T}_h)}\\ &+ h\|\nabla\times\kappa\nabla\times(\mathbf{E}-\mathcal{C}_h\mathbf{E})\|_{\mathbf{L}^2(\mathcal{T}_h)}\\ &+ h^{-\alpha}\|p-\mathcal{P}_h p\|_{L^2(\Omega)} + h^{\frac{1}{2}-\alpha}\|p-\mathcal{P}_h p\|_{L^2(\Sigma)}\big).\end{aligned}$$

Using the approximation properties of $\mathcal{C}_h$ together with (B.5.6), we infer

$$\begin{aligned}\|\mathbf{E}-\mathcal{C}_h\mathbf{E}, p-\mathcal{P}_h p\|_h &\leq ch^k\left(\|\mathbf{E}\|_{\mathbf{H}^{k+1}(\Omega)} + \|p\|_{H^{k+\alpha}(\Omega)}\right),\\ h^{\alpha-1}\|\mathbf{E}-\mathcal{C}_h\mathbf{E}\|_{\mathbf{L}^2(\Omega)} &\leq ch^{k+\alpha}\|\mathbf{E}\|_{\mathbf{H}^{k+1}(\Omega)},\\ h^{\sigma}\|\kappa\nabla\times(\mathbf{E}-\mathcal{C}_h\mathbf{E})\|_{\mathbf{H}^{\sigma}(\mathcal{T}_h)} &\leq ch^k\|\mathbf{E}\|_{\mathbf{H}^{k+1}(\Omega)},\\ h^{-\alpha}\|p-\mathcal{P}_h p\|_{L^2(\Omega)} &\leq ch^k\|p\|_{H^{k+\alpha}(\Omega)}.\end{aligned}$$

For the last term involving p, we use (B.7.5) for some $\sigma \in \left(\frac{1}{2}, 1\right)$:

$$\begin{aligned}h^{\frac{1}{2}-\alpha}\|p-\mathcal{P}_h p\|_{L^2(\Sigma)} &\leq ch^{\frac{1}{2}-\alpha}\|p-\mathcal{P}_h p\|_{L^2(\Omega)}^{1-\frac{1}{2\sigma}}\|p-\mathcal{P}_h p\|_{H^{\sigma}(\Omega)}^{\frac{1}{2\sigma}}\\ &\leq ch^{\frac{1}{2}-\alpha}h^{k+\alpha-\frac{1}{2}}\|p\|_{H^{k+\alpha}(\Omega)} = ch^k\|p\|_{H^{k+\alpha}(\Omega)}.\end{aligned}$$

For the last term involving $\mathbf{E}$, we distinguish two cases depending whether $k < 1$ or $k \geq 1$. If $k < 1$, we use an inverse inequality together with the approximation properties of $\mathcal{C}_h$ to deduce that

$$\begin{aligned}h\|\nabla\times\kappa\nabla\times(\mathbf{E}-\mathcal{C}_h\mathbf{E})\|_{\mathbf{L}^2(\mathcal{T}_h)} &\leq h\|\nabla\times\kappa\nabla\times\mathbf{E}\|_{\mathbf{L}^2(\Omega)} + ch\|\mathcal{C}_h\mathbf{E}\|_{\mathbf{H}^2(\mathcal{T}_h)}\\ &\leq h\|\mathbf{g}\|_{\mathbf{L}^2(\Omega)} + h^k\|\mathbf{E}\|_{\mathbf{H}^{k+1}(\Omega)}.\end{aligned}$$

If $k \geq 1$, we use the approximation properties of $\mathcal{C}_h$ to get

$$h\|\nabla\times\kappa\nabla\times(\mathbf{E}-\mathcal{C}_h\mathbf{E})\|_{\mathbf{L}^2(\mathcal{T}_h)} \leq ch\|\mathbf{E}-\mathcal{C}_h\mathbf{E}\|_{\mathbf{H}^2(\mathcal{T}_h)} \leq ch^k\|\mathbf{E}\|_{\mathbf{H}^{k+1}(\Omega)}.$$

In both cases, we have:

$$h\|\nabla\times\kappa\nabla\times(\mathbf{E}-\mathcal{C}_h\mathbf{E})\|_{\mathbf{L}^2(\mathcal{T}_h)} \leq ch^k\left(\|\mathbf{E}\|_{\mathbf{H}^{k+1}(\Omega)} + \|\mathbf{g}\|_{\mathbf{L}^2(\Omega)}\right).$$

Gathering all the above estimates and using (B.5.6) gives the desired result (B.5.5). □

Remark B.5.2. Note that the error estimate (B.5.5) is optimal since it implies that $\|\nabla\times(\mathbf{E}-\mathbf{E}_h)\|_{\mathbf{L}^2(\Omega)} \leq c\,h^k$, which is the best that can be expected from the piece-wise polynomial approximation of degree k. Note also that there is no lower bound on α to get convergence when the solution of (B.2.10) is smooth, i.e., any α in the range $[0, 1]$ is acceptable.

B.5.2 Convergence in the $\mathbf{L}^2$-norm.

Before proving that the discrete solution converges to the exact solution in the $\mathbf{L}^2$-norm, we prove a global version of Lemma B.7.4 that will be useful in the proof of Theorem B.5.3.

Lemma B.5.1. *Let $s \in \left(0, \frac{1}{2}\right)$. Then there exists $c > 0$, uniform in h, such that the following holds, for any $\boldsymbol{\psi} \in \mathbf{H}_{\mathrm{curl}}(\Omega) \cap \mathbf{H}^s(\Omega)$ and any $\mathbf{F}_h \in \mathbf{X}_h$:*

$$|(\boldsymbol{\psi}, [\![\mathbf{F}_h \times \mathbf{n}]\!])_{\Sigma \cup \Gamma}| \leq c\, h^{-\frac{1}{2}} \|[\![\mathbf{F}_h \times \mathbf{n}]\!]\|_{\mathbf{L}^2(\Sigma \cup \Gamma)} \left(h^s \|\boldsymbol{\psi}\|_{\mathbf{H}^s(\Omega)} + h \|\nabla \times \boldsymbol{\psi}\|_{\mathbf{L}^2(\Omega)}\right). \tag{B.5.7}$$

Proof. Let us consider $\boldsymbol{\psi} \in \mathbf{H}_{\mathrm{curl}}(\Omega) \cap \mathbf{H}^s(\Omega)$ and $\mathbf{F}_h \in \mathbf{X}_h$. Notice that the left hand side is well defined owing to Lemma B.7.4. We start from

$$\left|\left(\boldsymbol{\psi}, [\![\mathbf{F}_h \times \mathbf{n}]\!]\right)_{\Sigma \cup \Gamma}\right| \leq \underbrace{|(\boldsymbol{\psi} - \mathcal{K}_\delta \boldsymbol{\psi}, [\![\mathbf{F}_h \times \mathbf{n}]\!])_{\Sigma \cup \Gamma}|}_{:= I_1} + \underbrace{|(\mathcal{K}_\delta \boldsymbol{\psi}, [\![\mathbf{F}_h \times \mathbf{n}]\!])_{\Sigma \cup \Gamma}|}_{:= I_2},$$

for some δ to be defined later. We handle the two terms I_1, I_2 separately. For the first one, we apply Lemma B.7.4 with $\mathbf{v} = [\![\mathbf{F}_h \times \mathbf{n}]\!]$, $\boldsymbol{\phi} = \boldsymbol{\psi} - \mathcal{K}_\delta \boldsymbol{\psi}$ and $\sigma = s$, and we sum over all the faces $F \in \Sigma \cup \Gamma$. This leads to

$$\begin{aligned}
I_1 &\leq c\, h^{-\frac{1}{2}} \|[\![\mathbf{F}_h \times \mathbf{n}]\!]\|_{\mathbf{L}^2(\Sigma \cup \Gamma)} \big(h^s \|\boldsymbol{\psi} - \mathcal{K}_\delta \boldsymbol{\psi}\|_{\mathbf{H}^s(\mathcal{T}_h)} \\
&\quad + h \|\nabla \times (\boldsymbol{\psi} - \mathcal{K}_\delta \boldsymbol{\psi})\|_{\mathbf{L}^2(\mathcal{T}_h)} + \|\boldsymbol{\psi} - \mathcal{K}_\delta \boldsymbol{\psi}\|_{\mathbf{L}^2(\Omega)}\big) \\
&\leq c\, h^{-\frac{1}{2}} \|[\![\mathbf{F}_h \times \mathbf{n}]\!]\|_{\mathbf{L}^2(\Sigma \cup \Gamma)} \big(h^s \|\boldsymbol{\psi} - \mathcal{K}_\delta \boldsymbol{\psi}\|_{\mathbf{H}^s(\mathcal{T}_h)} \\
&\quad + h \|\nabla \times \boldsymbol{\psi}\|_{\mathbf{L}^2(\mathcal{T}_h)} + h \|\nabla \times \mathcal{K}_\delta \boldsymbol{\psi}\|_{\mathbf{L}^2(\mathcal{T}_h)} + \|\boldsymbol{\psi} - \mathcal{K}_\delta \boldsymbol{\psi}\|_{\mathbf{L}^2(\Omega)}\big).
\end{aligned}$$

Using the approximation properties of $\mathcal{K}_\delta$ (B.3.16) and (B.3.18), we arrive at

$$\begin{aligned}
I_1 &\leq c\, h^{-\frac{1}{2}} \|[\![\mathbf{F}_h \times \mathbf{n}]\!]\|_{\mathbf{L}^2(\Sigma \cup \Gamma)} \big(h^s \|\boldsymbol{\psi}\|_{\mathbf{H}^s(\Omega)} \\
&\quad + h \|\nabla \times \boldsymbol{\psi}\|_{\mathbf{L}^2(\Omega)} + \delta^s \|\boldsymbol{\psi}\|_{\mathbf{H}^s(\Omega)} + h \|\mathcal{K}_\delta \boldsymbol{\psi}\|_{\mathbf{H}^1(\Omega)}\big) \\
&\leq c\, h^{-\frac{1}{2}} \|[\![\mathbf{F}_h \times \mathbf{n}]\!]\|_{\mathbf{L}^2(\Sigma \cup \Gamma)} \big((h^s + \delta^s + h\delta^{s-1}) \|\boldsymbol{\psi}\|_{\mathbf{H}^s(\Omega)} + h \|\nabla \times \boldsymbol{\psi}\|_{\mathbf{L}^2(\Omega)}\big).
\end{aligned}$$

We handle I_2 by using the Cauchy-Schwarz inequality on every $\partial\Omega_i$, $i = 1, \cdots, N$.

$$I_2 \leq c\, h^{-\frac{1}{2}} \|[\![\mathbf{F}_h \times \mathbf{n}]\!]\|_{\mathbf{L}^2(\Sigma \cup \Gamma)} \sum_{i=1}^{N} h^{\frac{1}{2}} \|\mathcal{K}_\delta \boldsymbol{\psi}\|_{\mathbf{L}^2(\partial\Omega_i)}.$$

We use (B.7.6) on every Ω_i with $\Theta := \frac{1-2s}{2(1-s)}$, this leads to

$$\begin{aligned}
I_2 &\leq c\, h^{-\frac{1}{2}} \|[\![\mathbf{F}_h \times \mathbf{n}]\!]\|_{\mathbf{L}^2(\Sigma \cup \Gamma)} \sum_{i=1}^{N} h^{\frac{1}{2}} \|\mathcal{K}_\delta \boldsymbol{\psi}\|_{\mathbf{H}^s(\Omega_i)}^{1-\Theta} \|\mathcal{K}_\delta \boldsymbol{\psi}\|_{\mathbf{H}^1(\Omega_i)}^{\Theta} \\
&\leq c\, h^{-\frac{1}{2}} \|[\![\mathbf{F}_h \times \mathbf{n}]\!]\|_{\mathbf{L}^2(\Sigma \cup \Gamma)} h^{\frac{1}{2}} \|\mathcal{K}_\delta \boldsymbol{\psi}\|_{\mathbf{H}^s(\Omega)}^{1-\Theta} \|\mathcal{K}_\delta \boldsymbol{\psi}\|_{\mathbf{H}^1(\Omega)}^{\Theta},
\end{aligned}$$

where the constant c depends on N, which we recall is a fixed number. Using again the approximation properties of $\mathcal{K}_\delta$ we infer that

$$\begin{aligned}
I_2 &\leq c\, h^{-\frac{1}{2}} \|[\![\mathbf{F}_h \times \mathbf{n}]\!]\|_{\mathbf{L}^2(\Sigma \cup \Gamma)} h^{\frac{1}{2}} \delta^{(s-1)\Theta} \|\boldsymbol{\psi}\|_{\mathbf{H}^s(\Omega)} \\
&\leq c\, h^{-\frac{1}{2}} \|[\![\mathbf{F}_h \times \mathbf{n}]\!]\|_{\mathbf{L}^2(\Sigma \cup \Gamma)} h^{\frac{1}{2}} \delta^{s-\frac{1}{2}} \|\boldsymbol{\psi}\|_{\mathbf{H}^s(\Omega)}.
\end{aligned}$$

Then (B.5.7) is obtained by gathering the above estimates and setting $\delta = h$. □

Remark B.5.3. The proof of Lemma B.5.7 can done by using the decomposition $\boldsymbol{\psi} = \boldsymbol{\psi} - \mathcal{C}_h\boldsymbol{\psi} + \mathcal{C}_h\boldsymbol{\psi}$ instead of $\boldsymbol{\psi} = \boldsymbol{\psi} - \mathcal{K}_\delta\boldsymbol{\psi} + \mathcal{K}_\delta\boldsymbol{\psi}$.

Theorem B.5.3. *Let* $\mathbf{g} \in \mathbf{L}^2(\Omega)$ *and denote* $(\mathbf{E}, p)$ *the solution of* (B.2.10). *Let* $\tau < \min(\tau_\varepsilon, \tau_\mu)$ *where* τ_ε *and* τ_μ *are defined in Theorem B.2.1. Denote* $(\mathbf{E}_h, p_h)$ *the solution of* (B.4.13). *Then, for any* $\alpha \in \left(\frac{\ell(1-\tau)}{\ell-\tau}, 1\right)$, *there exists* $c > 0$, *uniform in* h, *such that*

$$\|\mathbf{E} - \mathbf{E}_h\|_{\mathbf{L}^2(\Omega)} \leq c\, h^{2r} \|\mathbf{g}\|_{\mathbf{L}^2(\Omega)}, \tag{B.5.8}$$

with $r := \min\left(1-\alpha, \alpha - 1 + \tau\left(1 - \frac{\alpha}{\ell}\right)\right)$. *If in addition* $\mathbf{E}$ *and* p *are smooth, say* $\mathbf{E} \in \mathbf{H}^{k+1}(\Omega)$ *and* $p \in H^{k+\alpha}(\Omega)$ *for some* $0 < k < \ell - 1$, *then the following holds:*

$$\|\mathbf{E} - \mathbf{E}_h\|_{\mathbf{L}^2(\Omega)} \leq c\, h^{k+r} \left(\|\mathbf{g}\|_{\mathbf{L}^2(\Omega)} + \|\mathbf{E}\|_{\mathbf{H}^{k+1}(\Omega)} + \|p\|_{H^{k+\alpha}(\Omega)} \right). \tag{B.5.9}$$

Proof. We are going to use a duality argument à la Nitsche-Aubin. In the following we denote a_h^1 the extension to $\left[(\mathbf{Z}^\tau(\Omega) + \mathbf{X}_h) \times H_0^1(\Omega)\right]^2$ of the bilinear form defined on $[\mathbf{X}_h \times M_h]^2$ in (B.4.12) with $\theta = 1$. Then the following symmetry property holds:

$$a_h^1\left((\mathbf{F}, q), (\mathbf{G}, r)\right) = a_h^1\left((\mathbf{G}, -r), (\mathbf{F}, -q)\right).$$

for all $((\mathbf{F}, q), (\mathbf{G}, r)) \in \left[(\mathbf{Z}^\tau(\Omega) + \mathbf{X}_h) \times H_0^1(\Omega)\right]^2$. Let $(\mathbf{w}, q) \in \mathbf{H}_{0,\mathrm{curl}}(\Omega) \times H_0^1(\Omega)$ be the solution of the following (adjoint) problem:

$$\nabla\times\kappa\nabla\times\mathbf{w} - \varepsilon\nabla q = \varepsilon\left(\mathbf{E} - \mathbf{E}_h\right), \quad \nabla\cdot(\varepsilon\mathbf{w}) = 0.$$

Recall that Theorem B.2.1 implies that $\mathbf{w} \in \mathbf{Z}^\tau(\Omega) \cap \mathbf{H}^\tau(\Omega)$ for any $s < \tau$ and that

$$\|\mathbf{w}\|_{\mathbf{H}^\tau(\Omega)} + \|\kappa\nabla\times\mathbf{w}\|_{\mathbf{H}^\tau(\Omega)} + \|\nabla\times\kappa\nabla\times\mathbf{w}\|_{\mathbf{L}^2(\Omega)} \leq c\, \|\mathbf{E} - \mathbf{E}_h\|_{\mathbf{L}^2(\Omega)}. \tag{B.5.10}$$

The definition of the pair $(\mathbf{w}, q)$ implies that $(\varepsilon\nabla q, \nabla\varphi)_\Omega = -(\varepsilon(\mathbf{E}-\mathbf{E}_h, \nabla\varphi)$ for all $\varphi \in H_0^1(\Omega)$, and the following identities hold:

$$\begin{aligned}
\|\varepsilon^{\frac{1}{2}}(\mathbf{E} - \mathbf{E}_h)\|_{\mathbf{L}^2(\Omega)}^2 &= a_h^1\left((\mathbf{w}, -q), (\mathbf{E} - \mathbf{E}_h, p_h - p)\right) + c_\alpha h^{2(1-\alpha)} \left(\varepsilon\nabla q, \nabla(p_h - p)\right)_\Omega \\
&= a_h^1\left((\mathbf{E} - \mathbf{E}_h, p - p_h), (\mathbf{w}, q)\right) + c_\alpha h^{2(1-\alpha)} \left(\varepsilon(\mathbf{E} - \mathbf{E}_h), \nabla(p - p_h)\right)_\Omega \\
&= a_h\left((\mathbf{E} - \mathbf{E}_h, p - p_h), (\mathbf{w}, q)\right) + c_\alpha h^{2(1-\alpha)} \left(\varepsilon(\mathbf{E} - \mathbf{E}_h), \nabla(p - p_h)\right)_\Omega \\
&\quad + (1-\theta)\left(\{\!\{\kappa\nabla\times\mathbf{w}\}\!\}, [\![-\mathbf{E}_h\times\mathbf{n}]\!]\right)_{\Sigma\cup\Gamma}
\end{aligned}$$

We now use the Galerkin orthogonality and introduce $\mathcal{C}_h\mathcal{K}_\delta\mathbf{w}$, $\mathcal{P}_h q$, with $\delta = h^{1-\frac{\alpha}{\ell}}$:

$$\begin{aligned}
\|\varepsilon^{\frac{1}{2}}(\mathbf{E} - \mathbf{E}_h)\|_{\mathbf{L}^2(\Omega)}^2 &= a_h\left((\mathbf{E} - \mathbf{E}_h, p - p_h), (\mathbf{w} - \mathcal{C}_h\mathcal{K}_\delta\mathbf{w}, q - \mathcal{P}_h q)\right) \\
&\quad + c_\alpha h^{2(1-\alpha)} \left(\varepsilon(\mathbf{E} - \mathbf{E}_h), \nabla(p - p_h)\right)_\Omega - (1-\theta)\left(\kappa\nabla\times\mathbf{w}, [\![\mathbf{E}_h\times\mathbf{n}]\!]\right)_{\Sigma\cup\Gamma}.
\end{aligned} \tag{B.5.11}$$

Note that we replaced $\{\!\{\kappa\nabla\times\mathbf{w}\}\!\}$ by $\kappa\nabla\times\mathbf{w}$ since the tangent component of $\kappa\nabla\times\mathbf{w}$ is continuous across the interfaces owing to $\nabla\times(\kappa\nabla\times\mathbf{w}) \in \mathbf{L}^2(\Omega)$.

We now handle the three terms in the right hand side separately. For the first one, we use Proposition B.4.4 with $s = 1 - \alpha$, $\mathbf{F} = \mathbf{w}$ and $\mathbf{F}_h = \mathcal{C}_h\mathcal{K}_\delta\mathbf{w}$ (note that $\mathbf{F}_h \in \mathbf{X}_h \cap \mathbf{H}_{0,\mathrm{curl}}(\Omega)$

since $\mathcal{K}_\delta \mathbf{w} \in \mathcal{C}_0^\infty(\Omega)$); we then infer that

$$\begin{aligned}\big|a_h\big((\mathbf{E}-\mathbf{E}_h, p-p_h), (\mathbf{w}-\mathcal{C}_h\mathcal{K}_\delta\mathbf{w}, q-\mathcal{P}_h q)\big)\big| \leq \\ c\,\|\mathbf{E}-\mathbf{E}_h, p-p_h\|_h \big(\|\mathbf{w}-\mathcal{C}_h\mathcal{K}_\delta\mathbf{w}, q-\mathcal{P}_h q\|_h \\ + h^{\alpha-1}\|\mathbf{w}-\mathcal{C}_h\mathcal{K}_\delta\mathbf{w}\|_{\mathbf{L}^2(\Omega)} + h^{-\alpha}\|q-\mathcal{P}_h q\|_{L^2(\Omega)} + h^{\frac{1}{2}-\alpha}\|q-\mathcal{P}_h q\|_{L^2(\Sigma)} \\ + h\|\nabla\times\kappa\nabla\times(\mathbf{w}-\mathcal{C}_h\mathcal{K}_\delta\mathbf{w})\|_{\mathbf{L}^2(\mathcal{T}_h)} + h^{1-\alpha}\|\nabla\times(\mathbf{w}-\mathcal{C}_h\mathcal{K}_\delta\mathbf{w})\|_{\mathbf{H}^{1-\alpha}(\Omega)}\big).\end{aligned}$$

The right hand side has already been estimated in the proof of Theorem B.5.1. We then have

$$\begin{aligned}\big|a_h\big((\mathbf{E}-\mathbf{E}_h, p-p_h),&(\mathbf{w}-\mathcal{C}_h\mathcal{K}_\delta\mathbf{w}, \mathcal{P}_h q-q)\big)\big| \\ &\leq c\,\|\mathbf{E}-\mathbf{E}_h, p-p_h\|_h h^r \|\mathbf{E}-\mathbf{E}_h\|_{\mathbf{L}^2(\Omega)}.\end{aligned} \tag{B.5.12}$$

The second term in (B.5.11) is estimated by using the Cauchy-Schwarz inequality, the definition of the norm $\|\cdot\|_h$ and inequality $r \leq 1-\alpha$,

$$\begin{aligned}\Big|h^{2(1-\alpha)}\,(\varepsilon(\mathbf{E}-\mathbf{E}_h), \nabla(p-p_h))_\Omega\Big| &\leq c\,h^{1-\alpha}\|\nabla(p-p_h)\|_{\mathbf{L}^2(\Omega)} h^{1-\alpha}\|\mathbf{E}-\mathbf{E}_h\|_{\mathbf{L}^2(\Omega)} \\ &\leq c\,\|\mathbf{E}-\mathbf{E}_h, p-p_h\|_h h^r \|\mathbf{E}-\mathbf{E}_h\|_{\mathbf{L}^2(\Omega)}.\end{aligned} \tag{B.5.13}$$

The last term in (B.5.11) is estimated by using Lemma B.5.1 with $\boldsymbol{\psi} := \kappa\nabla\times\mathbf{w}$ and $s := \tau$:

$$\begin{aligned}\big|(1-\theta)\big(\kappa\nabla\times\mathbf{w}, [\![\mathbf{E}_h\times\mathbf{n}]\!]\big)_{\Sigma\cup\Gamma}\big| & \\ &\leq c\,\|\mathbf{E}-\mathbf{E}_h\|_h \left(h^\tau\|\kappa\nabla\times\mathbf{w}\|_{\mathbf{H}^\tau(\Omega)} + h\|\nabla\times(\kappa\nabla\times\mathbf{w})\|_{\mathbf{L}^2(\Omega)}\right) \\ &\leq c\,\|\mathbf{E}-\mathbf{E}_h\|_h\, h^r \|\mathbf{E}-\mathbf{E}_h\|_{\mathbf{L}^2(\Omega)},\end{aligned} \tag{B.5.14}$$

where we have used (B.5.10) and $r \leq \frac{\tau}{2} < \tau$. Upon inserting (B.5.12)-(B.5.13)-(B.5.14) in (B.5.11) we obtain

$$\|\varepsilon^{\frac{1}{2}}(\mathbf{E}-\mathbf{E}_h)\|^2_{\mathbf{L}^2(\Omega)} \leq c h^r \|\mathbf{E}-\mathbf{E}_h\|_{\mathbf{L}^2(\Omega)} \|\mathbf{E}-\mathbf{E}_h, p-p_h\|_h.$$

Owing to the uniform positivity of ε, this leads to:

$$\|\mathbf{E}-\mathbf{E}_h\|_{\mathbf{L}^2(\Omega)} \leq c h^r \|\mathbf{E}-\mathbf{E}_h, p-p_h\|_h.$$

Now we consider two cases. Assuming only minimal regularity, Theorem B.5.1 gives a bound on $\|\mathbf{E}-\mathbf{E}_h, p-p_h\|_h$ that leads to (B.5.8). If $\mathbf{E}$ and p are smooth, then we can apply Theorem B.5.2 and we obtain (B.5.9). □

Remark B.5.4. Let $\tau \in (0, \frac{1}{2})$ and denote $(\mathbf{E}, p)$ the solution of (B.2.10). Assume that $\mathbf{E} \in \mathbf{H}^\tau(\Omega)$ and $\mathbf{E} \notin \mathbf{H}^{\tau^+}(\Omega)$ for all $\tau^+ > \tau$. Then the best choice of α is $\alpha = \frac{\ell(2-\tau)}{2\ell-\tau}$, which gives the convergence rate $2r = \tau\frac{\ell-1}{\ell-\frac{\tau}{2}}$; this convergence rate approaches the optimal rate, τ, when the approximation degree ℓ is large.

Remark B.5.5. It is interesting to notice that the degree of the polynomials used for M_h is not involved in the convergence rate when minimal regularity is assumed. This means that we can use different degrees of polynomials for $\mathbf{X}_h$ and M_h, and that it is sufficient to take polynomials of degree 1 for M_h.

B.5.3 Numerical illustrations

We present in this section some numerical illustrations of the performance of the method on a boundary value problem. We consider the L-shaped domain

$$\Omega = (-1,1)^2 \backslash ([0,+1]\times[-1,0])\,.$$

We assume that Ω is composed of three subdomains:

$$\Omega_1 = (0,1)^2, \qquad \Omega_2 = (-1,0)\times(0,1), \qquad \Omega_3 = (-1,0)^2.$$

We use $\kappa \equiv 1$ in Ω, $\varepsilon_{|\Omega_2} = 1$ and $\varepsilon_{|\Omega_1} = \varepsilon_{|\Omega_3} =: \varepsilon_r$. Denoting $\lambda > 0$ a real value such that

$$\tan\left(\frac{\lambda\pi}{4}\right)\tan\left(\frac{\lambda\pi}{2}\right) = \varepsilon_r,$$

we define the scalar potential $S_\lambda(r,\theta) = r^\lambda \phi_\lambda(\theta)$, where (r,θ) are the polar coordinates, and ϕ_λ is defined by

$$\begin{aligned}
&\phi_\lambda(\theta) = \sin(\lambda\theta) && \text{if } 0 \le \theta < \frac{\pi}{2},\\
&\phi_\lambda(\theta) = \frac{\sin\left(\frac{\lambda\pi}{2}\right)}{\cos\left(\frac{\lambda\pi}{4}\right)}\cos\left(\lambda\left(\theta - \frac{3\pi}{4}\right)\right) && \text{if } \frac{\pi}{2} \le \theta < \pi,\\
&\phi_\lambda(\theta) = \sin\left(\lambda\left(\frac{3\pi}{2} - \theta\right)\right) && \text{if } \pi \le \theta \le \frac{3\pi}{2}.
\end{aligned}$$

Then we solve the problem

$$\nabla\times\nabla\times\mathbf{E} = 0, \qquad \nabla\cdot(\varepsilon\mathbf{E}) = 0, \qquad \mathbf{E}\times\mathbf{n}_{|\partial\Omega} = \nabla S_\lambda\times\mathbf{n}.$$

The exact solution is given by $\mathbf{E} = \nabla S_\lambda$. We present two series of simulations. In table B.1, we use $\lambda = 0.535$, which leads to $\varepsilon_r = 0.499 \pm 10^{-3}$. In table B.2, we use $\lambda = 0.24$, which leads to $\varepsilon_r \simeq 7.55\ 10^{-2}$. In both case, we have computed the relative error in the $\mathbf{L}^2$-norm, and the column "COC" stands for the computed order of convergence. We have used several values of α, to show the effect of λ and α on the convergence rates. It seems that the convergence

h	$\alpha = 0.4$		$\alpha = 0.6$		$\alpha = 0.9$	
	rel.tol.	coc	rel.tol.	coc	rel.tol.	coc
0.2	2.332E-1	-	1.444E-1	-	1.249E-1	-
0.1	2.473E-1	-0.08	1.168E-1	0.31	8.846E-2	0.50
0.05	2.631E-1	-0.09	9.452E-2	0.31	6.186E-2	0.52
0.025	2.797E-1	-0.09	7.700E-2	0.30	4.289E-2	0.53
0.0125	2.968E-1	-0.09	6.312E-2	0.29	2.962E-2	0.53

Table B.1: $\mathbf{L}^2$-errors and computed order of convergence for $\lambda = 0.535$. We expect a convergence rate that is at most 0.535: it is almost optimal with $\alpha = 0.9$

rate improves when α is close to 1, which seems to be in contradiction with Remark B.5.4. Actually, if we write the example used here in the form of (B.2.10), we can use $\mathbf{g}$ which is divergence free. Then one can notice in the convergence proofs that in this case, we have only

$$r = \alpha - 1 + \tau\left(1 - \frac{\alpha}{\ell}\right),$$

which increases with α.

h	$\alpha = 0.4$		$\alpha = 0.6$		$\alpha = 0.9$	
	rel.tol.	coc	rel.tol.	coc	rel.tol.	coc
0.2	5.773E-1	-	4.739E-1	-	4.426E-1	-
0.1	6.209E-1	-0.11	4.507E-1	0.07	3.801E-1	0.22
0.05	6.711E-1	-0.11	4.413E-1	0.03	3.259E-1	0.22
0.025	7.180E-1	-0.10	4.452E-1	-0.01	2.788E-1	0.23
0.0125	7.564E-1	-0.08	4.602E-1	-0.05	2.380E-1	0.23

Table B.2: $\mathbf{L}^2$-errors and computed order of convergence for $\lambda = 0.24$. We expect a convergence rate that is at most 0.24: it is almost optimal with $\alpha = 0.9$

B.6 Eigenvalue problem

Now we turn our attention to the following problem: find $(\mathbf{E}, \lambda) \in \mathbf{H}_{0,\mathrm{curl}}(\Omega) \cap \mathbf{H}_{\mathrm{div}}(\Omega, \varepsilon) \times \mathbb{R}$ such that

$$\nabla \times \kappa \nabla \times \mathbf{E} = \lambda \varepsilon \mathbf{E}.$$

Using our discrete approximation, we want to prove an approximation result for the solutions of this problem.

B.6.1 Framework

In the rest of this section, we equip $\mathbf{L}^2(\Omega)$ with the inner product $(\mathbf{f}, \mathbf{g})_\varepsilon := \int_\Omega \varepsilon \mathbf{f} \cdot \mathbf{g}$. This inner product is equivalent to the usual inner product, owing to (B.2.13). The associated norm is denoted $\|\cdot\|_\varepsilon$. We introduce an operator A, using (B.2.10). For any $\mathbf{g} \in \mathbf{L}^2(\Omega)$, we denote $(\mathbf{E}, p)$ the solution of (B.2.10) and we set $A\mathbf{g} := \mathbf{E}$. Then A is well-defined $\mathbf{L}^2(\Omega) \to \mathbf{L}^2(\Omega)$, self-adjoint and, owing to Theorem B.2.1, compact. We want to study whether or not the discrete formulation can lead to a spectrally correct approximation in the sense of Theorem B.6.1.

Theorem B.6.1 (Spectral convergence [10, 116])**.** *Let X be an Hilbert space, and $A : X \to X$ a self-adjoint and compact operator. Let $\Theta = \{h_n;\ n \in \mathbb{N}\}$ be a discrete subset of $\mathbb{R}$ such that $h_n \to 0$ as $n \to +\infty$. Assume that there exists a family of operators $A_h : X \to X$ such that:*

- *for all $h \in \Theta$, A_h is a linear self-adjoint operator,*
- *A_h converges pointwise to A,*
- *the family is collectively compact.*

Let μ be an eigenvalue of A of multiplicity m and denote $\{\phi_j\}$, $j = 1, \cdots, m$, a set of associated orthonormal eigenvectors.

(i) For any $\epsilon > 0$ such that the disk $B(\mu, \epsilon)$ contains no other eigenvalues of A, there exists h_ϵ such that, for all $h < h_\epsilon$, A_h has exactly m eigenvalues (repeated according to their multiplicity) in the disk $B(\mu, \epsilon)$.

(ii) In addition, for $h < h_\epsilon$, if we denote $\mu_{h,j}$, $j = 1, \cdots, m$ the set of the eigenvalues of A_h in $B(\mu, \epsilon)$, there exists $c > 0$ such that

$$c|\mu - \mu_{h,j}| \leq \sum_{j,l=1}^{m} |\left((A - A_h)\phi_j, \phi_l\right)_X| + \sum_{j=1}^{m} \|(A - A_h)\phi_j\|_X^2. \tag{B.6.1}$$

We will check the assumptions of Theorem B.6.1 with the family $\{A_h\}$ defined by: for any $\mathbf{g} \in \mathbf{L}^2(\Omega)$, denote $(\mathbf{E}_h, p_h)$ the solution of (B.4.13) and set $A_h\mathbf{g} := \mathbf{E}_h - h^{2(1-\alpha)}\nabla p_h$. In this section, we consider (B.4.13) in the symmetric case, i.e. with $\theta = 1$ in the definition of a_h (B.4.12). We denote $\tau < \frac{1}{2}$ the minimal regularity of the problem (B.2.10), and we use in the following

$$\alpha \in \left(\frac{\ell(1-\tau)}{\ell-\tau}, 1\right), \qquad r := \min\left(1-\alpha, \alpha - 1 + \tau\left(1 - \frac{\alpha}{\ell}\right)\right).$$

In the following, we prove that the family A_h satisfies all the properties required in Theorem B.6.1.

B.6.2 Approximation result

We start by proving that the family $\{A_h\}$ is a family of self-adjoint bounded operators. Then we prove the pointwise convergence and we finally establish the collective compactness.

Lemma B.6.1. *For any h, $A_h : \mathbf{L}^2(\Omega) \to \mathbf{L}^2(\Omega)$ is a self-adjoint operator, i.e. for any $\mathbf{E}, \mathbf{F} \in \mathbf{L}^2(\Omega)$, the following holds*

$$(A_h\mathbf{E}, \mathbf{F})_\varepsilon = (\mathbf{E}, A_h\mathbf{F})_\varepsilon . \tag{B.6.2}$$

Proof. Let $\mathbf{E}, \mathbf{F} \in \mathbf{L}^2(\Omega)$ and denote $(\mathbf{E}_h, p_h), (\mathbf{F}_h, q_h) \in \mathbf{X}_h \times M_h$ the solutions of (B.4.13) with $\mathbf{g} = \mathbf{E}$ and $\mathbf{g} = \mathbf{F}$ respectively. By definition of $\mathbf{E}_h, p_h$, we have

$$a_h\left((\mathbf{E}_h, p_h), (\mathbf{F}_h, -q_h)\right) = (\mathbf{E}, \mathbf{F}_h)_\varepsilon - h^{2(1-\alpha)}\,(\mathbf{E}, \nabla q_h)_\varepsilon = (\mathbf{E}, A_h\mathbf{F})_\varepsilon .$$

Using the symmetry properties of a_h, together with the definition of $\mathbf{F}_h, q_h$, we infer

$$\begin{aligned} a_h\left((\mathbf{E}_h, p_h), (\mathbf{F}_h, -q_h)\right) &= a_h\left((\mathbf{F}_h, q_h), (\mathbf{E}_h, -p_h)\right) \\ &= (\mathbf{F}, \mathbf{E}_h)_\varepsilon - h^{2(1-\alpha)}\,(\mathbf{F}, \nabla p_h)_\varepsilon = (\mathbf{F}, A_h\mathbf{E})_\varepsilon . \end{aligned}$$

As a result, the operator A_h is self-adjoint on $\mathbf{L}^2(\Omega)$ equipped with the inner product $(\cdot,\cdot)_\varepsilon$. □

Lemma B.6.2. *With the above notations, there exists $c > 0$, uniform with respect to h such that,*

$$\forall \mathbf{E} \in \mathbf{L}^2(\Omega), \qquad \|A_h\mathbf{E} - A\mathbf{E}\|_\varepsilon \leq ch^{2r}\|\mathbf{E}\|_\varepsilon. \tag{B.6.3}$$

Proof. Let $\mathbf{E} \in \mathbf{L}^2(\Omega)$ and denote $(\mathbf{E}_h, p_h) \in \mathbf{X}_h \times M_h$ the solution of (B.4.13) with $\mathbf{g} = \mathbf{E}$. We also denote $p \in H_0^1(\Omega)$ such that $\nabla\times\kappa\nabla\times A\mathbf{E} + \varepsilon\nabla p = \varepsilon\mathbf{E}$. Using the triangular inequality, Theorems B.5.3 and B.5.1, the equivalence between the norms on $\mathbf{L}^2(\Omega)$ and the fact that $r \leq 1 - \alpha$, we infer

$$\begin{aligned} \|A_h\mathbf{E} - A\mathbf{E}\|_\varepsilon &\leq \|A\mathbf{E} - \mathbf{E}_h\|_\varepsilon + h^{2(1-\alpha)}\|\nabla p_h - \nabla p\|_\varepsilon + h^{2(1-\alpha)}\|\nabla p\|_\varepsilon \\ &\leq ch^{2r}\|\mathbf{E}\|_\varepsilon + ch^{1-\alpha}\|A\mathbf{E} - \mathbf{E}_h, p - p_h\|_h + ch^{2(1-\alpha)}\|\mathbf{E}\|_\varepsilon \leq ch^{2r}\|\mathbf{E}\|_\varepsilon. \end{aligned}$$

□

Note that this result is even stronger than pointwise convergence. Now let us turn our attention to the collective compactness. Recall that a set $\mathcal{A} := \{A_h : X \to X,\ h \in \Theta\}$ is said to be collectively compact if, for each bounded set $U \subset X$, the image set

$$\mathcal{A}U := \{A_h\mathbf{F},\ \mathbf{F} \in U,\ A_h \in \mathcal{A}\}$$

is relatively compact in X.

Lemma B.6.3. *The family $\{A_h\}_{h>0}$ is collectively compact.*

Proof. Owing to the compact embedding $\mathbf{H}^s(\Omega) \subset \mathbf{L}^2(\Omega)$ for any $s > 0$, it is sufficient to prove that there exists $s > 0$ and $c > 0$ such that, for any $\mathbf{g} \in \mathbf{L}^2(\Omega)$ and any $h > 0$,

$$\|A_h\mathbf{g}\|_{\mathbf{H}^s(\Omega)} \leq c\|\mathbf{g}\|_{\mathbf{L}^2(\Omega)}.$$

Let us take $\mathbf{g} \in \mathbf{L}^2(\Omega)$. Owing to the definition of $\mathbf{X}_h$ and M_h, we know that, for any $s \in \left(0, \frac{1}{2}\right)$, $A_h\mathbf{g} \in \mathbf{H}^s(\Omega)$. Moreover, there exists c only depending on s such that

$$\|A_h\mathbf{g}\|_{\mathbf{H}^s(\Omega)} \leq ch^{-s}\|A_h\mathbf{g}\|_{\mathbf{L}^2(\Omega)}.$$

Let us consider $s < r$. Notice that, in addition, $2s < \tau$. Using the triangular inequality, interpolation results, inverse inequality together with Theorems B.5.3 and B.2.1 leads to:

$$\begin{aligned}
\|A_h\mathbf{g}\|_{\mathbf{H}^s(\Omega)} &\leq \|A_h\mathbf{g} - A\mathbf{g}\|_{\mathbf{H}^s(\Omega)} + \|A\mathbf{g}\|_{\mathbf{H}^s(\Omega)} \\
&\leq c\|A_h\mathbf{g} - A\mathbf{g}\|^{\frac{1}{2}}_{\mathbf{L}^2(\Omega)}\|A_h\mathbf{g} - A\mathbf{g}\|^{\frac{1}{2}}_{\mathbf{H}^{2s}(\Omega)} + c\|\mathbf{g}\|_{\mathbf{L}^2(\Omega)} \\
&\leq ch^r\|\mathbf{g}\|^{\frac{1}{2}}_{\mathbf{L}^2(\Omega)}\left(h^{-s}\|A_h\mathbf{g}\|^{\frac{1}{2}}_{\mathbf{L}^2(\Omega)} + \|A\mathbf{g}\|^{\frac{1}{2}}_{\mathbf{H}^{2s}(\Omega)}\right) + c\|\mathbf{g}\|_{\mathbf{L}^2(\Omega)} \\
&\leq c\left(h^{r-s} + 1\right)\|\mathbf{g}\|_{\mathbf{L}^2(\Omega)}.
\end{aligned}$$

Since $r > s$, we have the collective compactness of $\{A_h\}$. □

Combining these three lemma, we conclude that the approximation is spectrally correct, in the sense of Theorem B.6.1.

B.6.3 Numerical illustration

In this section, we present some eigenvalues computations. We consider the square $\Omega = (-1, 1)^2$ in the plane. We split Ω in four subdomains

$$\Omega_1 = (0,1)^2, \qquad \Omega_2 = (-1,0)\times(0,1), \qquad \Omega_3 = (-1,0)^2, \qquad \Omega_4 = (0,1)\times(-1,0).$$

We use $\kappa \equiv 1$ in Ω, $\varepsilon_{|\Omega_1} = \varepsilon_{|\Omega_3} = 1$ and $\varepsilon_{|\Omega_2} = \varepsilon_{|\Omega_4} = \varepsilon_r$. A benchmark is provided for $\varepsilon_r^{-1} \in \{2, 10, 100, 10^8\}$ by M. Dauge, cf. [40]. Tables B.3 and B.4 show results for $\varepsilon_r = 0.5$ and $\varepsilon_r = 0.1$ respectively. The column "rel. tol." stands for the ratio $\frac{|\lambda_c - \lambda_r|}{\lambda_r}$, where λ_c (resp. λ_r) is the computed (resp. reference) eigenvalue. The reference values are those from the benchmark. The column "COC" stands for the computed order of convergence. The computations have been done using ARPACK (cf. [91]) with tolerance 10^{-8}. It is interesting to notice that, for every eigenvalue, the computed order of convergence seems to be constant for sufficiently small h. This expected behaviour is especially visible in the case $\varepsilon_r = 0.5$.

h	$\lambda_r \simeq 3.3175$		$\lambda_r \simeq 3.3663$		$\lambda_r \simeq 6.1863$		$\lambda_r \simeq 13.926$	
	rel. err.	COC	rel. err.	COC	rel. err.	COC	rel. err.	COC
0.2	9.364E-4	-	3.943E-3	-	1.439E-1	-	6.104E-1	-
0.1	1.833E-4	2.35	2.147E-3	0.88	1.734E-4	9.70	4.484E-1	0.44
0.05	3.751E-5	2.29	1.188E-3	0.85	2.241E-5	2.95	1.599E-1	1.49
0.025	8.405E-6	2.16	6.463E-4	0.88	2.833E-6	2.98	1.120E-5	13.8
0.0125	2.081E-6	2.01	3.439E-4	0.91	3.667E-7	2.95	1.478E-6	2.92

Table B.3: Approximation of the first four eigenvalues for $\varepsilon_r = 0.5$. We used $\alpha = 0.7$ in the simulations.

h	$\lambda_r \simeq 4.5339$		$\lambda_r \simeq 6.2503$		$\lambda_r \simeq 7.0371$		$\lambda_r \simeq 22.342$	
	rel. err.	COC	rel. err.	COC	rel. err.	COC	rel. err.	COC
0.2	4.559E-1	-	6.052E-1	-	6.410E-1	-	8.869E-1	-
0.1	2.859E-1	0.67	4.731E-1	0.36	5.310E-1	0.27	8.512E-1	0.06
0.05	3.306E-2	3.11	2.982E-1	0.67	3.763E-1	0.50	8.033E-1	0.08
0.025	2.154E-6	13.9	7.748E-2	1.94	1.772E-1	1.09	7.406E-1	0.12
0.0125	2.608E-7	3.05	3.258E-3	4.57	5.946E-7	18.2	6.602E-1	0.17

Table B.4: Approximation of the first four eigenvalues for $\varepsilon_r = 0.1$. We used $\alpha = 0.8$ in the simulations.

B.7 Appendix: Technical Lemmas

Let $\{\mathcal{T}_h\}_{h>0}$ be an affine shape-regular mesh family in $\mathbb{R}^d$, $d = 2, 3$. Let $T_K : \widehat{K} \longrightarrow K$ be the affine mapping that maps the reference element $\widehat{K}$ to K and let J_K be the Jacobian of T_K. It is a standard result that there are constants that depend only on $\widehat{K}$ and the shape regularity constants of the mesh family so that

$$\|J_K\| \le ch_K, \quad \|J_K^{-1}\| \le ch_K^{-1}, \qquad |\det(J_K)| \le ch_K^d, \quad |\det(J_K^{-1})| \le ch_K^{-d}, \tag{B.7.1}$$

where h_K is the diameter of K.

Lemma B.7.1. *For all $s \in [0,1]$, there is a constant c, uniform with respect to the mesh family, so that the following holds for all cells $K \in \mathcal{T}_h$ and all $\psi \in H^s(K)$ with zero average over K:*

$$\|\widehat{\psi}\|_{H^s(\widehat{K})} \le ch_K^{s-\frac{d}{2}} \|\psi\|_{H^s(K)}, \qquad \textit{where} \qquad \widehat{\psi}(\mathbf{x}) := \psi(T_K(\mathbf{x})) \tag{B.7.2}$$

Proof. Upon making the change of variable $\mathbf{x} = T_K(\widehat{\mathbf{x}})$ we obtain

$$\|\widehat{\psi}\|_{L^2(\widehat{K})} = |\det(J_K)|^{-\frac{1}{2}} \|\psi\|_{L^2(K)} \le ch_K^{-\frac{d}{2}} \|\psi\|_{L^2(K)}.$$

Likewise, using the fact that $\widehat{\psi}$ is of zero average, the Poincaré inequality implies

$$\begin{aligned} \|\widehat{\psi}\|_{H^1(\widehat{K})} &= \left(\|\widehat{\psi}\|^2_{L^2(\widehat{K})} + \|\nabla\widehat{\psi}\|^2_{L^2(\widehat{K})} \right)^{\frac{1}{2}} \le (c_p(\widehat{K}) + 1)^{\frac{1}{2}} \|\widehat{\nabla}\widehat{\psi}\|_{H^1(\widehat{K})} \\ &\le c|\det(J_K)|^{-\frac{1}{2}} \|J_K\| \|\nabla\psi\|_{L^2(K)} \le ch_K^{-\frac{d}{2}+1} \|\psi\|_{H^1(K)}. \end{aligned}$$

Then, the Riesz-Thorin theorem implies that

$$\|\widehat{\psi}\|_{\dot{H}^s(\widehat{K})} \leq c\, h_K^{s-\frac{3}{2}} \|\psi\|_{\dot{H}^s(K)},$$

where we defined $\dot{H}^s(E) := [\dot{L}^2(E), \dot{H}^1(E)]_{s,2}$ with $\dot{L}^2(E)$ and $\dot{H}^1(E)$ being the subspaces of the functions of zero average in $L^2(E)$ and $H^1(E)$, respectively. We conclude using Lemma B.7.2 □

Lemma B.7.2. *The spaces $[\dot{L}^2(E), \dot{H}^1(E)]_s$ and $[L^2(E), H^1(E)]_s \cap \dot{L}^2(E)$ are identical and the induced norms are identical, i.e., $\|v\|_{\dot{H}^s(E)} = \|v\|_{H^s(E)}$ for all for all $v \in [L^2(E), H^1(E)]_s \cap \dot{L}^2(E)$.*

Proof. One can use Lemma A1 from [64] with T being the projection onto $\dot{L}^2(\Omega)$. □

Lemma B.7.3. *The following holds for all $s \in [0,1]$ and for all $v \in H^s(\Omega)$,*

$$\sum_{K \in \mathcal{T}_h} \|v_{|K}\|^2_{H^s(K)} \leq \|v\|^2_{H^s(\Omega)}. \tag{B.7.3}$$

Proof. The result is evident for $s = 0$ and $s = 1$. Let us assume now that $s \in (0,1)$. Let v be a member of $H^s(\Omega)$. Recall that

$$\|v\|_{H^s(\Omega)} := \left(\int_0^\infty \mathcal{K}(t, v, \Omega)^2 t^{-1-2s} \mathrm{d}t \right)^{\frac{1}{2}},$$
$$\mathcal{K}(t, v, \Omega)^2 := \inf_{w \in H^1(\Omega)} \left(\|v - w\|^2_{L^2(\Omega)} + t^2 \|w\|^2_{H^1(\Omega)} \right).$$

For all $t \in \mathbb{R}_+$, let us denote v_t the function in $H^1(\Omega)$ that minimizes $\mathcal{K}(t, v, \Omega)$, i.e., $-t^2 \Delta v_t + t^2 v_t + (v_t - v) = 0$ over Ω with homogeneous Neumann boundary condition. Then

$$\begin{aligned}
\sum_{K \in \mathcal{T}_h} \|v_{|K}\|^2_{H^s(K)} &= \sum_{K \in \mathcal{T}_h} \int_0^\infty \mathcal{K}(t, v_{|K}, K)^2 t^{-1-2s} \mathrm{d}t \\
&\leq \sum_{K \in \mathcal{T}_h} \int_0^\infty \left(\|v_{|K} - v_{t|K}\|^2_{L^2(\Omega)} + t^2 \|v_{t|K}\|^2_{H^1(K)} \right) t^{-1-2s} \mathrm{d}t \\
&= \int_0^\infty \left(\sum_{K \in \mathcal{T}_h} \|v_{|K} - v_{t|K}\|^2_{L^2(K)} + t^2 \|v_{t|K}\|^2_{H^1(K)} \right) t^{-1-2s} \mathrm{d}t \\
&= \int_0^\infty \mathcal{K}(t, v, \Omega)^2 t^{-1-2s} \mathrm{d}t := \|v\|^2_{H^s(\Omega)}.
\end{aligned}$$

This completes the proof. □

We now state the main result of this section. It is a variant of Lemma 8.2 in [25] with the extra term $\|\boldsymbol{\phi}\|_{\mathbf{L}^2(K)}$. Our proof slightly differs from that in [25] since the proof therein did not appear convincing to us (actually, the embedding inequality at line 9, page 2224 in [25] has a constant that depends on the size of the cell; as result the estimate (8.11) therein is not uniform with respect to h).

Lemma B.7.4. *For all $k \in \mathbb{N}$ and all $\sigma \in (0, \frac{1}{2})$ there is c, uniform with respect to the mesh family, so that the following holds for all faces $F \in \mathcal{F}_h$ in the mesh, all polynomial function $\mathbf{v}$ of degree at most k, and all function $\boldsymbol{\phi} \in \mathbf{H}^\sigma(K) \cap \mathbf{H}(\mathrm{curl}, K)$*

$$\int_F (\mathbf{v}\times\mathbf{n})\cdot\boldsymbol{\phi} \le c\|\mathbf{v}\|_{\mathbf{L}^2(F)} h_F^{-\frac{1}{2}} (h_K^\sigma \|\boldsymbol{\phi}\|_{\mathbf{H}^\sigma(K)} + h_K \|\nabla\times\boldsymbol{\phi}\|_{\mathbf{L}^2(K)} + \|\boldsymbol{\phi}\|_{\mathbf{L}^2(K)}), \tag{B.7.4}$$

where K is either one of the two elements sharing the face F.

Proof. We restrict ourselves to three space dimensions. In two space dimensions $\boldsymbol{\phi}$ is scalar-valued and the proof must be modified accordingly. Let K be either one of the two elements sharing the face F. Let $\overline{\boldsymbol{\phi}}$ the average of $\boldsymbol{\phi}$ over K and let us denote $\boldsymbol{\psi} := \boldsymbol{\phi} - \overline{\boldsymbol{\phi}}$. Upon denoting $\widehat{\mathbf{v}}(\widehat{\mathbf{x}}) = J_K^T \mathbf{v}(T_K(\widehat{\mathbf{x}}))$ and $\widehat{\boldsymbol{\psi}}(\widehat{\mathbf{x}}) = J_K^T \boldsymbol{\psi}(T_K(\widehat{\mathbf{x}}))$, it is a standard result (see [111, 3.82]) that

$$\int_F (\mathbf{v}\times\mathbf{n})\cdot\boldsymbol{\psi} = \int_{\widehat{F}} (\widehat{\mathbf{v}}\times\widehat{\mathbf{n}})\cdot\widehat{\boldsymbol{\psi}},$$

where $\widehat{\mathbf{n}}$ is one of the two unit normals on $\widehat{F}$. Let us extend $\widehat{\mathbf{v}}$ by zero on $\partial\widehat{K}\backslash\widehat{F}$; then $\widehat{\mathbf{v}} \in: \mathbf{H}^{\frac{1}{2}-\sigma}(\partial\widehat{K})$ for all $\sigma > 0$. Note that it is not possible to have $\sigma = 0$. Now let $R : \mathbf{H}^{\frac{1}{2}-\sigma}(\partial\widehat{K}) \longrightarrow \mathbf{H}^{1-\sigma}(\widehat{K})$ be a standard lifting operator. There is a constant depending only on $\widehat{K}$ and σ so that

$$\|R\widehat{\mathbf{v}}\|_{\mathbf{L}^2(\widehat{K})} + \|\widehat{\nabla}\times R\widehat{\mathbf{v}}\|_{\mathbf{H}^{-\sigma}(\widehat{K})} \le c(\widehat{K},\sigma)\|R\widehat{\mathbf{v}}\|_{\mathbf{H}^{1-\sigma}(\widehat{K})} \le c' c(\widehat{K},\sigma)\|\widehat{\mathbf{v}}\|_{\mathbf{H}^{\frac{1}{2}-\sigma}(\widehat{F})},$$

where $\widehat{\nabla}\times$ is the curl operator in the coordinate system of $\widehat{K}$. Then we have

$$\begin{aligned}
\left|\int_{\widehat{F}} (\widehat{\mathbf{v}}\times\widehat{\mathbf{n}})\cdot\widehat{\boldsymbol{\psi}}\right| &= \left|\int_{\widehat{K}} \Big((R\widehat{\mathbf{v}})\cdot\widehat{\nabla}\times\widehat{\boldsymbol{\psi}} - \widehat{\boldsymbol{\psi}}\cdot\widehat{\nabla}\times(R\widehat{\mathbf{v}})\Big)\right| \\
&\le c\left(\|(R\widehat{\mathbf{v}})\|_{\mathbf{L}^2(\widehat{K})}\|\widehat{\nabla}\times\widehat{\boldsymbol{\psi}}\|_{\mathbf{L}^2(\widehat{K})} + \|\widehat{\boldsymbol{\psi}}\|_{\mathbf{H}_0^\sigma(\widehat{K})}\|\widehat{\nabla}\times(R\widehat{\mathbf{v}})\|_{\mathbf{H}^{-\sigma}(\widehat{K})}\right) \\
&\le c\left(\|\widehat{\nabla}\times\widehat{\boldsymbol{\psi}}\|_{\mathbf{L}^2(\widehat{K})} + \|\widehat{\boldsymbol{\psi}}\|_{\mathbf{H}_0^\sigma(\widehat{K})}\right)\|\widehat{\mathbf{v}}\|_{\mathbf{H}^{\frac{1}{2}-\sigma}(\widehat{F})} \\
&\le c\left(\|\widehat{\nabla}\times\widehat{\boldsymbol{\psi}}\|_{\mathbf{L}^2(\widehat{K})} + \|\widehat{\boldsymbol{\psi}}\|_{\mathbf{H}^\sigma(\widehat{K})}\right)\|\widehat{\mathbf{v}}\|_{\mathbf{H}^{\frac{1}{2}-\sigma}(\widehat{F})},
\end{aligned}$$

where we used that $\mathbf{H}^\sigma(\widehat{K}) = \mathbf{H}_0^\sigma(\widehat{K})$ for $\sigma \in [0, \frac{1}{2})$. Due to norm equivalence for discrete functions over $\widehat{K}$ and using that $\|J_K\| \le ch_K$, $h_K/h_F \le c$ and $|F| \le ch_F^2$ in three space dimensions, where c depends of the shape-regularity constant of the mesh family and the polynomial degree k, we have

$$\|\widehat{\mathbf{v}}\|_{\mathbf{H}^{\frac{1}{2}-\sigma}(\widehat{F})} \le c\|\widehat{\mathbf{v}}\|_{\mathbf{L}^2(\widehat{F})} \le c\|J_K\||F|^{-\frac{1}{2}}\|\mathbf{v}\|_{\mathbf{L}^2(F)} \le ch_K h_F^{-1}\|\mathbf{v}\|_{\mathbf{L}^2(F)} \le c'\|\mathbf{v}\|_{\mathbf{L}^2(F)}.$$

Using the identity (see [111, Cor. 3.58])

$$(\nabla\times\boldsymbol{\psi})(T_K(\widehat{\mathbf{x}})) = \frac{1}{\det(J_K)} J_K(\widehat{\nabla}\times\widehat{\boldsymbol{\psi}})(\widehat{\mathbf{x}}),$$

we obtain

$$\|\widehat{\nabla}\times\widehat{\boldsymbol{\psi}}\|_{\mathbf{L}^2(K)} \le c|\det(J_K)|^{\frac{1}{2}}\|J_K^{-1}\|\|\nabla\times\boldsymbol{\psi}\|_{\mathbf{L}^2(K)} \le ch_K^{\frac{1}{2}}\|\nabla\times\boldsymbol{\psi}\|_{\mathbf{L}^2(K)}.$$

Since the average of $\boldsymbol{\psi}$ over K is zero, we can use Lemma B.7.1 (with an extra scaling by $\|J_K\|$ for $\widehat{\boldsymbol{\psi}} = J_K^T \boldsymbol{\psi}(T_K)$) to deduce

$$\|\widehat{\boldsymbol{\psi}}\|_{\mathbf{H}^\sigma(\widehat{K})} \leq c h_K^{\sigma-\frac{1}{2}} \|\boldsymbol{\psi}\|_{\mathbf{H}^\sigma(K)}.$$

In conclusion we have obtained the following estimate:

$$\int_F (\mathbf{v}\times\mathbf{n})\cdot(\boldsymbol{\phi}-\overline{\boldsymbol{\phi}}) \leq c\left(h_K \, \|\nabla\times\boldsymbol{\phi}\|_{\mathbf{L}^2(K)} + h_K^\sigma \|\boldsymbol{\phi}-\overline{\boldsymbol{\phi}}\|_{\mathbf{H}^\sigma(K)}\right) h_K^{-\frac{1}{2}} \|\mathbf{v}\|_{\mathbf{L}^2(F)}.$$

Observing that $\|1\|_{\mathbf{H}^\sigma(K)} \leq \|1\|^{1-\sigma}_{\mathbf{L}^2(K)} \|1\|^{\sigma}_{\mathbf{H}^1(K)} = \|1\|_{\mathbf{L}^2(K)} = |K|^{\frac{1}{2}}$, we infer that

$$\|\boldsymbol{\phi}-\overline{\boldsymbol{\phi}}\|_{\mathbf{H}^\sigma(K)} \leq \|\boldsymbol{\phi}\|_{\mathbf{H}^\sigma(K)} + |\overline{\boldsymbol{\phi}}||K|^{\frac{1}{2}}$$

The Cauchy-Schwarz inequality yields $|\overline{\boldsymbol{\phi}}| \leq |K|^{-\frac{1}{2}} \|\boldsymbol{\phi}\|_{\mathbf{L}^2(K)}$; as a result,

$$\|\boldsymbol{\phi}-\overline{\boldsymbol{\phi}}\|_{\mathbf{H}^\sigma(K)} \leq \|\boldsymbol{\phi}\|_{\mathbf{H}^\sigma(K)} + \|\boldsymbol{\phi}\|_{\mathbf{L}^2(K)} \leq 2\|\boldsymbol{\phi}\|_{\mathbf{H}^\sigma(K)}.$$

Now we evaluate a bound from above on $\int_F (\mathbf{v}\times\mathbf{n})\cdot\overline{\boldsymbol{\phi}}$ as follows:

$$\begin{aligned}\left|\int_F (\mathbf{v}\times\mathbf{n})\cdot\overline{\boldsymbol{\phi}}\right| &\leq |\overline{\boldsymbol{\phi}}||F|^{\frac{1}{2}} \|\mathbf{v}\|_{\mathbf{L}^2(F)} \leq |K|^{-\frac{1}{2}} \|\boldsymbol{\phi}\|_{\mathbf{L}^2(K)} |F|^{\frac{1}{2}} \|\mathbf{v}\|_{\mathbf{L}^2(F)} \\ &\leq c\|\mathbf{v}\|_{\mathbf{L}^2(F)} h_F^{-\frac{1}{2}} \|\boldsymbol{\phi}\|_{\mathbf{L}^2(K)}.\end{aligned}$$

The result follows by combining all the above estimates. □

Lemma B.7.5. *Let $\alpha \in (\frac{1}{2}, 1)$. There is exists a constant $c(\alpha)$ so that*

$$\|u\|_{L^2(\Gamma)} \leq c(\alpha) \|u\|^{1-\frac{1}{2\alpha}}_{L^2(\Omega)} \|u\|^{\frac{1}{2\alpha}}_{H^\alpha(\Omega)}, \qquad \forall u \in H^\alpha(\Omega). \tag{B.7.5}$$

Similarly, for $s \in \left(0, \frac{1}{2}\right)$, there exists a constant $c(s)$ so that, for $\Theta := \frac{1-2s}{2(1-s)}$,

$$\|u\|_{L^2(\Gamma)} \leq c(s) \|u\|^{1-\Theta}_{H^s(\Omega)} \|u\|^{\Theta}_{H^1(\Omega)}, \qquad \forall u \in H^1(\Omega). \tag{B.7.6}$$

Proof. We start with the standard estimate

$$\|u\|_{L^2(\Gamma)} \leq c\|u\|^{\frac{1}{2}}_{L^2(\Omega)} \|u\|^{\frac{1}{2}}_{H^1(\Omega)}, \qquad \forall u \in H^1(\Omega),$$

which allows us to apply Lemma B.7.6. This implies that the trace operator is a continuous linear mapping from $[L^2(\Omega), H^1(\Omega)]_{\frac{1}{2},1}$ to $L^2(\Gamma)$. Then the re-iteration lemma implies that

$$\begin{aligned}[L^2(\Omega), H^\alpha(\Omega)]_{\frac{1}{2\alpha},1} &= [L^2(\Omega), [L^2(\Omega), H^1(\Omega)]_{\alpha,2}]_{\frac{1}{2\alpha},1} = [L^2(\Omega), H^1(\Omega)]_{\frac{1}{2},1} \\ [H^s(\Omega), H^1(\Omega)]_{\Theta,1} &= [[L^2(\Omega), H^1(\Omega)]_{s,2}, H^1(\Omega)]_{\Theta,1} = [L^2(\Omega), H^1(\Omega)]_{\frac{1}{2},1}\end{aligned}$$

The norms being equivalent, we can write:

$$\begin{aligned}\|u\|_{L^2(\Gamma)} \leq c\|u\|_{[L^2(\Omega),H^1(\Omega)]_{\frac{1}{2},1}} \leq c(\alpha)\|u\|_{[L^2(\Omega),H^\alpha(\Omega)]_{\frac{1}{2\alpha},1}} \leq c(\alpha)\|u\|^{1-\frac{1}{2\alpha}}_{L^2(\Omega)} \|u\|^{\frac{1}{2\alpha}}_{H^\alpha(\Omega)}, \\ \|u\|_{L^2(\Gamma)} \leq c\|u\|_{[L^2(\Omega),H^1(\Omega)]_{\frac{1}{2},1}} \leq c(s)\|u\|_{[H^s(\Omega),H^1(\Omega)]_{\Theta,1}} \leq c(s)\|u\|^{1-\Theta}_{H^s(\Omega)} \|u\|^{\Theta}_{H^1(\Omega)}.\end{aligned}$$

□

Lemma B.7.6 (Lions-Petree)**.** *Let $E_1 \subset E_0$ be two Banach spaces, with continuous embedding. Let L be a linear mapping $E_1 \to F$ with F another Banach space. For $s \in (0,1)$, L extends to a linear mapping from $[E_0, E_1]_{s,1}$ to F if and only if there exists $C > 0$ such that*

$$\forall u \in E_1, \qquad \|Lu\|_F \leq C\|u\|_{E_0}^{1-s}\|u\|_{E_1}^{s}.$$

Proof. See Lemma 25.3 in Tartar [143]. □

Annexe C

Electromagnetic induction in non-uniform domains

A. Giesecke [a], C. Nore [b,c], F. Stefani [a], G. Gerbeth [a], J. Léorat [d], F. Luddens [b,e], J.-L. Guermond [b,e]

Abstract

Kinematic simulations of the induction equation are carried out for different setups suitable for the von-Kármán-Sodium (VKS) dynamo experiment. The material properties of the flow driving impellers are modeled by means of high conducting and high permeability disks in a cylindrical volume filled with a conducting fluid. Two entirely different numerical codes are mutually validated by showing quantitative agreement on Ohmic decay and kinematic dynamo problems using various configurations and physical parameters. Field geometry and growth rates are strongly modified by the material properties of the disks even if the disks are thin. In contrast the influence of external boundary conditions remains small.

Utilizing a VKS like mean fluid flow and high permeability disks yields a reduction of the critical magnetic Reynolds number Rm^c for the onset of dynamo action of the simplest non-axisymmetric field mode. However this threshold reduction is not sufficient to fully explain the VKS experiment. We show that this reduction of Rm^c is influenced by small variations in the flow configuration so that the observed reduction may be changed with respect to small modifications of setup and properties of turbulence.

C.1 Introduction

Magnetic fields of galaxies, stars or planets are produced by dynamo action in a homogenous medium in which a conducting fluid flow provides for generation of field energy. During the past decade the understanding of the field generation mechanism has considerably benefitted from the examination of dynamo action in the laboratory. However, realization of dynamo action in laboratories at least requires the magnetic Reynolds number $\mathrm{Rm} = UL/\eta$ (where U

[a] Helmholtz-Zentrum Dresden-Rossendorf, PO Box 510119, 01314 Dresden, Germany
[b] Laboratoire d'Informatique pour la Mécanique et les Sciences de l'Ingénieur, CNRS, BP 133, 91403 Orsay Cedex, France
[c] Institut Universitaire de France, 103 Bd Saint-Michel, 75005 Paris, France
[d] Luth, Observatoire de Paris-Meudon, place Janssen, 92195 Meudon, France
[e] Department of Mathematics, Texas A&M University 3368 TAMU, College Station, TX 77843-3368, USA

and L represent typical velocity and length scales and η denotes the magnetic diffusivity) to exceed a threshold of the order of $\mathrm{Rm}^c \sim 10...100$. From the parameter values of liquid sodium – the best known liquid conductor – at standard laboratory conditions ($\eta = 1/\mu_0\sigma \approx 0.1$ m^2/s and $L \approx 1$ m, where μ_0 is the vacuum permeability and σ the electrical conductivity) it becomes immediately obvious that self excitation of magnetic fields in the laboratory needs typical velocity magnitudes of $U \sim 10$ m/s, which is already quite demanding. Therefore, the first successful dynamo experiments performed by [98, 99] utilized soft-iron material so that the magnetic diffusivity is reduced (this issue deserves indeed a specific study and is examined below) and the magnetic Reynolds number is (at least locally) increased. Although these experiments cannot be classified as hydromagnetic dynamos (no fluid flow and therefore no backreaction of the field on a fluid motion is possible) they allowed the examination of distinct dynamical regimes manifested in steady, oscillating or reversing fields. It is interesting to note that these results did not initiate further numerical studies on induction in the presence of soft iron domains.

The effects of internal and external walls with finite permeability and conductivity have been examined in [9, 8] by analytically solving a one dimensional kinematic dynamo driven by an α-effect. A facilitation of dynamo action is obtained for increasing conductivity and/or permeability of given inner and outer walls. This threshold reduction is monotonous in the case of a stationary dynamo mode but non monotonous in the case of a time dependent dynamo due to dissipation from eddy currents induced within the container walls. The authors also assumed that a mean flow may increase the dynamo threshold due to additional dissipation. More recently, [127] performed nonlinear simulations in a sphere with a flow driven by the counter rotation of the two hemispherical parts of the outer sphere. Their setup and geometry are only roughly representative for the VKS configuration (they also included an inner sphere made of a solid electrical insulator). They performed nonlinear simulations simultaneously varying permeability and conductivity of the external walls, applying thin wall conditions (where the wall thickness $h \to 0$ and the permeability $\mu_\mathrm{r} \to \infty$ and conductivity $\sigma \to \infty$ so that the product $h\mu_\mathrm{r}$ ($h\sigma$) remains finite). Only a few runs exhibit dynamo action and their results cannot yield any general conclusion about the influence of the wall permeability or conductivity on the dynamo threshold.

A possibility to increase the effective magnetic Reynolds number in fluid flow driven dynamo experiments arises from the addition of tiny ferrous particles to the fluid medium leading to an uniform enlargement of the relative permeability [50, 43]. Since the amount of particles is limited so as to retain reasonable fluid properties, the maximum fluid permeability achievable by this technique is $\mu_\mathrm{r} \approx 2$. The main effect found in the simulations of [43] was a reduced decay of the initial field but not a smaller threshold (essentially because of nonmonotonous behavior of the growth rate with respect to Rm).

Another type of ferromagnetic influence on dynamo action is observed in the von-Kármán-sodium (VKS) dynamo. In the VKS experiment a turbulent flow of liquid sodium is driven by two counterotating impellers located at the opposite end caps of a cylindrical domain [110]. Dynamo action is only obtained when the impellers are made of soft-iron with $\mu_\mathrm{r} \sim 100$ [153]. Recently it has been shown in [58] that these soft-iron impellers essentially determine the geometry and the growth rates of the magnetic field by locally enhancing the magnetic Reynolds number and by enforcing internal boundary conditions for the magnetic field at the material interfaces. We conjecture that non-homogenous distributions of the material coefficients μ_r and σ may support dynamo action because gradients of μ_r and σ modify the induction equation by coupling toroidal and poloidal components of the magnetic fields which

is essential for the occurrence of dynamo action. An example for this dynamo type has been presented in [28] where it was shown that even a straight flow without shear over an (infinite) conducting plate with sinusoidal variation of the conductivity is able to produce dynamo action. However, an experimental realization of this setup would require either an unachievable large magnetic Reynolds number or rather large variations of the conductivity ($\gtrsim$ factor of 100 and with a mean value which should be of the order of the fluid conductivity). On the other hand, large permeability variations are more easily achievable experimentally, for instance the relative permeability of soft-iron alloys easily attains values of several thousands. Although these dynamos are of little astrophysical relevance the experiments of Lowes and Wilkinson and in particular the rich dynamical behavior of the VKS dynamo demonstrate the usefulness of such models.

The purpose of the present work is to validate the numerical tool necessary to establish a basic understanding of the influence of material properties on the induction process. Emphasis is given to the problem of free decay in cylindrical geometry where two disks characterized by high conductivity/permeability and their thickness are inserted in the interior of a cylindrical container filled with a conducting fluid. To demonstrate the reliability of our results we use two different numerical approaches and show that both methods give results in agreement. The study is completed by an application of a mean flow as it occurs in the VKS experiment in combination with two high permeability disks.

C.2 Induction equation in heterogenous domains

From Faraday's Law in combination with Ohm's Law one immediately retrieves the induction equation that determines the temporal behavior of the magnetic flux density $\mathbf{B}$:

$$\frac{\partial \mathbf{B}}{\partial t} = \nabla \times (\mathbf{u} \times \mathbf{B} - \frac{1}{\mu_0 \sigma} \nabla \times \frac{\mathbf{B}}{\mu_\mathrm{r}}), \tag{C.2.1}$$

where $\mathbf{u}$ denotes the flow velocity, σ the electric conductivity, μ_0 the vacuum permeability and μ_r the relative permeability. In case of spatially varying distributions of conductivity and permeability equation (C.2.1) can be rewritten in the form:

$$\begin{aligned} \frac{\partial \mathbf{B}}{\partial t} &= \nabla \times (\mathbf{u} \times \mathbf{B}) + \frac{1}{\mu_0 \mu_\mathrm{r} \sigma} \nabla^2 \mathbf{B} + \frac{1}{\mu_0 \mu_\mathrm{r} \sigma} \nabla \times (\nabla \ln \mu_\mathrm{r} \times \mathbf{B}) \\ &\quad - \frac{1}{\mu_0 \mu_\mathrm{r} \sigma} (\nabla \ln \mu_\mathrm{r} + \nabla \ln \sigma) \times (\nabla \ln \mu_\mathrm{r} \times \mathbf{B}) + \frac{1}{\mu_0 \mu_\mathrm{r} \sigma} (\nabla \ln \mu_\mathrm{r} + \nabla \ln \sigma) \times (\nabla \times \mathbf{B}). \end{aligned} \tag{C.2.2}$$

The terms on the right-hand-side that involve gradients of μ_r and σ potentially couple the toroidal and poloidal field components which is known to be essential for the existence of a dynamo. The lack of symmetry between the terms containing $\nabla \mu_\mathrm{r}$ and $\nabla \sigma$ indicates a distinct impact of σ and μ_r. This difference of behavior can also be anticipated by looking at the jump conditions that the electric and magnetic fields have to fulfill at material interfaces. At interfaces between materials 1 and 2 that exhibit a jump in conductivity σ and/or in relative permeability μ_r the normal component of the magnetic flux density is continuous whereas the tangential components exhibit a jump described by the ratio of the permeabilities. In case of conductivity discontinuities, the tangential components of the electric field are continuous and the normal component of the electric current is continuous. Mathematically these jump

conditions are given by (see e.g. [74] [74])

$$\begin{aligned} \mathbf{n}\cdot(\mathbf{B}_1-\mathbf{B}_2) &= 0, \qquad \mathbf{n}\times\left(\frac{\mathbf{B}_1}{\mu_{\mathrm{r},1}}-\frac{\mathbf{B}_2}{\mu_{\mathrm{r},2}}\right) = 0, \\ \mathbf{n}\cdot(\mathbf{j}_1-\mathbf{j}_2) &= 0, \qquad \mathbf{n}\times(\mathbf{E}_1-\mathbf{E}_2) = 0, \end{aligned} \tag{C.2.3}$$

where $\mathbf{n}$ denotes the unit vector in the normal direction on the interface between materials 1 and 2. If there is no contribution of the flow, the continuity of the normal current leads to the discontinuity of the normal electric field in the ratio of the conductivities. Although the transmission conditions (C.2.3) are standard, their dynamical consequences in flows at large Rm are largely unknown.

C.3 Numerical schemes

Two different numerical algorithms and codes are used for the numerical solution of problems involving the kinematic induction equation (C.2.1). The first one is a combined finite volume/boundary element method FV/BEM [136]. It is a grid based approach which provides a flexible scheme that utilizes a local discretization and intrinsically maintains the solenoidal character of the magnetic field.

The second solution method is based on a Spectral/Finite Element approximation technique denoted SFEMaNS for Spectral/Finite Elements for Maxwell and Navier-Stokes equations. Taking advantage of the cylindrical symmetry of the domains, Fourier modes are used in the azimuthal direction and finite elements are used in the meridional plane. For each Fourier mode this leads to independent two-dimensional-problems in the meridian plane.

C.3.1 Hybrid finite volume/boundary element method

We start with the induction equation in conservative form

$$\frac{\partial\mathbf{B}}{\partial t}+\nabla\times\mathbf{E}=\mathbf{0}, \tag{C.3.1}$$

where the electric field $\mathbf{E}$ is given by

$$\mathbf{E}=-\mathbf{u}\times\mathbf{B}+\eta\nabla\times\frac{\mathbf{B}}{\mu_{\mathrm{r}}} \tag{C.3.2}$$

and $\eta=1/\mu_0\sigma$ is the magnetic diffusivity. For the sake of simplicity we give a short sketch for the treatment of inhomogeneous conductivity and permeability only in Cartesian coordinates. The scheme can easily be adapted to different (orthogonal) coordinate systems (e.g. cylindrical or spherical coordinate system) making use of generalized coordinates [140, 141].

In the finite volume scheme the grid representation of the magnetic field is given by a staggered collocation of the field components that are interpreted as an approximation of the (cell-)face average:

$$\overline{B}_x^{i-1/2,j,k}\approx\frac{1}{\Delta y\Delta z}\int_{\Gamma_{yz}}B_x(x_{i-1/2},y,z)\mathrm{d}y\mathrm{d}z, \tag{C.3.3}$$

where the integration domain Γ corresponds to the surface of a single cell-face: $\Gamma_{yz}=[y_{j-1/2},y_{j+1/2}]\times[z_{k-1/2},z_{k+1/2}]$ (see figure C.1). A comparable definition is applied to the

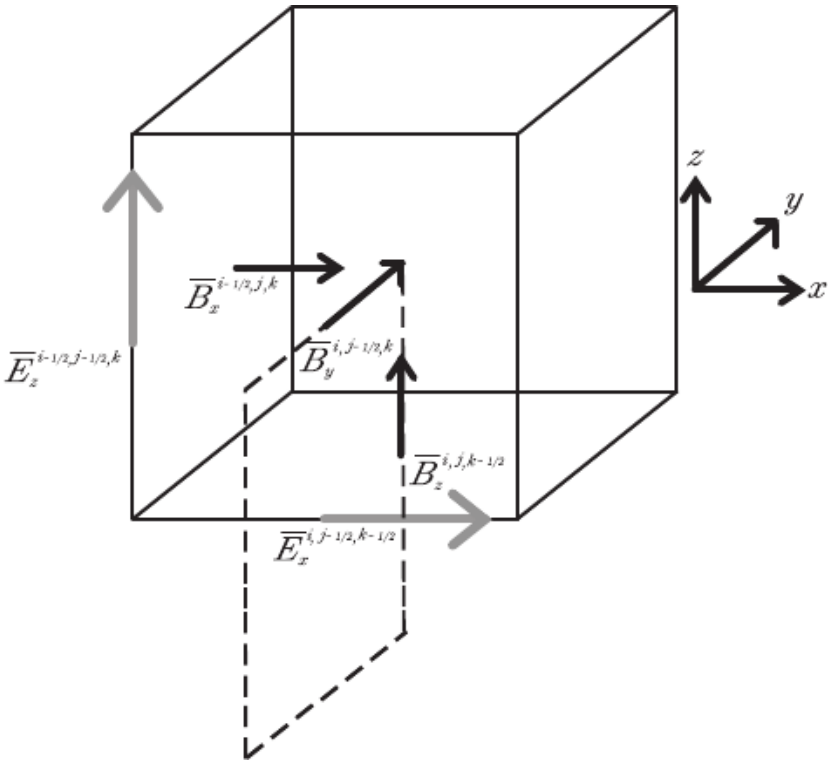

Figure C.1: Localization of vector quantities on a grid cell ijk with the cell center located at (x_i, y_j, z_k). The dotted curve denotes the path along which the integration of $\mathbf{B}$ is executed for the computation of $\overline{E}_x^{i,j-1/2,k-1/2}$.

electric field which is localized at the center of a cell edge and which is defined as the line average (see figure C.1):

$$\overline{E}_x^{i,j-1/2,k-1/2} \approx \frac{1}{\Delta x}\int_{x^{i-1/2}}^{x^{i+1/2}} E_x(x, y_{j-1/2}, z_{k-1/2})\mathrm{d}x. \tag{C.3.4}$$

Similar definitions hold for the components $\overline{B}_y^{i,j-1/2,k}$ and $\overline{B}_z^{i,j,k-1/2}$, and for $\overline{E}_y^{i-1/2,j,k-1/2}$ and $\overline{E}_z^{i-1/2,j-1/2,k}$, respectively.

The finite volume discretization of the induction equation reads

$$\begin{aligned}\frac{\mathrm{d}}{\mathrm{d}t}\overline{B}_x^{i-1/2,j,k} &= -\frac{\overline{E}_z^{i-1/2,j+1/2,k}(t) - \overline{E}_z^{i-1/2,j-1/2,k}(t)}{\Delta y} \\ &\quad + \frac{\overline{E}_y^{i-1/2,j,k+1/2}(t) - \overline{E}_y^{i-1/2,j,k-1/2}(t)}{\Delta z}\end{aligned} \tag{C.3.5}$$

and it can easily been shown that this approach preserves the $\nabla \cdot \mathbf{B}$ constraint for all times (to machine accuracy) if the initial field is divergence free.

Material coefficients

In the following we only discuss the treatment of the diffusive part of the electric field, $\mathbf{E} = \eta\nabla \times \mathbf{B}/\mu_r$ because the induction contribution ($\propto -\mathbf{u} \times \mathbf{B}$) does not involve the material

properties and can be treated separately in the framework of an operator splitting scheme (see e.g. [72] [72], [57] [57], [157] [157]). To obtain the computation directive for the electric field the magnetic field has to be integrated along a (closed path) around $\overline{E}_{x(,y,z)}$ at the edge of a grid cell (see dotted curve in figure C.1).

$$\overline{E}_x \approx \frac{1}{\Gamma}\int_{\Gamma_{yz}} E_x \mathrm{d}A = \frac{1}{\Gamma}\int_{\Gamma_{yz}} \eta\left(\nabla\times\frac{\mathbf{B}}{\mu_\mathrm{r}}\right)\mathrm{d}A \approx \frac{\overline{\eta}}{\Delta y\Delta z}\int_{\partial\Gamma_{yz}}\frac{\mathbf{B}}{\mu_\mathrm{r}}\mathrm{d}\mathbf{l}, \tag{C.3.6}$$

where $\Gamma = \Delta y\Delta z$ is the surface surrounded by the path Γ_{yz} and $\overline{\eta}$ is the average diffusivity ($\eta = (\mu_0\sigma)^{-1}$) "seen" by the electric field. Unlike vectorial quantities the material coefficients are scalar quantities that are localized in the center of a grid cell. The consideration of spatial variations and/or jumps in conductivity respectively permeability is straightforward if corresponding averaging procedures for σ or μ_r are applied [68]. For the component $\overline{E}_x$ the discretization of equation (C.3.6) leads to

$$\begin{aligned}\overline{E}_x^{i,j-1/2,k-1/2} = \overline{\eta}_{i,j-1/2,k-1/2}\Bigg[&\frac{1}{\Delta y}\left(\frac{\overline{B}_z^{i,j,k-1/2}}{(\overline{\mu}_\mathrm{r})_{i,j,k-1/2}} - \frac{\overline{B}_z^{i,j-1,k-1/2}}{(\overline{\mu}_\mathrm{r})_{i,j-1,k-1/2}}\right)\\ &-\frac{1}{\Delta z}\left(\frac{\overline{B}_y^{i,j-1/2,k}}{(\overline{\mu}_\mathrm{r})_{i,j-1/2,k}} - \frac{\overline{B}_y^{i,j-1/2,k-1}}{(\overline{\mu}_\mathrm{r})_{i,j-1/2,k-1}}\right)\Bigg].\end{aligned} \tag{C.3.7}$$

In equation (C.3.7), $\overline{\eta}_{i,j-1/2,k-1/2}$ represents the diffusivity that is seen by the electric field component $\overline{E}_x^{i,j-1/2,k-1/2}$ at the edge of the grid cell (ijk) and which is given by the arithmetic average of the diffusivity of the four adjacent cells:

$$\overline{\eta}_{i,j-1/2,k-1/2} = \frac{1}{4}\left(\eta_{i,j,k} + \eta_{i,j-1,k} + \eta_{i,j,k-1} + \eta_{i,j-1,k-1}\right). \tag{C.3.8}$$

Similarly, $\overline{\mu_\mathrm{r}}$ denotes the relative permeability that is seen by the magnetic field components ($\overline{B}_y$ and $\overline{B}_z$) at the interface between two adjacent grid cells. For instance, for the case considered in equation (C.3.7), μ_r is defined as follows:

$$\begin{aligned}\text{for } \overline{B}_y^{i,j-1/2,k}\text{:}\quad (\overline{\mu}_\mathrm{r})_{i,j-1/2,k} &= \frac{2(\mu_\mathrm{r})_{i,j,k}(\mu_\mathrm{r})_{i,j-1,k}}{(\mu_\mathrm{r})_{i,j,k}+(\mu_\mathrm{r})_{i,j-1,k}},\\ \text{for } \overline{B}_z^{i,j,k-1/2}\text{:}\quad (\overline{\mu}_\mathrm{r})_{i,j,k-1/2} &= \frac{2(\mu_\mathrm{r})_{i,j,k}(\mu_\mathrm{r})_{i,j,k-1}}{(\mu_\mathrm{r})_{i,j,k}+(\mu_\mathrm{r})_{i,j,k-1}}.\end{aligned} \tag{C.3.9}$$

For the computation of $\overline{E}_y^{i-1/2,j,k-1/2}$ and $\overline{E}_z^{i-1/2,j-1/2,k}$ equations (C.3.8) and (C.3.9) have to be adjusted according to the localization and the field components involved. Applying the averaging rules (C.3.8) and (C.3.9) to the computation of the "diffusive" part of the electric field results in a scheme that intrinsically fulfills the jump conditions (C.2.3) at material interfaces. The scheme is robust and simple to implement, however, the averaging procedure results in a artificial smoothing of parameter jumps at interfaces and in concave corners additional difficulties might occur caused by ambiguous expressions for μ_r. Furthermore in the simple realization presented above, the parameter range is restricted. For larger jumps of μ_r or σ a more careful treatment of the discontinuities at the material interfaces is necessary which would require a more elaborate field reconstruction that makes use of slope limiters.

Boundary conditions

In numerical simulations of laboratory dynamo action insulating boundary conditions are often simplified by assuming vanishing tangential fields (VTF, sometimes also called pseudo vacuum condition). In fact, a restriction of the boundary magnetic field to its normal component resembles an artifical but numerically convenient setup where the exterior of the computational domain is characterized by an infinite permeability. VTF boundary conditions usually overestimate the field growth rates in many dynamo problems. Therefore a more elaborate treatment of the field behavior at the boundary is recommended which is nontrivial in non-spherical coordinate systems. Insulating domains are characterized by a vanishing current $\mathbf{j} \propto \nabla \times \mathbf{B} = \mathbf{0}$ so that $\mathbf{B}$ can be expressed as the gradient of a scalar field Φ (assuming that the insulating domain is simply connected) which fulfills the Laplace equation:

$$\mathbf{B} = -\nabla\Phi \quad \text{with} \quad \nabla^2\Phi = 0, \quad \Phi \to \mathrm{O}(r^{-2}) \text{ for } r \to \infty. \tag{C.3.10}$$

Integrating $\nabla^2\Phi = 0$ and adoption of Green's 2nd theorem leads to

$$\Phi(\mathbf{r}) = 2\int_\Gamma G(\mathbf{r},\mathbf{r}') \underbrace{\frac{\partial\Phi(\mathbf{r}')}{\partial n}}_{-B^{\mathrm{n}}(\mathbf{r}')} - \Phi(\mathbf{r}')\frac{\partial G(\mathbf{r},\mathbf{r}')}{\partial n}\mathrm{d}\Gamma(\mathbf{r}'), \tag{C.3.11}$$

where $G(\mathbf{r},\mathbf{r}') = -(4\pi\,|\mathbf{r}-\mathbf{r}'|)^{-1}$ is the Greens function (with $\nabla^2 G(\mathbf{r},\mathbf{r}') = -\delta(\mathbf{r}-\mathbf{r}')$) and $\partial/\partial n$ is the normal derivative on the surface element $\mathrm{d}\Gamma$ so that $\partial_n\Phi = -B^{\mathrm{n}}$ yields the normal component of $\mathbf{B}$ on $\mathrm{d}\Gamma$. The tangential components of the magnetic field at the boundary $B^\tau = \mathbf{e}_\tau \cdot \mathbf{B} = -\mathbf{e}_\tau \cdot \nabla\Phi(\mathbf{r})$ are computed from equation (C.3.11) as follows :

$$B^\tau = 2\int_\Gamma \mathbf{e}_\tau \cdot \left(\Phi(\mathbf{r}')\nabla_r\frac{\partial G(\mathbf{r},\mathbf{r}')}{\partial n} + B^{\mathrm{n}}(\mathbf{r}')\nabla_r G(\mathbf{r},\mathbf{r}')\right)\mathrm{d}\Gamma(\mathbf{r}'), \tag{C.3.12}$$

where $\mathbf{e}_\tau$ represents a tangential unit vector on the surface element $\mathrm{d}\Gamma(\mathbf{r}')$. In fact, there are two orthogonal tangential directions on the boundary and equation (C.3.12) is valid independently for both orientations. After the subdivision of the surface Γ in boundary elements Γ_j with $\Gamma = \cup\Gamma_j$ the approximate potential $\Phi_i = \Phi(\mathbf{r_i})$ and the tangential field $B_i^\tau = B^\tau(\mathbf{r}_i) = -\mathbf{e}_\tau \cdot (\nabla\Phi_i)$ in discretized form are given by

$$\begin{aligned}
\frac{1}{2}\Phi_i &= -\sum_j \left(\int_{\Gamma_j}\frac{\partial G}{\partial n}(\mathbf{r}_i,\mathbf{r}')\mathrm{d}\Gamma'_j\right)\Phi_j, -\sum_j\left(\int_{\Gamma_j} G(\mathbf{r}_i,\mathbf{r}')\mathrm{d}\Gamma'_j\right)B_j^{\mathrm{n}} \\
B_i^\tau &= \sum_j\left(\int_{\Gamma_j} 2\mathbf{e}_\tau\cdot\nabla_r\frac{\partial G}{\partial n}(\mathbf{r}_i,\mathbf{r}')\mathrm{d}\Gamma'_j\right)\Phi_j + \sum_j\left(\int_{\Gamma_j} 2\mathbf{e}_\tau\cdot\nabla_r G(\mathbf{r}_i,\mathbf{r}')\mathrm{d}\Gamma'_j\right)B_j^{\mathrm{n}}.
\end{aligned} \tag{C.3.13}$$

The system of equations (C.3.13) gives a linear, non local relation for the tangential field components at the boundary in terms of the normal components and closes the problem of magnetic induction in finite (connected) domains with insulating boundaries [73]. A more detailed description of the scheme can be found in [57].

C.3.2 Spectral/Finite Elements for Maxwell equations

The conducting part of the computational domain is denoted Ω_c, the non-conducting part (vacuum) is denoted Ω_v, and we set $\Omega := \Omega_c \cup \Omega_v$. We use the subscript c for the conducting

part and v for the vacuum. We assume that Ω_c is partitioned into subregions $\Omega_{c1}, \cdots, \Omega_{cN}$, so that the magnetic permeability in each subregion Ω_{ci}, say μ^{ci}, is smooth. We denote Σ_μ the interface between all the conducting subregions. We denote Σ the interface between Ω_c and Ω_v. A sketch of the computational domain is displayed on figure D.1(a).

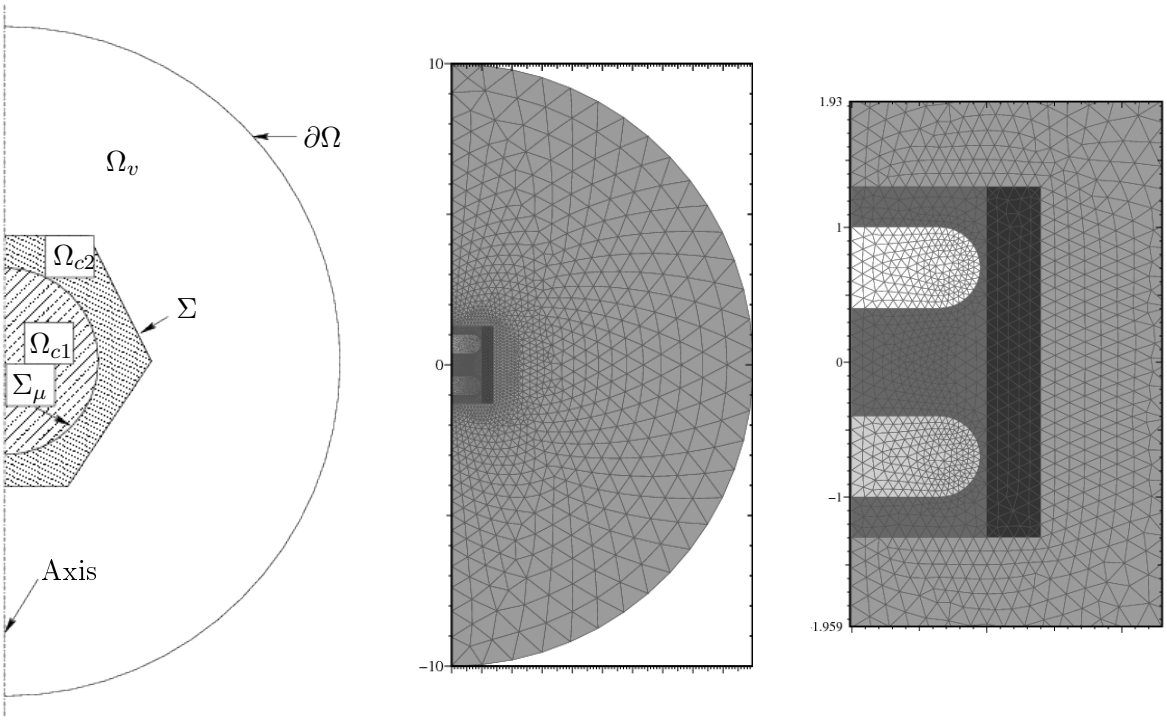

(a) (b) (c)

Figure C.2: Example of a computational domain Ω with various boundaries: (a) sketch with arbitrary axisymmetrical domains showing the conducting domain Ω_c (shaded regions) and the vacuum Ω_v (non-shaded domain) with the interfaces Σ_μ and Σ, (b) meridian triangular mesh used in section C.4 with disks of $d = 0.6$ thickness with SFEMaNS (1 point out of 4 has been represented), (c) zoom of (b).

The electric field $\mathbf{E}$ and magnetic field $\mathbf{H}$ in Ω_c and Ω_v solve the following system:

$$\text{(C.3.14)} \qquad \frac{\partial(\mu^c \mathbf{H}^c)}{\partial t} = -\nabla \times \mathbf{E}^c, \qquad \frac{\partial(\mu^v \mathbf{H}^v)}{\partial t} = -\nabla \times \mathbf{E}^v,$$

$$\text{(C.3.15)} \qquad \nabla\cdot(\mu^c \mathbf{H}^c) = 0, \qquad \nabla\cdot(\mu^v \mathbf{H}^v) = 0,$$

$$\text{(C.3.16)} \qquad \mathbf{E^c} = -\mathbf{u} \times \mu^c \mathbf{H^c} + \frac{1}{\sigma}\nabla\times\mathbf{H^c}, \qquad \nabla\times\mathbf{H}^v = \mathbf{0}$$

and the following transmission conditions hold across Σ_μ and Σ:

$$\text{(C.3.17)} \qquad \mathbf{H}^{ci} \times \mathbf{n}^{ci} + \mathbf{H}^{cj} \times \mathbf{n}^{cj} = \mathbf{0}, \qquad \mathbf{H}^c \times \mathbf{n}^c + \mathbf{H}^v \times \mathbf{n}^v = \mathbf{0},$$

$$\text{(C.3.18)} \qquad \mu^{ci}\mathbf{H}^{ci} \cdot \mathbf{n}^{ci} + \mu^{cj}\mathbf{H}^{cj} \cdot \mathbf{n}^{cj} = 0, \qquad \mu^c\mathbf{H}^c \cdot \mathbf{n}^c + \mu^v\mathbf{H}^v \cdot \mathbf{n}^v = 0,$$

$$\text{(C.3.19)} \qquad \mathbf{E}^{ci} \times \mathbf{n}^{ci} + \mathbf{E}^{cj} \times \mathbf{n}^{cj} = \mathbf{0}, \qquad \mathbf{E}^c \times \mathbf{n}^c + \mathbf{E}^v \times \mathbf{n}^v = \mathbf{0},$$

where $\mathbf{n}^c$ (resp. $\mathbf{n}^v$) is the unit outward normal on Σ, i.e. $\mathbf{n}^c$ points from Ω_c to Ω_v (resp. from Ω_v to Ω_c), and $\mathbf{n}^{ci}$ is the unit normal on Σ_μ, i.e. $\mathbf{n}^{ci}$ points from Ω_{ci} to Ω_{cj}.

Weak formulation

The finite element solution is computed by solving a weak form of the system (C.3.14)-(C.3.19). We proceed as follows in Ω_{ci}. Multiplying the induction equation in Ω_{ci} by a test-function $\mathbf{b}$, integrating over Ω_{ci}, integrating by parts and using (C.3.16) gives

$$\begin{aligned} 0 &= \int_{\Omega_{ci}} \frac{\partial(\mu^{ci}\mathbf{H}^{ci})}{\partial t}\cdot\mathbf{b} + \int_{\Omega_{ci}} \nabla\times\mathbf{E}^{ci}\cdot\mathbf{b} \\ &= \int_{\Omega_{ci}} \frac{\partial(\mu^{ci}\mathbf{H}^{ci})}{\partial t}\cdot\mathbf{b} + \int_{\Omega_{ci}} \mathbf{E}^{ci}\cdot\nabla\times\mathbf{b} + \int_{\partial\Omega_{ci}} (\mathbf{n}^{ci}\times\mathbf{E}^{ci})\cdot\mathbf{b} \\ &= \int_{\Omega_{ci}} \frac{\partial(\mu^{ci}\mathbf{H}^{ci})}{\partial t}\cdot\mathbf{b} + \int_{\Omega_{ci}} \left(-\mathbf{u}\times\mu^{ci}\mathbf{H}^{ci} + \frac{1}{\sigma}\nabla\times\mathbf{H}^{ci}\right)\cdot\nabla\times\mathbf{b} + \int_{\partial\Omega_{ci}} \mathbf{E}^{ci}\cdot(\mathbf{b}\times\mathbf{n}^{ci}). \end{aligned} \tag{C.3.20}$$

Note that, in the weak formulation, the variable of integration is omitted. We proceed slightly differently in Ω_v. From (C.3.16) we infer that $\mathbf{H}^v$ is a gradient for a simply connected vacuum, i.e., $\mathbf{H}^v = \nabla\phi^v$. Thus taking a test-function of the form $\nabla\psi$, where ψ is a scalar potential defined on Ω_v, multiplying (C.3.14) by $\nabla\psi$ and integrating over Ω_v, we obtain

$$\int_{\Omega_v} \frac{\partial(\mu^v\nabla\phi^v)}{\partial t}\cdot\nabla\psi + \int_\Sigma \mathbf{E}^v\cdot\nabla\psi\times\mathbf{n}^v + \int_{\partial\Omega} \mathbf{E}^v\cdot\nabla\psi\times\mathbf{n}^v = 0. \tag{C.3.21}$$

We henceforth assume that $\mathbf{a} := \mathbf{E}_{|\partial\Omega}$ is a data. Since only the tangential parts of the electric field are involved in the surface integrals in (C.3.20) and (C.3.21), we can use the jump conditions (C.3.19) to write

$$\int_{\Sigma_\mu} \mathbf{E}^{ci}\cdot\mathbf{b}\times\mathbf{n}^{ci} = \int_{\Sigma_\mu} \{\mathbf{E}^c\}\cdot\mathbf{b}\times\mathbf{n}^{ci}, \qquad \int_\Sigma \mathbf{E}^v\cdot\nabla\psi\times\mathbf{n}^v = \int_\Sigma \mathbf{E}^c\cdot\nabla\psi\times\mathbf{n}^v,$$

where $\{\mathbf{E}^c\}$ is defined on Σ_μ by $\{\mathbf{E}^c\} = \frac{1}{2}\left(\mathbf{E}^{ci} + \mathbf{E}^{cj}\right)$. We now add (C.3.20) (for $i = 1,\dots,N$) and (C.3.21) to obtain

$$\begin{aligned} \int_{\Omega_c} \frac{\partial(\mu^c\mathbf{H}^c)}{\partial t}\cdot\mathbf{b} + \int_{\Omega_v} \frac{\partial(\mu^v\nabla\phi^v)}{\partial t}\cdot\nabla\psi + \int_{\cup_{i=1}^N\Omega_{ci}} \left(\frac{1}{\sigma}\nabla\times\mathbf{H}^{ci} - \mathbf{u}\times\mu^{ci}\mathbf{H}^{ci}\right)\cdot\nabla\times\mathbf{b} \\ + \int_{\Sigma_\mu} \{\mathbf{E}^c\}\cdot[\![\mathbf{b}\times\mathbf{n}]\!] + \int_\Sigma \mathbf{E}^c\cdot(\mathbf{b}\times\mathbf{n}^c + \nabla\psi\times\mathbf{n}^v) = -\int_{\partial\Omega} \mathbf{a}\cdot\nabla\psi\times\mathbf{n}^v, \end{aligned}$$

where we have set $[\![\mathbf{b}\times\mathbf{n}]\!] := \left(\mathbf{b}_i\times\mathbf{n}^{ci} + \mathbf{b}_j\times\mathbf{n}^{cj}\right)$ with $\mathbf{b}_i := \mathbf{b}|_{\Omega_{ci}}$ and $\mathbf{b}_j := \mathbf{b}|_{\Omega_{cj}}$. We finally get rid of $\mathbf{E}^c$ by using Ohm's law in the conductor:

$$\begin{aligned} &\int_{\Omega_c} \frac{\partial(\mu^c\mathbf{H}^c)}{\partial t}\cdot\mathbf{b} + \int_{\Omega_v} \frac{\partial(\mu^v\nabla\phi^v)}{\partial t}\cdot\nabla\psi + \int_{\cup_{i=1}^N\Omega_{ci}} \left(\frac{1}{\sigma}\nabla\times\mathbf{H}^{ci} - \mathbf{u}\times\mu^{ci}\mathbf{H}^{ci}\right)\cdot\nabla\times\mathbf{b} \\ &\quad + \int_{\Sigma_\mu} \{\frac{1}{\sigma}\nabla\times\mathbf{H}^c - \mathbf{u}\times\mu^c\mathbf{H}^c\}\cdot[\![\mathbf{b}\times\mathbf{n}]\!] + \int_\Sigma \left(\frac{1}{\sigma}\nabla\times\mathbf{H}^c - \mathbf{u}\times\mu^c\mathbf{H}^c\right)\cdot(\mathbf{b}\times\mathbf{n}^c + \nabla\psi\times\mathbf{n}^v) \\ &\quad = -\int_{\partial\Omega} \mathbf{a}\cdot\nabla\psi\times\mathbf{n}^v. \end{aligned} \tag{C.3.22}$$

This formulation is the starting point for the finite element discretization.

Space discretization

As already mentioned, SFEMaNS takes advantage of the cylindrical symmetry. We denote Ω_v^{2d} and Ω_{ci}^{2d} the meridian sections of Ω_v and Ω_{ci}, respectively. These sections are meshed using quadratic triangular meshes (we assume that Ω_v^{2d} and the sub-domains $\Omega_{c1}^{2d} \dots \Omega_{cN}^{2d}$ have piecewise quadratic boundaries). We denote $\{\mathcal{F}_h^v\}_{h>0}$, $\{\mathcal{F}_h^{c1}\}_{h>0} \dots \{\mathcal{F}_h^{cN}\}_{h>0}$ the corresponding regular families of non-overlapping quadratic triangular meshes where h denotes the typical size of a mesh element. Figure D.1(b-c) displays a meridian triangular mesh used in section C.4 with disks of thickness $d = 0.6$ (see section C.4 for details). We use the same mesh strategy for all the sub-domains. We can use refinement, but the ratio between the maximum size of an element and the minimum one is of order 1. For every triangle K in the mesh we denote $T_K : \hat{K} \longrightarrow K$ the quadratic transformation that maps the reference triangle $\hat{K} := \{(\hat{r}, \hat{z}) \in \mathbb{R}^2,\ 0 \leq \hat{r},\ 0 \leq \hat{z},\ \hat{r} + \hat{z} \leq 1\}$ to K. Given ℓ_H and ℓ_ϕ two integers in $\{1, 2\}$ with $\ell_\phi \geqslant \ell_H$ we first define the meridian finite element spaces

$$\mathbf{X}_h^{H,2d} := \left\{\mathbf{b}_h \in \mathbf{L}^1(\Omega_c) \,/\, \mathbf{b}_h|_{\Omega_{ci}} \in \mathcal{C}^0(\overline{\Omega}_{ci}),\ \forall i = 1, \dots, N,\ \mathbf{b}_h(T_K) \in \mathbb{P}_{\ell_H},\ \forall K \in \cup_{i=1}^N \mathcal{F}_h^{ci}\right\},$$
$$X_h^{\phi,2d} := \left\{\psi_h \in \mathcal{C}^0(\overline{\Omega}_v) \,/\, \psi_h(T_K) \in \mathbb{P}_{\ell_\phi},\ \forall K \in \mathcal{F}_h^v\right\},$$

where $\mathbb{P}_k$ denotes the set of (scalar or vector valued) bivariate polynomials of total degree at most k. Then, using the complex notation $\mathrm{i}^2 = -1$, the magnetic field and the scalar potential are approximated in the following spaces:

$$\mathbf{X}_h^H := \left\{\mathbf{b}_h = \sum_{m=-M}^{M} \mathbf{b}_h^m(r,z)\mathrm{e}^{\mathrm{i}m\theta};\ \forall m = 0, \dots, M,\ \mathbf{b}_h^m \in \mathbf{X}_h^{H,2d} \text{ and } \mathbf{b}_h^m = \overline{\mathbf{b}_h^{-m}}\right\},$$
$$X_h^\phi := \left\{\psi_h = \sum_{m=-M}^{M} \psi_h^m(r,z)\mathrm{e}^{\mathrm{i}m\theta};\ \forall m = 0, \dots, M,\ \psi_h^m \in \mathbf{X}_h^{H,2d} \text{ and } \psi_h^m = \overline{\psi_h^{-m}}\right\},$$

where $M + 1$ is the maximum number of complex Fourier modes.

Time discretization

We approximate the time derivatives using the second-order Backward Difference Formula (BDF2). The terms that are likely to mix Fourier modes are made explicit. Let Δt be the time step and set $t^n := n\Delta t,\ n \geqslant 0$. After proper initialization at t^0 and t^1, the algorithm proceeds as follows. For $n \geqslant 1$ we set

$$\mathbf{H}^* = 2\mathbf{H}^{c,n} - \mathbf{H}^{c,n-1} \quad \text{and} \quad \begin{cases} D\mathbf{H}^{c,n+1} := \dfrac{1}{2}\left(3\mathbf{H}^{c,n+1} - 4\mathbf{H}^{c,n} + \mathbf{H}^{c,n-1}\right), \\ D\phi^{v,n+1} := \dfrac{1}{2}\left(3\phi^{v,n+1} - 4\phi^{v,n} + \phi^{v,n-1}\right), \end{cases}$$

and the discrete fields $\mathbf{H}^{c,n+1} \in \mathbf{X}_h^H$ and $\phi^{v,n+1} \in X_h^\phi$ are computed so that the following holds for all $\mathbf{b} \in \mathbf{X}_h^H,\ \psi \in X_h^\phi$:

$$\mathcal{L}\left((\mathbf{H}^{c,n+1}, \phi^{v,n+1}), (\mathbf{b}, \psi)\right) = \mathcal{R}(\mathbf{b}, \psi), \tag{C.3.23}$$

where the linear for $\mathcal{R}$ is defined by

$$\mathcal{R}(\mathbf{b},\psi) = -\int_{\partial\Omega} \mathbf{a}\cdot\nabla\psi\times\mathbf{n}^v + \int_{\Omega_c} \mathbf{u}\times\mu^c\mathbf{H}^*\cdot\nabla\times\mathbf{b} + \int_{\Sigma_\mu} \{\mathbf{u}\times\mu^c\mathbf{H}^*\}\cdot[\![\mathbf{b}\times\mathbf{n}]\!] + \int_{\Sigma} \mathbf{u}\times\mu^c\mathbf{H}^*\cdot\left(\mathbf{b}\times\mathbf{n}^c + \nabla\psi\times\mathbf{n}^v\right),$$

the bilinear form $\mathcal{L}$ is defined by

$$\begin{aligned}\mathcal{L}\big((\mathbf{H}^{c,n+1},\phi^{v,n+1}),(\mathbf{b},\psi)\big) := &\int_{\Omega_c} \mu^c\frac{D\mathbf{H}^{c,n+1}}{\Delta t}\cdot\mathbf{b} + \int_{\Omega_v} \mu^v\frac{\nabla D\phi^{v,n+1}}{\Delta t}\cdot\nabla\psi \\ &+ \int_{\Omega_c} \frac{1}{\sigma}\nabla\times\mathbf{H}^{c,n+1}\cdot\nabla\times\mathbf{b} + g\left((\mathbf{H}^{c,n+1},\phi^{v,n+1}),(\mathbf{b},\psi)\right) \\ &+ \int_{\Sigma_\mu} \{\frac{1}{\sigma}\nabla\times\mathbf{H}^{c,n+1}\}\cdot[\![\mathbf{b}\times\mathbf{n}]\!] + \int_{\Sigma} \frac{1}{\sigma}\nabla\times\mathbf{H}^{c,n+1}\cdot\left(\mathbf{b}\times\mathbf{n}^c + \nabla\psi\times\mathbf{n}^v\right)\end{aligned}$$

and the bilinear form g is defined by

$$\begin{aligned} g((\mathbf{H}_h,\psi_h),(\mathbf{b}_h,\psi_h)) \;:=\; & \beta_1 h_F^{-1}\int_{\Sigma_\mu} (\mathbf{H}_{h,1}\times\mathbf{n}_1^c + \mathbf{H}_{h,2}\times\mathbf{n}_2^c)\cdot(\mathbf{b}_{h,1}\times\mathbf{n}_1^c + \mathbf{b}_{h,2}\times\mathbf{n}_2^c) \\ +\; & \beta_2 h_F^{-1}\int_{\Sigma} (\mathbf{H}_h\times\mathbf{n}^c + \nabla\psi_h\times\mathbf{n}^v)\cdot(\mathbf{b}_h\times\mathbf{n}^c + \nabla\psi_h\times\mathbf{n}^v),\end{aligned}$$

where h_F denotes the typical size of $\partial K\cup\Sigma_\mu$ or $\partial K\cup\Sigma$ for all K in the mesh such that $\partial K\cup\Sigma_\mu$ or $\partial K\cup\Sigma$ is not empty. The constant coefficients β_1 and β_2 are chosen to be of order 1. The purpose of the bilinear form g is to penalize the tangential jumps $[\![\mathbf{H}^{c,n+1}\times\mathbf{n}]\!]$ and $\mathbf{H}^{c,n+1}\times\mathbf{n}^c + \nabla\psi^{v,n+1}\times\mathbf{n}^v$, so that they converge to zero when the mesh-size goes to zero.

Addition of a magnetic pressure

The above time-marching algorithm is convergent on finite time intervals but may fail to provide a convergent solution in a steady state regime since errors may accumulate on the divergence of the magnetic induction. We now detail the technique which is employed to control the divergence of $\mathbf{B}^c$ on arbitrary time intervals.

To avoid non-convergence properties that could occur in non-smooth domains and discontinuous material properties, we have designed a non standard technique inspired from [17] to control $\nabla\cdot\mathbf{B}$. We replace the induction equation in Ω_c by the following:

$$\frac{\partial(\mu^c\mathbf{H}^c)}{\partial t} = -\nabla\times\mathbf{E}^c + \mu^c\nabla p^c, \quad (-\Delta_0)^\alpha p^c = \nabla\cdot\mu^c\mathbf{H}^c, \quad p^c|_{\partial\Omega_c} = 0, \tag{C.3.24}$$

where α is a real parameter, Δ_0 is the Laplace operator with zero boundary condition on Ω_c, and p^c is a new scalar unknown. A simple calculation shows that $p^c = 0$ if the initial magnetic induction is solenoidal; hence, (D.3.9) enforces $\nabla\cdot\mu^c\mathbf{H}^c = 0$. Taking $\alpha = 0$ amounts to penalizing $\nabla\cdot\mu^c\mathbf{H}^c$ in $\mathbf{L}^2(\Omega_c)$, which turns out to be non-convergent with Lagrange finite elements when the boundary of Ω_c is not smooth, (see [36] for details). The mathematical analysis shows that the method converges with Lagrange finite elements when $\alpha\in(\frac{1}{2},1)$. In practice we take $\alpha = 0.7$.

We introduce new finite elements spaces to approximate the new scalar unknown p^c

$$X_h^{p,2d} := \left\{ p_h \in L^1(\Omega_c) \,/\, p_h \in \mathcal{C}^0(\overline{\Omega_c}),\ p_h(T_K) \in \mathbb{P}_{\ell_p},\ \forall K \in \cup_{i=1}^N \mathcal{F}_h^{ci},\ p_h = 0 \text{ on } \partial\Omega_c \right\},$$

$$X_h^p := \left\{ p = \sum_{m=-M}^{M} p^m(r,z)\mathrm{e}^{\mathrm{i}m\theta} \,/\, \forall m = 1\ldots,M,\ p^m \in X_h^{p,2d} \text{ and } p^m = \overline{p^{-m}} \right\}.$$

Here ℓ_p is an integer in {1,2}. The final form of the algorithm is the following: after proper initialization, we solve for $\mathbf{H}^{c,n+1} \in \mathbf{X}_h^H$, $\phi^{v,n+1} \in X_h^\phi$ and $p^{n+1} \in X_h^p$ so that the following holds for all $\mathbf{b} \in \mathbf{X}_h^H$, $\psi \in X_h^\phi$, $q \in X_h^p$:

(C.3.25)
$$\mathcal{L}\left((\mathbf{H}^{c,n+1}, \phi^{v,n+1}), (\mathbf{b}, \psi)\right) + \mathcal{D}\left((\mathbf{H}^{c,n+1}, p^{c,n+1}, \phi^{v,n+1}), (\mathbf{b}, q, \psi)\right) + \mathcal{P}(\phi^{v,n+1}, \psi) = \mathcal{R}(\mathbf{b}, \psi)$$

with

(C.3.26)
$$\mathcal{D}\left((\mathbf{H}, p, \phi), (\mathbf{b}, q, \psi)\right) := \sum_{i=1}^{N} \int_{\Omega_{ci}} \left(\mu^c \mathbf{b}\cdot\nabla p - \mu^c \mathbf{H}\cdot\nabla q + h^{2\alpha} \nabla\cdot\mu^c\mathbf{H}\ \nabla\cdot\mu^c\mathbf{b} + h^{2(1-\alpha)} \nabla p\cdot\nabla q \right),$$

where h denotes the typical size of a mesh element. The term $\sum_{i=1}^N \int_{\Omega_{ci}} h^{2\alpha} \nabla\cdot\mu^c\mathbf{H}^{c,n+1}\ \nabla\cdot\mu^c\mathbf{b}$ is a stabilization quantity which is added in to have discrete well-posedness of the problem irrespective of the polynomial degree of the approximation for p^c. The additional stabilizing bilinear form $\mathcal{P}$ is defined by

$$\mathcal{P}(\phi, \psi) = \int_{\Omega_v} \nabla\phi\cdot\nabla\psi - \int_{\partial\Omega_v} \psi\mathbf{n}\cdot\nabla\phi.$$

This bilinear form is meant to help ensure that $\Delta\phi^{v,n+1} = 0$ for all times.

Taking advantage of the cylindrical symmetry for Maxwell and Navier-Stokes equations

SFEMaNS is a fully nonlinear code integrating the coupled Maxwell and Navier-Stokes equations ([65, 66]). As mentioned above, any term that could mix different Fourier modes has been made explicit. Owing to this property, there are $M+1$ independent linear systems to solve at each time step ($M+1$ being the maximum number of complex Fourier modes). This immediately provides a parallelization strategy. In practice we use one processor per Fourier mode. The computation of the nonlinear terms in the right-hand side is done using a parallel Fast Fourier Transform. Note that, in the present paper, we use only the kinematic part of the code with an axisymmetric steady flow. A typical time step is $\Delta t = 0.01$ and a typical mesh size is $h = 1/80$. When necessary, the mesh is refined in the vicinity of the curved interface Σ_μ so that we have $h = 1/400$ locally.

C.4 Ohmic decay in heterogenous domains

The inspection of equations (C.2.3) shows that even in the absence of flow, heterogeneous domains can lead to non trivial Ohmic decay problems. Therefore the reliability and the application range of both numerical schemes are first examined by studying pure Ohmic decay

problems in the absence of fluid flow. A cylindrical geometry is chosen with radius $R = 1.4$ and height $H = 2.6$ which is in accordance with setting of the VKS experiment. The cylinder is filled with a conductor with diffusivity $\eta = (\mu_0\sigma_0)^{-1} = 1$ and relative permeability $\mu_r = 1$. Two disks are introduced inside the domain, characterized by thickness $d \in \{0.6, 0.3, 0.1\}$,

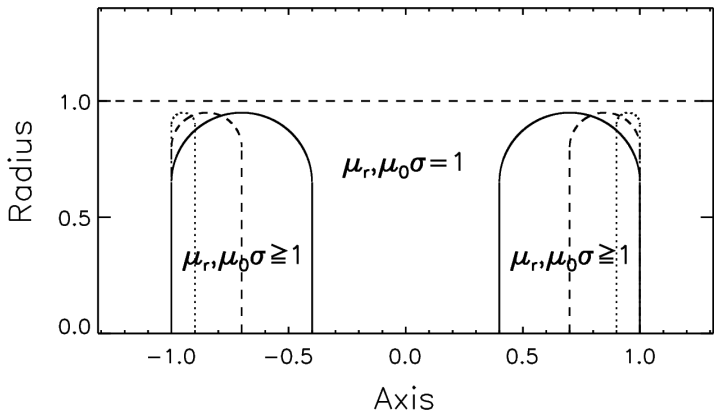

Figure C.3: Sketch of the set up. Two disks with thickness $d = 0.6, 0.3, 01$ (solid, dashed, dotted curve) are introduced in a cylinder with height $H = 2.6$ and radius $R = 1.4$. In all runs the location of the backside of each disk is fixed at $z = \pm 1$. At the outer disk edge a circular shape is applied with a curvature radius corresponding to half of the disk thickness. The radial extension of the disks is fixed and given by $R_{\text{disk}} = 0.95$. The dashed horizontal line denotes the inner boundary that separates the dynamical active region from the stagnant outer layer in the runs with $\text{Rm} > 0$ (see Sec. C.5).

conductivity σ and permeability μ_r (see figure C.3). The thickness $d = 0.1$ is representative of the VKS impellers but the other d have been tested to study the scaling law with an effective permeability or an effective conductivity and also to estimate the impact of the numerical resolutions.

In a freely decaying system azimuthal Fourier modes are independent one from another as long as μ_r and σ are axisymmetric. Moreover the axisymmetric mode ($m = 0$) can be split into decoupled poloidal (B_r, B_z) and toroidal (B_φ) components which decay independently and exhibit two distinct decay rates. The three components of the magnetic field of each Fourier mode $m \geq 1$ are coupled, i.e. the poloidal and toroidal components interact and have the same decay rate when $m \geq 1$. The Ohmic decay rates are computed with SFEMaNS by solving an eigenvalue problem using the ARPACK package. Between 10 to 40 eigenvectors are computed for each azimuthal Fourier mode, and the dominant eigenvector, i.e., the one whose eigenvalue has the largest real part, is extracted. Applying the grid-based FV/BEM algorithm equation (C.2.1) is time stepped and the growth (respectively decay) rates are estimated from the time behavior of the magnetic field amplitude. Initial conditions are given by a divergence free random magnetic field which ensures that all possible eigen vectors are excited.

In the following we limit our examinations to the decay of the axisymmetric mode ($m = 0$) and the simplest non-axisymmetric mode, i.e. the ($m = 1$)-mode ($B \propto \cos\varphi$).

C.4.1 External boundary conditions and field pattern

A couple of simulations have been performed utilizing vanishing tangential field boundary conditions in order to make comparisons with the vacuum boundary conditions. Figure C.4 shows the structure of the field geometry with the container embedded in vacuum (upper panels) and with VTF boundary conditions (lower panels). We observe that the boundary conditions have significant impacts when the conductivity and the permeability are uniform in the whole computational domain. This impact becomes negligible when the disk permeability or conductivity is large enough. More noticeable differences occur when comparing the axisymmetric eigenmode of the magnetic field obtained with high permeability disks with that obtained with high conductive disks. In the first case (as μ_r increase) the axisymmetric mode changes from a poloidal dominant structure to a toroidal dominant structure (see figure C.7 for $d = 0.6$). The change of structure occurs irrespective of d around $\mu_r^{\text{eff}} \approx 1.5$, where μ_r^{eff} denotes the effective value for permeability defined by $\mu_r^{\text{eff}} = V^{-1} \int \mu_r(\mathbf{r}) dV$ (with V the volume of the cylindrical domain). The field structure is dominated by two distinct azimuthal annular structures essentially located within the disks. When the conductivity is large the axial component of the magnetic field dominates and has a slab like structure concentrated around the axis. A remarkable change in the field structure is obtained when the thickness of the disks is small ($d = 0.1$, see figure C.5 & C.6). When μ_r is large the azimuthal component of the field is dominated by two ring like structures centered on the outer part of both disks. The radial field component is concentrated within two highly localized paths on the outer edge of the disk. The axial component is nearly independent from z except close to the disks where the jump conditions require H_z to be very small within the disks. The differences in the field patterns between $d = 0.6$ and $d = 0.1$ are less significant when the conductivity is large where a torus-like structure of the poloidal field component dominates in all cases (see right panel in figure C.6).

Note the equatorial symmetry breaking in the toroidal field when the conductivity is large ($\mu_0 \sigma = 100$, central column in figure C.4). The asymmetry in H_φ results from the occurrence of combined contributions with dipole-like symmetry (even with respect to the equator) and quadrupolar-like symmetry (odd with respect to the equator). Using ARPACK the SFEMaNS scheme yields decay rates for both symmetries which are close but not equal (the dipole mode has always a larger decay time than the quadrupole mode).

C.4.2 Decay rates and dominating mode

The temporal behavior of the magnetic eigenmodes follows an exponential law $B \propto e^{\gamma t}$ where γ denotes the growth or decay rate. Figure C.8 shows the magnetic field decay rates for a thick disk ($d = 0.6$) and a thin disk ($d = 0.1$) against μ_r^{eff} (left column) and against σ^{eff} (right column). σ^{eff} denotes the effective values for the conductivity defined similarly to μ_r^{eff} (see above) by $\sigma^{\text{eff}} = V^{-1} \int \sigma(\mathbf{r}) \mathrm{d}V$. The essential properties of the field behavior can be summarized as follows: The presence of high permeability/conductivity material enhances axisymmetric and ($m = 1$) modes. However, for thin disks the enhancement works selectively for the axisymmetric toroidal field (in case of large μ_r), respectively for the poloidal axisymmetric mode (in case of large σ) and the decay rate of the poloidal (respectively toroidal) field component remains nearly independent of the permeability (respectively conductivity).

Small differences can be observed between the results obtained by the SFEMaNS and FV/BEM algorithms. These are particularly noticeable for the axisymmetric poloidal mode

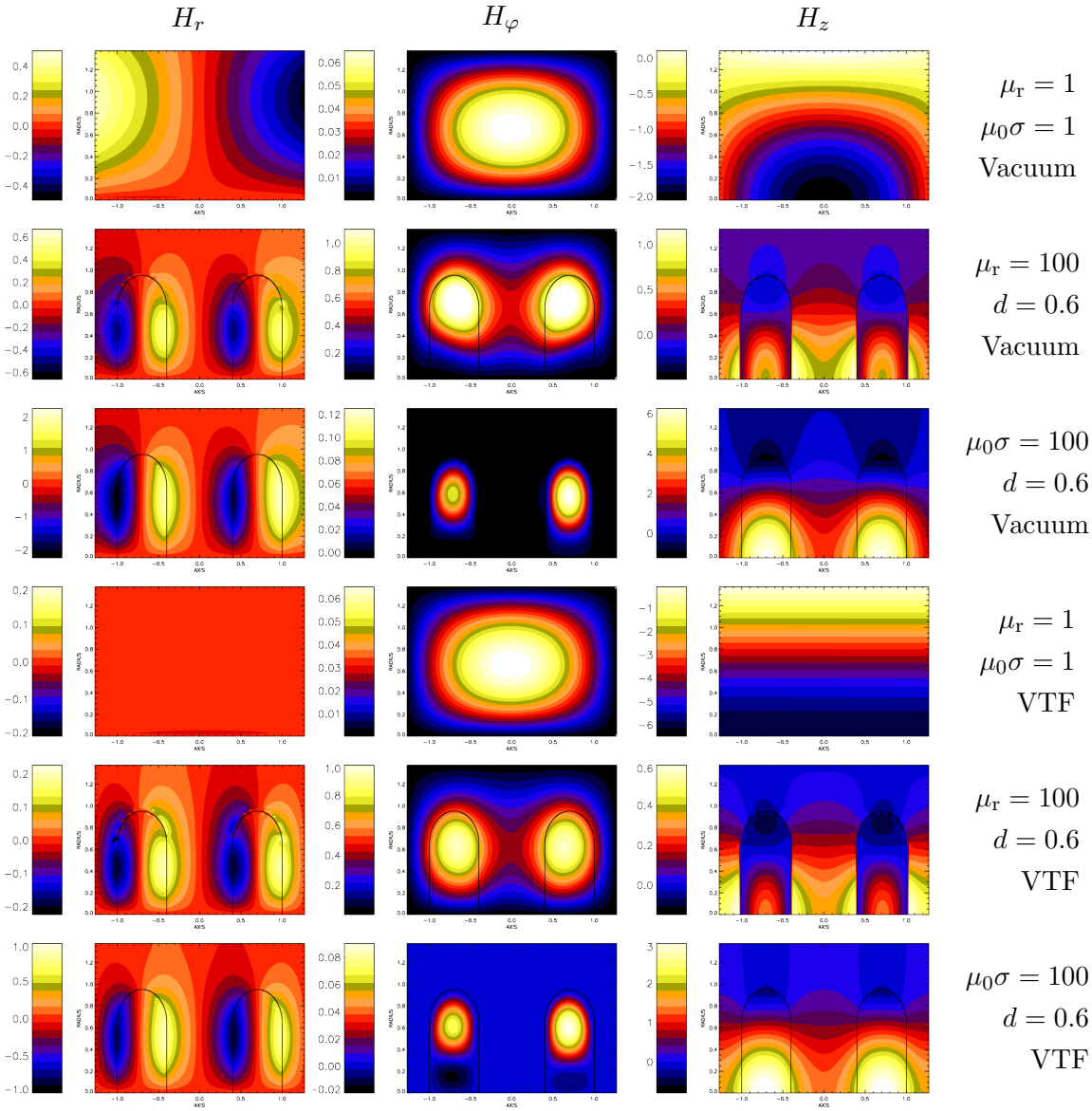

Figure C.4: (Color online) Ohmic decay. Axisymmetric eigenmodes of the magnetic field $\mathbf{H} = \mu_r^{-1}\mathbf{B}$ (from left to right: H_r, H_φ, H_z); From top to bottom: $\mu_r = \mu_0\sigma = 1$ (no disks), $\mu_r = 100$, $\mu_0\sigma = 100$ (all with insulating boundary conditions and $d = 0.6$), $\mu_r = \mu_0\sigma = 1$ (no disks), $\mu_r = 100$, $\mu_0\sigma = 100$ (all with vanishing tangential field boundary conditions and $d = 0.6$). Note that the absolute amplitudes denoted by the respective color bars are meaningless and only serve to compare the relative amplitudes of the different components within one case.

and for the $(m = 1)$ mode when the disks are thin $(d = 0.1)$. A couple of simulations with higher resolution in the axial direction (marked by the blue, red and the yellow stars in the lower right panel of figure C.8) show that these deviations are most probably the result of the poor resolution of the FV/BEM scheme. Only 6 mesh points are used to resolve the vertical structure of the disk in FV/BEM whereas SFEMaNS uses 40 mesh points. More systematic

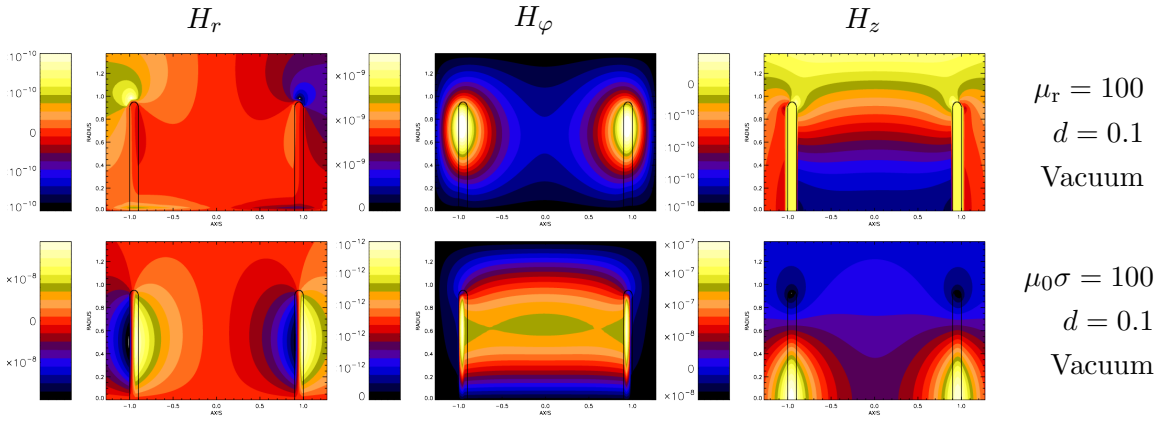

Figure C.5: (Color online) Ohmic decay. Axisymmetric field $\mathbf{H} = \mu_r^{-1}\mathbf{B}$ for the thin disk case ($d = 0.1$, from left to right: H_r, H_φ, H_z); Top row: $\mu_r = 100$, bottom row: $\mu_0\sigma = 100$. Insulating boundary conditions. Note that the absolute amplitudes denoted by the respective color bars are meaningless and only serve to compare the relative amplitudes of the different components within one case.

discrepancies between both algorithms become obvious by means of the behavior of the decay time τ defined by the reciprocal value of the decay rate (see figure C.9). For sufficiently large values of μ_r^{eff} (respectively σ^{eff}), τ follows a scaling law $\tau \propto c\mu_r^{\text{eff}}$ (respectively $\propto c\sigma^{\text{eff}}$) as reported in table C.1. For increasing μ_r^{eff} the decay time of the ($m = 0$) toroidal mode slightly increases as d decreases whereas the axisymmetric poloidal mode exhibits an opposite behavior. The variation of the decay time with σ^{eff} for the ($m = 0$) components (toroidal and poloidal) is the opposite to the behavior obtained with varying μ_r^{eff}. These variations with respect to d suggest that the decay time scaling law not only depends on the ferromagnetic volume of the impellers but also depends on the geometric constraints associated with the jump conditions (C.2.3).

Further evaluation of the discrepancies in the scaling behavior obtained by both numerical schemes is difficult, since it would require doing simulations with larger values for μ_r^{eff} and/or σ^{eff}, which is not possible at the moment without significantly improving the numerical schemes. In particular for the thin disk case ($d = 0.1$) the achievable values for μ_r and/or σ are restricted to μ_r^{eff} (respectively $\mu_0\sigma^{\text{eff}}$) $\lesssim 5$ and, with the available data, it is not obvious whether the asymptotic linear scaling has been reached. In any case the absolute values for the decay rates obtained by both algorithms are close, giving confidence that the results imply a sufficient accurate description of the magnetic field behavior in the presence of non-heterogenous materials. As already indicated by the marginal differences in the field pattern for both examined boundary conditions, we find no qualitative change in the behavior of the decay rates or decay times with vacuum boundary conditions or VTF boundary conditions (see figure C.10). Although for small values of μ_r^{eff} and σ^{eff} the absolute values of the decay rates differ by 30% the scaling behavior of the decay time is nearly independent of the external boundary conditions (see Tab. C.2). The influence of these boundary conditions is smaller as μ_r increases. Although the decay rates (for the thick disks) differ by approximately 30% when $\mu_r \lesssim 5$ there are nearly no differences in γ for higher values of the permeability. This behavior is less obvious in case of a high conductivity disk where the poloidal axisymmetric field exhibits differences in the decay rates of 15% even at the highest available conductivity

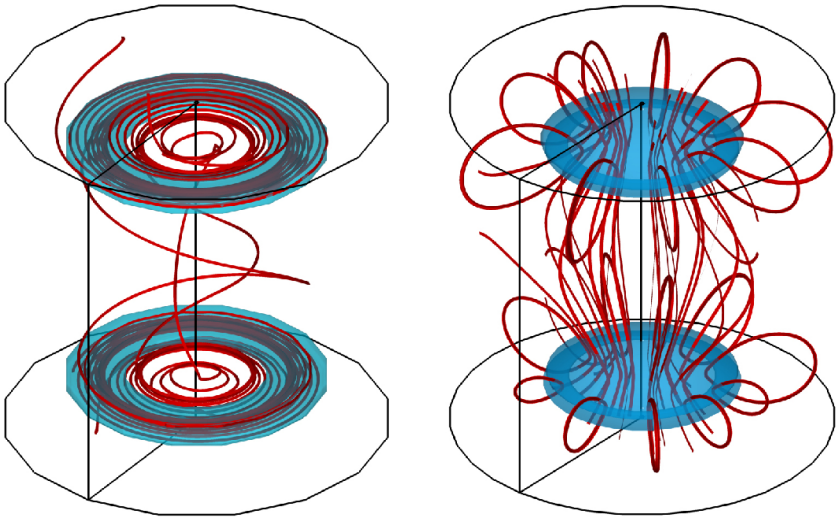

Figure C.6: (Color online) Ohmic decay for thin disks ($d = 0.1$). Left panel: $\mu_\mathrm{r} = 100$, right panel: $\mu_0\sigma = 100$. The isosurfaces present the magnetic energy density at 25% of its maximum value.

	$\mu_\mathrm{r}^\mathrm{eff}$			σ^eff			
d	0.6	0.3	0.1	0.6	0.3	0.1	**Algorithm**
$\tau(B^\mathrm{tor}_{m=0})$	0.29	0.32	0.33	0.12	0.07	0.00	FV/BEM
	0.28	–	0.34	0.12	–	0.00	SFEMaNS
$\tau(B^\mathrm{pol}_{m=0})$	0.12	0.08	0.00	0.32	0.36	0.33	FV/BEM
	0.11	–	0.00	0.35	–	0.45	SFEMaNS
$\tau(B_{m=1})$	0.12	0.21	0.25	0.14	0.20	0.20	FV/BEM
	0.17	–	0.25	0.18	–	0.28	SFEMaNS

Table C.1: Scaling coefficient c for the decay time as $\tau \propto c\mu_\mathrm{r}^\mathrm{eff}$ (respectively $c\mu_0\sigma^\mathrm{eff}$) for different $m = 0$ and $m = 1$ modes as indicated (vacuum BC).

(see figure C.11). Note that the axisymmetric toroidal field behaves exactly in the same way for both kinds of boundary conditions because insulating boundary conditions and vanishing tangential field conditions are identical for the axisymmetric part of B_φ.

C.5 Kinematic Dynamo

In the following, the kinematic induction equation is solved numerically with $\mathrm{Rm} > 0$ in order to examine whether the behavior of the magnetic field obtained in the free decay regime is maintained when interaction with a mean flow is allowed. To approximately mimic the VKS

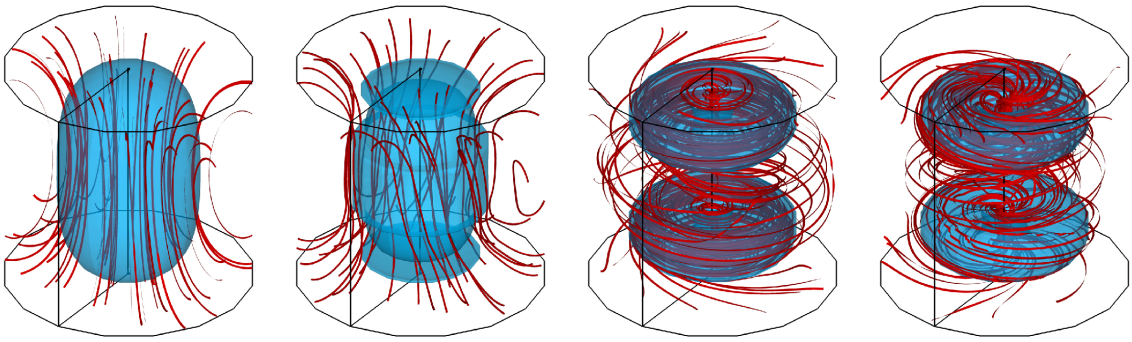

Figure C.7: (Color online) Ohmic decay. The blue transparent isosurfaces present the magnetic energy density at 25% of the maximum value and the red fieldlines show the field structure for $d = 0.6$ and (from left to right): $\mu_r = 1, 2, 10, 100$ (corresponding to $\mu_r^{\rm eff} = 1, 1.2, 2.7, 19.5$).

	$\mu_r^{\rm eff}$	$\sigma^{\rm eff}$	
$\tau(B^{\rm tor}_{m=0})$	0.29	0.12	FV/BEM VTF
	0.28	0.12	SFEMaNS VTF
$\tau(B^{\rm pol}_{m=0})$	0.12	0.37	FV/BEM VTF
	0.10	0.42	SFEMaNS VTF
$\tau(B_{m=1})$	0.11	0.14	FV/BEM VTF
	0.17	0.19	SFEMaNS VTF

Table C.2: Scaling coefficient c for the decay time as $\tau \propto c\mu_r^{\rm eff}$ for thick disks ($d = 0.6$) and VTF boundary conditions.

experiment we apply the so called MND-flow [102] given by

$$\begin{aligned} u_r(r,z) &= -(\pi/H)\cos(2\pi z/H)\, r(1-r)^2(1+2r), \\ u_\varphi(r,z) &= 4\epsilon r(1-r)\sin(\pi z/H), \\ u_z(r,z) &= (1-r)(1+r-5r^2)\sin(2\pi z/H), \end{aligned} \tag{C.5.1}$$

where $H = 1.8$ denotes the distance between the impeller disks and ϵ measures the ratio between toroidal and poloidal component of the velocity (here, $\epsilon = 0.7259$ is chosen following previous work, e.g. [137] [137]). The flow magnitude is characterized by the magnetic Reynolds number which is defined as

$$\mathrm{Rm} = \mu_0\sigma_0 U_{\max} R, \tag{C.5.2}$$

where $U_{\max}$ is the maximum of the flow velocity and σ_0 denotes the fluid conductivity. Figure C.12 shows the structure of the velocity field where equations (E.2.3) are only applied in the region between the two impellers. The flow active region with radius $R = 1$ (corresponding to 20.5 cm in the experiment) is surrounded by a layer of stagnant fluid with a thickness of $0.4R$ (the side layer) which significantly reduces Rm^c ([137] [137]). In the domain of the impellers a purely azimuthal velocity is assumed given by the azimuthal velocity of the MND flow (see (E.2.3)) at $z = \pm H/2$. A so called lid layer is added behind each impeller

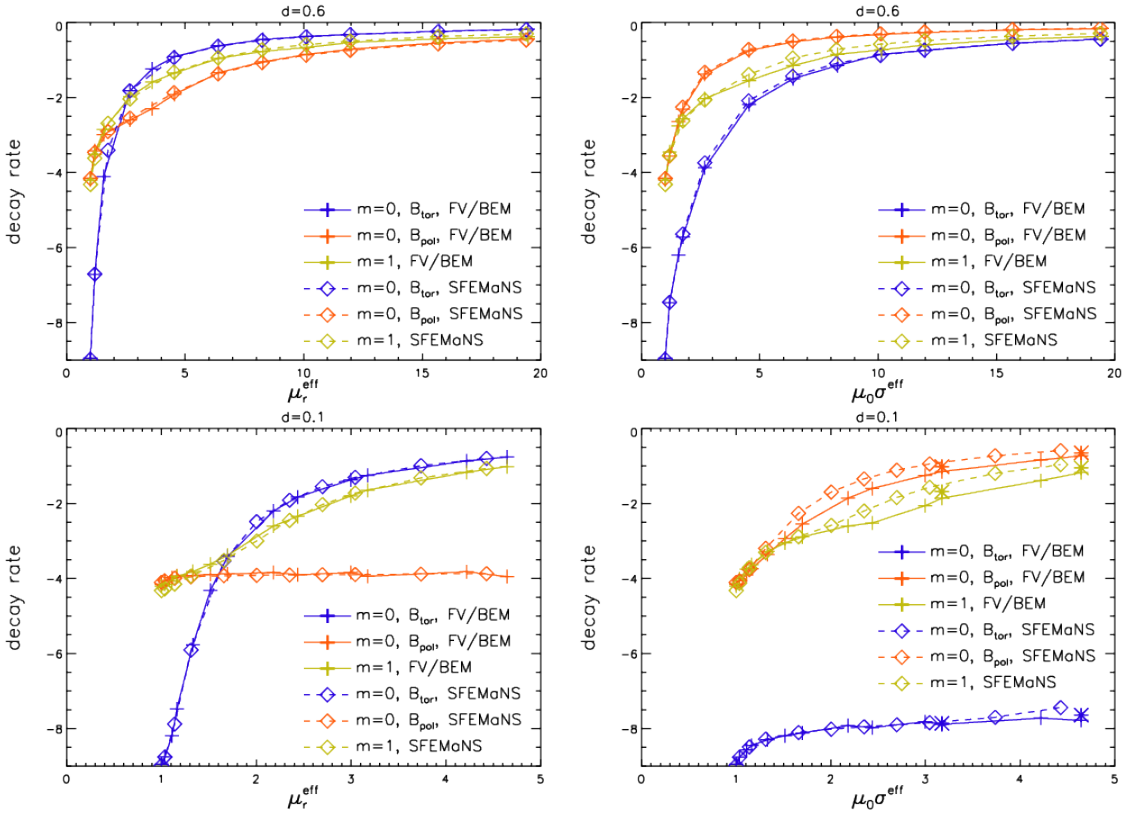

Figure C.8: (Color online) Decay rates with vacuum BC against μ_r^{eff} (left column) and against $\mu_0\sigma^{\text{eff}}$ (right column) for $d = 0.6$ (top row) and $d = 0.1$ (bottom row). The solid curves show the results obtained from the hybrid FV/BEM scheme and the dashed curves denote the results from the SFEMaNS scheme. The stars in the lower right panel present the results of a FV/BEM run with higher resolution demonstrating that the FV/BEM algorithm might approach the SFEMaNS data.

disk. A purely rotating flow is assumed within these lid layers, and it is modeled by a linear interpolation along the z-axis between the azimuthal velocity at the outer side of the impeller disk and zero at the end cap of the cylindrical domain. Here we limit our examinations to disks with a height $d = 0.1$. Note that the impellers are modeled only by the permeability and/or conductivity distribution and no particular flow boundary conditions are enforced on the (assumed) interface between the impellers and the fluid. This setup is comparable to the configuration in [58] except that we now assume that permeability and conductivity are axisymmetric.

Figure C.13 shows the growth rates for the $(m = 1)$ mode for different magnetic Reynolds numbers. Compared to the free decay, we obtain a remarkable distinct behavior of the growth rate if induction from a mean flow is added. High permeability disks together with $\mathrm{Rm} > 0$ enhance the $(m = 1)$ mode when compared to the case $\mu_r = 1$ resulting in a non-negligible impact on the critical magnetic Reynolds number for the onset of dynamo action (of this mode): Rm^c is reduced from around 76 at $\mu_r = 1$ to Rm^c around 55 at $\mu_r = 100$. The behavior of Rm^c indicates a saturation around $\mathrm{Rm}^c \approx 55$ for $\mu_r \gg 1$ which is still above 50 which is the highest achievable experimental value. The enhancement of the $(m = 1)$ mode

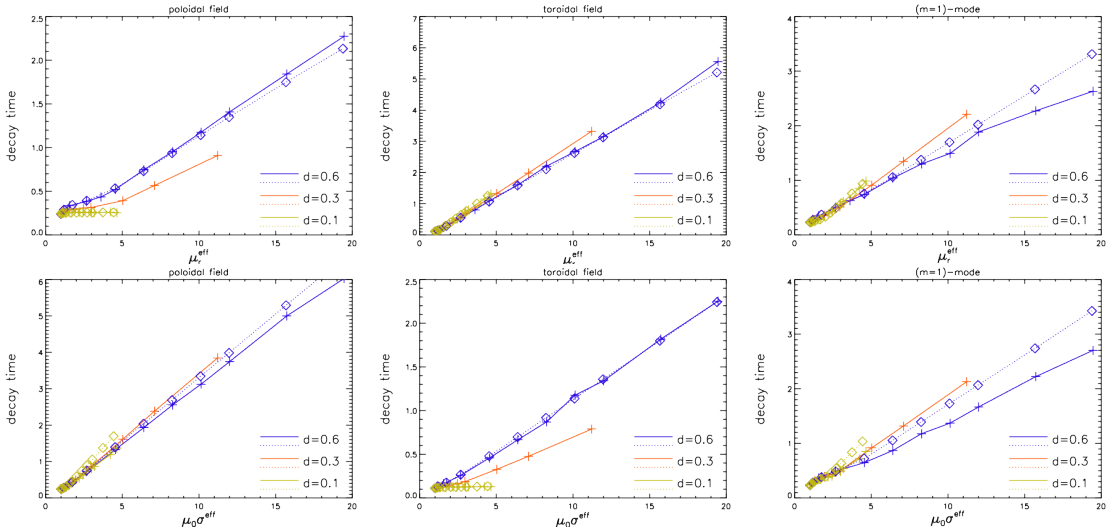

Figure C.9: (Color online) Ohmic decay. Decay times against μ_r^{eff} (top row) and against $\mu_0\sigma^{\text{eff}}$ (bottom row) for three disk thicknesses $d = 0.6, 0.3, 0.1$ (blue, red, yellow). The solid curves show the results obtained from the hybrid FV/BEM scheme and the dotted curves denote the results from the SFEMaNS scheme.

for $\text{Rm} \neq 0$ is weaker compared to the Ohmic decay (green curve in left panel of figure C.13). An opposite behavior is obtained for a high conducting disk where a reduction of the $(m = 1)$ growth rate is obtained (see right panel of figure C.13).

In both cases the $(m = 1)$ decay rate remains independent of μ_r (respectively σ) for values exceeding approximately $\mu_r \approx 20$ (or $\mu_0\sigma \approx 20$). The critical magnetic Reynolds number has also been computed for a different set-up with the flow restricted to the bulk region : $0 \leq r \leq 1.4, -0.9 \leq z \leq 0.9$ with VTF conditions applied at the boundary of this region. We obtained in $\text{Rm}^c = 39$ in this case. Note that this pseudo-vacuum set-up under-estimates the threshold by more than 30% when compared to $\text{Rm}^c = 55$ in the limit $\mu_r \gg 1$. This confirms that a realistic description of the soft iron impellers is crucial to get correct estimates.

The robustness of the results reported above exhibits a rather delicate dependence of the field behavior on the details of the flow distribution, in particular from the flow in the lid layers. Beside the dynamo killing influence of the lid flow [137] this is also true for the radial flow in the vicinity of the inner side of the disks. In order to estimate the relative impact of velocity jumps on the two codes, some simulations have been performed by smoothing the radial component of the velocity at the transition between the bulk of the domain and the impeller disk (where $u_r = 0$). The resulting decay rates at $\text{Rm} = 50$ (black stars in the left panel of figure C.13 and table C.3) are slightly different at $\mu_r = 1$ but the difference is more significant for $\mu_r = 60$.

C.6 Conclusions

In addition to its well recognized effects in magnetostatics, experimental dynamos have shown that soft-iron material may also find important applications in the field of magnetohydrodynamics. For instance, at least one of the two impellers of the Cadarache experiment must be made of soft iron and must rotate in order to achieve dynamo action (F. Daviaud, private

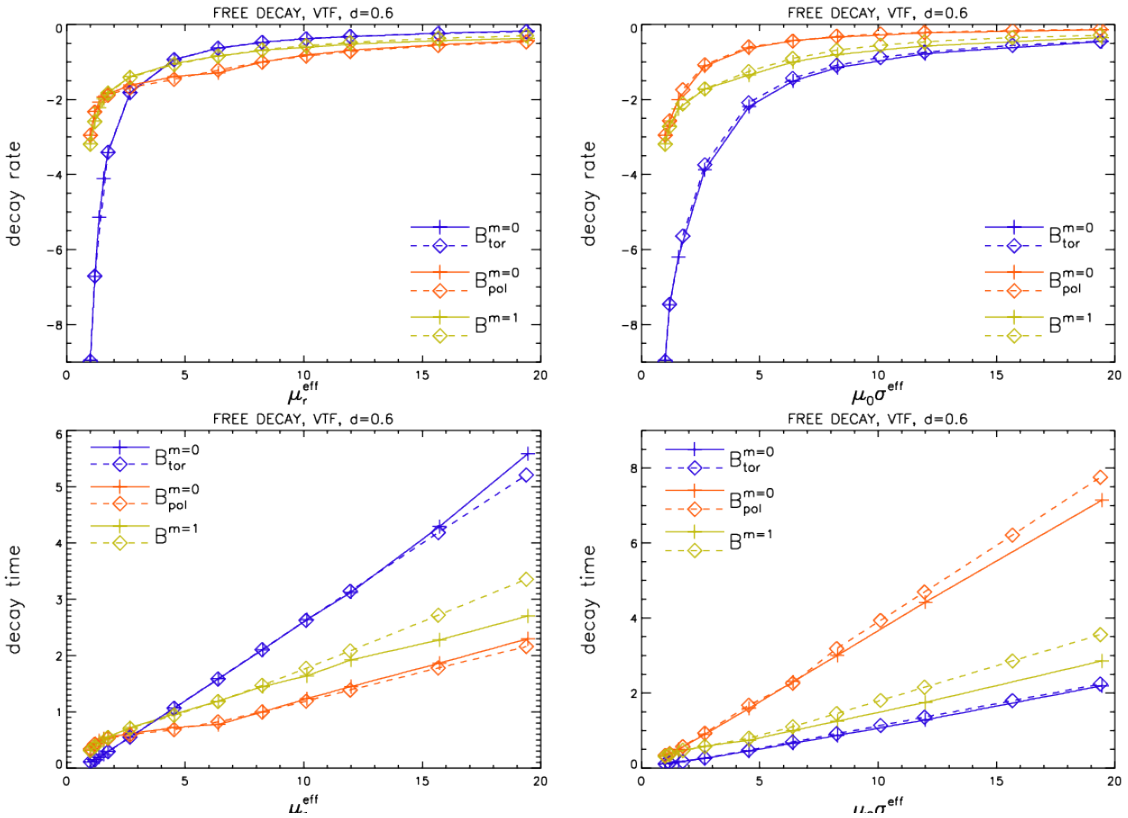

Figure C.10: (Color online) Decay rates and decay times against μ_r^{eff} (left column) and against $\mu_0\sigma^{eff}$ (right column) for vanishing tangential fields boundary conditions. $d = 0.6$. The solid (dashed) curves denote the results from the FV/BEM (SFEMaNS) scheme.

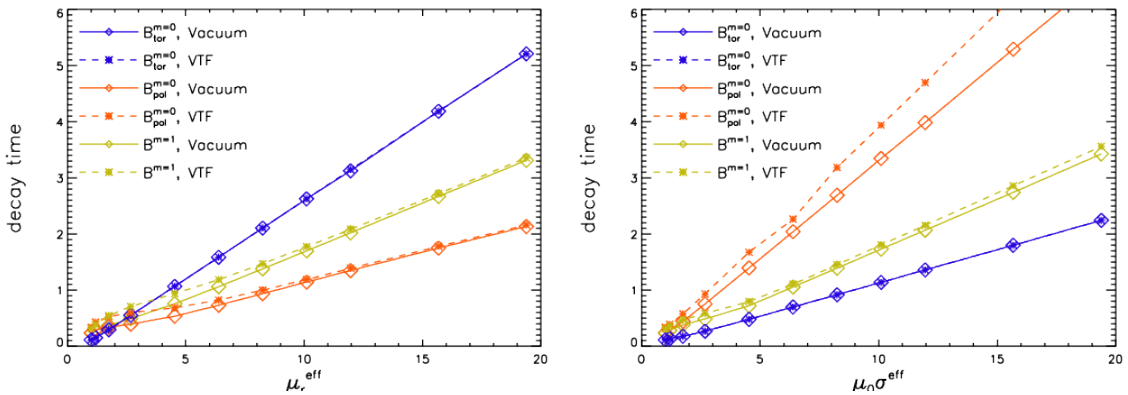

Figure C.11: (Color online) Comparison of boundary conditions. Decay times against μ_r^{eff} (left panel) and against $\mu_0\sigma^{eff}$ (right panel) for vacuum BC (solid curves) and VTF boundary conditions (dashed curves). $d = 0.6$. All data results from the SFEMaNS scheme.

communication). This unexplained fact raises the question whether the role of this material

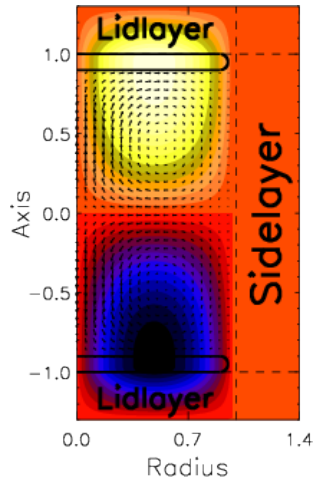

Figure C.12: (Color online) Structure of the prescribed axisymmetric velocity field. The color coded pattern represents the azimuthal velocity and the arrows show the poloidal velocity field. The black solid lines represent the shape of the impeller disk.

m=1, Rm=50	$\mu_r = 1$		$\mu_r = 60$	
	FV/BEM	SFEMaNS	FV/BEM	SFEMaNS
MND	-1.218	-1.327	-0.550	-0.655
$SMND$	-1.51	-1.667	-1.16	-1.291

Table C.3: Decay rate for $m = 1$ mode for 2 flows MND and a similar flow with slightly modified (smoothed) radial velocity component (SMND).

is only to lower the critical magnetic Reynolds number in the domain of experimental feasibility or if the dynamo mechanism is fundamentally different when the conducting medium is no longer homogenous. This issue can be addressed numerically in principle . However, to face such problems with heterogenous domains, specific algorithms must be implemented and validated. This was the aim of the present study. Our comparative runs of Ohmic decay problems proved in practice to be extremely useful to optimize both codes and to select some numerical coefficients occurring in the algorithms (such as in penalty terms).

The problems which have been successively presented above are standard in MHD, but we were forced to reduce the dimension of the parameter space to configurations more or less related to the Cadarache experiment, where the impellers may be treated as disks in a conducting flow bounded by a cylinder of a given aspect ratio. We have thus considered axisymmetric domains only (see [58] for non-axisymmetric cases), and azimuthal modes of low order ($m = 0$ and 1).

We have first studied Ohmic decay problems, with disk impellers of various thicknesses to investigate scaling laws and the impact of the spatial resolution. The effects of internal assemblies of high permeability material within the fluid container are different from those of an enhanced, but homogenous fluid permeability because of inner boundary conditions for the magnetic field (in case of high permeability material), and for the electric field/current (in case of conductivity jumps). In the free decay problem with thin high permeability disks a selective enhancement of the axisymmetric toroidal field and the ($m = 1$) mode is observed whereas the axisymmetric poloidal field component is preferred in case of high conductive

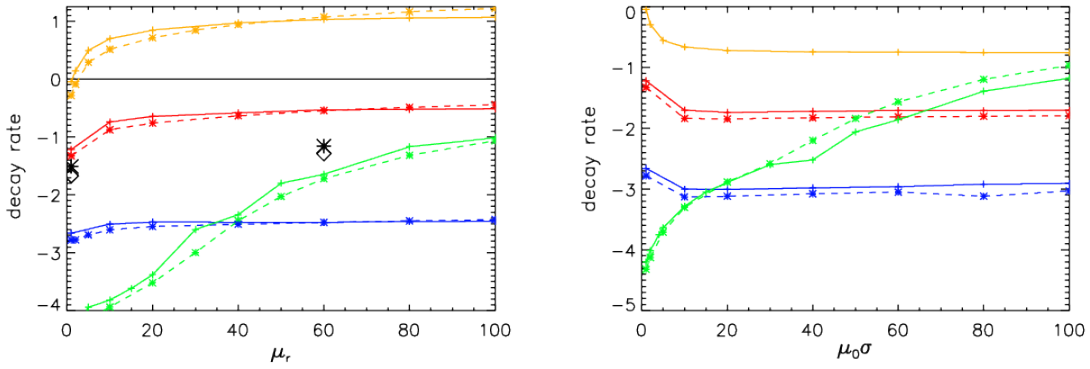

Figure C.13: Growth rates for the MND flow driven dynamo against μ_r (left panel) and against $\mu_0\sigma$ (right panel). Solid curves denote data obtained from the FV/BEM scheme, dashed curves denote the results from the SFEMaNS scheme. The green, blue, red, yellow colors denote the cases $\mathrm{Rm} = 0, 30, 50, 70$. The black stars in the left panel show the results for the SMND flow at $\mathrm{Rm} = 50$ (see text) as reported in Tab. C.3.

disks.

We have also shown that pseudo-vacuum boundary conditions, which are easier to implement on the cylinder walls than the jump conditions on the impellers, have only a slight influence on the decay rates. The impact of the outer container boundaries on the field behavior is limited to a shift of the decay/growth rates. This is surprising, insofar as pseudo vacuum boundary conditions resemble the conditions that correspond to an external material with infinite permeability. Nevertheless, the presence of high permeability/conductivity disks within the liquid hides the influence of outer boundary conditions, and the simplifying approach applying vanishing tangential field conditions at the end caps of the cylinder in order to mimic the effects of the high permeability disks in the VKS experiment ([61]) is not sufficient to describe the correct field behavior. The consideration of impeller disks with (large but finite) permeability remains indispensable in order to describe the influence of the material properties.

For completeness, we have also considered conductivity domains. From the experimental point of view the utilization of disks with a conductivity that is 100 times larger than the conductivity of liquid sodium remains purely academic. Nevertheless, the simulations show a crucial difference between heterogeneous permeabilities and conductivities: even if these two quantities may appear in the definition of an effective Reynolds number $\mathrm{Rm}^{\mathrm{eff}} = \mu_0 \mu_{\mathrm{r}}^{\mathrm{eff}} \sigma^{\mathrm{eff}} UL$, they do not play the same role and they select different geometries of the dominant decaying mode. It is not only a change of magnetic diffusivity that matters.

We have considered kinematic dynamo action, using analytically defined flows in accordance with the setting of the VKS mean flow. Since these flows and the variation of μ and σ are axisymmetric, the azimuthal modes are decoupled. An important Fourier mode is the $(m = 1)$ mode which will be excited eventually through dynamo action. We have shown that our codes give comparable growth rates for this mode. We have examined also the growth rate of the $(m = 0)$ magnetic field in presence of soft iron impellers and the axisymmetric MND flow. Since convergence of results is not achieved in all the cases considered, this comparative

study is still in progress and it has thus not been included in the present paper. We recall that the main surprise of the Cadarache experiment was perhaps the occurrence of the mode $(m = 0)$, which pointed out the possible role of the non-axisymmetric flow fluctuations. Non-axisymmetric velocity contributions might be considered in terms of an α-effect as it has been proposed in [119] and [89, 88]. Preliminary examinations applying simple α-distributions are presented in [55] and [58]. However, there is still a lack of knowledge on the details and physical justification of a precise α-distribution which requires a non-linear hydrodynamic code. The questions related to this empirical fact represent a main issue of the experimental and numerical approaches of the fluid dynamo problem and deserve a dedicated study. Our axisymmetric model is not intended to explain the main features of the VKS experiment, which are the dominating axisymmetric field mode and the surprising low critical magnetic Reynolds number of $\mathrm{Rm} \approx 32$. However, our results give a hint why the $(m = 1)$ mode remains absent in the experiment.

A source term on the $m = 0$ mode appears when the flow axisymmetry is broken. Although the relative amplitude of this source cannot be discussed here, we note that the decay time of the $(m = 0)$ toroidal mode becomes the largest when the effective permeability is high enough (see for example figure C.8). It may thus appear as the dominant mode of the dynamo, as it seems to be observed in the VKS experiment. Stated otherwise, the impact of soft-iron impellers on the critical magnetic Reynolds number of the $(m = 1)$-mode could be rather low (decrease from ~ 76 to ~ 55 in the MND case) and could remain unobservable, while it could be strong for the $(m = 0)$ mode (down to 32 in the VKS geometry) when conjugated with a slight departure from axisymmetry of the flow. Numerical evidences for this picture require the consideration of non-axisymmetric velocity contributions, either in terms of vortices as e.g. observed in water experiments by [152] or applying a physically established profile of an α-effect.

Acknowledgments

Financial support from Deutsche Forschungsgemeinschaft (DFG) in frame of the Collaborative Research Center (SFB) 609 is gratefully acknowledged and from European Commission under contract 028679. The computations using SFEMaNS were carried out on the IBM SP6 computer of Institut du Développement et des Ressources en Informatique Scientifique (IDRIS) (project # 0254).

Annexe D

Effects of discontinuous magnetic permeability on magnetodynamic problems

J.-L. Guermond [a], J. Léorat [b], F. Luddens [a,c], C. Nore [c,d,e], A. Ribeiro [c]

Abstract

A novel approximation technique using Lagrange finite elements is proposed to solve magneto-dynamics problems involving discontinuous magnetic permeability and non-smooth interfaces. The algorithm is validated on benchmark problems and is used for kinematic studies of the Cadarache von Kármán Sodium 2 (VKS2) experimental fluid dynamo.

D.1 Introduction

This paper is the third part of a research program whose goal is to develop a solution method for solving the magnetohydrodynamic equations in heterogeneous axisymmetric domains. The computational domain is assumed to be composed of non-conducting and conducting media. The electromagnetic field is represented by the pair $\mathbf{H}-\phi$, where $\mathbf{H}$ denotes the magnetic field in the conducting region and ϕ denotes the magnetic scalar potential in the non-conducting region. The basic ideas for approximating this class of problems have been introduced in [65]. Lagrange finite elements are used in the median section and variations in the azimuthal direction are approximated with Fourier expansions. The approximation is discontinuous across the interface separating the conducting and the non-conducting domains. This choice allows us to use Lagrange elements. The coupling between the $\mathbf{H}$ and ϕ representations is done by using an Interior Penalty technique [7, 11]. The method has been applied in [65] to the Maxwell equations forced by given velocity fields; this is the so-called kinematic dynamo

[a] Department of Mathematics, Texas A&M University 3368 TAMU, College Station, TX 77843-3368, USA
[b] Luth, Observatoire de Paris-Meudon, place Janssen, 92195 Meudon, France
[c] Laboratoire d'Informatique pour la Mécanique et les Sciences de l'Ingénieur, CNRS, BP 133, 91403 Orsay Cedex, France
[d] Université Paris Sud 11, 91405 Orsay Cedex, France
[e] Institut Universitaire de France, 103 Bd Saint-Michel, 75005 Paris, France

problem. The solution method has been shown to be stable and convergent. In [66], the method has been generalized to the full magnetohydrodynamic (MHD) problems and has been shown to be capable of solving nontrivial nonlinear dynamo problems. The Navier-Stokes/Maxwell coupling together with details on a parallelization technique for the Fast Fourier Transform (FFT) method are described in [66].

The main restriction of the method introduced in [65, 66] is that the magnetic permeability must be smooth in the conducting region. This is a major impediment since magnetic permeability heterogeneousness is suspected to play a key role in the confinement of the magnetic field in some dynamo experiments (we refer in particular to the VKS2 (von Kármán Sodium 2) successful dynamo experiment [110]) and thus significantly lowers the dynamo threshold, [89]. The second restriction is that our using Lagrange finite elements and penalizing the divergence of the magnetic induction in L^2 requires all the interfaces to be either smooth or the convexity of the interfaces be oriented towards the non-conducting region. This geometrical restriction is sometimes cumbersome. The objective of the present work is to address the two above issues. We show in the present work that the approximation framework proposed in [65, 66] can be generalized to account for magnetic permeability jumps and possible lack of smoothness of the interfaces where the electric conductivity and the magnetic permeability are discontinuous.

The paper is organized as follows. Notation and basic notions regarding the continuous problem are introduced and discussed in §D.2. The finite element approximation is presented in §D.3. In addition to accounting for discontinuous magnetic permeability, the main novelty of the method is condensed in the bilinear form $\mathcal{D}$ in the weak formulation (D.3.11). The new method is tested numerically on various academic benchmark problems in §D.4. The method is shown therein to be robust with respect to geometric singularities and high magnetic permeability contrasts. The method is finally used in § D.5 to explore various aspects of the VKS2 experiment. Our numerical results confirm the experimental observation that using soft iron components in the VKS2 experiment significantly lowers the dynamo threshold.

D.2 Setting of the magnetic problem

The purpose of this section is to describe the PDE setting. We focus our attention on the magnetic features of the problem since the main novelty that we are going to introduce with respect to [65, 66] consists of accounting for the discontinuities of magnetic permeability field. The Navier-Stokes part of the full MHD problem is thus not considered in this paper.

D.2.1 The geometric setting

We consider the MHD equations in a bounded axisymmetric domain $\Omega \subset \mathbb{R}^3$ (Ω could be a truncated version of an unbounded domain). The boundary of Ω is denoted by $\Gamma = \partial\Omega$ and is henceforth assumed to be at least Lipschitz continuous. Ω is assumed to be partitioned into a conducting region (subscript c) and an insulating region (subscript v) as follows:

$$\overline{\Omega} = \overline{\Omega}_c \cup \overline{\Omega}_v, \qquad \Omega_c \cap \Omega_v = \emptyset. \tag{D.2.1}$$

Ω_c is referred to as the conducting domain and Ω_v is referred to as the non-conducting domain. The interface between the conducting region and the non-conducting region is given and denoted by

$$\Sigma = \partial\Omega_c \cap \partial\Omega_v. \tag{D.2.2}$$

The magnetic permeability, μ, is assumed to be axisymmetric and piece-wise smooth over Ω_c. More precisely, we assume that the conducting region, Ω_c, can be partitioned into subregions $\Omega_{c1}, \ldots, \Omega_{cN}$ so that the restriction of μ over each subregion, Ω_{ci}, $i \in \overline{1,N}$, is smooth. In other words,

$$\overline{\Omega_c} = \overline{\Omega_{c1}} \cup \ldots \cup \overline{\Omega_{cN}}, \qquad \Omega_{ci} \cap \Omega_{cj} = \emptyset, \ \forall i,j \in \overline{1,N}. \tag{D.2.3}$$

The interface between all the conducting subregions is also given and denoted by Σ_μ,

$$\Sigma_\mu = \cup_{i,j\in\overline{1,N}} \overline{\Omega_{ci}} \cap \overline{\Omega_{cj}}. \tag{D.2.4}$$

The interfaces Σ and Σ_μ are fixed and given; they correspond to changes of material properties and one side of these interfaces is always a non-deformable solid.

To easily refer to boundary conditions, we introduce

$$\Gamma_c = \Gamma \cap \partial\Omega_c, \quad \Gamma_v = \Gamma \cap \partial\Omega_v. \tag{D.2.5}$$

Note that $\Gamma = \Gamma_v \cup \Gamma_c$. Moreover, we denote by Γ_v^0 the connected component of $\partial\Omega_v$ that contains Γ_v. We assume that $\partial\Omega_v$ has $J+1$ connected components, say

$$\Gamma_v^0, \Gamma_v^1, \ldots, \Gamma_v^J. \tag{D.2.6}$$

Observe that $\Sigma = (\Gamma_v^0 \setminus \Gamma_v) \cup \Gamma_v^1 \cup \ldots \cup \Gamma_v^J$

The notation is illustrated in Figure D.1 on two examples. The vertical dashed line represents the symmetry axis. Only the meridional section of each region is shown. The geometry shown in the left panel (a) has $J = 2$ (3 conducting torii), and $\Sigma = (\Gamma_v^0 \setminus \Gamma_v) \cup \Gamma_v^1 \cup \Gamma_v^2$. The conducting region is composed of 5 subregions. The geometry shown in the right panel (b) has $J = 1$, $\Gamma_v^0 = \Gamma_v$, $\Gamma_c = \emptyset$, and $\Sigma = \Gamma_v^1$. The conducting region is composed of 2 subregions of different electric conductivities and magnetic diffusivities.

D.2.2 The PDE setting

The conducting region is composed of fluid and solid domains, with conductivity and permeability jumps. The time evolution of the magnetic and electric fields is modeled by the Maxwell equations. To simplify the presentation, we assume in this paper that the velocity field of the fluid and that of the solid moving parts are known and we denote this quantity by $\tilde{\mathbf{u}}$. No notational distinction is made to separate the fluid and the solid regions.

The time evolution of the electromagnetic field is modeled as follows:

$$\begin{cases} \mu\partial_t \mathbf{H} = -\nabla\times\mathbf{E}, \ \text{in } \Omega \\ \nabla\times\mathbf{H} = \begin{cases} \sigma(\mathbf{E} + \tilde{\mathbf{u}}\times\mu\mathbf{H}) + \mathbf{j}^s, & \text{in } \Omega_c \\ 0, & \text{in } \Omega_v \end{cases} \\ \nabla\cdot\mathbf{E} = 0, \ \text{in } \Omega_v \\ \mathbf{E}\times\mathbf{n}|_\Gamma = \mathbf{a}, \qquad \mathbf{H}|_{t=0} = \mathbf{H}_0, \ \text{in } \Omega_c \\ \displaystyle\int_{\Gamma_v^i} \mathbf{E}\cdot\mathbf{n} = 0, \quad 1 \le i \le J \end{cases} \tag{D.2.7}$$

where $\mathbf{n}$ is the outward normal on Γ. The independent variables are space and time. The dependent variables are the magnetic field, $\mathbf{H}$, and the electric field, $\mathbf{E}$. The physical parameters are the magnetic permeability, μ, and the electric conductivity, σ. The data are $\mathbf{H}_0$, $\mathbf{a}$

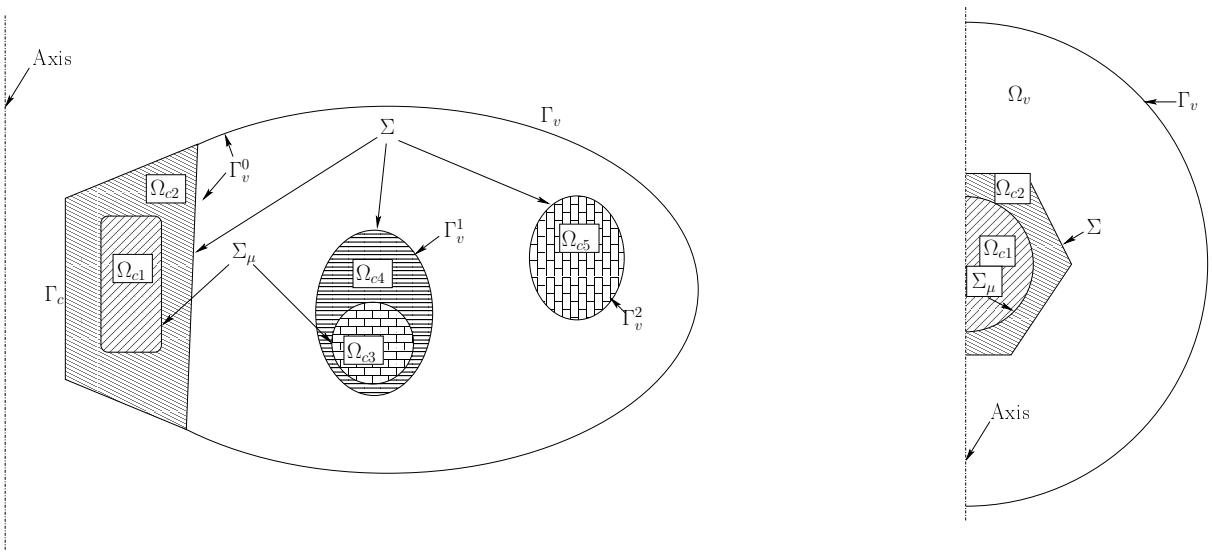

(a) (b)

Figure D.1: Examples of computational domains with various boundaries. The left line is the revolution axis. The shaded regions constitute the conducting domain Ω_c, the non-shaded domain is vacuum Ω_v. The dashed subregions may have different electric conductivities and magnetic permeabilities.

and $\mathbf{j}^s$: $\mathbf{H}_0$ is an initial data; $\mathbf{a}$ is a boundary data; $\mathbf{j}^s$ is an externally imposed distribution of current. The initial magnetic induction field, $\mu\mathbf{H}_0$, is assumed to satisfy the compatibility condition $\nabla\cdot(\mu\mathbf{H}_0) = 0$.

Let $\mathcal{U}$ be the characteristic scale of $\tilde{\mathbf{u}}$ and let $\mathfrak{c}$ be the speed of light. The MHD approximation consists of assuming that the ratio $\mathcal{U}/\mathfrak{c}$ is extremely small. This hypothesis leads to neglect the displacement currents $\epsilon\partial_t\mathbf{E}$ in the Ampère-Maxwell equation. Note however that the conditions $\nabla\cdot\mathbf{E}|_{\Omega_v} = 0$ and $\int_{\Gamma_v^i}\mathbf{E}\cdot\mathbf{n} = 0$, $1 \le i \le J$ are what is left from the Ampère-Maxwell equation when passing to the limit to zero on the ratio $\mathcal{U}/\mathfrak{c}$ (assuming that the total electrostatic charge in each conducting region is zero). These extra conditions ensure that $\mathbf{E}$ is uniquely defined, i.e., they have no effect on $\mathbf{H}$. Note finally that the condition $\int_{\Gamma_v^0}\mathbf{E}\cdot\mathbf{n} = 0$ needs not be enforced since it is a consequence of the J other conditions, $\int_{\Gamma_v^i}\mathbf{E}\cdot\mathbf{n} = 0$, $i = 1,\ldots,J$, together with $\mathbf{E}$ being solenoidal. We refer to [19, 3] for more details on the asymptotic analysis leading to (D.2.7).

When σ is uniformly positive over Ω, i.e., $\Omega_c = \Omega$ and $\Omega_v = \emptyset$, an evolution equation for $\mathbf{H}$ can be obtained after eliminating the electric field. This shortcut is no longer possible when Ω_v is non trivial, and determining the complete solution, including the electric field, is no longer straightforward.

We henceforth assume that the conductivity σ is zero in Ω_v and is bounded from below and from above in Ω_c by positive constants. We also assume that the restriction of μ to Ω_v is a smooth function, and that μ is piece-wise smooth on Ω_c, i.e., $\mu|_{\Omega_{ci}}$ is smooth for all $i = 1,\ldots,N$.

D.2.3 Non-dimensionalization of the equations

We now non-dimensionalize (D.2.7). We denote by $\mathcal{L}$ and $\mathcal{U}$ reference length and velocity scales, respectively. Our basic assumption is that $\mathcal{U} \ll \mathfrak{c}$, where $\mathfrak{c}$ is the speed of light. The reference (advective) time scale is $\mathcal{T} := \mathcal{L}/\mathcal{U}$. The fluid density is assumed to be a constant ρ. The reference magnetic permeability and electric conductivity are denoted by μ_0 and σ_0, respectively. We choose the reference scale for the magnetic field to be so that the reference Alfvén speed is one, i.e., $\mathcal{H} := \mathcal{U}\sqrt{\rho/\mu_0}$. The reference scale for the electric field is set to be $\mathcal{E} := \mu_0 \mathcal{H}\mathcal{U}$. The source current $\mathbf{j}^s$ and the data $\mathbf{H}_0$, $\mathbf{a}$ are non-dimensionalized by $\mathcal{H}\mathcal{L}^{-1}$, $\mathcal{H}$ and $\mathcal{H}$, respectively. This leaves one non-dimensional parameter which we refer to as the magnetic Reynolds number, $R_{\rm m}$, and which is defined as follows:

$$R_{\rm m} := \mathcal{U}\mathcal{L}\sigma_0\mu_0. \tag{D.2.8}$$

Henceforth we abuse the notation by using the same symbols for the non-dimensional and the corresponding dimensional quantities. The non-dimensional set of equations is re-written as follows:

$$\begin{cases} \mu\partial_t \mathbf{H} = -\nabla\times\mathbf{E}, \text{ in } \Omega \\ \nabla\times\mathbf{H} = \begin{cases} R_{\rm m}\sigma(\mathbf{E} + \tilde{\mathbf{u}}\times\mu\mathbf{H}) + \mathbf{j}^s, & \text{in } \Omega_c \\ 0, & \text{in } \Omega_v \end{cases} \\ \nabla\cdot\mathbf{E} = 0, \text{ in } \Omega_v \\ \mathbf{E}\times\mathbf{n}|_\Gamma = \mathbf{a}, \qquad \mathbf{H}|_{t=0} = \mathbf{H}_0, \text{ in } \Omega_c \\ \displaystyle\int_{\Gamma_v^i} \mathbf{E}\cdot\mathbf{n} = 0, \quad 1 \le i \le J, \end{cases} \tag{D.2.9}$$

where σ and μ are the relative conductivity and permeability, respectively.

D.2.4 Introduction of ϕ and elimination of E

In addition to the above geometrical hypotheses on Ω, we henceforth assume that the initial data $\mathbf{H}_0$ is smooth and is such that $\nabla\cdot(\mu\mathbf{H}_0)|_\Omega = 0$ and $\nabla\times\mathbf{H}_0|_{\Omega_v} = 0$. We also assume that either Ω_v is simply connected or that the circulation of $\mathbf{H}$ along any path in the insulating media is zero for all time. The condition $\nabla\times\mathbf{H}|_{\Omega_v} = 0$ together with the above assumption implies that there is a scalar potential ϕ, defined up to an arbitrary constant, such that $\mathbf{H}|_{\Omega_v} = \nabla\phi$. The same holds for $\mathbf{H}_0$, i.e., there is ϕ_0 such that $\mathbf{H}_0|_{\Omega_v} = \nabla\phi_0$.

To clarify in which domain we work, we now define

$$\mathbf{H} = \begin{cases} \mathbf{H}^c & \text{in } \Omega_c \\ \nabla\phi & \text{in } \Omega_v, \end{cases} \qquad \mu = \begin{cases} \mu^c & \text{in } \Omega_c \\ \mu^v & \text{in } \Omega_v, \end{cases} \tag{D.2.10}$$

and we denote by $\mathbf{n}^c$ and $\mathbf{n}^v$ the outward normal on $\partial\Omega_c$ and $\partial\Omega_v$, respectively. Similarly, to distinguish between the limits $\lim_{\Omega_{ci}\ni\mathbf{y}\to\mathbf{x}}$ and $\lim_{\Omega_{cj}\ni\mathbf{y}\to\mathbf{x}}$ whenever $\mathbf{x}$ is on the interface Σ_μ and $\mathbf{x} \in \overline{\Omega_{ci}} \cap \overline{\Omega_{cj}}$, we set

(D.2.11)

$$\mathbf{H}_1^c(\mathbf{x}) = \begin{cases} \lim_{\Omega_{ci}\ni\mathbf{y}\to\mathbf{x}} \mathbf{H}^c(\mathbf{y}) & \text{if } i < j \\ \lim_{\Omega_{cj}\ni\mathbf{y}\to\mathbf{x}} \mathbf{H}^c(\mathbf{y}) & \text{otherwise,} \end{cases} \qquad \mathbf{H}_2^c(\mathbf{x}) = \begin{cases} \lim_{\Omega_{cj}\ni\mathbf{y}\to\mathbf{x}} \mathbf{H}^c(\mathbf{y}) & \text{if } i < j \\ \lim_{\Omega_{ci}\ni\mathbf{y}\to\mathbf{x}} \mathbf{H}^c(\mathbf{y}) & \text{otherwise,} \end{cases}$$

and we have similar definitions for $\mu_1^c(\mathbf{x})$ and $\mu_2^c(\mathbf{x})$. For any (scalar- or vector-valued) function f that is two-valued at $\mathbf{x} \in \overline{\Omega_{ci}} \cap \overline{\Omega_{cj}}$ we define the average of f at $\mathbf{x}$ as follows:

$$\{\!\{f\}\!\}(\mathbf{x}) = \frac{1}{2}(f_1(\mathbf{x}) + f_2(\mathbf{x})). \tag{D.2.12}$$

Furthermore, we denote by $\mathbf{n}^{ci}(\mathbf{x})$ and $\mathbf{n}^{cj}(\mathbf{x})$ the outward normal at $\mathbf{x}$ on $\partial\Omega_{ci}$ and $\partial\Omega_{cj}$, respectively. Assuming that $i < j$, we set $\mathbf{n}_1^c(\mathbf{x}) = \mathbf{n}^{ci}(\mathbf{x})$ and $\mathbf{n}_2^c(\mathbf{x}) = \mathbf{n}^{cj}(\mathbf{x})$.

It is possible to eliminate the electric field from the problem (see e.g. [65] for the details), and once this is done we obtain:

$$\begin{cases} \mu^c \partial_t \mathbf{H}^c = -\nabla\times(R_{\mathrm{m}}^{-1}\sigma^{-1}(\nabla\times\mathbf{H}^c - \mathbf{j}^s) - \tilde{\mathbf{u}}\times\mu^c\mathbf{H}^c), & \text{in every } \Omega_{ci},\ i \in \overline{1,N} \\ \mu^v \partial_t \Delta\phi = 0 & \text{in } \Omega_v \\ (R_{\mathrm{m}}^{-1}\sigma^{-1}(\nabla\times\mathbf{H}^c - \mathbf{j}^s) - \tilde{\mathbf{u}}\times\mu^c\mathbf{H}^c)\times\mathbf{n}^c = \mathbf{a} & \text{on } \Gamma_c \\ \mu^v \partial_{\mathbf{n}^v}(\partial_t\phi) = -\mathbf{n}^v\cdot\nabla\times(\mathbf{n}^v\times\mathbf{a}), & \text{on } \Gamma_v \\ \mathbf{H}_1^c\times\mathbf{n}_1^c + \mathbf{H}_2^c\times\mathbf{n}_2^c = 0 & \text{on } \Sigma_\mu \\ \mu_1^c\mathbf{H}_1^c\cdot\mathbf{n}_1^c + \mu_2^c\mathbf{H}_2^c\cdot\mathbf{n}_2^c = 0 & \text{on } \Sigma_\mu \\ \mathbf{H}^c\times\mathbf{n}^c + \nabla\phi\times\mathbf{n}^v = 0 & \text{on } \Sigma \\ \mu^c\mathbf{H}^c\cdot\mathbf{n}^c + \mu^v\nabla\phi\cdot\mathbf{n}^v = 0 & \text{on } \Sigma \\ \mathbf{H}^c|_{t=0} = \mathbf{H}_0^c, \qquad \phi|_{t=0} = \phi_0. \end{cases} \tag{D.2.13}$$

The first equation in (D.2.13) is obtained by substituting the electric field in the Faraday equation in the conducting domain by $\mathbf{E}^c := (R_{\mathrm{m}}\sigma)^{-1}(\nabla\times\mathbf{H}^c - \mathbf{j}^s) - \tilde{\mathbf{u}}\times\mu^c\mathbf{H}^c$. The second equation is obtained by taking the divergence of the Faraday equation in the insulating region, $\mu^v\partial_t\nabla\phi = -\nabla\times\mathbf{E}^v$. The third and fourth equations are the boundary condition on the electric field on $\Gamma_c \cup \Gamma_v$. The fifth, sixth, seventh and eighth equations require that the tangential component of the magnetic field and the normal component of the magnetic induction are continuous across $\Sigma\cup\Sigma_\mu$. Observe that the operator $\mathbf{n}^v\cdot\nabla\times(\cdot)$ involves only tangential derivatives; hence, it is meaningful to have it acting on the field $\mathbf{n}^v\times\mathbf{a}$ which is only defined on Γ. Note also that the two conditions $(\mu^c\mathbf{H}^c\cdot\mathbf{n}^c + \mu^v\nabla\phi\cdot\mathbf{n}^v)|_\Sigma = 0$ and $(\mu_1^c\mathbf{H}^c\cdot\mathbf{n}_1^c + \mu_2^c\mathbf{H}^c\cdot\mathbf{n}_2^c)|_{\Sigma_\mu} = 0$ express the continuity of the normal component of the magnetic induction across Σ and Σ_μ, respectively. These constraints are consequences of the continuity of the tangential components of the electric field across Σ and Σ_μ, respectively.

If the electric field is needed, it is computed in the conducting domain by using Ohm's law, i.e., by setting $\mathbf{E}^c := (R_{\mathrm{m}}\sigma)^{-1}(\nabla\times\mathbf{H}^c - \mathbf{j}^s) - \tilde{\mathbf{u}}\times\mu^c\mathbf{H}^c$. The electric field is computed in the non-conducting medium by solving the Cauchy-Riemann problem: $\nabla\times\mathbf{E}^v = -\mu^v\partial_t\nabla\phi$, $\nabla\cdot\mathbf{E}^v = 0$, $\mathbf{E}^v\times\mathbf{n}^v|_\Sigma = -\mathbf{E}^c\times\mathbf{n}^c|_\Sigma$, $\mathbf{E}^v\times\mathbf{n}^v|_{\Gamma_v} = \mathbf{a}$, and $\int_{\Gamma_v^i}\mathbf{E}^v\cdot\mathbf{n}^v = 0$, $1 \le i \le J$. Note that (D.2.13) does not involve the Γ_v^i's, $1 \le i \le J$, and whether μ is continuous or not does not matter when computing the electric field.

D.2.5 Weak formulation

A weak formulation of (D.2.7) with the electric field eliminated (i.e., (D.2.13)) has been derived in [65] assuming that μ is continuous. We handle the discontinuous situation similarly. For this purpose, we introduce the following Hilbert spaces:

$$\mathbf{L} = \{(\mathbf{b},\varphi) \in \mathbf{L}^2(\Omega_c)\times H^1_{\int=0}(\Omega_v)\}, \tag{D.2.14}$$

$$\mathbf{X} = \{(\mathbf{b},\varphi) \in \mathbf{H}_{\mathrm{curl}}(\Omega_c)\times H^1_{\int=0}(\Omega_v);\ (\mathbf{b}\times\mathbf{n}^c + \nabla\varphi\times\mathbf{n}^v)|_\Sigma = 0\}, \tag{D.2.15}$$

and we equip $\mathbf{L}$ and $\mathbf{X}$ with the norm of $\mathbf{L}^2(\Omega_c)\times H^1(\Omega_v)$ and $\mathbf{H}_{\rm curl}(\Omega_c)\times H^1(\Omega_v)$, respectively. $H^1_{\int=0}(\Omega_v)$ is the subspace of $H^1(\Omega_v)$ composed of the functions of zero mean value. The space $\mathbf{H}_{\rm curl}(\Omega_c)$ is composed of the vector-valued functions on Ω_c that are component-wise L^2-integrable and whose curl is also component-wise L^2-integrable. The space $\mathbf{H}_{\rm div}(\Omega)$ is composed of the vector-valued functions on Ω that are component-wise L^2-integrable and whose divergence is L^2-integrable. We recall that, for any field $\mathbf{b}$ in $\mathbf{H}_{\rm curl}(\Omega_c)$, the tangential components of $\mathbf{b}$ are continuous across Σ_μ, i.e., $\mathbf{b}_1\times\mathbf{n}_1^c+\mathbf{b}_2\times\mathbf{n}_2^c=0$.

By proceeding as in [65] and taking inspiration from the so-called Interior Penalty method [7, 11], we reformulate the problem as follows: Seek the pair $(\mathbf{H}^c,\phi)\in L^2((0,+\infty);\mathbf{X})\cap L^\infty((0,+\infty);\mathbf{L})$ (with $\partial_t\mathbf{H}^c$ and $\partial_t\phi$ in appropriate spaces) such that for all pairs $(\mathbf{b},\varphi)\in\mathbf{X}$ and a.e. $t\in(0,+\infty)$,

(D.2.16)

$$
\left\{\begin{array}{l}
\mathbf{H}^c|_{t=0}=\mathbf{H}_0^c;\quad \nabla\phi|_{t=0}=\nabla\phi_0,\\
\displaystyle\int_{\Omega_c}\big[\mu^c(\partial_t\mathbf{H}^c)\cdot\mathbf{b}+((R_{\rm m}\sigma)^{-1}(\nabla\times\mathbf{H}^c-\mathbf{j}^s)-\tilde{\mathbf{u}}\times\mu^c\mathbf{H}^c)\cdot\nabla\times\mathbf{b}\big]+\int_{\Omega_v}\mu^v(\partial_t\nabla\phi)\cdot\nabla\varphi\\
\qquad\displaystyle+\int_{\Sigma_\mu}\big\{\!\!\big\{(R_{\rm m}\sigma)^{-1}(\nabla\times\mathbf{H}^c-\mathbf{j}^s)-\tilde{\mathbf{u}}\times\mu^c\mathbf{H}^c\big\}\!\!\big\}\cdot(\mathbf{b}_1\times\mathbf{n}_1^c+\mathbf{b}_2\times\mathbf{n}_2^c)\\
\qquad\displaystyle+\int_{\Sigma}((R_{\rm m}\sigma)^{-1}(\nabla\times\mathbf{H}^c-\mathbf{j}^s)-\tilde{\mathbf{u}}\times\mu^c\mathbf{H}^c)\cdot(\mathbf{b}\times\mathbf{n}^c+\nabla\varphi\times\mathbf{n}^v)\\
\qquad\displaystyle=\int_{\Gamma_c}(\mathbf{a}\times\mathbf{n})\cdot(\mathbf{b}\times\mathbf{n})+\int_{\Gamma_v}(\mathbf{a}\times\mathbf{n})\cdot(\nabla\varphi\times\mathbf{n}).
\end{array}\right.
$$

The interface integrals over Σ and Σ_μ are zero since $\mathbf{b}\times\mathbf{n}^c+\nabla\varphi\times\mathbf{n}^v=0$ and $\mathbf{b}_1\times\mathbf{n}_1^c+\mathbf{b}_2\times\mathbf{n}_2^c=0$, but we nevertheless retain these two integrals since they will not vanish when we construct the non-conforming finite element approximation, see §D.3. In the same spirit, observe that the tangential components of the average of $\big\{\!\!\big\{\big((R_{\rm m}\sigma)^{-1}(\nabla\times\mathbf{H}^c-\mathbf{j}^s)-\tilde{\mathbf{u}}\times\mu^c\mathbf{H}^c\big)\big\}\!\!\big\}\times\mathbf{n}_1^c$ are equal to the average of the tangential components of the electric field. Since the tangential components of electric field are continuous, the two terms composing the average across Σ_μ are actually equal. We nevertheless retain the average notation since this is the formulation that we shall use when we construct the non-conforming finite element approximation, see §D.3.

The main novelty with respect to [65, 66] is the presence in (D.2.16) of the boundary integral over Σ_μ. It is this term that will allow us to account for jumps on the magnetic permeability. The boundary integral over Σ_μ appears when one tests the Faraday equation in (D.2.13) with a test function $\mathbf{b}$ that is piecewise smooth on $\Omega_{c1},\ldots,\Omega_{cN}$ but with discontinuous tangential components across Σ_μ, and when one integrates by parts over each Ω_{ci}, $i\in\overline{1,N}$.

Showing that the problem (D.2.16) is well-posed under suitable assumption on the velocity field $\tilde{\mathbf{u}}$ is a standard exercise in functional analysis; it is essentially a consequence of Lions' theorem (see e.g. [23, p .218], [95, pp. 253–258]). We refer e.g. [3, 19], [65, Thm 2.1] for more details on the well-posedness issue.

At this point it may not seem clear to the reader that the weak formulation (D.2.16) naturally enforces the interface condition $\mu_1^c\mathbf{H}_1^c\cdot\mathbf{n}_1^c+\mu_2^c\mathbf{H}_2^c\cdot\mathbf{n}_2^c=0$ across Σ_μ. To see that this is indeed true, let us set $\mathbf{E}^c:=(R_{\rm m}\sigma)^{-1}(\nabla\times\mathbf{H}^c-\mathbf{j}^s)-\tilde{\mathbf{u}}\times\mu^c\mathbf{H}^c$ on Ω_c. By using test functions compactly supported on Ω_c, one infers from (D.2.16) that $\mathbf{H}^c$ and $\mathbf{E}^c$ are related by Faraday's law: $\mu^c\partial_t\mathbf{H}^c=-\nabla\times\mathbf{E}^c$ (integrate by parts over Ω_c and apply a distribution

argument). Similarly, by using test functions whose support is compact on Ω_c and has a non-empty intersection with Σ_μ, one infers from (D.2.16) that the tangential components of $\mathbf{E}^c$ are continuous across Σ_μ, i.e., $\mathbf{E}_1^c \times \mathbf{n}_1^c + \mathbf{E}_2^c \times \mathbf{n}_2^c = 0$ (integrate by parts over Ω_{c1} and over Ω_{c2}). This immediately implies that $(\nabla \times \mathbf{E}_1^c)\cdot\mathbf{n}_1^c + (\nabla \times \mathbf{E}_2^c)\cdot\mathbf{n}_2^c = 0$ across Σ_μ, which, owing to Faraday's law, implies $\partial_t(\mu_1 \mathbf{H}_1^c\cdot\mathbf{n}_1^c + \mu_2 \mathbf{H}_2^c\cdot\mathbf{n}_2^c) = 0$ across Σ_μ. One then concludes that $\mu_1 \mathbf{H}_1^c\cdot\mathbf{n}_1^c + \mu_2 \mathbf{H}_2^c\cdot\mathbf{n}_2^c = 0$ across Σ_μ, since this relation holds at time $t = 0$, (recall that $\mathbf{H}_0$ is smooth and $\nabla\cdot(\mu^c \mathbf{H}_0) = 0$ in Ω_c).

D.3 Approximation

The purpose of this section is to explain how (D.2.16) is discretized in space and time. We proceed as in [65, 66], taking into account that μ^c is discontinuous, but the divergence-free condition on the magnetic induction is treated differently so as to handle quite general geometries.

D.3.1 The geometry

The algorithm that we propose takes advantage of the cylindrical symmetry of the domain Ω and the interfaces Σ and Σ_μ. The symmetry axis is denoted Oz and the cylindrical coordinates are denoted (r, θ, z): r is the distance to the Oz axis; θ, $(0 \le \theta \le 2\pi)$, is the angular coordinate; and z is the position along the Oz axis. We denote by Ω_v^{2D}, Ω_c^{2D} and Ω_{ci}^{2D} $(i = 1, \ldots, N)$, the meridional sections of Ω_v, Ω_c and Ω_{ci}, respectively. We assume that Ω_v, Ω_c and Ω_{ci} have piecewise quadratic boundaries. These sections are meshed using quadratic triangular meshes.

We denote by $\{\mathcal{F}_h^v\}_{h>0}$, $\{\mathcal{F}_h^c\}_{h>0}$ and $\{\mathcal{F}_h^{ci}\}_{h>0}$ the corresponding regular families of non-overlapping quadratic triangular meshes. We assume for the sake of simplicity that, for every given mesh index h, $\mathcal{F}_h^{ci}$ is a subset of $\mathcal{F}_h^c$. We denote by Σ_h^{2D} and $\Sigma_{\mu h}^{2D}$ the collection of triangle faces that compose the meridional section of Σ and Σ_μ, respectively. The collection of cylindrical surfaces generated by rotation around the symmetry axis by the faces in Σ_h^{2D} and $\Sigma_{\mu h}^{2D}$ are denoted by Σ_h and $\Sigma_{\mu h}$, respectively. For every cylindrical surface F in $\Sigma_h \cup \Sigma_{\mu h}$, we denote by h_F the diameter of the triangle face that generates F.

For every element K in the mesh $\mathcal{F}_h^v \cup \mathcal{F}_h^c$ we denote by $T_K : \hat{K} \longrightarrow K$ the quadratic transformation that maps the reference triangle $\hat{K} := \{(\hat{r}, \hat{z}) \in \mathbb{R}^2,\ 0 \le \hat{r},\ 0 \le \hat{z},\ \hat{r} + \hat{z} \le 1\}$ to K, and we denote by h_K the diameter of K. Finally, we denote by K^{3D} the volume generated by rotation around the symmetry axis by an element K.

D.3.2 Space discretization for the Maxwell equations

The electromagnetic part of the problem is approximated by using the technique introduced in [65]. The main feature of the space approximation is that the method is non-conforming, i.e., the continuity constraint $(\mathbf{b}\times\mathbf{n}^c + \nabla\varphi\times\mathbf{n}^v)|_\Sigma = 0$ and $(\mathbf{b}_1\times\mathbf{n}_1^c + \mathbf{b}_2\times\mathbf{n}_2^c)|_{\Sigma_\mu} = 0$ in $\mathbf{X}$ (see (D.2.15)) are relaxed and enforced by means of an interior penalty method.

Let $\ell_{\mathbf{H}}$ and ℓ_ϕ be two integers in $\{1, 2\}$ with $\ell_\phi \ge \ell_{\mathbf{H}}$. We first define the meridional finite

element spaces

(D.3.1)
$$\mathbf{X}_h^{\mathbf{H},2D} := \{\mathbf{b}_h \in \mathbf{L}^2(\Omega_c);\, \mathbf{b}_h|_{\Omega_{ci}} \in \boldsymbol{\mathcal{C}}^0(\overline{\Omega_{ci}}), \forall i = 1,\dots,N, \mathbf{b}_h(T_K)|_K \in \mathbb{P}_{\ell_{\mathbf{H}}},\ \forall K \in \mathcal{F}_h^c\},$$

(D.3.2)
$$X_h^{\phi,2D} := \{\varphi_h \in \mathcal{C}^0(\overline{\Omega_v});\, \varphi_h(T_K)|_K \in \mathbb{P}_{\ell_\phi},\ \forall K \in \mathcal{F}_h^v\},$$

where $\mathbb{P}_k$ denotes the set of bivariate polynomials of total degree at most k, and $\mathbb{P}_k := \mathbb{P}_k \times \mathbb{P}_k \times \mathbb{P}_k$. Then, using the complex notation $\mathrm{i}^2 = -1$, the magnetic field and the scalar potential are approximated in the following spaces:

$$\mathbf{X}_h^{\mathbf{H}} := \{\mathbf{b} = \sum_{m=-M}^{M} \mathbf{b}_h^m(r,z)e^{\mathrm{i}m\theta};\, \mathbf{b}_h^m \in \mathbf{X}_h^{\mathbf{H},2D},\ \overline{\mathbf{b}_h^m} = \mathbf{b}_h^{-m},\ k \in \overline{0,M}\}, \tag{D.3.3}$$

$$X_h^{\phi} := \{\varphi = \sum_{m=-M}^{M} \varphi_h^m(r,z)e^{\mathrm{i}m\theta};\, \varphi_h^m \in X_h^{\phi,2D},\ \overline{\varphi_h^m} = \varphi_h^{-m},\ m \in \overline{0,M}\}, \tag{D.3.4}$$

where $M+1$ is the maximum number of complex Fourier modes.

D.3.3 Time discretization

We use the same time discretization as in [66]. We just recall the main steps without going through the details. The time derivatives are approximated using the second-order Backward Difference Formula (BDF2). All the terms that are likely to mix the modes are made explicit (e.g. cross products). Let Δt be the time step and set $t^n := n\Delta t$, $n \geq 0$. A first version of the algorithm is written as follows: after appropriate initialization at t^0 and t^1, define the following fields for all $n \geq 1$

$$\mathbf{H}^* = 2\mathbf{H}^{c,n} - \mathbf{H}^{c,n-1} \tag{D.3.5}$$

$$\begin{cases} D\mathbf{H}^{c,n+1} := \frac{1}{2}(3\mathbf{H}^{c,n+1} - 4\mathbf{H}^{c,n} + \mathbf{H}^{c,n-1}), \\ D\phi^{n+1} := \frac{1}{2}(3\phi^{n+1} - 4\phi^n + \phi^{n-1}). \end{cases} \tag{D.3.6}$$

The solution to the Maxwell part of the problem is computed in one step by solving for $\mathbf{H}^{c,n+1}$ in $\mathbf{X}_h^{\mathbf{H}}$ and ϕ^{n+1} in X_h^{ϕ} so that the following holds for all $\mathbf{b}$ in $\mathbf{X}_h^{\mathbf{H}}$ and all φ in X_h^{ϕ}

$$\int_{\Omega_c} \mu^c \frac{D\mathbf{H}^{c,n+1}}{\Delta t}\cdot\mathbf{b} + \int_{\Omega_v} \mu^v \frac{\nabla D\phi^{n+1}}{\Delta t}\cdot\nabla\varphi + \mathcal{L}\left((\mathbf{H}^{c,n+1}, \phi^{n+1}), (\mathbf{b},\varphi)\right) = \mathcal{R}_n\left(\mathbf{b},\varphi\right), \tag{D.3.7}$$

where we have defined the linear form $\mathcal{R}_n$

$$\mathcal{R}_n(\mathbf{b},\varphi) := \int_{\Gamma_v} (\mathbf{a}\times\mathbf{n}^v)\cdot(\nabla\varphi\times\mathbf{n}^v) + \int_{\Gamma_c} (\mathbf{a}\times\mathbf{n}^c)\cdot(\mathbf{b}\times\mathbf{n}^c) + \int_{\Omega_c} \left((R_{\mathrm{m}}\sigma)^{-1}\mathbf{j}^s + \tilde{\mathbf{u}}\times\mu^c\mathbf{H}^*\right)\cdot\nabla\times\mathbf{b}$$
$$+ \int_{\Sigma_\mu} \left\{(R_{\mathrm{m}}\sigma)^{-1}\mathbf{j}^s + \tilde{\mathbf{u}}\times\mu^c\mathbf{H}^*\right\}\cdot[\![\mathbf{b}\times\mathbf{n}]\!] + \int_{\Sigma} \left((R_{\mathrm{m}}\sigma)^{-1}\mathbf{j}^s + \tilde{\mathbf{u}}\times\mu^c\mathbf{H}^*\right)\cdot(\mathbf{b}\times\mathbf{n}^c + \nabla\varphi\times\mathbf{n}^v),$$

and $[\![\mathbf{b}\times\mathbf{n}]\!]$ stands for $\mathbf{b}_1\times\mathbf{n}_1^c+\mathbf{b}_2\times\mathbf{n}_2^c$. The bilinear form $\mathcal{L}$ in (D.3.7) is defined by

$$\mathcal{L}\left((\mathbf{H}^{c,n+1},\phi^{n+1}),(\mathbf{b},\varphi)\right) := \int_{\Omega_c}(R_{\mathrm{m}}\sigma)^{-1}\nabla\times\mathbf{H}^{c,n+1}\cdot\nabla\times\mathbf{b}+\int_{\Sigma_\mu}\left\{(R_{\mathrm{m}}\sigma)^{-1}\nabla\times\mathbf{H}^{c,n+1}\right\}\cdot[\![\mathbf{b}\times\mathbf{n}]\!]$$
$$+\,g\left((\mathbf{H}^{c,n+1},\phi^{n+1}),(\mathbf{b},\varphi)\right)+\int_{\Sigma}(R_{\mathrm{m}}\sigma)^{-1}\nabla\times\mathbf{H}^{c,n+1}\cdot\left(\mathbf{b}\times\mathbf{n}^c+\nabla\varphi\times\mathbf{n}^v\right)$$

where g is defined by

(D.3.8)

$$g((\mathbf{H}^{c,n+1},\phi^{n+1}),(\mathbf{b},\varphi)) := \beta_2\sum_{F\in\Sigma_{\mu h}}h_F^{-1}\int_F[\![\mathbf{H}^{c,n+1}\times\mathbf{n}^c]\!]\cdot[\![\mathbf{b}\times\mathbf{n}^c]\!]$$
$$+\,\beta_1\sum_{F\in\Sigma_h}h_F^{-1}\int_F(\mathbf{H}^{c,n+1}\times\mathbf{n}^c+\nabla\phi^{n+1}\times\mathbf{n}^v)\cdot(\mathbf{b}\times\mathbf{n}^c+\nabla\varphi\times\mathbf{n}^v),$$

The purpose of the bilinear form g is to penalize the quantities $\mathbf{H}^{c,n+1}\times\mathbf{n}^c+\nabla\phi^{n+1}\times\mathbf{n}^v$ and $[\![\mathbf{H}^{c,n+1}\times\mathbf{n}^c]\!]$ across Σ and Σ_μ, respectively, so that they converge to zero when the mesh-size goes to zero. The coefficients β_1 and β_2 are user-dependent. We usually take

$$\beta_1=\gamma_1/(R_{\mathrm{m}}\min_{\mathbf{x}\in\Omega_c}(\sigma(\mathbf{x}))),\qquad \beta_2=\gamma_2/(R_{\mathrm{m}}\min_{\mathbf{x}\in\Omega_c}(\sigma(\mathbf{x}))),$$

with $\gamma_1=\gamma_2=1$. This scaling can be justified by arguments from the Interior Penalty theory [7, 65, 66].

D.3.4 Addition of a magnetic pressure

At this point, the only novelty with respect to [66] is that the approximate magnetic field is discontinuous across the interface $\Sigma_{\mu h}$. This method has been proven to be convergent on finite time intervals, but it may fail to converge in the steady state regime. Indeed, in the time-dependent case, taking the divergence of Faraday's equation, we observe that provided the initial magnetic induction is divergence-free, the following holds for all times

$$\nabla\cdot(\mu\mathbf{H})=0.$$

Unfortunately, in the steady state case, this condition is a constraint that the above technique may fail to respect. We describe in this section the modifications we have made in order to enforce the divergence-free condition in both conducting and insulating part, even in time-independent situations.

Motivation for a magnetic pressure.

In [66], the solenoidality constraint is enforced by means of a penalty term added to the bilinear form $\mathcal{L}$, namely

$$\beta_0\int_{\Omega_c}\nabla\cdot(\mu^c\mathbf{H}^{c,n+1})\cdot\nabla\cdot(\mu^c\mathbf{b}),$$

where $\beta_0=0$ or 1 depending on the regularity of the domain. Taking $\beta_0=1$ requires that the approximate solution converges to the exact solution in the $\mathbf{H}_{\mathrm{curl}}(\Omega)\cap\mathbf{H}_{\mathrm{div}}(\Omega)$ norm. We point out the fact that we want to use $\mathbf{H}^1$-conforming Lagrange finite elements. It is known

since the ground-breaking work of Costabel (cf. [36]) that, for non-smooth and non-convex domains (e.g. a L-shape domain), $\mathbf{H}^1$ is a genuine closed subspace of $\mathbf{H}_{\rm curl}(\Omega) \cap \mathbf{H}_{\rm div}(\Omega)$. This means that one can find elements in $\mathbf{H}_{\rm curl}(\Omega) \cap \mathbf{H}_{\rm div}(\Omega)$ that cannot be approximated by elements of $\mathbf{H}^1$. We thus need to find another way to deal with the divergence-free constraint in non-smooth domains.

In the conducting region.

Taking inspiration from [17], we propose a non standard technique, which consists of replacing the induction equation in the conducting part by

$$\partial_t(\mu^c \mathbf{H}^c) = -\nabla \times \mathbf{E}^c - \mu^c \nabla p^c, \quad (-\Delta_0)^\alpha p^c = -\nabla\cdot(\mu^c \mathbf{H}^c), \quad p^c|_{\partial\Omega_c} = 0, \tag{D.3.9}$$

where α is a yet-to-be-chosen real parameter, Δ_0 is the Laplace operator on Ω_c with zero Dirichlet boundary condition, and p^c is a new scalar unknown which we call magnetic pressure. A simple calculation shows that if the initial magnetic induction is solenoidal, then $p^c \equiv 0$ so that (D.3.9) indeed enforces the condition $\nabla\cdot(\mu^c \mathbf{H}^c) = 0$. Taking $\alpha = 0$ in the above formulation amounts to penalize $\nabla\cdot(\mu^c \mathbf{H}^c)$ in $\mathbf{L}^2(\Omega_c)$, as in the previous subsection. For $\alpha \in (\frac{1}{2}, 1]$, this new formulation can be shown to be convergent, even if the domain is non-smooth and non-convex. We refer to [17] for the mathematical analysis of this method. Although $\alpha = 1$ is a legitimate value when solving boundary value problems, it is shown in [17] that α should be taken away from 1 when solving eigenvalue problems in non-smooth domains to avoid spurious eigenvalues. In practice, we use $\alpha \in [0.6, 0.8]$ and we do not observe any significative dependence of the method with respect to α when the interfaces are non-smooth. When the interfaces are smooth the method works properly for any value $\alpha \in [0, 1]$ both for boundary value and eigenvalue problems.

In the vacuum.

We proceed slightly differently in Ω_v. The induction equation is replaced by the following

$$\partial_t(\mu^v \nabla\phi) = -\nabla\times\mathbf{E}^v - \mu^v \nabla p^v, \quad \Delta p^v = \Delta\phi, \quad \nabla p^v\cdot\mathbf{n}^v|_{\partial\Omega_v} = 0, \tag{D.3.10}$$

where p^v is a new scalar unknown, and μ^v is the magnetic permeability in the vacuum which we assume to be constant. Once again, a simple calculation shows that if the initial magnetic induction is solenoidal, then $p^v \equiv 0$, so that (D.3.10) indeed enforces $\Delta\phi = 0$. Moreover, upon observing that

$$\int_{\Omega_v} \nabla p^v\cdot\nabla\varphi = \int_{\Omega_v} \nabla\phi\cdot\nabla\varphi - \int_{\partial\Omega_v} (\mathbf{n}\cdot\nabla\phi)\varphi, \qquad \forall\varphi \in H^1(\Omega_v)$$

The weak formulation of (D.3.10) can be re-written as follows:

$$\int_{\Omega_v} \mu^v(\partial_t\nabla\phi)\cdot\nabla\varphi = -\int_{\Omega_v} \nabla\times\mathbf{E}^v\cdot\nabla\varphi - \int_{\Omega_v} \mu^v\nabla\phi\cdot\nabla\varphi + \int_{\partial\Omega_v} \mu^v(\mathbf{n}\cdot\nabla\phi)\varphi, \qquad \forall\varphi \in H^1(\Omega_v)$$

so that p^v is eliminated from the formulation.

Final algorithm.

Finally, we have three unknown fields (one vector-field $\mathbf{H}^c$, two scalar fields ϕ, p^c) instead of two ($\mathbf{H}^c$, ϕ).

We introduce a new finite element space to approximate the new scalar unknown p^c:

$$X_h^{p,2D} := \left\{ p_h \in L^2(\Omega_c) \,/\, p_h \in \mathcal{C}^0(\overline{\Omega_c}),\ p_h(T_K) \in \mathbb{P}_{\ell_p},\ \forall K \in \mathcal{F}_h^c,\ p_h = 0 \text{ on } \partial\Omega_c \right\},$$

$$X_h^{p} := \left\{ p = \sum_{m=-M}^{M} p_h^m(r,z)\mathrm{e}^{\mathrm{i}m\theta} \,/\, \forall m = 1\ldots,M,\ p^m \in X_h^{p,2D} \text{ and } p_h^m = \overline{p_h^{-m}} \right\}$$

Here ℓ_p is an integer in {1,2}.

The final form of the algorithm is the following : after proper initialization, we solve for $\mathbf{H}^{c,n+1} \in \mathbf{X}_h^H$, $\phi^{n+1} \in X_h^\phi$ and $p^{c,n+1} \in X_h^p$ so that the following holds for all $\mathbf{b} \in \mathbf{X}_h^H$, $\psi \in X_h^\phi$, $q \in X_h^p$

$$\begin{aligned} \int_{\Omega_c} \mu^c \frac{D\mathbf{H}^{c,n+1}}{\Delta t}\cdot\mathbf{b} + \int_{\Omega_v} \mu^v \frac{\nabla D\phi^{n+1}}{\Delta t}\cdot\nabla\varphi + \mathcal{L}\left((\mathbf{H}^{c,n+1},\phi^{n+1}),(\mathbf{b},\varphi)\right) \\ + \mathcal{P}(\phi^{n+1},\varphi) + \mathcal{D}\left((\mathbf{H}^{c,n+1},p^{c,n+1}),(\mathbf{b},q)\right) = \mathcal{R}_n\left(\mathbf{b},\varphi\right) \end{aligned} \tag{D.3.11}$$

where $\mathcal{P}$ denotes the stabilizing bilinear form defined by

$$\mathcal{P}(\phi,\psi) = \int_{\Omega_v} \mu^v \nabla\phi\cdot\nabla\psi - \int_{\partial\Omega_v} \mu^v \psi\mathbf{n}\cdot\nabla\phi,$$

and $\mathcal{D}$ is defined by

$$\mathcal{D}\left((\mathbf{H},p),(\mathbf{b},q)\right) := \beta_0 \left(\int_{\Omega_c} \mu^c \nabla p\cdot\mathbf{b} - \int_{\Omega_c} \mu^c \mathbf{H}\cdot\nabla q + \sum_{K\in\mathcal{F}_h^c} \int_{K^{3D}} h_K^{2(1-\alpha)} \nabla p\cdot\nabla q + s(\mathbf{H}^{c,n+1},\mathbf{b}) \right),$$

where the last bilinear form s is defined by

$$s(\mathbf{H},\mathbf{b}) := \sum_{K\in\mathcal{F}_h^c} \int_{K^{3D}} h_K^{2\alpha} \nabla\cdot(\mu^c\mathbf{H})\nabla\cdot(\mu^c\mathbf{b}).$$

$\mathcal{P}$ accounts for the addition of p^v and $\mathcal{D}$ is a discrete approximation for the weak formulation of (D.3.9). Finally, s is a stabilization term that makes the discrete formulation well-posed irrespective of the polynomial degree of the approximation for p^c. The coefficient β_0 is scaled as follows:

$$\beta_0 = \gamma_0/(R_\mathrm{m} \min_{\mathbf{x}\in\Omega_c}(\sigma(\mathbf{x}))),$$

with $\gamma_0 = 1$. This scaling can be justified by arguments from the Interior Penalty theory [7, 65, 66].

D.4 Convergence tests

The new formulation (D.3.11) presents two major novelties with respect to that introduced in [66]: it now accounts for non-smooth geometries and discontinuous magnetic permeability fields. The purpose of this section is to illustrate numerically these new features on benchmark problems.

D.4.1 The L-shape domain

We first illustrate the positive effect of the magnetic pressure in the case of steady-state regime in a non-smooth and non-convex domain. The setting is the following: we consider the conducting L-shape domain (two dimensional case)

$$\Omega = \Omega_c = (-1,+1)^2 \backslash ([0,+1]\times[-1,0]). \tag{D.4.1}$$

with no insulating region, $\Omega_v = \emptyset$, (cf. Fig. D.2). We take $\mu = 1$, $\tilde{\mathbf{u}} = 0$, and $\sigma = 1$.

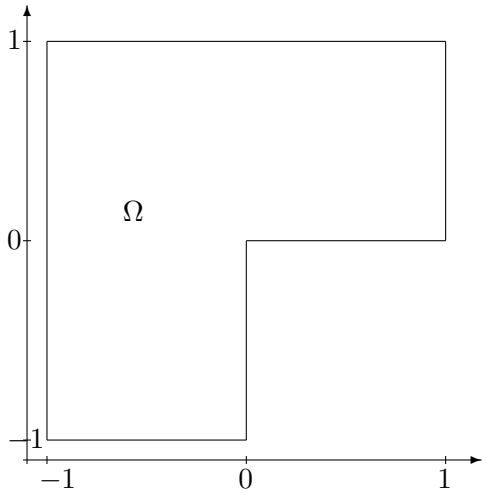

Figure D.2: Two-dimensional L-shape domain with constant μ^c

Boundary value problem

Consider the following boundary value problem in the above defined L-shape domain: find $\mathbf{H}$ such that

$$\nabla\times\nabla\times\mathbf{H} = 0, \qquad \nabla\cdot\mathbf{H} = 0, \qquad \mathbf{H}\times\mathbf{n}|_\Gamma = \mathbf{G}\times\mathbf{n}, \tag{D.4.2}$$

where the Cartesian components of the boundary data $\mathbf{G}$ are given by

$$\mathbf{G}(r,\theta) = \frac{2}{3} r^{-\frac{1}{3}} \begin{pmatrix} -\sin(\frac{\theta}{3}) \\ \cos(\frac{\theta}{3}) \end{pmatrix}, \tag{D.4.3}$$

and (r,θ) are the polar coordinates centered at the re-entrant corner of the domain. The solution to the above problem is $\mathbf{H} = \nabla\psi$, where $\psi(r,\theta) = r^{\frac{2}{3}}\sin(\frac{2}{3}\theta)$.

Five quasi-uniform (non-nested) Delaunay meshes are considered of mesh-sizes $h = 1/10$, $1/20$, $1/40$, $1/80$, $1/160$, respectively. The meshes are composed of triangles. Two types of approximation are tested; we use $\mathbb{P}_1$ elements in the first case and $\mathbb{P}_2$ elements in the second case. The magnetic field and the magnetic pressure are approximated using equal order polynomials in each case.

Denoting by $\mathbf{H}_h$ the approximate magnetic field, we report in Table D.1 the relative errors $\|\mathbf{H}_h - \mathbf{H}\|_{\mathbf{L}^2}/\|\mathbf{H}\|_{\mathbf{L}^2}$ for $\alpha = 0.75$ and $\alpha = 1$. Table D.1 also shows the computed order of convergence (COC). Convergence is observed for the $\mathbb{P}_1$ and $\mathbb{P}_2$ approximations. The best possible convergence rate is $\frac{2}{3}$ and this rate is achieved numerically when using $\mathbb{P}_2$ elements.

h	$\mathbb{P}_1$				$\mathbb{P}_2$			
	$\alpha = 0.75$		$\alpha = 1$		$\alpha = 0.75$		$\alpha = 1$	
	Rel. Error	COC	Rel. Error	COC	Rel. Error	COC	Rel. Error	COC
0.1	$2.390\,10^{-1}$	N/A	$2.303\,10^{-1}$	N/A	$1.290\,10^{-1}$	N/A	$1.110\,10^{-1}$	N/A
0.05	$1.843\,10^{-1}$	0.38	$1.826\,10^{-1}$	0.34	$8.178\,10^{-2}$	0.66	$7.016\,10^{-2}$	0.66
0.025	$1.405\,10^{-1}$	0.39	$1.367\,10^{-1}$	0.42	$5.978\,10^{-2}$	0.45	$5.017\,10^{-2}$	0.48
0.0125	$1.031\,10^{-1}$	0.45	$1.010\,10^{-1}$	0.44	$3.759\,10^{-2}$	0.67	$3.191\,10^{-2}$	0.65
0.00625	$7.544\,10^{-2}$	0.45	$7.656\,10^{-2}$	0.4	$2.232\,10^{-2}$	0.75	$1.938\,10^{-2}$	0.72

Table D.1: $L^2(\Omega)$ relative errors and computed order of convergence for the boundary value problem (D.4.2)-(D.4.3) using $\mathbb{P}_1$ elements (2nd and 3rd columns) and $\mathbb{P}_2$ elements (4th and 5th columns) with $\alpha = 0.75$ and $\alpha = 1$; h is the typical diameter of the Delaunay meshes.

Eigenvalue problem

We now study Ohmic decay in the conducting L-shape domain. Assuming that the magnetic field has the following behavior $\mathbf{H}(\mathbf{x}, t) = \mathbf{H}(\mathbf{x})\mathrm{e}^{-\lambda t}$, where $\lambda > 0$, we are lead to consider the following eigenvalue problem: find $(\lambda, \mathbf{H})$ such that

$$\nabla\times\nabla\times\mathbf{H} = \lambda\mathbf{H}, \qquad \nabla\cdot\mathbf{H} = 0, \qquad \mathbf{H}\times\mathbf{n}|_\Gamma = 0, \tag{D.4.4}$$

Approximations of the first five eigenvalues with 10^{-11} tolerance are provided in [40]: $\lambda_1 \approx 1.47562182408$, $\lambda_2 \approx 3.53403136678$, $\lambda_3 = \lambda_4 = \pi^2 \approx 9.86960440109$, and $\lambda_5 \approx 11.3894793979$. We solve (D.4.4) using ARPACK [91] with a relative tolerance of 10^{-8}.

Table D.2 shows the first eigenvalue computed with $\alpha = 0.9$ on five quasi-uniform (non-nested) Delaunay meshes of mesh-sizes 1/10, 1/20, 1/40, 1/80, 1/160, respectively. As explained in [17], taking α close to 1 improves the convergence rate on the first eigenvalue. The method is clearly convergent although the eigenvector has a strong unbounded singularity.

h	$\mathbb{P}_1$			$\mathbb{P}_2$		
	λ_1	Rel. Error	COC	λ_1	Rel. Error	COC
0.1	1.555	$5.256\,10^{-2}$	N/A	1.508	$2.192\,10^{-2}$	N/A
0.05	1.541	$4.353\,10^{-2}$	0.27	1.493	$1.167\,10^{-2}$	0.9
0.025	1.522	$3.094\,10^{-2}$	0.49	1.487	$7.371\,10^{-3}$	0.66
0.0125	1.507	$2.126\,10^{-2}$	0.54	1.481	$3.726\,10^{-3}$	0.98
0.00625	1.497	$1.465\,10^{-2}$	0.54	-	-	N/A

Table D.2: Relative errors and COC for λ_1 using $\mathbb{P}_1$ elements and $\mathbb{P}_2$ elements with $\alpha = 0.9$. The symbol "-" indicates that the pair (Linear Solver + ARPACK) did not converge with the assigned tolerances.

Table D.3 shows the first five eigenvalues computed with $\alpha = 0.7$ on five quasi-uniform (non-nested) Delaunay meshes of mesh-sizes 1/10, 1/20, 1/40, 1/80, 1/160, respectively. Here again we observe convergence and there is no spurious eigenvalue. As expected the worst rate of convergence is observed for the first eigenvalue which corresponds to the most singular eigenvector. The second eigenvector is in $H^1(\Omega)$, the third and fourth eigenvectors are analytic, the fifth one has a strong unbounded singularity. The theory developed in [17] shows that

the accuracy of the method improves when $\alpha \to 1$, but the absence of spurious eigenvalues is assured only for $\alpha < 1$. This phenomenon can be observed on the first eigenvalue by comparing Table D.2 and Table D.3. The COC stalls for the eigenvalues λ_3 and λ_4 using $\mathbb{P}_2$ since the accuracy of the computed eigenvalues is limited by the tolerance in ARPACK (10^{-8}).

h	$\mathbb{P}_1$			$\mathbb{P}_2$		
	λ_1	Rel. Error	COC	λ_1	Rel. Error	COC
0.1	1.930	$2.668\,10^{-1}$	N/A	1.707	$1.452\,10^{-1}$	N/A
0.05	1.845	$2.224\,10^{-1}$	0.26	1.623	$9.522\,10^{-2}$	0.61
0.025	1.765	$1.788\,10^{-1}$	0.32	1.586	$7.240\,10^{-2}$	0.4
0.0125	1.696	$1.389\,10^{-1}$	0.36	1.545	$4.614\,10^{-2}$	0.65
0.006256	1.644	$1.080\,10^{-1}$	0.36	-	-	N/A

h	$\mathbb{P}_1$			$\mathbb{P}_2$		
	λ_2	Rel. Error	COC	λ_2	Rel. Error	COC
0.1	3.573	$1.101\,10^{-2}$	N/A	3.537	$8.266\,10^{-4}$	N/A
0.05	3.551	$4.716\,10^{-3}$	1.22	3.535	$2.380\,10^{-4}$	1.8
0.025	3.540	$1.578\,10^{-3}$	1.58	3.534	$6.640\,10^{-5}$	1.8
0.0125	3.536	$6.245\,10^{-4}$	1.33	3.534	$1.726\,10^{-5}$	1.9
0.006256	3.535	$2.768\,10^{-4}$	1.17	-	-	N/A

h	$\mathbb{P}_1$			$\mathbb{P}_2$		
	λ_3	Rel. Error	COC	λ_3	Rel. Error	COC
0.1	5.450	$5.770\,10^{-1}$	N/A	7.828	$2.307\,10^{-1}$	N/A
0.05	7.852	$2.277\,10^{-1}$	1.34	9.870	$3.799\,10^{-7}$	19.21
0.025	9.873	$3.075\,10^{-4}$	2.89	9.870	$3.856\,10^{-8}$	3.3
0.0125	9.870	$7.714\,10^{-5}$	2.0	9.870	$3.444\,10^{-8}$	0.16
0.006256	9.870	$1.934\,10^{-5}$	2.0	-	-	N/A

h	$\mathbb{P}_1$			$\mathbb{P}_2$		
	λ_4	Rel. Error	COC	λ_4	Rel. Error	COC
0.1	5.455	$5.761\,10^{-1}$	N/A	7.841	$2.291\,10^{-1}$	N/A
0.05	7.858	$2.270\,10^{-1}$	1.34	9.870	$4.712\,10^{-7}$	18.9
0.025	9.873	$3.100\,10^{-4}$	9.52	9.870	$3.856\,10^{-8}$	3.61
0.0125	9.870	$7.768\,10^{-5}$	2.0	9.870	$1.990\,10^{-8}$	0.95
0.006256	9.870	$1.935\,10^{-5}$	2.0	-	-	N/A

h	$\mathbb{P}_1$			$\mathbb{P}_2$		
	λ_5	Rel. Error	COC	λ_5	Rel. Error	COC
0.1	5.506	$6.964\,10^{-1}$	N/A	7.903	$3.614\,10^{-1}$	N/A
0.05	7.877	$3.646\,10^{-1}$	0.93	11.39	$2.374\,10^{-5}$	13.89
0.025	11.39	$4.326\,10^{-4}$	9.72	11.39	$7.786\,10^{-6}$	1.61
0.0125	11.39	$1.457\,10^{-4}$	1.57	11.39	$2.168\,10^{-6}$	1.85
0.006256	11.39	$5.303\,10^{-5}$	1.46	-	-	N/A

Table D.3: First five eigenvalues using $\mathbb{P}_1$ elements and $\mathbb{P}_2$ elements with $\alpha = 0.7$. The symbol "-" indicates that the pair (Linear Solver + ARPACK) did not converge with the assigned tolerances.

D.4.2 Induction in a composite sphere

We now turn our attention to three-dimensional induction problems with discontinuous permeability fields.

Description of the problem

The domain is $\Omega := \mathbb{R}^3$ and the conductor is composed of two concentric spheres centered at 0. The radius of the inner sphere, say Ω_1, is R_1 and its magnetic permeability is μ_1. The radius of the outer conducting sphere, say Ω_2, is R_2 and its magnetic permeability is μ_2. This composite sphere is surrounded by vacuum of magnetic permeability μ_0. The magnetic field at infinity is the vertical uniform field $\mathbf{H}_0 := H_0\mathbf{e}_z$. The magnetic field solves

$$\nabla\times\mathbf{H} = 0, \quad \nabla\cdot(\mu\mathbf{H}) = 0, \quad \lim_{\|\mathbf{x}\|\to+\infty} \mathbf{H}_0(\mathbf{x}) = H_0\mathbf{e}_z. \tag{D.4.5}$$

This problem has an analytical steady state solution which is derived in [45] and which we briefly recall for the sake of completeness.

There is a scalar potential ψ so that $\mathbf{H} = \nabla\psi$ in $\mathbb{R}^3$, and ψ solves $\nabla\cdot(\mu\nabla\psi) = 0$ in $\mathbb{R}^3$ with $\nabla\psi \to H_0\mathbf{e}_z$ at infinity. Using the spherical coordinates $(\varrho, \vartheta, \theta)$, where ϱ is the distance to the origin, $\vartheta \in [0, \pi]$ is the colatitude and $\theta \in [0, 2\pi)$ is the azimuth, the potential is given by

$$\psi(\varrho,\vartheta,\theta) = \begin{cases} -A\varrho\cos\vartheta, & \text{for } \varrho \le R_1 \\ -\left(B\varrho + C\frac{R_1^3}{\varrho^2}\right)\cos\vartheta & \text{for } R_1 \le \varrho \le R_2 \\ -\left(D\frac{R_1^3}{\varrho^2} - H_0\varrho\right)\cos\vartheta & \text{for } R_2 \le \varrho, \end{cases} \tag{D.4.6}$$

where A, B, C and D are constants. The constants can be computed by enforcing ψ and $\mu\partial_\varrho\psi$ to be continuous across Σ_μ and Σ, (the continuity of ψ guarantees that the tangential components of the magnetic field $\mathbf{H}$ are continuous and the continuity of $\mu\partial_\varrho\psi$ guarantees that the normal component of the magnetic induction $\mu\mathbf{H}$ is continuous). To simplify the expressions of A, B, C and D we assume that $\mu_1 = \mu_0$ and we abuse the notation by setting $\mu := \mu_2/\mu_0$. Then,

$$\begin{aligned} A &= -\frac{9\mu H_0}{(2\mu+1)(\mu+2) - 2(\mu-1)^2\left(\frac{R_1}{R_2}\right)^3} \\ D &= \frac{(2\mu+1)(\mu-1)\left[\left(\frac{R_2}{R_1}\right)^3 - 1\right] H_0}{(2\mu+1)(\mu+2) - 2(\mu-1)^2\left(\frac{R_1}{R_2}\right)^3} \\ B &= \frac{1}{3}\left(2+\frac{1}{\mu}\right)A, \qquad C = \frac{1}{3}\left(1-\frac{1}{\mu}\right)A. \end{aligned}$$

The magnetic field in Ω_1 is $\mathbf{H}|_{\Omega_1} = -A\mathbf{e}_z$. Whether the spheres are composed of conducting material or not does not matter since the conductivity coefficient does not appear in any formula. As a result, the inner sphere can be viewed from two different perspectives: we can either consider Ω_1 to be part of the conducting medium (with $\mu_1 = \mu_0$), in which case $\Omega_c = \Omega_1 \cup \Omega_2$, or we can consider Ω_1 to be part of the non-conducting medium, in which

μ	h	$\mathbf{H}$, L^2	COC	$\nabla\times\mathbf{H}$, L^2	COC	$\nabla\cdot(\mu^c\mathbf{H}^c)$, L^2	COC	ϕ, H^1	COC
2	0.16	$1.688\,10^{-3}$	-	$7.328\,10^{-3}$	-	$2.665\,10^{-2}$	-	$9.536\,10^{-5}$	-
	0.08	$2.691\,10^{-4}$	2.65	$2.094\,10^{-3}$	1.81	$1.068\,10^{-2}$	1.32	$2.018\,10^{-5}$	2.24
	0.04	$3.898\,10^{-5}$	2.79	$4.889\,10^{-4}$	2.10	$3.831\,10^{-3}$	1.48	$3.431\,10^{-6}$	2.56
	0.02	$7.088\,10^{-6}$	2.46	$1.239\,10^{-4}$	1.98	$1.480\,10^{-3}$	1.37	$5.945\,10^{-7}$	2.53
	0.01	$1.363\,10^{-6}$	2.38	$3.114\,10^{-5}$	1.99	$5.980\,10^{-4}$	1.31	$1.032\,10^{-7}$	2.53
20	0.16	$8.044\,10^{-3}$	-	$3.729\,10^{-2}$	-	$1.314\,10^{-2}$	-	$3.218\,10^{-4}$	-
	0.08	$1.004\,10^{-3}$	3.00	$6.180\,10^{-3}$	2.59	$6.699\,10^{-3}$	0.97	$7.065\,10^{-5}$	2.19
	0.04	$1.089\,10^{-4}$	3.21	$4.273\,10^{-4}$	3.85	$1.845\,10^{-3}$	1.86	$1.253\,10^{-5}$	2.50
	0.02	$2.048\,10^{-5}$	2.41	$4.570\,10^{-5}$	3.22	$4.856\,10^{-4}$	1.93	$2.220\,10^{-6}$	2.50
	0.01	$3.832\,10^{-6}$	2.42	$1.069\,10^{-5}$	2.10	$1.310\,10^{-4}$	1.89	$3.885\,10^{-7}$	2.51
200	0.16	$1.067\,10^{-1}$	-	$3.728\,10^{-1}$	-	$3.876\,10^{-3}$	-	$3.984\,10^{-4}$	-
	0.08	$2.439\,10^{-2}$	2.13	$9.239\,10^{-2}$	2.01	$2.620\,10^{-3}$	0.57	$8.331\,10^{-5}$	2.26
	0.04	$4.321\,10^{-3}$	2.50	$1.571\,10^{-2}$	2.56	$1.076\,10^{-3}$	1.28	$1.444\,10^{-5}$	2.53
	0.02	$6.547\,10^{-4}$	2.72	$2.233\,10^{-3}$	2.81	$4.114\,10^{-4}$	1.39	$2.577\,10^{-6}$	2.49
	0.01	$9.008\,10^{-5}$	2.86	$2.956\,10^{-4}$	2.92	$1.223\,10^{-4}$	1.75	$4.536\,10^{-7}$	2.51

Table D.4: Case 1, $\mathbb{P}2/\mathbb{P}2$; one iteration ($\Delta t = 10^9$); $\alpha = 0.75$

case $\Omega_c = \Omega_2$. Both cases are described by the same steady solution but the numerical approximations computed by our method are computed differently.

Note that $A \to 0$, $B \to 0$, $C \to 0$, $D \to (R_2/R_1)^3 H_0$, and $\mu B \to 3H_0/(1-(R_1/R_2)^3)$, $\mu C \to 6H_0/(1-(R_1/R_2)^3)$ when $\mu \to \infty$; as a result, the magnetic field tends to zero in $\Omega_1 \cup \Omega_2$ but the magnetic induction converges to a non-zero limit in Ω_2 when $\mu \to \infty$. The magnetic field penetrates more or less in the spheres depending on the value of μ, and it is completely expelled from the spheres in the limit $\mu \to \infty$.

Case 1: Inner sphere is a conductor

We assume that $\Omega_c = \Omega_1 \cup \Omega_2$, i.e., the conducting medium is composed of the inner and the outer spheres. We take $\mathcal{L} := R_2$ as reference length scale and we set $R_1 = \frac{1}{2}R_2$. We set $\mathcal{H} := H_0$ to non-dimensionalize the magnetic field since there is no velocity to construct a reference magnetic field.

The infinite vacuum region is truncated at $\varrho = 10R_2$. We enforce the time-independent Dirichlet condition $\phi = H_0 z := H_0 \varrho \cos\vartheta$ at the outer boundary of the vacuum region, Γ_v. The steady solution is computed in one time step using $\Delta t = 10^9$. (Recall that the steady-state problem is now well-posed thanks to our introducing the magnetic pressure.)

The above problem is solved using various uniformly refined meshes and various values of μ. The stabilizing exponent α is equal to 0.75. The magnetic pressure is approximated using $\mathbb{P}_1$ elements, the magnetic field is approximated using $\mathbb{P}_2$ elements, and the scalar potential is approximated using $\mathbb{P}_2$ elements. For each computation we measure the relative error on $\mathbf{H}^c$, $\nabla\times\mathbf{H}^c$, $\nabla\cdot(\mu^c\mathbf{H}^c)$ in the $\mathbf{L}^2(\Omega_c)$-norm, and the error on ϕ in the $H^1(\Omega_v)$-norm. The results are reported in Table D.4. The method converges well in the range $\mu \in [2, 200]$.

Figure D.3 shows the computed solution for $\mu = 200$. We observe that the radial component H_r^c (panel (a)) is continuous at ($\varrho = R_1$ and $\vartheta = 0$, $\vartheta = \pi$) and that the vertical component H_z^c (panel (b)) is continuous at ($\varrho = R_1$, $\vartheta = \pi/2$). This shows that the IP

method enforces well the continuity of the tangential component of the magnetic field. The panel (c) shows the magnetic field lines of $\mathbf{H}^c$ $(0 \leq \varrho \leq R_2)$ and those of $\nabla\phi$ $(R_2 \leq \varrho)$. The magnetic lines in the vacuum region arrive nearly perpendicularly at the ferromagnetic interface. This phenomenon is a feature of $\mu \to \infty$.

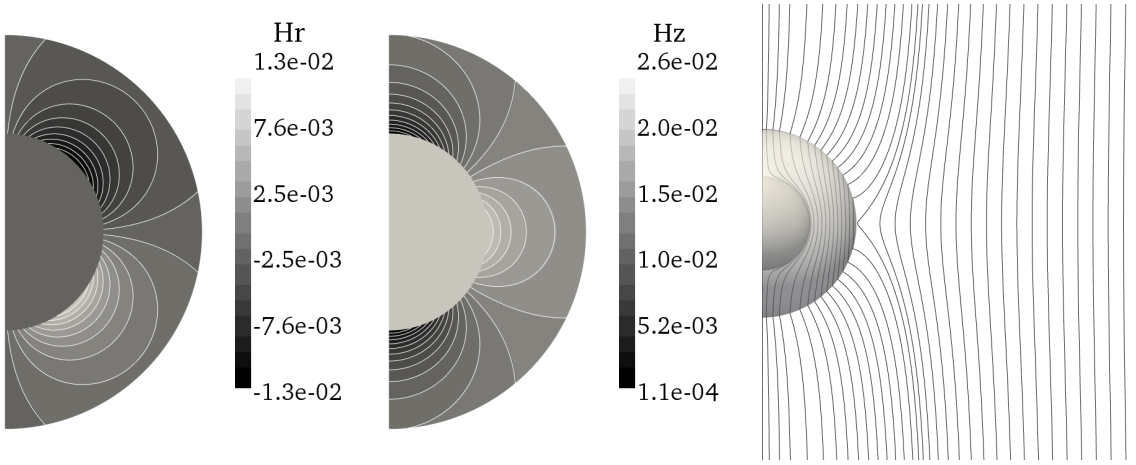

Figure D.3: Steady solution for a composite sphere embedded in a vertical uniform magnetic field: (a-b) H_r and H_z for conducting inner and outer spheres with relative permeability $\mu = 200$; (c) magnetic field lines.

Case 2: Hollow sphere

We use the same geometric setting as in case 1, but we now assume that the inner sphere is an insulator, i.e., $\Omega_c = \Omega_2$. The non-conducting medium, Ω_v, is composed of the inner sphere Ω_1 plus the spherical annulus $\varrho \in (R_2, 10R_2)$. The exact solution to this problem is the same as in case 1.

We repeat the same convergence tests as in case 1. The results are reported in Table D.5. We observe that the method converges well in the range $\mu \in [2, 200]$ and that the convergence rates are almost identical to those shown in Table D.4.

D.4.3 Induction in rotating devices

We test in this section the proposed method on rotating conductors embedded in a uniform external magnetic field. We make two numerical tests: the first one assesses the robustness of the method with respect to geometrical singularities and the second one assesses the robustness of the method with respect to high permeability contrasts. These tests have been preformed with $\alpha = 0.7$.

Induction in a finite rotating solid cylinder

Let Ω_c be a conducting cylinder of non-dimensional radius $R = 1$ and height $L_z^c = 1.6$. This cylinder is embedded in vacuum in $\mathbb{R}^3$ and rotates about the z-axis with angular speed $\varpi = 1$.(The reference velocity $\mathcal{U}$ is equal to the product of the radius of the cylinder and the angular

μ	h	$\mathbf{H}$, L^2	COC	$\nabla\times\mathbf{H}$, L^2	COC	$\nabla\cdot(\mu^c\mathbf{H}^c)$, L^2	COC	ϕ, H^1	COC
2	0.16	$1.590\,10^{-3}$	-	$7.314\,10^{-3}$	-	$2.424\,10^{-2}$	-	$1.362\,10^{-4}$	-
	0.08	$2.913\,10^{-4}$	2.45	$2.002\,10^{-3}$	1.87	$9.423\,10^{-3}$	1.36	$2.679\,10^{-5}$	2.35
	0.04	$2.898\,10^{-5}$	3.33	$4.525\,10^{-4}$	2.15	$3.285\,10^{-3}$	1.52	$3.924\,10^{-6}$	2.77
	0.02	$4.910\,10^{-6}$	2.56	$1.088\,10^{-4}$	2.06	$1.189\,10^{-3}$	1.47	$6.694\,10^{-7}$	2.55
	0.01	$1.109\,10^{-6}$	2.15	$2.665\,10^{-5}$	2.03	$4.637\,10^{-4}$	1.36	$1.162\,10^{-7}$	2.53
20	0.16	$9.418\,10^{-3}$	-	$3.924\,10^{-2}$	-	$1.282\,10^{-2}$	-	$3.423\,10^{-4}$	-
	0.08	$1.494\,10^{-3}$	2.66	$6.749\,10^{-3}$	2.54	$6.627\,10^{-3}$	0.95	$7.261\,10^{-5}$	2.24
	0.04	$1.952\,10^{-4}$	2.94	$5.859\,10^{-4}$	3.53	$1.832\,10^{-3}$	1.85	$1.245\,10^{-5}$	2.54
	0.02	$2.409\,10^{-5}$	3.02	$7.075\,10^{-5}$	3.05	$4.819\,10^{-4}$	1.93	$2.203\,10^{-6}$	2.50
	0.01	$2.889\,10^{-6}$	3.06	$1.255\,10^{-5}$	2.49	$1.291\,10^{-4}$	1.90	$3.862\,10^{-7}$	2.51
200	0.16	$1.098\,10^{-1}$	-	$3.934\,10^{-1}$	-	$3.861\,10^{-3}$	-	$4.013\,10^{-4}$	-
	0.08	$2.474\,10^{-2}$	2.15	$9.847\,10^{-2}$	2.00	$2.596\,10^{-3}$	0.57	$8.380\,10^{-5}$	2.26
	0.04	$4.415\,10^{-3}$	2.49	$1.740\,10^{-2}$	2.50	$1.067\,10^{-3}$	1.28	$1.472\,10^{-5}$	2.51
	0.02	$7.451\,10^{-4}$	2.57	$2.658\,10^{-3}$	2.71	$4.091\,10^{-4}$	1.38	$2.642\,10^{-6}$	2.48
	0.01	$1.211\,10^{-4}$	2.62	$3.999\,10^{-4}$	2.73	$1.217\,10^{-4}$	1.75	$4.668\,10^{-7}$	2.50

Table D.5: Case 2, $\mathbb{P}2/\mathbb{P}2$; one iteration ($\Delta t = 10^9$); $\alpha = 0.75$

velocity.) The non-dimensional conductivity is $\sigma = 1$ and the magnetic Reynolds number is $R_m = 100$. The non-dimensional magnetic permeability in the entire electromagnetic domain is constant and equal to one, i.e., $\mu^c = \mu^v = 1$. The imposed magnetic field at infinity is $H_0\mathbf{e}_x$. This is a benchmark test case thoroughly investigated in [105].

The time-dependent problem is solved with initial data $\mathbf{H}_0 = H_0\mathbf{e}_x$ on a Delaunay mesh which is quasi-uniform in the conducting region and of mesh-size $h = 1/100$. We use $\mathbb{P}_2$ elements for both the magnetic field and the magnetic potential. The magnetic pressure is approximated using $\mathbb{P}_1$ elements. The time step is $\Delta t = 5\,10^{-2}$. The truncated numerical domain is $\Omega = \{r \in (0, 1.6), \theta \in [0, 2\pi], z \in (-4, 4)\}$ and the non-conducting domain is $\Omega_v = \Omega\backslash\Omega_c$. The imposed boundary condition on Γ_v is $\phi|_{\Gamma_v} = H_0 r\cos\theta$. The only active Fourier mode is $m = 1$.

The time evolution of the magnetic energy is shown in Figure D.4(a). The graph shows oscillations that correspond to reconnections of the magnetic lines. Figure D.4(b) shows the radial profile of H_z at $z = 0.8$ in the meridian plane $\theta = 0$ at steady state. Note that the point $r = 1$, $\theta = 0$, $z = 0.8$ is located on the upper sharp edge of the cylinder. The profile is compared with that obtained in [105]. The agreement is excellent considering that the gradient of the solution is discontinuous at the edges of the cylinder.

Figures D.5(a), D.5(b) show the contour lines of the $m = 1$ azimuthal Fourier mode of H_θ at $t = 100$. Observe that H_θ is symmetric with respect to the equatorial plane. Plotting the contour lines of H_θ emphasizes the skin effect. The lines shown in Figures D.5(a), D.5(b) are very close to those reported in Figure 5 from [105] even at the corners. Figure D.5(c) shows the streamlines of the Fourier mode $m = 1$ of the electric current in the cylinder. The current is mainly contained in a thin layer (of the order of the skin depth). It varies smoothly in the azimuthal direction and bends sharply at the corners. This behavior is a direct consequence of the presence of the cylindrical interface with vacuum. The current creates the z-component of the magnetic field and is responsible for the strong extremum of H_z at the sharp edges of

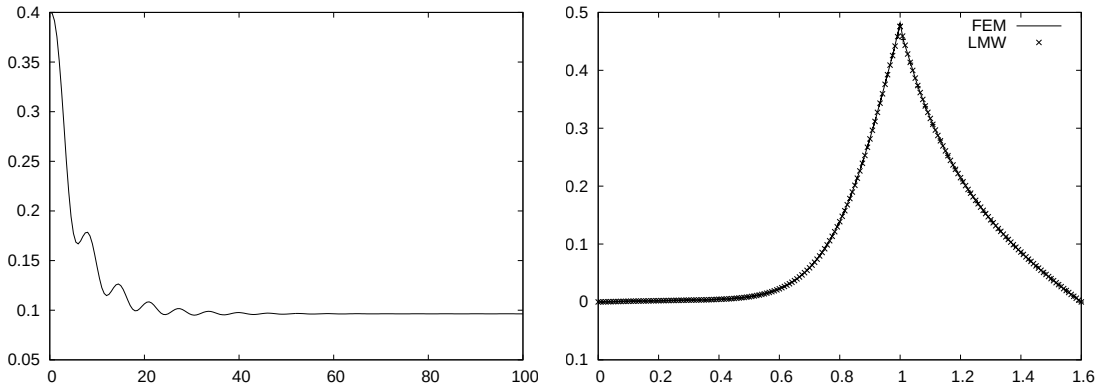

(a) Time evolution of the magnetic energy (b) Radial profile of $H_z(r, z = 0.8)$

Figure D.4: Induction in a finite rotating solid cylinder at $R_m = 100$. 'LMW' is the result from [105], 'FEM' is our result with $\mathbb{P}_2$ finite elements for $\mathbf{H}$ and $\mathbb{P}_2$ finite elements for ϕ with $h = 1/100$.

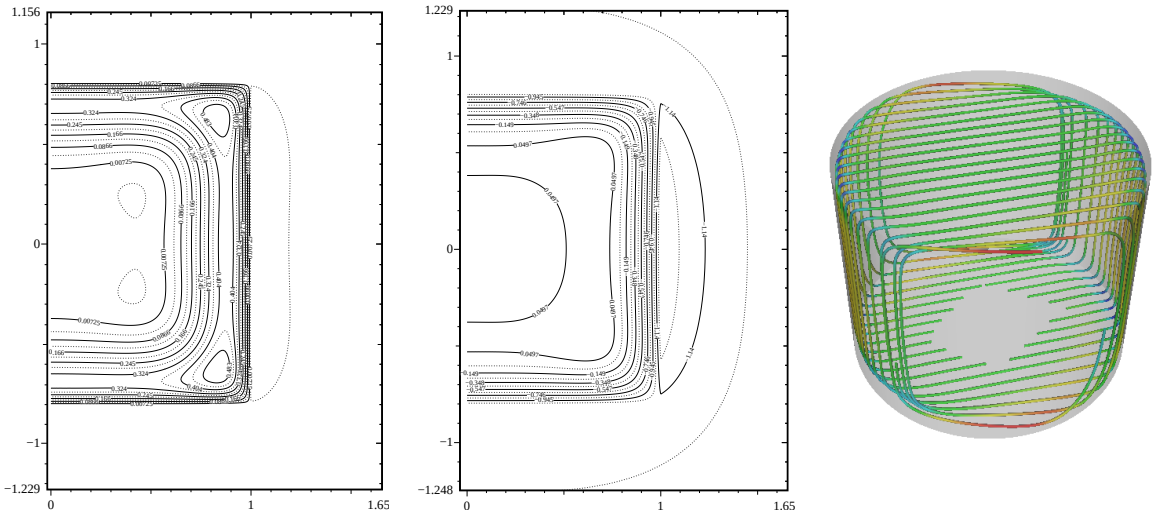

(a) $\theta = 0$, (b) $\theta = \pi/2$. (c) Electric current

Figure D.5: Rotating cylinder at $R_m = 100$ at steady state. Contours of H_θ of the $m = 1$ mode in azimuthal planes and streamlines of the electric current of the $m = 1$ mode colored by the norm of the current.

the cylinder $(r = 1, \theta \in [0, 2\pi], z = \pm 0.8)$

Induction in counter-rotating disks made of soft iron

In order to measure the impact of soft iron disks on induction fields, we now consider two counter-rotating disks embedded in a cylindrical conductor which is itself embedded in vacuum. This test case is a qualitative illustration of the Cadarache VKS2 fluid dynamo studied in more details in Section D.5.

The conducting domain is a cylinder of non-dimensional radius $R = 1$ and of rectangular cross section of non-dimensional height $L = 2.55$: $\Omega_c = \{(r, \theta, z); r \in [0, 1), \ z \in$

$(-1.275, 1.275),\ \theta \in [0, 2\pi)\}$. Two counter-rotating disks, $\Omega_c^{\rm top}$, $\Omega_c^{\rm bot}$, are embedded in Ω_c. The upper rotating conducting disk is a cylinder whose cross section is defined as follows:

$$\begin{cases} 0.775 \le z \le 0.975 & \text{if } r \le 0.65, \\ (r-0.65)^2 + (z-0.875)^2 \le (0.1)^2 & \text{if } r \ge 0.65. \end{cases}$$

The lower rotating conducting disk is the image by reflection about the equatorial plane $z = 0$ of the upper disk. There is no analytical solution to this problem, but asymptotic solutions are given in [69] assuming that the disks are of rectangular cross section. The upper and lower disks rotate with non-dimensional angular speed $\varpi_{\rm top} = -1$ and $\varpi_{\rm bot} = 1$, respectively. The non-dimensional magnetic permeability and conductivity of the non-rotating solid container, $\Omega_c \backslash (\Omega_c^{\rm top} \cup \Omega_c^{\rm bot})$, are $\mu_0 = 1$ and $\sigma_0 = 1$, respectively. The non-dimensional magnetic permeability and conductivity of the two counter-rotating disks, $\Omega_c^{\rm top} \cup \Omega_c^{\rm bot}$, are μ_d and σ_d, respectively. The non-dimensional magnetic permeability of the vacuum is $\mu_0 = 1$. The imposed velocity field in Ω_c is

$$\tilde{\mathbf{u}}^{n+1}(\mathbf{x}) = \begin{cases} 0 & \text{in } \Omega_c \backslash (\Omega_c^{\rm top} \cup \Omega_c^{\rm bot}) \\ \varpi_{\rm top} \mathbf{e}_z \times \mathbf{x} & \text{in } \Omega_c^{\rm top} \\ \varpi_{\rm bot} \mathbf{e}_z \times \mathbf{x} & \text{in } \Omega_c^{\rm bot} \end{cases}$$

The device is placed in a transverse uniform magnetic field $\mathbf{H}_0 := H_0 \mathbf{e}_x = H_0(\cos\theta \mathbf{e}_r - \sin\theta \mathbf{e}_\theta)$ and we look for the steady state solution in two cases: (a) $\mu_d = 200\mu_0$, $\sigma_d = 1$; (b) $\mu_d = 1$, $\sigma_d = 200\sigma_0$. In both cases the effective magnetic Reynolds number is the same for the disks $R_{\rm m}^{\rm disks} = \mu_d \sigma_d \varpi_{\rm bot} R^2 = 200\mu_0\sigma_0$.

For computational purposes the vacuum region is truncated and restricted to the sphere of non-dimensional radius $R_v = 10$. The time-independent Dirichlet condition $\phi = H_0 x := H_0 r \cos\theta$ is enforced at the outer boundary of the vacuum region, Γ_v. The steady solution is computed by advancing (D.3.11) in time until convergence to steady state is reached. We use the $\mathbb{P}_2/\mathbb{P}_2$ finite element pair for $\mathbf{H}$ and ϕ and $\mathbb{P}_1$ elements for the magnetic pressure.

Some three-dimensional representations of the computed solutions are shown in Figure D.6. Panels (a) and (d) show some magnetic field streamlines near the top disk seen from the side of the cylinder. Panels (b) and (e) show the same magnetic field streamlines seen from the top of the cylinder. Panels (c) and (f) show the contour of the magnetic energy corresponding to 10% of the maximum energy. The top panels correspond to the solution with $\mu_d = \mu_0$ and $\sigma_d = 200\sigma_0$ and the bottom panels (c,d,e) correspond to the solution with $\mu_d = 200\mu_0$ and $\sigma_d = \sigma_0$. The two steady solutions are very different although the two configurations have the same effective magnetic Reynolds number. When the disks are non-ferromagnetic, the magnetic field lines are distorted horizontally due to the eddy current in each disk. When the disks are ferromagnetic, the field lines are distorted inside the disks but also outside as they connect nearly perpendicularly to the disks.

D.5 Kinematic dynamo

The kinematic code based on the new formulation (D.3.11) has been further validated on kinematic dynamo problems by making comparisons with a finite-volume/boundary-element method code [56] using analytical axisymmetric flows. We now illustrate the efficiency of the new method by applying it to VKS2-like kinematic dynamo problems. These tests have been preformed with $\alpha = 0.7$.

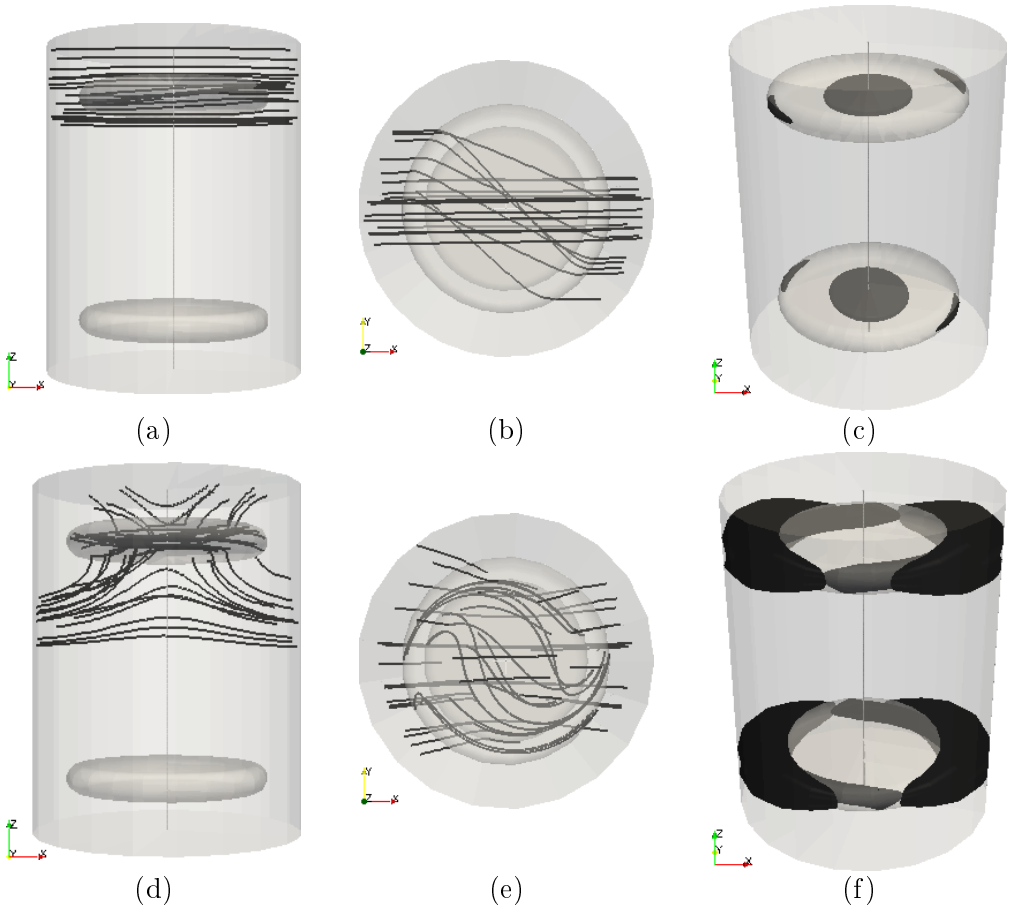

Figure D.6: Steady solutions for two counter-rotating disks in a cylindrical vessel: (a,b,c) $\mu_d = \mu_0$ and $\sigma_d = 200\sigma_0$; (c,d,e) $\mu_d = 200\mu_0$ and $\sigma_d = \sigma_0$; magnetic line near the top disk seen from the side (a,d) and from the top (b,e); (c,f) contours corresponding to 10% of the maximum magnetic energy.

D.5.1 The VKS2 experiment

The interest of the scientific community for dynamo action in liquid metals has been renewed since 2000 in the wake of successful experiments [51, 139, 110]. We show in this section that the numerical method proposed in this paper is suitable, to some extent, to model the Cadarache von Kármán Sodium 2 (VKS2) experiment [110] which has been done in liquid sodium.

The experimental set-up is schematically represented on Figure D.7 together with the simplified geometry that we use in the numerical simulations. The 'bulk flow', composed of liquid sodium, is contained in a cylinder of radius $r = 206$ mm, height 524 mm and thickness 5 mm. This cylinder is made of copper and is henceforth referred to as the envelope. The liquid sodium is stirred by two counter-rotating impellers located at the top and bottom of the container. Each impeller is composed of a supporting disk and eight curved blades. The impellers act on the liquid sodium as efficient centrifugal pumps: the fluid is pumped in and expelled out radially, thus forming an helicoidal flow. The top and bottom flows recirculate alongside the envelope wall and meet at the mid-plane. This creates a strong azimuthal shear-layer between the two toroidal recirculation flows. A layer of stationary liquid sodium

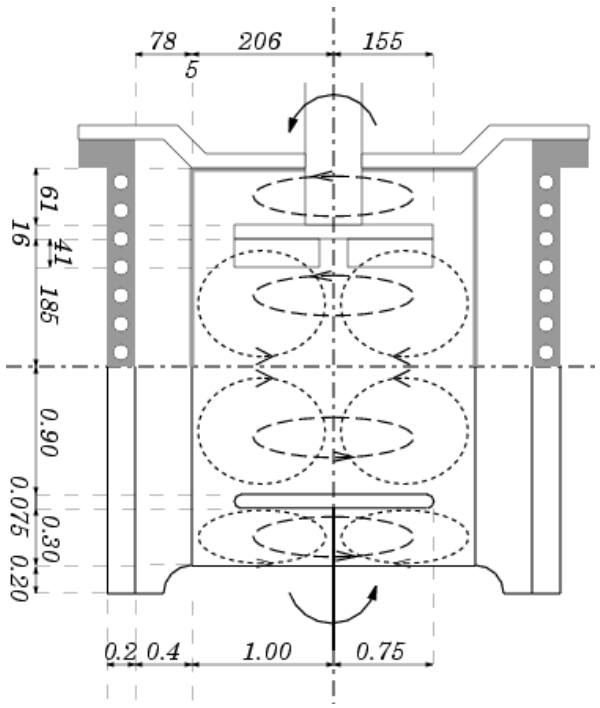

Figure D.7: VKS design and mean-flow structure. Top: dimensions (in millimeters) and technical details of the set-up. Are represented the copper vessel with the embedded cooling system, the thin copper envelope of radius $r = 206$ mm, height 524 mm and thickness 5 mm separating the flow and the stagnant liquid sodium, the impellers (disks with attached blades), and the shafts (courtesy of the VKS team). Bottom: simplified geometry in non-dimensional units for numerical simulations; the thickness of the copper envelope is zero.

is trapped between the envelope and the cooling system. This stationary fluid zone is called 'side layer'. Due to experimental and technical constraints, two additional layers of liquid sodium exist between the impellers and the top and bottom lids of the copper container and are referred to as 'lid flows'.

Dynamo action was first observed in the VKS2 set-up once the two counter-rotating impellers, which were initially made of stainless steel, were replaced by soft iron ones and the injected power was high enough [110]. Once dynamo action occurs, the measured time-averaged magnetic field is that of a steady axisymmetric axial dipole with a strong azimuthal component in the equatorial plane [109]. This contradicts the kinematic dynamo computations based on axisymmetric time-averaged von Kármán flows reported in [101, 123, 137, 87, 93]. In these simulations the generated magnetic field is non-axisymmetric as a consequence of Cowling's theorem [39] (the Fourier mode $m = 1$ is always found to be the most unstable mode). Until now, there is no satisfying explanation that could throw light on the generation of the mainly axisymmetric magnetic field which is observed in the VKS2 experiment. Cowling's theorem [39] implies that there exists a mechanism in the VKS2 experiment that breaks the flow axisymmetry, and this mechanism has yet to be clearly identified. One possible scenario to explain this behavior is that small scale helical turbulence may have induction effects via the so called α-effect. A source for the α-effect could be the helical flow induced by the shear

between outwardly expelled fluid trapped between the impeller blades and the slower moving fluid in the bulk of the container [89, 119, 55]. Another possible scenario proposed in [60] is based on non-axisymmetric velocity fluctuations created by nonlinearities on the induction equation.

Notwithstanding the above scenarii, recent experimental observations (F. Daviaud, private communication, 2010) have shown that the role of moving ferromagnetic material is crucial. With the same available power, the dynamo effect has been obtained only when at least one of the rotating impellers is made of soft iron. In particular, the following material substitutions have led to subcritical behavior: (1) replacing the copper envelope by a soft iron one while using steel impellers, (2) using steel impellers enclosed in a copper envelope and filling the space occupied by the 'lid flow' with copper plates, (3) using one non-rotating impeller (disk+blades) made of soft iron, the other rotating impeller being made of steel, and removing the envelope, (4) placing non-rotating soft iron disk behind the steel impellers and removing the envelope, (5) using two rotating composite impellers (either composed of soft iron disks with steel blades or steel disks with soft iron blades) and removing the envelope. The main conclusion of all these experiments is that at least one of the impellers (disk+blades) must be made of soft iron and must rotate for the dynamo effect to be observed.

Obviously the experiment is quite complex. The purpose of the present study is not to explain the generation of the observed axisymmetric magnetic field in the VKS2 experiment but rather to investigate the role played by the magnetic permeability of the impellers on the dynamo threshold for the $m = 1$ Fourier mode. That this mode has not been observed may be related to the limited range of magnetic Reynolds numbers available in the VKS device ($R_{\rm m} \leq 50$).

D.5.2 Simplified model

Before going through the analysis of a VKS2-like device we investigate the effect of the 'side layer' and compare the so-called Vanishing Tangential Field (VTF) boundary condition with the vacuum boundary condition. The VTF boundary condition, $\mathbf{H}\times\mathbf{n}|_\Gamma = 0$, models walls of infinite permeability.

We consider two simplified geometries of the VKS device. The first one (vessel Nb1) is a cylinder of rectangular cross section $(r, z) \in [0, 1.6R_0]\times[-\frac{1}{2}H_0, \frac{1}{2}H_0]$ with $H_0 = 1.8R_0$. The moving fluid is contained in the cylinder of cross section $(r, z) \in [0, R_0]\times[-\frac{1}{2}H_0, \frac{1}{2}H_0]$ and the 'side layer' is the torus of cross section $(r, z) \in [R_0, 1.4R_0]\times[-\frac{1}{2}H_0, \frac{1}{2}H_0]$. The outer part of the vessel of cross section $(r, z) \in [1.4R_0, 1.6R_0]\times[-\frac{1}{2}H_0, \frac{1}{2}H_0]$ is made of copper, cf. Figure D.8(a). The second simplified vessel (vessel Nb2) is a cylinder of rectangular cross section $(r, z) \in [0, R_0]\times[-\frac{1}{2}H_0, \frac{1}{2}H_0]$ with $H_0 = 1.8R_0$ filled with moving fluid cf. Figure D.8(b). Note that the impellers are not accounted for in these two simplified models. The conductivity of the fluid is σ_0 and that of copper is $\sigma = 4.5\sigma_0$. The magnetic permeability is assumed to be uniformly constant, μ_0.

Three different kinematic dynamo scenarii with prescribed velocity field $\tilde{\mathbf{u}}$ are considered:

Case 1 The conducting region is vessel Nb1. The device is embedded in a truncated sphere of vacuum of radius $10R_0$. The usual vacuum/conductor transmission condition is enforced on the interface Σ which separate the conducting material from the vacuum region (see (D.2.13)).

Case 2 The conducting region is again modeled by the vessel Nb1, but in order to replicate

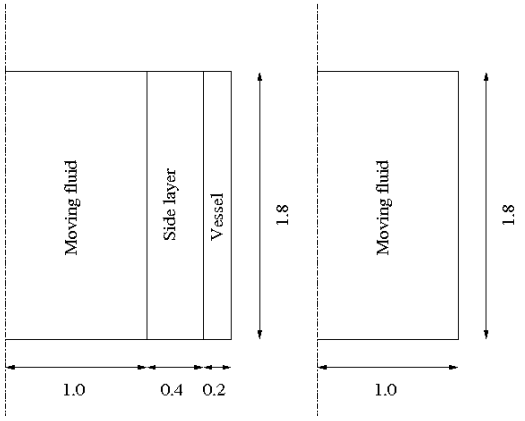

(a) Cases 1-2 (b) Case 3

Figure D.8: Two simplified domains where the thickness of the copper envelope is zero.

the VKS2 experiment, we now model the presence of soft iron impellers at the top and bottom of the moving fluid region by enforcing the infinite permeability boundary condition $\mathbf{H}\times\mathbf{n} = 0$ at $\{z = \pm\frac{1}{2}H_0, 0 \leq r \leq R_0\}$. The device is again embedded in a truncated sphere of vacuum of radius $10R_0$. The usual vacuum/conductor transmission condition is enforced on the remaining part of the interface Σ where the VTF condition is not applied (see (D.2.13)).

Case 3 The conducting region is modeled by the vessel Nb2. The infinite permeability boundary condition $\mathbf{H}\times\mathbf{n} = 0$ is enforced on the entire boundary of the vessel. This boundary condition is expected to model an envelope made of soft iron in the VKS2 experiment. There is no insulating region.

The velocity field $\tilde{\mathbf{u}}$ that has been chosen for these tests is the axisymmetric time-averaged flow field measured in a water experiment which is documented in [123]. The flow is interpolated on the finite element grid and normalized by the maximum of the euclidian norm of the velocity, $U_{\max}$. Henceforth we use $\mathcal{L} = R_0$ as reference length scale and $\mathcal{U} = U_{\max}$ as reference velocity scale. The magnetic Reynolds number is

$$R_{\mathrm{m}} = \mu_0\sigma_0 U_{\max} R_0. \tag{D.5.1}$$

>From Cowling's theorem [39], only magnetic fields with Fourier modes $m \geq 1$ can be generated by a prescribed axisymmetric velocity field. Furthermore, the azimuthal modes are uncoupled since $\nabla\times(\tilde{\mathbf{u}}\times\mathbf{H}^c)$ cannot transfer energy between the azimuthal modes of $\mathbf{H}^c$. It is also known that the Fourier mode $m = 1$ is the most unstable one [123, 102, 137, 87]; therefore, we investigate only this mode. We denote $\mathbf{H}^c(m = 1)$ the Fourier mode $m = 1$ of $\mathbf{H}^c$.

The above three problems are solved by advancing (D.3.11) in time using a small random divergence-free magnetic field as initial data. The magnetic energy of $\mathbf{H}^c(m = 1)$, $\frac{1}{2}\int_{\Omega_c^{2D}} \|\mathbf{H}^c(m = 1)\|^2 \mathrm{d}\mathbf{x}$, is recorded as a function of time for various magnetic Reynolds numbers $R_{\mathrm{m}} \in [25, 100]$. The critical magnetic Reynolds number R_{mc} correspond to zero growth rate. The critical magnetic Reynolds number for the three cases defined above are reported in Table D.6. By comparing cases 1 and 2, we observe that the critical magnetic

Reynolds number decreases when the VTF condition is used to model the soft iron impellers, thereby confirming that using soft iron impellers may indeed help to lower the dynamo threshold in the VKS2 experiment. The results of the third experiment (Case 3) show that using an envelope made of soft iron to confine the magnetic field within the 'bulk flow' region is counter-productive. Another interpretation of this result is that the presence of the 'side layer' may help the dynamo effect in the VKS2 experiment.

case	boundary condition	R_{mc}
1	Vacuum transmission condition	45
2	VTF at $z = \pm\frac{1}{2}H_0$, $0 \le r \le R_0$	40
3	VTF everywhere	52

Table D.6: Critical magnetic Reynolds number for Cases 1 to 3.

D.5.3 More realistic models

We now model the VKS2 experiment with more realistic geometries, electric conductivities, and magnetic permeabilities (see Figure D.7).

The conducting domain is partitioned into a moving region (comprising the 'bulk flow', 'lid flows', and the 'disk flows') and a stationary region (comprising the 'side layer' and the copper vessel), see Figure D.9.

The moving fluid region is $(r, z) \in [0, R_0]\times[-1.275, 1.275]$ and the stagnant sodium 'side layer' is $r \in [R_0, R_1]$, $R_1 = 1.4R_0$. The moving fluid region is divided into the 'bulk flow' subregion $(r, z) \in [0, R_0]\times[-0.9, 0.9]$, the 'disk flows' subregions $(r, z) \in [0, R_0]\times[-0.975, -0.9] \cup [0.9, 0.975]$, and the 'lid flows' subregions $(r, z) \in [0, R_0]\times([-1.275, -0.975] \cup [0.975, 1.275])$. The purpose of the 'disk flows' is to model the two impellers and the fluid moving between the blades. To account for the presence of solids of various material properties in the 'disk flows' subregions, we also introduce two 'flat disks' of width $H_i = 0.075R_0$, radius $R_i = 0.75R_0$ and round edges.

The copper walls of the device are $(r, z) \in [R_1, R_2]\times[-1.475, 1.475]$, $R_2 = 1.6R_0$. Other geometrical dimensions are reported in Figure D.7.

The fluid is assigned the conductivity of liquid sodium σ_0, ($\sigma_1 = \sigma_0$). The outer wall of the device is assigned the conductivity of copper, $\sigma_2 = 4.5\sigma_0$. The magnetic permeability of every component of the device is equal to that of the vacuum μ_0 except for the two 'flat disks'. Two different material compositions are tested for the 'flat disks'. In what we hereafter refer to as Case 1' and Case 2' the 'flat disks' are made of stainless steel, $\sigma_i = 0.14\sigma_0$ and $\mu_i = \mu_0$, but in Case 3' and Case 4' the 'flat disks' are made of soft iron, $\sigma_i = \sigma_0$ and $\mu_i = 60\mu_0$.

The prescribed axisymmetric velocity field $\tilde{\mathbf{u}}$ is defined separately in the 'bulk flow', 'disk flow', and 'lid flow' regions. In the 'bulk flow' region $\tilde{\mathbf{u}}$ is modeled as in the previous section by using the axisymmetric time-averaged flow field measured in a water experiment which is documented in [123]. The flow is interpolated on the finite element grid and normalized by the maximum of the Euclidian norm of the velocity, $U_{\max}$. The quantity $U_{\max}$ is chosen to be the reference velocity scale, $\mathcal{U} := U_{\max}$. Let us denote by $u_0(r, z)\mathbf{e}_\theta$ the axisymmetric 'bulk flow'. Then the flow in the top 'disk flow' region is defined to be equal to $u_0(r, 0.9)\mathbf{e}_\theta$ and the flow in the bottom 'disk flow' region is defined to be equal to $u_0(r, -0.9)\mathbf{e}_\theta$. Finally, two different models are tested for the 'lid flow'. In the first model the top 'lid flow' velocity field is defined to be the linear interpolation with respect to z between $u_0(r, 0.9)\mathbf{e}_\theta$ and the zero,

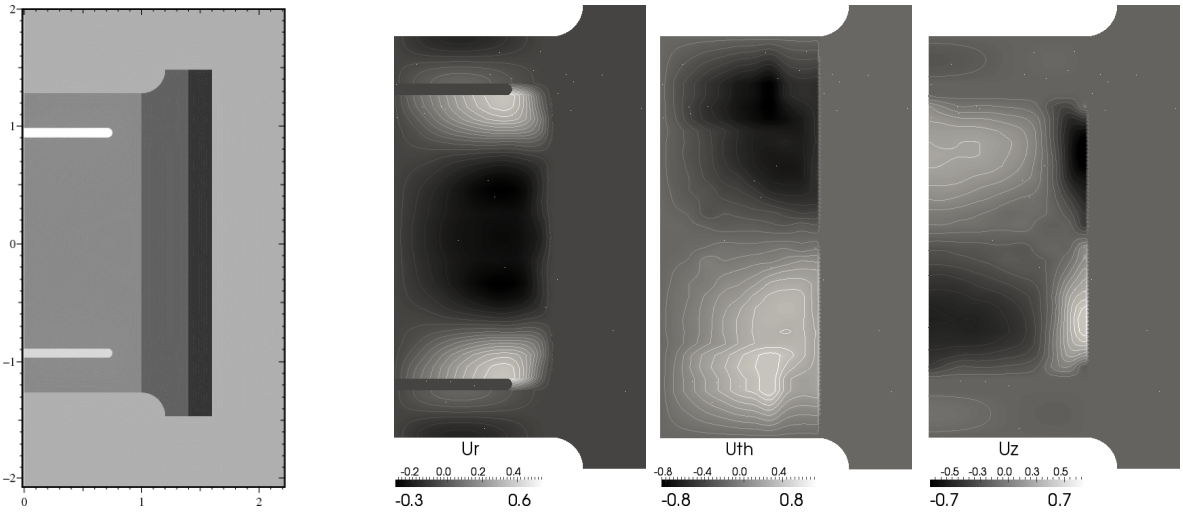

Figure D.9: Simplified VKS2 setting and imposed axisymmetric velocity field $\tilde{\mathbf{u}}$ for Case 2' and Case 4'.

and the bottom flow is defined similarly. The 'lid flow' thus defined is denoted $\mathbf{u}_\theta^{\rm lin}$. In the second model the 'lid flow' velocity is defined to be the sum of $\mathbf{u}_\theta^{\rm lin}$ and 10% of an analytical poloidal recirculation flow $\mathbf{u}^{\rm pol}$ that has been introduced in [102]. The flow $\mathbf{u}^{\rm pol}$ is normalized so that the maximum of Cartesian norm of $\mathbf{u}^{\rm pol}$ is $U_{\rm max}$.

We use $\mathbf{u}_\theta^{\rm lin}$ in the 'lid flow' region in Case 1' and Case 3', and we use $\mathbf{u}_\theta^{\rm lin}+10^{-1}\mathbf{u}^{\rm pol}$ in the 'lid flow' region in Case 2' and Case 4'. The three components of the velocity field $\tilde{\mathbf{u}}$ which is used in Case 2' and Case 4' are shown in Figure D.9. The velocity has a continuous azimuthal component and shows a small recirculation in the 'lid flow' region.

The critical magnetic Reynolds numbers are computed in the four cases defined above by solving (D.3.11) for various Reynolds numbers and evaluating the growth rate of the magnetic energy in each case. The critical magnetic Reynolds number $R_{\rm mc}$ corresponds to zero growth rate. The results are reported in Table F.1.

Case	Composition of disk	Lid flow	$R_{\rm mc}$
1'	Stainless steel	$\mathbf{u}_\theta^{\rm lin}$	82
2'	Stainless steel	$\mathbf{u}_\theta^{\rm lin}+10^{-1}\mathbf{u}^{\rm pol}$	75
3'	Soft iron	$\mathbf{u}_\theta^{\rm lin}$	66
4'	Soft iron	$\mathbf{u}_\theta^{\rm lin}+10^{-1}\mathbf{u}^{\rm pol}$	64

Table D.7: Critical magnetic Reynolds number for the Fourier mode $m=1$ in VKS2 simplified setting.

When comparing Case 1 from Table D.6 with Case 1' from Table F.1, one realizes that adding counter-rotating disks (modeled by the 'disk flows') and purely azimuthal 'lid flows' dramatically increases the dynamo thresholds; $R_{\rm mc}$ goes from 45 to 82. The adverse effect of the 'lid flows' was first demonstrated in [137]. Adding a poloidal component to the 'lid flow' with 10% recirculation intensity (Case 2') lowers the threshold from 82 to 75 which is still larger than 45. Hence, changing the magnetic permeability has more effect than tweaking the 'lid flow'. The threshold goes further down to $R_{\rm mc}=65\pm1$ in both Cases 3' and 4'.

We show in Figure D.10 the two unstable modes of the magnetic field corresponding to Cases 2' and 4'. They look similar in the 'bulk flow' region. There is an equatorial dipole and two vertical structures of opposite sign. Noticeable differences become apparent when observing the magnetic lines close to the counter-rotating disks as shown in Figure D.11.

The general conclusion of this parametric study is that ferromagnetic disks have a measurable impact on the dynamo threshold, which is crucial since the experimental magnetic Reynolds number is constrained to be below 50 in the VKS2 experiment. A provisional result about ferromagnetic disks is that they may screen the 'bulk flow' from the influence of the 'lid flow', thereby lowering the dynamo threshold for the Fourier mode $m = 1$ of the magnetic field. These numerical experiments also confirm the importance of moving soft iron material in the VKS2 dynamo. This may be one piece of the big maze that constitutes the VKS2 experiment, but more experimental and numerical investigations need to be done to fully understand this experiment. This illustrates clearly the unending interplay between MHD experiments and simulations.

D.6 Conclusion

We have developed a novel approximation technique using Lagrange finite elements for solving magneto-dynamics problems involving discontinuous magnetic permeability and non-smooth interfaces. The method has been applied to model the VKS2 experiment in a kinematic dynamo context. In the future, we will investigate nonlinear regimes with the full MHD equations in a VKS2 set-up using impellers modeled by flat disks together with an axisymmetric volumic forcing term acting at the location of the blades.

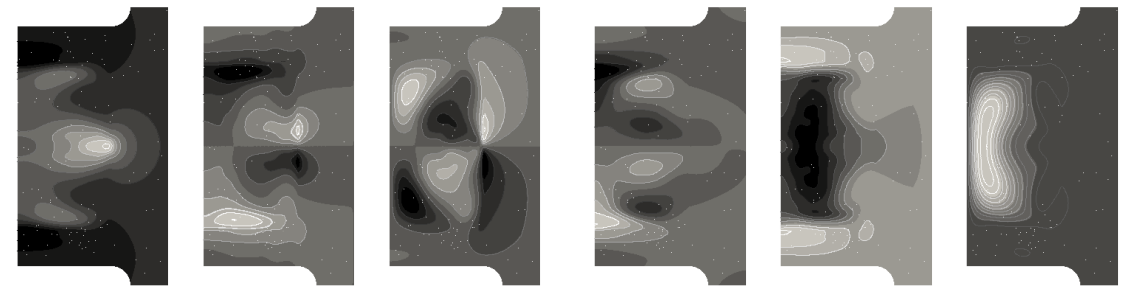

(a) H_r^c, H_θ^c, H_z^c at $\theta = 0$, $\mu = 1$, $R_\mathrm{m} = 75$ (b) H_r^c, H_θ^c, H_z^c at $\theta = \frac{\pi}{2}$ and $\mu = 1$, $R_\mathrm{m} = 75$

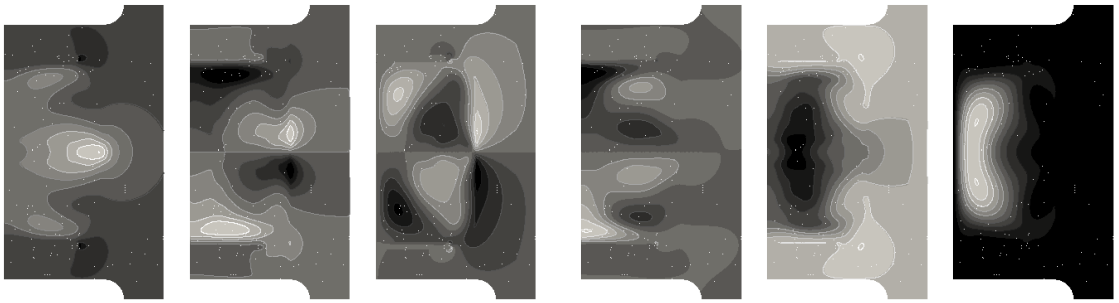

(c) H_r^c, H_θ^c, H_z^c at $\theta = 0$ and $\mu = 60$, $R_\mathrm{m} = 65$ (d) H_r^c, H_θ^c, H_z^c at $\theta = \frac{\pi}{2}$ and $\mu = 60$, $R_\mathrm{m} = 65$

Figure D.10: Magnetic field in two perpendicular azimuthal planes in Cases 2' and 4'.

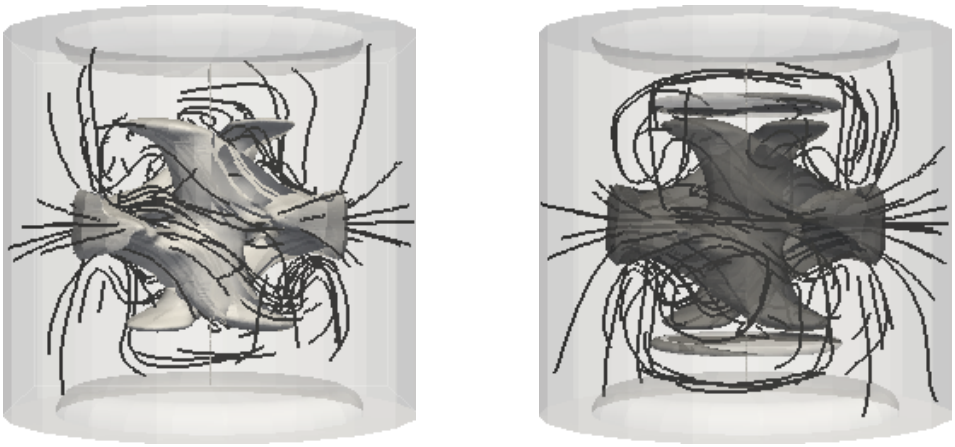

(a) $\mu = 1$, $R_m = 75$ (b) $\mu = 60$, $R_m = 65$

Figure D.11: Magnetic lines and iso-value of the magnetic energy density corresponding to 25% of the maximum magnetic energy for Cases 2' and 4'.

Acknowledgments

This work was granted access to the HPC resources of IDRIS under the allocation 2010-[0254] made by GENCI (Grand Equipement National de Calcul Intensif). JLG is thankful to University Paris Sud 11 for supporting him in June 2009, January 2010, and January 2011. F.L. is thankful to Texas A&M University for supporting him in 2010/2011.

Annexe E

Influence of high-permeability discs in an axisymmetric model of the Cadarache dynamo experiment

A. Giesecke [a], C. Nore [b,c], F. Stefani [a], G. Gerbeth [a], J. Léorat [d], W. Herreman [b,c], F. Luddens [b], J.-L. Guermond [b,e]

Abstract

Numerical simulations of the kinematic induction equation are performed on a model configuration of the Cadarache von-Kármán-Sodium dynamo experiment. The effect of a localized axisymmetric distribution of relative permeability μ_r that represents soft iron material within the conducting fluid flow is investigated. The critical magnetic Reynolds number Rm^c for dynamo action of the first non-axisymmetric mode roughly scales like $\mathrm{Rm}^\mathrm{c}_{\mu_\mathrm{r}} - \mathrm{Rm}^\mathrm{c}_\infty \propto \mu_r^{-1/2}$ i.e. the threshold decreases as μ_r increases. This scaling law suggests a skin effect mechanism in the soft iron disks. More important with regard to the Cadarache dynamo experiment, we observe a purely toroidal axisymmetric mode localized in the high permeability disks which becomes dominant for large μ_r. In this limit, the toroidal mode is close to the onset of dynamo action with a (negative) growth-rate that is rather independent of the magnetic Reynolds number. We qualitatively explain this effect by paramagnetic pumping at the fluid/disk interface and propose a simplified model that quantitatively reproduces numerical results. The crucial role of the high permeability disks for the mode selection in the Cadarache dynamo experiment cannot be inferred from computations using idealized pseudo-vacuum boundary conditions ($\boldsymbol{H}\times\boldsymbol{n} = 0$).

E.1 Introduction

Astrophysical magnetic fields are a ubiquitous phenomenon. They affect formation and behavior of galaxies, stars or planets and might even be important for structure formation on cosmic scales. On astrophysical scales fluid flow driven field generation by virtue of the dynamo effect

[a] Helmholtz-Zentrum Dresden-Rossendorf, PO Box 510119, 01314 Dresden, Germany
[b] Laboratoire d'Informatique pour la Mécanique et les Sciences de l'Ingénieur, CNRS, BP 133, 91403 Orsay Cedex, France
[c] Université Paris Sud 11, 91405 Orsay Cedex, France
[d] Luth, Observatoire de Paris-Meudon, place Janssen, 92195 Meudon, France
[e] Department of Mathematics, Texas A&M University 3368 TAMU, College Station, TX 77843-3368, USA

is relatively uncomplicated because the magnetic Reynolds number is always huge. However, due to their limited size the realization of dynamo action in laboratory experiments is a demanding task and requires an elaborate design that makes use of optimizations like an ideal guidance of a fluid flow or a selective choice of materials. Material properties like electrical conductivity or relative permeability have always been important for experimental dynamos. For example, the use of soft iron in the dynamo experiments of Lowes & Wilkinson [98, 99] was crucial for the occurrence of magnetic self excitation. More recently, the addition of high permeability material (soft iron spheres) into a conducting fluid was examined to test magnetic self excitation [43] in a flow that otherwise would not be able to sustain a dynamo.

The work presented here is motivated by the Cadarache von-Kármán-Sodium (VKS) dynamo [110]. In this experiment liquid sodium contained in a cylindrical vessel is driven by two counter–rotating impellers that are located close to the lids of the vessel. Dynamo action is obtained only when (at least one of) the flow driving impellers are made of soft iron with a relative permeability $\mu_\mathrm{r} \approx 65$ [153]. Moreover the observed magnetic field is dominated by an axisymmetric mode [109]. It can be conjectured that the occurrence of dynamo action with soft iron impellers and the axisymmetry of the magnetic field are linked but, so far, the very nature of the axisymmetric dynamo is still unknown.

A well-known necessary condition for the occurrence of dynamo action is a sufficiently complex conducting fluid flow that couples the toroidal and poloidal components of the magnetic field. The interaction between these components gives rise to the so-called dynamo cycle which consists of regenerating the toroidal field from the poloidal field and vice versa. This coupling can take place on large scales [44] as well as on small scales by virtue of the well known α-effect [82]. It is less well known that non-homogeneities in the electrical conductivity can also introduce such coupling and, by this, favour dynamo action. For example, a uniform flow over an infinite plate with varying conductivity can produce dynamo action [28, 154]. It is likely that inhomogeneous magnetic permeability can lead to dynamo action as well.

In this paper we investigate the impact of a localized disk-like permeability distribution embedded in a conducting axisymmetric fluid flow on the growth-rates of the first axisymmetric and non-axisymmetric magnetic eigenmodes. Induction effects due to non-axisymmetric perturbations (turbulence, small-scale or large-scale flow or conductivity/permeability distributions) are not taken into account. First, we briefly re-examine the threshold of the equatorial dipole mode as in [56] and propose an explanation for the scaling law that relates the critical magnetic Reynolds number to the permeability in the impeller disks. Second we investigate the influence of the concentrated high permeability on the axisymmetric field modes. Even though they are always damped, according to Cowling's theorem [39, 71], for large μ_r we find a dominant toroidal mode very close to the onset of dynamo action. We suggest that this eigenmode plays a significant role in the dominance of the axisymmetric mode in the dynamo observed in the VKS experiment [110].

In the following, toroidal and poloidal components always refer to the axisymmetric case so that the toroidal component corresponds to the azimuthal field $\boldsymbol{B}_\mathrm{tor} = B_\varphi \boldsymbol{e}_\varphi$ and the poloidal component is given by $\boldsymbol{B}_\mathrm{pol} = B_r \boldsymbol{e}_r + B_z \boldsymbol{e}_z$, where $(\boldsymbol{e}_r, \boldsymbol{e}_\varphi, \boldsymbol{e}_z)$ are the cylindrical unit vectors.

E.2 Model

The induction equation with nonuniform material coefficients, i.e. spatially dependent electrical conductivity $\sigma = \sigma(\boldsymbol{r})$ and relative permeability $\mu_\mathrm{r} = \mu_\mathrm{r}(\boldsymbol{r})$, reads:

$$\frac{\partial \boldsymbol{B}}{\partial t} = \nabla\times\left(\boldsymbol{u}\times\boldsymbol{B} + \frac{1}{\mu_\mathrm{r}\mu_0\sigma}\frac{\nabla\mu_\mathrm{r}}{\mu_\mathrm{r}}\times\boldsymbol{B} - \frac{1}{\mu_\mathrm{r}\mu_0\sigma}\nabla\times\boldsymbol{B}\right), \tag{E.2.1}$$

where $\boldsymbol{u}$ is the prescribed (mean) flow, $\boldsymbol{B}$ the magnetic flux density and μ_0 the vacuum permeability ($\mu_0 = 4\pi\times 10^{-7}$Vs/Am). The middle term in the right hand side of Eq. (E.2.1) proportional to $\sim \nabla\mu_\mathrm{r}\times\boldsymbol{B}$ represents the so-called "paramagnetic pumping" [43]. This term is responsible for the suction of the magnetic field into the regions with large permeability and involves a (non divergence free) velocity-like field that we henceforth call "pumping velocity"

$$\boldsymbol{V}^\mu = \frac{1}{\mu_\mathrm{r}\mu_0\sigma}\frac{\nabla\mu_\mathrm{r}}{\mu_\mathrm{r}}. \tag{E.2.2}$$

The eigenvalue problem associated with equation (E.2.1) is solved numerically by using two different methods. One is based on a spectral/finite element approach described in [67] (SFEMaNS, spectral/finite element method for Maxwell and Navier-Stokes equations) which solves the eigenvalue problem using ARPACK. The second approach utilizes a combined finite volume/boundary element method for timestepping equation (E.2.1), [57]. Both approximation methods can account for insulating boundaries and non-uniform permeability and/or conductivity distributions. In the FV/BEM scheme insulating boundary conditions are treated by solving an integral equation on the boundary which allows a direct computation of the (unknown) tangential field components by correlating the (known) normal field components on the surface of the computational domain [72, 57]. In the SFEMaNS code the magnetic field is computed numerically in a certain domain outside of the cylinder and matching conditions are used at the interfaces with the insulator [65].

The respective discretizations are done so that the transmission conditions across the material interfaces are satisfied. In addition to having passed independent convergence tests on manufactured solutions, the two codes have been cross-validated by comparing their outputs on various common test cases (see Giesecke et al. [55, 56] and Table E.1 below).

We use the same configuration as applied in [58]. The computational domain is inspired from the VKS configuration. The conducting fluid is contained in a cylinder of height $H = 2.6$ and radius $R_\mathrm{out} = 1.4$, surrounded by an insulator. The fluid fills two unconnected compartments. The moving fluid is contained in an inner cylinder of radius $R_\mathrm{in} = 1$. The fluid contained in the annular region comprised between the cylinders of radius $R_\mathrm{in} = 1$ and $R_\mathrm{out} = 1.4$ is at rest; this region is referred to as the side layer (see figure E.1). Two discoidal subdomains of radius $R_\mathrm{imp} = 0.95$ are located in the intervals $z \in [-1.0; -0.9]$ and $z \in [0.9; 1.0]$ and are meant to model soft iron impeller disks of thickness $d = 0.1$; the relative magnetic permeability in these two disks is denoted μ_r. The velocity field $\boldsymbol{u}$ and the permeability distribution μ_r are assumed to be axisymmetric. The velocity field between the impeller disks

At the interface between two materials denoted 1 and 2, the transmission conditions on the magnetic field and the electric field/current are given by:

$$\begin{aligned} \boldsymbol{n}\cdot(\boldsymbol{B}^1 - \boldsymbol{B}^2) &= 0 \quad \text{and} \quad \boldsymbol{n}\times\left(\frac{\boldsymbol{B}^1}{\mu_\mathrm{r}^1} - \frac{\boldsymbol{B}^2}{\mu_\mathrm{r}^2}\right) = 0 \quad \text{for permeability jumps and} \\ \boldsymbol{n}\cdot(\boldsymbol{j}^1 - \boldsymbol{j}^2) &= 0 \quad \text{and} \quad \boldsymbol{n}\times(\boldsymbol{E}^1 - \boldsymbol{E}^2) = 0 \quad \text{for conductivity jumps.} \end{aligned}$$

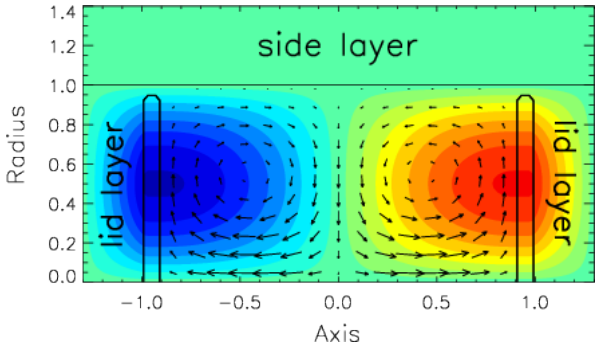

Figure E.1: Velocity field used in the kinematic simulations. The azimuthal velocity, u_φ, is shown in color and the poloidal component of the velocity, $u_r \boldsymbol{e}_r + u_z \boldsymbol{e}_z$, is shown with arrows. The black structures in the intervals $z \in [-1.0; -0.9]$ and $z \in [0.9; 1.0]$ represent two axisymmetric impellers of relative permeability $\mu_\mathrm{r} > 1$. Note that the flow is mixed (poloidal and toroidal) between the two impeller disks and purely toroidal within and behind the impeller disks.

in the inner cylinder is given by the so-called MND fluid flow [102]:

$$\begin{aligned} u_r(r,z) &= -(\pi/h)\cos(2\pi z/h)\, r(1-r)^2(1+2r), \\ u_\varphi(r,z) &= 4\epsilon r(1-r)\sin(\pi z/h), \\ u_z(r,z) &= (1-r)(1+r-5r^2)\sin(2\pi z/h), \end{aligned} \tag{E.2.3}$$

where h is the distance between the two impeller disks ($h = 1.8$) and ϵ parametrizes the toroidal to poloidal ratio of the flow (in the following we choose $\epsilon = 0.7259$) . A purely azimuthal velocity equal to the azimuthal velocity of the MND flow at $z = \pm h/2$ is assumed in the two impeller disks. A so-called lid layer [137] is added behind each impeller disk, and the velocity field therein is modeled by linear interpolation along the z-axis between the azimuthal velocity at the outer side of the impeller disk and the no-slip condition at the lid of the vessel. The velocity field and the impeller disks (two thin structures shown in black solid lines) are displayed in Figure E.1. The conductivity is assumed to be uniform in the liquid metal and the soft iron disks. We focus in this paper on non-uniform permeability distributions only, which seems roughly justified for soft iron disks embedded in liquid sodium.

The equations are nondimensionalized so that $\mathcal{R} = R_\mathrm{in}$ is the reference length-scale (R_in is the radius of the flow active region) and $\mathcal{U} = \max[(u_r^2 + u_\varphi^2 + u_z^2)^{1/2}]$ is the reference velocity scale (maximum absolute value of the velocity field). The control parameter is the magnetic Reynolds number defined by $\mathrm{Rm} = \mu_0 \sigma \mathcal{U} \mathcal{R}$.

---

where $\boldsymbol{n}$ denotes the unit normal vector at the interface between both materials, $\boldsymbol{j}$ the current density and $\boldsymbol{E}$ the electrical field.

This value is close to the optimum relation between poloidal and toroidal flow that has been estimated in various comparable configurations [123] and has frequently been utilized in previous studies of dynamo action driven by the MND flow (e.g. Stefani et al. [137], Gissinger et al. [61], Giesecke et al. [56]).

E.3 Results

The eigenvalues of the differential operator in the right-hand side of equation (E.2.1) are denoted $\lambda = \gamma + i\omega$; the real part γ is the growth-rate of the field amplitude ($\gamma < 0$ corresponds to decay) and the imaginary part ω is the frequency. All the computations reported below give non-oscillatory eigen-modes (i.e. $\omega = 0$). An immediate consequence of the axisymmetric setup is that the eigenmodes of the kinematic dynamo problem can be computed for each azimuthal wavenumber m.

E.3.1 Overview

We show in Table E.1 sample values of growth-rates obtained by FV and SFEMaNS for the above simplified VKS model problem. This table confirms that FV and SFEMaNS converge to the same solutions up to 2% on the growth-rates. We use the following notation in Table E.1 and in the rest of the paper: γ_{m0} is the growth-rate of a mixed poloidal/toroidal mode. This mode degenerates to a purely poloidal mode when Rm $= 0$, and when there is no permeability jump (e.g. for stainless steel disks) this mode always determines the behavior of the axisymmetric field. Furthermore, $\gamma^{\rm t}_{m0}$ is the growth-rate of the first axisymmetric mode ($m = 0$) that is purely toroidal and γ_{m1} is the growth-rate of the first non-axisymmetric mode ($m = 1$).

When $R_{\rm m} = 0$, the dominant and the second dominant $m0$-modes at $\mu_{\rm r} = 1$ are purely poloidal and purely toroidal, respectively; the situation is reversed at $\mu_{\rm r} = 60$: the dominant mode is purely toroidal. All growth-rates increase with $\mu_{\rm r}$. When $R_{\rm m} > 0$, the growth-rate of the $m0$-mode is always negative in agreement with Cowling's theorem [39], but we observe that its relaxation time becomes longer as the permeability in the impeller disks increases.

Rm	$\mu_{\rm r}$	$\gamma^{\rm t}_{m0}$	γ_{m0}	γ_{m1}	Scheme
0	1	-8.950	-4.159	-4.273	FV
0	1	-8.977	-4.162	-4.322	SFEMaNS
0	60	-1.292	-3.887	-1.715	FV
0	60	-1.305	-3.893	-1.722	SFEMaNS
30	1	-8.748	-3.591	-2.690	FV
30	1	-8.770	-3.597	-2.780	SFEMaNS
30	60	-1.134	-3.404	-2.511	FV
30	60	-1.155	-3.478	-2.476	SFEMaNS
70	1	-8.079	-3.467	-0.119	FV
70	1	-8.119	-3.471	-0.215	SFEMaNS
70	60	-1.203	-3.232	1.012	FV
70	60	-1.219	-3.264	0.969	SFEMaNS

Table E.1: Comparison of growth-rates obtained with FV (hybrid finite volume/boundary element method) and SFEMaNS (spectral/finite element method for Maxwell and Navier-Stokes equations). Rm is the magnetic Reynolds number, $\mu_{\rm r}$ the disk permeability, $\gamma^{\rm t}_{m0}$ the growth-rate of the axisymmetric toroidal field, γ_{m0} the growth-rate of the axisymmetric mixed field, γ_{m1} the growth-rate of the first non-axisymmetric field ($m1$-mode). The thickness of the impeller disks is $d = 0.1$.

We also observe that dynamo action occurs on the $m1$-mode and that increasing μ_r lowers the critical threshold on R_{m}.

Snapshots of the dominant magnetic eigenmode are shown in Figure E.2. The structure of the $m1$-mode does not change very much with respect to μ_{r} and Rm; it is an equatorial dipole with two opposite axial structures mainly localized in the bulk of the fluid. In contrast, the $m0$-mode is essentially localized in the two impeller disks and does barely differ from the pattern obtained in the free decay case (see Figure E.6 below).

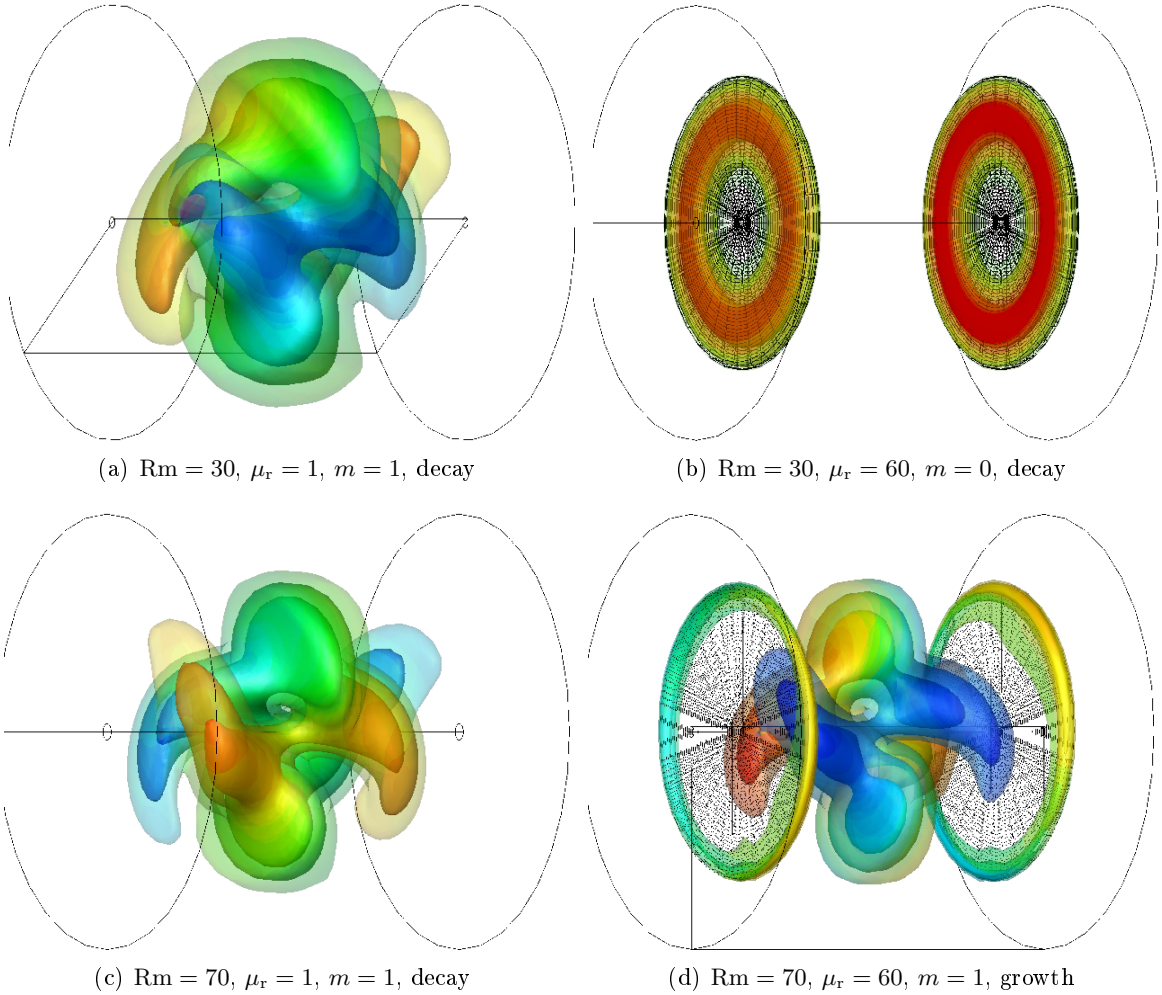

(a) Rm $= 30$, $\mu_{\mathrm{r}} = 1$, $m = 1$, decay

(b) Rm $= 30$, $\mu_{\mathrm{r}} = 60$, $m = 0$, decay

(c) Rm $= 70$, $\mu_{\mathrm{r}} = 1$, $m = 1$, decay

(d) Rm $= 70$, $\mu_{\mathrm{r}} = 60$, $m = 1$, growth

Figure E.2: Dominant magnetic eigenmodes. The isosurfaces show the magnetic energy density at $10\%, 20\%, 40\%$ of the maximum value. The colors show $H_\varphi = \mu_{\mathrm{r}}^{-1} B_\varphi$ and the meshes show the location of the soft iron disks (in the right column). Note that all eigenmodes are decaying except the case $\mathrm{Rm} = 70, \mu_{\mathrm{r}} = 60$ (lower right panel) which is above the dynamo threshold and therefore presents a growing $m1$–mode.

E.3.2 Effect of the disk permeability on the $m1$-mode

Figure E.3 shows the growth-rate of the $m1$-mode as a function of the relative permeability of the impeller disks for four values of the Reynolds number. This figure is similar to figure 13a in

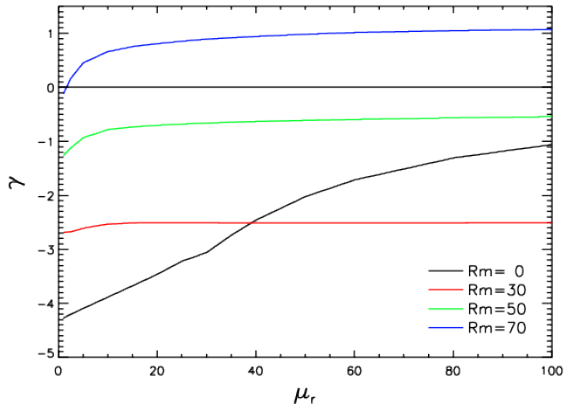

Figure E.3: Growth-rate of the $m1$-mode as a function of $\mu_{\rm r}$ for $\mathrm{Rm} = 0, 30, 50, 70$.

[56]. The growth-rate reaches quickly an asymptotic value when $\mathrm{Rm} > 0$, which is not the case when $\mathrm{Rm} = 0$. The $m1$-mode clearly depends on Rm and exhibits dynamo action when Rm is large enough. It can be seen in the left panel in Figure E.4 that the threshold for dynamo action goes from $\mathrm{Rm}^{\rm c} \approx 76$ when $\mu_{\rm r} = 1$ to $\mathrm{Rm}^{\rm c}_{\infty} \approx 53.95$ when $\mu_{\rm r} \to \infty$. The asymptotic

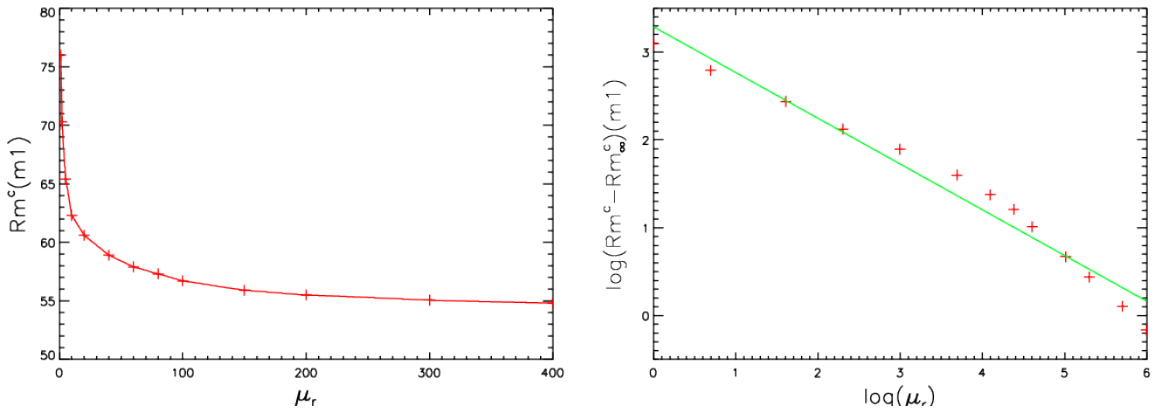

Figure E.4: Left panel: Dynamo threshold for the $m1$-mode as a function of μ_r. Right panel: Linear fit on log-log scale provides the scaling $\mathrm{Rm}^{\rm c} - \mathrm{Rm}^{\rm c}_{\infty} \propto \mu_r^{-0.52}$.

threshold for $\mu_{\rm r} \to \infty$ has been calculated by enforcing the boundary condition $\boldsymbol{H}\times\boldsymbol{n} = 0$ on the impeller disks (pseudo-vacuum or Vanishing Tangential Field condition) while keeping the flow pattern (E.2.3) unchanged. This computation shows that, as far as the $m1$-mode is concerned, the impeller disks behave like an idealized ferromagnetic material in the limit $\mu_{\rm r} \to \infty$. Upon inspection of the right panel in Figure E.4, where $\mathrm{Rm}^{\rm c} - \mathrm{Rm}^{\rm c}_{\infty}$ is displayed as a function of μ_r in log-log scale, we infer the following scaling law: $\mathrm{Rm}^{\rm c} - \mathrm{Rm}^{\rm c}_{\infty} \propto \mu_r^{-0.52}$. This

type of scaling is an indication that a boundary layer effect is at play which can be explained as follows. Starting with the idea that the stationary $m1$-dynamo is generated within the fluid flow, it is reasonable to expect that the rotating disks see this field as a quickly varying imposed field. The magnetic field cannot penetrate the disks when the permeability is infinite but, according to the classical skin effect, it can diffuse through a thin boundary layer of thickness $\delta = (\sigma\mu_r\Omega)^{-1/2}$ when μ_r is finite (Ω is the mean angular velocity). This diffusion effect adds a supplementary $\mu_r^{-1/2}$ damping to the magnetic field mode compared to the infinite permeability case.

E.3.3 Effect of the disk permeability on the $m0$-mode

Figure E.5 shows the growth-rates of the axisymmetric mode as a function of μ_r. Contrary to what we have observed for the $m1$-mode, the dependence of the $m0$-mode with respect to Rm seems to be small; more precisely, the flow does not seem to play a significant role when the permeability is large.

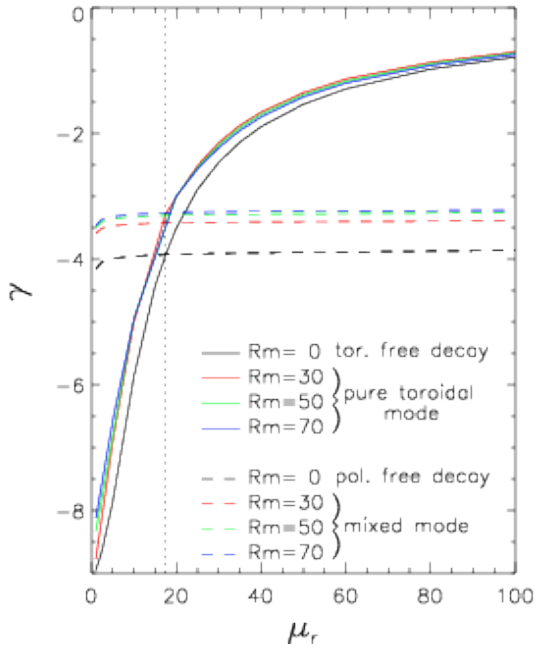

Figure E.5: Growth-rates of the $m0$-mode. The dotted vertical line marks the transitional value $\mu_\mathrm{r}^\mathrm{t} \approx 17.5$ at which the pure toroidal mode becomes dominant.

In the free decay case (Rm = 0) the poloidal (dashed black line) and toroidal (solid black line) modes are decoupled and the growth-rates of these two modes are $\gamma_{m0} = -4.159$ and $\gamma_{m0}^\mathrm{t} = -8.950$, respectively. The decay time of the poloidal eigenmode is significantly larger than that of the toroidal one. The dominant poloidal eigenmode exhibits a typical dipolar pattern as shown in the left panel of Figure E.6. Increasing the disk permeability (still at Rm = 0) the poloidal mode remains nearly unaffected (dashed black curve in Figure E.5) whereas the purely toroidal mode is significantly enhanced and eventually becomes dominant

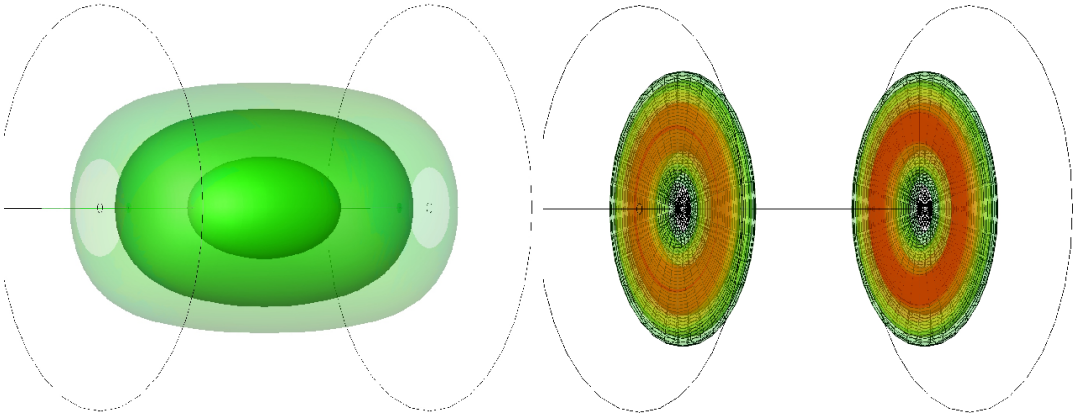

Figure E.6: Spatial structure of $m0$-mode in free decay (Rm = 0). Left panel: $\mu_\mathrm{r} = 1$, right panel: $\mu_\mathrm{r} = 60$. The isosurfaces show the energy density at 20%, 40%, 80% of the maximum value. The colors code the azimuthal component $H_\varphi = \mu_\mathrm{r}^{-1} B_\varphi$.

when $\mu_\mathrm{r} \gtrsim \mu_\mathrm{r}^\mathrm{t} \approx 17.5$ (see solid curves in figure E.5 and right panel in Figure E.6). The growth-rate of the toroidal mode increases monotonically with μ_r and roughly scales $\propto -\mu_\mathrm{r}^{-1}$.

The introduction of a velocity field (Rm > 0) transfers poloidal field components into toroidal field components, but not vice versa. Therefore for increasing Rm a mixed mode is generated from the purely poloidal field that is observed at Rm $= 0$ (see dashed lines in Figure E.5). The dependence of the growth-rate of the mixed mode with respect to the Reynolds number and the permeability is small. This mixed mode is dominant when $\mu_\mathrm{r} \lesssim \mu_\mathrm{r}^\mathrm{t}$, but above this transitional point it is the purely toroidal eigenmode that dominates (see solid colored curves in Figure E.5). The purely toroidal mode hardly depends on the magnetic Reynolds number and its growth-rate increases with μ_r like in the free decay situation.

Surprisingly, the value of the transitional permeability $\mu_\mathrm{r}^\mathrm{t}$ is more or less the same for all the considered Reynolds numbers (see the vertical dotted line in Figure E.5 that marks the transition).

E.4 Discussion on the $m0$-mode

E.4.1 The coupling

Using the cylindrical coordinate system (r, φ, z), and assuming axisymmetry, the induction equation can be written as follows:

$$\left(\frac{\partial}{\partial t} + u_r\frac{\partial}{\partial r} + u_z\frac{\partial}{\partial z}\right) B_r = \left(B_r\frac{\partial}{\partial r} + B_z\frac{\partial}{\partial z}\right) u_r + \eta_0\left[\frac{\partial}{\partial z}\left(\frac{\partial}{\partial z}\frac{B_r}{\mu_\mathrm{r}} - \frac{\partial}{\partial r}\frac{B_z}{\mu_\mathrm{r}}\right)\right], \tag{E.4.1}$$

$$\left[\frac{\partial}{\partial t} + u_r\left(\frac{\partial}{\partial r} - \frac{1}{r}\right) + u_z\frac{\partial}{\partial z}\right] B_\varphi = \left[B_r\left(\frac{\partial}{\partial r} - \frac{1}{r}\right) + B_z\frac{\partial}{\partial z}\right] u_\varphi + \eta_0\Delta_*\frac{B_\varphi}{\mu_r}, \tag{E.4.2}$$

$$\left(\frac{\partial}{\partial t} + u_r\frac{\partial}{\partial r} + u_z\frac{\partial}{\partial z}\right) B_z = \left(B_r\frac{\partial}{\partial r} + B_z\frac{\partial}{\partial z}\right) u_z - \eta_0\frac{1}{r}\frac{\partial}{\partial r}\left[r\left(\frac{\partial}{\partial z}\frac{B_r}{\mu_\mathrm{r}} - \frac{\partial}{\partial r}\frac{B_z}{\mu_\mathrm{r}}\right)\right] \tag{E.4.3}$$

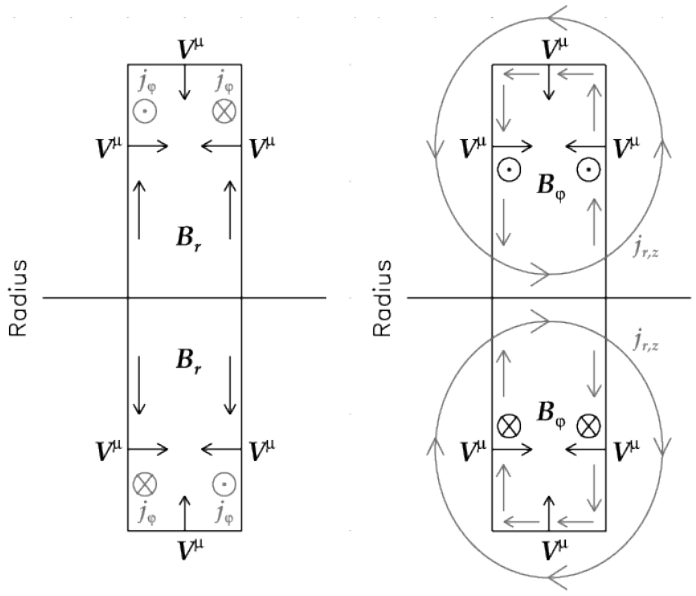

Figure E.7: Left panel: current generation at the fluid-disk interface by paramagnetic pumping for a radial magnetic field B_r. Right panel: current generation from paramagnetic pumping for the azimuthal magnetic field B_φ.

where $\Delta_* = \frac{\partial^2}{\partial r^2} + \frac{1}{r}\frac{\partial}{\partial r} + \frac{\partial^2}{\partial z^2} - \frac{1}{r^2}$, and $\eta_0 = \frac{1}{\sigma\mu_0}$. This form of the induction equation clearly shows that $B_r = B_z = 0$ and $B_\varphi \neq 0$ can be an axisymmetric solution: this is the purely toroidal mode. If $B_r \neq 0$, $B_z \neq 0$, then their shearing by the nonzero azimuthal flow u_φ, the so-called Ω-effect, will always generate $B_\varphi \neq 0$ which then results in a mixed mode. The growth-rate of the mixed mode will however remain entirely fixed by its poloidal components B_r and B_z (see Figure E.5).

Purely toroidal and purely poloidal fields cannot exist if μ_r depends on φ. The same remark holds if σ depends on φ; for instance, spatial variation of the electric conductivity is used in [28] to produce dynamo action. When the permeability μ_r is axisymmetric there is no mechanism to transfer magnetic energy from the toroidal component B_φ to the poloidal pair (B_r, B_z) (see Eqs. E.4.1 and E.4.3).

E.4.2 Selective enhancement of B_φ

We start by explaining qualitatively why, for large values of μ_r, the purely toroidal mode is the least damped one and why the mixed mode is so little influenced by the disk. The argument is based on the paramagnetic pumping term (E.2.2) that is at the origin of an electromotive force (EMF):

$$\boldsymbol{\mathcal{E}}^\mu = \boldsymbol{V}^\mu \times \boldsymbol{B} = \frac{1}{\mu_0 \mu_\mathrm{r} \sigma} \frac{\nabla \mu_\mathrm{r}}{\mu_\mathrm{r}} \times \boldsymbol{B}. \tag{E.4.4}$$

Since the permeability jump is restricted to the material interface there is only a contribution to the EMF within that localized area. For sufficiently thin disks, as considered here, it is reasonable to assume that the permeability jump at the rim of the impeller disks plays a

minor role. We therefore assume that the pumping velocity is mainly axial: $\boldsymbol{V}^{\mu} \propto \frac{\partial}{\partial z}\mu_{\mathrm{r}}\boldsymbol{e}_z$. The interaction of $\boldsymbol{V}^{\mu}$ with the axial field $B_z\boldsymbol{e}_z$ is henceforth neglected.

The interaction between $\boldsymbol{V}^{\mu} \propto \frac{\partial}{\partial z}\mu_{\mathrm{r}}\boldsymbol{e}_z$ and the radial field $B_r\boldsymbol{e}_r$ creates an azimuthal current $j_\varphi\boldsymbol{e}_\varphi$ at the interface between the impeller disks and the fluid (see left panel in Figure E.7). Since the impeller disks are thin, it is reasonable to assume that the orientation and the amplitude of B_r do not change across the disks. This implies that the signs of the pumping term (E.2.2) at the back and at the front side of the disks are opposite, which in turn implies that the induced azimuthal currents mostly cancel each other and the overall azimuthal current is close to zero. This cancellation mechanism would not occur with thick disks. When the impeller disks are thick, the mixed mode and the purely toroidal mode have similar growth-rates as can be observed in the left panels on figure 8 in [56] where the above phenomenon is illustrated for two thicknesses of the impeller disks, $d = 0.1$ and $d = 0.6$.

The behavior is very different concerning the EMF that results from the interaction of the azimuthal component $B_\varphi\boldsymbol{e}_\varphi$ with $\boldsymbol{V}^{\mu}$ (see right panel in Figure E.7). In this case the currents generated at the front and at the back of the impeller disks add up and the EMF drives a

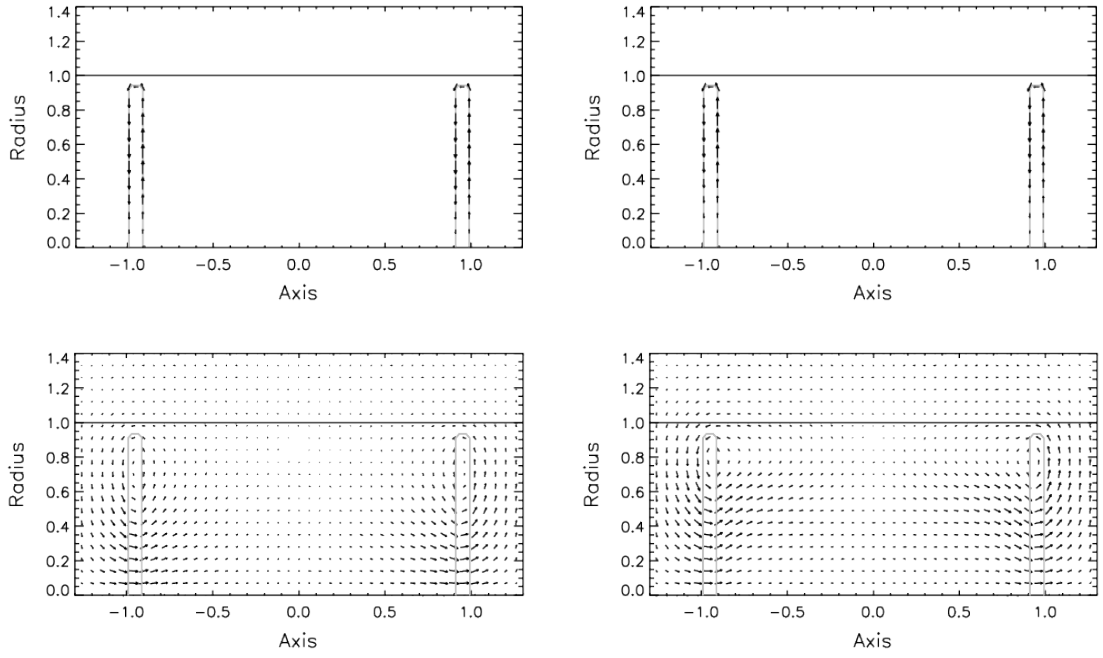

Figure E.8: Paramagnetic pumping at $\mu_{\mathrm{r}} = 60$. Upper row: electromotive force (EMF) $\mathcal{E}^{\mu} = (\mu_0\mu_{\mathrm{r}}\sigma)^{-1}\mu_{\mathrm{r}}^{-1}\nabla\mu_{\mathrm{r}} \times B_\varphi\boldsymbol{e}_\varphi$ at $\mathrm{Rm} = 0$ (left) and $\mathrm{Rm} = 30$ (right). Lower row: (poloidal) current density $\boldsymbol{j} = (\mu_0)^{-1}\nabla \times \boldsymbol{B}/\mu_{\mathrm{r}}$ at $\mathrm{Rm} = 0$ (left) and $\mathrm{Rm} = 30$ (right). The light grey lines show soft iron disks and the solid horizontal line shows the separation between the moving fluid and stagnant side layer. The azimuthal current is negligible. Note the close similarity between free decay (left column) and the case $\mathrm{Rm} = 30$ (right column) illustrating the marginal impact of the fluid flow.

poloidal current along the surface of the disk which in turn re-enforces B_φ. Typical patterns of the EMF and current density from our numerical simulations are shown in Figure E.8. These graphics confirm the presence of the poloidal current and confirm also that the influence of the fluid flow is marginal.

E.4.3 Simplified model for the toroidal $m0$-mode

Our numerical results clearly indicate that the influence of the flow on the toroidal axisymmetric mode is negligible and that this mode is mostly localized inside the impeller disks. In order to better understand the dynamics of the toroidal $m0$-mode, we consider an idealized disk-fluid model in free decay situation ($R_\mathrm{m} = 0$).

Let us assume a disk of radius 1, permeability $\mu_r \gg 1$ and thickness d, sandwiched between two semi-infinite cylindrical fluid regions with $\mu_\mathrm{r} = 1$. We further assume the boundary condition $\boldsymbol{H}\times\boldsymbol{n} = 0$ at the wall $r = 1$. This simplifying assumption will allow us to find analytical solutions. We solve

$$\begin{aligned} \mu_r\gamma B_\varphi &= \Delta_* B_\varphi, & r<1, \quad |z|<d/2 \\ \gamma B_\varphi &= \Delta_* B_\varphi, & r<1, \quad |z|>d/2 \end{aligned} \tag{E.4.5}$$

where $\Delta_* = \frac{\partial^2}{\partial r^2} + \frac{1}{r}\frac{\partial}{\partial r} + \frac{\partial^2}{\partial z^2} - \frac{1}{r^2}$. Note that the non-dimensionalization is done so that the reference scale of the growth-rate is $(\sigma\mu_0 R^2)^{-1}$. The boundary condition is $B_\varphi = 0$ at $r = 1$, and the transmission condition across the material interface is that H_φ and $E_r = \partial_z H_\varphi/\sigma$ be continuous at $z = \pm d/2$.

The numerical simulations show that the dominating eigenmodes are symmetric with respect to the equatorial plane of the disk $z = 0$. This leads to the following ansatz

$$\begin{aligned} B_\varphi &= A_1\, J_1(kr)\cos l_1 z, & r<1, \quad 0<z<d/2 \\ B_\varphi &= A_2\, J_1(kr)\, e^{-L_2 z}, & r<1, \quad z>d/2, \end{aligned}$$

where J_1 is the Bessel function of the first kind and

$$l_1 = \sqrt{-\gamma\mu_r - k^2}, \qquad L_2 = \sqrt{k^2+\gamma}. \tag{E.4.6}$$

The amplitudes A_1 and A_2 are arbitrary for the moment. The fields are obtained by symmetry for $z < 0$. To ensure that the solution decays at infinity (i.e. it remains bounded when $z \to \pm\infty$), it is necessary that l_1 and L_2 be real. This imposes the constraints

$$\mu_r > 1 \quad , \quad \gamma \in [-k^2, -k^2/\mu_r]. \tag{E.4.7}$$

The boundary condition at $r = 1$ implies that $J_1(k) = 0$, i.e. k is a zero of J_1. We choose the first zero, say k_1, so that the solution is composed of one radial cell only,

$$k_1 \approx 3.8317. \tag{E.4.8}$$

This value specifically depends on the idealized boundary condition that we have assumed at $r = 1$; the effect of small deviations $k = (1 \pm 0.1)k_1$ is considered further below. Due to the assumed symmetry, we need to impose the transmission conditions at the $z = d/2$ interface only:

$$\begin{aligned} \left(\frac{1}{\mu_r}\cos\frac{l_1 d}{2}\right) A_1 - \left(e^{-L_2 d/2}\right) A_2 &= 0, \\ \left(\frac{l_1}{\sigma\mu_r}\sin\frac{l_1 d}{2}\right) A_1 - \left(\frac{L_2}{\sigma}\, e^{-L_2 d/2}\right) A_2 &= 0. \end{aligned} \tag{E.4.9}$$

The determinant of the above linear system must be zero for a solution to exist,

$$L_2 \cos\frac{l_1 d}{2} - l_1 \sin\frac{l_1 d}{2} = 0. \tag{E.4.10}$$

Upon inserting the definitions of l_1 and L_2 from (E.4.6) into this dispersion relation, we obtain an implicit nonlinear equation for the growth-rate γ as a function of d and $\mu_{\rm r}$.

We show in the left panel of Figure E.9 the graph of the function $\gamma(\mu_{\rm r})$ deduced from (E.4.10) with $d = 0.1$ and $k = k_1 = 3.8317$. Two further analytical graphs computed with $k = (1 \pm 0.1)k_1$ show the very weak sensitivity of the growth rate on relaxing the strict boundary condition $\boldsymbol{H} \times \boldsymbol{n} = 0$ (e.g. by using an outer shell of different conductivity). We also show in this figure the numerical outcome for the growth-rate of the purely toroidal mode at $\mathrm{Rm} = 0$ (see also black solid line in Figure E.5). The agreement is quite satisfactory and thereby confirms our analysis. When representing $\gamma(\mu_{\rm r})$ in log-log scale (not shown) we see that $\gamma(\mu_{\rm r})$ scales like μ_r^{-1} in the limit $\mu_r \to \infty$. Actually this behavior depends on the choice that we have made for the non-dimensionalization. Involving the disks permeability for defining the new timescale $(\sigma\mu_r\mu_0 R^2)$ instead of $(\sigma\mu_0 R^2)$, we obtain the rescaled growth-rate $\tilde{\gamma} = \gamma\mu_r$ shown in the right-panel of Figure E.9. This representation shows that the growth-rate $\tilde{\gamma}$ reaches a constant value for very high permeabilities ($\tilde{\gamma}_\infty = -86.6631$). This observation immediately implies that the following power law $\gamma \sim \tilde{\gamma}_\infty/\mu_{\rm r}$ holds in the original units when $\mu_{\rm r} \to +\infty$.

In conclusion, the above simplified model explains why the growth-rate of the purely toroidal mode goes to zero when $\mu_r \to \infty$. The model shows also that although the dominant purely toroidal mode is localized to a very small volume, its decay time determines the overall decay of the axisymmetric azimuthal magnetic field. Note finally that this mode would not be observed in numerical simulations of VKS-dynamos that use the idealized boundary condition $\boldsymbol{H}\times\boldsymbol{n} = 0$ on the disk's surface (see e.g. [61]).

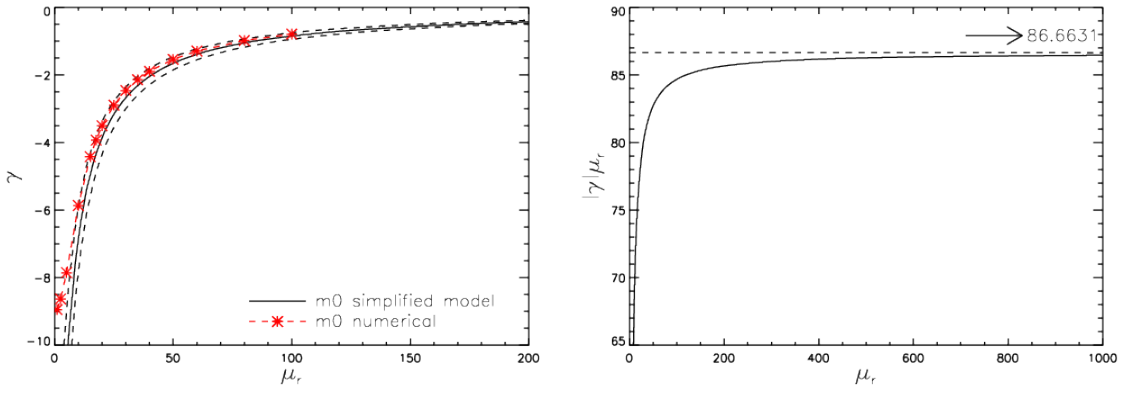

Figure E.9: (left) Growth-rate γ as a function of μ_r for the dominant axisymmetric toroidal eigenmode from the simplified model. $d = 0.1$, $k = k_1$ and $k = (1\pm0.1)k_1$. (right) Using the proper time scale $\sigma\mu_r\mu_0 R^2$ involving the permeability of the impeller disk, the growth-rate $\tilde{\gamma} = \gamma\mu_r$ reaches an asymptote at high μ_r.

E.5 Conclusions

The aim of this paper is to study the influence of thin high permeability disks on a VKS-like dynamo model. This work goes well beyond the study of [56] in the sense that we investigate thoroughly the axisymmetric mode and present novel details on the scaling behavior of the dynamo $m1$-mode. The high permeability disks facilitate the occurrence of non-axisymmetric dynamo action by enhancing the growth-rate of the equatorial dynamo $m1$-mode. Compared to the idealized limit ($\mu_r \to \infty$) the presence of a finite but high permeability material adds a small supplementary damping effect and therefore slightly increases the dynamo threshold. We propose that the observed $\mu_r^{-1/2}$-scaling for the dynamo threshold can be explained by a skin-effect so that that the disk's role on the $m1$-mode is quite passive. Although the reduction of the magnetic Reynolds number is substantial (from $\mathrm{Rm}^{\mathrm{c}} \approx 76$ at $\mu_{\mathrm{r}} = 1$ to $\mathrm{Rm}^{\mathrm{c}} \approx 54$ in the limit $\mu_{\mathrm{r}} \to \infty$) the spatial structure of the $m1$-mode is hardly changed.

The effects of the high permeability of the impeller disks on the axisymmetric mode turn out to be more fundamental. In the presence of a mean flow the axisymmetric $m0$-modes are split up in two separate families, one consisting of a purely toroidal mode and one consisting of a mixed mode composed of a poloidal and a toroidal component. The growth-rate of the mixed $m0$-mode slightly increases with Rm but is nearly independent of the disk permeability. The growth-rate of the purely toroidal $m0$-mode is not significantly influenced by the flow amplitude, but it is considerably enhanced $\propto \mu_{\mathrm{r}}^{-1}$ for large values of μ_r. This selective enhancement of the purely toroidal $m0$-mode can be explained qualitatively by paramagnetic pumping. A simplified analytical model that interprets the purely toroidal mode as a localized free decay solution confirms the scaling obtained in the numerical simulations. This slowly decaying purely toroidal mode promoted through the high permeability disks may play an important role in axisymmetric dynamo action. However, in our simple axisymmetric set-up no possibility for a closure of the dynamo cycle is provided since the poloidal component remains decoupled from the dominant toroidal field so that such dynamo remains impossible [39, 71].

Our study shows that the ideal boundary conditions $\boldsymbol{H} \times \boldsymbol{n} = 0$ is indeed a reasonable assumption for the $m1$-mode, but it is not appropriate for the analysis of the toroidal $m0$-mode. The purely toroidal $m0$-mode can be obtained only by explicitly considering the internal permeability distribution and the corresponding jump conditions at the fluid/disk interface. This mode cannot be obtained numerically by simulations of VKS-like dynamos that use either the idealized boundary condition $\boldsymbol{H} \times \boldsymbol{n} = 0$ at the fluid/disk interface or the thin-wall approximation from [127].

In conclusion, we have seen that the high (but finite) permeability in the impeller disks is very important to promote axisymmetric modes in our model and we suppose that it may also play a nontrivial role in the real VKS experiment. For example, in the presence of more complex (non-axisymmetric) flows containing small scale turbulence modeled by an α-effect [89, 55], or in the presence of non-axisymmetric permeability distributions that resemble the soft-iron blades attached to the disks [58], the purely toroidal $m0$-modes can be coupled with poloidal field components thus providing the required mechanism to close the dynamo loop.

Acknowledgement

We acknowledge intense and fruitful discussions with J.-F. Pinton and G. Verhille. AG is grateful to the assistence from T. Wondrak in the implementation of the cublas library. Fi-

nancial support from Deutsche Forschungsgemeinschaft (DFG) in frame of the Collaborative Research Center (SFB) 609 is gratefully acknowledged. The computations using SFEMaNS were carried out on IBM SP6 of IDRIS (project 0254).

Annexe F

Nonlinear dynamo in a short Taylor-Couette setup

C. Nore [a,b,c], J.-L. Guermond [d], R. Laguerre [a,e], J. Léorat [f], F. Luddens [a]

Abstract

It is numerically demonstrated by means of a magnetohydrodynamics code that a short Taylor-Couette setup with a body force can sustain dynamo action. The magnetic threshold is comparable to what is usually obtained in spherical geometries. The linear dynamo is characterized by a rotating equatorial dipole. The nonlinear regime is characterized by fluctuating kinetic and magnetic energies and a tilted dipole whose axial component exhibits aperiodic reversals during the time evolution. These numerical evidences of dynamo action in a short Taylor-Couette setup may be useful for developing an experimental device.

F.1 Introduction

Still a century after Larmor suggested that dynamo action can be a source of magnetic field in astrophysics, the exact mechanism by which a fluid dynamo can be put in action in astrophysical bodies remains an open challenge. In addition to the numerous analytical and numerical studies that have been done since Larmor's work, it is only recently that fluid dynamos have been produced experimentally [51, 139, 110]. These experimental dynamos have been helpful in particular to explore the nonlinear saturation regime. For instance, the dynamo produced in the Cadarache experiment [110] has an axial dipolar component and exhibits polarity reversals that are not unlike those observed in astronomical dynamos. The design of this experiment, however, has peculiar features that distinguishes it from natural dynamos. The most notable one is that the flow motion is induced by counter-rotating impellers. This driving mechanism induces an unrealistic differential rotation in the equatorial plane and produces a large turbulent dissipation. Even with a mechanical power injection close to 300 kW, the magnetic

[a] Laboratoire d'Informatique pour la Mécanique et les Sciences de l'Ingénieur, CNRS, BP 133, 91403 Orsay Cedex, France
[b] Université Paris Sud 11, 91405 Orsay Cedex, France
[c] Institut Universitaire de France, 103 Bd Saint-Michel, 75005 Paris, France
[d] Department of Mathematics, Texas A&M University 3368 TAMU, College Station, TX 77843-3368, USA
[e] Observatoire Royal de Belgique, Avenue Circulaire 3, B-1180, Bruxelles, Belgium
[f] Luth, Observatoire de Paris-Meudon, place Janssen, 92195 Meudon, France

Reynolds number of the flow of liquid sodium hardly reaches $R_m = 45$. Another peculiarity of this experiment is that dynamo action has not yet been obtained by using blades made of steel. The dynamo threshold has been reached at $R_m = 32$ by using blades made of soft iron instead. The objective of the present work is to investigate an alternative driving mechanism that shares the fundamental symmetry properties of natural dynamos, i.e., axisymmetry and equatorial symmetry (so-called SO(2)-Z2 symmetry). The Taylor-Couette geometry is a natural candidate for this purpose, since this configuration is already known to produce dynamos both in axially periodic geometries [155] and in finite vessels of large aspect ratio [66]. We examine in the present paper the dynamo capabilities of Taylor-Couette flows in vessels of small aspect ratio, and we compare the results obtained in this setting with those from more popular spherical dynamos [44].

The paper is organized as follows. The formulation of the problem and the physical setting of the Taylor-Couette configuration under consideration are described in §F.2. The formulation of the problem and the physical setting of the Taylor-Couette configuration under consideration are described in §F.2. Three types of flows are considered in the paper and are discussed in §F.3. These flows are the standard Taylor-Couette flow driven by viscous stresses, a manufactured Taylor-Couette flow, and an optimized flow driven by a body force that models rotating blades attached to the lids. Two kinematic dynamo configurations are investigated in §G.4. It is found that the poloidal to toroidal ratio of the velocity field generated by viscous driving only (standard Taylor-Couette) is not large enough to generate a dynamo at $R_m \leq 200$. Dynamo action is obtained by using the strengthen Taylor-Couette flow and the forced Taylor-Couette flow. In both cases the poloidal to toroidal ratio of the velocity field is close to one. A nonlinear dynamo obtained with the forced Taylor-Couette flow is described in §F.5. In the early linear phase of the dynamo, the magnetic field at large distance is dominated by an equatorial rotating dipole. In the established nonlinear regime, an axial axisymmetric component of the magnetic dipole is excited and exhibits aperiodic reversals. Concluding remarks are reported in §F.6.

F.2 Formulation of the problem

F.2.1 The physical setting

We consider an incompressible conducting fluid of constant density ρ and constant kinematic viscosity ν. This fluid is contained between two coaxial cylinders of height L_z. The radius of the inner cylinder is R_i and that of the outer one is R_o. The inner cylinder is composed of a solid conducting material. The inner cylindrical wall and the top and bottom lids corotate at angular velocity Ω_i. The outer cylindrical wall is motionless. The inner solid core may rotate or not, i.e., the inner core and the inner cylindrical wall may have different angular velocities. The electrical conductivity and magnetic permeability of the inner cylinder are significant elements of the parameter space. For instance, using sodium at 140^o Celsius, the ratio of the conductivity of the inner cylinder to that of the liquid metal is 1 if the inner cylinder is made of soft iron, it is about 0.16 if the inner cylinder is made of stainless steel, and it is about 4.5 if the inner cylinder is made of copper. Using soft iron implies jumps of the magnetic permeability, and using steel or copper implies jumps of the conductivity. Although our code can cope with discontinuous physical parameters [67], we postpone the optimization stage with respect to these parameters and focus on the simplest choice which consists of assuming that the conductivities of the fluid and of the inner solid are equal. The conductivity in the

solid and in the fluid is denoted σ_0. The magnetic permeability μ_0 is assumed to be constant in the entire space.

Let $\mathcal{U}$ be a reference velocity scale yet to be defined. We then consider the following reference scales for length, $\mathcal{L} = R_o - R_i$, magnetic field, $\mathcal{H} = \mathcal{U}\sqrt{\rho/\mu_0}$, and pressure, $\mathcal{P} = \rho\mathcal{U}^2$. The non-dimensional parameters of the system are the kinetic Reynolds number, R_e, the magnetic Reynolds number, R_m, the radius ratio η, and the aspect ratio Γ:

$$R_\mathrm{e} = \frac{\mathcal{U}\mathcal{L}}{\nu}, \quad R_\mathrm{m} = \mu_0\sigma_0\mathcal{U}\mathcal{L}, \quad \eta = \frac{R_i}{R_o}, \quad \Gamma = \frac{L_z}{\mathcal{L}}. \tag{F.2.1}$$

To limit the number of geometrical parameters, we restrict ourselves in this paper to $\eta = 0.5$ and $\Gamma = 2$. Abusing the notation, this immediately implies that $R_i = 1$ and $R_o = 2$ in non-dimensional units. We did not explore other aspect ratios (see for example [144, 1, 104, 70] for short aspect ratios and different angular velocities). The conducting domain Ω_c is partitioned into its fluid part enclosed between the two walls, Ω_{cf}, and its solid part enclosed in the inner cylinder, Ω_{cs}. Using non-dimensional cylindrical coordinates (r, θ, z), we have $\Omega_{cf} = [1,2]\times[0,2\pi)\times[-1,1]$ and $\Omega_{cs} = [0,1]\times[0,2\pi)\times[-1,1]$. The conducting material is embedded in a non-conducting region denoted Ω_v, which we refer to as the vacuum region.

The non-dimensional set of equations that we consider is written as follows in the conducting material:

$$\partial_t\mathbf{u} + (\mathbf{u}\cdot\nabla)\mathbf{u} + \nabla p = \frac{1}{R_\mathrm{e}}\boldsymbol{\Delta}\mathbf{u} + (\nabla\times\mathbf{H}^c)\times\mathbf{H}^c + \mathbf{f}_I \tag{F.2.2}$$

$$\nabla\cdot\mathbf{u} = 0 \tag{F.2.3}$$

$$\partial_t\mathbf{H}^c - \nabla\times(\mathbf{u}\times\mathbf{H}^c) = \frac{1}{R_\mathrm{m}}\boldsymbol{\Delta}\mathbf{H}^c \tag{F.2.4}$$

$$\nabla\cdot\mathbf{H}^c = 0, \tag{F.2.5}$$

where $\mathbf{u}$, p, and $\mathbf{H}^c$ are the velocity field, pressure, and magnetic field, respectively. The magnetic field in Ω_v is assumed to derive from a harmonic scalar potential: $\mathbf{H}^v = \nabla\phi$, $\Delta\phi = 0$. The transmission conditions across the interface separating the conducting and nonconducting material are such that the tangent components of the magnetic and electric fields are continuous (see [65]).

We consider three different settings: (i) The incompressible Navier-Stokes setting ($\mathbf{H}^c = 0$); (ii) The Maxwell or kinematic dynamo setting; (iii) The nonlinear magnetohydrodynamics setting (MHD). In the Navier-Stokes setting, $\mathbf{H}^c$ is set to zero in the Lorentz force and the induction equation is not solved. The source term $\mathbf{f}_I$ is an ad hoc body force that models blades fixed at the endwalls, see §F.3.3. When $\mathbf{f}_I = 0$, the viscous stress induced by the rotating walls is the only source of momentum, see §F.3.1. In the Maxwell setting, only the induction equation is solved assuming that some ad hoc velocity field $\mathbf{u}$ is given. In the MHD setting, the full set of equations is solved.

Since the definition of the reference velocity in similar dynamo configurations may be different (velocity at a given point, maximal speed in the flow, etc.), we introduce the root mean square (rms) velocity to facilitate comparisons:

$$\mathcal{U}^{*2} = \frac{1}{\mathrm{vol}(\Omega_{cf})}\int_{\Omega_{cf}} \|\mathbf{u}(\mathbf{x},t)\|^2 \mathrm{d}\mathbf{x}, \tag{F.2.6}$$

where the dimensionless fluid volume is $\mathrm{vol}(\Omega_{cf}) = 6\pi$ in the present case.

F.2.2 Numerical details

The code (SFEMaNS) that we have developed solves the coupled Navier-Stokes and Maxwell equations in the MHD limit in heterogeneous axisymmetric domains composed of conducting and nonconducting regions by using a mixed Fourier/Lagrange finite element technique. Continuous Lagrange Finite elements are used in the meridian plane and Fourier modes are used in the azimuthal direction. Parallelization is done with respect to the Fourier modes. Continuity conditions across interfaces are enforced using an interior penalty technique [65, 66]. SFEMaNS can account for discontinuous electrical conductivity and magnetic permeability distributions [56, 67]. An original technique for the control of the divergence of the magnetic induction has been developed to ensure the convergence of the method in the presence of corner singularities [67, 17]. The magnetic field in the nonconducting regions is assumed to derive from a scalar magnetic potential, i.e., the configurations that we model are such that there is some mechanism that ensures that the circulation of the magnetic field along any path in the insulating medium is zero (this happens for instance when the vacuum is simply connected). Finite elements naturally take care of corner singularities induced by the boundary conditions of the hydrodynamic problem. The velocity field in Ω_{cf} and the magnetic field in Ω_c are approximated using continuous $\mathbb{P}_2$ polynomials, and the pressure field in Ω_{cf} is approximated using continuous $\mathbb{P}_1$ polynomials. In the vacuum Ω_v, the magnetic potential ϕ is approximated using continuous $\mathbb{P}_2$ polynomials. Typical characteristics of the meshes in the meridian section of all the cases studied in this paper are summarized in Table F.1.

Run	Δx	Δt	$np(P)$	$np(V)$	$np(H)$	$np(\phi)$	M
§F.3.1	1/100	0.025	5911	23341	-	-	8
§F.3.3, §F.3.2	1/100	0.025	5911	23341	-	-	12
§F.4.1, §F.4.2	1/100	0.005	5911	23341	29821	14041	4
§F.5	1/100	0.005	5911	23341	29821	14041	32

Table F.1: Characteristics of the runs: Δx is the quasi-uniform meshsize in Ω_c; Δt is the timestep; $np(P)$ is the number of $\mathbb{P}_1$ nodes for the pressure field in Ω_{cf}; $np(V)$ is the number of $\mathbb{P}_2$ nodes for the velocity field in Ω_{cf}; $np(H)$ is the number of $\mathbb{P}_2$ nodes for the magnetic field in Ω_c; $np(\phi)$ is the number of $\mathbb{P}_2$ nodes for the magnetic potential in Ω_v. The numbers $np(P)$, $np(V)$, $np(H)$ refer only to the meridian section. The total number of grid points for each unknown Y is obtained by multiplying $np(Y)$ by 2 times the number of Fourier modes, M, minus one.

The performance of SFEMaNS has been validated on various kinematic and nonlinear dynamo configurations. In particular, a study of two Taylor-Couette setups using SFEMaNS is reported in [66]. In the first case $\Gamma = 4$, $\eta = 0.5$, and z-periodicity is assumed; in the second case $\Gamma = 2\pi$, $\eta = 0.5$ and the vessel is finite, i.e., no z-periodicity is assumed and the vessel is closed at both ends. In both cases the inner wall rotates, but the outer wall and the two endwalls (when present) are motionless. The self-consistent saturated dynamo found in [155] in the z-periodic case has been reproduced in [66], and a new nonlinear dynamo has been found in the finite vessel at $R_e = 120$, $R_m = 240$. The behaviors of the z-periodic and finite-vessel dynamos, as observed in [66], significantly differ. After some transient, the kinetic and magnetic energies of the z-periodic dynamo converge to a stationary value. The final nonlinear MHD state is a steady rotating wave resulting from the balance between the driving effect of the viscous shear and the braking effect of the Lorentz force. The nonlinear dynamo action

found in the finite vessel shows a different behavior in which the spatial symmetry about the equatorial plane (or mid-plane) of the velocity and magnetic fields plays a key role. The dynamo is cyclic in time and the fields rotate rigidly with modulated amplitude. In these two cases (periodic and finite extension), the wavelength of the magnetic eigenvector is about twice that of the flow; as a result, the velocity field in the median plane of a single magnetic structure is directed inwards. This feature is shared by the spherical kinematic dynamos studied in [44]. It is reported in [44] that the lowest critical magnetic Reynolds number is obtained when the velocity field forms two poloidal cells that flow inwards in the equatorial plane. Note in passing that the two numerical experiments reported in [66] clearly confirm that assuming periodicity or enforcing finite boundary conditions give rise to dynamos with fundamentally different behaviors, i.e., assuming periodicity or ad hoc boundary conditions for the sake of numerical convenience may have nontrivial consequences. The series of observations above have led us to investigate more thoroughly the Taylor-Couette configuration with aspect ratio $\Gamma = 2$.

F.3 Hydrodynamic forcing

Since a number of dynamo studies have shown that the ratio of poloidal to toroidal speed should be close to unity to obtain the lowest critical magnetic Reynolds number, it is important to control this ratio. We describe in this section the mechanisms that we use to optimize the velocity field for dynamo action.

F.3.1 Taylor-Couette flow (viscous driving only)

When the aspect ratio is about 2 and the kinematic Reynolds number is moderate, two counter-rotating poloidal cells form with a toroidal angular velocity oriented in the same direction as that of the inner cylinder. In order to enforce the equatorial jet to flow inwards, we let the lids of the vessel rotate with the angular velocity of the inner cylinder and we keep the outer cylinder motionless. Note that it is important to have the lids and the inner cylindrical wall of the vessel to corotate; this makes the equatorial jet flow inwards and makes the overall velocity field similar to the spherical flows that are known to yield dynamo action [44] at $Rm_c \approx 100$. With an outward equatorial jet flow (in case of static lids), the dynamo threshold is expected to be enhanced following Livermore and Jackson's results [97]. These authors gave an intuitive argument: the magnetic field is stretched up and down by the poloidal circulation associated to an inwards jet and aligns with the direction of the maximal strain rate, whereas it is compressed with the reversed circulation and the alignment is less effective. They computed the magnetic energy instability thresholds in both cases for a Modified Dudley and James flow and found a factor of 2 between the two thresholds.

We define the velocity reference scale to be

$$\mathcal{U} = \Omega_i R_i, \tag{F.3.1}$$

when the only source of momentum is the viscous stress at the boundary.

At $R_e = 120$ in the Navier-Stokes regime, the flow is steady, and forms the expected two toroidal cells invariant under the SO(2)-Z2 symmetry, i.e., axisymmetric and symmetric with respect to the equatorial plane, see Figure F.1. This flow, henceforth generically referred to

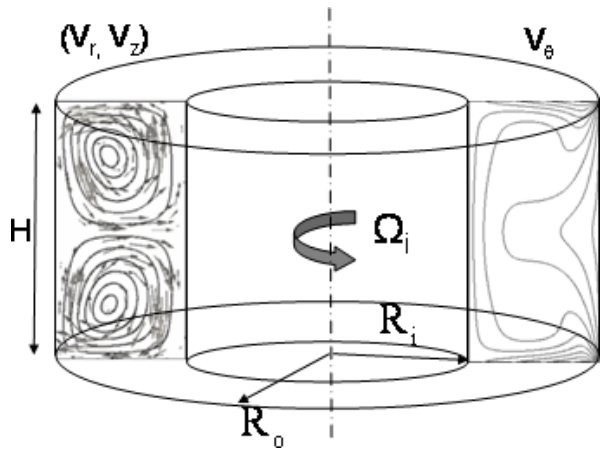

Figure F.1: Taylor-Couette flow $\mathcal{V}_0$, $\Gamma = 2$, $R_\mathrm{e} = 120$. The angular velocity of the lids and the inner cylinder is $\Omega_i = 1$; the outer cylinder is motionless. A radial jet flows inward at the equator. Represented are the poloidal flow (vectors and streamlines) $-0.2 \le V_r \le 0.3$, and $-0.25 \le V_z \le 0.25$, and the toroidal (or azimuthal) flow $0.25 \le V_\theta \le 2$ (every 0.25).

as $\mathcal{V}_0$, is characterized by its rms velocity, V_0^*, defined as follows:

$$V_0^{*2} = V_{0p}^{*2} + V_{0t}^{*2} = \frac{1}{\mathrm{vol}(\Omega_{cf})} \int_{\Omega_{cf}} (V_r^2 + V_z^2) \mathrm{d}\mathbf{x} + \frac{1}{\mathrm{vol}(\Omega_{cf})} \int_{\Omega_{cf}} V_\theta^2 \mathrm{d}\mathbf{x},$$

where V_{0p}^* and V_{0t}^* are the rms poloidal and toroidal velocities of the reference hydrodynamic flow, respectively, and $\mathrm{vol}(\Omega_{cf}) = 6\pi$ is the volume of the vessel. Our computations give $V_0^* = 0.272$; this value is significantly lower than the maximum speed at the rim of the endwalls which is equal to 2. The poloidal to toroidal ratio is $\Lambda_0 = V_{0p}^*/V_{0t}^* = 0.235$.

We have verified that the flow $\mathcal{V}_0$ is stable with respect to non-axisymmetric perturbations supported on the Fourier modes $m = 1, \cdots, 7$ at $R_\mathrm{e} = 120$. The velocity field $\mathbf{V}_0$ together with a sketch of the setup is shown in Figure F.1. This reference flow is used in §F.4.1 to perform kinematic dynamo simulations .

F.3.2 A modified Taylor-Couette flow

In order to perform kinematic dynamo simulations with a velocity field that has a poloidal to toroidal ratio that can be controlled easily, we construct an ad hoc field based on $\mathcal{V}_0$. We use the poloidal and toroidal components of the vector field $\mathbf{V}_0$ to define a kinematic field, $\mathbf{V}_\epsilon$, with a pre-assigned poloidal to toroidal ratio as follows:

$$\mathbf{V}_\epsilon = \frac{\epsilon}{\alpha(\epsilon)} \mathbf{V}_{0p} + \frac{1}{\alpha(\epsilon)} \mathbf{V}_{0t}. \tag{F.3.2}$$

The normalization is done so that the rms of $\mathbf{V}_\epsilon$ is the same as that of $\mathbf{V}_0$. This gives

$$\alpha^2(\epsilon) = \frac{1 + \epsilon^2 \Lambda_0^2}{1 + \Lambda_0^2}, \qquad \Lambda(\epsilon) = \epsilon \Lambda_0. \tag{F.3.3}$$

Since the toroidal component of the velocity at the inner cylinder is equal to $1/\alpha(\epsilon)$, the angular velocity of the inner wall is $\Omega_i = 1/\alpha(\epsilon)$, and this also means that the reference velocity scale is

$$\mathcal{U} = \alpha(\epsilon)\Omega_i R_i. \tag{F.3.4}$$

Although the vector field $\mathbf{V}_\epsilon$ is not a solution of the Navier-Stokes equations, it is nevertheless solenoidal. This flow is henceforth generically referred to as $\mathcal{V}_\epsilon$. Computations have been done (see §F.4.1) for the values of ϵ reported in Table F.2. The quantity denoted $V_{\max}$ in Table F.2 is the maximum of the velocity modulus; $V_{\max}$ depends on ϵ.

ϵ	1	3	4	5	6	6.5	8	10	12	16
$\alpha(\epsilon)$	1	1.19	1.34	1.50	1.69	1.78	2.08	2.49	2.92	3.80
$\Lambda(\epsilon)$	0.235	0.71	0.94	1.18	1.41	1.53	1.89	2.36	2.83	3.77
$V_{\max}$	2.00	1.67	1.49	1.32	1.20	1.21	1.23	1.25	1.26	1.27

Table F.2: Modified Taylor-Couette flow: normalization factor $\alpha(\epsilon)$, poloidal to toroidal ratio $\Lambda(\epsilon)$ and maximum of the velocity modulus $V_{\max}$.

F.3.3 Forced Taylor-Couette flow (viscous driving plus body force)

A number of dynamo studies have shown that the ratio of poloidal to toroidal speed should be close to unity to obtain a low critical magnetic Reynolds number. Viscous driving by the rotating walls yields a value for this ratio that is not close to unity ($\Lambda_0 = 0.235$ at $R_e = 120$, see section above). At low Reynolds numbers, the flow is steady and axisymmetric. It is relatively easy to vary the relative amplitude of the toroidal component in experimental setups by using blades fixed to the corotating endwalls to act as centrifugal pumps. This configuration, however, is difficult to implement in a computer code. In order to better control the poloidal to toroidal ratio in our simulations, we have chosen to model the toroidal driving by a body force. The action of blades on the top and bottom lids is modeled by an ad hoc axisymmetric divergence-less force given in dimensional form as follows:

$$\mathbf{f}_I(r,z) = \begin{cases} \rho\dfrac{A}{r}\mathcal{U}^2\mathbf{e}_r & \text{if } 0.8 \le |z| \le 1 \text{ and } 1.2 \le r \le 1.8 \\ 0 & \text{otherwise,} \end{cases} \tag{F.3.5}$$

where the non-dimensional parameter A has been tuned to optimize the poloidal to toroidal ratio. Note that (F.3.5) defines the reference velocity $\mathcal{U}$. The resulting velocity field is denoted $\mathbf{V}_I$ and the flow is generically called $\mathcal{V}_I$.

We have found that using $A = 2.5$ at $R_e = 120$ gives $\Lambda_I = V^*_{Ip}/V^*_{It} = 1.04$ and the rms velocity is $V^*_I = 0.219$. We have observed that the azimuthal velocity in the vicinity of the inner radius is close to 0.55; hence, to reduce the viscous boundary layer at the inner wall and endwalls, we have set the dimensionless angular velocity to $\Omega_i = 0.55$. The steady axisymmetric flow $\mathcal{V}_\mathrm{I}$ is shown in Figure F.2, (see Figure F.1 for a comparison with the pure Taylor-Couette flow). We have verified, by performing nonlinear Navier-Stokes simulations, that the flow $\mathcal{V}_I$, at $Re = 120$, is stable with respect to three-dimensional perturbations supported on Fourier modes up to $m = 11$. The first hydrodynamic non-axisymmetric instability occurs on the Fourier mode $m = 3$ at $R_e = 168$. The steady and axisymmetric forced Taylor-Couette flow $\mathcal{V}_\mathrm{I}$ is used in §F.4.2 to perform kinematic dynamo simulations.

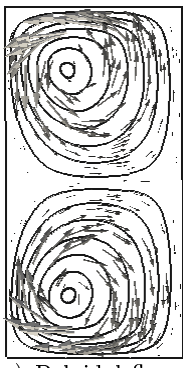

(a) Poloidal flow, $\theta = \pi$

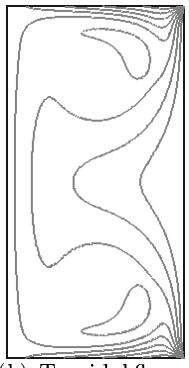

(b) Toroidal flow, $\theta = 0$

Figure F.2: Forced Taylor-Couette flow $\mathcal{V}_{\rm I}$, $\Gamma = 2$, $R_{\rm e} = 120$, and $A = 2.5$. The lids and the inner cylinder rotate with angular speed $\Omega_i = 0.55$; the outer cylinder is motionless. A radial jet flows inwards at the equator. Represented are the poloidal flow (vectors and streamlines), $-0.7 \leq V_r \leq 1.4$, $-1.1 \leq V_z \leq 1.1$, and the toroidal (or azimuthal) flow, $0 \leq V_\theta \leq 1.6$ (10 levels)

F.3.4 Summary

To compare the flows $\mathcal{V}_0$, $\mathcal{V}_I$, and $\mathcal{V}_\epsilon$, we show in Table F.3 the following characteristics of these three flows: rms velocity, V^*; maximum of the velocity modulus in the fluid domain, $V_{\rm max}$; poloidal to toroidal ratio, Λ.

Run	V^*	$V_{\rm max}$	Λ
Viscous flow $\mathcal{V}_0$, §F.3.1	0.272	2.00	0.235
Modified flow $\mathcal{V}_\epsilon$, §F.3.2,§F.4.1	0.272	(1.20,2.00)	$0.235\times\epsilon$
Forced flow $\mathcal{V}_{\rm I}$, §F.3.3,§F.4.2,§F.5	0.219	1.09	1.04

Table F.3: Characteristics of the flows $\mathcal{V}_0$, $\mathcal{V}_\epsilon$ and $\mathcal{V}_{\rm I}$: V^* is the r.m.s. speed; $V_{\rm max}$ is the maximum of the velocity modulus in the fluid domain; Λ is the poloidal to toroidal ratio.

F.4 Kinematic Dynamos

We evaluate in this section the properties of the kinematic dynamos generated by the flows $\mathcal{V}_\epsilon$ (viscous driving) and $\mathcal{V}_I$ (viscous driving plus body force).

F.4.1 Parametric study of the poloidal to toroidal ratio using $\mathcal{V}_\epsilon$

We investigate the dynamo properties of the manufactured flow $\mathcal{V}_\epsilon$ in the kinematic regime, see §F.3.2. The reference velocity scale is defined in (F.3.4). To ensure that the velocity is continuous across the solid/fluid interface, the angular velocity of the inner core is set to be $\Omega_i = 1/\alpha(\epsilon)$ with $\alpha(\epsilon)$ given by Table F.2. The conductivities of the solid inner core and the fluid are identical.

We perform two studies at $R_{\rm m} = 100$ and $R_{\rm m} = 200$ to determine the optimal weight ϵ that gives the largest growthrate of the dynamo action in the kinematic regime. The computations are done with SFEMaNS in Maxwell mode. The magnetic field is initialized to some small random values and the growth rate (i.e., the real part of the leading eigenvalue) is computed by running short time simulations for various ratios $\epsilon \in [3, 16]$ shown in Table F.2. As the vector field $\mathbf{V}_\epsilon$ is axisymmetric, the term $\nabla\times(\mathbf{V}_\epsilon\times\mathbf{H}^c)$ cannot transfer energy between the Fourier modes of $\mathbf{H}^c$, i.e., the Fourier modes are uncoupled. The first bifurcation is of Hopf type and the most unstable eigenvector is the Fourier mode $m = 1$. The growthrate of the magnetic energy is reported in Figure F.3. There is no dynamo action at $R_{\rm m} = 100$. Dynamo action occurs at $R_{\rm m} = 200$ in the range $4.2 < \epsilon < 15.4$, which corresponds to $1.0 < \Lambda(\epsilon) < 3.8$. Note that the purely viscous driving, which corresponds to $\epsilon = 1$ and $\Lambda_0 = 0.235$, cannot sustain a dynamo at $R_{\rm m} = 100$ and $R_{\rm m} = 200$.

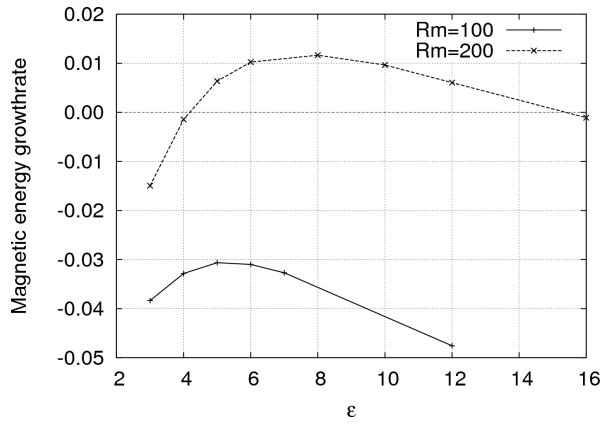

Figure F.3: Kinematic dynamo. Growthrate of Fourier mode $m = 1$ for the modified Taylor-Couette flow, $\mathcal{V}_\epsilon$, as a function of ϵ for $R_{\rm m} = 100$ and $R_{\rm m} = 200$; $\Gamma = 2$ and $R_{\rm e} = 120$.

Figure F.4 the magnetic eigenvector for the Fourier mode $m = 1$ at $R_{\rm e} = 120$, $R_{\rm m} = 200$ and $\epsilon_{opt} = 8$. This eigenvector is a rigid wave that rotates in the same direction as the inner cylinder and top/bottom lids, and its period of rotation is $T \simeq 870$, i.e., more than 66 rotation periods of the inner cylinder. Since $\Omega_i = 1/\alpha(\epsilon)$ and $\epsilon = 8$, the angular velocity of the inner cylinder is $\Omega_i = 0.481$; this in turn implies that the rotation period of the inner cylinder is $T_i = \frac{2\pi}{\Omega_i} = 13.1$. Upon introducing the equatorial symmetry operator $\mathcal{S}_{\rm Z2}\mathbf{H} = (H_r,\ H_\theta,\ -H_z)(r, \theta, -z)$. the magnetic field has the following symmetry property:

$$\mathbf{H}^c = \mathcal{S}_{\rm Z2}\mathbf{H}^c. \tag{F.4.1}$$

i.e., the magnetic field has the same symmetry as the velocity field.

We now evaluate the critical magnetic Reynolds number and its minimal value with respect to ϵ. We assume that the growthrate depends smoothly on $R_{\rm m}$. Upon inspecting Figure F.3 we see that the growth rate is maximum for $\epsilon_{opt} \approx 5$ at $R_{\rm m} = 100$ and for $\epsilon_{opt} \approx 8$ ate $R_{\rm m} = 200$. Then, by drawing the line connecting the two maximum points in Figure F.3, we observe that this line crosses the horizontal line of zero growth rate in the interval $\epsilon \in [6.5, 7]$. We have chosen to explore the value $\epsilon = 6.5$, which gives the poloidal to toroidal ratio $\Lambda = 1.53$. The growth rate for various magnetic Reynolds numbers in the range $[125, 200]$ has been

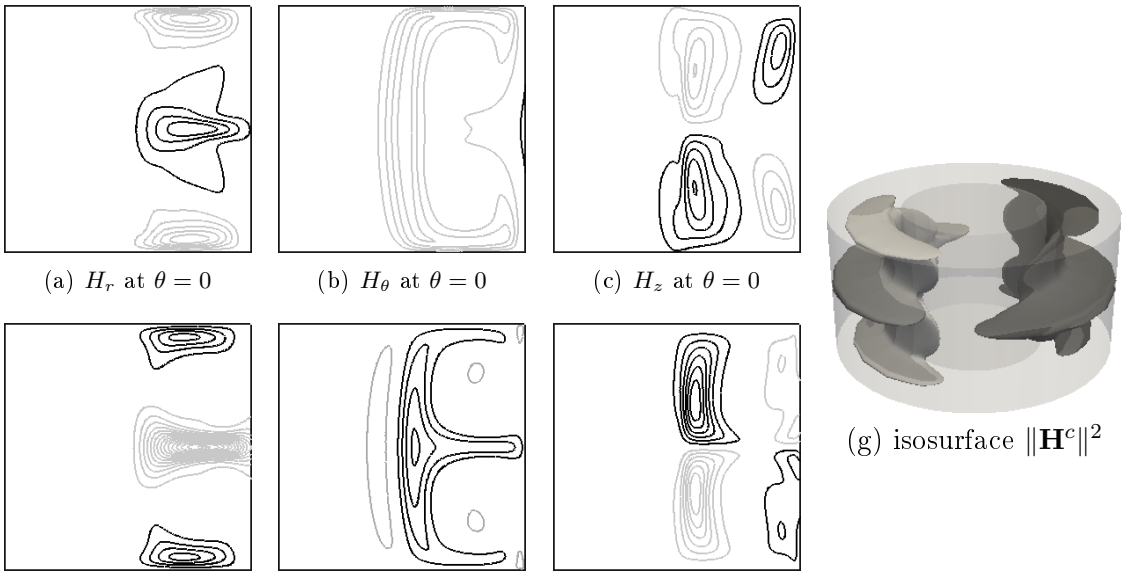

(a) H_r at $\theta = 0$ (b) H_θ at $\theta = 0$ (c) H_z at $\theta = 0$

(g) isosurface $\|\mathbf{H}^c\|^2$

(d) H_r at $\theta = \frac{\pi}{2}$ (e) H_θ at $\theta = \frac{\pi}{2}$ (f) H_z at $\theta = \frac{\pi}{2}$

Figure F.4: Kinematic dynamo with flow $\mathcal{V}(\epsilon = 8)$ at $R_\mathrm{e} = 120$, $R_\mathrm{m} = 200$. Magnetic eigenvector for Fourier mode $m = 1$. Represented in (a) to (f) are the radial, azimuthal, and vertical components, normalized by the square root of the magnetic energy, in two complementary planes, with $0 \leq r \leq 2$, $-1 \leq z \leq 1$ (the $z-$axis is on the left): for $\theta = 0$, $-0.85 \leq H_r \leq 0.85$ (every 0.17), $-0.1 \leq H_\theta \leq 0.68$ (every 0.17) and $-0.85 \leq H - z \leq 0.85$ (every 0.17); for $\theta = \frac{\pi}{2}$, $-1 \leq H_r \leq 3.75$ (every 0.25), $-1 \leq H_\theta \leq 0.15$ (every 0.25) and $-1.5 \leq H_z \leq 1.5$ (every 0.25). Represented in (g) is the isosurface $\|\mathbf{H}^c\|^2$ (7% of maximum value) colored by the azimuthal component. Note the $m = 1$ structure.

computed. The results are shown in Figure F.5. We have found that the critical magnetic Reynolds number for the Fourier mode $m = 1$ is $R_\mathrm{m} = 155$ with $\epsilon = 6.5$ and $\Lambda = 1.53$.

F.4.2 Kinematic dynamo in the forced Taylor-Couette setup

We use the steady axisymmetric forced flow, $\mathcal{V}_\mathrm{I}$, at $R_\mathrm{e} = 120$ to perform kinematic dynamo computations. The reference velocity scale is defined in (F.3.5) with $A = 2.5$. To determine whether the rotation of the inner solid core has any impact on the dynamo threshold, we have compared growth rates when the solid inner core is motionless and when the inner wall and solid inner core corotate with angular speed Ω_i. Whether the inner core rotates or not, the magnetic eigenvector $m = 1$ is always the most unstable. We show in Figure F.6 the computed growth rates in the two cases in the range $R_\mathrm{m} \in [175, 200]$. The motion of the inner core does not seem to have a significant influence; in both cases the dynamo threshold is $R_\mathrm{m} = 180$ for the Fourier mode $m = 1$.

The structure of the magnetic eigenvector corresponding to the Fourier mode $m = 1$ with a rotating inner core is shown in Figure F.7 (at $R_\mathrm{e} = 120$, $R_\mathrm{m} = 200$). It is a rigid wave that rotates in the same direction as the inner cylinder and top/bottom lids with period $T \simeq 120$, corresponding to 10.5 rotation periods of the inner cylinder rotating with angular velocity

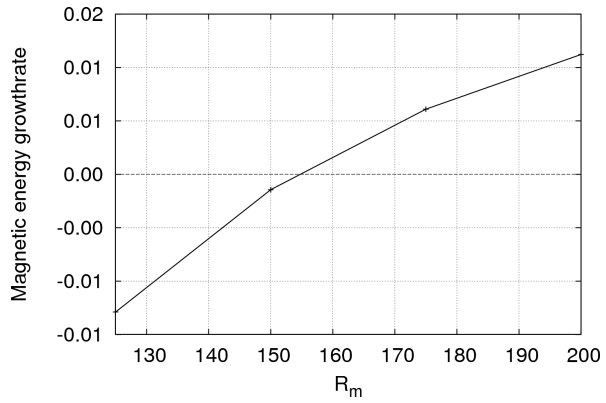

Figure F.5: Kinematic dynamo of flow $\mathcal{V}(\epsilon = 6.5)$, $\Gamma = 2$, $R_{\rm e} = 120$. Growthrate of the Fourier mode $m = 1$ as a function of $R_{\rm m}$.

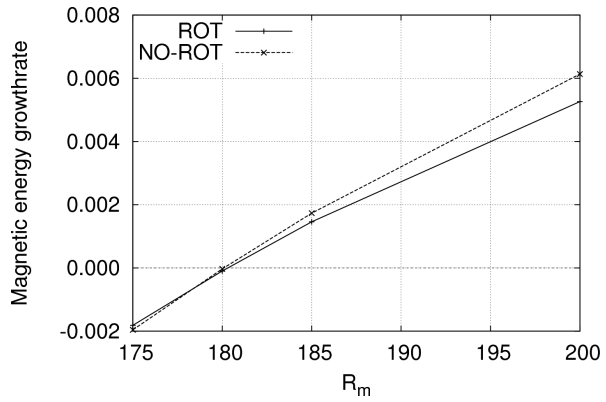

Figure F.6: Kinematic dynamo with $\mathcal{V}_I$ flow, $\Gamma = 2$ and $R_{\rm e} = 120$. Growthrate of the Fourier mode $m = 1$ as a function of $R_{\rm m}$. ROT: rotating inner core; NO-ROT: non-rotating inner core (but inner wall rotates).

$\Omega_i = 0.55$.

F.5 Nonlinear dynamo action

We report in this section on nonlinear dynamo computations done with the forced Taylor-Couette setup at $R_{\rm e} = 120$ and $R_{\rm m} = 200$.

F.5.1 Description of the setting

We consider the forced Taylor-Couette setup described in §F.4.2. The reference velocity scale is defined in (F.3.5) with $A = 2.5$. We perform nonlinear dynamo computations with the parameters $R_{\rm e} = 120$, $R_{\rm m} = 200$. The inner core is kept motionless. We work with 32 azimuthal modes ($m = 0, \ldots, 31$), and the meridional finite element mesh is the same as in the kinematic runs. The total number of degrees of freedom to be updated at each time step is 11,353,104. The initial velocity field is the axisymmetric flow $\mathcal{V}_{\rm I}$ that we computed in the Navier-Stokes regime at $R_{\rm e} = 120$. The initial magnetic seed is the growing Fourier mode

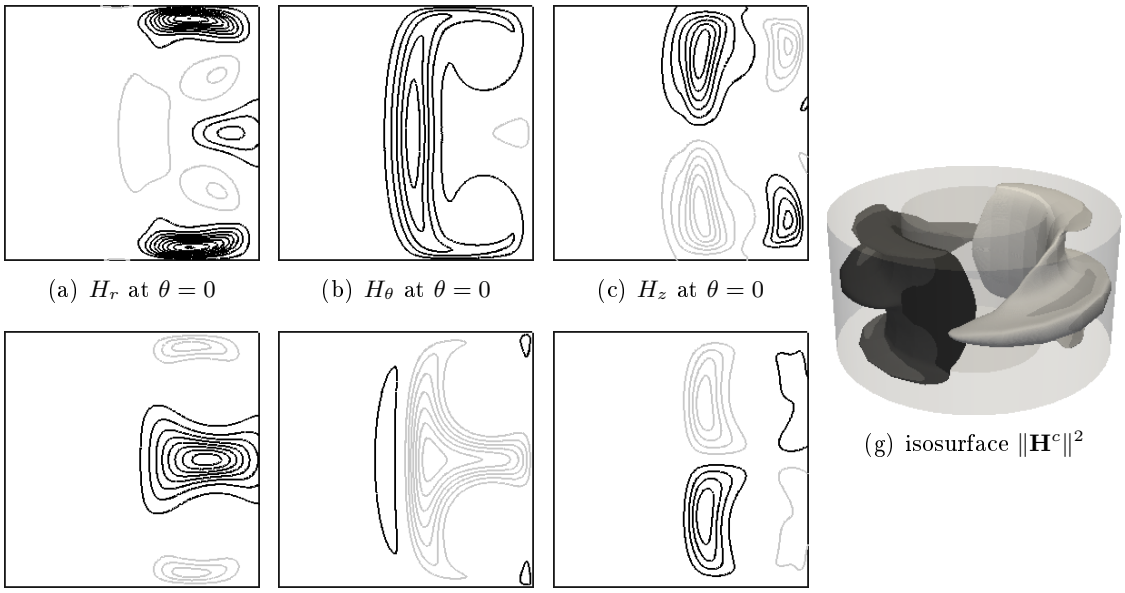

(a) H_r at $\theta = 0$ (b) H_θ at $\theta = 0$ (c) H_z at $\theta = 0$

(g) isosurface $\|\mathbf{H}^c\|^2$

(d) H_r at $\theta = \frac{\pi}{2}$ (e) H_θ at $\theta = \frac{\pi}{2}$ (f) H_z at $\theta = \frac{\pi}{2}$

Figure F.7: Kinematic dynamo with flow $\mathcal{V}_I$ at $R_\mathrm{e} = 120$, $R_\mathrm{m} = 200$. Magnetic eigenvector for Fourier mode $m = 1$. Represented in (a) to (f) are the radial, azimuthal, and vertical components, normalized by the square root of the magnetic energy, in two complementary planes: for $\theta = 0$, $-0.9 \leq H_r \leq 0.2$ (every 0.1), $-1.4 \leq H_\theta \leq 0.35$ (every 0.25) and $-0.6 \leq H_z \leq 0.6$ (every 0.1); for $\theta = \pi/2$, $-2.2 \leq H_r \leq 0.9$ (every 0.25), $-0.25 \leq H_\theta \leq 1.75$ (every 0.25) and $-1.25 \leq H_z \leq 1.25$ (every 0.1). Represented in (g) is the isosurface $\|\mathbf{H}^c\|^2$ (14% of maximum value) colored by the azimuthal component. Note the $m = 1$ structure.

$m = 1$ obtained in the kinematic computations described in §F.4.2 at $R_\mathrm{m} = 200 > R_\mathrm{mc} = 180$. The initial magnetic field has been rescaled so that nonlinear saturation occurs within reasonable CPU time.

When dynamo action occurs, the magnetic energy grows exponentially until the Lorentz force is capable of modifying the base flow. This transient phase lasts about 5 rotation periods. When the Lorentz force is strong enough, a new regime settles where the magnetic energy saturates. Nonlinear saturation is a slow process that lasts at least 200 rotation periods (see Figure 11 in [66]). Although SFEMaNS is parallel with respect to the Fourier modes, the volume of computation required by this type of simulation is such that we have not been able to explore other kinematic and magnetic Reynolds numbers within the resources allocated to this project. The nonlinear run presented in this section used about 15600 cumulated CPU hours with 32 processors on an IBM Power 6 cluster.

F.5.2 Time evolution of the energy

The time evolutions of the kinetic and magnetic energies are reported in Figure F.8(a-b), where the kinetic and magnetic energies are defined as follows: $\frac{1}{2}\int_{\Omega_{cf}} \|\mathbf{u}\|^2 \mathrm{d}\mathbf{x}$, $\frac{1}{2}\int_{\Omega_c} \|\mathbf{H}^c\|^2 \mathrm{d}\mathbf{x}$, respectively. From $t = 0$ to $t = 500$ (first transition), the kinetic energy decreases and the magnetic energy grows exponentially with a growthrate similar to that of the kinematic

dynamo. Then both the magnetic and the kinetic energies seem to saturate in a first nonlinear regime, $500 \lesssim t \lesssim 1100$. During the first transition, the fluid flow loses the axial symmetry, $m = 0$, and the magnetic field loses the symmetry associated with the Fourier mode $m = 1$. The flow being forced by the Lorentz force $(\nabla\times\mathbf{H}^c)\times\mathbf{H}^c$, the velocity thereby acquires a contribution on the Fourier mode $m = 2$. The magnetic field being deformed by the action of the induction term $\mathbf{u}\times\mathbf{H}^c$ acquires a contribution on the Fourier mode $m = 3$. The cascade of nonlinear couplings generate even velocity modes, $m = 0, 2, \ldots$, and odd magnetic modes, $m = 1, 3, \ldots$ During this transitional phase that consists of populating the Fourier modes, the axisymmetry of the velocity field is broken but the equatorial (mid-plane) symmetry is preserved for both the velocity and the magnetic field.

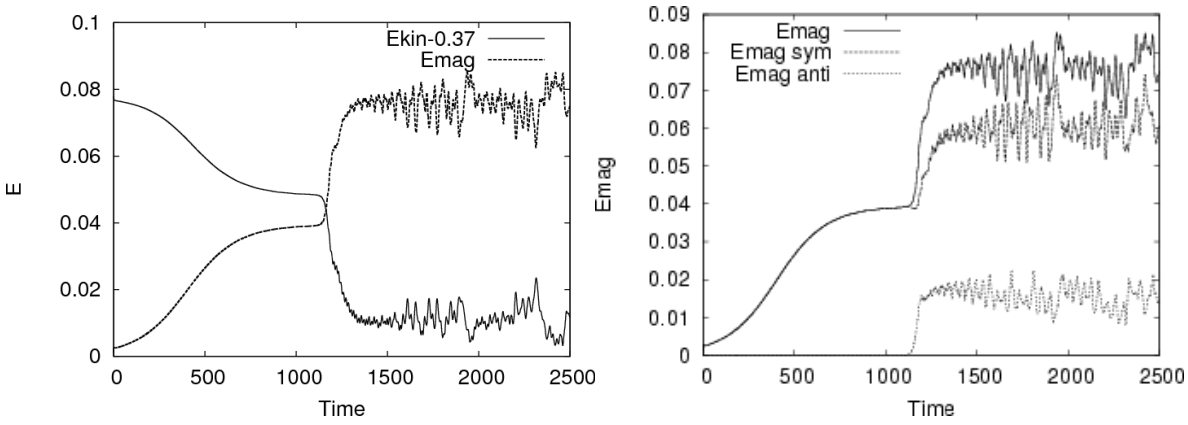

(a) Kinetic (-0.37) and magnetic energies

(b) Splitting of magnetic energy

Figure F.8: Nonlinear dynamo in the forced Taylor-Couette setup. (a) Time evolution of kinetic (-0.37) and magnetic energies in the conducting region $0 \le r \le R_o$ and $-\Gamma/2 \le z \le \Gamma/2$. Panel (b) shows the symmetric and anti-symmetric components of the magnetic energy.

A second nonlinear transition starts at $t = 1100$ and lasts until $t = 1175$. In this time interval the magnetic energy increases and the kinetic energy decreases. This change of behavior is due to the breaking of the equatorial symmetry. This phenomenon is well illustrated by computing the energy of the symmetric part, $\frac{1}{2}(\mathbf{H}^c + \mathcal{S}_{Z2}\mathbf{H}^c)$, and anti-symmetric part, $\frac{1}{2}(\mathbf{H}^c - \mathcal{S}_{Z2}\mathbf{H}^c)$, of the magnetic field. The time evolution of these two quantities is shown in Figure F.8(c). The equatorial symmetry breaking is driven by the small even azimuthal modes of the magnetic field as can be seen on Figure F.9 (a)(b), especially the magnetic mode $m = 2$.

In the time interval $1175 \le t \le 1600$, the system enters a second nonlinear regime characterized by large fluctuations and a dynamics dominated by the large Fourier modes. Between $t = 1600$ and $t = 2200$, we observe a third transition during which the small even modes of the magnetic field increase again until they reach the final saturated state. A third and final nonlinear regime settles beyond $t = 2200$. Figure F.9(c) shows that the large Fourier modes, exemplified by $m = 30$ and $m = 31$, basically fluctuate within some asymptotic range for $t > 1250$, whereas the small even modes grow until they become energetically significant.

We show in Figure F.10(a) the time series of the azimuthal component of the magnetic field at the point $(r = 1.2, \theta = 0, z = -0.5)$. The envelop of the signal first grows then

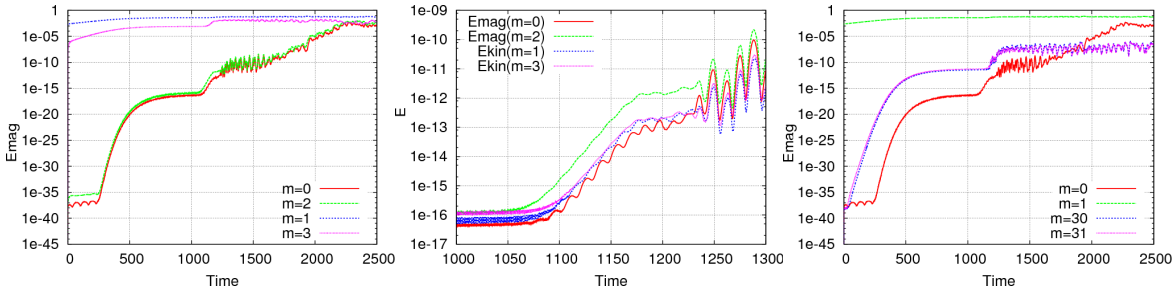

(a) Magnetic energy, $m = 0, 1, 2, 3$ (b) Kin. $m = 1$, 3; Mag. $m = 0$, 2 (c) Magnetic energy, $m = 0, 1, 30, 31$

Figure F.9: Time evolution of different modal energies; (a) magnetic energies $m = 0$, 2 (bottom curves) and $m = 1$, 3 (top curves); (b) kinetic energies $m = 1$, 3 and magnetic energies $m = 0$, 2; (c) magnetic energies $m = 1$ (top curve), $m = 30$, 31 (middle curves) and $m = 0$.

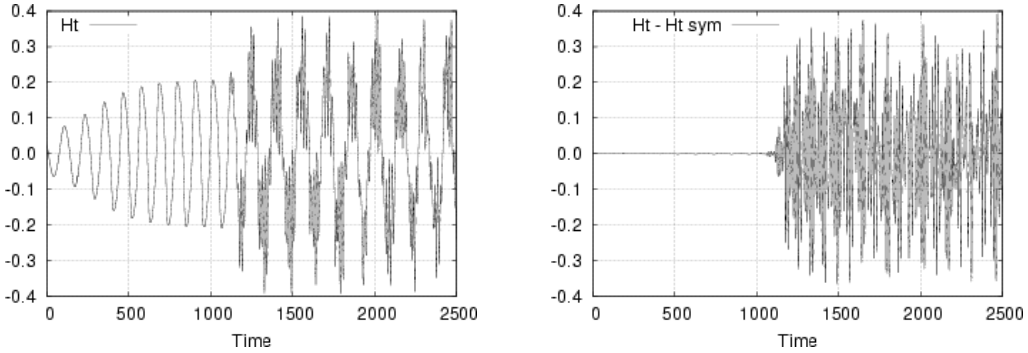

(a) $H_\theta(1.2, 0, -0.5, t)$ (b) $H_\theta(1.2, 0, -0.5, t) - H_\theta(1.2, 0, 0.5, t)$

Figure F.10: Time series of (a) H_θ at $(r = 1.2, \theta = 0, z = -0.5)$ and (b) twice the anti-symmetric part of H_θ at $(r = 1.2, \theta = 0, z = -0.5)$.

reaches a maximum range. The period of the signal is $T \approx 112.5$; this corresponds to a wave that rotates in the same direction as the inner cylinder and top/bottom lids. More frequencies appear beyond $t = 1100$; the signal is the superposition of an oscillation of period $T \approx 150$ and a modulation of period $T_{\text{mod}} \approx 17$, which happens to be of the same order as the wall rotation period $T_{\text{lids}} = 2\pi/0.55 \approx 11.4$. The modulation of the time series of H_θ has similarities with the solar activity modulation reproduced by some mean-field dynamo models (see e.g. [151]). The breaking of the equatorial symmetry is measured by monitoring the anti-symmetric part of the magnetic field. We show in Figure F.10(b) the time evolution of twice the anti-symmetric part of H_θ at $(r = 1.2, \theta = 0, z = -0.5)$.

F.5.3 Spatial structure of the dynamo

To have a better understanding of the structure of the velocity and magnetic fields during the three nonlinear regimes identified above, we show in Figure F.11 the isosurfaces of the magnetic and kinetic energies at $t = 1000$, $t = 1400$, and $t = 2500$. Since the axisymmetric velocity mode $m = 0$ is dominant (see Figure F.11(d-f)), we show in Figure F.11(g-i) the kinetic energy

without its axisymmetric contribution to better distinguish the fine structures. The magnetic field at $t = 1000$ is dominated by the odd azimuthal modes (see Figure F.11(a)) and resembles the eigenvector shown in Figure F.7(g). The velocity field is composed of even modes as can be seen on Figure F.11(g), see e.g. the two dark structures that are diametrically opposed. Similar spatial distributions are observed at time $t = 1400$ with the addition of smaller scales. At time $t = 2500$ the small scale modes are even more apparent, and the magnetic and velocity structures in the fluid domain are more deformed.

Isosurface $\|\mathbf{H}^c\|^2$ (25% of maximum value)

(a) $t = 1000$ (b) $t = 1400$ (c) $t = 2500$

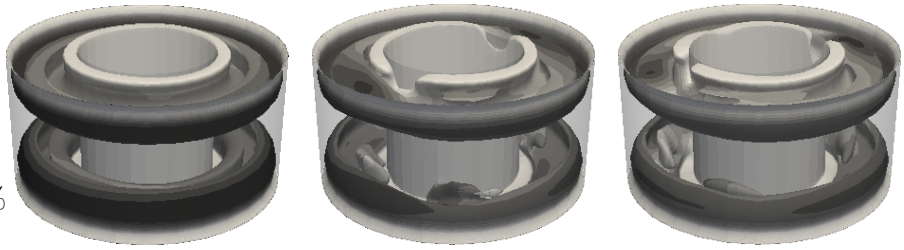

Isosurface $\|\mathbf{V}\|^2$ (25% of maximum value)

(d) $t = 1000$ (e) $t = 1400$ (f) $t = 2500$

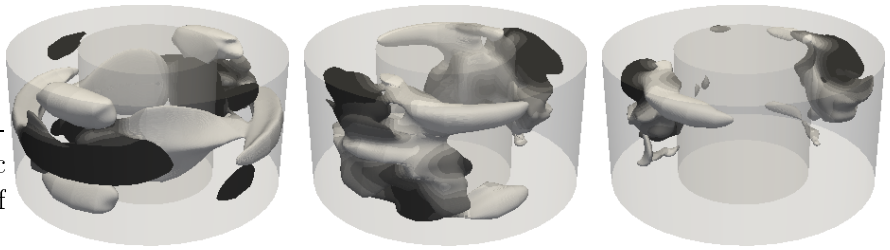

Isosurface $\|\mathbf{V}\|^2$ without the axisymmetric mode $m=0$ (10% of maximum value)

(g) $t = 1000$ (h) $t = 1400$ (i) $t = 2500$

Figure F.11: Nonlinear dynamo at $t = 1000$, $t = 1400$ and $t = 2500$, for $R_\mathrm{e} = 120$, $R_\mathrm{m} = 200$: (a-c) isosurface of $\|\mathbf{H}^c\|^2$ (25% of maximum value); (d-f) isosurface of $\|\mathbf{V}\|^2$ (25% of maximum value); (g-i) isosurface of $\|\mathbf{V}\|^2$ without the axisymmetric mode (10% of maximum value); color scale proportional to azimuthal component.

To characterize the long distance influence of the magnetic field, we have recorded the time evolution of the magnetic dipole defined by $\mathbf{D} = \int_{\Omega_c} \mathbf{r}\times(\nabla\times\mathbf{H}^c)\mathrm{d}\mathbf{x}$. Figure F.12 shows the time series of the three Cartesian components of the magnetic dipole in the time interval $0 \leq t \leq 2500$. During the first two transitions and nonlinear regimes, i.e., $0 \leq t \leq 1600$, the dipolar moment is purely equatorial and rotates at the same frequency as the magnetic field. The axial moment starts to grow at the beginning of the third transition ($t > 1600$) and changes sign several times afterward (note that the time series in (a) is under sampled in this range). Figure F.12(b) presents a zoom of the time evolution of D_z showing two reversals.

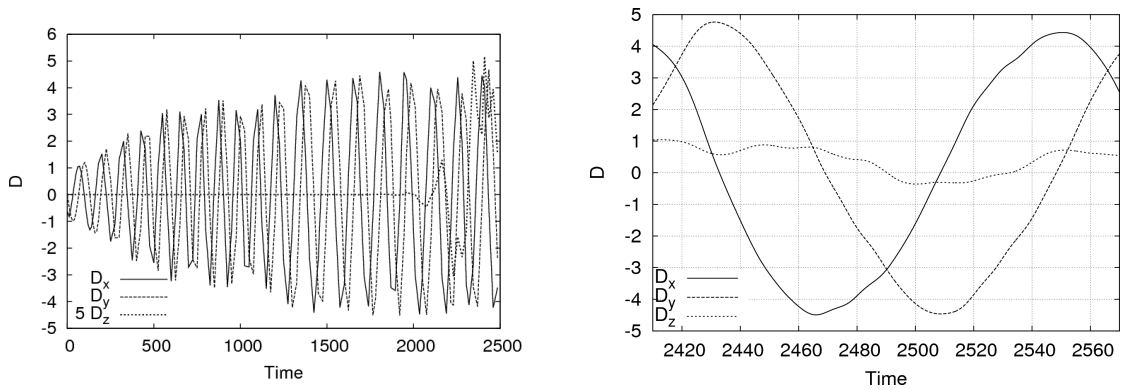

(a) $0 \leq t \leq 2500$ (b) Zoom in $2410 \leq t \leq 2570$

Figure F.12: Time evolution of the dipolar magnetic moment. Note that the vertical component has been multiplied by 5 in the left panel.

The magnitude of the quadrupolar moments (data not shown) stay below 10^{-3} until $t = 1175$, then increase and saturate to values four times smaller than the magnitude of the dipolar moment. Magnetic field lines in the vacuum at $t = 2500$ show a pattern characteristics of an equatorial dipole (see Figure F.13).

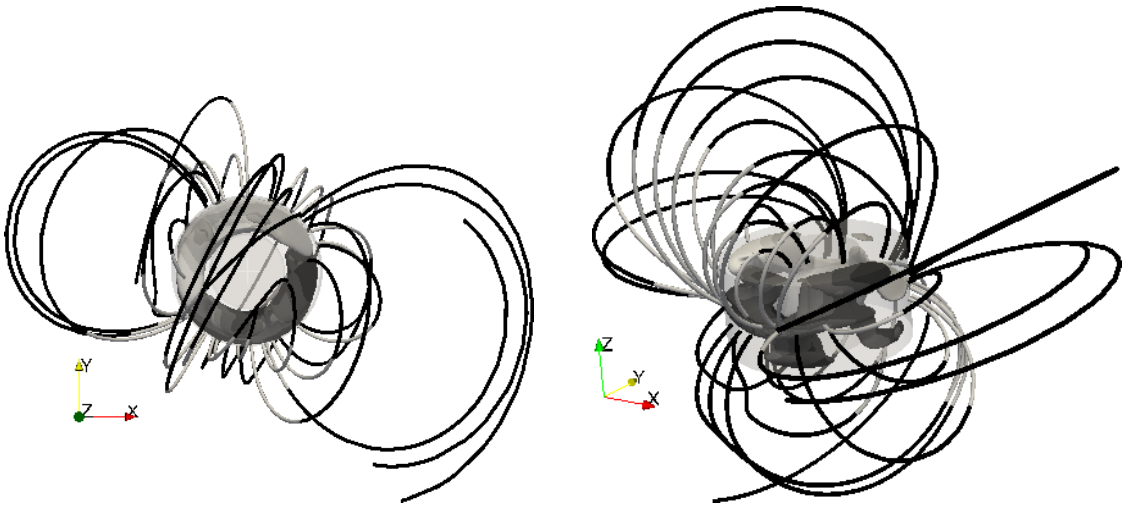

(a) From above (b) From a perspective point of view

Figure F.13: Isosurface of $\|\mathbf{H}^c\|^2$ (25% of maximum value) and magnetic field lines at $t = 2500$.

F.6 Concluding remarks

We have numerically demonstrated that pure viscous driving by smooth rotating walls in a short Taylor-Couette setup does not lead to dynamo action for $R_\mathrm{m} \leq 200$ since the poloidal to toroidal ratio of the velocity field is too small. An adjustment of the poloidal to toroidal ratio is needed to achieve dynamo action in the kinematic regime. We have implemented

an ad hoc body force to produce a poloidal to toroidal ratio that is of the same order as what is needed in the kinematic simulations to trigger the dynamo action. This force may be thought of as a model for the action of blades fixed to the static or to the rotating walls/lids at convenient angles. This force has also the same symmetry properties as the geodynamo, i.e., the SO(2)×Z2 symmetry (axisymmetry and equatorial symmetry). The critical magnetic Reynolds number of this setup based on the inner cylinder speed $\mu_0\sigma\Omega_i R_i^2 = 0.55\times180 = 99$ is in the range of what has been obtained in the kinematic studies of [44] in a spherical container with the same symmetries. This magnetic Reynolds number is also comparable to what has been reported in [66] for Taylor-Couette simulations in vessels of larger aspect ratios and with pure viscous driving.

A nonlinear simulation has been performed at $R_\mathrm{e} = 120$, $R_\mathrm{m} = 200$ over 225 rotation periods. In the early linear phase of the dynamo, the external field is dominated by an equatorial rotating dipole. In the established nonlinear regime, an axial axisymmetric component is excited and exhibits reversals. The relation between the main flow parameters of the time-dependent angle formed by the dipole and the rotation axis calls for further investigations, since it is a basic feature of observed planetary dynamos.

Exploring the feasibility of an experimental fluid dynamo based on the present design will require expertise from many different experimental and numerical fields [93]. To achieve a magnetic Reynolds number equal to 100 in a flow of liquid sodium requires that the kinematic Reynolds number be of order 10^7. It is well known that such a value corresponds to a highly turbulent flow that can be studied only in experimental facilities, since it is far beyond the capacity of direct numerical simulations. The objective of such experiments should be to recover optimized poloidal and toroidal components after time averaging, which presumably would guide the design of the blades fixed to the endwalls. These experiments would also inform about the power requirements. Using a standard rotation frequency of 50 Hz, a magnetic Reynolds number of 100 can be obtained in liquid sodium at 150°C with an inner radius of approximatively 18 cm and an outer radius and height of 36 cm. This seems feasible since these dimensions are not far from those of the Cadarache experiment [110]. We conjecture however that the power required by this experiment at a given rotation frequency should be smaller, since the turbulence rate induced by co-rotating lids/impellers should be smaller than that of counter-rotating lids/impellers. A dynamo facility presenting similarities with the present proposal is currently investigated by Colgate and collaborators [34]. Their MHD device uses also a Taylor-Couette forcing in a short cylindrical container with size and targeted magnetic Reynolds number similar to those studied in the present paper. There are however differences: the flow in their experiment forms an outwards jet in the equatorial plane and is driven by viscous stresses only. More detailed comparisons of the respective merits of both designs should certainly be instructive.

Acknowledgments

JLG is thankful to University Paris-Sud for constant support over the years. The computations were carried out on the IBM Power 6 cluster of Institut du Développement et des Ressources en Informatique Scientifique (IDRIS) (project # 0254).

Annexe G

Nonlinear dynamo action in a precessing cylindrical container

C. Nore [a], J. Léorat [b], J.-L. Guermond [a,c], F. Luddens [a,c]

Abstract

It is numerically demonstrated by means of a magnetohydrodynamics (MHD) code that precession can trigger the dynamo effect in a cylindrical container. When the Reynolds number, based on the radius of the cylinder and its angular velocity, increases, the flow, which is initially centro-symmetric, loses its stability and bifurcates to a quasi-periodic motion. This unsteady and asymmetric flow is shown to be capable of sustaining dynamo action in the linear and nonlinear regimes. The magnetic field thus generated is unsteady and quadrupolar. These numerical evidences of dynamo action in a precessing cylindrical container may be useful for an experiment now planned at the DREsden Sodium facility for DYNamo and thermohydraulic studies facility in Germany (DRESDYN).

G.1 Introduction

The interest of astronomers and physicists for the dynamo action finds its origins in the quest for a reasonable explanation for the source of terrestrial and solar magnetism. Dynamo action is obtained when the conversion rate of kinetic energy in magnetic energy in the Earth liquid core is larger than the ohmic dissipation. This phenomenon is turbulent and reproducing it either numerically or experimentally constitutes an enormous challenge.

For a long time the analysis of the dynamo action has been restricted to kinematic dynamo theories which postulate that the velocity field is known a priori. For instance the so-called mean field theory consists of assuming that the velocity and magnetic length scales are well separated and the magnetic Reynolds number is small. Although the mean-field theory is widely used, its validity in the range of large magnetic Reynolds number is questionable [108, 82].

Some models like the so-called alpha-quenching include some sort of nonlinear retro-action of the fluid flow on the magnetic field through a modelling of the velocity perturbations as a

[a] Laboratoire d'Informatique pour la Mécanique et les Sciences de l'Ingénieur, CNRS, BP 133, 91403 Orsay Cedex, France

[b] Luth, Observatoire de Paris-Meudon, place Janssen, 92195 Meudon, France

[c] Department of Mathematics, Texas A&M University 3368 TAMU, College Station, TX 77843-3368, USA

function of the local magnetic field. These models do give saturated nonlinear dynamics, but, again, the theoretical foundations of these approaches are questionable.

One can imagine that, as the number-crunching capacity of computers is ever growing, some of the short-comings of the above phenomenological theories and models can be overcome by direct numerical simulation (DNS) of the magnetohydrodynamics equations (MHD). Although the main advantage of the direct numerical simulation approach is that the nonlinear coupling between the Navier-Stokes equations and the induction equation is represented exactly, some level of modelling of the boundary conditions and forcing is still required by DNS. For instance, the question of the nature of the forcing that needs to be applied to the MHD system so that the resulting dynamo has experimental or astronomical significance needs to be somewhat modelled. The purpose of the remainder of this introduction is to briefly review this issue, and the objective of this paper is to show that precession is an efficient forcing that can be used for experimental purposes and does not require any modelling.

DNS of the dynamo action is very demanding computationally since obtaining statistically stationary solutions requires very long integration times. Two types of DNS are performed in practice to address this problem. If one is interested in the dynamics of length scales that are significantly smaller than those of the forcing term (i.e., the source of energy in the system), one can use periodic boundary conditions together with the very efficient arsenal of Fourier/spectral techniques. This is the choice usually made for the study of *turbulent dynamos*. If on the contrary one is interested in the dynamics of scales that are close to the characteristic scales of the forcing term, one must represent the boundary conditions more accurately and thus use numerical methods that are not yet as efficient as spectral methods and thus cannot reach very high Reynolds numbers. This type of choice is made when one wants to study *large scale dynamos*. Forcing by precession, which is the object of this paper, can be put in this category. Let us now review the various types of nonlinear dynamos known so far to better appreciate the qualities of precession forcing.

In the standard framework of homogeneous MHD turbulence, the mechanical power injected in the system is modelled by a large scale forcing term that can be either time independent or random with zero or finite correlation time. The purpose of the turbulent dynamos thus generated is to study the dynamics of the energy transfers between scales and between the velocity and the magnetic fields [113, 142, 130, 122]. It is sufficient to use periodic boundary conditions to achieve this program. Let us emphasize though that this type of simulation is not yet capable of drawing reasonable conclusions concerning the terrestrial magnetism, since the magnetic Prandtl numbers explored so far, P_{m}, are larger than 0.01, whereas the terrestrial magnetic Prandtl number is very small, $P_{\mathrm{m}} \approx 10^{-5}$.

Contrary to turbulent dynamos, it is critical to impose realistic boundary conditions in large scale dynamos. Although natural and experimental dynamos have simple geometries in general, modelling their forcing for numerical purposes is non trivial. For instance, thermal convection is known to be a source of stellar dynamos, and it is also suspected to be one of the possible sources of the geodynamo [79], but enforcing a realistic boundary condition to control the thermal convection is a particularly tricky question for the geodynamo. It is now recognized that various numerical scenarios can be obtained depending on the nature of the boundary condition which is imposed at the boundary of the iron core, see for instance [62], [84], and [115]. The situation is similar for experimental dynamos driven either by rotors or pumps [51, 139, 110]. In this case also forcing is usually modelled by inserting ad hoc forces in the momentum equation, see for instance [15, 81, 60].

Contrary to the above examples, precession has the rare quality of generating a flow dy-

namics free of modelling, since exact boundary conditions are imposed in this case. The boundary conditions prescribe the action of the container walls on the flow and thus create a realistic forcing at the largest scale available. Simulating numerically precession-driven rotating flows is useful for experimental fluid dynamos and opens perspectives for real astrophysical dynamos [26, 100]. To the best of our knowledge, only two precession-driven dynamos have been successfully simulated so far. Tilgner [148, 149] has first proved the capability of precession to drive the dynamo effect in a spherical shell. However, due to the symmetry properties of the sphere, the precessing flow thus obtained is driven by viscosity, which makes it difficult to be used in experimental and astrophysical applications at large kinetic Reynolds numbers. Wu and Roberts [156] have obtained the dynamo effect in a precessing spheroid using a flow obtained as a stress free fluctuation of an analytical Poincaré solution. The objective of the paper is to show that dynamo action can also be achieved in a precessing cylinder. The precession forcing in a cylinder is large scale, i.e., comes from the walls, and is not purely viscous. Although the spheroidal geometry is more relevant in an astrophysical context, the cylindrical geometry is more suitable for experimental purposes. A first attempt to realize an experimental turbulent homogeneous dynamo in a precessing cylindrical container is reported in [54]. A new experiment using a cylindrical vessel is now planned in the large scale MHD facility DRESDYN currently being built at Helmholtz-Zentrum Dresden-Rossendorf in Germany. The action of precession will be tested there, among other things (F. Stefani [133]).

The objective of the present article is to report numerical evidences supporting the idea that precession is indeed a potent mechanism to drive dynamo action in cylindrical containers. The paper is organized as follows. The formulation of the problem is described in section G.2. We present in section G.3 the hydrodynamical regimes that are obtained at different Reynolds numbers, focusing on the two largest ones. Section G.4 explores the dynamo action in linear and nonlinear regimes. The role of symmetries is also investigated in this section. Section G.5 is devoted to a discussion of the results.

G.2 Formulation of the problem

The conducting domain considered in this article is a cylindrical vessel $\mathcal{C}$ of radius R and length L. The vessel contains a conducting fluid and is embedded in vacuum. The solid walls of the vessel are assumed to be so thin that their influence is henceforth neglected. The container rotates about its axis of symmetry with angular velocity $\Omega_r \mathbf{e}_z$ and is assumed to precess about a second axis spanned by the unit vector $\mathbf{e}_p$ forming an angle α with $\mathbf{e}_z$, $(0 < \alpha < \pi)$. The angular velocity of the precession is $\Omega_p \mathbf{e}_p$. A cylindrical coordinate system about the axis of the cylinder is defined as follows: the origin of the coordinate system is the center of mass of the cylinder, say O; the Oz axis is the line passing through O and parallel to $\mathbf{e}_z$; the origin of the angular coordinate $\theta\,(0 \leq \theta \leq 2\pi)$ is the half plane passing through O, spanned by $\mathbf{e}_z$ and $\mathbf{e}_p$, and containing the vector $\Omega_p \mathbf{e}_p$. The third coordinate, denoted r, is the distance to the Oz axis.

We denote by $\mathcal{L} = R$ and $\mathcal{U} = R\Omega_r$ the reference length and velocity scales, respectively. The fluid density, ρ, is assumed to be constant and the reference pressure scale is $\mathcal{P} := \rho\mathcal{U}^2$. The magnetic permeability is uniform throughout the entire space, μ_0, and the electric conductivity of the conducting fluid is constant, σ_0. The quantities μ_0 and σ_0 are used as reference magnetic permeability and electric conductivity, respectively. The reference scale for the magnetic field is chosen so that the reference Alfvén speed is 1, i.e., $\mathcal{H} := \mathcal{U}\sqrt{\rho/\mu_0}$. We

are left with five non-dimensional parameters: one geometrical parameter L/R (aspect ratio); two forcing parameters α (precession angle) and $\varepsilon = \Omega_p/\Omega_r$ (precession rate); and two fluid parameters, namely the Ekman number $E = \nu/R^2\Omega_r$ (where ν is the kinematic viscosity) and the magnetic Prandtl number $P_\mathrm{m} = \nu\mu_0\sigma_0$. We finally define the kinetic Reynolds number $R_\mathrm{e} = 1/E$ and the magnetic Reynolds number $R_\mathrm{m} = P_\mathrm{m}R_\mathrm{e}$.

The non-dimensional set of equations that we consider is written as follows in the precessing frame of reference:

$$\begin{aligned}
\partial_t\mathbf{u} + (\mathbf{u}\cdot\nabla)\mathbf{u} + 2\varepsilon\mathbf{e}_p\times\mathbf{u} + \nabla p &= \frac{1}{R_\mathrm{e}}\boldsymbol{\Delta}\mathbf{u} + \mathbf{f},\\
\nabla\cdot\mathbf{u} &= 0,\\
\partial_t\mathbf{h} - \nabla\times(\mathbf{u}\times\mathbf{h}) &= \frac{1}{R_\mathrm{m}}\boldsymbol{\Delta}\mathbf{h},\\
\nabla\cdot\mathbf{h} &= 0,
\end{aligned}$$

where $\mathbf{u}$, p, and $\mathbf{h}$ are the velocity field, the pressure, and the magnetic field, respectively. In the following we consider three different settings to solve these equations: (i) The incompressible Navier-Stokes setting; (ii) The Maxwell or kinematic dynamo setting; (iii) The nonlinear magnetohydrodynamics setting (MHD). In the Navier-Stokes setting the source term $\mathbf{f}$ is set to zero and $\mathbf{h}$ is not computed. In the Maxwell setting, only the induction equation is solved assuming that the velocity field $\mathbf{u}$ is given. In the MHD setting the full set of equations is solved and the source term $\mathbf{f}$ is the Lorentz force per unit mass, $\mathbf{f} := (\nabla\times\mathbf{h})\times\mathbf{h}$. The no-slip boundary condition on the velocity field is written as follows in the precessing frame of reference: $\mathbf{u} = \mathbf{e}_\theta$ at $r = 1$ and $\mathbf{u} = r\mathbf{e}_\theta$ at $z = \pm 1$. The magnetic field is represented as the gradient of a scalar potential, $\nabla\phi$, in the vacuum. The magnetic boundary transmission conditions enforce that the magnetic field is continuous across the walls of the vessel, say Σ, i.e., $\mathbf{h}|_\Sigma = \nabla\phi|_\Sigma$.

The above equations are solved numerically by means of a code which is specialized to axisymmetric domains and has been presented in details in [66, 56]. The code is called SFEMaNS for Spectral/Finite Elements for Maxwell and Navier-Stokes equations. It is an hybrid algorithm that uses finite element representations in the meridian section of the axisymmetric domain and Fourier representations in the azimuthal direction. The magnetic field is represented as a vector field in the conducting region and as the gradient of a scalar potential in the insulating region. SFEMaNS can account for discontinuous distributions of electric conductivity and magnetic permeability, and all the required continuity conditions across the interfaces are enforced using an interior penalty technique. The solution technique is parallel and parallelization is done with respect to the Fourier modes.

The typical spatial resolution in the meridional plane of the conducting domain is $\Delta x = 1/160$. The grid is non-uniform in the vacuum with $\Delta x = 1/160$ close to the cylindrical vessel and $\Delta x = 1$ at the outer boundary of the numerical domain, which is a sphere of radius ten times larger than that of the cylinder. We take 24 or 32 Fourier modes ($m = 0, \ldots, 23$ or $m = 0, \ldots, 31$) for Navier-Stokes runs and 64 Fourier modes ($m = 0, \ldots, 63$) for MHD runs. The typical time-step is $\Delta t = 0.001$. A typical MHD run requires about 1000 cumulated CPU hours per rotation ($t = 2\pi$) on 64 processors on an IBM-SP6.

G.3 Hydrodynamical regime

Let us now briefly recall what is observed in a typical precessing fluid experiment starting with the fluid at rest, (see e.g. [92, 86, 90]). The vessel is first set in rotation without precession. The fluid motion is then governed by the formation of a viscous Ekman boundary layer during the acceleration ramp. The resulting flow is a stable solid rotation independently of the strength of the acceleration phase. Once precession is applied, the Coriolis force generates an axial motion of the flow driven by the Fourier mode $m = 1$. When R_e is large enough, the flow undergoes a transition from laminar to turbulent even for small precession rates and small angles [86]. The range $\varepsilon \in [0.1, 0.15]$ has been shown in [92] to maximize the axial energy in a cylinder of aspect ratio 2 in the range $R_\mathrm{e} \in [500, 5000]$ when $\alpha = \pi/2$. Although a parametric study varying the aspect ratio, the precession angle and the precession rate is interesting per se, due to limited numerical resource we are going to reduce the dimensionality of the parametric space to one aspect ratio, $L/R = 2$, one precession angle, $\alpha = \pi/2$, one precession rate, $\varepsilon = 0.15$, four values of $R_\mathrm{m} \in \{600, 800, 1200, 2400\}$ and a larger range of $R_\mathrm{e} \in [400, 1200]$.

G.3.1 Axial and total kinetic energies

We start our investigations with a Navier-Stokes run at $R_\mathrm{e} = 1000$. The initial velocity field is the solid rotation in the precessing frame: $\mathbf{u}_0 = \mathbf{e}_z \times \mathbf{r}$. The onset of the axial circulation induced by precession is monitored by recording the time evolution of the normalized total kinetic energy $K(t) = \frac{1}{2}\int_\mathcal{C} \mathbf{u}^2(\mathbf{r}, t)\,\mathrm{d}\mathbf{r}/K_0$ and normalized axial kinetic energy $K_z(t) = \frac{1}{2}\int_\mathcal{C} u_z^2(\mathbf{r}, t)\,\mathrm{d}\mathbf{r}/K_0$ where $K_0 = \frac{1}{2}\int_\mathcal{C} \mathbf{u}_0^2\,\mathrm{d}\mathbf{r}$ is the kinetic energy of the initial motion. The time evolution of $K(t)$ and $K_z(t)$ for $t \in [0, 297]$ is reported in figure G.1. The time $t = 297$ corresponds to 47.3 rotation periods. After a transient that lasts 5 rotation periods and peaks at two rotation periods, the axial kinetic energy oscillates around a plateau value $K_z \approx 0.1$. Meanwhile, the total kinetic energy decreases and oscillates around a plateau value $K \approx 0.418$ after 5 rotation periods also. These values are in very good agreement with those reported in figure 1 of [92]. The time evolution of the total kinetic energy shown in figure G.1(b) presents doubly periodic oscillations with one long period of about 9 rotation periods and one small period of about one rotation period.

To enrich the dynamics of the system we have restarted the computation at $t = 72$ (i.e., 11.5 rotation periods) and increased the Reynolds number to $R_\mathrm{e} = 1200$. The time evolution of $K(t)$ and $K_z(t)$ at $R_\mathrm{e} = 1200$ for $t \in [72, 342]$ and at $R_\mathrm{e} = 1000$ for $t \in [0, 275]$ is reported in figure G.2. At saturation, the time evolution of the total kinetic energy exhibits doubly periodic oscillations as can be seen in figure G.2(c) for $R_\mathrm{e} = 1200$. The short period oscillations correspond to energy exchanges between the north and south halves of the container, with a period of about 2 rotation periods. The energy exchange mechanism is visible in figure G.2(d) where we have reported the time evolution of the kinetic energy of the north and south halves of the cylinder for $t \in [312, 342]$. Similar oscillations between north and south hemispheres have been reported to occur in a spheroidal cavity in [156].

More can be learned by examining spectra instead of integrated quantities like the total kinetic energy K. We show for instance in figure G.3 the time averaged azimuthal spectra of the three velocity components at $R_\mathrm{e} = 1200$. More precisely, the quantities shown are $K_i(m) := \frac{1}{T}\int_0^T [\int \frac{1}{2}|\hat{u}_i(r, m, z, t)|^2 \mathrm{d}r\mathrm{d}z]\mathrm{d}t$ where $\hat{u}_i(r, m, z, t)$ is the m-th Fourier component of the velocity component $u_i(r, \theta, z, t)$, $i \in \{r, \theta, z\}$. The maximum at $m = 0$ of the azimuthal

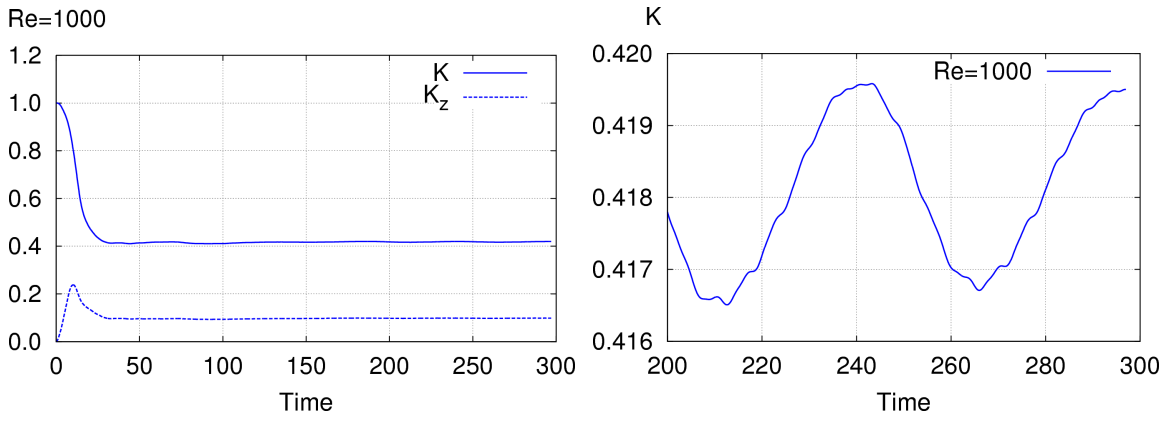

(a) (b) zoom

Figure G.1: (Color online) Time evolution of the total kinetic energy K and axial kinetic energy K_z at $R_e = 1000$, and zoom of K.

energy spectrum $K_\theta(m)$ corresponds to the large scale forcing induced by the rotating walls. The maximum at $m = 1$ of $K_z(m)$ corresponds to the Coriolis acceleration. The radial energy spectrum $K_r(m)$ presents also a maximum at $m = 1$. The three velocity components show parallel spectra at large wave numbers as a consequence of nonlinear coupling and transfer towards the dissipation scale.

In the MHD runs reported below, we have used $R_e = 1200$ since the corresponding hydrodynamical regime has broken the centro-symmetry and thus seems favourable for dynamo action.

G.3.2 Transition at low kinetic Reynolds numbers

Before investigating the dynamo regime we want to explore the dynamics of the centro-symmetry breaking in the Navier-Stokes regime as the Reynolds number increases.

Figure G.4 displays the total kinetic energy in the range $R_e \in [400, 1200]$. Note that K is a decreasing function of R_e in this range (see discussion in §G.5). At low Reynolds numbers, e.g. at $R_e = 700$, the velocity field is steady and centro-symmetric, meaning that $\mathbf{u}(\mathbf{r}, t) = \mathbf{u}(\mathbf{r}) = -\mathbf{u}(-\mathbf{r})$.

At larger Reynolds numbers, the loss of centro-symmetry of the velocity field can be monitored by inspecting its symmetric and antisymmetric components: $\mathbf{u}_s(\mathbf{r}, t) = \frac{1}{2}(\mathbf{u}(\mathbf{r}, t) - \mathbf{u}(-\mathbf{r}, t))$ and $\mathbf{u}_a(\mathbf{r}, t) = \frac{1}{2}(\mathbf{u}(\mathbf{r}, t) + \mathbf{u}(-\mathbf{r}, t))$. In the Navier-Stokes simulations reported below, we monitor the loss of centro-symmetry by tracking the time evolution of the asymmetric kinetic energy $K_a(t) = \frac{1}{2}\int_{\mathcal{C}} \mathbf{u}_a^2(\mathbf{r}, t) d\mathbf{r}/K_0$ and the asymmetry ratio $r_a(t) = K_a(t)/K(t)$. These computations have been done on centro-symmetric grids, but centro-symmetry has not been otherwise enforced. Figure G.5 shows that the asymmetric ratio decreases as time grows at $R_e = 750$ (see also the enlarged view in figure G.6(a)) and is always below 10^{-6} at $R_e = 700$ and 730. At $R_e = 800$, the velocity field is unsteady and asymmetric; the asymmetry ratio $r_a(t)$ oscillates around the asymptotic value 0.0022 as shown in figure G.6(b). At $R_e = 900$ and above, the flow is clearly asymmetric and the time evolution of the total kinetic energy is quasi-periodic with a short period of about one rotation period and a long period of about 9 rotation periods, see figure G.4.

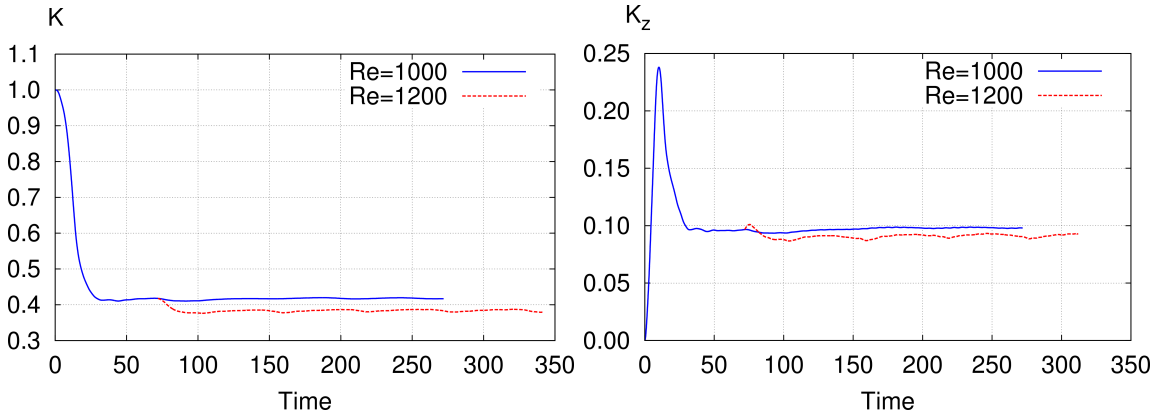

(a) total kinetic energy K, $R_e = 1000$, $R_e = 1200$ (b) axial kinetic energy K_z, $R_e = 1000$, $R_e = 1200$

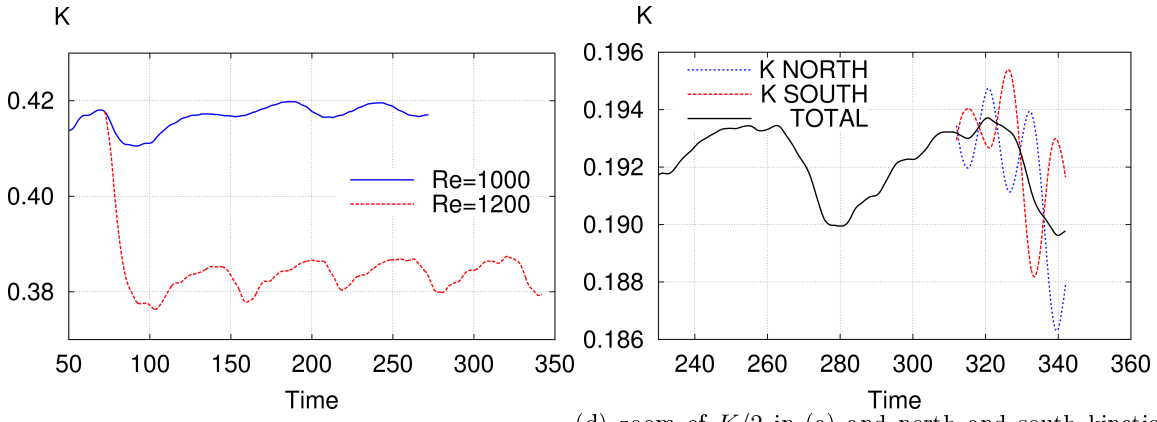

(c) zoom of (a), $t \in [50, 342]$, $R_e = 1000$, $R_e = 1200$ (d) zoom of $K/2$ in (a) and north and south kinetic energies, $R_e = 1200$, $t \in [230, 342]$

Figure G.2: (Color online) Time evolution of the total kinetic energy K, axial kinetic energy K_z, and total north and south kinetic energies as indicated.

G.4 Dynamo action

G.4.1 Linear regime

We now solve the full MHD system using as initial velocity field the velocity computed at $t = 192$ during the Navier-Stokes run at $R_e = 1200$. The initial magnetic field and the boundary conditions on the scalar potential are defined as follows in order to trigger efficiently the dynamo instability. The zero Dirichlet boundary condition that was imposed on the scalar potential ϕ on the outer sphere is replaced by $\hat{\phi}_0 = 0.05 z f(t)$ for $m = 0$ and $\hat{\phi}_1 = 0.05 r f(t)$ for $m = 1$, where $f(t) = \frac{\tau_a^3}{1+\tau_a^3}\left(1 - \frac{\tau_e^4}{1+\tau_e^4}\right)$ with $\tau_a = \frac{t}{0.4}$ and $\tau_e = \frac{t}{2}$, and the amplitude of each Fourier mode of the initial magnetic field components is set to 10^{-5} for $m \geq 2$. It has been verified in [65] that imposing vanishing Dirichlet boundary conditions on ϕ on a sphere of radius ten times larger than the typical scale of the conducting region gives results that are very close to those obtained by imposing Neumann or Robin boundary conditions.

Various MHD runs are done at $R_e = 1200$ for different values of the magnetic Prandtl number. The onset of dynamo action is monitored by recording the time evolution of the magnetic energy in the conducting fluid, $M(t) = \frac{1}{2}\int_{\mathcal{C}} \mathbf{h}^2(\mathbf{r}, t) d\mathbf{r}/K_0$. Linear dynamo action

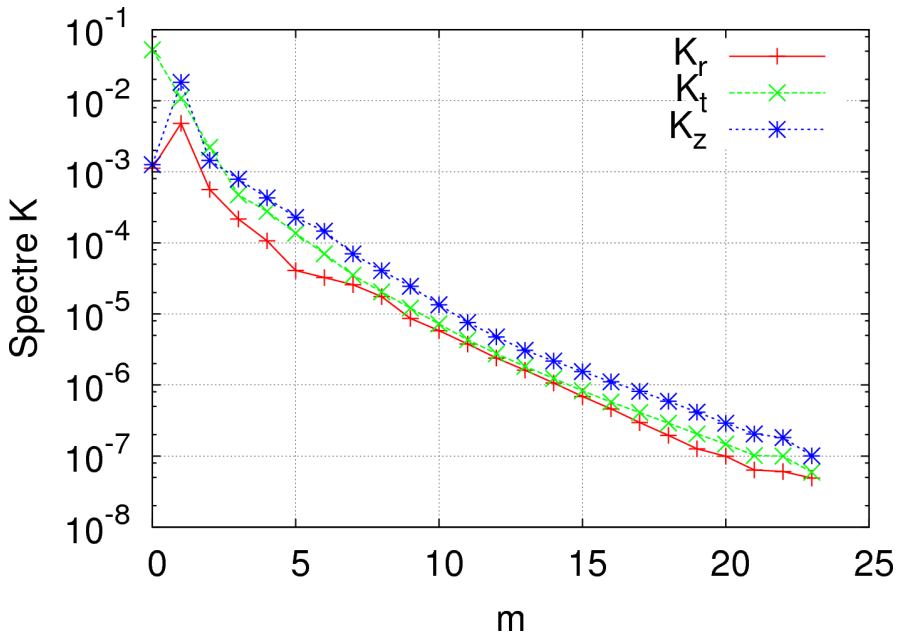

Figure G.3: (Color online) Time averaged spectra of the three components of the velocity field as a function of the azimuthal mode $m = 0, \ldots, 23$ at $R_e = 1200$.

occurs when $M(t)$ is an increasing function of time for large times. The time evolution of M for $P_m \in \{2, 1, \frac{2}{3}, \frac{1}{2}\}$ is shown in figure G.7(a). The runs at $P_m \in \{1, \frac{2}{3}, \frac{1}{2}\}$ are done by using the velocity and magnetic fields obtained from the run $P_m = 2$ at $t = 211$ as initial velocity and magnetic fields. The flow is observed to above the dynamo threshold at $P_m = 1$ and $P_m = \frac{2}{3}$ but is subcritical at $P_m = \frac{1}{2}$. Linear interpolation of the growth-rates gives the critical magnetic Prandtl number $P_m^* \approx 0.625$ corresponding to the critical magnetic Reynolds number $R_m^* \approx 750$.

G.4.2 Nonlinear saturation

We now want to observe the nonlinear saturation and evaluate the impact of the magnetic Prandtl number on the nonlinear regime. To reach nonlinear saturation in reasonable CPU time, we have used as initial data for the velocity and magnetic fields the velocity and magnetic fields from the MHD run at $t = 217$ with $P_m = 2$. The velocity field has been kept unchanged but we have multiplied by 300 the amplitude of the Fourier modes $m = 0, \ldots, 5$ of the magnetic field. The time evolution of the magnetic energy of this nonlinear run in the time interval $t \in [192, 287.5]$ is shown in figure G.7(b). We observe that M grows smoothly in one turnover time (i.e., until $t \approx 222$) and begins to oscillate thereafter. The ratio M/K is observed to be of order $6\,10^{-2}$ during the nonlinear oscillating regime. After restarting the MHD run at $t = 241$ with $P_m = 1$ and running it until $t = 346$, we observe that the dynamo is still active. After restarting the MHD run at $t = 271$ with $P_m = \frac{1}{2}$ and running it until $t = 307$, we observe that the dynamo dies in a short time lapse, suggesting that the dynamo bifurcation is not sub-critical for this set of control parameters. These nonlinear results indicate that P_m^* lies in the interval $[\frac{1}{2}, 1]$. Recall that the threshold determined in the linear regime is $P_m^* \approx 0.625$.

A snapshot of the vorticity and magnetic lines at $R_e = 1200$, $R_m = 2400$ is shown in figure G.8. We observe a central S-shaped vortex which is deformed by the precession and

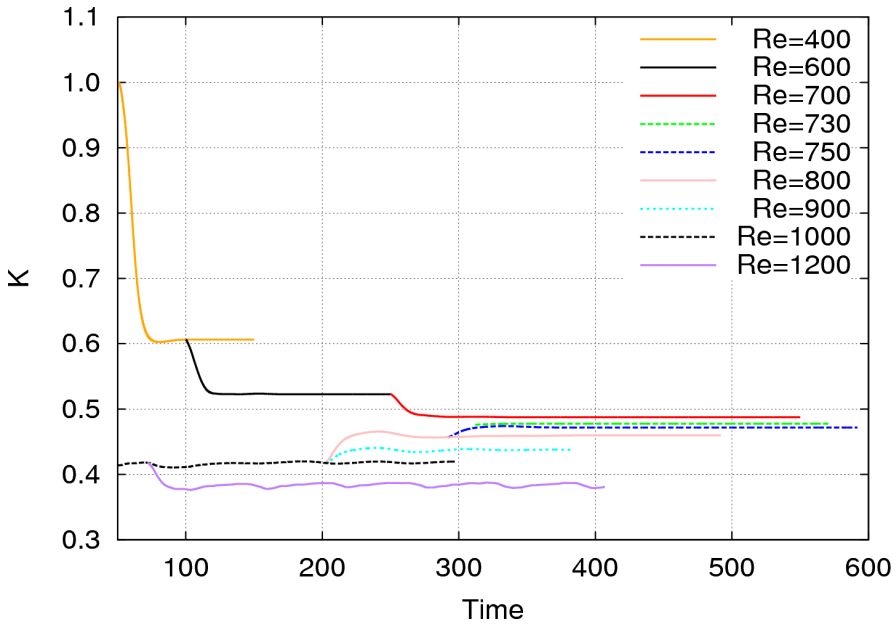

Figure G.4: (Color online) Time evolution of the total kinetic energy K for different Reynolds numbers $R_e \in [400, 1200]$.

reconnects at the walls through viscous boundary layers, (see figure G.8(a)). The magnetic field lines exhibit a quadrupolar shape which is best seen in the vacuum from the top of the cylinder (see figure G.8(b)). These lines connect mainly to the lateral wall where the current is concentrated. The magnetic energy in the cylinder is dominated by the azimuthal modes $m = 1, 2, 3$.

G.4.3 Role of the flow symmetries

Tilgner [148] has observed that unsteadiness and breaking of the centro-symmetry of the flow facilitate dynamo action. A similar observation has been made in [156], and dynamo action is reported therein to occur when cyclic oscillations of the kinetic energy between the north and south halves of the spheroidal cavity occur. Although the loss of centro-symmetry is not a necessary condition for dynamo action, we now want to test this idea in the present cylindrical setting.

The time evolution of the asymmetry ratio r_a for the Navier-Stokes run at $R_e = 1200$ is shown in figure G.9 in the time range $t \in [72, 407]$ (dotted line). The ratio r_a varies between 0.004 and 0.01 when the nonlinear regime is well established, i.e., $t \geq 220$.

In order to evaluate the impact of the dynamo on the centro-symmetry of the flow, we have started the MHD run at $t = 192$ with $P_m = 2$ (i.e., $R_m = 2400$). The time evolution of r_a in this MHD run is shown in solid line in figure G.9. Note that the solid and dotted lines coincide since the dynamo regime is linear in the time interval $t \in [192, 217]$ and the magnetic field is too weak to have an impact on the kinetic energy ratio r_a. We have restarted the MHD run at $t = 217$ after multiplying the amplitude of the magnetic field by 300 as already mentioned. The ratio r_a (solid line) clearly departs from its Navier-Stokes value thereafter as seen in the figure. At saturation, r_a oscillates between 0.008 and 0.012; these values are slightly larger than those reported in [148] for a precessing sphere. We have restarted the MHD run again at

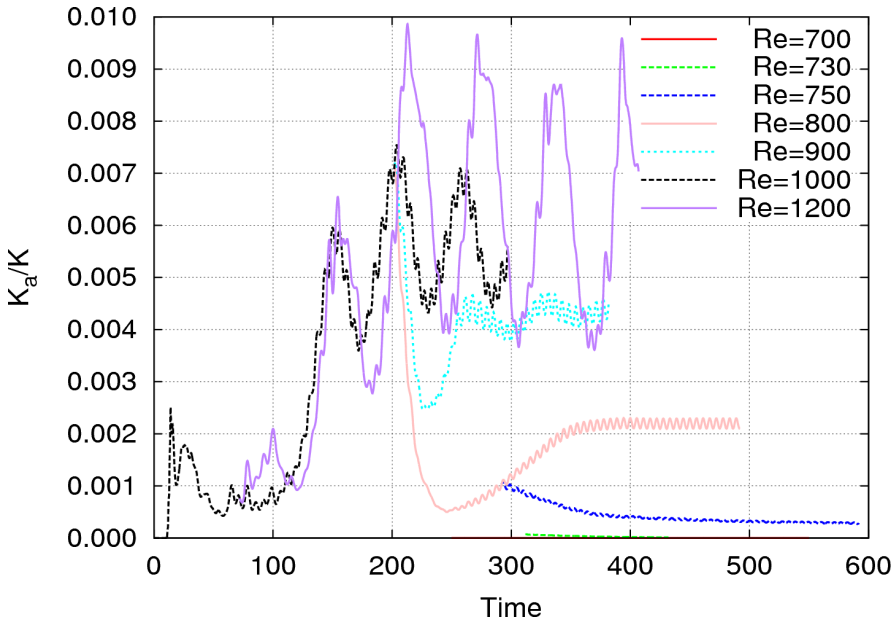

Figure G.5: (Color online) Time evolution of the asymmetry ratio r_a for different Reynolds numbers $R_e \in [700, 1200]$.

$t = 241$ after reducing the value of P_m to 1, thereby reducing the magnetic Reynolds number to $R_m = 1200$. The asymmetry factor (dotted blue line) also departs from its Navier-Stokes value, as seen on the figure. We have finally restarted the MHD run at $t = 271$ after reducing the value of the magnetic Prandtl number to $\frac{1}{2}$. As expected the dynamo dies and r_a decreases to 0.003 close to the hydrodynamical level. These computations show that the dynamo action reinforces the loss of centro-symmetry of the flow.

In order to assess the impact of the centro-symmetry and of the unsteadiness of the flow on the dynamo action, we have performed two Maxwell runs at $R_m = 1200$ with the following characteristics: (i) the velocity field at $R_e = 1200$ is frozen at $t = 211$, (ii) the velocity field at $R_e = 1200$ is frozen at $t = 211$ but only its symmetric component is retained so that the resulting velocity field is centro-symmetric. The time evolution of the magnetic energy of the MHD run and the two Maxwell runs (i) and (ii) are shown in figure G.10. It is remarkable that, in the two considered kinematic runs, the dynamo keeps growing with a rate similar to that of the MHD run. These computations show that neither the temporal oscillations nor the flow asymmetry play a crucial role on the dynamo action in the precessing cylinder at $R_m = 1200$.

G.5 Discussion

Although the range of Reynolds numbers that we have explored in our Navier-Stokes simulations is modest, it is wide enough to suggest a scaling law for the average kinetic energy, K, as a function of the Reynolds number R_e for the precession rate $\epsilon = 0.15$. To substantiate this claim we show in figure G.11(b) the average K as a function of R_e. The run at $R_e = 2000$ has not been discussed in this paper and the points at $R_e = 2500, 4000, 5000$ have been extracted from Lallemand et al. [92]. The log-log representation of the data suggests that in range

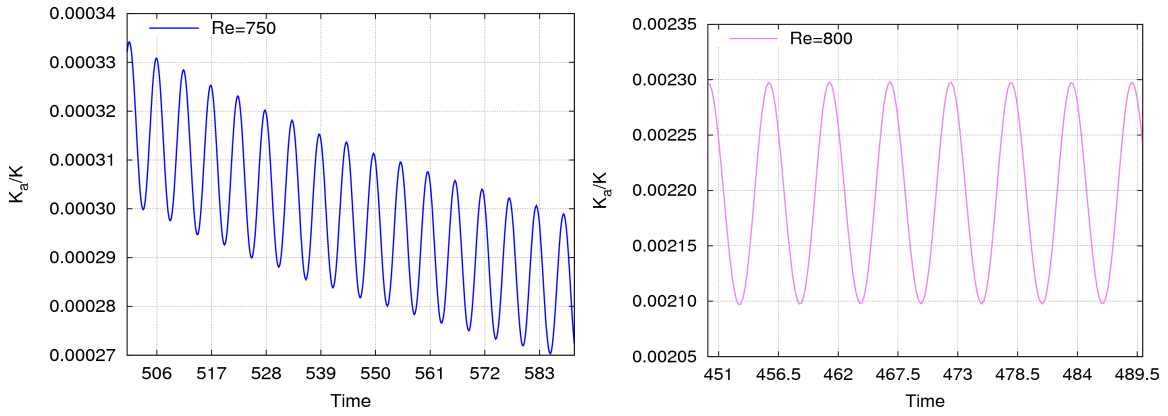

(a) zoom of r_a at $R_e = 750$ (b) zoom of r_a at $R_e = 800$

Figure G.6: (Color online) Time evolution of the asymmetry ratio r_a at $R_e = 750$ and $R_e = 800$ to show the short period of oscillations.

$R_e \in [400 : 5000]$ the energy scales like $K \simeq R_e^{-0.4}$ (see figure G.11(b)), which in turn suggests the following scaling law for the velocity $u \simeq R_e^{-1/5} = E^{1/5}$. This scaling predicts that the average flow vanishes at large R_e. This property is not paradoxical since, in an axisymmetric container with a rotation axis parallel to its symmetry axis, the azimuthal flow is driven only by viscous forces at the wall. Since in the limit of zero viscosity the rotation does not force the flow, one expects to get at the inviscid limit a static fluid in the precessing frame and a solid body motion around the precession axis in the inertial frame.

The above scaling for the velocity reminds of the Stewartson-Roberts analysis [138] of the critical layer in a precessing sphere. Note that the range of Reynolds numbers explored here spans one decade only and the values are not large enough to reach an asymptotic regime. We mention this scaling as a possible venue for future theoretical investigations.

Forty years after the promising experiments with liquid sodium by Gans [54], we have numerically demonstrated that dynamo action can occur in a precessing cylindrical tank. The bifurcations through symmetry breaking and cyclic time dependence are similar to those already observed in dynamo flows in spherical or spheroidal precession-driven cavities. There is however a large gap between the control parameters used in the present simulations and those achieved in experimental set-ups and planetary dynamos, where $E = 1/R_e$ and P_m are many orders of magnitude smaller. Following these evidences for dynamo action, it seems that the following two directions need to be thoroughly investigated: (1) the study of parity breaking and unsteadiness through variations of the forcing parameters (precession angle and rate); (2) the search for a scaling law for the critical magnetic Reynolds number as a function of the hydrodynamic Reynolds number. Such a relation has been proposed by Tilgner in a precessing sphere [148], who argues that it is the asymmetric part of the flow that plays a key role in the dynamo. The research program (2) will be time consuming as it will necessitate large scale computations to explore a wide range of Reynolds numbers. It will also require to develop nonlinear stabilization techniques to simulate small scale viscous dissipation. We are currently working on a second level of parallelization of the code: in addition to the parallelization with respect to the azimuthal modes which is already implemented, we are implementing a domain decomposition technique based on PETSc [13] to solve the two-dimensional problems in the meridional domains. This will hopefully speed-up the code and will permit us to

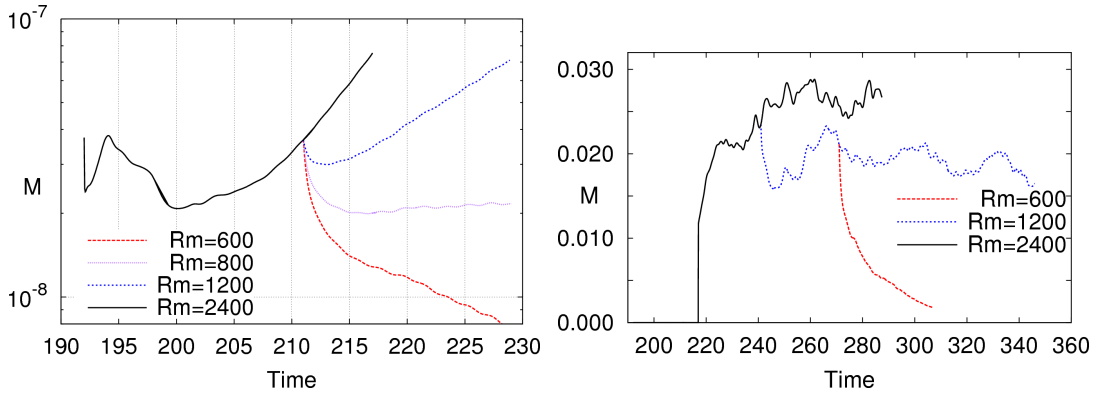

(a) linear regime (b) nonlinear regime

Figure G.7: (Color online) Time evolution of the magnetic energy M in the conducting fluid (a) in the linear regime from $t = 192$ at $R_e = 1200$ and various R_m as indicated (in lin-log scale) and (b) in the nonlinear regime from $t = 192$ to $t = 287.5$ ($R_e = 1200$, $R_m = 2400$), from $t = 241$ to $t = 346$ ($R_e = 1200$, $R_m = 1200$) and from $t = 271$ to $t = 307$ ($R_e = 1200$, $R_m = 600$).

perform higher Reynolds number computations. The empirical scaling $K \simeq R_e^{-0.4}$ that we have observed so far needs to be confirmed on smaller Ekman numbers before being considered seriously.

A major step in the understanding of precession dynamo will hopefully be achieved in the near future with the construction of the large scale MHD facility DRESDYN at Helmholtz-Zentrum Dresden-Rossendorf (Germany). The cooperation between simulations and experiments will lead to a better understanding of natural dynamos, including the geodynamo.

This work was performed using HPC resources from GENCI-IDRIS (Grant 2010-0254). We acknowledge fruitful discussions with D. Cébron, W. Herreman, P. Lallemand, P. H. Roberts, F. Stefani and A. Tilgner.

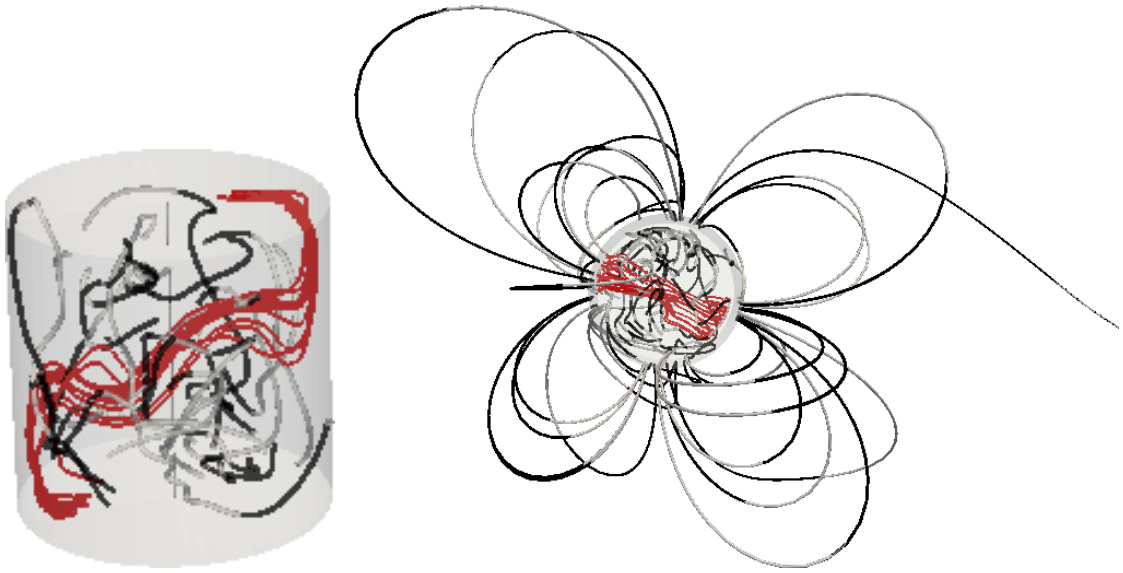

(a) from the side (b) from the top

Figure G.8: (Color online) Snapshot at $t = 241$ for $R_e = 1200$, $R_m = 2400$ showing vorticity field lines (red) and magnetic field lines colored by the axial component (grey/black for positive/negative H_z component).

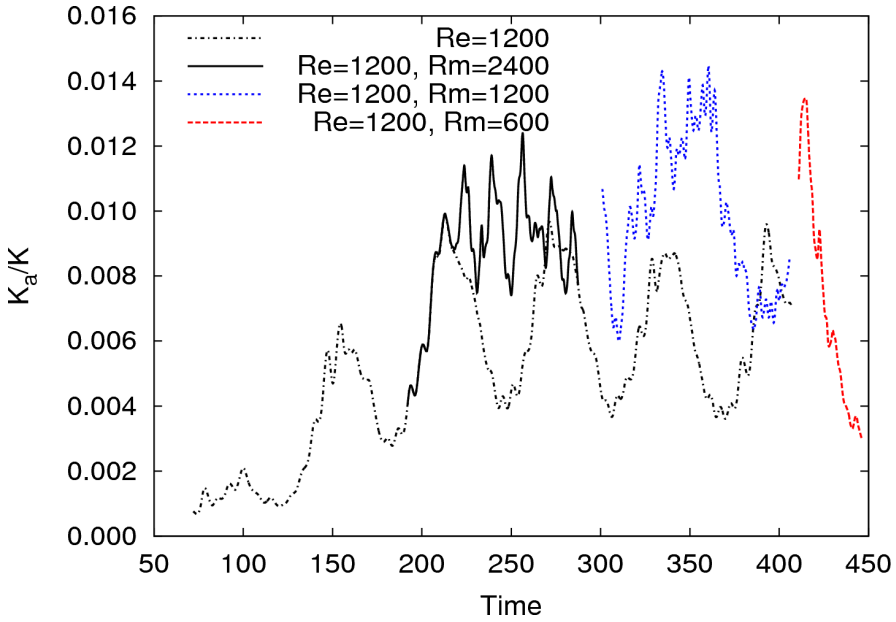

Figure G.9: (Color online) Time evolution of the asymmetry ratio r_a at $R_e = 1200$ for $t \in [72, 407]$ in the Navier-Stokes setting and $R_e = 1200$, $R_m = 2400$ for $t = [192, 287.5]$, $R_e = 1200$, $R_m = 1200$ for $t = [241, 346]$, and $R_e = 1200$, $R_m = 600$ for $t = [271, 307]$ in the MHD setting. The curves at $R_e = 1200$, $R_m = 1200$ and $R_e = 1200$, $R_m = 600$ have been shifted for easy reading.

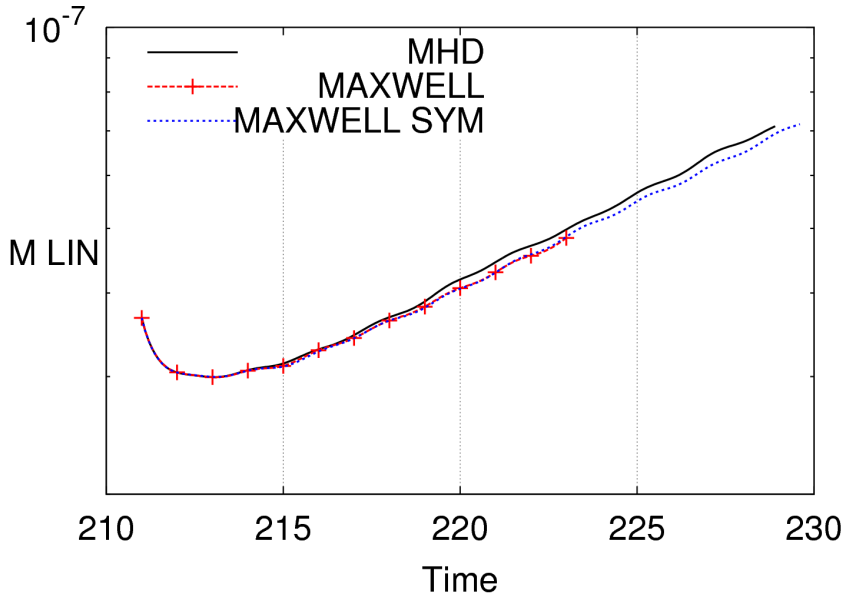

Figure G.10: (Color online) Time evolution of the magnetic energy M at $R_e = 1200$ and $R_m = 1200$ for $t \in [211, 229]$ in the MHD setting (denoted as 'MHD'), in the Maxwell setting with the velocity frozen at $t = 211$ (denoted as 'MAXWELL') and in the Maxwell setting with the symmetrized velocity frozen at $t = 211$ (denoted as 'MAXWELL SYM').

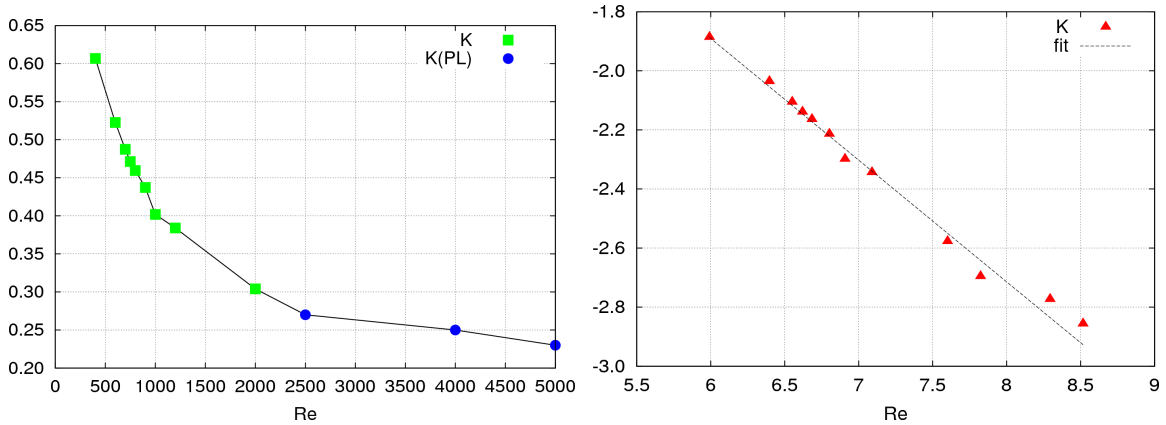

(a) K vs. R_e

(b) K vs. R_e in log-log scale

Figure G.11: (Color online) Total (time averaged) kinetic energy K in the precessing frame as a function of the Reynolds number R_e: (a) the points denoted PL are from reference [92], (b) log-log scale with the fit $R_e^{-2/5}$.

Annexe H

Remarks on the stability of the Navier-Stokes equations supplemented with stress boundary conditions

J.L. Guermond [a,b], J. Léorat [c], F. Luddens [a,b], C. Nore [a,d]

Abstract

The purpose of this note is to analyze the long term stability of the Navier-Stokes equations augmented with the Coriolis force and supplemented stress boundary conditions. It is shown that spurious stability behaviors can occur depending whether the Coriolis force is active or not when the flow domain is axisymmetric.

H.1 Introduction

The liquid core of the Earth is often modeled as a heated conducting fluid enclosed between the solid inner core and the mantle. Numerically simulating the dynamics of the liquid core is difficult in many respects; one of the difficulties comes from the presence of viscous layers that develop at the boundaries of the fluid domain, i.e., the so-called inner core boundary (ICB) and core mantle boundary (CMB). It is a common practice in the geophysics literature to use stress-free boundary conditions in order to minimize the role played by the viscous layers. Although this choice of boundary condition is convenient, it is not clear that it is more physically justified than using the no-slip condition. Actually, enforcing either the no-slip or the stress-free boundary condition may lead to significantly different results when it comes to simulating the geodynamo. For example, Glatzmaier and Roberts [62] and Kuang and Bloxham [83, 84] have used the above two different sets of boundary conditions and have reported numerical buoyancy-driven dynamos in rapidly rotating spherical shells that differ in some fundamental aspects, see e.g. [115]. The simulations reported in [83] use the stress-free condition whereas those reported in [62] use the no-slip condition. The dynamo simulated in [83] has a magnetic field outside the core-mantle boundary that is dominated by an axial

[a] Laboratoire d'Informatique pour la Mécanique et les Sciences de l'Ingénieur, CNRS, BP 133, 91403 Orsay Cedex, France

[b] Department of Mathematics, Texas A&M University 3368 TAMU, College Station, TX 77843-3368, USA

[c] Luth, Observatoire de Paris-Meudon, place Janssen, 92195 Meudon, France

[d] Institut Universitaire de France, 103 Bd Saint-Michel, 75005 Paris, France

dipole component, like that of the Earth, and its intensity is close to the present geomagnetic dipole moment. The internal magnetic field outside the core-mantle boundary is comparable to that obtained by Glatzmaier and Roberts [62], but important differences in the velocity and magnetic fields between these two dynamos can be observed within the outer core and the Taylor-Proudman tangent cylinder. (It is known that rotation of the Earth rigidifies the flow field in the direction parallel to the rotation axis through a mechanism known as the Taylor-Proudman effect. This effect makes the imaginary cylinder that is tangent to the equator of the solid inner core and whose axis is parallel to the rotation axis of the Earth acts like a solid boundary.) In the dynamo reported in [83] the fluid flow is almost stagnant inside the tangent cylinder and has a strong azimuthal component outside; the magnetic field is active throughout the outer core and is composed of two opposite toroidal cells and a simple dipolar poloidal structure. In the dynamo reported in [62] the fluid flow is composed of an intense polar vortex that is located inside the tangent cylinder and extends in the two hemispheres; the toroidal component of the magnetic field is active only inside the tangent cylinder and is concentrated near the ICB; the poloidal component has a complicated dipolar structure with extra closed loops near the ICB. It is suggested in [115] that the significantly different structures of the above two dynamos should be attributed to the nature of the boundary conditions that are imposed at the ICB and CMB interfaces. Note finally that different thermal boundary conditions (i.e., fixed temperature or fixed heat-flux boundary conditions) lead also to different magnetic and fluid solutions [128].

In addition to thermal or compositional convection due to buoyancy, precession is also believed to be a possible source of energy for the geodynamo. The precession hypothesis has been formulated for the first time in [26] and experimentally investigated using a water model in [100]. It has since then been actively studied from the theoretical, experimental and numerical perspectives. However, it seems that it is only recently that numerical examples of precession dynamos have been reported in spheres [148, 149], in spheroidal cavities [156] and in cylinders [114]. Recently, Wu and Roberts [156] have numerically studied the dynamo effect in a precessing oblate spheroid. To facilitate their analysis the authors have split the total velocity field into a basic stationary analytic (polynomial) solution (the so-called Poincaré flow) and a fluctuating part. Following ideas of Kerswell and Mason [106], they have implemented the stress-free boundary condition on the fluctuating component of the velocity in order to reduce the impact of the viscous layers at the rigid boundaries.

The purpose of the present paper is to show that the use of stress boundary conditions poses mathematical difficulties. We prove for instance that, if the fluid domain is not axisymmetric, the flow always returns to rest for large times when the stress-free boundary condition is enforced (see Proposition H.2.1), but this may not be the case when the flow domain is axisymmetric (see Proposition H.2.3). Various scenarios can occur depending whether the domain undergoes precession or not.

The note is organized as follows. We analyze the stress-free boundary condition in general fluid domains in §H.2. We show that this boundary condition is admissible if and only if the domain is not axisymmetric (see Proposition H.2.2). We revisit the same question in axisymmetric domains that undergo precession in §H.3 and §H.4. We show in §H.3 that the problem exhibits a spurious stability behavior if the stress-free condition is enforced on the velocity field minus the Poincaré flow (i.e., on the perturbation to the Poincaré flow; see Proposition H.3.1). We show in §H.4 that the problem always returns to rest for large times if the homogeneous stress-free boundary condition is enforced. The theoretical argumentation developed in §H.3 and §H.4 is numerically illustrated in §H.5. Concluding remarks are reported

in §H.6.

H.2 Stress-free boundary condition without precession

The objective of this section is to investigate the long term stability of the Navier-Stokes equations equipped with the stress-free boundary condition. The fluid domain is denoted Ω and is assumed to be open, bounded and Lipschitz.

H.2.1 Position of the problem

We are interested in the motion of an incompressible fluid in a container Ω with boundary Γ. The container is assumed to be at rest in an inertial reference frame. Denoting $\mathbf{u}$ the velocity of the fluid and p the pressure, the fluid motion is modeled by means of the incompressible Navier-Stokes equations:

$$\partial_t \mathbf{u} + \mathbf{u}\cdot\nabla\mathbf{u} - 2\nu\nabla\cdot\boldsymbol{\epsilon}(\mathbf{u}) + \nabla p = 0, \tag{H.2.1}$$

$$\nabla\cdot\mathbf{u} = 0, \tag{H.2.2}$$

$$\mathbf{u}_{|t=0} = \mathbf{u}_0, \tag{H.2.3}$$

where ν is the kinematic viscosity, $\boldsymbol{\epsilon}(\mathbf{u}) := \frac{1}{2}\left(\nabla\mathbf{u} + \nabla\mathbf{u}^T\right)$ is the strain rate tensor, and $\mathbf{u}_0$ is an initial data in $\mathbf{H} := \{\mathbf{v} \in \mathbf{L}^2(\Omega) : \ \nabla\cdot\mathbf{v} = 0, \ \mathbf{v}\cdot\mathbf{n}_\Gamma = 0\}$. It is a common practice to replace the term $\nabla\cdot\left(\nabla\mathbf{u} + \nabla\mathbf{u}^T\right)$ in the momentum equation by $\Delta\mathbf{u}$ since $\nabla\cdot\nabla\mathbf{u}^T = 0$ for incompressible flows. We nevertheless keep the original form of the viscous stress since we want to enforce the so-called stress-free boundary condition:

$$(\mathbf{n}\cdot\boldsymbol{\epsilon}(\mathbf{u}))\times\mathbf{n}_{|\Gamma} = 0, \tag{H.2.4}$$

together with the impenetrable boundary condition:

$$\mathbf{n}\cdot\mathbf{u}_{|\Gamma} = 0, \tag{H.2.5}$$

where $\mathbf{n}$ is the unit outward normal on Γ. The stress-free condition means that the tangent component of the stress at the boundary is zero. We shall see that this boundary condition is admissible in general for non-axisymmetric domains, but it yields pathological stability behaviors if the fluid domain is a solid of revolution.

We are not going to discuss the well-posedness of the above problem in its full generality since it is still unknown whether the three-dimensional Navier-Stokes equations are well-posed under the much simpler no-slip boundary condition. We nevertheless recognize as a symptom of pathological stability behavior the fact that there are solutions to (H.2.1)-(H.2.2)-(H.2.3)-(H.2.4)-(H.2.5) that do not return to rest as $t \to +\infty$ if Ω is axisymmetric.

Definition H.2.1. *We say that Ω is stress-free admissible if there is a constant $K > 0$, possibly depending on Ω, so that the following holds*

$$K\int_\Omega \mathbf{v}^2 \leqslant \int_\Omega \boldsymbol{\epsilon}(\mathbf{v}):\boldsymbol{\epsilon}(\mathbf{v}), \qquad \forall\mathbf{v} \in \mathbf{H}^1(\Omega), \ \mathbf{v}\cdot\mathbf{n}_{|\Gamma} = 0 \tag{H.2.6}$$

where ":" denotes the tensor double product.

Proposition H.2.1. *Assume that* Ω *is stress-free admissible, then* $\{0\}$ *is the global attractor of* (H.2.1)-(H.2.2)-(H.2.3)-(H.2.4)-(H.2.5).

Proof. We omit the details concerning the existence of Leray-Hopf solutions, which can be constructed using standard Galerkin techniques [94, 145, 132], and we focus only on the aspects of the question which are relevant to our discussion. It is clear that $\{0\}$ is an invariant set of (H.2.1)-(H.2.2)-(H.2.3)-(H.2.4)-(H.2.5). Let $\mathbf{B}$ be a bounded set in $\mathbf{H}$ and let $\mathbf{u}_0 \in \mathbf{B}$. Let $\mathbf{u}$ be a Leray-Hopf solution corresponding to the initial data $\mathbf{u}_0$ and let $\mathbf{v}$ be a smooth solenoidal vector field satisfying the impenetrable boundary condition. Upon multiplying the momentum equation by $\mathbf{v}$ and integrating over the domain we obtain

$$\int_\Omega \partial_t \mathbf{u}\cdot\mathbf{v} + \int_\Omega \mathbf{u}\cdot\nabla\mathbf{u}\cdot\mathbf{v} - 2\nu\int_\Omega \nabla\cdot\boldsymbol{\epsilon}(\mathbf{u})\cdot\mathbf{v} + \int_\Omega \nabla p\cdot\mathbf{v} = 0.$$

Solenoidality and the impenetrable boundary condition imply that $\int_\Omega \nabla p\cdot\mathbf{v} = -\int_\Omega p\nabla\cdot\mathbf{v} + \int_\Gamma p\mathbf{v}\cdot\mathbf{n} = 0$. Now, using the decomposition

$$\mathbf{v} = (\mathbf{n}\cdot\mathbf{v})\mathbf{n} - \mathbf{n}\times(\mathbf{n}\times\mathbf{v}),$$

and integrating by parts the viscous term we obtain:

$$\begin{aligned} -\int_\Omega \nabla\cdot\boldsymbol{\epsilon}(\mathbf{u})\cdot\mathbf{v} &= \int_\Omega \boldsymbol{\epsilon}(\mathbf{u}):\nabla\mathbf{v} - \int_\Gamma \mathbf{n}\cdot\boldsymbol{\epsilon}(\mathbf{u})\cdot\mathbf{v} \\ &= \int_\Omega \boldsymbol{\epsilon}(\mathbf{u}):\boldsymbol{\epsilon}(\mathbf{v}) + \int_\Gamma (\mathbf{n}\cdot\boldsymbol{\epsilon}(\mathbf{u})\times\mathbf{n})\cdot(\mathbf{n}\times\mathbf{v}) = \int_\Omega \boldsymbol{\epsilon}(\mathbf{u}):\boldsymbol{\epsilon}(\mathbf{v}). \end{aligned}$$

The transport term is re-written in the following form

$$\int_\Omega \mathbf{u}\cdot\nabla\mathbf{u}\cdot\mathbf{v} = \int_\Omega \frac{1}{2}\nabla\cdot(\mathbf{u}(\mathbf{u}\cdot\mathbf{v})) + \frac{1}{2}\int_\Omega (\mathbf{u}\cdot\nabla\mathbf{u}\cdot\mathbf{v} - \mathbf{u}\cdot\nabla\mathbf{v}\cdot\mathbf{u}) = \frac{1}{2}\int_\Omega (\mathbf{u}\cdot\nabla\mathbf{u}\cdot\mathbf{v} - \mathbf{u}\cdot\nabla\mathbf{v}\cdot\mathbf{u}).$$

We now apply the above identities by replacing $\mathbf{v}$ by a sequence $\{\mathbf{v}_n\}_{n\in\mathbb{N}}$ that converges in the appropriate norm to $\mathbf{u}$. By integrating in time over an arbitrary interval (t_1, t_2) and by passing to the limit (we omit the details again, see Sell [132, §2.3]), we finally obtain

$$\frac{1}{2}\int_\Omega \mathbf{u}^2(t_2,\mathbf{x})\,\mathrm{d}\mathbf{x} + 2\nu\int_{t_1}^{t_2}\int_\Omega \boldsymbol{\epsilon}(\mathbf{u}):\boldsymbol{\epsilon}(\mathbf{u})\,\mathrm{d}\mathbf{x}\,\mathrm{d}\tau \le \frac{1}{2}\int_\Omega \mathbf{u}^2(t_1,\mathbf{x})\,\mathrm{d}\mathbf{x}. \tag{H.2.7}$$

Note that equality is lost in the passage to the limit. Then using (H.2.6), we infer the following inequality:

$$\frac{1}{2}\int_\Omega \mathbf{u}^2(t_2,\mathbf{x})\,\mathrm{d}\mathbf{x} + 2K\nu\int_{t_1}^{t_2}\int_\Omega \mathbf{u}^2\,\mathrm{d}\mathbf{x}\,\mathrm{d}\tau \leqslant \frac{1}{2}\int_\Omega \mathbf{u}^2(t_1,\mathbf{x})\,\mathrm{d}\mathbf{x},$$

which, owing to the Gronwall lemma (see Lemma H.4.1), immediately leads to $\|\mathbf{u}\|_{\mathbf{L}^2(\Omega)} \leqslant \|\mathbf{u}_0\|_{\mathbf{L}^2(\Omega)}\mathrm{e}^{-2K\nu t}$, thereby proving that $\mathbf{u}\to 0$ as $t\to+\infty$. □

We shall see that the stress-free admissibility condition (H.2.6) does not hold for axisymmetric fluid domains, which are common in geoscience.

Remark H.2.1. *Note that whether equality holds in* (H.2.7) *in three space dimensions is an open question related to the Navier-Stokes Millennium Prize from the Clay institute. For this reason we refrain from invoking the time derivative of the kinetic energy in the proof of Proposition H.2.1. The mapping* $t \longmapsto \int_\Omega \mathbf{u}^2\,\mathrm{d}\mathbf{x}$ *is a priori lower semi-continuous only, and, upon denoting* $\mathbf{L}^2_w(\Omega)$ *the space* $\mathbf{L}^2(\Omega)$ *equipped with the weak topology, the mapping* $t \longmapsto \mathbf{u} \in \mathbf{L}^2_w(\Omega)$ *is continuous.*

H.2.2 The non-axisymmetric case

To better understand the stress-free admissibility condition (H.2.6), we first prove that it holds if and only if Ω is not axisymmetric.

Definition H.2.2. *We say that Ω is axisymmetric (or is a solid of revolution) if and only if there is a rotation $\mathbf{R} : \Omega \longrightarrow \Omega$ which is tangent on Γ.*

Upon introducing the average operator over Ω, $\langle v \rangle := \frac{1}{|\Omega|} \int_\Omega v$, where $|\Omega|$ is the volume of Ω, the following lemma gives a characterization of non-axisymmetric domains:

Lemma H.2.1 (Desvillettes-Villani [42])**.** *Assume that the domain Ω is of class $\mathcal{C}^1$ but is not a solid of revolution, then there is $c > 0$ so that*

$$c|\Omega|\langle \nabla \times \mathbf{v} \rangle^2 \leq \|\boldsymbol{\epsilon}(\mathbf{v})\|_{\mathbf{L}^2(\Omega)}, \qquad \forall \mathbf{v} \in \mathbf{H}^1(\Omega),\ \mathbf{v}\cdot\mathbf{n}_{|\Gamma} = 0.$$

We are now in measure to state the main result of this section:

Proposition H.2.2. *Assume that the domain Ω is of class $\mathcal{C}^1$, then Ω is stress-free admissible if and only if Ω is not a solid of revolution.*

Proof. Let us assume first that Ω is not a solid of revolution. Let us now assume that (H.2.6) does not hold. We start from the Korn inequality (cf. e.g. [46]): there exists a constant $c > 0$ such that, for all $\mathbf{v} \in \mathbf{H}^1(\Omega)$,

$$\|\mathbf{v}\|_{\mathbf{L}^2(\Omega)} + \|\nabla \mathbf{v}\|_{\mathbf{L}^2(\Omega)} \leq c \left(\|\mathbf{v}\|_{\mathbf{L}^2(\Omega)} + \|\nabla \mathbf{v} + \nabla \mathbf{v}^T\|_{\mathbf{L}^2(\Omega)} \right). \tag{H.2.8}$$

Since (H.2.6) does not hold, for any $n \in \mathbb{N}$, one can find $\mathbf{u}_n \in \mathbf{H}^1(\Omega)$ such that

$$\mathbf{u}_n\cdot\mathbf{n}_{|\Gamma} = 0, \qquad \|\mathbf{u}_n\|_{\mathbf{L}^2(\Omega)} = 1, \quad \text{and} \quad \|\nabla \mathbf{u}_n + \nabla \mathbf{u}_n^T\|_{\mathbf{L}^2(\Omega)} \leqslant \frac{1}{n}.$$

The Korn inequality implies that the sequence $\mathbf{u}_n$ is bounded in $\mathbf{H}^1(\Omega)$. Since the inclusion $\mathbf{H}^1(\Omega) \subset \mathbf{L}^2(\Omega)$ is compact, there exists $\mathbf{u} \in \mathbf{H}^1(\Omega)$ such that (we keep using $\mathbf{u}_n$ after extraction of the converging sub-sequence) $\|\mathbf{u}_n - \mathbf{u}\|_{\mathbf{L}^2(\Omega)} \to 0$ and $\mathbf{u}_n \rightharpoonup \mathbf{u}$ in $\mathbf{H}^1(\Omega)$. We also have

$$\nabla \mathbf{u}_n + \nabla \mathbf{u}_n^T \to 0 \text{ in } \mathbf{L}^2(\Omega) \text{ and } \nabla \mathbf{u}_n + \nabla \mathbf{u}_n^T \to \nabla \mathbf{u} + \nabla \mathbf{u}^T \text{ in } \boldsymbol{\mathcal{D}}'(\Omega),$$

which finally gives $\nabla \mathbf{u} + \nabla \mathbf{u}^T = 0$ ($\boldsymbol{\mathcal{D}}(\Omega)$ is the space of smooth vector-valued functions with compact support in Ω and $\boldsymbol{\mathcal{D}}'(\Omega)$ is the space of vector-valued distributions over Ω, i.e., the linear forms acting on $\boldsymbol{\mathcal{D}}(\Omega)$.) Applying the Korn inequality to $\mathbf{u} - \mathbf{u}_n$ and using the fact that

$$\|\mathbf{u}_n - \mathbf{u}\|_{\mathbf{L}^2(\Omega)} + \|\nabla \mathbf{u}_n + \nabla \mathbf{u}_n^T - \nabla \mathbf{u} - \nabla \mathbf{u}^T\|_{\mathbf{L}^2(\Omega)} \to 0,$$

we infer that $\|\mathbf{u}_n - \mathbf{u}\|_{\mathbf{H}^1(\Omega)} \to 0$. This allows us to pass to the limit on the boundary condition $\mathbf{u}\cdot\mathbf{n}_{|\Gamma} = 0$. The condition $\boldsymbol{\epsilon}(\mathbf{u}) = 0$ implies that there are two vectors $\mathbf{t} \in \mathbb{R}^3$, $\boldsymbol{\omega} \in \mathbb{R}^3$ so that $\mathbf{u} = \mathbf{t} + \boldsymbol{\omega} \times \mathbf{x}$. This means that $\nabla \times \mathbf{u} = \langle \nabla \times \mathbf{u} \rangle = \boldsymbol{\omega}$. Using Lemma H.2.1, we conclude that $\boldsymbol{\omega} = 0$, which means that $\mathbf{u} = \mathbf{t}$. The boundary condition $\mathbf{u}\cdot\mathbf{n}_{|\Gamma} = 0$ implies $\mathbf{t} = 0$; this in turn means $\mathbf{u} = 0$, which is impossible because $\|\mathbf{u}\|_{\mathbf{L}^2(\Omega)} = 1$. In conclusion, (H.2.6) holds.

Let us assume now that Ω is axisymmetric. This means that there is a rotation $\mathbf{R} : \Omega \longrightarrow \Omega$ which is tangent on Γ. Without loss of generality we assume that the rotation axis is parallel to $\mathbf{e}_z$ and the coordinate origin is located on this axis. Then $\mathbf{R}(\mathbf{x}) = \omega \mathbf{e}_z \times \mathbf{x}$ and clearly $\mathbf{R} \in \mathbf{H}^1(\Omega)$, $\mathbf{R}(\mathbf{x})\cdot\mathbf{n}(\mathbf{x})_{|\Gamma} = 0$, $\|\mathbf{R}\|_{\mathbf{L}^2(\Omega)} \neq 0$ but (H.2.6) does not hold since $\boldsymbol{\epsilon}(\mathbf{R}) = 0$. □

H.2.3 The Axisymmetry curse

Let us assume that Ω is axisymmetric. We are going to show the following statement in this section.

Claim H.2.1. *The zero velocity field,* 0*, is in the global attractor of* (H.2.1)-(H.2.2)-(H.2.3)-(H.2.4)-(H.2.5)*, but the rest state,* $\{0\}$*, is not an attractor. There are initial data that create flows that never return to rest. In particular, if the initial data is a rigid-body rotation, the flow will rotate for ever without losing energy.*

Recall that it can be shown that Ω is axisymmetric if and only if Ω is either a sphere (and all the directions are symmetry axes) or Ω has a unique symmetry axis. Without a loss of generality, we assume that Oz is the only symmetry axis of Ω. Recall that all the rigid-body rotations about Oz can be written as follows $\mathbf{x} \longmapsto \omega \mathbf{e}_z \times \mathbf{x}$, $\omega \in \mathbb{R}$, where $\mathbf{x}$ is the position vector. We introduce the following space

$$\mathcal{R} := \operatorname{span}\{\mathbf{e}_z \times \mathbf{x}\}, \tag{H.2.9}$$

and its orthogonal complement in $\mathbf{L}^2(\Omega)$, say $\mathcal{R}^\perp$.

Lemma H.2.2. *Let* Ω *be an open, bounded, connected, domain of class* $\mathcal{C}^1$ *with unique symmetry axis* Oz*. There exists* $K > 0$ *such that the following holds for every* $\mathbf{v} \in \mathcal{R}^\perp \cap \mathbf{H}^1(\Omega)$ *with* $\mathbf{v}\cdot\mathbf{n} = 0$*:*

$$K\|\mathbf{v}\|^2_{\mathbf{L}^2(\Omega)} \leq \int_\Omega |\boldsymbol{\epsilon}(\mathbf{v})|^2 \, \mathrm{d}\mathbf{x},$$

where we denote $|\boldsymbol{\epsilon}(\mathbf{v})|^2 := \boldsymbol{\epsilon}(\mathbf{v}){:}\boldsymbol{\epsilon}(\mathbf{v})$.

Proof. The proof is similar to that of Proposition H.2.2 and proceeds by contradiction. We consider a sequence $\mathbf{v}_n \in \mathcal{R}^\perp \cap \mathbf{H}^1(\Omega)$ with vanishing normal component such that

$$\|\mathbf{v}_n\|_{\mathbf{L}^2} = 1 \text{ and } \|\boldsymbol{\epsilon}(\mathbf{v}_n)\|_{\mathbf{L}^2} \leqslant \frac{1}{n}.$$

Using Korn's inequality, we can prove that (up to extraction) $\mathbf{v}_n$ converges in $\mathbf{H}^1(\Omega)$, and the limit $\mathbf{v}$ satisfies

$$\mathbf{v} \in \mathcal{R}^\perp, \ \mathbf{v}\cdot\mathbf{n} = 0 \text{ and } \boldsymbol{\epsilon}(\mathbf{v}) = 0.$$

This implies that $\mathbf{v}$ is the sum of a translation plus a rigid-body rotation. But Ω being bounded the translation is zero. The unique symmetry axis of Ω being Oz, the condition $\mathbf{v}\cdot\mathbf{n} = 0$ implies that $\mathbf{v}$ is a rigid-body rotation about the Oz-axis, i.e., $\mathbf{v} \in \mathcal{R} \cap \mathcal{R}^\perp = \{0\}$, which contradicts $\|\mathbf{v}\|_{\mathbf{L}^2(\Omega)} = 1$. □

We claim that the Navier-Stokes problem (H.2.1)-(H.2.2) equipped with boundary conditions (H.2.4)-(H.2.5) has spurious stability properties due to the following proposition.

Proposition H.2.3. *(i)* $\mathcal{R}$ *is the global attractor of* (H.2.1)-(H.2.2)-(H.2.3)-(H.2.4)-(H.2.5)*. (ii) No element in* $\mathcal{R}$ *is an attractor.*

Proof. (i) Let $\mathbf{u} \in L^2((0,+\infty);\mathbf{L}^2(\Omega)) \cap L^\infty((0,+\infty);\mathbf{H}^1(\Omega))$ be a Leray-Hopf solution of (H.2.1)–(H.2.5) and consider the following decomposition:

$$\mathbf{u}(t) = \mathbf{u}^\perp(t) + \lambda(t)\mathbf{e}_z \times \mathbf{x}, \text{ where } \mathbf{u}^\perp(t) \in \mathcal{R}^\perp, \ \lambda(t) \in \mathbb{R}, \ \forall t \in [0,+\infty).$$

Invoking Lemma H.3.1 we infer that $\frac{\mathrm{d}\lambda(t)}{\mathrm{d}t} = 0$, implying that $\lambda(t) = \lambda(0) := \lambda_0$. Let $t_2 > t_1 > 0$ be two positive times, then $\mathbf{u}$ being a Leray-Hopf solution implies that

$$\|\mathbf{u}^\perp(t_2)\|^2_{\mathbf{L}^2(\Omega)} + c_z\lambda(t_2)^2 + 4\nu\int_{t_1}^{t_2}\int_\Omega |\boldsymbol{\epsilon}(\mathbf{u})|^2\,\mathrm{d}\mathbf{x}\,\mathrm{d}\tau \le \|\mathbf{u}^\perp(t_1)\|^2_{\mathbf{L}^2(\Omega)} + c_z\lambda(t_1)^2,$$

where $c_z := \|\mathbf{e}_z\times\mathbf{x}\|^2_{\mathbf{L}^2(\Omega)}$. Since $\lambda(t_2) = \lambda(t_1)$, Lemma H.2.2 implies

$$\|\mathbf{u}^\perp(t_2)\|^2_{\mathbf{L}^2(\Omega)} + 4\nu K\int_{t_1}^{t_2}\|\mathbf{u}^\perp\|^2_{\mathbf{L}^2(\Omega)}\,\mathrm{d}\tau \le \|\mathbf{u}^\perp(t_1)\|^2_{\mathbf{L}^2(\Omega)}.$$

Using the Gronwall-Bellmann inequality (see Lemma H.4.1), we infer that $\|\mathbf{u}^\perp(t)\|_{\mathbf{L}^2(\Omega)} \le \|\mathbf{u}_0\|_{\mathbf{L}^2(\Omega)}\mathrm{e}^{-2\nu Kt}$.

In conclusion

$$\|\mathbf{u}(t) - \lambda_0\mathbf{e}_z\times\mathbf{x}\|_{\mathbf{L}^2(\Omega)} = \|\mathbf{u}^\perp(t)\|_{\mathbf{L}^2(\Omega)} \le \|\mathbf{u}_0\|_{\mathbf{L}^2(\Omega)}\mathrm{e}^{-2\nu Kt}.$$

This implies that the global attractor, say $\mathcal{A}$, is such that $\mathcal{A}\subset\mathcal{R}$, but since λ_0 spans $\mathbb{R}$, we conclude that $\mathcal{A} = \mathcal{R}$.

(ii) Let us consider the rigid-body rotation field $\mathbf{u} = \omega\mathbf{e}_z\times\mathbf{x} \in \mathcal{R}$. It is clear that $\{\mathbf{u}\}$ is an invariant set, i.e., $\mathbf{u}$ is a steady-state solution. Let $\mathbf{B}(\mathbf{u},\rho)\in\mathbf{H}$ be the ball centered at $\mathbf{u}$ of arbitrary radius $\rho > 0$. Let $\mathbf{v} = \mu\mathbf{e}_z\times\mathbf{x}\in\mathcal{R}$, $\mu\neq 0$, be another rigid-body rotation and assume that μ is small enough so that $\mathbf{u}+\mathbf{v}\in\mathbf{B}(\mathbf{u},\rho)$. Clearly $\mathbf{u}+\mathbf{v}$ satisfies (H.2.2), (H.2.4), (H.2.5) (recall that $\boldsymbol{\epsilon}(\mathbf{u}+\mathbf{v}) = 0$). Let us observe that $\partial_t(\mathbf{u}+\mathbf{v}) - 2\nu\nabla\cdot(\boldsymbol{\epsilon}(\mathbf{u}+\mathbf{v})) = 0$ and

$$(\mathbf{u}+\mathbf{v})\cdot\nabla(\mathbf{u}+\mathbf{v}) = 2(\mathbf{u}+\mathbf{v})\cdot\boldsymbol{\epsilon}(\mathbf{u}+\mathbf{v}) - (\mathbf{u}+\mathbf{v})\cdot(\nabla(\mathbf{u}+\mathbf{v}))^T = -\frac{1}{2}\nabla|\mathbf{u}+\mathbf{v}|^2,$$

since $\mathbf{u}+\mathbf{v}$ is a rigid-body rotation. Upon setting $p = \frac{1}{2}|\mathbf{u}+\mathbf{v}|^2$ we conclude that $\mathbf{u}+\mathbf{v}$ solves (H.2.1). This proves that $\mathbf{u}+\mathbf{v}$ is invariant (i.e., a steady-state solution). In other words $\mathbf{u}+\mathbf{v}$ does not converge to $\mathbf{u}$, no matter how small ρ is, thereby proving that the set $\{\mathbf{u}\}$ is not an attractor, no matter how large ν is. □

H.2.4 An admissible stress-free-like boundary condition

The principal motivation to consider the so-called stress-free boundary condition is that it minimizes viscous layers and is thus less computationally demanding than the no-slip boundary condition. We have seen above that it unfortunately leads to pathological stability properties when the computational domain is axisymmetric. One possible remedy to this problem is to consider the following non-symmetric boundary condition:

$$(\mathbf{n}\cdot\nabla\mathbf{u})\times\mathbf{n}_{|\Gamma} = 0. \tag{H.2.10}$$

This condition expresses that the tangent components of the normal derivative of the velocity field are zero. The physical interpretation of this condition is definitely less appealing than that of the stress-free boundary condition. However (H.2.10) and the stress-free condition are equally numerically convenient. The main advantage we see in (H.2.10) over the stress-free condition is that it yields standard stability properties, i.e., $\{0\}$ is the global attractor.

Lemma H.2.3. *The following holds for all smooth solenoidal vector field* $\mathbf{u}$ *that satisfies* $(\mathbf{n}\cdot\nabla\mathbf{u})\times\mathbf{n}_{|\Gamma}=0$*:*

$$\int_\Omega -\nabla\cdot(\boldsymbol{\epsilon}(\mathbf{u}))\cdot\mathbf{v}=\tfrac{1}{2}\int_\Omega \nabla\mathbf{u}:\nabla\mathbf{v},\qquad \forall\mathbf{v}\in\mathbf{H}^1(\Omega),\ \mathbf{v}\cdot\mathbf{n}_{|\Gamma}=0. \tag{H.2.11}$$

Proof. Upon observing that $\nabla\cdot(\boldsymbol{\epsilon}(\mathbf{u}))=\frac{1}{2}\nabla\cdot(\nabla\mathbf{u})$ since $\mathbf{u}$ is solenoidal, we infer that

$$\begin{aligned}\int_\Omega -\nabla\cdot(\boldsymbol{\epsilon}(\mathbf{u}))\cdot\mathbf{v}&=\int_\Omega -\tfrac{1}{2}\nabla\cdot(\nabla\mathbf{u})\cdot\mathbf{v}=\tfrac{1}{2}\int_\Omega\nabla\mathbf{u}:\nabla\mathbf{v}-\tfrac{1}{2}\int_\Gamma(\mathbf{n}\cdot\nabla\mathbf{u})\cdot\mathbf{v}\\&=\tfrac{1}{2}\int_\Omega\nabla\mathbf{u}:\nabla\mathbf{v}-\tfrac{1}{2}\int_\Gamma(\mathbf{n}\cdot\nabla\mathbf{u})\cdot((\mathbf{n}\cdot\mathbf{v})\mathbf{n})+\tfrac{1}{2}\int_\Gamma((\mathbf{n}\cdot\nabla\mathbf{u})\times\mathbf{n})\cdot(\mathbf{n}\times\mathbf{v})\\&=\tfrac{1}{2}\int_\Omega\nabla\mathbf{u}:\nabla\mathbf{v},\end{aligned}$$

where we used again the decomposition $\mathbf{v}_{|\Gamma}=(\mathbf{n}\cdot\mathbf{v})\mathbf{n}-\mathbf{n}\times(\mathbf{n}\times\mathbf{v})$. □

Proposition H.2.4. *Assume that* Ω *is an open, connected, bounded Lipschitz domain, then* $\{0\}$ *is the global attractor of* (H.2.1)-(H.2.2)-(H.2.3)-(H.2.10)-(H.2.5)*.*

Proof. Repeat the argument in the proof of Proposition H.2.1 using Lemma H.2.3 together with the following Poincaré-like inequality

$$K\int_\Omega\mathbf{v}^2\le\int_\Omega|\nabla\mathbf{v}|^2,\qquad\forall\mathbf{v}\in\mathbf{H}^1(\Omega),\ \mathbf{v}\cdot\mathbf{n}_{|\Gamma}=0,$$

which can be shown to hold by proceeding as in the proof of Proposition H.2.2. □

H.3 Precession driven flow with Poincaré stress

If the fluid domain is a spheroid that undergoes precession, the time-independent Navier-Stokes equations supplemented with the impenetrable condition admit a so-called Poincaré solution. We show in this section that, independently of the value of the viscosity, the Poincaré solution is not an attractor of the problem if the tangential stress at the boundary is enforced to be equal to that of the steady-state Poincaré solution.

H.3.1 Geometry and equations

The container is an ellipsoid of revolution of center O and symmetry axis Oz. The unit vector along the Oz-axis is $\mathbf{e}_z$. The unit vectors along the other two orthogonal axes Ox and Oy are $\mathbf{e}_x$ and $\mathbf{e}_y$, respectively. The surface of the spheroid is defined by the equation

$$x^2+y^2+(1+\beta)z^2=1, \tag{H.3.1}$$

where $\beta>-1$ and $\beta\neq0$. We assume that the Ox-axis is fixed in an inertial reference frame and the container rotates about the Ox-axis with angular velocity $\varepsilon\mathbf{e}_x$. The reference frame $(O,\mathbf{e}_x,\mathbf{e}_y,\mathbf{e}_z)$ is non-inertial, and the non-dimensional Navier-Stokes equations describing the motion of the fluid in this reference frame are written as follows:

$$\partial_t\mathbf{u}+\mathbf{u}\cdot\nabla\mathbf{u}-2\nu\nabla\cdot\boldsymbol{\epsilon}(\mathbf{u})+2\varepsilon\mathbf{e}_x\times\mathbf{u}+\nabla p=0, \tag{H.3.2}$$

$$\nabla\cdot\mathbf{u}=0, \tag{H.3.3}$$

$$\mathbf{u}_{|t=0}=\mathbf{u}_0. \tag{H.3.4}$$

The only inertial effect to be considered in this frame is the Coriolis force induced by the rotation about the Ox-axis. Note that the definition of the pressure has been changed to account for the centripetal acceleration, $\varepsilon\mathbf{e}_x\times(\varepsilon\mathbf{e}_x\times\mathbf{x})$. We additionally enforce the impenetrable boundary condition,

$$\mathbf{u}\cdot\mathbf{n}_{|\Gamma}=0. \tag{H.3.5}$$

The system (H.3.2)-(H.3.3)-(H.3.5) is known to admit a steady-state solution called the Poincaré flow (see e.g. [156]) whose expression is as follows:

$$\mathbf{u}_P=-y\mathbf{e}_x+\left(x-\frac{2\varepsilon}{\beta}(1+\beta)z\right)\mathbf{e}_y+\frac{2\varepsilon}{\beta}y\mathbf{e}_z. \tag{H.3.6}$$

Of course, $\mathbf{u}_P$ does not solve the Navier-Stokes system (H.3.2)-(H.3.3) equipped with the no-slip boundary condition. However, it has been shown formally in Stewartson and Roberts [138] that if the ellipsoid additionally rotates about the Oz-axis with angular velocity $\mathbf{e}_z$ and if $\nu\to 0$ and $\varepsilon\to 0$, the no-slip Navier-Stokes solution converges to $\mathbf{u}_P$ when $t\to+\infty$, except in thin Ekman layers on Γ. This result is the main reason why we are interested in the Poincaré solution.

One way to force $\mathbf{u}_P$ to be a Navier-Stokes solution consists of proceeding as in [156] and to consider the problem (H.3.2)-(H.3.3)-(H.3.5) equipped with the additional non-homogeneous boundary condition

$$(\mathbf{n}\cdot\boldsymbol{\epsilon}(\mathbf{u}))\times\mathbf{n}_{|\Gamma}=(\mathbf{n}\cdot\boldsymbol{\epsilon}(\mathbf{u}_P))\times\mathbf{n}_{|\Gamma}. \tag{H.3.7}$$

That is, we want the tangential component of the normal stress to be equal to that of the Poincaré solution. As mentioned in [156], it is clear that

Claim H.3.1 (See [156]). *$\mathbf{u}_P$ is a steady state solution of* (H.3.2)-(H.3.3)-(H.3.5)-(H.3.7).

H.3.2 Long term stability

The question that we now want to investigate is whether there is a threshold on ν beyond which $\mathbf{u}_P$ is a stable solution as $t\to+\infty$; i.e., does the flow return to $\mathbf{u}_P$ independently of the initial data as $t\to+\infty$ if ν is large enough. We show in this section that the answer to this question is no, the fundamental reason being that rigid-body rotations cannot be dampened by viscous dissipation, no matter how large ν is.

Proposition H.3.1. *(i) For all $\nu>0$, $\{\mathbf{u}_P\}$ is not an attractor of the Navier-Stokes problem* (H.3.2)-(H.3.3) *equipped with the boundary conditions* (H.3.5)-(H.3.7).
(ii) $\{\mathbf{u}_P\}+\mathcal{R}$ is the global attractor if $\varepsilon/\nu<2K$ where K is the Korn constant introduced in Lemma H.2.2, and the convergence to the attractor is exponential.

Proof. Let us first prove item (i). Let $\rho>0$ be an arbitrary positive number. Let $\mathbf{B}(\mathbf{u}_P,\rho)\subset\mathbf{H}$ be a ball of radius ρ centered at $\mathbf{u}_P$. Let $\mathbf{w}=\omega\mathbf{e}_z\times\mathbf{r}$ is a rigid-body rotation about the Oz-axis, and assume that $\omega\neq 0$ is small enough so that $\mathbf{u}_P+\mathbf{w}\in\mathbf{B}(\mathbf{u}_P,\rho)$. Let us prove that $\mathbf{u}_P+\mathbf{w}$ is a steady state solution of (H.3.2)-(H.3.3)-(H.3.5)-(H.3.7). Owing to $\boldsymbol{\epsilon}(\mathbf{w})=0$, $\mathbf{w}\cdot\mathbf{n}_{|\Gamma}=0$, $\nabla\cdot\mathbf{w}=0$, it is clear that $\mathbf{u}_P+\mathbf{w}$ is solenoidal and satisfies the boundary conditions (H.3.5)-(H.3.7). Let us now show that it is possible to find a pressure field so that the steady

state momentum equation holds. Let us first prove that $\mathbf{u}_P\cdot\nabla\mathbf{w} + \mathbf{w}\cdot\nabla\mathbf{u}_P + 2\varepsilon\mathbf{e}_x\times\mathbf{w}$ is a gradient. A straightforward computation gives:

$$\mathbf{u}_P\cdot\nabla\mathbf{w} = \omega\begin{pmatrix}\frac{2\varepsilon}{\beta}(1+\beta)z - x\\ -y\\ 0\end{pmatrix},\quad \mathbf{w}\cdot\nabla\mathbf{u}_P = \omega\begin{pmatrix}-x\\ -y\\ \frac{2\varepsilon}{\beta}x\end{pmatrix},\quad 2\varepsilon\mathbf{e}_x\times\mathbf{w} = \omega\begin{pmatrix}0\\ 0\\ 2\varepsilon x\end{pmatrix},$$

so that

$$\mathbf{u}_P\cdot\nabla\mathbf{w} + \mathbf{w}\cdot\nabla\mathbf{u}_P + 2\varepsilon\mathbf{e}_x\times\mathbf{w} = -\nabla\left(\omega(x^2+y^2)\right) + \nabla\left(\frac{2\varepsilon\omega}{\beta}(1+\beta)xz\right). \tag{H.3.8}$$

Let us then define $q(\mathbf{x}) := -\omega(x^2+y^2)+\frac{2\varepsilon\omega}{\beta}(1+\beta)xz$. Observe that we can define the pressure field $r(\mathbf{x})$ so that $\nabla r := -\mathbf{u}_P\cdot\nabla\mathbf{u}_P - 2\varepsilon\mathbf{e}_x\times\mathbf{u}_P$, since $\mathbf{u}_P$ solves (H.3.2). Let us finally observe that

$$\mathbf{w}\cdot\nabla\mathbf{w} = -\frac{1}{2}\nabla|\mathbf{w}|^2. \tag{H.3.9}$$

Then we conclude that $\mathbf{u}_P + \mathbf{w}$ solves (H.3.2) with $p = q + r - \frac{1}{2}|\mathbf{w}|^2$. In particular if we set $\mathbf{u}_0 = \mathbf{u}_P + \mathbf{w}$, then $\mathbf{u}_P + \mathbf{w}$ remains a solution forever, i.e., the solution does not converge to $\mathbf{u}_P$ as $t\to+\infty$, no matter how small ρ is and no matter how large ν is. This proves that although $\{\mathbf{u}_P\}$ is an invariant set, it is not an attracting set.

We now prove item (ii). Let $\mathbf{u}\in L^2((0,+\infty);\mathbf{L}^2(\Omega))\cap L^\infty((0,+\infty);\mathbf{H}^1(\Omega))$ be a Leray-Hopf solution of (H.3.2)-(H.3.3)-(H.3.5)-(H.3.7). Similarly to what has been done in the proof of Proposition H.2.3 we consider the following decomposition

$$\mathbf{u}(t) - \mathbf{u}_P = \mathbf{u}^\perp(t) + \lambda(t)\mathbf{e}_z\times\mathbf{x},\ \text{where } \mathbf{u}^\perp(t)\in\mathcal{R}^\perp,\ \lambda(t)\in\mathbb{R},\ \forall t\in[0,+\infty),$$

and let us denote $\mathbf{w} = \lambda(t)\mathbf{e}_z\times\mathbf{x}$. Upon testing the momentum equation with $\mathbf{u}^\perp(t)$ we formally obtain:

$$\frac{1}{2}\|\mathbf{u}^\perp(t_2)\|^2_{\mathbf{L}^2(\Omega)} - \frac{1}{2}\|\mathbf{u}^\perp(t_1)\|^2_{\mathbf{L}^2(\Omega)} + 2\nu\int_{t_1}^{t_2}\|\boldsymbol{\epsilon}(\mathbf{u}^\perp(t))\|^2_{\mathbf{L}^2(\Omega)}\,\mathrm{d}t$$
$$+\int_{t_1}^{t_2}\int_\Omega\left((\mathbf{u}-\mathbf{u}_P)\cdot\nabla\mathbf{u} + \mathbf{u}_P\cdot\nabla(\mathbf{u}-\mathbf{u}_P) + 2\varepsilon\mathbf{e}_x\times(\mathbf{u}-\mathbf{u}_P)\right)\cdot\mathbf{u}^\perp(t)\,\mathrm{d}\mathbf{x}\,\mathrm{d}t \le 0,$$

A rigorous proof would require a passage to the limit à la Sell [132, §2.3]. Using the decomposition $\mathbf{u}-\mathbf{u}_P = \mathbf{u}^\perp + \mathbf{w}$ together with (H.3.8) and (H.3.9), we obtain

$$\frac{1}{2}\|\mathbf{u}^\perp(t_2)\|^2_{\mathbf{L}^2(\Omega)} - \frac{1}{2}\|\mathbf{u}^\perp(t_1)\|^2_{\mathbf{L}^2(\Omega)} + 2K\nu\int_{t_1}^{t_2}\|\mathbf{u}^\perp(t)\|^2_{\mathbf{L}^2(\Omega)}\,\mathrm{d}t$$
$$+\int_{t_1}^{t_2}\int_\Omega\left(\mathbf{u}^\perp(t)\cdot\nabla(\mathbf{u}_P+\mathbf{w})\cdot\mathbf{u}^\perp(t)\right)\mathrm{d}\mathbf{x}\,\mathrm{d}t \le 0.$$

Using that $\mathbf{v}\cdot\nabla\mathbf{w}\cdot\mathbf{v} = 0$ for any vector field $\mathbf{v}$, we finally infer the following energy estimate:

$$\frac{1}{2}\|\mathbf{u}^\perp(t_2)\|^2_{\mathbf{L}^2(\Omega)} - \frac{1}{2}\|\mathbf{u}^\perp(t_1)\|^2_{\mathbf{L}^2(\Omega)} + 2K\nu\int_{t_1}^{t_2}\|\mathbf{u}^\perp(t)\|^2_{\mathbf{L}^2(\Omega)}\,\mathrm{d}t$$
$$-2\varepsilon\int_{t_1}^{t_2}\int_\Omega u_y^\perp(t)u_z^\perp(t)\,\mathrm{d}\mathbf{x}\,\mathrm{d}t \le 0,$$

where we used $\mathbf{v}\cdot\nabla\mathbf{u}_P\cdot\mathbf{v} = -2\varepsilon v_y v_z$ for any vector field $\mathbf{v}$. Then using Lemma H.4.1 and assuming that $\varepsilon/\nu < 2K$, we conclude that $\|\mathbf{u}^\perp(t)\|^2_{\mathbf{L}^2(\Omega)} \leq \|\mathbf{u}_0^\perp\|^2_{\mathbf{L}^2(\Omega)} e^{-2(2K\nu-\varepsilon)t}$. Using (H.3.13), we deduce that

$$(\lambda(t_2)-\lambda(t_1))\int_\Omega(\mathbf{e}_z\times\mathbf{x})^2 = -\varepsilon\int_{t_1}^{t_2}\int_\Omega \mathbf{e}_y\cdot(\mathbf{x}\times(\lambda(\tau)(\mathbf{e}_z\times\mathbf{x})+\mathbf{u}^\perp)).$$

But Lemma H.3.2 implying that

$$\begin{aligned}\int_\Omega \mathbf{e}_y\cdot(\mathbf{x}\times(\lambda(\tau)(\mathbf{e}_z\times\mathbf{x}))) &= \lambda(\tau)\int_\Omega \mathbf{e}_y\cdot(\mathbf{x}\times(\mathbf{e}_z\times\mathbf{x}))\\ &= 2\lambda(\tau)\int_\Omega(\mathbf{e}_z\times\mathbf{x})\cdot(\mathbf{e}_x\times(\mathbf{e}_z\times\mathbf{x})) = 0,\end{aligned}$$

we finally infer that

$$|\lambda(t_2)-\lambda(t_1)|\int_\Omega(\mathbf{e}_z\times\mathbf{x})^2 \leq \varepsilon\int_{t_1}^{t_2}\int_\Omega|\mathbf{e}_y\cdot(\mathbf{x}\times\mathbf{u}^\perp)| \leq c\mu^{-1}\left(e^{-\mu t_1}-e^{-\mu t_2}\right),$$

where c is a generic constant and $\mu := 2K\nu-\varepsilon$. This immediately implies that $\lambda(t)$ converges exponentially to a constant. In conclusion $\mathbf{u}(t)-\mathbf{u}_P$ converges exponentially fast to an element in $\mathcal{R}$ as t tends to infinity. □

Remark H.3.1. *Proposition H.3.1 is the generalization of Proposition H.2.3 with $\varepsilon \neq 0$. Item (ii) of Proposition H.3.1 is similar in spirit to the result of Stewartson and Roberts [138].*

H.3.3 Angular momentum balance

Let us now mention a result on the balance of the angular momentum. Let us assume that $\mathbf{u}$ solves (H.3.2)-(H.3.3) with the boundary conditions

$$\mathbf{n}\cdot\mathbf{u} = 0 \qquad \text{on } \Gamma, \tag{H.3.10}$$

$$(\mathbf{n}\cdot\boldsymbol{\epsilon}(\mathbf{u}))\times\mathbf{n} = \mathbf{g}\times\mathbf{n} \qquad \text{on } \Gamma, \tag{H.3.11}$$

where the field $\mathbf{g}$ is a boundary data. Let us now define the angular momentum

$$\mathbf{M} := \int_\Omega \mathbf{x}\times\mathbf{u}. \tag{H.3.12}$$

Lemma H.3.1. *Denoting by M_z and M_y the z- and y-component of $\mathbf{M}$, respectively, all the weak solutions of* (H.3.2)-(H.3.3)-(H.3.10)-(H.3.11) *satisfy*

$$\partial_t M_z + \varepsilon M_y = -\int_\Gamma \nu(\mathbf{g}\times\mathbf{n})\cdot((\mathbf{e}_z\times\mathbf{x})\times\mathbf{n}), \qquad \text{a.e. } t\in(0,+\infty). \tag{H.3.13}$$

Proof. Observing that $M_z = \int_\Omega(\mathbf{e}_z\times\mathbf{x})\cdot\mathbf{u}$, we multiply (H.3.2) by $\mathbf{e}_z\times\mathbf{x}$ and integrate over Ω. Using the divergence free condition together with (H.3.10) and integrating by parts, we infer that

$$\int_\Omega(\mathbf{e}_z\times\mathbf{x})\cdot(\mathbf{u}\cdot\nabla\mathbf{u}) = \int_\Omega\nabla\cdot(\mathbf{u}\otimes\mathbf{u})\cdot(\mathbf{e}_z\times\mathbf{x}) = \int_\Gamma(\mathbf{u}\cdot\mathbf{n})\,(\mathbf{u}\cdot(\mathbf{e}_z\times\mathbf{x})) = 0,$$

where we used that $(\mathbf{u}\otimes\mathbf{u})$:$\nabla(\mathbf{e}_z\times\mathbf{x})=0$ since the matrix $\mathbf{u}\otimes\mathbf{u}$ is symmetric and $\nabla(\mathbf{e}_z\times\mathbf{x})$ is anti-symmetric. The same argument applies to the viscous term

$$\int_\Omega(\mathbf{e}_z\times\mathbf{x})\cdot\nu\nabla\cdot(\boldsymbol{\epsilon}(\mathbf{u}))=\int_\Gamma\nu(\boldsymbol{\epsilon}(\mathbf{u})\cdot\mathbf{n})\cdot(\mathbf{e}_z\times\mathbf{x})=\int_\Gamma\nu(\mathbf{g}\times\mathbf{n})\cdot((\mathbf{e}_z\times\mathbf{x})\times\mathbf{n}),$$

where we used $\mathbf{e}_z\times\mathbf{x}=(\mathbf{e}_z\times\mathbf{x})\times\mathbf{n}$ since $(\mathbf{e}_z\times\mathbf{x})\cdot\mathbf{n}_{|\Gamma}=0$. The same argument applies again for the pressure term since $\nabla p=\nabla\cdot(pI)$ where I is the identity matrix.

$$\int_\Omega(\mathbf{e}_z\times\mathbf{x})\cdot\nabla p=\int_\Gamma p(\mathbf{e}_z\times\mathbf{x})\cdot\mathbf{n}=0.$$

We now deal with the Coriolis term by applying Lemma H.3.2:

$$\int_\Omega(\mathbf{e}_z\times\mathbf{x})\cdot(\mathbf{e}_x\times\mathbf{u})=\frac{1}{2}\int_\Omega\mathbf{e}_y\cdot(\mathbf{x}\times\mathbf{u})=\frac{1}{2}M_y.$$

The conclusion follows readily. □

Lemma H.3.2. *Let $\mathbf{v}\in\mathbf{L}^1(\Omega)$ be an integrable vector field such that $\nabla\cdot\mathbf{v}=0$ and $\mathbf{v}\cdot\mathbf{n}_{|\Gamma=0}$, then*

$$\int_\Omega\mathbf{e}_y\cdot(\mathbf{x}\times\mathbf{v})=2\int_\Omega(\mathbf{e}_z\times\mathbf{x})\cdot(\mathbf{e}_x\times\mathbf{v}). \tag{H.3.14}$$

Proof. Let us first observe that $\int_\Omega(\mathbf{e}_z\times\mathbf{x})\cdot(\mathbf{e}_x\times\mathbf{v})=-\int_\Omega xv_z$. Noticing that $\int_\Omega xv_z+zv_x=\int_\Omega\mathbf{v}\cdot\nabla(zx)=0$ since $\nabla\cdot\mathbf{v}=0$ and $\mathbf{v}\cdot\mathbf{n}_{|\Gamma}=0$, we infer that

$$\int_\Omega(\mathbf{e}_z\times\mathbf{x})\cdot(\mathbf{e}_x\times\mathbf{v})=-\int_\Omega xv_z=\frac{1}{2}\int_\Omega zv_x-xv_z=\frac{1}{2}\int_\Omega\mathbf{e}_y\cdot(\mathbf{x}\times\mathbf{v}),$$

which concludes the proof. □

Remark H.3.2. *If we choose $\mathbf{g}=\boldsymbol{\epsilon}(\mathbf{u}_P)\cdot\mathbf{n}$ like in* (H.3.7)*, then $-\int_\Gamma\nu(\mathbf{g}\times\mathbf{n})\cdot((\mathbf{e}_z\times\mathbf{x})\times\mathbf{n})$ is equal to $-\int_\Omega(\mathbf{e}_z\times\mathbf{x})\cdot\nu\nabla\cdot(\boldsymbol{\epsilon}(\mathbf{u}_P))=0$ and the balance equation of the angular momentum in the z direction simplifies to $\partial_tM_z+\varepsilon M_y=0$.*

Remark H.3.3. *Note that* (H.3.13) *is just a consequence of* (H.3.2)-(H.3.3)-(H.3.10)-(H.3.11)*. This balance holds whether the long term stability of* (H.3.2)-(H.3.3)-(H.3.10)-(H.3.11) *is spurious or not. It is false to consider that* (H.3.13) *is an additional equation that fixes the long term stability behavior of the system.*

H.4 Precession driven flow with stress-free boundary conditions

We show in this section that if we enforce $(\mathbf{n}\cdot\boldsymbol{\epsilon}(\mathbf{u}))\times\mathbf{n}_{|\Gamma}=0$, instead of enforcing $(\mathbf{n}\cdot\boldsymbol{\epsilon}(\mathbf{u}))\times\mathbf{n}_{|\Gamma}=(\mathbf{n}\cdot\boldsymbol{\epsilon}(\mathbf{u}_P))\times\mathbf{n}_{|\Gamma}$ in (H.3.2)-(H.3.3)-(H.3.10), then 0 becomes the unique stable solution as $t\to+\infty$, i.e., $\{0\}$ is the global attractor.

H.4.1 Long time stability

The setting of the problem is the same as in Section H.3.1 except that we enforce the tangential component of the normal stress to be zero at the boundary.

$$\partial_t \mathbf{u} + \mathbf{u}\cdot\nabla\mathbf{u} - 2\nu\nabla\cdot\boldsymbol{\epsilon}(\mathbf{u}) + 2\varepsilon\mathbf{e}_x\times\mathbf{u} + \nabla p = 0 \qquad \text{in } \Omega \tag{H.4.1}$$

$$\nabla\cdot\mathbf{u} = 0 \qquad \text{in } \Omega \tag{H.4.2}$$

$$\mathbf{n}\cdot\mathbf{u} = 0 \qquad \text{on } \Gamma \tag{H.4.3}$$

$$(\mathbf{n}\cdot\boldsymbol{\epsilon}(\mathbf{u}))\times\mathbf{n} = 0 \qquad \text{on } \Gamma \tag{H.4.4}$$

$$\mathbf{u}_{|t=0} = \mathbf{u}_0 \qquad \text{in } \Omega. \tag{H.4.5}$$

The result that we want to emphasize is that contrary to what we observed in Section H.3, 0 becomes the unique stable solution of (H.4.1)–(H.4.5) as $t \to +\infty$. The main result that we want to prove here is that any solution of the system (H.4.1)-(H.4.4) returns to rest as $t \to +\infty$. This fact has been mentioned in [156] without proof. The key argument is that rigid-body rotations about the Oz axis are not stationary solutions of (H.4.1).

Theorem H.4.1. $\{0\}$ *is the global attractor of* (H.4.1)–(H.4.5).

Proof. Let us start by observing that $\{0\}$ is indeed an invariant set of (H.4.1)–(H.4.5). Let $\mathbf{B}(0,\rho)$ be the unit ball in $\mathbf{H}$ centered at 0 and of radius ρ. Let $\mathbf{u}_0 \in \mathbf{B}(0,\rho)$ and let $\mathbf{u} \in L^2((0,+\infty);\mathbf{L}^2(\Omega)) \cap L^\infty((0,+\infty);\mathbf{H}^1(\Omega))$ be a Leray-Hopf solution of (H.4.1)–(H.4.5) and consider the following decomposition:

$$\mathbf{u}(t) = \mathbf{u}^\perp(t) + \lambda(t)\mathbf{e}_z\times\mathbf{x}, \text{ where } \mathbf{u}^\perp(t) \in \mathcal{R}^\perp, \ \lambda(t) \in \mathbb{R}, \ \forall t \in [0,+\infty).$$

Lemma H.2.2 together with $\mathbf{u}$ being a Leray-Hopf solution implies that

$$\|\mathbf{u}^\perp(t)\|^2_{\mathbf{L}^2(\Omega)} + c_z\lambda(t)^2 + 4\nu K\int_0^t \|\mathbf{u}^\perp(\tau)\|^2_{\mathbf{L}^2(\Omega)}\,\mathrm{d}\tau \le \|\mathbf{u}_0\|^2_{\mathbf{L}^2(\Omega)}.$$

where $c_z = \|\mathbf{e}_z\times\mathbf{x}\|^2_{\mathbf{L}^2}$ (recall $t \longmapsto \mathbf{u}(t)$ is continuous in the $\mathbf{L}^2$-weak topology). Let $t_2 > t_1$ in $(0,+\infty)$, then (H.3.13) means that

$$|\lambda(t_2) - \lambda(t_1)|\int_\Omega (\mathbf{e}_z\times\mathbf{x})^2 \le \varepsilon\int_{t_1}^{t_2}\int_\Omega |(\mathbf{e}_y\times\mathbf{x})\cdot\mathbf{u}| \le \varepsilon|t_2-t_1|\|\mathbf{u}_0\|_{\mathbf{L}^2}\|(\mathbf{e}_y\times\mathbf{x})\|_{\mathbf{L}^2},$$

thereby proving that $t \longmapsto \lambda(t)$ is uniformly Lipschitz over $(0,+\infty)$. Since $\mathbf{u}$ is a Leray-Hopf solution we also have

$$\|\mathbf{u}^\perp(t_2)\|^2_{\mathbf{L}^2} - \|\mathbf{u}^\perp(t_1)\|^2_{\mathbf{L}^2} + (\lambda(t_2)^2 - \lambda(t_1)^2)\|\mathbf{e}_z\times\mathbf{x}\|^2_{\mathbf{L}^2} + 4\nu\int_{t_1}^{t_2}\int_\Omega |\boldsymbol{\epsilon}(\mathbf{u})|^2 \le 0.$$

This in turn implies that

$$\begin{aligned}\frac{\|\mathbf{u}^\perp(t_2)\|^2_{\mathbf{L}^2} - \|\mathbf{u}^\perp(t_1)\|^2_{\mathbf{L}^2}}{t_2-t_1} &\le (|\lambda(t_2)+\lambda(t_1)|)\frac{|\lambda(t_2)-\lambda(t_1)|}{|t_2-t_1|}\|\mathbf{e}_z\times\mathbf{x}\|^2_{\mathbf{L}^2}\\ &\le 2\varepsilon\|\mathbf{u}_0\|^2_{\mathbf{L}^2}\|\mathbf{e}_y\times\mathbf{x}\|_{\mathbf{L}^2}\|\mathbf{e}_z\times\mathbf{x}\|^{-1}_{\mathbf{L}^2} =: \gamma.\end{aligned}$$

In conclusion the function $t \longmapsto \|\mathbf{u}^\perp(t)\|^2_{\mathbf{L}^2}$ satisfies the assumptions of Lemma H.4.2. We then infer that $\|\mathbf{u}^\perp\|_{L^\infty((t,+\infty);\mathbf{L}^2)} \to 0$ as $t \to +\infty$.

Let $\delta > 0$ be an arbitrarily small number. Let t_δ be so that $\|\mathbf{u}^\perp\|_{L^\infty((t,+\infty);\mathbf{L}^2)} \leq \delta$ for all $t \geq t_\delta$. Let $t_2 > t_1 \geq t_\delta$ in $(0,+\infty)$ then the energy balance implies

$$\|\mathbf{u}^\perp(t_2)\|^2_{\mathbf{L}^2} + c_z\lambda(t_2)^2 \leq \|\mathbf{u}^\perp(t_1)\|^2_{\mathbf{L}^2} + c_z\lambda(t_1)^2,$$

which also gives

$$\lambda(t_2)^2 \leq \lambda(t_1)^2 + 2c_z^{-1}\delta^2.$$

Lemma H.4.3 in turn implies that $\lambda(t)$ converges to real a number λ_∞ as t goes to infinity, since λ is a continuous function. Using (H.3.13) again, we infer that

$$(\lambda(t_2) - \lambda(t_1)) \int_\Omega (\mathbf{e}_z \times \mathbf{x})^2 = -\varepsilon \int_{t_1}^{t_2} \int_\Omega \mathbf{e}_y \cdot (\mathbf{x} \times (\lambda(\tau)(\mathbf{e}_z \times \mathbf{x}) + \mathbf{u}^\perp)).$$

But Lemma H.3.2 implying that

$$\begin{aligned}\int_\Omega \mathbf{e}_y \cdot (\mathbf{x} \times (\lambda(\tau)(\mathbf{e}_z \times \mathbf{x}))) &= \lambda(\tau) \int_\Omega \mathbf{e}_y \cdot (\mathbf{x} \times (\mathbf{e}_z \times \mathbf{x})) \\ &= 2\lambda(\tau) \int_\Omega (\mathbf{e}_z \times \mathbf{x}) \cdot (\mathbf{e}_x \times (\mathbf{e}_z \times \mathbf{x})) = 0,\end{aligned}$$

we finally infer that

$$|\lambda(t_2) - \lambda(t_1)| \int_\Omega (\mathbf{e}_z \times \mathbf{x})^2 \leq \varepsilon \int_{t_1}^{t_2} \int_\Omega |\mathbf{e}_y \cdot (\mathbf{x} \times \mathbf{u}^\perp)| \leq c\delta |t_2 - t_1|,$$

where c is a generic constant that depends on Ω and may vary at each occurrence from now on. Let us take $\boldsymbol{\varphi} \in \boldsymbol{\mathcal{D}}(\Omega)$ independent of time and divergence-free. Since $\mathbf{u}$ is a Leray solution we have

$$\begin{aligned}0 = &\int_\Omega (\mathbf{u}(t_2, \mathbf{x}) - \mathbf{u}(t_1, \mathbf{x})) \cdot \boldsymbol{\varphi}(\mathbf{x}) \, \mathrm{d}\mathbf{x} + \int_{t_1}^{t_2} \int_\Omega 2\varepsilon \mathbf{u}(\tau, \mathbf{x}) \cdot (\boldsymbol{\varphi}(\mathbf{x}) \times \mathbf{e}_x) \, \mathrm{d}\mathbf{x} \, \mathrm{d}\tau \\ &- \int_{t_1}^{t_2} \int_\Omega 2\nu \mathbf{u}(\tau, \mathbf{x}) \cdot \nabla \cdot \boldsymbol{\epsilon}(\boldsymbol{\varphi}) \, \mathrm{d}\mathbf{x} \, \mathrm{d}\tau - \int_{t_1}^{t_2} \int_\Omega (\mathbf{u}(\mathbf{x}) \otimes \mathbf{u}(\mathbf{x})) : \nabla \boldsymbol{\varphi}(\mathbf{x}) \mathrm{d}\mathbf{x} \, \mathrm{d}\tau.\end{aligned}$$

Let us now set $t_2 = t_1 + 1$. Upon observing that $\int_\Omega ((\mathbf{e}_z \times \mathbf{x}) \otimes (\mathbf{e}_z \times \mathbf{x})) : \nabla \boldsymbol{\varphi}(\mathbf{x}) \mathrm{d}\mathbf{x} = 0$ and $\int_\Omega (\mathbf{e}_z \times \mathbf{x}) \cdot \nabla \cdot \boldsymbol{\epsilon}(\boldsymbol{\varphi}) \, \mathrm{d}\mathbf{x} = 0$. This implies that there is a constant $c(\boldsymbol{\varphi}) \geq 0$ so that

$$\begin{aligned}2\varepsilon \left| \int_{t_1}^{t_2} \lambda(\tau) \, \mathrm{d}\tau \int_\Omega (\mathbf{e}_z \times \mathbf{x}) \cdot (\boldsymbol{\varphi}(\mathbf{x}) \times \mathbf{e}_x) \, \mathrm{d}\mathbf{x} \right| \leq &\left| (\lambda(t_2) - \lambda(t_1)) \int_\Omega (\mathbf{e}_z \times \mathbf{x}) \cdot \boldsymbol{\varphi}(\mathbf{x}) \, \mathrm{d}\mathbf{x} \right| \\ &+ c(\boldsymbol{\varphi})\delta.\end{aligned}$$

Let us choose $\boldsymbol{\varphi}$ so that $2\varepsilon \int_\Omega (\mathbf{e}_z \times \mathbf{x}) \cdot (\boldsymbol{\varphi}(\mathbf{x}) \times \mathbf{e}_x) \, \mathrm{d}\mathbf{x} = 1$. The above estimate implies that

$$\left| \int_{t_1}^{t_1+1} \lambda(\tau) \, \mathrm{d}\tau \right| \leq c(\boldsymbol{\varphi})\delta.$$

This implies that $\lambda_\infty = \lim_{t_1 \to \infty} \int_{t_1}^{t_1+1} \lambda(\tau) \, \mathrm{d}\tau \leq c(\boldsymbol{\varphi})\delta$, which means that $\lambda_\infty = 0$. In conclusion

$$\lim_{t \to +\infty} \|\mathbf{u}\|_{L^\infty((t,+\infty);\mathbf{L}^2)} = 0, \tag{H.4.6}$$

which concludes the proof. □

H.4.2 Useful lemmas

We start by recalling a standard version of the Gronwall-Bellman inequality.

Lemma H.4.1. *Let $u \in L^\infty((0,T);\mathbb{R}_+)$ and assume that u is lower-semi-continuous and there exists $\lambda \in \mathbb{R}$ so that the following holds*

$$u(t_2) + \lambda \int_{t_1}^{t_2} u(\tau)\,\mathrm{d}\tau \leq u(t_1), \qquad \forall t_2 > t_1 > 0,$$

then

$$0 \leq u(t) \leq u(0)e^{-\lambda t}, \qquad \forall t \in [0,T]. \tag{H.4.7}$$

Lemma H.4.2. *Let $\alpha \in L^1((0,+\infty);\mathbb{R}_+)$ be an nonnegative integrable function. Assume that there exists a constant β so that*

$$\operatorname{ess\,sup}_{t\neq\tau} \frac{\alpha(t)-\alpha(\tau)}{t-\tau} \leq \gamma, \tag{H.4.8}$$

then $\lim_{t\to+\infty} \|\alpha\|_{L^\infty((t,+\infty);\mathbb{R}_+)} = 0$.

Proof. Let $M = \{t > 0, \operatorname{ess\,sup}_{t\neq\tau} \frac{\alpha(t)-\alpha(\tau)}{t-\tau} < +\infty\}$ and for all $t \in M$ let $M_t = \{\tau > 0, \sup_{t\neq\tau} \frac{\alpha(t)-\alpha(\tau)}{t-\tau} < +\infty\}$. Note that $\mathrm{meas}(\mathbb{R}_+\backslash M) = 0$ and $\mathrm{meas}(\mathbb{R}_+\backslash M_t) = 0$. Let us proceed by contradiction. Assume that there exists $c > 0$ so that for all $t > 0$, $\|\alpha\|_{L^\infty((t,+\infty);\mathbb{R}_+)} \geq c$. Let us set $t_0 = 0$. Since α is integrable, there is a set $A_1^* \subset (t_0+1,+\infty)$ of positive measure and diameter 1 so that $\alpha(\tau) \leq \frac{1}{2}c$, for all τ in A_1^*. Let $t_1^* \in A_1^* \cap M$ (note that this set cannot be empty). Then, there is set $A_1 \subset (t_1^*+1,\infty)$ of positive measure and diameter 1 so that $\alpha(\tau) \geq \frac{3}{4}c$, for all τ in A_1. Let $t_1 \in A_1 \cap M_{t_1^*}$ (note that this set cannot be empty). By repeating the above argument we construct an increasing sequence $t_1^* < t_1 < t_2^* < t_2 < \ldots$ Note that the hypothesis $(\alpha(t_i)-\alpha(t_i^*))/(t_i-t_i^*) \leq \gamma$ implies that $t_i - t_i^* \geq c/(4\gamma)$ for all $i \geq 1$. Let us consider the time $\widehat{t}_i := t_i - c/4\gamma \geq t_i^* > t_{i-1}$. The following holds owing to (H.4.8)

$$\frac{c}{2} \leq \frac{3c}{4} - \frac{c}{4} \leq \alpha(t_i) - \gamma(t_i-\tau) \leq \alpha(\tau), \qquad \text{a.e. } \tau \in (\widehat{t}_i, t_i).$$

This means that $\int_{\widehat{t}_i}^{t_i} \alpha(\tau)\,\mathrm{d}\tau \geq \frac{c^2}{8\gamma}$ for all $\widehat{t}_i$, which contradicts the fact that α is integrable. □

Lemma H.4.3. *Let $\psi \in \mathcal{C}^0([0,+\infty);\mathbb{R}_+)$ so that for all $\delta > 0$ there is $t_\delta \geq 0$ so that for all $t_2 \geq t_1 \geq t_\delta$, $\psi(t_1) + \delta \geq \psi(t_2)$, then $\psi(t)$ converges to a finite limit as t goes to infinity.*

Proof. Let $\overline{\psi} := \limsup_{t\geq 0} \psi(t)$ and $\underline{\psi} := \liminf_{t\geq 0} \psi(t)$. Let $\delta > 0$ be a positive real number. There are $t_1 \geq t_\delta$ and $t_2 \geq t_1 \geq t_\delta$ so that

$$\psi(t_1) \leq \underline{\psi} + \delta, \qquad \text{and} \qquad \overline{\psi} - \delta \leq \psi(t_2),$$

which in turn implies that

$$\overline{\psi} - \delta \leq \psi(t_2) \leq \psi(t_1) + \delta \leq \underline{\psi} + 2\delta.$$

In conclusion $\overline{\psi} \leq \underline{\psi} + 3\delta$, which implies $\overline{\psi} = \underline{\psi}$ since δ is arbitrary. This completes the proof. □

H.5 Numerical illustrations

We now illustrate the mathematical results from §H.3-§H.4 by performing numerical simulations with the geometry used in [156]. The simulations are performed using the SFEMaNS code [67] which has been extensively validated on precession flows [114]. The authors of [156] study the dynamo action in an oblate spheroid defined by equation (H.3.1) with $\beta = 0.5625$ (this corresponds to the value $b = 0.8$ for the semi-minor axis used in [156], $b := (1+\beta)^{-\frac{1}{2}}$). This spheroid rotates about the Oz-axis and precesses about the Ox-axis with a precession rate ε. Two sets of boundary conditions are considered: either the homogeneous stress-free boundary or the Poincaré stress condition is enforced. The normalization is done so that the Reynolds number is equal to ν^{-1}.

H.5.1 Stress-free boundary condition

The first simulation solves the equations (H.4.1)-(H.4.2)-(H.4.3)-(H.4.4) with stress-free boundary conditions using the initial data $\mathbf{u}_{|t=0} = 0.1\mathbf{e}_z \times \mathbf{x} = 0.1(-y\mathbf{e}_x + x\mathbf{e}_y)$. The normalized viscosity is $\nu = 0.024$ and the precession rate is $\varepsilon = 0.25$ as in [156]. The left panel in Figure H.1 shows the time derivative of the total energy $E_K = \frac{1}{2}\|\mathbf{u}\|^2_{\mathbf{L}^2}$ in the precessing frame. Note that $\partial_t E_K$ is always negative, establishing that E_K is a decreasing function. This graph is in excellent agreement with figure 1(a) of [156]. It also shows that $\mathbf{u} \to 0$ as $t \to \infty$ in agreement with (H.4.6) (i.e., $\{0\}$ is indeed the global attractor). The right panel in the figure shows the time derivative of the angular momentum along the Oz-axis and the quantity $50(\partial_t M_z + \varepsilon M_y)$ evaluated numerically at each time step (see Lemma H.3.1). We observe that $\partial_t M_z + \varepsilon M_y$ is zero up to truncation errors as expected. This graph is also in excellent agreement with figure 1(b) of [156].

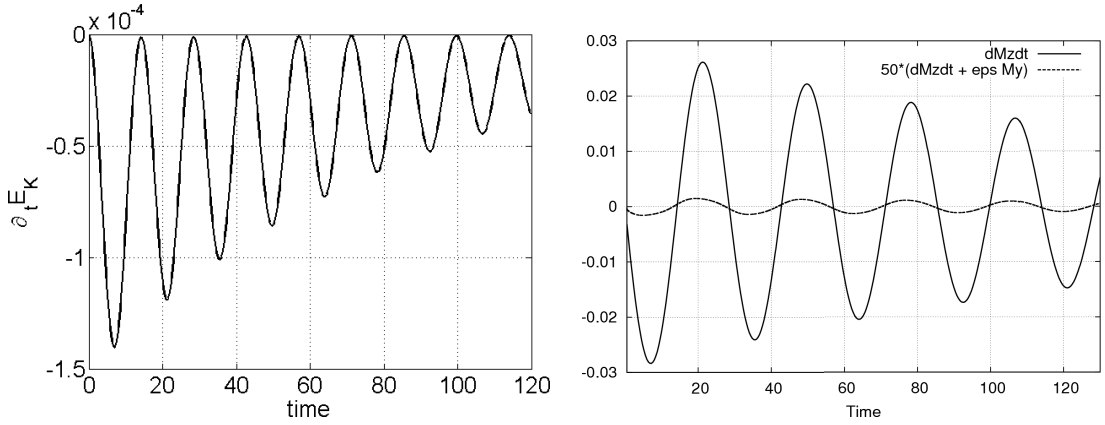

Figure H.1: Precessing spheroid with $\beta = 0.5625$, $\varepsilon = 0.25$ and $\nu = 0.024$ with the stress-free boundary condition (solution of (H.4.1)-(H.4.2)-(H.4.3)-(H.4.4)): (left) time evolution of $\partial_t E_K$ of the solution, (right) time evolution of $\partial_t M_z$ and $50(\partial_t M_z + \varepsilon M_y)$.

H.5.2 Poincaré stress boundary condition

Small Reynolds number flows

The second series of simulations solves equations (H.3.2)-(H.3.3)-(H.3.5)-(H.3.7) with the Poincaré stress boundary condition using different initial data and with the precession rate $\varepsilon = 0.025$. This precession rate is chosen so that ε/ν is small. The spatial resolution of the meridian mesh is 1/40, and 16 Fourier modes are used in the azimuthal direction. We test two different perturbations denoted PERT1 and PERT2. PERT1 corresponds to the initial condition $\mathbf{u}_0 = \mathbf{u}_P + (1 + \text{rand}(r,z))\mathbf{e}_z \times \mathbf{x}$ where $\mathbf{u}_P$ is the Poincaré solution and rand(r,z) is a random function of amplitude in the range $[-0.5, 0.5]$. PERT2 corresponds to the initial condition $\mathbf{u}_0 = \mathbf{u}_P + \mathbf{e}_z \times \mathbf{x} + \mathbf{v}$ where $\mathbf{v}$ is a perturbation without rigid-body rotation, $\mathbf{v}(r,\theta,z) = (\frac{r}{2}\sin(\theta), r\cos(\theta), 0)$, where (r,θ,z) are the cylindrical coordinates about the Oz-axis. The y- and z-components of the angular momentum of the initial data of PERT1 are $(0, 2.67842046)$. The y- and z-components of the angular momentum of the initial data of PERT2 are $(0, 2.68077560)$. The z-component of the angular momentum is a measure of the rigid-body rotation of the initial data. Note that the z-component of the angular momentum of the initial data of PERT2 is the same as that of the rigid-body rotation $2\mathbf{e}_z \times \mathbf{x}$. We show in Figures H.2 the time evolution of the quantities $\delta E_K = \frac{1}{2}\|\mathbf{u} - \mathbf{u}_P\|^2_{\mathbf{L}^2(\Omega)}$ and $\|\mathbf{u}^\perp(t)\|_{\mathbf{L}^2(\Omega)}$ and of the y- and z- components of the angular momentum (denoted M_y and M_z in the figures, respectively). The two solutions tend to two different steady states with two different rigid-body rotations about the Oz-axis, and these rigid-body rotations are different from those of the initial data (see figure H.2(d)). This is due to the fact that, even if the y-component of the angular momentum of the initial data is zero for both initial data, the angular momentum balance implies that the y-component of the angular momentum departs from zero when $t > 0$, thereby perturbing the z-component of the angular momentum via the conservation equation $\partial_t M_z + \varepsilon M_y = 0$ (see figure H.2(c)). The velocity component $\mathbf{u}^\perp$ of the two steady states is zero as expected, up to truncation errors induced by the space discretization, (see figure H.2(b)). These results illustrate the fact that, provided ε/ν is mall enough, $\{\mathbf{u}_P\} + \mathcal{R}$ is the global attractor of (H.3.2)-(H.3.3)-(H.3.5)-(H.3.7), but no element in $\{\mathbf{u}_P\} + \mathcal{R}$ is an attracting set, meaning that the rigid-body rotation of the final steady state can differ from that of its initial data.

Large Reynolds number flows

In the third series of simulations we solve equations (H.3.2)-(H.3.3)-(H.3.5)-(H.3.7) with the Poincaré stress boundary condition at a larger Reynolds number with the precession rate $\varepsilon = 0.25$ that is used in [156]. We use $\nu = 0.00375$ and the initial data is the Poincaré solution. Figure H.3(a) shows the time evolution of $\delta E_K = \frac{1}{2}\|\mathbf{u} - \mathbf{u}_P\|^2_{\mathbf{L}^2(\Omega)}$ from $t = 0$ to $t = 2800$, obtained with the SFEMaNS code. The mesh size in the meridian section is of order 1/80 and 16 Fourier modes are used in the azimuthal direction. Note that contrary to what is shown in figures 5 and 6 of reference [156], the system does not converge to an oscillating state, and the order of magnitude of δE_K in our computation is at least 6 times larger than that reported in figure 6 of [156]. This contradictory result is reproduced in figure H.3(b) by another colleague using a totally different and independent code based on a Finite Volume algorithm (courtesy of S. Vantieghem, ETH, Zurich, Switzerland). The quantity δE_K from the Finite Volume code is at least 3 times larger than that reported in figure 6 of [156]. These results illustrate the fact that the attractor of (H.3.2)-(H.3.3)-(H.3.5)-(H.3.7) with the

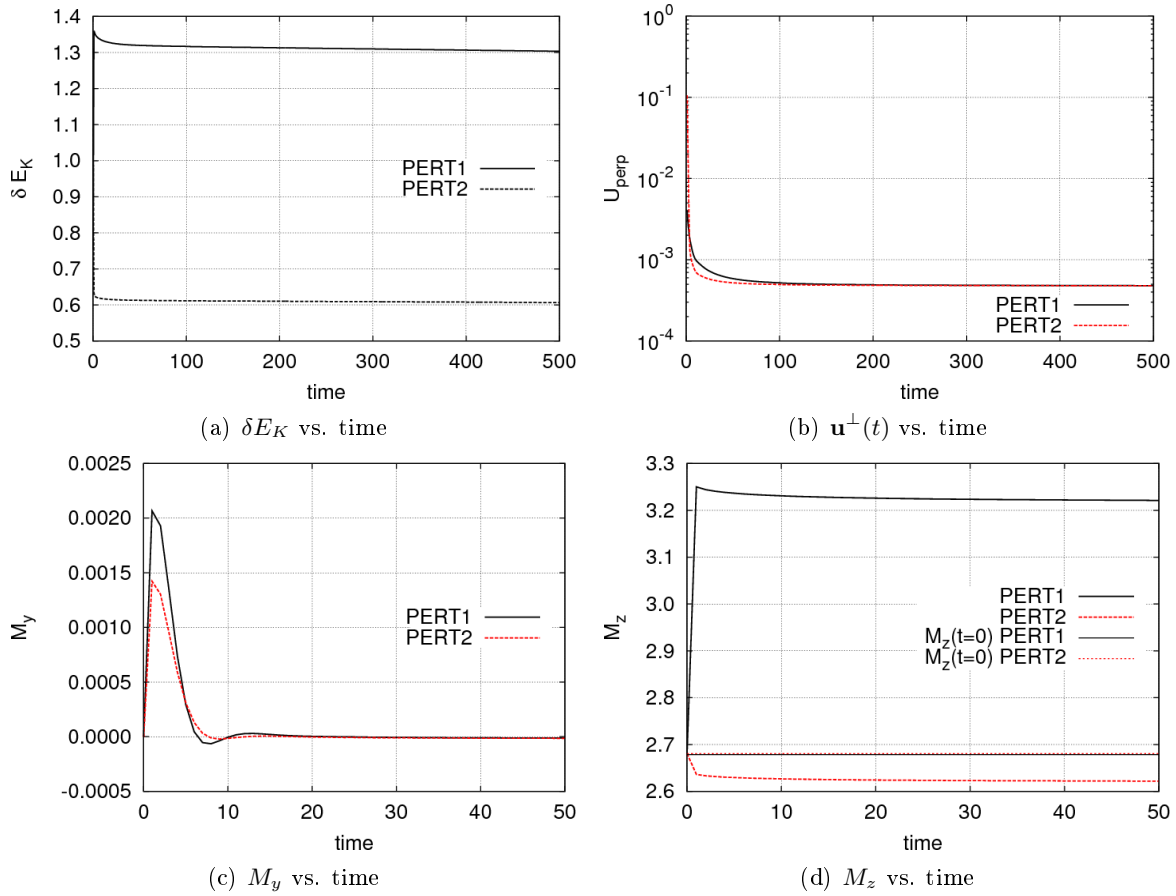

(a) δE_K vs. time

(b) $\mathbf{u}^{\perp}(t)$ vs. time

(c) M_y vs. time

(d) M_z vs. time

Figure H.2: (Color online) Precessing spheroid with $\beta = 0.5625$, $\varepsilon = 0.025$ and $\nu = 1$ with the Poincaré stress boundary condition (solutions of (H.3.2)-(H.3.3)-(H.3.5)-(H.3.7)). Time evolution of (a) the kinetic energy, $\delta E_K = \frac{1}{2}\|\mathbf{u}-\mathbf{u}_P\|^2_{\mathbf{L}^2(\Omega)}$, with two different perturbations (PERT1 and PERT2, see text) as initial data, (b) $\|\mathbf{u}^{\perp}(t)\|_{\mathbf{L}^2(\Omega)}$, (c) M_y, (d) M_z.

Poincaré stress boundary condition has pathological properties. The dynamo results of [156] based on the Poincaré stress boundary condition may therefore be questioned.

H.6 Discussion

The so-called stress-free boundary condition $(\mathbf{n}\cdot\boldsymbol{\epsilon}(\mathbf{u}))\times\mathbf{n}_{|\Gamma} = 0$ is often used in the geophysics literature to avoid issues induced by viscous layers. For example, an anelastic dynamo benchmark [78] was conducted very recently in a rotating spherical shell. The authors emphasize in their concluding section the difficulties they encountered to obtain the same hydrodynamical solutions using four different codes in a model with stress-free boundary conditions applied to the ICB and the CMB. Since the container in this benchmark has the spherical symmetry (spherical shell), the balance equation (H.3.13) gives $\partial_t \mathbf{M} = 0$ in the inertial reference frame, and each group had to apply some remedy in order to numerically conserve the three components of the angular momentum. But, more importantly, they also had to use the same initial

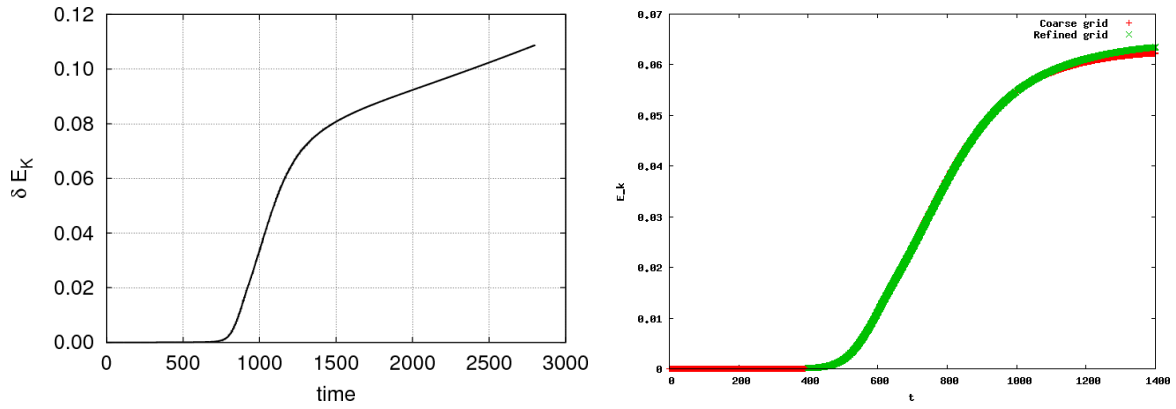

(a) δE_K vs. time with SFEMaNS (b) δE_K vs. time with Finite Volume Code

Figure H.3: (Color online) Precessing spheroid with $\beta = 0.5625$, $\varepsilon = 0.25$, $\nu = 0.00375$, and the Poincaré stress boundary condition (solutions of (H.3.2)-(H.3.3)-(H.3.5)-(H.3.7)). Time evolution of the kinetic energy, $\delta E_K = \frac{1}{2}\|\mathbf{u} - \mathbf{u}_P\|^2_{\mathbf{L}^2(\Omega)}$, with the Poincaré solution as initial data: (a) solution with the SFEMaNS code and (b) solution with a Finite Volume code (courtesy of S. Vantieghem, ETH, Zurich, Switzerland).

condition. This difficulty did not arise in the older dynamo benchmark [31] using the same geometry because the no-slip boundary condition was prescribed at the ICB and CMB.

We have proved in this work that the stress-free boundary condition with no precession leads to spurious stability behaviors when the fluid domain is axisymmetric. This problem is still present when precession is accounted for and the Poincaré stress boundary condition is imposed. One recovers stability at large times with precession when the stress-free boundary condition is enforced.

We hope that the present work will help draw the attention of the geodynamo community on this problem. The above pathological stability behaviors can be avoided by enforcing one additional condition. For instance, for problem (H.3.2)–(H.3.5) and (H.3.7), one could think of enforcing the vertical component of the angular momentum of the difference $\mathbf{u} - \mathbf{u}_P$, say

$$\int_\Gamma (\mathbf{u} - \mathbf{u}_P)\cdot(\mathbf{e}_z \times \mathbf{x})\, d\mathbf{s} = 0, \tag{H.6.1}$$

or enforcing $\mathbf{u} - \mathbf{u}_P$ and $\mathbf{u}_P$ to be orthogonal in average over the boundary, say

$$\int_\Gamma (\mathbf{u} - \mathbf{u}_P)\cdot\mathbf{u}_P\, d\mathbf{s} = 0. \tag{H.6.2}$$

For problem (H.2.1)–(H.2.5), one could think of enforcing the vertical component of the total angular momentum

$$\int_\Gamma \mathbf{u}\cdot(\mathbf{e}_z \times \mathbf{x})\, d\mathbf{s} = 0, \tag{H.6.3}$$

as was done for the three components in the anelastic dynamo benchmark [78].

We have suggested in §H.2.4 to use a boundary condition that does not have the stability problems mentioned above. For the problem (H.2.1)–(H.2.5) this condition is

$$(\mathbf{n}\cdot\nabla\mathbf{u})\times\mathbf{n}_{|\Gamma} = 0, \tag{H.6.4}$$

and for the problem (H.3.2)–(H.3.5) this condition is

$$(\mathbf{n}\cdot\nabla\mathbf{u})\times\mathbf{n}_{|\Gamma} = (\mathbf{n}\cdot\nabla\mathbf{u}_P)\times\mathbf{n}_{|\Gamma}. \tag{H.6.5}$$

Let us finally emphasize that it is false to consider that the momentum balance equation (H.3.13) is an additional equation that makes (H.3.2)-(H.3.3)-(H.3.5)-(H.3.7) a well-behaved dynamical system. The equation (H.3.13) is a redundant consequence of (H.3.2)-(H.3.3)-(H.3.5)-(H.3.7). For instance, (H.6.1) (or (H.6.2) or (H.6.3)) is an additional equation whereas (H.3.13) is not.

In conclusion, using the stress boundary condition to evaluate nonlinear behaviors of Navier-Stokes systems may sometimes be dubious when the domain is axisymmetric.

Acknowledgments

The authors are happy to acknowledge helpful email discussions with P.H. Roberts and P. Boronski. They also want to thank David Cébron, Wietze Herreman, and Stijn Vantieghem for stimulating discussions.

Table des figures

Liste des tableaux

Bibliographie

[1] J. Abshagen, K.A. Cliffe, J. Langenberg, T. Mullin, G. Pfister, and S.J. Tavener. Taylor–Couette flow with independently rotating end plates. *Theoretical and Computational Fluid Dynamics*, 18 :129–136, 2004. 10.1007/s00162-004-0135-3.

[2] Robert A. Adams and John J.F. Fournier. *Sobolev spaces. 2nd ed.* Pure and Applied Mathematics 140. New York, NY : Academic Press. xiii, 305 p., 2003.

[3] A. Alonso. A mathematical justification of the low-frequency heterogeneous time-harmonic Maxwell equations. *Math. Models Methods Appl. Sci.*, 9(3) :475–489, 1999.

[4] P. R. Amestoy, I. S. Duff, J. Koster, and J.-Y. L'Excellent. A fully asynchronous multifrontal solver using distributed dynamic scheduling. *SIAM Journal on Matrix Analysis and Applications*, 23(1) :15–41, 2001.

[5] P. R. Amestoy, A. Guermouche, J.-Y. L'Excellent, and S. Pralet. Hybrid scheduling for the parallel solution of linear systems. *Parallel Computing*, 32(2) :136–156, 2006.

[6] P.R. Amestoy *et al.* MUMPS : a MUltifrontal Massively Parallel sparse direct Solver. `http://graal.ens-lyon.fr/MUMPS`.

[7] D.N. Arnold. An interior penalty finite element method with discontinuous elements. *SIAM J. Numer. Anal.*, 19 :742–760, 1982.

[8] R. Avalos-Zuñiga and F. Plunian. Influence of inner and outer walls electromagnetic properties on the onset of a stationary dynamo action. *Eur. Phys. J. B*, 47 :127–135, 2005.

[9] R. Avalos-Zuñiga, F. Plunian, and A. Gailitis. Influence of electromagnetic boundary conditions onto the onset of dynamo action in laboratory experiments. *Phys. Rev. E.*, 68 :066307, 2003.

[10] I. Babuška and J. Osborn. Eigenvalue problems. In *Finite Element Methods (Part 1)*, volume 2 of *Handbook of Numerical Analysis*, pages 641 – 787. Elsevier, 1991.

[11] G.A. Baker. Finite element methods for elliptic equations using nonconforming elements. *Math. Comp.*, 31(137) :45–59, 1977.

[12] S. Balay, J. Brown, K. Buschelman, V. Eijkhout, W.D. Gropp, D. Kaushik, M.G. Knepley, L. Curfman McInnes, B.F. Smith, and H. Zhang. PETSc users manual. Technical Report ANL-95/11 - Revision 3.3, Argonne National Laboratory, 2012.

[13] S. Balay, J. Brown, K. Buschelman, W.D. Gropp, D. Kaushik, M.G. Knepley, L. Curfman McInnes, B.F. Smith, and H. Zhang. PETSc Web page, 2012. `http://www.mcs.anl.gov/petsc`.

[14] S. Balay, W.D. Gropp, L. Curfman McInnes, and B.F. Smith. Efficient management of parallelism in object oriented numerical software libraries. In E. Arge, A. M. Bruaset,

and H. P. Langtangen, editors, *Modern Software Tools in Scientific Computing*, pages 163–202. Birkhäuser Press, 1997.

[15] R. A. Bayliss, C. B. Forest, M. D. Nornberg, E. J. Spence, and P. W. Terry. Numerical simulations of current generation and dynamo excitation in a mechanically forced turbulent flow. *Phys. Rev. E*, 75 :id. 026303, 2007.

[16] C. Bernardi. Optimal finite element interpolation on curved domains. *SIAM J. Numer. Anal.*, 26 :1212–1240, 1989.

[17] A. Bonito and J.-L. Guermond. Approximation of the eigenvalue problem for the time harmonic Maxwell system by continuous Lagrange finite elements. *Math. Comp.*, 80(276) :1887–1910, 2011.

[18] A. Bonito, J.-L. Guermond, and F. Luddens. Note on the regularity of the Maxwell equations in heterogeneous media. submitted, 2012.

[19] A. Bossavit. *Computational Electromagnetism, Variational Formulations, Complementary, Edge Elements*, volume 2 of *Electromagnetism*. Academic Press, New York, NY, 1998.

[20] M. Bourgoin, F. Pétrélis, C. Gasquet, A. Guigon, J.-B. Luciani, M. Moulin, F. Namer, J. Burguete, A. Chiffaudel, F. Daviaud, S. Fauve, P. Odier, and J.-F. Pinton. Magnetohydrodynamics measurements in the Von Kármán Sodium experiment. *Phys. Fluids*, 14 :3046–3058, 2002.

[21] J.H. Bramble, T.V. Kolev, and J.E. Pasciak. The approximation of the Maxwell eigenvalue problem using a least-squares method. *Math. Comp.*, 74(252) :1575–1598, 2005. electronic.

[22] J.H. Bramble and J.E. Pasciak. A new approximation technique for div-curl systems. *Math. Comp.*, 73(248) :1739–1762, 2004. electronic.

[23] H. Brezis. *Analyse fonctionnelle. Théorie et applications. [Functional Analysis. Theory and applications]*. Applied Mathematics Series for the Master's Degree. Masson, Paris, France, 1983.

[24] A. Buffa, P. Ciarlet Jr, and E. Jamelot. Solving electromagnetic eigenvalue problems in polyhedral domains with nodal finite elements. *Numer. Math.*, 113 :497–518, 2009.

[25] A. Buffa and I. Perugia. Discontinuous Galerkin approximation of the Maxwell eigenproblem. *SIAM J. Numer. Anal.*, 44(5) :2198–2226 (electronic), 2006.

[26] E. Bullard. The magnetic field within the Earth. *Proc. Roy. Soc. Lond. A*, 197(1051) :433–453, 1949.

[27] E. Bullard. The stability of a homopolar dynamo. *Mathematical Proceedings of the Cambridge Philosophical Society*, 51 :744–760, 1955.

[28] F. H. Busse and J. Wicht. A simple dynamo caused by conductivity variations. *Geophysical & Astrophysical Fluid Dynamics*, 64(1-4) :135–144, 1992.

[29] P. Cardin, E. Dormy, and D. Jault. MHD flow in a slightly differentially rotating spherical shell, with conducting inner core, in a dipolar magnetic field. *Earth and Planetary Science Letters*, 160 :15–30, 1998.

[30] J.E.T. Channell, D.A. Hodell, J. McManus, and B. Lehman. Orbital modulation of the Earth's magnetic field intensity. *Nature*, 394 :464–468, 1998.

[31] U.R. Christensen, J. Aubert, P. Cardin, E. Dormy, S. Gibbons, G.A. Glatzmaier, E. Grote, Y. Honkura, C. Jones, M. Kono, M. Matsushima, A. Sakuraba, F. Takahashi, A. Tilgner, J. Wicht, and K. Zhang. A numerical dynamo benchmark. *Physics of the Earth and Planetary Interiors*, 128(1-4) :25 – 34, 2001. Dynamics and Magnetic Fields of the Earth's and Planetary Interiors.

[32] P. Ciarlet Jr, F. Lefèvre, S. Lohrengel, and S. Nicaise. Weighted regularization for composite materials in electromagnetism. *Modélisation Mathématique et Analyse Numérique*, 44 :75–108, 2010.

[33] P. Clément. Approximation by finite element functions using local regularization. *RAIRO, Anal. Num.*, 9 :77–84, 1975.

[34] S. A. Colgate, H. Beckley, J. Si, J. Martinic, D. Westpfahl, J. Slutz, C. Westrom, B. Klein, P. Schendel, C. Scharle, T. McKinney, R. Ginanni, I. Bentley, T. Mickey, R. Ferrel, H. Li, V. Pariev, and J. Finn. High magnetic shear gain in a liquid sodium stable Couette flow experiment : A prelude to an α-ω dynamo. *Phys. Rev. Lett.*, 106 :175003, Apr 2011.

[35] M. Costabel. A remark on the regularity of solutions of Maxwell's equations on Lipschitz domains. *Math. Methods Appl. Sci.*, 12(4) :365–368, 1990.

[36] M. Costabel. A coercive bilinear form for Maxwell's equations. *J. Math. Anal. Appl.*, 157(2) :527–541, 1991.

[37] M. Costabel and M. Dauge. Weighted Regularization of Maxwell Equations in Polyhedral Domains. *Numer. Math.*, 93(2) :239–278, 2002.

[38] M. Costabel, M. Dauge, and S. Nicaise. Singularities of Maxwell interface problems. *Math. Mod. Num. Anal*, 33(3) :627–649, 1999.

[39] T.G. Cowling. The magnetic field of sunspots. *Mon. Not. Roy. Astr. Soc.*, 94 :39–48, 1934.

[40] M. Dauge. Benchmark for Maxwell, 2009. `http://perso.univ-rennes1.fr/monique.dauge/benchmax.html`.

[41] R. Dautray and J.-L. Lions. *Mathematical Analysis and Numerical Methods for Science and Technology. Vol. 2. Functional and variational methods.* Springer-Verlag, Berlin, Germany, 1988.

[42] L. Desvillettes and C. Villani. On a variant of Korn's inequality arising in statistical mechanics. *ESAIM Control Optim. Calc. Var.*, 8 :603–619 (electronic), 2002. A tribute to J. L. Lions.

[43] W. Dobler, P. Frick, and R. Stepanov. Screw dynamo in a time-dependent pipe flow. *Phys. Rev. E.*, 67 :056309, 2003.

[44] M.L. Dudley and R.W. James. Time-dependent kinematic dynamos with stationary flows. *Proc. Roy. Soc. London A*, 425 :407–429, 1989.

[45] E. Durand. *Magnétostatique.* Masson, Paris, 1968.

[46] G. Duvaut and J.-L. Lions. *Les inéquations en mécanique et en physique.* Dunod, Paris, 1972.

[47] A. Ern and J.-L. Guermond. *Elements finis : Théorie, applications, mise en œuvre*, volume 36 of *SMAI Series on Mathematics and Applications.* Springer-Verlag, Paris, France, 2002.

[48] A. Ern and J.-L. Guermond. *Theory and practice of finite elements*, volume 159 of *Applied Mathematical Sciences*. Springer-Verlag, New York, 2004.

[49] M. Fortin. An analysis of the convergence of mixed finite element methods. *RAIRO, Anal. Num.*, 11 :341–354, 1977.

[50] P. Frick, S. Khripchenko, S. Denisov, D. Sokoloff, and J.-F. Pinton. Effective magnetic permeability of a turbulent fluid with macroferroparticles. *Eur. Phys. J. B*, 25 :399–402, 2002.

[51] A. Gailitis, O. Lielausis, S. Dement'ev, E. Platacis, and A. Cifersons. Detection of a flow induced magnetic field eigenmode in the Riga dynamo facility. *Phys. Rev. Lett.*, 84 :4365, 2000.

[52] A. Gailitis, O. Lielausis, E. Platacis, G. Gerbeth, and F. Stefani. Riga dynamo experiment and its theoretical background. *Phys. Fluids*, 11 :2838–2843, 2004.

[53] B. Gallet, F. Pétrélis, and S. Fauve. Dynamo action due to spatially dependent magnetic permeability. *EPL (Europhysics Letters)*, 97(6) :69001, 2012.

[54] R. F. Gans. On hydromagnetic precession in a cylinder. *J. Fluid Mech.*, 45 :111–130, 1970.

[55] A. Giesecke, C. Nore, F. Plunian, R. Laguerre, A. Ribeiro, F. Stefani, G. Gerbeth, J. Léorat, and J.-L. Guermond. Generation of axisymmetric modes in cylindrical kinematic mean-field dynamos of VKS type. *Geophys. Astrophys. Fluid Dyn.*, 104(2) :249–271, 2010.

[56] A. Giesecke, C. Nore, F. Stefani, G. Gerbeth, J. Léorat, F. Luddens, and J.-L. Guermond. Electromagnetic induction in non-uniform domains. *Geophys. Astrophys. Fluid Dyn.*, 104(5) :505–529, 2010.

[57] A. Giesecke, F. Stefani, and G. Gerbeth. Kinematic simulations of dynamo action with a hybrid boundary-element/finite-volume method. *Magnetohydrodynamics*, 44(3) :237–252, 2008.

[58] A. Giesecke, F. Stefani, and G. Gerbeth. Role of Soft-Iron Impellers on the Mode Selection in the von Kármán–Sodium Dynamo Experiment. *Phys. Rev. Lett.*, 104 :044503, 2010.

[59] V. Girault and P.-A. Raviart. *Finite Element Methods for Navier-Stokes Equations. Theory and Algorithms*. Springer Series in Computational Mathematics. Springer-Verlag, Berlin, Germany, 1986.

[60] C. Gissinger, S. Fauve, and E. Dormy. Bypassing Cowling's theorem in axisymmetric fluid dynamos. *Phys. Rev. Lett.*, 101 :144502, 2008.

[61] C. Gissinger, A. Iskakov, S. Fauve, and E. Dormy. Effect of magnetic boundary conditions on the dynamo threshold of von Kármán swirling flows. *EPL*, 82 :29001, 2008.

[62] G.A. Glatzmaier and P.H. Roberts. A three-dimensional self-consistent computer simulation of a geomagnetic field reversal. *Nature*, 377 :203–209, 1995.

[63] P. Grisvard. *Elliptic problems in nonsmooth domains*, volume 24 of *Monographs and Studies in Mathematics*. Pitman (Advanced Publishing Program), Boston, MA, 1985.

[64] J.-L. Guermond. The LBB condition in fractional sobolev spaces and applications. *IMA, Numer. Anal.*, 2006, Submitted.

[65] J.-L. Guermond, R. Laguerre, J. Léorat, and C. Nore. An interior penalty Galerkin method for the MHD equations in heterogeneous domains. *J. Comput. Phys.*, 221(1) :349–369, 2007.

[66] J.-L. Guermond, R. Laguerre, J. Léorat, and C. Nore. Nonlinear magnetohydrodynamics in axisymmetric heterogeneous domains using a fourier/finite element technique and an interior penalty method. *J. Comput. Phys.*, 228 :2739–2757, 2009.

[67] J.-L. Guermond, J. Léorat, F. Luddens, C. Nore, and A. Ribeiro. Effects of discontinuous magnetic permeability on magnetodynamic problems. *J. Comput. Phys.*, 230 :6299–6319, 2011.

[68] E. Haber and U.M. Ascher. Fast Finite Volume Simulation of 3d electromagnetic problems with highly discontinuous coefficients. *SIAM J. Sci. Comput.*, 22 :1943–1961, 2001.

[69] A. Herzenberg and F.J. Lowes. Electromagnetic Induction in Rotating Conductors. *Phil. Trans. Roy. Soc. of London. Series A, Mathematical and Physical Sciences*, 249(970) :507–584, 1957.

[70] R.E Hewitt, T Mullin, S.J Tavener, M.A.I Khan, and P.D Treacher. Nonlinear vortex development in rotating flows. *Philosophical Transactions of the Royal Society A : Mathematical, Physical and Engineering Sciences*, 366(1868) :1317–1329, 2008.

[71] R. Hide and T.N. Palmer. Generalization of Cowling's theorem. *Geophysical & Astrophysical Fluid Dynamics*, 19 :301–309, 1982.

[72] A.B. Iskakov, S. Descombes, and E. Dormy. An integro-differential formulation for magnetic induction in bounded domains : boundary element-finite volume method. *J. Comput. Phys.*, 197 :540–554, 2004.

[73] A.B. Iskakov and E. Dormy. On magnetic boundary conditions for non-spectral dynamo simulations. *Geophysical & Astrophysical Fluid Dynamics*, 99 :481–492, 2005.

[74] J.D. Jackson. *Classical electrodynamics*. Wiley, 1975.

[75] D.S. Jerison and C.E. Kenig. The Neumann problem in Lipschitz domains. *Bull. Amer. Math. Soc. (N.S.)*, 4(2) :203–207, 1981.

[76] D.S. Jerison and C.E. Kenig. The inhomogeneous Dirichlet problem in Lipschitz domains. *J. Func. Anal.*, 130(1) :161–219, 1995.

[77] F. Jochmann. An H^s-regularity result for the gradient of solutions to elliptic equations with mixed boundary conditions. *J. Math. Anal. Appl.*, 238 :429–450, 1999.

[78] C.A. Jones, P. Boronski, A.S. Brun, G.A. Glatzmaier, T. Gastine, M.S. Miesch, and J. Wicht. Anelastic convection-driven dynamo benchmarks. *Icarus*, 216(1) :120 – 135, 2011.

[79] A. Kageyama, T. Miyagoshi, and T. Sato. Formation of current coils in geodynamo simulations. *Nature (London)*, 454 :1106–1109, 2008.

[80] G. Karypis and V. Kumar. A Fast and Highly Quality Multilevel Scheme for Partitioning Irregular Graphs. *SIAM Journal on Scientific Computing*, 20(1) :359–392, 1999.

[81] S. Kenjereš and K. Hanjalić. Numerical simulation of a turbulent magnetic dynamo. *Phys. Rev. Lett.*, 98(10) :104501, 2007.

[82] F. Krause and K.-H. Radler. *Mean-Field Magnetohydrodynamics and Dynamo Theory*. Pergamon Press Oxford, 1980.

[83] W. Kuang and J. Bloxham. An Earth-like numerical dynamo model. *Nature*, 389 :371–374, 1997.

[84] W. Kuang and J. Bloxham. Numerical modeling of magnetohydrodynamic convection in a rapidly rotating spherical shell : Weak and strong field dynamo action. *J. Comput. Phys.*, 153(1) :51 – 81, 1999.

[85] Karypis Lab. METIS Homepage. `http://glaros.dtc.umn.edu/gkhome/metis/metis/overview`.

[86] R. Lagrange, C. Eloy, F. Nadal, and P. Meunier. Instability of a fluid inside a precessing cylinder. *Phys. Fluids*, 20(8) :081701, 2008.

[87] R. Laguerre. *Approximation des équations de la MHD par une méthode hybride spectrale-éléments finis nodaux : application à l'effet dynamo*. PhD thesis, University of Paris VII, 2006.

[88] R. Laguerre, C. Nore, A. Ribeiro, J. Léorat, J.-L. Guermond, and F. Plunian. Erratum : Impact of impellers on the axisymmetric magnetic mode in the VKS2 dynamo experiment. *Phys. Rev. Lett.*, 101(10) :219902, 2008.

[89] R. Laguerre, C. Nore, A. Ribeiro, J. Léorat, J.-L. Guermond, and F. Plunian. Impact of impellers on the axisymmetric magnetic mode in the VKS2 dynamo experiment. *Phys. Rev. Lett.*, 101(10) :104501, 2008.

[90] T. Lehner, W. Mouhali, J. Léorat, and A. Mahalov. Mode coupling analysis and differential rotation in a flow driven by a precessing cylindrical container. *Geophys. Astrophys. Fluid Dyn.*, 104(4) :369–401, 2010.

[91] R.B. Lehoucq, D.C. Sorensen, and C. Yang. *ARPACK users' guide*, volume 6 of *Software, Environments and Tools*. Society for Industrial and Applied Mathematics (SIAM), Philadelphia, PA, 1998. Solution of large-scale eigenvalue problems with implictly restarted Arnoldi methods.

[92] J. Léorat, P. Lallemand, J.-L. Guermond, and F. Plunian. Dynamo action, between numerical experiments and liquid sodium devices. In P. Chossat, D. Armbruster, and I. Oprea, editors, *Dynamo and dynamics, a Mathematical challenge*, volume 26 of *NATO Science Series, II Mathematics, Physics and Chemistry*, pages 25–33. Kluwer, Dordrecht, 2001.

[93] J. Léorat and C. Nore. Interplay between experimental and numerical approaches in the fluid dynamo problem. *Comptes Rendus Physique*, 9 :741–748, September 2008.

[94] J.-L. Lions. *Quelques méthodes de résolution des problèmes aux limites non linéaires*, volume 1. Dunod, Paris, France, 1969.

[95] J.-L. Lions and E. Magenes. *Problèmes aux limites non homogènes et applications*, volume 1. Dunod, Paris, France, 1968.

[96] J.-L. Lions and J. Peetre. Sur une classe d'espaces d'interpolation. *Inst. Hautes Études Sci. Publ. Math.*, 19 :5–68, 1964.

[97] P. W. Livermore and A. Jackson. On magnetic energy instability in spherical stationary flows. *Proceedings of the Royal Society of London. Series A : Mathematical, Physical and Engineering Sciences*, 460(2045) :1453–1476, 2004.

[98] F.J. Lowes and I. Wilkinson. Geomagnetic dynamo : a laboratory model. *Nature*, 198 :1158, 1963.

[99] F.J. Lowes and I. Wilkinson. Geomagnetic dynamo : an improved laboratory model. *Nature*, 219 :717, 1968.

[100] W. V. R. Malkus. Precession of the Earth as the cause of geomagnetism : Experiments lend support to the proposal that precessional torques drive the Earth's dynamo. *Science*, 160(3825) :259–264, 1968.

[101] L. Marié, J. Burguete, F. Daviaud, and J. Léorat. Numerical study of homogeneous dynamo based on experimental von Kármán type flows. *European Physical Journal B*, 33 :469–485, June 2003.

[102] L. Marié, C. Normand, and F. Daviaud. Galerkin analysis of kinematic dynamos in the von Kármán geometry. *Phys. Fluids*, 18 :017102, 2006.

[103] L. Marié, F. Pétrélis, M. Bourgoin, J. Burguete, A. Chiffaudel, F. Daviaud, S. Fauve, P. Odier, and J.-F. Pinton. Open questions about homogeneous fluid dynamos : the VKS experiment. *Magnetohydrodynamics*, 38 :156–169, 2002.

[104] F. Marques and J. M. Lopez. Onset of three-dimensional unsteady states in small-aspect-ratio Taylor–Couette flow. *Journal of Fluid Mechanics*, 561 :255–277, 2006.

[105] L. Martin Witkowski, P. Marty, and J.S. Walker. Multidomain analytical-numerical solution for a rotating magnetic field with finite-length conducting cylinder. *IEEE Trans. on Magnetics*, 36 :452–460, 2000.

[106] R.M. Mason and R.R. Kerswell. Chaotic dynamics in a strained rotating flow : a precessing plane fluid layer. *J. Fluid Mech.*, 471 :71–106, 2002.

[107] N.G. Meyers. An L^pe-estimate for the gradient of solutions of second order elliptic divergence equations. *Ann. Scuola Norm. Sup. Pisa (3)*, 17 :189–206, 1963.

[108] H.K. Moffatt. *Magnetic Field Generation in Electrically Conducting Fluids*. Cambridge Monographs on Mechanics and Applied Mathematics. Cambridge University Press, Cambridge, 1978.

[109] R. Monchaux, M. Berhanu, S. Aumaitre, A. Chiffaudel, F. Daviaud, B. Dubrulle, F. Ravelet, S. Fauve, N. Mordant, F. Pétrélis, M. Bourgoin, Ph. Odier, J.-F. Pinton, N. Plihon, and R. Volk. The von Kármán sodium experiment : Turbulent dynamical dynamos. *Phys. Fluids*, 21 :035108, 2009.

[110] R. Monchaux, M. Berhanu, M. Bourgoin, Ph. Odier, M. Moulin, J.-F. Pinton, R. Volk, S. Fauve, N. Mordant, F. Pétrélis, A. Chiffaudel, F. Daviaud, B. Dubrulle, C. Gasquet, L. Marié, and F. Ravelet. Generation of magnetic field by a turbulent flow of liquid sodium. *Phys. Rev. Lett.*, 98 :044502, 2007.

[111] P. Monk. *Finite element methods for Maxwell's equations*. Numerical Mathematics and Scientific Computation. Oxford University Press, New York, 2003.

[112] U. Müller, R. Stieglitz, and S. Horanyi. A two-scale hydromagnetic dynamo experiment. *Journal of Fluid Mechanics*, 498 :31–71, 2004.

[113] C. Nore, M. Brachet, H. Politano, and A. Pouquet. Dynamo action in the Taylor–Green vortex near threshold. *Phys. Plasmas*, 4 :1–4, 1997.

[114] C. Nore, J. Léorat, J.-L. Guermond, and F. Luddens. Nonlinear dynamo action in a precessing cylindrical container. *Phys. Rev. E*, 84 :016317, Jul 2011.

[115] P. Olson. Probing Earth's dynamo. *Nature*, 389 :337–338, 1997.

[116] J.E. Osborn. Spectral Approximation for Compact Operators. *Mathematics of Computation*, 29(131) :712–725, 1975.

[117] E.N. Parker. Hydromagnetic dynamo models. *Astrophys. J.*, 122 :293, 1955.

[118] F. Pétrélis, M. Bourgoin, L. Marié, J. Burguete, A. Chiffaudel, F. Daviaud, S. Fauve, P. Odier, and J.-F. Pinton. Nonlinear magnetic induction by helical motion in a liquid sodium turbulent flow. *Phys. Rev. Lett.*, 90 :174501, 2003.

[119] F. Pétrélis, N. Mordant, and S. Fauve. On the magnetic fields generated by experimental dynamos. *Geophysical & Astrophysical Fluid Dynamics*, 101 :289–323, 2007.

[120] O. Pironneau, F. Hecht, A. Le Hyaric, and J. Morice. freeFEM Homepage. `http://www.freefem.org`.

[121] Yu.B. Ponomarenko. Theory of the hydrodynamic generator. *J. Appl. Mech. Tech. Phys.*, 14 :775–778, 1973.

[122] Y. Ponty, P.D. Mininni, J.-F. Pinton, H. Politano, and A. Pouquet. Dynamo action at low magnetic Prandtl numbers : mean flow vs. fully turbulent motion. *New J. Phys.*, 9 :296, 2007.

[123] F. Ravelet, A. Chiffaudel, F. Daviaud, and J. Léorat. Towards an experimental von Kármán dynamo : numerical studies for an optimized design. *Phys. Fluids*, 17 :117104, 2005.

[124] A. Ribeiro. *Approche spectrale/éléments finis pour des problèmes de magnétohydrodynamique non-linéaires.* PhD thesis, University of Paris XI, 2010.

[125] G.O. Roberts. Dynamo action of fluid motions with two-dimensional periodicity. *Phil. Trans. Roy. Soc. of London. Series A*, 271 :411–454, 1972.

[126] P.H. Roberts. *An introduction to Magnetohydrodynamics.* Longmans, first edition, 1967.

[127] P.H. Roberts, G.A. Glatzmaier, and T.L. Clune. Numerical simulation of a spherical dynamo excited by a flow of von Kármán type. *Geophysical & Astrophysical Fluid Dynamics*, 104 :207–220, 2010.

[128] A. Sakuraba and P.H. Roberts. Generation of a strong magnetic field using uniform heat flux at the surface of the core. *Nature Geoscience*, 2 :802–805, 2009.

[129] G. Savaré. Regularity results for elliptic equations in Lipschitz domains. *J. Func. Anal.*, 152 :176–201, 1998.

[130] A. Schekochihin, A. Iskakov, S. Cowley, J. Mc Williams, M. Proctor, and T. Yousef. Fluctuation dynamo and turbulent induction at low magnetic prandtl numbers. *New J. Phys.*, 9 :300, 2007.

[131] R.L. Scott and S. Zhang. Finite element interpolation of nonsmooth functions satisfying boundary conditions. *Math. Comp.*, 54(190) :483–493, 1990.

[132] G. Sell. Global attractors for the three-dimensional Navier-Stokes equations. *Journal of Dynamics and Differential Equations*, 8 :1–33, 1996. 10.1007/BF02218613.

[133] F. Stefani. Personal communication, 2011.

[134] F. Stefani, S. Eckert, G. Gerbeth, A. Giesecke, Th. Gundrum, C. Steglich, T. Weier, and B. Wustmann. DresDyn - A new facility for MHD experiments with liquid sodium. *Magnetohydrodynamics*, 48 :103–113, 2012.

[135] F. Stefani, G. Gerbeth, and A. Gailitis. Velocity profile optimization for the Riga dynamo experiment. In A. Alemany, P. Marty, and J. P. Thibault, editors, *Transfer Phenomena in Magnetohydrodynamic and Electroconducting Flows*, page 31, 1999.

[136] F. Stefani, A. Giesecke, and G. Gerbeth. Numerical simulations of liquid metal experiments on cosmic magnetic fields. *Theor. Comp. Fluid Dyn.*, 23 :405–429, 2009.

[137] F. Stefani, M. Xu, G. Gerbeth, F. Ravelet, A. Chiffaudel, F. Daviaud, and J. Léorat. Ambivalent effects of added layers on steady kinematic dynamos in cylindrical geometry : application to the VKS experiment. *Eur. J. Fluid Mech, B*, 25 :894, 2006.

[138] K. Stewartson and P. H. Roberts. On the motion of liquid in a spheroidal cavity of a precessing rigid body. *J. Fluid Mech.*, 17 :1–20, 1963.

[139] R. Stieglitz and U. Müller. Experimental demonstration of a homogeneous two-scale dynamo. *Phys. Fluids*, 13 :561, 2001.

[140] J.M. Stone and Norman M.L. ZEUS-2D : A radiation magnetohydrodynamics code for astrophysical flows in two space dimensions. I - The hydrodynamic algorithms and tests. *Astrophys. J. Supp.*, 80 :753–790, 1992.

[141] J.M. Stone and Norman M.L. ZEUS-2D : A Radiation Magnetohydrodynamics Code for Astrophysical Flows in Two Space Dimensions. II. The Magnetohydrodynamic Algorithms and Tests. *Astrophys. J. Supp.*, 80 :791, 1992.

[142] K. Subramanian, A. Shukurov, and N. E. L. Haugen. Evolving turbulence and magnetic fields in galaxy clusters. *MNRAS*, 366 :1437, 2006.

[143] L. Tartar. *An introduction to Sobolev spaces and interpolation spaces*, volume 3 of *Lecture Notes of the Unione Matematica Italiana*. Springer, Berlin, 2007.

[144] S. J. Tavener, T. Mullin, and K. A. Cliffe. Novel bifurcation phenomena in a rotating annulus. *Journal of Fluid Mechanics*, 229 :483–497, 1991.

[145] R. Temam. *Navier-Stokes Equations : Theory and Numerical Analysis*. North-Holland, Amsterdam, 1984.

[146] A. Tilgner. On models of precession driven core flow. *Studia geoph. et geod.*, 42(232), 1998.

[147] A. Tilgner. Numerical simulation on the onset of dynamo action in an experimental two-scale dynamo. *Phys. Fluids*, 14(11) :40–91, 2002.

[148] A. Tilgner. Precession driven dynamos. *Phys. Fluids*, 17(3) :034104, 2005.

[149] A. Tilgner. Kinematic dynamos with precession driven flow in a sphere. *Geophys. Astrophys. Fluid Dyn.*, 101(1) :1, 2007.

[150] A. Tilgner and F.H. Busse. Simulation of the bifurcation diagram of the Karlsruhe dynamo. *Magnetohydrodynamics*, 38 :35–40, 2002.

[151] S.M. Tobias. Modulation of solar and stellar dynamos. *Astronomische Nachrichten*, 323(3-4) :417–423, 2002.

[152] A. de la Torre and J. Burguete. Slow Dynamics in a Turbulent von Kármán Swirling Flow. *Phys. Rev. Lett.*, 99 :05401, 2007.

[153] G. Verhille, N. Plihon, M. Bourgoin, P. Odier, and J. Pinton. Induction in a von Kármán flow driven by ferromagnetic impellers. *New J. Phys.*, 12 :033006, 2010.

[154] J. Wicht and F.H. Busse. Dynamo Action Induced by Lateral Variation of the Electrical Conductivity. in M.R.E Proctor, P.C. Matthews & A.M. Rucklidge, ed.,*Solar and Planetary Dynamos*, pages 329–337, 1993.

[155] A. P. Willis and C. F. Barenghi. A Taylor-Couette dynamo. *Astronomy and Astrophysics*, 393 :339–343, 2002.

[156] C.-C. Wu and P.H. Roberts. On a dynamo driven by topographic precession. *Geophysical & Astrophysical Fluid Dynamics*, 103(6) :467–501, 2009.

[157] U. Ziegler. A three-dimensional Cartesian adaptive mesh code for compressible magnetohydrodynamics. *Comp. Phys. Comm.*, 116 :65–77, 1999.